Transactions of the ASME

Technical Editor
ARTHUR J. WENNERSTROM
Senior Associate Editor
G. K. SEROVY
Associate Editors
Advanced Energy Systems
S. I. FREEDMAN
Environmental Control
H. E. HESKETH
Fuels and Combustion Technologies
R. E. BARRETT
Gas Turbine
S. KUO
Internal Combustion Engine
K. J. SPRINGER
Nuclear Engineering
S. M. CHO
Power
R. W. PORTER

BOARD ON COMMUNICATIONS
Chairman and Vice-President
K. N. REID, JR.

Members-at-Large
W. BEGELL
J. T. COKONIS
M. FRANKE
W. G. GOTTENBERG
M. KUTZ
F. LANDIS
J. R. LLOYD
T. C. MIN
R. E. NICKELL
R. E. REDER
F. W. SCHMIDT

President, N. D. FITZROY
Executive Director,
PAUL ALLMENDINGER
Treasurer, ROBERT A. BENNETT

PUBLISHING STAFF
Mng. Dir., Publ., J. J. FREY
Dep. Mng. Dir., Pub.,
JOS. SANSONE
Managing Editor,
CORNELIA MONAHAN
Sr. Production Editor,
VALERIE WINTERS
Editorial Prod. Asst.,
MARISOL ANDINO

Transactions of the ASME, Journal of Turbomachinery (ISSN 0889-504X) is published quarterly (Jan., Apr., July, Oct.) for $85 per year by The American Society of Mechanical Engineers, 345 East 47th Street, New York, NY 10017. Application to mail at second-class postage rates is pending at New York, NY and additional mailing offices. POSTMASTER: Send address change to The Journal of Turbomachinery, c/o The AMERICAN SOCIETY OF MECHANICAL ENGINEERS, 22 Law Drive, Box 2300, Fairfield, NJ 07007-2300."

CHANGES OF ADDRESS must be received at Society headquarters seven weeks before they are to be effective. Please send old label and new address.

PRICES: To members, $24.00, annually; to nonmembers, $85.00. Add $6.00 for postage to countries outside the United States and Canada.

INDEXED by Engineering Information

Journal of Turbomachinery

Published Quarterly by The American Society of Mechanical Engineers

VOLUME 109 • NUMBER 2 • APRIL 1987

TECHNICAL PAPERS

DISCUSSIONS

ANNOUNCEMENTS

C. Rodgers
Chief, Aerothermal and Conceptual Design.

R. Geiser
Senior Development Engineer.

Turbomach,
Division of Sundstrand Corporation,
San Diego, CA 92123

Performance of a High-Efficiency Radial/Axial Turbine

This paper presents the test performance of a lightly loaded, combination radial/axial turbine for a 420-hp, two-shaft gas turbine. This two-stage turbine configuration, which included an interstage duct and an exhaust duct discharging vertically to ambient pressure conditions, was shown to be capable of attaining an overall isentropic efficiency of 89.7 percent. The influence of exhaust diffuser struts on the turbine performance under stalled power turbine conditions was shown to significantly affect compressor and turbine matching.

Introduction

Virtually all gas turbines with multistage turbines use the axial turbine configuration. A few gas turbines have been produced and developed, however, with a single-stage, radial inflow turbine followed by a single-stage axial turbine. Most notable among those produced are the AiResearch GTCP 105, the AiResearch GTCP 601, and Solar's T351 Spartan gas turbine.

The results of extensive experimental testing of a high pressure ratio radial/axial turbine configuration for an advanced auxiliary power unit are described by Kidwell and Large [1]. At an overall pressure ratio of 9.0, cold turbine rig tests showed an isentropic expansion efficiency of 87 percent.

The radial/axial turbine arrangement is particularly suitable for small gas turbines with reverse flow combustors or scroll combustors, since the combustor exit 180-deg bend can be supplanted by the radial nozzle and radial inflow rotor. Furthermore, the radial rotor is less sensitive to tip clearance than the small blade height axial rotor. Counteracting these advantages are the losses of the interstage duct between the exducer and the inlet of the axial nozzle, and the potentially higher inertia of the radial rotor.

Providing the interstage duct losses are minimized, the optimum radial/axial turbine arrangement is usually more efficient than the optimum two-stage axial arrangement at the same pressure ratio in the 2.0 to 10.0 pps flow engine category.

This paper describes the development test of a radial/axial turbine for the 420-hp, two-shaft T351 gas turbine, where it was demonstrated that an overall total-to-ambient turbine efficiency of 89.7 percent was attained based upon actual gas turbine test calibrations.

Radial Turbine Design Optimization

The aerodynamic excellence of both radial inflow and axial turbines is dominated by two major performance parameters:

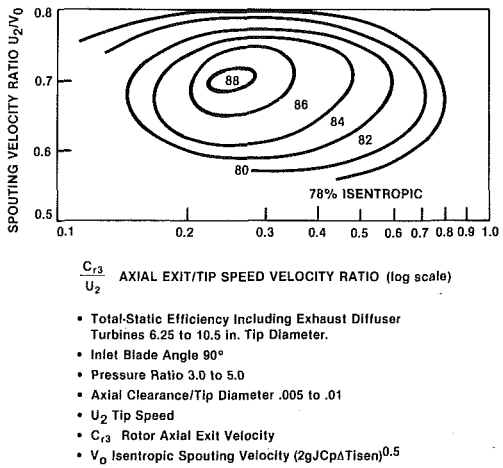

Fig. 1 Attainable efficiency levels of radial inflow turbines

- Velocity ratio $= U_2/Vo$
- Exit flow coefficient $= \phi = Cr_3/U_2$

The velocity ratio is a direct measure of the blade loading. The exit flow coefficient for a radial turbine is an indirect measure of the specific speed since for zero exit swirl and incompressible flow it can be shown that:

$$\text{Dimensionless specific speed } N_s \sim \phi^{1/2}\left(\frac{U_2}{Vo}\right)^{1.5}\frac{2.98}{\epsilon}$$

where

$$\epsilon = \text{Rotor diameter ratio} = D_2/D_{3\ \text{rms}}$$

State-of-the-art levels for the total-to-static efficiency of uncooled radial inflow turbines are shown in Fig. 1, indicating peak efficiencies are obtained with velocity ratios close to 0.7 with exit flow coefficients of 0.2 to 0.3.

Similar charts have been produced by Smith [2] for axial turbines showing comparable trends. For a particular turbine design, the level of efficiency is dependent upon specific criteria, such as:

- Solidity of nozzle and rotor
- Effects of diameter ratio ϵ
- Tip clearance losses

Contributed by the Gas Turbine Division of THE AMERICAN SOCIETY OF MECHANICAL ENGINEERS and presented at the 31st International Gas Turbine Conference and Exhibit, Düsseldorf, Federal Republic of Germany, June 8–12, 1986. Manuscript received at ASME Headquarters December 26, 1985. Paper No. 86-GT-18.

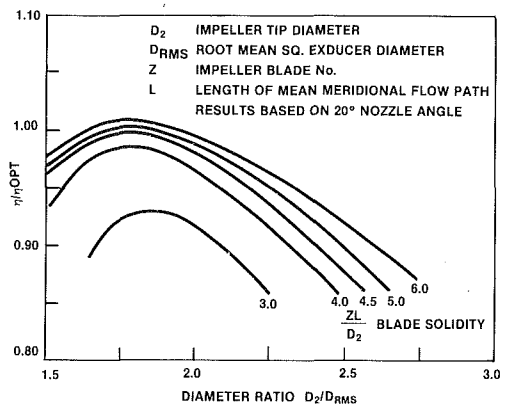

Fig. 2 Effect of rotor solidity on radial turbine efficiency

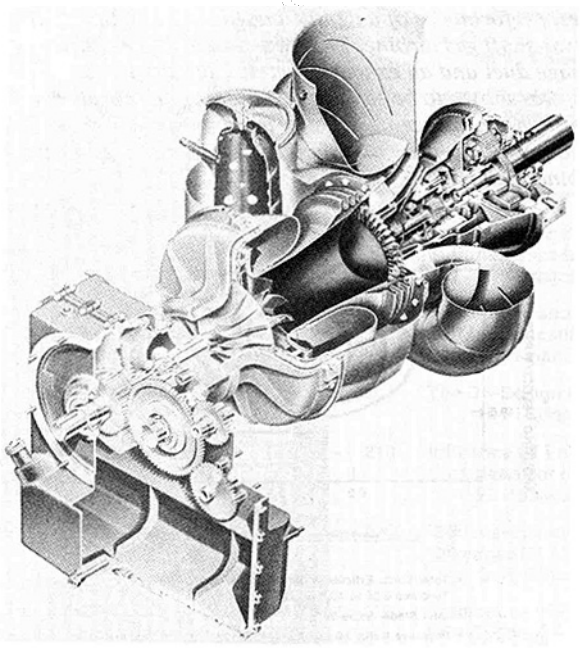

Fig. 3 T351 gas turbine

- Vane and blade trailing edge thickness
- Entry flow conditions
- Mach and Reynolds numbers

The effects of rotor solidity and diameter ratio upon radial turbine efficiency are correlated in Fig. 2, wherein small diameter ratios decrease efficiency as a consequence of nonuniform shroud loading.

A high-performance radial inflow turbine should be selected close to the maximum efficiency island of Fig. 1 and have an optimum diameter ratio ϵ and blading solidity. These basic guidelines were adopted in choosing the geometry of the T351 radial inflow turbine described herein.

Description of Test Gas Turbine

The T351 was designed as a two-shaft version of the T350 single-shaft gas turbine described in [3].

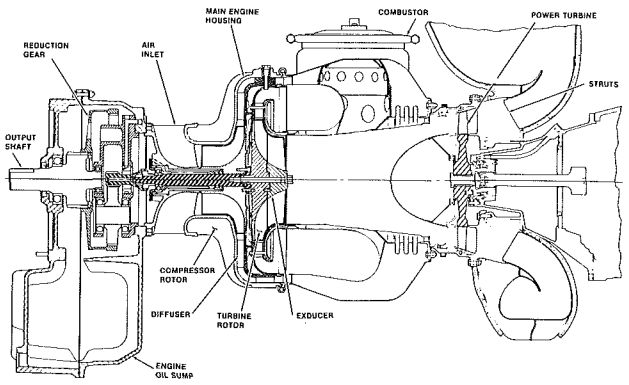

Fig. 4 T351 gas turbine cross section

Table 1 Test instrumentation

Instrumentation	Number	Type	Accuracy
Barometer	1	- - -	±.05 psi
Bellmouth Inlet Air Temperature	1	C/A Thermocouple	±3°
Bellmouth Static Pressure	3	.03 inch	±.05 psi
Compressor Inlet Temperature	3	C/A Thermocouple	±1°
Compressor Inlet Total Pressure	3	Kiel	±0.1 psi
Compressor Exit Total Pressure	3	Kiel	±0.1 psi
Compressor Exit Total Temperature	2	C/A Thermocouple	±3°
Gas Producer Turbine Inlet Total Pressure	2	Kiel	±0.1 psi
Gas Producer Turbine Exit Total Pressure	3	Kiel	±0.1 psi
Power Turbine Inlet Total Temperature	1	I/C Thermocouple	±10°F
Exhaust Total Temperature	6	I/C Thermocouple	±10°F
Rotational Speeds	2	Tachometers	±0.2%
Output Power	1	Water Dynamometer	±5 hp
Fuel Flow	1	Rotometer	±3 pph

The T351 gas turbine with its separate shaft power turbine is shown in Figs. 3 and 4. This gas turbine has a single-stage centrifugal compressor, driven by a single-stage gas producer radial inflow turbine, feeding into a single-stage axial power turbine, followed by an exhaust collector with a vertical discharge.

The gas turbine was designed to deliver an output power of 420 hp at sea level, 80°F conditions with a corresponding conservative turbine inlet temperature of 1450°F.

Compressor discharge air was collected in the outer combustor scroll and passed through a single can combustor to the inner turbine scroll. Combustor exit swirl entering the gas producer radial nozzles was on the order of 40 deg.

The axial power turbine was a modified second-stage turbine from Solar's Saturn gas turbine [4] fitted with interstage transition ducting to permit matching to the gas producer tailcone and existing Saturn turbine exhaust collector. The manner in which the interstage transition was accomplished is of particular interest in that for simplicity and cost reasons an inner cone was not used. Rapid acceleration into the power turbine nozzle was accomplished with a large centerbody.

The exhaust collector consists of an annular diffuser transitioning into a vertical collector. The centerbody and power turbine bearing housing was supported by eight airfoil, zero-camber struts located approximately one chord downstream of the power turbine blades. The effect of the close proximity of the struts on stalled power turbine performance is discussed later in this paper.

Nomenclature

C = velocity
D = diameter
g = gravitational constant
J = Joules equivalent
L = blade length
N_s = dimensionless specific speed
P = total pressure
p = static pressure
T = total temperature
U = tip speed
Vo = spouting velocity
W = flow
Z = blade number
η = isentropic efficiency
ϵ = diameter ratio
ϕ = exit flow coefficient

Subscripts

2 = radial turbine inlet
3 = radial turbine exit
4 = axial turbine inlet
5 = exhaust diffuser exit (ambient)
rms = root mean square
m = mean
t = turbine

Table 2 Radial turbine aerodynamic details

Parameter	Dimension
Inlet Total Temperature, °R	1910
Inlet Total Pressure, psia	58
Inlet Flow, pps	6.52
Rotational Speed, rpm	36,200
Nozzle Entry Diameter, in.	13.4
Nozzle Exit Diameter, in.	10.7
Nozzle Throat Area, sq. in.	10.6
Nozzle Vane Height, in.	0.75
Number of Nozzle Vanes	19
Number of Rotor Blades	12
Rotor Tip Height, in.	0.75
Rotor Tip Diameter, in.	9.8
Inlet Blade Angle, deg	90.0
Inlet Incidence, deg	-15.0
Exducer Tip Diameter, in.	7.5
Exducer Hub Diameter, in	1.5
Exducer RMS Blade Angle, deg	57
Exducer Exit Swirl, deg	-6.0
Pressure Ratio (Total-to-Total)	2.2
Velocity Ratio U_2/Vo	0.71
Exit Axial Velocity/Tip Speed, Cr_3/U_2	0.34
Total-to-Total Isentropic Efficiency, *	0.92
Dimensionless Specific Speed, N_s	0.77

*Indicates interstage duct

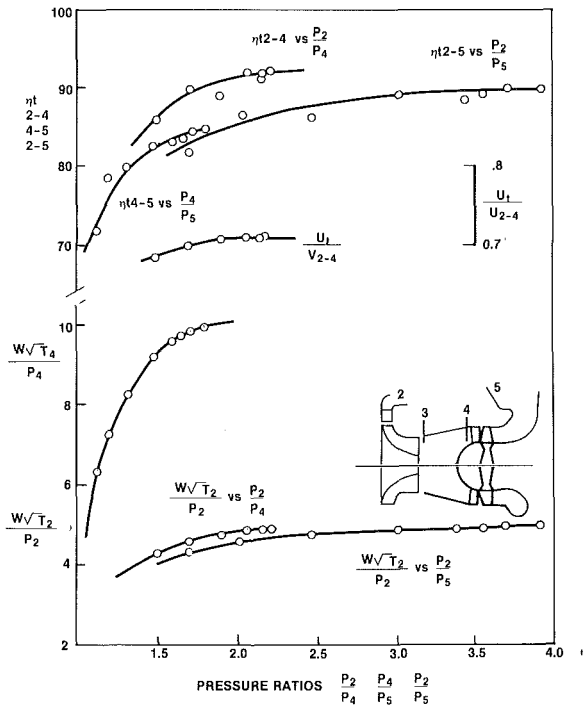

Fig. 5 T351 gas turbine test performances

Several test calibrations and gas turbine builds were completed, mostly operating the power turbine along its optimum efficiency locus. Some stalled power turbine testing was also conducted by locking the dynamometer arm.

The data from the gas turbine test instrumentation listed in Table 1 provided the input for a computerized performance analysis code. Gas producer radial turbine efficiency was computed from a work balance with the single-stage centrifugal compressor. Power turbine efficiency was computed from measurement of the pressure ratio, exit temperature, airflow, and output power. An average specific heat of 0.276 Btu/lb R and a specific heat ratio of 1.33 was used for the expansion process.

T351 Radial Turbine Performance

Extensive development previously conducted on the single-shaft version of the T350 Spartan gas turbine [3] produced

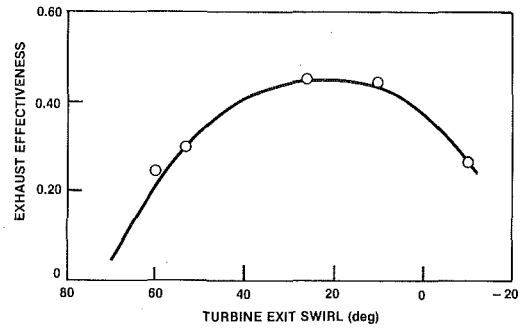

Fig. 6 Exhaust diffuser effectiveness

Table 3 Axial turbine aerodynamic details

Parameter	Dimension
Inlet Total Temperature, °R	1601
Inlet Total Pressure, psia	26.0
Inlet Flow, pps	6.52
Rotational Speed, rpm	22,000
Inlet Axial/Exducer Axial Velocity, *	1.16
Nozzle Entry Annulus Area, sq. in.	46.8
Nozzle Exit Angle*, deg	64.0
Nozzle Vane Number	41.0
Nozzle Solidity	1.46
Rotor Solidity	1.45
Rotor Blade Angle*, deg	11.0
Rotor Inlet Incidence*, deg	1.0
Rotor Blade Number	58
Rotor Exit Annulus Area, sq. in.	55.5
Rotor Exit Swirl*, deg	4.0
Exit Axial Velocity/Blade Speed, Cr_3/U_2	0.53
Work Coefficient, $gJ\Delta H/U_m^2$	1.07
Reaction	0.43
Velocity Ratio, Um/Vo	0.59
Overall Isentropic Efficiency, %	84.7
Total-to-Total Isentropic Efficiency, %	92.0
Pressure Ratio (Total-Ambient)	1.792

*Mean section 11.1-inch diameter

relatively good performance with overall total-to-ambient efficiencies of up to 88 percent including the exhaust at stage pressure ratios of up to 4.2. Design analyses for the T351 two-shaft gas turbine application showed that the total-to-total gas producer stage pressure ratio would decrease to 2.2, requiring a nozzle rematch and decrease in rotor tip diameter of 11 percent for operation at optimum velocity ratio.

Aerodynamic details of the gas producer radial turbine are listed in Table 2. The rotor was 9.8 in. in diameter with 12 radial element blades. At the design velocity ratio of 0.71, the measured total-to-total turbine efficiency was 92.0 percent with an inlet incidence of -15.0 deg and exit swirl of -6.0 deg.

Test performance of the radial turbine, as determined from test calibrations of the T351 gas turbine using the instrumentation itemized in Table 1, is shown in Fig. 5. This performance is based upon nozzle inlet total-to-power turbine inlet total pressures (i.e., including the interstage transition duct).

T351 Power Turbine Performance

Extensive development was also conducted on the three-stage axial turbine and exhaust diffuser for the Saturn gas turbine program. Design analyses for application of the Saturn's second-stage turbine for the T351 power turbine revealed that the only change required was to rematch the second-stage nozzle by increasing the throat area 7 percent.

Aerodynamic details of the axial power turbine are listed in Table 3. With a design rotational speed of 22,000 rpm, the meanline-velocity ratio was 0.59, at which a total-to-ambient isentropic efficiency including the exhaust diffuser of 84.7 percent was measured. The power test performance shown in Fig. 5, in combination with the radial gas producer turbine,

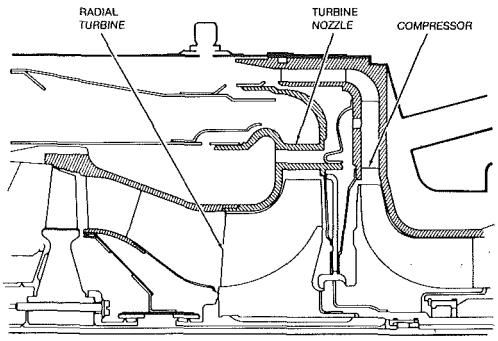

Fig. 7 S140 gas turbine configuration

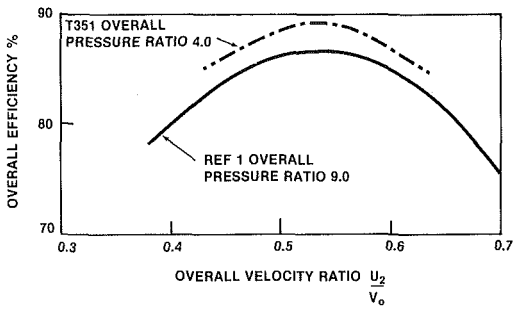

Fig. 8 Radial/axial turbine overall efficiency potential

resulted in the attainment of an overall expansion efficiency for both turbines of 89.7 percent at design point.

Meanline vector conditions were very close to optimum with an inlet incidence of one degree exit swirl of 4.0 degrees and reaction of 0.43. The ratio of the power turbine inlet and gas producer exducer axial velocities was 1.16.

Stalled Torque Performance

Application of the T351 two-shaft gas turbine was earmarked for cement cracking in the petroleum industry where the power turbine could be operated over a range of speeds for stall (zero speed) to runaway conditions.

Gas turbine development testing was therefore conducted operating the power turbine under simulated field conditions. During stalled power turbine testing, the compressor match point moved adjacent to the compressor surge line, and random surge "popping" was experienced close to design gas producer speed.

Component performance data indicated a reduction of power turbine flow function of 9 percent at stalled conditions. This prompted traversing of the power turbine exit to assess the influence of exit swirl upon the exhaust diffuser performance.

Exhaust diffuser static pressure effectiveness as calculated from the traverse pressure measurements is plotted in Fig. 6 versus diffuser inlet swirl angle. Maximum effectiveness was 0.45 near 15-deg swirl, rapidly reducing to zero as stalled conditions were approached. Similar trends are reported in [5]. Twelve equally spaced straight axial struts, as shown in Figs. 3 and 4, were used to support the power turbine bearing housing.

The reduction in power turbine flow capacity reduced the gas producer pressure ratio and flow capacity at rated speed, displacing the operating line closer to surge. The eventual solution to improve surge margin at stalled conditions was to open both the gas producer and power turbine nozzles by approximately 3 percent.

Discussion

Although the radial/axial turbine configuration is capable of attaining high overall turbine efficiency levels in small gas turbines, its popularity is limited. This may be due, in part, to selection of relatively low pressure ratio uncooled designs, for which a closely coupled, lightweight, two-stage axial design may attain comparable efficiencies.

An example of a closely coupled radial/axial turbine configuration for a small 140-hp gas turbine is shown in Fig. 7. This particular gas turbine, Solar's S140, was used as a gas turbine starter system and attained an overall turbine efficiency of 86 percent with an axial diffuser.

The desire to improve thermal efficiencies has motivated increased pressure ratios for single-stage centrifugal compressors to the level where the two-stage axial turbine becomes overloaded, and either a three-stage axial or radial/axial turbine offers higher performance.

The test performance of the radial/axial turbine described in this paper and supported by the work in [1] verifies that the radial/axial turbine configuration is an attractive candidate for fuel-efficient, low-cost, small gas turbines.

The combined overall performance potential of radial/axial turbines with fixed nozzles including the interstage and exhaust ducting is presented in Fig. 8, where overall efficiency is plotted versus velocity ratio based upon the tip speed of the radial stage. These potential performance levels will be attractive for higher pressure ratio small gas turbines, providing the cooling flow considerations for higher temperature operation of the radial turbine stage (with its larger hub surface area) do not incur additional cycle performance losses.

Acknowledgments

The authors wish to thank the Turbomach Division of Sundstrand Corporation for permission to publish this paper and acknowledge the efforts of their associates at Turbomach for their dedicated efforts in originating, designing, producing, selling, and supporting the small radial gas turbine APU over the past years.

References

1 Kidwell, T. R., and Large, G. D., "Advanced Technology Components for Model GTCP305-2 Aircraft Auxiliary Power System," AFAPL-TR-79-2106.

2 Smith, S. F., "A Simple Correlation and Turbine Efficiency," *Journal Royal Aeronautical Society*, Vol. 69, July 1965.

3 Carlson, P. G., and Pembleton, T. K., "A 300 Hp Recuperative Gas Turbine," ASME Paper No. 63-AHGT-75.

4 Pitt, P. A., "1100 Hp Gas Turbine for Marine Applications," ASME Paper No. 60-GTP-11.

5 Amman, C. A., and Dawson, D. W., "The Power Turbine and Its Diffuser," SAE 690032.

S. H. Moustapha
Staff Aerodynamicist.

U. Okapuu
Chief, Turbine Aerodynamics.

Pratt & Whitney Canada Inc.,
Longueuil, Canada

R. G. Williamson
Head, Gas Dynamics Laboratory,
National Research Council, Canada

Influence of Rotor Blade Aerodynamic Loading on the Performance of a Highly Loaded Turbine Stage

This paper describes the performance of a highly loaded single-stage transonic turbine with a pressure ratio of 3.76 and a stage loading factor of 2.47. Tests were carried out with three rotors, covering a range of blade Zweifel coefficient of 0.77 to 1.18. Detailed traversing at rotor inlet and exit allowed an assessment of rotor and stage performance as a function of blade loading under realistic operating conditions. The effect of stator endwall contouring on overall stage performance was also investigated using two different contours with the same vane design.

Introduction

Gas turbine engines designed for the propulsion of light helicopters and small turboprop aircraft generally incorporate single-stage axial gas generator turbines, for reasons of compactness and simplicity. To achieve acceptable fuel consumption, such turbines must operate with relatively high stage pressure ratios. The resulting large enthalpy drop ΔH calls for high rotor blade speeds for the achievement of good turbine efficiency.

However, considerable benefits to engine weight, cost, and handling characteristics would result if blade speeds could be kept low without compromising turbine efficiency. The results of one design study (of a 600-hp turboshaft/turboprop engine) indicated that if the rotor blade diameter were reduced so that the gas generator turbine stage loading ($\Delta H/U_m^2$) increased by 37 percent over conventional levels, the weight of the turbine rotor would reduce by 31 percent, the number of rotor blades by 24 percent, and the polar moment of inertia of the turbine rotor by 39 percent. The latter is particularly important for turboshaft versions of small engines, where rotational inertia has a strong influence on the handling characteristics of light helicopters. The only major disadvantage is the predicted reduction in turbine efficiency, caused by the increase in stage loading.

A research program on the aerodynamics of highly loaded turbine stages was therefore undertaken. This program, which is a cooperative activity involving the National Research Council of Canada and Pratt & Whitney Canada, has as its objective the extension of turbine design methods to regimes combining high stage loadings with high pressure ratios, with special emphasis on small blade sizes. The primary test vehicle is a small, single-stage gas generator turbine having a stage loading of 2.47, a flow factor of 0.64, and a pressure ratio of 3.76. Figure 1 shows a comparison of design points of this NRC/PWC turbine with other similar designs, as reported in [1–5]. The effects of pressure ratio, downstream traverse location, and outer wall contouring on the (isolated) nozzle performance of this turbine are presented in [6, 7]. The present paper discusses the overall performance of the complete research stage with two different endwall contours and three rotors covering a range of blade midspan Zweifel coefficient of 0.77 to 1.18.

Turbine Stage Aerodynamic Design

Stage Design. The research stage was modeled on a realistic gas generator turbine for a small, low-cost, advanced aeroengine. This engine would employ a single-stage gas generator turbine operating at sufficiently high inlet gas temperatures to require at least stator cooling. The stage mean reaction was

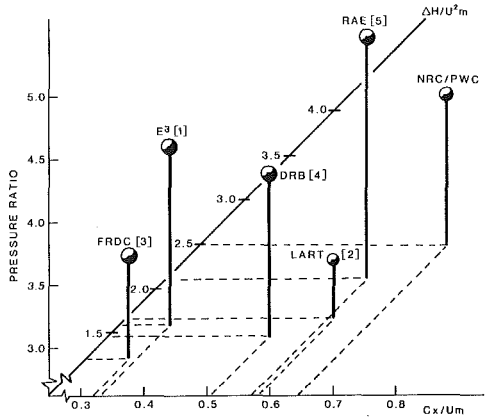

Fig. 1 High-pressure research turbine characteristics

Contributed by the Gas Turbine Division of THE AMERICAN SOCIETY OF MECHANICAL ENGINEERS and presented at the 31st International Gas Turbine Conference and Exhibit, Düsseldorf, Federal Republic of Germany, June 8–12, 1986. Manuscript received at ASME Headquarters January 10, 1986. Paper No. 86-GT-56.

Table 1 Stage average and midspan design point parameters

Inlet Total Pressure	=	0.9 Bar
Inlet Total Temperature	=	400 K
Mass Flow Rate	=	4.38 Kg/s
Rotational Speed	=	8852 R.P.M.
Turbine Pressure Ratio	=	3.76
Stage Loading Factor, $\Delta H/U^2m$	=	2.47
Flow Factor, Cx/Um	=	0.64
Work Capacity, $\Delta H/T_{01m}$	=	265 J/Kg K
Blade Speed Function, $Um/\sqrt{T_{01m}}$	=	10.3 m/s $\sqrt{K}$

kept low (30 percent) to reduce the exit swirl and the blade relative temperatures. Availability of a large exhauster plant permitted a rig three times full size, maintaining blade Reynolds numbers at realistic values in a cool rig and facilitating aerodynamic measurements with minimal probe interference. Figure 2 shows the highly loaded turbine rig and Table 1 gives the stage design point parameters. Midspan velocity triangles (Fig. 3) show the nozzle and rotor transonic exit Mach numbers and the large amount of flow turning needed for high stage work requirements. A radial work distribution was used to unload the hub and tip sections and hence reduce the endwall losses. Selection of number of airfoils was based on a compromise between optimum loading (pitch-to-chord ratio), minimum trailing edge, and secondary (aspect ratio) losses. After the mechanical considerations, 14 vanes and 51 blades were chosen. Using the correlations presented in [8], the vane and blade mean total pressure loss coefficients (based on exit dynamic head) were 0.15 and 0.36, respectively. This resulted in a gas path turbine total efficiency of 83.5 percent for a rotor tip clearance of 1.5 percent of the blade height.

Nozzle Design. The nozzle had 14 vanes of aspect ratio of 0.6 (based on mean true chord), a turning angle of 77 deg, and an exit Mach number of 1.15 at the vane mean section. Vane sections were stacked such that the trailing edge was straight (no tilt) and radial (no lean) in the meridional and axial views, respectively. Details of the nozzle design and comparisons between predicted and measured vane surface Mach number distributions at various pressure ratios have been given in [6].

The improvements in overall efficiency available from meridional endwall contouring of gas generator turbine stators have been demonstrated in different investigations [3, 4, 10]. Contouring the stator endwall has the potential of controlling the secondary loss mechanism by reducing the cross-channel and radial pressure gradients. In order to investigate the effects of endwall contouring on the performance of a

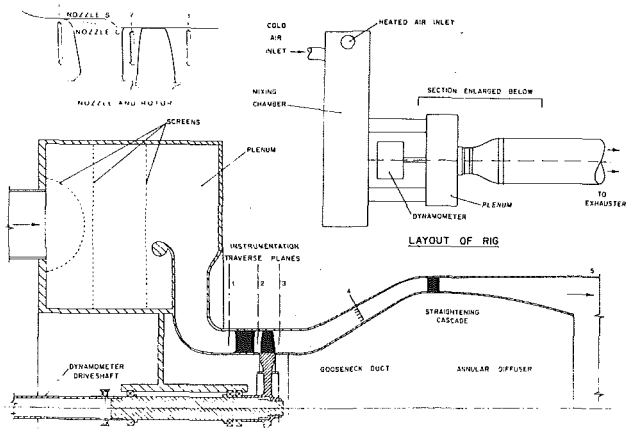

Fig. 2 The highly loaded turbine rig

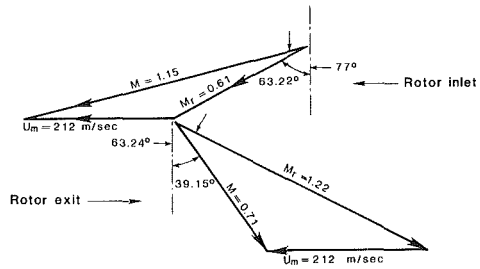

Fig. 3 Design point velocity triangles at midspan

highly loaded stage, where secondary flows and losses become more pronounced, two endwall contours were tested with the same vane sections (Fig. 2). Nozzle S had a contoured S-shaped outer wall starting near the throat, while nozzle C used a conical contour from inlet to exit. The modified tip contour, for variant C, necessitated the restagger of the vane sections by 0.72 deg open to match the throat area of variant S. The effect of the two endwall contours on nozzle performance has been presented in [7].

Rotor Design. The rotor design in a highly loaded turbine generally poses some conflicting design requirements. On the one hand low mean reaction is required to give lower blade metal temperatures, and on the other hand the highest possible hub reaction is required to give good blade hub acceleration and low rotor inlet flow angle and Mach number. From stress considerations, especially for uncooled blades, a minimum hub-to-tip ratio of blade metal area should be satisfied which makes the root section design a difficult one. The research tur-

Nomenclature

bx = axial chord
Cx = axial velocity, m/s
C_{p0} = nozzle local total pressure loss coefficient = $(P_{01m}-P_{02})/(P_{01m}-P_{s2m})$
$\overline{C_{p0}}$ = circumferential average of C_{p0}
$\overline{\overline{C_{p0}}}$ = area-weighted radial average of $\overline{C_{p0}}$
H = stagnation enthalpy, J/kg
M = Mach number
$\dot{m}$ = mass flow rate, kg/s
$N.$ = rotational speed, rpm
P = pressure
$P.R.$ = stage total pressure ratio
S = pitch
T = temperature, K
U = blade speed, m/s
Y_r = rotor loss coefficient = $(P_{0r2}-P_{0r3})/(P_{0r3m}-P_{s3m})$
Z = rotor blade Zweifel coefficient = $2\,(S/bx)\cos^2\alpha_{r3}\,[(C_{x2}/C_{x3})\tan\alpha_{r2}+\tan\alpha_{r3}]$
α = local flow angle, degrees from axial
$\bar{\alpha}$ = circumferential average of α
$\bar{\bar{\alpha}}$ = area-weighted radial average of $\bar{\alpha}$
Δ = change
η = stage total-to-total efficiency

Subscripts

1,2,3 . . . = plane number (Fig. 2)
m = mean
0 = total
r = relative
s = static

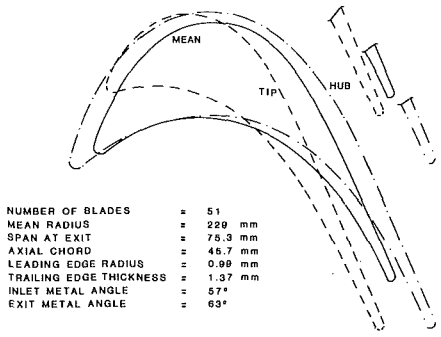

Fig. 4 Blade sections and midspan geometric parameters

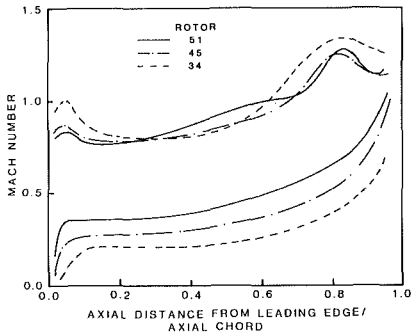

Fig. 5 Predicted rotor blade surface Mach number distributions at midspan

bine was designed for subimpulse conditions at the blade root with a resultant large flow deflection (130 deg) and high inlet relative Mach number (0.8). The tip section was designed to have surface velocity distributions and loading such that there would be a minimum pressure difference across the tip from pressure to suction surface to decrease the tip leakage flow and its adverse effects on stage performance. Blade root, mean, and tip Zweifel loading coefficients were 0.69, 0.77, and 0.79, respectively. The blade sections were stacked on a radial line which passed through the center of gravity of the various sections. Figure 4 shows the blade sections and the midspan geometric parameters.

From weight and cost considerations it is advantageous to minimize the number of rotor blades in a turbine. However, without increasing the stage reaction this implies higher blade loading, for the same axial chord, and possible performance penalties. In order to establish the optimum Zweifel loading coefficient for this class of turbine three rotor configurations were tested, each employing the same blading and designated by the number of blades in the build. Mean Zweifel coefficients were as follows: Rotor 51, 0.77; Rotor 45, 0.87; Rotor 34, 1.18. The hub and tip Zweifel coefficients for Rotor 34 were 1.07 and 1.23, respectively. In the case of Rotors 45 and 34, throat area was maintained at the datum value by restaggering the blades closed by 0.7 deg and 3.0 deg, respectively. Figure 5 shows the predicted blade surface Mach number distributions at midspan for the three rotor configurations as obtained by a two-dimensional Euler flow solver due to Ni [11]. The effect of increased blade loading is manifested as increased diffusion levels near the blade leading edge. This was more pronounced for the rotor root section due to the higher inlet Mach number levels. Figure 6 shows the 51 and 34 rotor configurations.

Test Arrangements

The test facility (Fig. 2), which has been described in [6, 7], was designed to accommodate single turbine stages of about 53 cm o.d. with blade heights up to 7.5 cm. Turbine power was absorbed in a water brake dynamometer with a speed range up

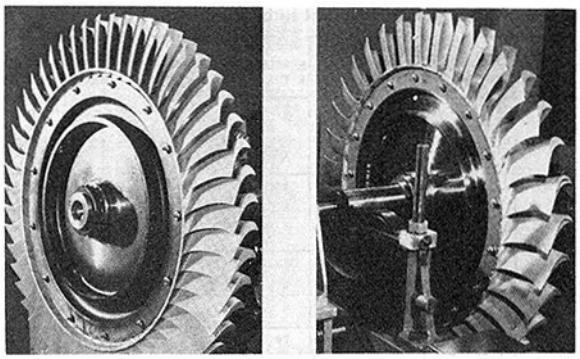

Fig. 6 Rotor configurations

to 10,000 rpm. Air was drawn through the rig by an exhauster plant, and was prewarmed by thorough mixing with the output of a propane combustor.

Plenum conditions, which were assumed to represent inlet stagnation conditions, were sensed by sixteen partially shielded thermocouples equispaced around the circumference, and by four static pressure tappings. Three static pressure tappings on both the hub and tip walls at the nozzle inlet plane completed the stage inlet measurements.

In order to allow for circumferential variations in static pressure at nozzle exit, mean wall exit static pressures were derived from subsurface chambers connected to circumferential slits extending over one nozzle blade pitch. Provision was made at nozzle exit (plane 2) for radial/circumferential traversing by a wedge probe equipped with a partially shielded thermocouple. Similar radial/circumferential traversing capability was also available at rotor exit (plane 3), together with hub and tip static pressure tappings at five circumferential locations. Rotor exit conditions could also be sensed by four total pressure rakes, each with five probes disposed at centers of equal areas, equispaced circumferentially in the exit duct (plane 4). The rakes, located some six axial chords downstream of the rotor exit (a location previously found to best represent engine measured performance) could be aligned and locked to conform with the mean exit swirl angle. A straightening cascade restored axial flow in the downstream ducting, where further mixing of remaining temperature nonuniformities could occur. Four rakes of partially shielded thermocouples, located at approximately nine rotor diameters from rotor exit (plane 5), were used to determine the final mixed-out temperature of the exit flow. Insulation of the entire rig, and careful adjustment of inlet temperature to maintain exit temperature within $\pm 1°C$ of cell ambient temperature, combined to reduce heat transfer in the downstream mixing process. For a discussion of instrumentation accuracy and averaging procedures the reader is referred to [6, 7, 12].

Performance of the Basic Stage

The overall performance of the basic turbine stage (which used the S nozzle variant and rotor 51) is presented in Figs. 7 and 8. Figure 7 shows the turbine hub and tip reaction increasing with pressure ratio up to the design values. With the nozzle becoming choked at a pressure ratio near 2.2, the effect of reducing the speed is to increase the rotor inlet relative Mach number. At low pressure ratios this will result in reduced stage reaction due to a decrease in flow acceleration in the rotor passages.

The variation in total efficiency (calculated as per method 1, Table 2) with stage total pressure ratio and rotor speed is shown in Fig. 8. At equivalent speeds between 80 and 100 percent, turbine efficiencies are nearly independent of pressure ratio over a wide range of that parameter. Slight reductions in

Table 2 Design point turbine efficiency (percent)

METHOD	PRESSURE MEASUREMENT	TOTAL TEMPERATURE MEASUREMENT	NOZZLE S ROTOR 51	NOZZLE C ROTOR 51	NOZZLE S ROTOR 45	NOZZLE S ROTOR 34	NOZZLE C ROTOR 34
1	Total Pressure Rakes, Plane 4	Mixing Pipe Rakes, Plane 5	80.0	79.8	79.8	77.6	77.6
2	Total Pressure Traverse, Plane 3	Mixing Pipe Rakes, Plane 5	83.0	82.0	82.7	81.6	81.3
3	Total Pressure Traverse, Plane 3	Traverse, Plane 3	79.4	78.7	79.5	76.3	76.0
4	Total Pressure Rakes, Plane 4	Dynamometer * (N, m)	79.7	78.6	79.3	77.7	78.2
5	Continuity Polm, Tolm, Ps3m, m, α)	Dynamometer * (N, m)	81.9	80.8	81.6	78.3	78.3
6	Wall Static Pressures, Plane 3	Mixing Pipe Rakes, Plane 5	70.8	69.2	69.7	68.4	68.1

* Uncorrected for bearing and windage losses.

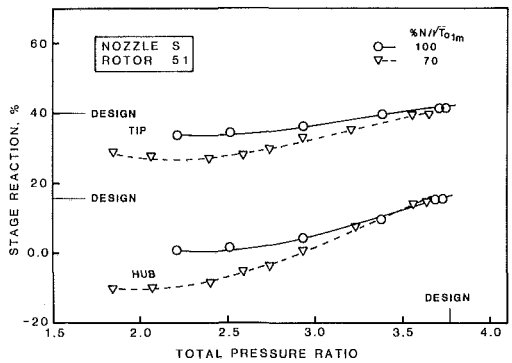

Fig. 7 Variation of reaction with pressure ratio for the basic stage

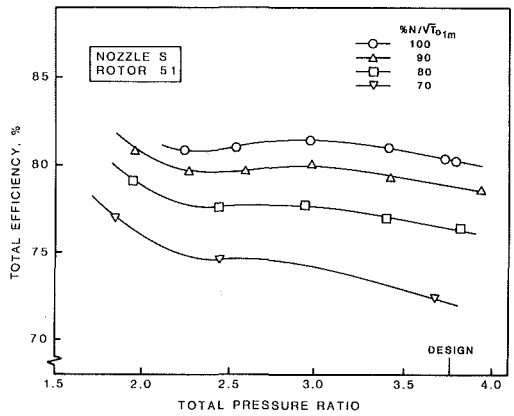

Fig. 8 Variation of efficiency with pressure ratio for the basic stage

efficiency at high pressure ratios probably stem from rotor shock losses, whereas transonic nozzle losses probably affect efficiencies at stage pressure ratios near 2.3. With almost constant nozzle exit conditions over much of the pressure ratio range, the decrease in efficiency due to speed reduction results from increased incidence and relative Mach number at the blade inlet and lower rotor flow acceleration (Fig. 7). For the design speed, peak efficiency of 81.5 percent occurs at a pressure ratio of about 3.0 and a turbine efficiency of 80.0 percent is measured at the design point. Although this measured efficiency is 2 percent below the predicted target efficiency of 82 percent [8] at the running tip clearance/blade height of 2.3 percent it is noted that small variations between predicted and calculated efficiencies depend significantly on the instrumentation used. Measured turbine efficiencies,

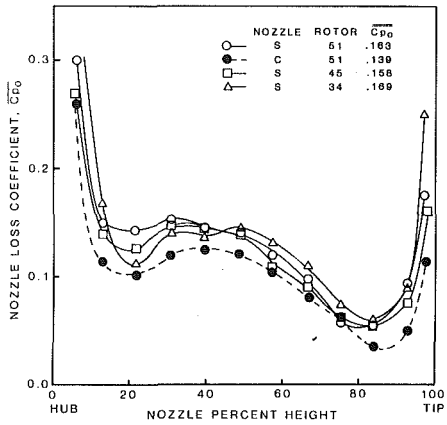

Fig. 9 Radial distribution of circumferentially averaged nozzle total pressure loss at design conditions

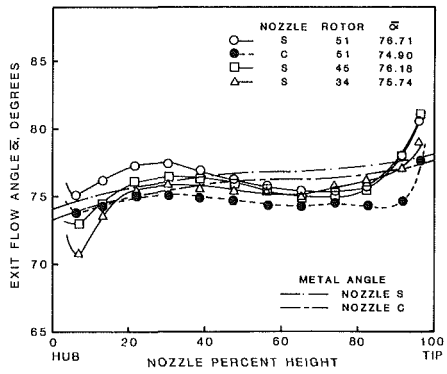

Fig. 10 Radial distribution of circumferentially averaged nozzle exit flow angle at design conditions

derived in different ways, are presented in Table 2 for design conditions. Effects relating to mixing distance, averaging techniques, and instrumentation accuracy are readily apparent.

Effect of Nozzle Contouring and Rotor Loading on Nozzle Performance

The effect of endwall contour on the performance of the nozzle, when tested with an unbladed stationary insert representing the rotor hub wall, has been presented in [7]. At the nozzle design pressure ratio of 2.3, significantly greater hub total pressure loss was measured at the exit of the C nozzle compared with the S variant. This difference was not offset by a corresponding decrease in tip loss and led to a 7 percent higher overall total pressure loss for the C nozzle. The thicker hub loss region at the C nozzle exit resulted in greater flow underturning when compared to the S variant.

With the basic 51-bladed rotor operating, the overall loss of the S nozzle exceeded that of the C design by about 15 percent. Substantial reductions of total pressure loss were measured at the hub, particularly for the C nozzle. The effect of the rotor in suppressing nozzle hub flow separation [6] was also evident in the radial distributions of the nozzle exit flow angle. An analysis of the influence of the rotor presence on the performance of these nozzles is given in [12]. Reducing the number of rotor blades affected the radial distribution of the nozzle losses and flow angles, particularly in the inner part of the annulus (Figs. 9 and 10). Similar behavior was obtained for the C nozzle exit parameters with various rotor builds.

Significantly more three dimensionality was evident in the S nozzle exit flow field in all the tests. This was reflected in the value of the corrected mass flow parameter, which was 4 percent lower than was found for the C nozzle despite the nominal similarity in geometric throat areas.

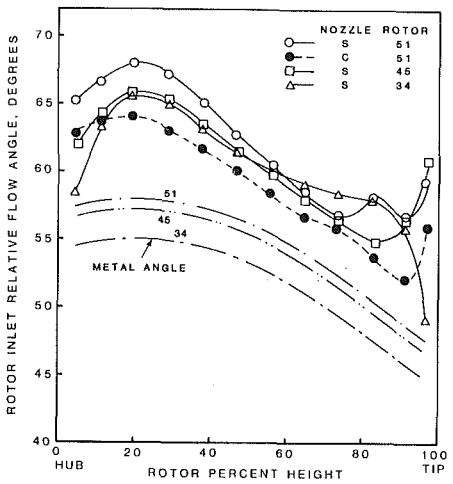

Fig. 11 Radial distribution of rotor inlet relative flow angle at design conditions

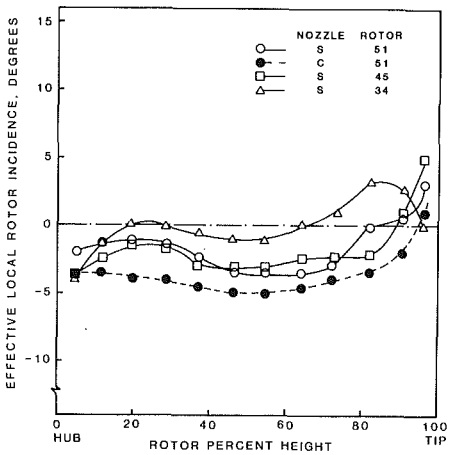

Fig. 12 Effect of nozzle contouring and rotor loading on rotor incidence

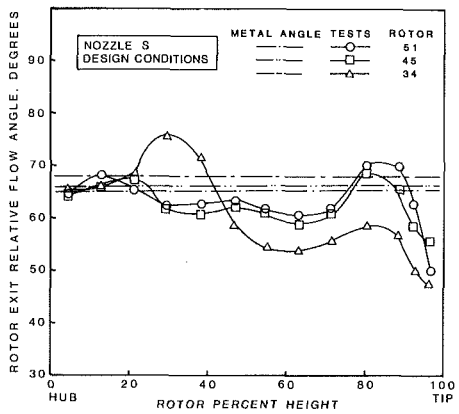

Fig. 13 Radial distribution of rotor exit relative flow angle

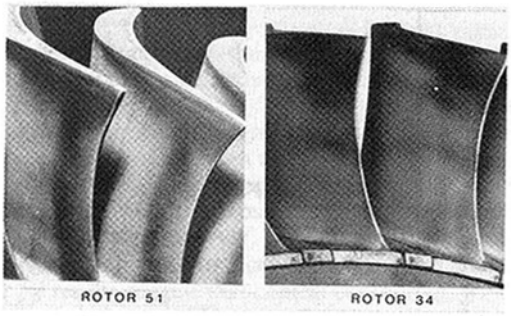

Fig. 14 Flow visualization on rotor blades

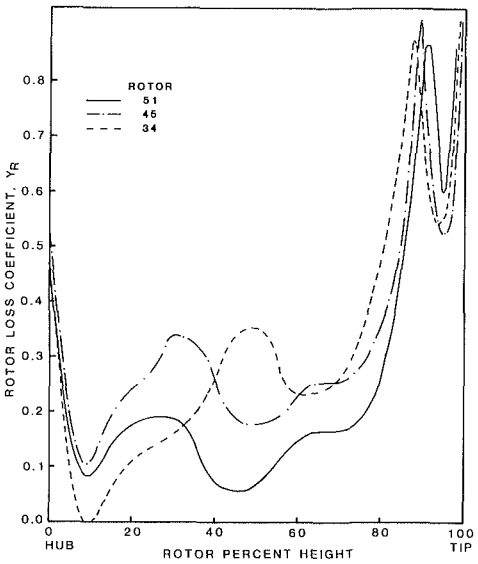

Fig. 15 Radial distribution of rotor loss coefficient

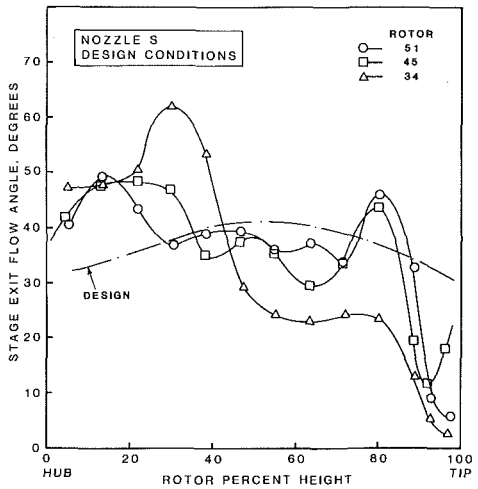

Fig. 16 Radial distribution of stage exit swirl

Effect of Nozzle Contouring and Rotor Loading on Rotor Performance

The measured nozzle exit conditions were used to calculate the rotor inlet flow parameters in the rotating frame of reference. Figure 11 presents the radial distribution of the rotor inlet relative flow angles for the various nozzle/rotor combinations at design speed and pressure ratio. Also plotted are the blade inlet metal angles for the three rotor variants. The difference between the inlet flow angle and the corresponding metal angle represents the total incidence experienced by the rotor. The effective local rotor incidence was estimated by subtracting from the rotor total incidence an analytically derived induced incidence which varied from +4 deg to +10 deg depending on the rotor inlet flow angle. The resulting local incidence on the rotor, plotted in Fig. 12, is seen to be within a range of 0 deg to −5 deg, except near the rotor tip where slightly higher incidences were experienced by Rotor 34.

A sector at rotor exit, corresponding to one nozzle vane pitch, was surveyed at 11 circumferential positions and 13 radial immersions for each of the three rotor configurations. Contour plotting of the traverse results confirmed that the large circumferential total pressure gradients associated with

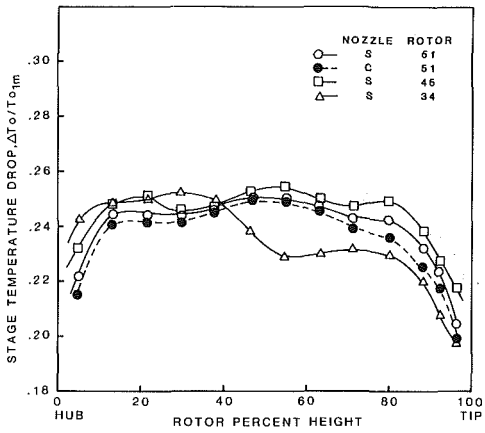

Fig. 17 Radial distribution of stage temperature drop

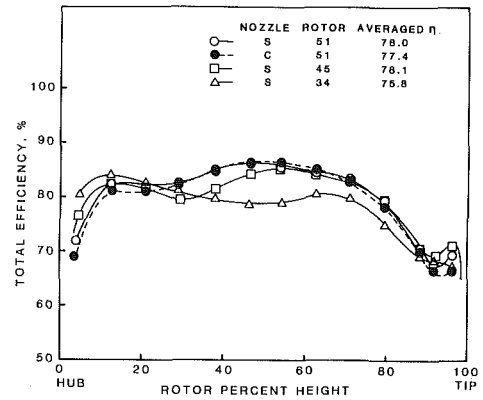

Fig. 18 Radial distribution of stage efficiency at design conditions

the vane wakes were considerably attenuated in passing through the rotor. Rotor exit relative flow angle distributions are presented in Fig. 13 together with the metal angles for each rotor build. The basic variant shows signs of the usual secondary flow pattern of underturning in the middle region and overturning nearer the endwalls. From the radial distribution it appears that the centers of the two secondary vortices were displaced inward to lie at about 25 and 75 percent span. The high turning angle of the rotor blades is probably responsible for the migration toward midspan of the two secondary vortices which originated at both endwalls. Figure 13 also reveals the presence of the tip leakage vortex located at about 90 percent span and causing large flow underturning near the rotor tip. Reducing the blade number from 51 to 34 results in a large change in flow angle in the midspan region indicating the presence of a strong vortex. Here the effect of increasing the blade loading is to further displace inward the two counter-rotating secondary vortices until they merge to produce a region of high flow deviations. The combined effect of this secondary flow pattern and the tip leakage flow leads to significant flow underturning over the outer part of the blade span. The flow angle distribution for Rotor 34 is in agreement with the results presented by Moustapha et al. [13] on a similar highly loaded blade tested in a stationary rig. In that work, a single large vortex was apparent in the middle of the passage with flow underturning of up to 12 deg.

Further confirmation of the flow pattern just described can be seen in the oil flow visualization on the blades of Rotor 34 (Fig. 14), which shows the midspan vortex streak as well as tip vortex trails. These indications of strong flow three dimensionality are quite different from those of Rotor 51 in which tip vortex trails persist to the trailing edge with no evidence of the midspan vortex. In that build an essentially two-dimensional shock impingement pattern is visible over most of the blade span. Radial distributions of rotor loss coefficient

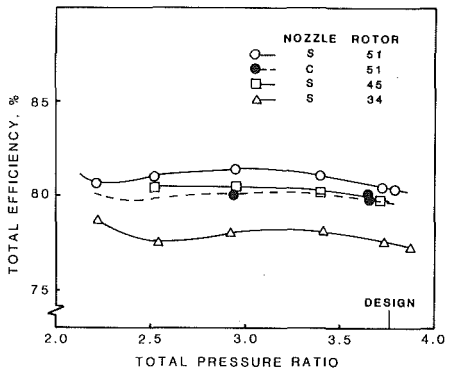

Fig. 19 Effect of nozzle contour and rotor loading on stage efficiency at design speed

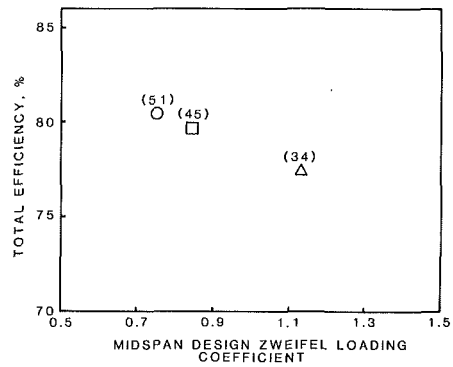

Fig. 20 Effect of rotor loading on stage efficiency at design conditions

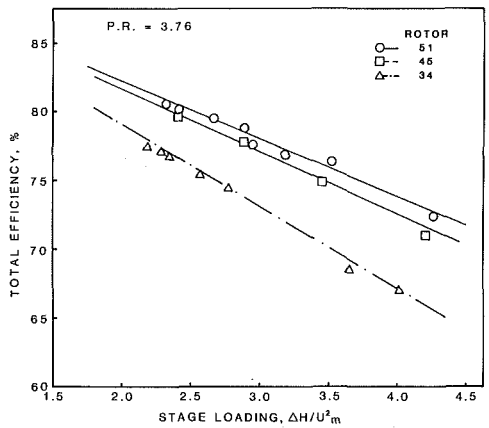

Fig. 21 Effect of stage loading on efficiency

are presented in Fig. 15. It is noted that such distributions assume no radial displacement of flow between rotor inlet and exit, an assumption which, as discussed above, suggests that at least the results for the Rotor 34 case should be viewed with some caution, although broad trends, including the loss peak near midspan, appear to be plausibly represented. The effect of increased blade loading is to increase and modify the position of the hub loss region, moving it toward midspan.

Effect of Nozzle Contouring and Rotor Loading on Stage Performance

The radial distributions of stage exit parameters for the three rotor configurations are presented in Figs. 16–18. Figure 16 shows the stage exit swirl variations which are similar to the distributions given in Fig. 13. The performance of a subsequent duct and nozzle would obviously be affected by those large variations in exit swirl, particularly for the high blade loading variant. The measured hub and tip stage reactions for

the various nozzle/rotor combinations agreed closely with the design reactions, thus indicating a correct restagger of the nozzle and rotor blades. The nondimensional total temperature drop across the stage (Fig. 17), which is directly related to the rotor performance, shows an improvement with the S nozzle as compared to the C variant from hub to tip, probably resulting from the more favorable rotor incidence shown in Fig. 12. This was reflected in a marginal improvement in the corresponding overall basic stage efficiency (Fig. 18), despite the lower loss level of the C nozzle (Fig. 9).

Figure 17 also shows some effect of the previously described midpassage vortex and tip leakage flows on the deterioration of the Rotor 34 performance in the outer 60 percent of the annulus. This is also seen in generally lower efficiency levels (Fig. 18). It is noted that, for the high blade loadings of Rotor 34, the effects of nozzle wall contouring on overall efficiency were less pronounced than for the basic stage. Data are presented in Table 2.

Figure 19 shows the variation of total efficiency with pressure ratio at design speed for various stage builds. At all pressure ratios, increasing the rotor blade loading from the datum values results in a drop in stage efficiency. Increasing the midspan blade Zweifel loading by 50 percent from the design value of 0.77 results in a loss of 2.5 percent in total efficiency at design point (Fig. 20). (Calculation of these Zweifel coefficients has been based on the velocity triangles of Fig. 3.) The total efficiency is finally plotted against the stage loading factor (Fig. 21). The envelope of the maximum efficiency attained at each stage loading is shown to have a slope which appears to be proportional to the rotor blade loading. These envelopes, obtained by operating three rotors at off-design conditions, are useful in providing at least lower bound estimates of efficiencies attainable at even higher stage loadings.

Conclusions

The performance of a highly loaded turbine stage with a pressure ratio of 3.76 and a stage loading of 2.47 has been presented for different pressure ratios and speeds. The effects of stator endwall geometry and rotor blade loading on the radial distributions of the nozzle and rotor flow parameters have been presented. The results lead to the following main conclusions:

1 The measured efficiency of the basic stage was within about 1 percent of the predicted target efficiency of 82 percent depending on the measurement technique adopted.

2 Increasing the rotor blade aerodynamic loading from the design value of 0.77 to 1.18 resulted in a drop of about 2.5 percent in stage efficiency. This efficiency loss is mainly attributed to the merging of the two endwall secondary vortices into a major vortex near midspan. The effect of this flow three dimensionality was to produce flow underturning over most of the blade span.

3 Off-design operation of the basic stage has permitted lower bound estimates to be derived for efficiencies at higher stage loadings.

4 Earlier data [7] without an operating rotor showed nozzle S with a 7 percent lower loss than the C variant. In the present tests with various rotors, the C nozzle demonstrated a loss up to 15 percent lower than the S build. The average stage efficiency in these tests was, however, still marginally higher using the S variant, probably due to more favorable rotor inlet flow angles. These results suggest that conical contouring, with appropriate rotor design, could be superior to the S wall type in terms of overall stage performance.

Acknowledgments

The authors are indebted to J. P. Huot for his assistance in the evaluation of these results, and to B. J. Day and D. L. Logan for their work in securing the experimental data.

References

1 Crow, D. E., Vanco, M. R., Welna, H., and Singer, I. D., "Results From Tests on a High Work Transonic Turbine for an Energy Efficient Engine," ASME Paper No. 80-GT-146.

2 Liu, H. C., Booth, T. C., and Tall, W. A., "An Application of 3D Viscous Flow Analysis to the Design of a Low Aspect Ratio Turbine," ASME Paper No. 79-GT-53.

3 Ewen, J. S., Huber, F. W., and Mitchell, J. P., "Investigation of the Aerodynamic Performance of Small Axial Turbines," ASME Paper No. 73-GT-3.

4 Okapuu, U., "Some Results From Tests on a High Work Axial Gas Generator Turbine," ASME Paper No. 74-GT-81.

5 Bryce, I. D., Litchfield, M. R., and Leversuch, N. P., "The Design, Performance and Analysis of a High Work Capacity Transonic Turbine," ASME Paper No. 85-GT-15.

6 Williamson, R. G., and Moustapha, S. H., "Annular Cascade Testing of Turbine Nozzles at High Exit Mach Numbers," ASME *Journal of Fluids Engineering*, Vol. 108, No. 3, 1986, pp. 313–320.

7 Moustapha, S. H., and Williamson, R. G., "Investigation of the Effect of Two Endwall Contours on the Performance of an Annular Nozzle Cascade," *AIAA Journal*, Vol. 84, No. 9, 1986, p. 1524.

8 Kacker, S. C., and Okapuu, U., "A Mean Line Prediction Method for Axial Flow Turbine Efficiency," ASME Paper No. 81-GT-58.

9 Morris, A. W. H., and Hoar, R. G., "Secondary Loss Measurements in a Cascade of Turbine Blades With Meridional Wall Profiling," ASME Paper No. 75-WA/GT-13.

10 Haas, J. E., and Boyle, R. J., "Analytical and Experimental Investigation of Stator Endwall Contouring in a Small Axial Flow Turbine," NASA TP-2309, Sept. 1984.

11 Ni, R. H., "A Multiple-Grid Scheme for Solving the Euler Equations," *AIAA Journal*, Vol. 20, No. 11, Nov. 1982.

12 Williamson, R. G., Moustapha, S. H., and Huot, J. P., "The Effect of a Downstream Rotor on the Measured Performance of a Transonic Turbine Nozzle," ASME JOURNAL OF TURBOMACHINERY, Vol. 108, No. 2, 1986, pp. 269–274.

13 Moustapha, S. H., Paron, G. J., and Wade, J. H. T., "Secondary Flows in Cascades of Highly Loaded Turbine Blades," ASME JOURNAL OF ENGINEERING FOR GAS TURBINES AND POWER, Vol. 107, No. 4, 1985, pp. 1031–1038.

the various nozzle/rotor combinations agreed closely with the design reactions, thus indicating a correct restagger of the nozzle and rotor blades. The nondimensional total temperature drop across the stage (Fig. 17), which is directly related to the rotor performance, shows an improvement with the S nozzle as compared to the C variant from hub to tip, probably resulting from the more favorable rotor incidence shown in Fig. 12. This was reflected in a marginal improvement in the corresponding overall basic stage efficiency (Fig. 18), despite the lower loss level of the C nozzle (Fig. 9).

Figure 17 also shows some effect of the previously described midpassage vortex and tip leakage flows on the deterioration of the Rotor 34 performance in the outer 60 percent of the annulus. This is also seen in generally lower efficiency levels (Fig. 18). It is noted that, for the high blade loadings of Rotor 34, the effects of nozzle wall contouring on overall efficiency were less pronounced than for the basic stage. Data are presented in Table 2.

Figure 19 shows the variation of total efficiency with pressure ratio at design speed for various stage builds. At all pressure ratios, increasing the rotor blade loading from the datum values results in a drop in stage efficiency. Increasing the midspan blade Zweifel loading by 50 percent from the design value of 0.77 results in a loss of 2.5 percent in total efficiency at design point (Fig. 20). (Calculation of these Zweifel coefficients has been based on the velocity triangles of Fig. 3.) The total efficiency is finally plotted against the stage loading factor (Fig. 21). The envelope of the maximum efficiency attained at each stage loading is shown to have a slope which appears to be proportional to the rotor blade loading. These envelopes, obtained by operating three rotors at off-design conditions, are useful in providing at least lower bound estimates of efficiencies attainable at even higher stage loadings.

Conclusions

The performance of a highly loaded turbine stage with a pressure ratio of 3.76 and a stage loading of 2.47 has been presented for different pressure ratios and speeds. The effects of stator endwall geometry and rotor blade loading on the radial distributions of the nozzle and rotor flow parameters have been presented. The results lead to the following main conclusions:

1 The measured efficiency of the basic stage was within about 1 percent of the predicted target efficiency of 82 percent depending on the measurement technique adopted.

2 Increasing the rotor blade aerodynamic loading from the design value of 0.77 to 1.18 resulted in a drop of about 2.5 percent in stage efficiency. This efficiency loss is mainly attributed to the merging of the two endwall secondary vortices into a major vortex near midspan. The effect of this flow three dimensionality was to produce flow underturning over most of the blade span.

3 Off-design operation of the basic stage has permitted lower bound estimates to be derived for efficiencies at higher stage loadings.

4 Earlier data [7] without an operating rotor showed nozzle S with a 7 percent lower loss than the C variant. In the present tests with various rotors, the C nozzle demonstrated a loss up to 15 percent lower than the S build. The average stage efficiency in these tests was, however, still marginally higher using the S variant, probably due to more favorable rotor inlet flow angles. These results suggest that conical contouring, with appropriate rotor design, could be superior to the S wall type in terms of overall stage performance.

Acknowledgments

The authors are indebted to J. P. Huot for his assistance in the evaluation of these results, and to B. J. Day and D. L. Logan for their work in securing the experimental data.

References

1 Crow, D. E., Vanco, M. R., Welna, H., and Singer, I. D., "Results From Tests on a High Work Transonic Turbine for an Energy Efficient Engine," ASME Paper No. 80-GT-146.

2 Liu, H. C., Booth, T. C., and Tall, W. A., "An Application of 3D Viscous Flow Analysis to the Design of a Low Aspect Ratio Turbine," ASME Paper No. 79-GT-53.

3 Ewen, J. S., Huber, F. W., and Mitchell, J. P., "Investigation of the Aerodynamic Performance of Small Axial Turbines," ASME Paper No. 73-GT-3.

4 Okapuu, U., "Some Results From Tests on a High Work Axial Gas Generator Turbine," ASME Paper No. 74-GT-81.

5 Bryce, I. D., Litchfield, M. R., and Leversuch, N. P., "The Design, Performance and Analysis of a High Work Capacity Transonic Turbine," ASME Paper No. 85-GT-15.

6 Williamson, R. G., and Moustapha, S. H., "Annular Cascade Testing of Turbine Nozzles at High Exit Mach Numbers," ASME *Journal of Fluids Engineering*, Vol. 108, No. 3, 1986, pp. 313–320.

7 Moustapha, S. H., and Williamson, R. G., "Investigation of the Effect of Two Endwall Contours on the Performance of an Annular Nozzle Cascade," *AIAA Journal*, Vol. 84, No. 9, 1986, p. 1524.

8 Kacker, S. C., and Okapuu, U., "A Mean Line Prediction Method for Axial Flow Turbine Efficiency," ASME Paper No. 81-GT-58.

9 Morris, A. W. H., and Hoar, R. G., "Secondary Loss Measurements in a Cascade of Turbine Blades With Meridional Wall Profiling," ASME Paper No. 75-WA/GT-13.

10 Haas, J. E., and Boyle, R. J., "Analytical and Experimental Investigation of Stator Endwall Contouring in a Small Axial Flow Turbine," NASA TP-2309, Sept. 1984.

11 Ni, R. H., "A Multiple-Grid Scheme for Solving the Euler Equations," *AIAA Journal*, Vol. 20, No. 11, Nov. 1982.

12 Williamson, R. G., Moustapha, S. H., and Huot, J. P., "The Effect of a Downstream Rotor on the Measured Performance of a Transonic Turbine Nozzle," ASME JOURNAL OF TURBOMACHINERY, Vol. 108, No. 2, 1986, pp. 269–274.

13 Moustapha, S. H., Paron, G. J., and Wade, J. H. T., "Secondary Flows in Cascades of Highly Loaded Turbine Blades," ASME JOURNAL OF ENGINEERING FOR GAS TURBINES AND POWER, Vol. 107, No. 4, 1985, pp. 1031–1038.

DISCUSSION

R. J. Roelke[1]

The authors are to be commended on the extent of the investigation undertaken. However, the very large number of design option investigations made it difficult at times to sort out which were beneficial to the turbine performance and which were not. For example, it is not clear whether the "S" contoured stator or the conical stator was better, or was it a draw?

I also would have liked more information defining the hub and tip flow conditions (such as velocity diagrams and blade surface velocities) since it was at those locations that most of the losses occurred. Having that information in the paper would have aided in the discussion of the test results.

Lastly, but perhaps most importantly, is the clear need for analysis and design tools that better model the flow physics of small turbomachines where viscous effects play such a dominant role.

[1]Aerospace Engineer, NASA Lewis Research Center, Cleveland, OH 44135.

Authors' Closure

The authors thank Mr. Roelke for his comments, and are keenly aware that space constraints precluded inclusion of all

aspects of the investigation. In particular, we agree that the optimum design is not a clear-cut choice. The example cited by Mr. Roelke is a good example of some of the complexities involved.

Initial work with the nozzle operating as an isolated annular cascade suggested that the "S" contour had lower losses than the "C" variant. Subsequent experiments in a stage environment showed that under those conditions the "C" nozzle had the lower overall loss, reflecting the rotor interaction effect discussed in [12]. The flow turning achieved with the "C" nozzle, however, did not match the design value, and this led to a reduction in rotor performance. In terms of overall stage efficiency, therefore, the stage with the "C" nozzle proved inferior to that with the "S" nozzle. The results suggest that, with appropriate redesign to accommodate the flow angles involved, the "C" contour could eventually prove superior in terms of overall stage efficiency. Further work is planned, and will be reported in due course.

M. F. Malak
Graduate Research Assistant.
Student Mem. ASME

A. Hamed
Professor.
Mem. ASME

W. Tabakoff
Professor.
Fellow ASME

Department of Aerospace Engineering and Engineering Mechanics,
University of Cincinnati,
Cincinnati, OH 45221

Three-Dimensional Flow Field Measurements in a Radial Inflow Turbine Scroll Using LDV

The results of an experimental study of the three-dimensional flow field in a radial inflow turbine scroll are presented. A two-color LDV system was used in the measurement of three orthogonal velocity components at 758 points located throughout the scroll and the unvaned portion of the nozzle. The cold flow experimental results are presented for through-flow velocity contours and the cross velocity vectors.

Introduction

Radial inflow turbines are used in a wide range of applications from small turbochargers of automotive engines to space auxiliary systems. For small power requirements, radial inflow turbines offer several advantages such as low manufacturing cost, simple construction, and good performance over a wide range of operating conditions. Several studies have been conducted to develop methods for predicting radial inflow turbine aerodynamic performance [1-5]. These methods are mainly based on a combination of one-dimensional flow analysis with appropriate loss models in the inlet volute, vaned and/or vaneless nozzles, rotor and exit duct. The differences between the various methods are in the loss models used in the various components. Benson [1] used the extensive performance measurements data of Hiett and Johnston [2] to develop loss correlations for the flow in rotors. Besides friction losses, Wallace et al. [3] included clearance, disc friction, and incidence effects in the rotor loss model, and took into consideration the incidence losses in the nozzle vanes. Evidence of good agreement between the measured and predicted turbine performance was demonstrated in [3, 4] over a wide range of operating conditions. Wallace et al. [3] showed also that the simpler model of Futral et al. [6] gave results that are in very good agreement with the measured performance.

The flow is actually three dimensional in the various components of radial inflow turbine and is also complicated by the interaction between the rotor and nozzle. Tabakoff et al. [7-9] obtained hot-wire measurements in scrolls of different cross-sectional geometries that revealed the presence of two counter-rotating vortices at three different scroll cross sections. Khalil et al. [10] presented maps of the measured total pressure, Mach number, and flow angles at the inlet and exit of the vaned nozzle. These measurements clearly demonstrate the three-dimensional flow behavior in this component. They also compared the measured losses in the vaned nozzles of a radial inflow turbine with the calculated friction and mixing losses of the boundary layers. Hashemi et al. [11] presented total pressure measurements at three radii downstream of different vaned nozzle geometries, and also conducted flow visualization which revealed the formation of secondary flow and the presence of leading edge vortex. The shape of the leading edge vortex was found to be strongly influenced by the incidence

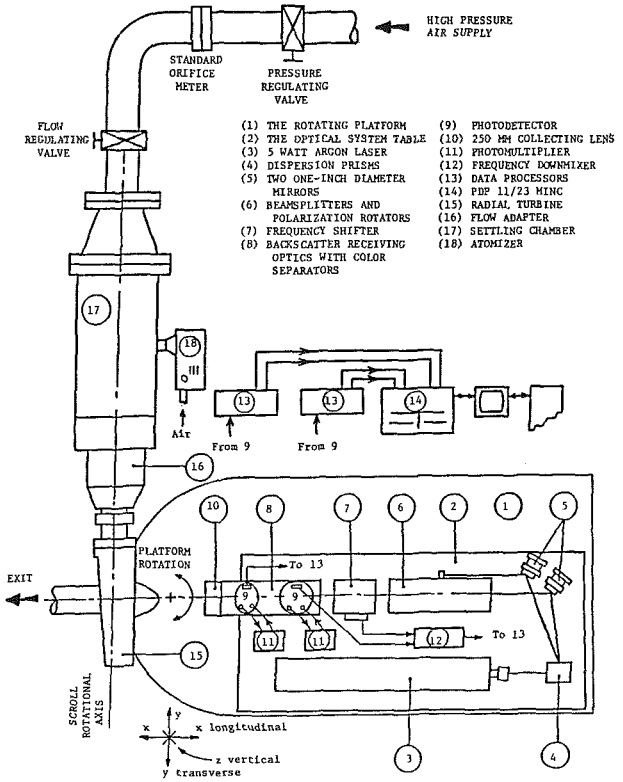

Fig. 1 Schematic showing the LDV experimental setup

Contributed by the Gas Turbine Division of THE AMERICAN SOCIETY OF MECHANICAL ENGINEERS and presented at the 31st International Gas Turbine Conference and Exhibit, Düsseldorf, Federal Republic of Germany, June 8-12, 1986. Manuscript received at ASME Headquarters January 24, 1986. Paper No. 86-GT-122.

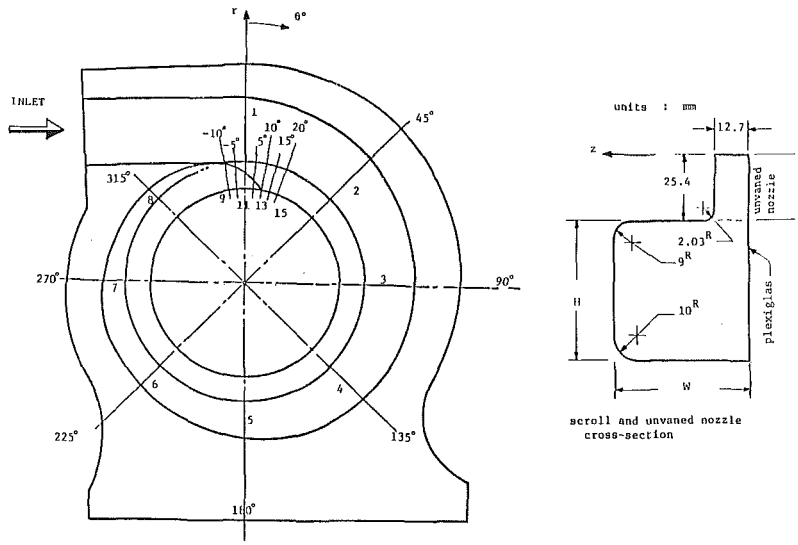

Fig. 2 Schematic showing the LDV measuring sections

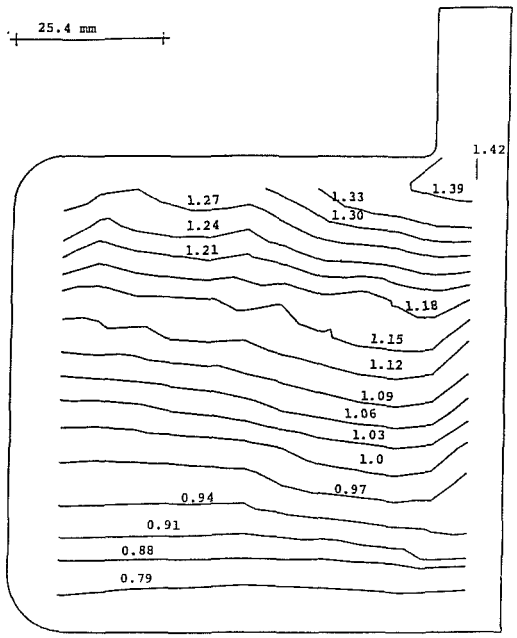

Fig. 3 Normalized circumferential velocity contours for cross section No. 1 ($\theta = 0$ deg)

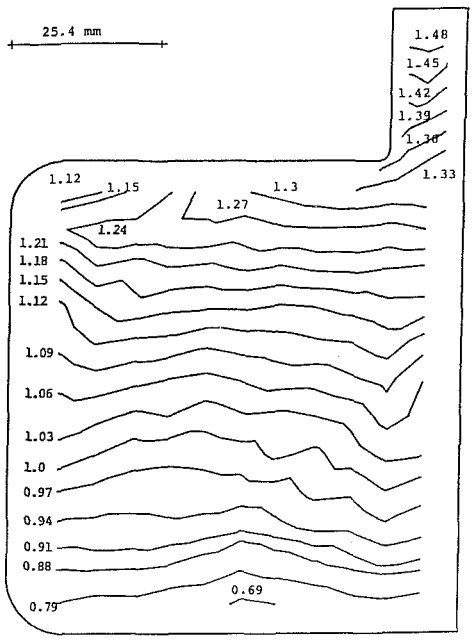

Fig. 4 Normalized circumferential velocity contours for cross section No. 2 ($\theta = 45$ deg)

angle which was found to vary between the vanes as determined by circumferential traverses.

Most turbine scroll designs [12–15] combine one-dimensional flow models with free vortex theory to determine either the scroll sectional area, or area to radius ratio variation along the circumference. While the purpose of these design methods is to provide uniform flow conditions around the nozzle periphery, Bhinder [16] reported that the measured flow angles in a vaneless turbine designed using this method showed significant variations around the rotor.

Codes for inviscid flow solutions in the rotors [17, 18] and scroll nozzle assemblies [19–21] do not reveal the secondary flow behavior, nor do they predict the flow losses. However, the numerical solutions of potential flow in scroll nozzle assemblies using the finite element method by Hamed et al. revealed circumferential variation in the flow angles at the vaneless nozzle exit [19, 20] and differences in the flow field and mass flow through the different vane passages [21].

One can conclude from the previous discussion that the three-dimensional flow behavior in the scroll and nozzle vanes, and the interaction between the scroll, nozzle, and rotor present a very complex flow field. Future developments of radial inflow turbines will depend on advanced theoretical research together with detailed experimental measurements in the various components in general and in the turbine scroll in particular.

The purpose of the present study is to obtain detailed measurements of the three velocity components through the scroll and the vaneless nozzles. The velocity measurements are obtained using Laser Doppler Velocimetry (LDV) and the experimental results are presented for the through and cross-flow velocities. The results show clearly the formation and development of the vortex pattern at the different scroll cross sections. The through-flow velocity patterns at the different cross sections reflect the complex interaction between the influence of the flow discharge to the nozzle and the cross velocity vortex pattern.

Experimental Setup

The experimental setup is shown schematically in Fig. 1. It consists of the test turbine, the seeding particle atomizer, the LDV, optical and data acquisition systems.

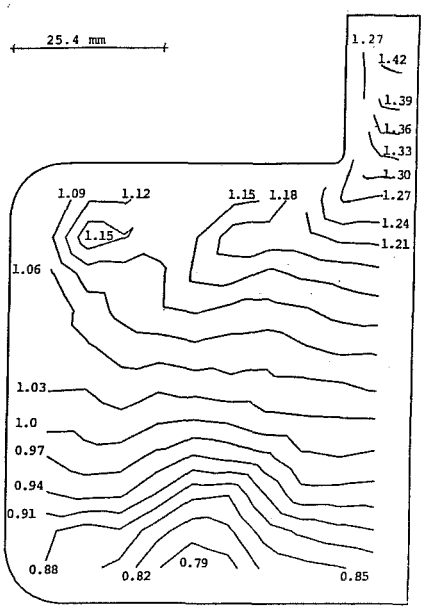

Fig. 5 Normalized circumferential velocity contours for cross section No. 3 ($\theta = 90$ deg)

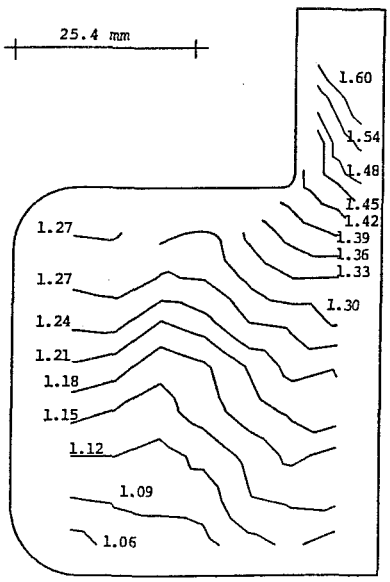

Fig. 7 Normalized circumferential velocity contours for cross section No. 5 ($\theta = 180$ deg)

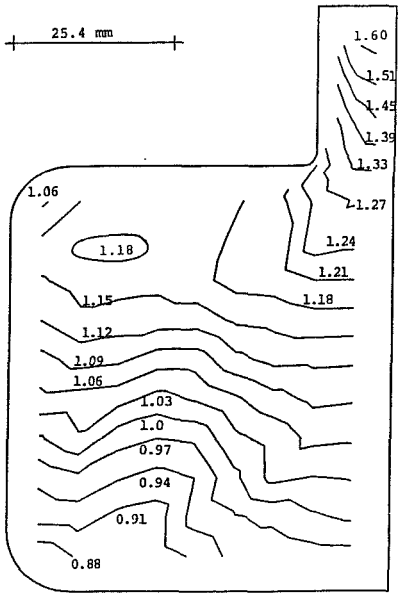

Fig. 6 Normalized circumferential velocity contours for cross-section No. 4 ($\theta = 135$ deg)

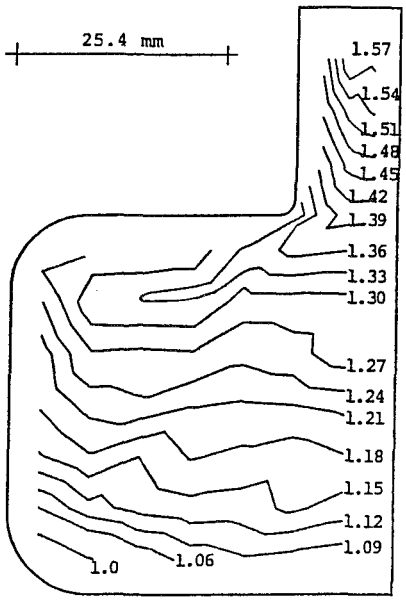

Fig. 8 Normalized circumferential velocity contours for cross section No. 6 ($\theta = 225$ deg)

Test Turbine. The turbine scroll has a nearly square cross section at the inlet and over most of the circumference. The asymmetric scroll cross section location relative to the nozzle is such that one side of the square cross section lines up with one of the nozzle side walls. This wall was made of 6.35-mm-thick plexiglass, through which the LDV measurements were obtained. The nozzle end walls are parallel and are 12.7 mm apart. The outer radius of the nozzle is 137.3 mm with a vaneless region followed by 18 nozzle vanes placed between the 112-mm and 82.6-mm radii. A rotor simulator, with no blades with an outer radius of 81.8 mm, follows the nozzle. A six-jet atomizer, which is connected to the bottom of the settling chamber through a 1.25-in-diameter flexible tube as shown in Fig. 1, was used to seed the flow with propylene glycol particles, at 1×10^5 particles/cm^3.

Laser and Optics. A 5-W argon-ion laser is used in the backward scatter mode to measure two simultaneous velocity components. Details of the laser, optics, and measuring volume were reported in [22].

The laser and optical systems are mounted on a table designed such that these systems can be traversed in the vertical direction, as well as along and perpendicular to the laser and optical axis in the horizontal plane. The whole table is mounted on a platform that rotates about a vertical axis. This additional degree of freedom was used to obtain measurements through inclined angles to the measuring surfaces. This technique was found to improve the signal-to-noise ratio, by reducing the effect of glare induced by the reflections from the plexiglass and scroll walls. Finally, the mountings of the sending and receiving optics are designed to allow for rotation around the optical axis up to 90 deg. This makes it possible to obtain the measurements of the two velocity components at an arbitrary angle to the vertical and horizontal directions.

Velocity Measuring Technique. A Digital MINC 11/23 minicomputer, equipped with preamp, a/d converter, and a clock modulus, was used on-line to acquire synchronized data for the simultaneous measurements of two perpendicular velocity components. A code was developed such that the data

set is tagged in the computer memory only if the time between the two data ready signals is less than a specified time. In the present experiment, the synchronization condition was set at 5 μs. In addition, time was allowed for the particle to clear the measuring volume before acquiring new velocity data, to insure that the sampled data are not obtained more than once from the same particle.

The experimental flow velocity measurements were obtained in the scroll and unvaned nozzle cross sections 1 through 8 which are shown in Fig. 2. Measurements were also obtained at seven additional sections, 9 through 15, located around the scroll tongue to investigate the details of the three-dimensional flow field in that region. The 758 measuring points were spaced at 3.175 mm (1/8 in.) intervals in both radial and axial directions in the vaneless nozzle region and at 6.35 mm (1/4 in.) intervals in the scroll sections. The signal-to-noise ratio was found to be unacceptably low for the velocity measurement close to the plexiglass when the optical axis was perpendicular to that surface. For that reason and to reduce the effect of glare, most of the flow velocity measurements were obtained with the optical axis not perpendicular to the measuring surface. This was accomplished either by keeping the turbine plexiglass back surface in a vertical position and rotating the laser-optics table platform in the horizontal plane or by fixing the optics axis and rotating the turbine and flow adapter around the horizontal line perpendicular to the optical axis. The first method was used in sections 1, 5, and 9 through 15 and the second in sections 2, 3, 4, 6, 7, and 8. Using this technique, some of the measuring points were blocked either by the scroll outer surface or by the surface of the unvaned nozzle. Since these blocked measuring points were deep and far from the plexiglass surface, which induced most of the glare reducing signal-to-noise ratio, one set of velocity measurements at these points was conducted with the optical axis perpendicular to the plexiglass surface. In some of the velocity measurements, a 40 MHz Bragg cell was introduced with downmixer in one of the colors to obtain frequency offsets ranging between 0 and 5 MHz. This was necessary to resolve the ambiguity in the direction of the radial velocity in the scroll at sections 1, 3, 5, and 7.

Uncertainty Analysis. The experimental uncertainties for the different variables and parameters are evaluated based on the methods described in [23–26]. An analysis [27] was conducted to optimize the number of velocity samples collected from the two velocimeter channels in order to reduce the statistical errors. Following the method of [27], the optimum size of the data ensemble was found to be 20. A sample size of

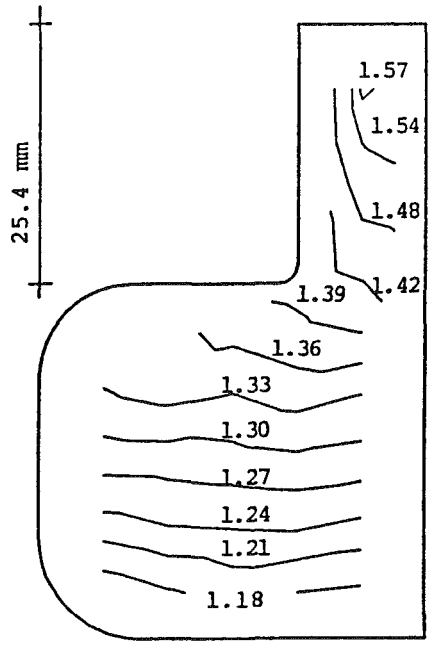

Fig. 9 Normalized circumferential velocity contours for cross section No. 7 ($\theta = 270$ deg)

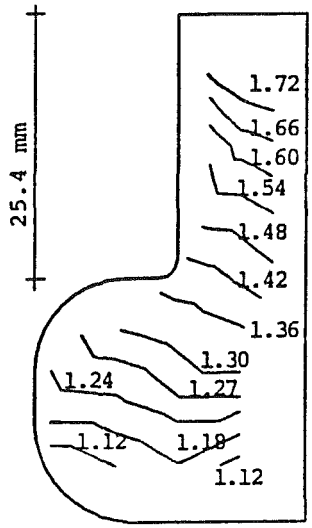

Fig. 10 Normalized circumferential velocity contours for cross section No. 8 ($\theta = 315$ deg)

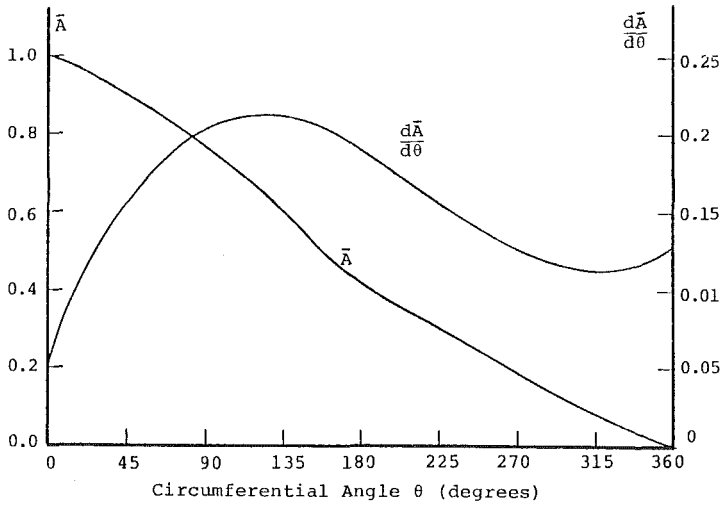

Fig. 11 Variation of the normalized scroll cross-sectional area and $d\bar{A}/d\theta$ with the circumferential angle

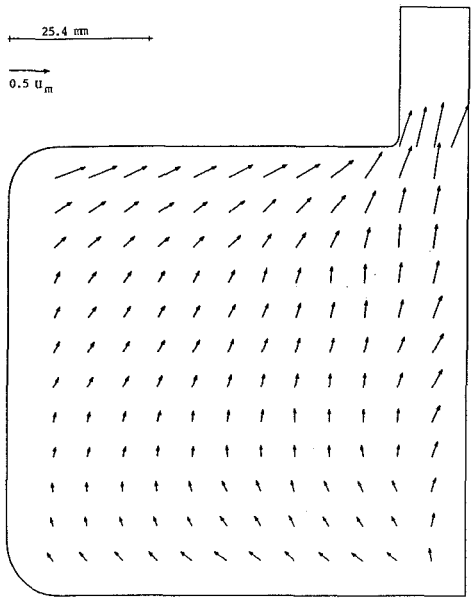

Fig. 12 Cross-flow velocity vectors for cross section No. 1 ($\theta = 0$ deg)

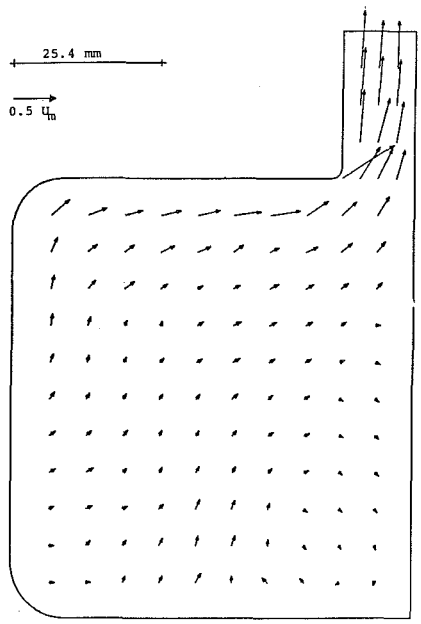

Fig. 14 Cross-flow velocity vectors for cross section No. 3 ($\theta = 90$ deg)

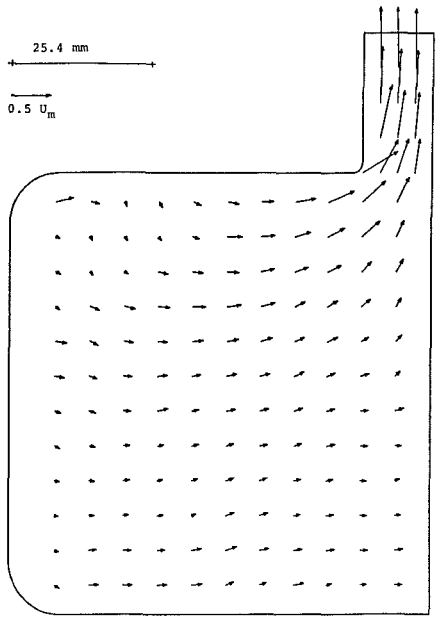

Fig. 13 Cross-flow velocity vectors for cross section No. 2 ($\theta = 45$ deg)

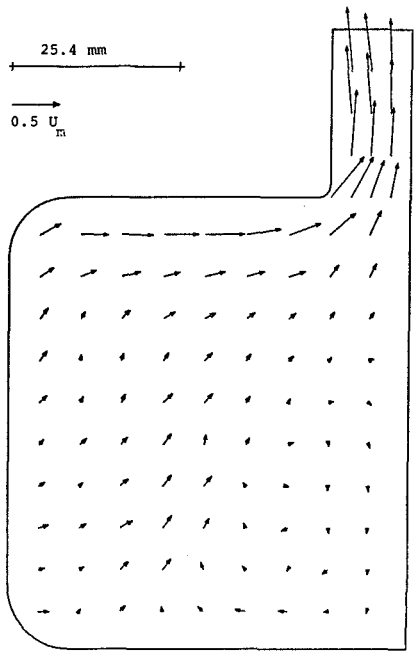

Fig. 15 Cross-flow velocity vectors for cross section No. 4 ($\theta = 135$ deg)

50 was used in the experiment to obtain the present results, without affecting the sampling time appreciably.

The uncertainties associated with the LDV measurements are listed below.

Results and Discussion

The high-pressure air supply from air storage tanks is regulated to a pressure of 1.379×10^5 N/m^2 gauge (20 psig) at the orifice meter, using a pressure-regulating valve, to give an air mass flow rate of 0.0907 kg/s (0.2 lb/s). This corresponds to a Reynolds number of 0.58536×10^5, based on the scroll inlet hydraulic diameter of 0.08452 m (0.2773 ft) and the cold air properties at 20°C (68°F). The results are presented for the three velocity components in the circumferential, radial, and axial directions, U_θ, U_r, and U_z, respectively, normalized with respect to the inlet mean velocity U_m, which is equal to 10.36 m/s (34.0 ft/s). The results of the velocity measurements are presented in Figs. 3–10 and 12–19.

Figures 3–10 show the measured through-flow velocities in the scroll sections 1 through 8. The contours have been drawn using linear interpolation between the measurement points, but with no extrapolation outside the measuring mesh. The influence of the scroll passage curvature is reflected in the gradient of the circumferential velocity in the radial direction. This influence can be observed in all figures, and it is present even at section 1 (Fig. 3). One can see in the same figure that the radial gradient in the through-flow velocity is much higher near the radially outward scroll surface due to the lower measured velocities in the flow boundary layer. Figure 4 shows that the slower boundary layer flow over the outer scroll curved surface is seen to move radially away from the two end walls and accumulate halfway between the scroll plane surfaces after a 45 deg turning angle. In a curved duct with plane endwalls, the slower endwall boundary layer flow moves under the influence of the pressure field away from the pressure side (outer radius) and toward the suction side (inner radius). This generates two counterrotating vortices, which cause lateral motions in the curved wall boundary layers [28].

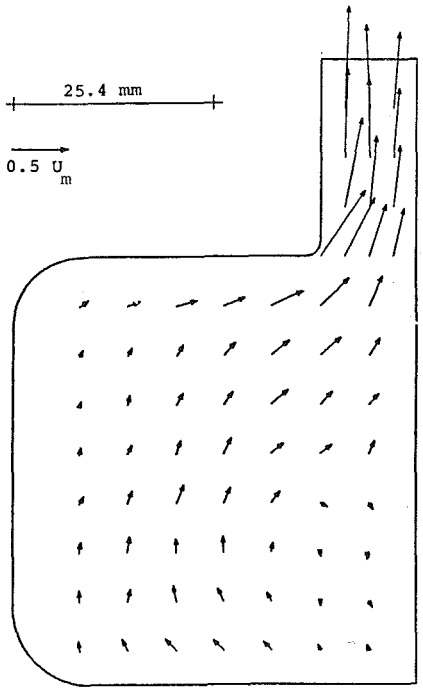

Fig. 16 Cross-flow velocity vectors for cross section No. 5 ($\theta = 180$ deg)

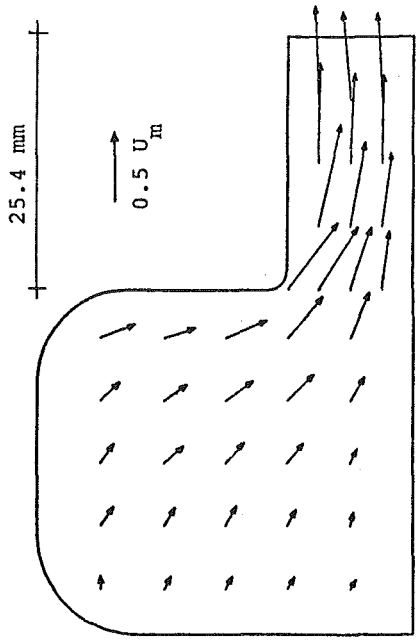

Fig. 18 Cross-flow contours for cross section No. 7 ($\theta = 270$ deg)

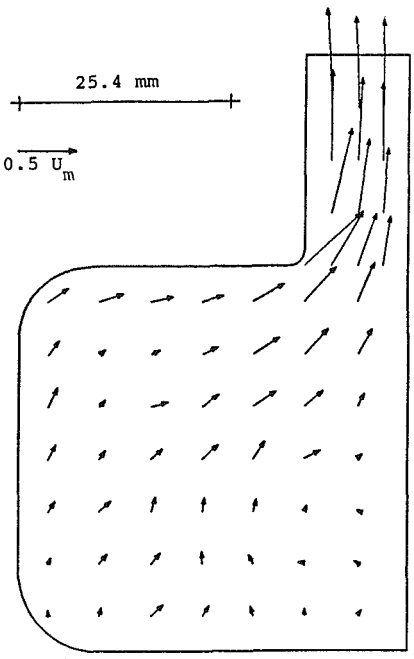

Fig. 17 Cross-flow velocity vectors for cross section No. 6 ($\theta = 225$ deg)

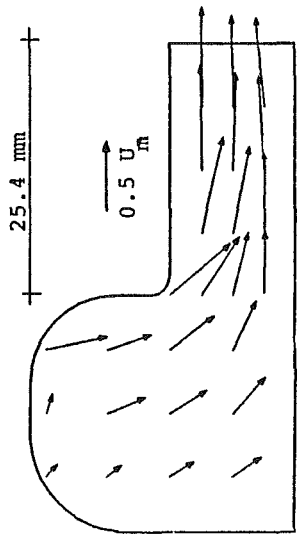

Fig. 19 Cross-flow velocity vectors for cross section No. 8 ($\theta = 315$ deg)

The slower boundary layer accumulation at the curved outer surface of the scroll halfway between the end walls, and at the corner of the curved inner surface furthest from the nozzle, does not conform with the familiar pattern in curved ducts. Figure 5 demonstrates that the same trend continues and becomes more predominant at section 3, where larger regions of slower moving flows are observed in the same two locations. One can see from Figs. 6 and 7 that the outer scroll curved surface boundary layer flow accumulation later moves away from the plexiglass surface and toward the other corner. An examination of Figs. 6–10 reveals that the slower moving flow regions do not grow further but start to diminish at section 4 (135 deg turning angle) and continuously decrease at subsequent sections. In order to find an explanation for this behavior, the scroll cross-sectional area variation and its rate of change were calculated and plotted in Fig. 11. This figure reflects a maximum rate of area change at section 4 (135 deg turning angle). In addition, the influence of discharge flow progressively extends over large portions of the scroll cross sections leading to higher flow velocities in the later cross sections. Both these factors combined provide an explanation of the above-mentioned favorable boundary layer behavior. The circumferential velocity contours, which are initially cylindrical near the nozzle at section 1, are also seen to distort at later sections under the influence of flow discharge to the nozzle.

Figures 12–19 show the combined flow velocity component in the cross-sectional plane as determined from the experimental values of the radial and axial velocity components. Figure 12 shows that the cross velocities are predominantly in the radially inward direction at the first measuring section 1. This radially inward motion of the flow is mainly to accommodate the establishment of a free vortex variation of the cir-

Table 1 Maximum possible uncertainties

Parameter	Bias	Precision
Longitudinal and lateral traverses (x, y)	±0.13 mm	±0.025 mm
Vertical traverses (z)	±0.5 mm	±0.025 mm
Circumferential traverses (θ)	±0.16 deg	±0.07 deg
Optics axis or plexiglass surface angular position (α, ϕ)	±0.25 deg	–
Effect of plexiglass on measuring location	–	±0.32 mm
Effect of plexiglass on measuring volume	–	±0.57 mm
Average inlet mean velocity ($\bar{U}_m$)	±0.5 percent	±0.5 percent
Average circumferential velocity ($\bar{U}_\theta/\bar{U}_m$)	±3 percent	±1.7
Average radial velocity ($\bar{U}_r/\bar{U}_m$)	±3 percent	±1.5
Average axial velocity ($\bar{U}_z/\bar{U}_m$)	±3 percent	±2.0

cumferential velocity. It appears that once the free vortex pattern is established, the radial velocities are reduced and Fig. 13 shows that the cross velocities at section 2 (45 deg turning angle) are predominantly in the axial direction. Figures 14–17 show that a recirculating secondary velocity zone is established at the scroll corner between the outer curved scroll wall and the plexiglass plane wall. This has the opposite sense of rotation expected of one of the familiar two counterrotating vortices that would exist in this region in the case of a curved duct. Its influence does not extend to the curved inner wall, where the influence of nozzle flow discharge is more pronounced. There is no evidence of the presence of the familiar counterrotating vortices, since the rest of the flow moves somewhat around the corner vortex in the general direction along the diagonal between the outer corner and the nozzle inlet, with increasing cross velocities. The low-velocity boundary layer flow accumulation at the corner of the inner scroll curved surface away from the nozzle at section 2 (Fig. 4) can be explained by the relatively strong radial inward velocity at section 1.

The velocity measurements around the tongue and the turbulent measurements will be reported at a later date in a NASA Report.

Conclusion

One can conclude from the previous results that the flow pattern in the scroll is strongly influenced by the geometry of the scroll cross sections and scroll-to-nozzle transition, as well as by the scroll area variation around the circumference. The accumulation of the low-energy flow regions, which affects the loss, is determined by the cross-sectional geometry. The cross velocities show the presence of one vortex, not the familiar two counterrotating vortices in curved ducts. The low energy accumulation is dominated by the cross-velocity pattern in the earlier scroll sections. At later sections, the flow discharge through the nozzle becomes more dominant and its influence is reflected in both through-flow velocity and cross-velocity patterns. In the present results the recirculating flow zone is limited to the corner between the outer scroll curved surface and the plexiglass wall and is observed in the cross sections at 45 to 270 deg turning angles.

Acknowledgments

This research was sponsored by NASA Contract NAG3-26. Useful discussions with Mr. K. L. McLallin of NASA Lewis Research Center are gratefully acknowledged.

References

1 Benson, R. S., "An Analysis of the Losses in a Radial Gas Turbine," *Proc. Instn. Mech. Engrs.*, Vol. 180, Part 3J, 1966, pp. 41–53.

2 Hiett, G. F., and Johnston, I. H., "Experiments Concerning the Aerodynamic Performance of Inward Flow Radial Turbines," *Proc. Instn. Mech. Engrs.*, Vol. 178, Pt. 3I(ii), 1964, pp. 28–41.

3 Wallace, F. J., Baines, N. C., and Whitfield, A., "A Unified Approach to the One-Dimensional Analysis and Design of Radial and Mixed Flow Turbines," ASME Paper No. 76-GT-100.

4 Kastner, L. J., and Bhinder, F. S., "A Method for Predicting the Performance of a Centripetal Gas Turbine Fitted With a Nozzle-less Volute Casing," ASME Paper No. 75-GT-65.

5 Futral, S. M., and Wasserbauer, C. A., "Off-Design Performance Prediction and Experimental Verification for a Radial-Inflow Turbine," NASA TND-2621, 1965.

6 Todd, C. A., and Futral, S. M., "A Fortran IV Program to Estimate the Off-Design Performance of Radial Inflow Turbines," NASA TND-5059, 1969.

7 Tabakoff, W., Vittal, B. V. R., and Wood, B., "Three Dimensional Flow Measurements in a Turbine Scroll," NASA CR-167920 Report, 1982.

8 Tabakoff, W., Wood, B., and Vittal, B. V. R., "Three Dimensional Flow Measurements in a Vaneless Radial Turbine," NASA CR-167994, Aug. 1982.

9 Tabakoff, W., Vittal, B. V. R., and Wood, B., "Three-Dimensional Flow Measurements in a Turbine Scroll," ASME JOURNAL OF ENGINEERING FOR GAS TURBINES AND POWER, Vol. 106, 1984, pp. 516–522.

10 Khalil, I. M., Tabakoff, W., and Hamed, A., "Losses in Radial Inflow Turbines," ASME *Journal of Fluids Engineering*, Vol. 98, Sept. 1976, pp. 364–373.

11 Hashemi, S. G. R., Lemak, R. J., and Owczarek, J. A., "An Investigation of the Flow Characteristics and of Losses in Radial Nozzle Cascades," ASME JOURNAL OF ENGINEERING FOR GAS TURBINES AND POWER, Vol. 106, 1984, pp. 502–510.

12 Chapple, P. M., Flynn, P. F., and Mulloy, J. M., "Aerodynamics Design of Fixed and Variable Geometry Nozzleless Turbine Casings," ASME JOURNAL OF ENGINEERING FOR POWER, Vol. 102, Jan. 1980, pp. 141–147.

13 Risika, J. W., et al., "The Design and Performance Analysis of Radial Inflow Turbines," Northern Research and Engineering Corp., Cambridge, MA, Reports No. 1067-1 and 1067-2, 1964.

14 Brown, W. B., and Bradshaw, G. R., "Method of Designing Vaneless Diffusers and Experimental Investigation of Certain Undetermined Parameters," NACA TN 1426, 1947.

15 Brown, W. B., and Bradshaw, G. R., "Design and Performance of Family of Diffusing Scrolls With Mixed-Flow Impeller and Vaneless Diffuser," NACA TN 936, 1947.

16 Bhinder, F. S., "Investigation of Flow in the Nozzle-less Spiral Casing of a Radial Inward-Flow Gas Turbine," *Proc. Inst. Mech. Engrs.*, Vol. 184, Part 3G(11), 1969–1970, pp. 66–71.

17 Katsanis, T., "Revised Fortran Program for Calculating Velocities and Streamlines on the Hub-Shroud Midchannel Stream Surface of an Axial-, Radial- or Mixed-Flow Turbomachine or Annular Duct. I: User's Manual," NASA TND-8430, July 1977.

18 Katsanis, T., "Computer Program for Calculating Velocities and Streamlines on a Blade-To-Blade Stream Surface of a Turbo-machine," NASA TND-4525, 1968.

19 Hamed, A., and Abou Ghantous, C., "Three-Dimensional Flow Computations in a Turbine Scroll," NASA CR 168003 Report, Aug. 1982.

20 Hamed, A., Tabakoff, W., and Malak, M. F., "The Three-Dimensional Compressible Flow in a Radial Inflow Turbine Scroll," GTSJ Paper No. 83-TOKYO-IGTC-66.

21 Hamed, A., and Baskharone, E., "Analysis of the Three Dimensional Flow in a Turbine Scroll," ASME *Journal of Fluids Engineering*, Vol. 102, No. 3, 1980, pp. 297–301.

22 Hamed, A., and Malak, M. F., "LDV Measurements of Three Dimensional Flow Development in a Curved Rectangular Duct With Inlet Shear Profile," AIAA 17th Fluid Dynamics, Plasma Dynamics and Lasers Conference, June 15–17, 1984, Snowmass, CO, Paper No. AIAA-84-1601.

23 Kline, S. J., "The Purposes of Uncertainty Analysis," ASME *Journal of Fluids Engineering*, Vol. 107, June 1985, pp. 153–160.

24 Abernathy, R. B., Benedict, R. P., and Dowdell, R. B., "ASME Measurement Uncertainty," ASME *Journal of Fluids Engineering*, Vol. 107, June 1985, pp. 161–164.

25 Smith, R. E., and Wehofer, S., "From Measurement Uncertainty to Measurement Communications, Credibility and Cost Control in Propulsion Ground Test Facilities," ASME *Journal of Fluids Engineering*, Vol. 107, June 1985, pp. 165–172.

26 Moffat, R. J., "Using Uncertainty Analysis in the Planning of an Experiment," ASME *Journal of Fluids Engineering*, Vol. 107, June 1985, pp. 173–178.

27 Snyder, P. K., Orloff, K. L., and Reinath, M. S., "Reduction of Flow-Measurement Uncertainties in Laser Velocimeters With Nonorthogonal Channels," *AIAA Journal*, Vol. 22, No. 8, Aug. 1984, pp. 1115–1123.

28 Hawthorne, W. R., "Secondary Circulation in Fluid Flow," *Proc. Roy. Soc.*, Vol. A206, 1951, pp. 374–387.

S. Wittig
Professor.

K. Dullenkopf
Research Assistant.

A. Schulz
Research Assistant.

R. Hestermann
Research Assistant.

Lehrstuhl und Institut für
Thermische Strömungsmaschinen,
Universität Karlsruhe (T.H.),
D-7500 Karlsruhe 1,
Federal Republic of Germany

Laser-Doppler Studies of the Wake-Effected Flow Field in a Turbine Cascade

The interaction between consecutive blade rows can be expected to have important effects on the heat transfer in cooled gas turbine cascades. In determining the local heat transfer under the influence of wake flow, nonintrusive optical measuring techniques were used to obtain the flow velocities and turbulence structures in the cascade inlet flow as well as along the test blade's surface. The main purpose of the measurements is to provide accurate experimental data for the development of predictive codes. The applicability primarily of the laser-Doppler technique is discussed and problems arising from the use of laser-dual-focus anemometry are reported. In simulating the effects of wake flow, a plane airfoil was traversed in front of the cascade. Both the axial distance between the airfoil and the cascade and the position in circumferential direction were changed in discrete steps. Turbulence intensities between 1.4 and 15 percent were recorded in cold gas flow. The effects on the blade heat transfer are illustrated.

Introduction

The development of high-performance gas turbines has always been connected with a rise of the thermal efficiency primarily due to the increasing turbine inlet temperatures and simultaneously increasing pressure ratios. Obviously, the high thermal loads of the turbine components exceedingly surpass the allowed data of modern alloys. Cooling, therefore, is a necessity which also has to be viewed with respect to safety and reliability. The durability analysis of turbine blades in a jet engine requires detailed knowledge of the heat transfer from the fluid to the blade surface, which has been of longstanding interest.

The heat transfer along turbine blades is determined by a variety of different parameters such as turbulence intensity, pressure gradient, curvature, temperature ratio between gas and blade surface, and periodic flow variations due to interaction of rotor and stator. As a consequence of the relative motion of stationary and rotating rows in an axial compressor or gas turbine, the flow around the blades is highly unsteady.

Measurements to predict the effects of a "wake-passing flow" on the heat transfer to turbine blades have been obtained by Bayley and Milligan [1]. They used a rotating (squirrel-type) cage as a turbulence generator, mounted upstream of a turbine cascade. In continuing this effort, Bayley and Priddy [2, 3] used this arrangement to demonstrate a strong dependence of the heat transfer on the turbulence induced. The frequency of the perturbation, however, was of minor importance. Utilizing a similar experimental setup Pfeil et al. [4, 5] analyzed the transition characteristics along a flat plate.

The influence of an unsteady wake flow on the heat transfer characteristics of a gas turbine blade has been described by Doorly et al. [6]. The short-duration wind tunnel experiment, however, did not provide a detailed flow analysis.

Several aspects of the wake influence on the heat transfer in an actual turbine have been described by Stöcker [7, 8].

In our opinion, a separation of the various effects is necessary for a full understanding of the heat exchange phenomena. In addition, it should be possible to support generalizations and similarity considerations. It should, however, be recognized that true wake effects are to be studied for a final comparison.

In the larger context of the present experimental and analytical study, Rüd et al. [9–11] made an attempt to describe the effects of turbulence parameters, pressure gradients, and temperature ratios on the heat transfer along a convectively cooled flat plate. Corresponding to these heat transfer measurements, Eriksen et al. [12–16] investigated the velocity profiles and turbulence intensities and associated moments of the plane boundary layer flow by means of laser-Doppler and laser-dual-focus velocimetry. The influence of different isotropic free-stream turbulence intensities and temperature ratios on the heat transfer along a turbine blade was the subject of several previous investigations by Wittig et al. [16–18]. In continuing the basic studies, an attempt was made to determine the influence of a wake flow with its turbulence structure on the heat transfer characteristics along the turbine blade (see Wittig et al. [17, 18]). For a detailed understanding, laser-velocimetry investigations of the wake flow, the cascade inlet flow, and the flow around the test blade were found to be of major interest and are discussed in the present paper.

Principally, a cascade consisting of five blades is subjected

Contributed by the Gas Turbine Division of THE AMERICAN SOCIETY OF MECHANICAL ENGINEERS and presented at the 31st International Gas Turbine Conference and Exhibit, Düsseldorf, Federal Republic of Germany, June 8–12, 1986. Manuscript received at ASME Headquarters February 7, 1986. Paper No. 86-GT-160.

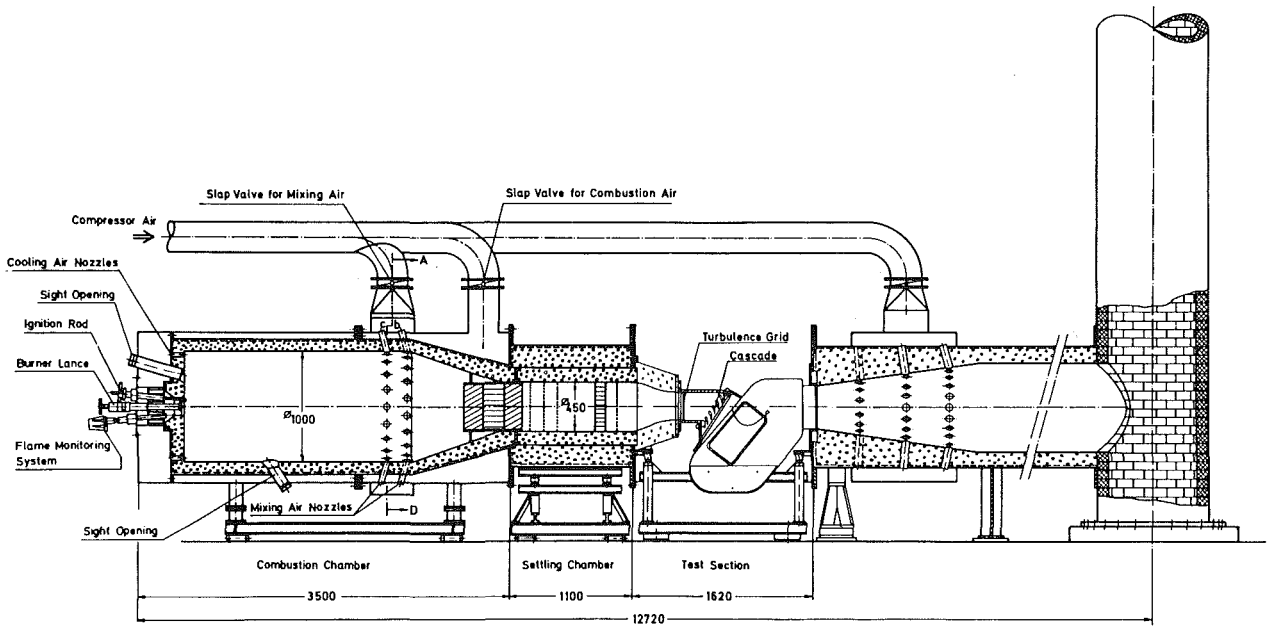

Fig. 1 High-temperature test facility

to the wake of a plane airfoil of similar design. The wake-producing airfoil is traversed in discrete steps in front of the cascade at different axial distances from the leading edge. This can be viewed as a first approximation of the real unsteady process within the turbine. The inlet conditions, thus, correspond to the design conditions. The wake cutting, though, is not verified. The approach is similar to that chosen by Stöcker [7, 8] in obtaining the temperature distribution, for this approach is to be seen in the attempt to resolve in a first step the effect of the turbulence characteristics of the wake on the heat transfer by comparing it with the measurements at isotropic mean flow turbulence.

Experimental Setup

The hot gas tunnel used for the experiments has been described previously [17] and is shown in Fig. 1. Air from the compressor is heated in the primary zone of an oil-fired combustor. Primary air and fuel injection are chosen and secondary air is added by means of 40 circumferential injection holes for the adjustment of the temperature level. A maximum thermal power of 2 MW can be verified in the combustor with maximum temperatures up to 1500°C. However, for reasons of accurate data acquisition lower temperatures are generally chosen.

The temperature and velocity profiles at the exit of the combustor which are not uniform originally are equalized in a settling chamber equipped with specially designed mixers and honeycombs. At the end of the settling chamber a probe is mounted to seed the flow with tracer particles. Relatively high accelerations are subsequently induced by a nozzle with rectangular cross section equipped with a transition from the circular settling tank.

The test section entrance itself has a cross section of 250 × 100 mm (see Fig. 2). In exiting the test section, the hot gas flow is mixed with additional air for cooling purposes and exhausted. Special inserts behind the cascade serve to avoid circulation and vortices re-entering the test section and influencing the measurements. Within limited ranges, independent variation of pressure and temperature can be accomplished.

In simulating the effects of wake flow, a straight blade profile is mounted in the cascade entrance flow. To achieve relatively realistic flow conditions, the relative location of the wake flow can be changed. The traverse of the airfoil is illustrated in Fig. 2. The mechanism allows a parallel displacement in front of the cascade. The profile of the wake-producing airfoil is derived from the thickness distribution of the test blade. Figure 3 demonstrates the geometric arrangement of the cascade and the leading airfoil.

The cascade consists of five untwisted blades as shown in Fig. 3. Basically it is a high-performance profile. The three inner blades are fixed between transparent windows. At lower temperatures Lucite of 10 mm thickness has been used. It is therefore possible to achieve optical accessibility of the flow field around the central measurement blade with its adjacent flow channels as well as the entering flow area ahead of the leading edge. For an optimum signal quality and in order to avoid background light scatter the blades were covered by a matte black coating (compare Fig. 3).

Optical Techniques

The optical system, using a forward scattering one-component fringe-type arrangement, is shown in Fig. 4. In earlier papers [15, 16] we described the principal components of the setup and the data acquisition and reduction. In order to obtain better signal-to-noise ratios, only the forward scattering mode was used. The modular optic is equipped with an argon-ion laser operating at a wavelength of 488 nm with a maximum power of 1 W. The incoming laser beam is split into

Nomenclature

a = axial distance between airfoil and cascade inlet plane
l = chord length
Ma = Mach number
Re = Reynolds number
s = distance along surface
T = temperature
t = blade spacing
Tu_u = turbulence intensity in mean flow direction
Tu_v = turbulence intensity perpendicular to the mean flow direction
u = velocity
u^* = velocity at cascade inlet plane
x = airfoil position with respect to the test blade's stagnation plane
α = heat transfer coefficient
λ = wavelength

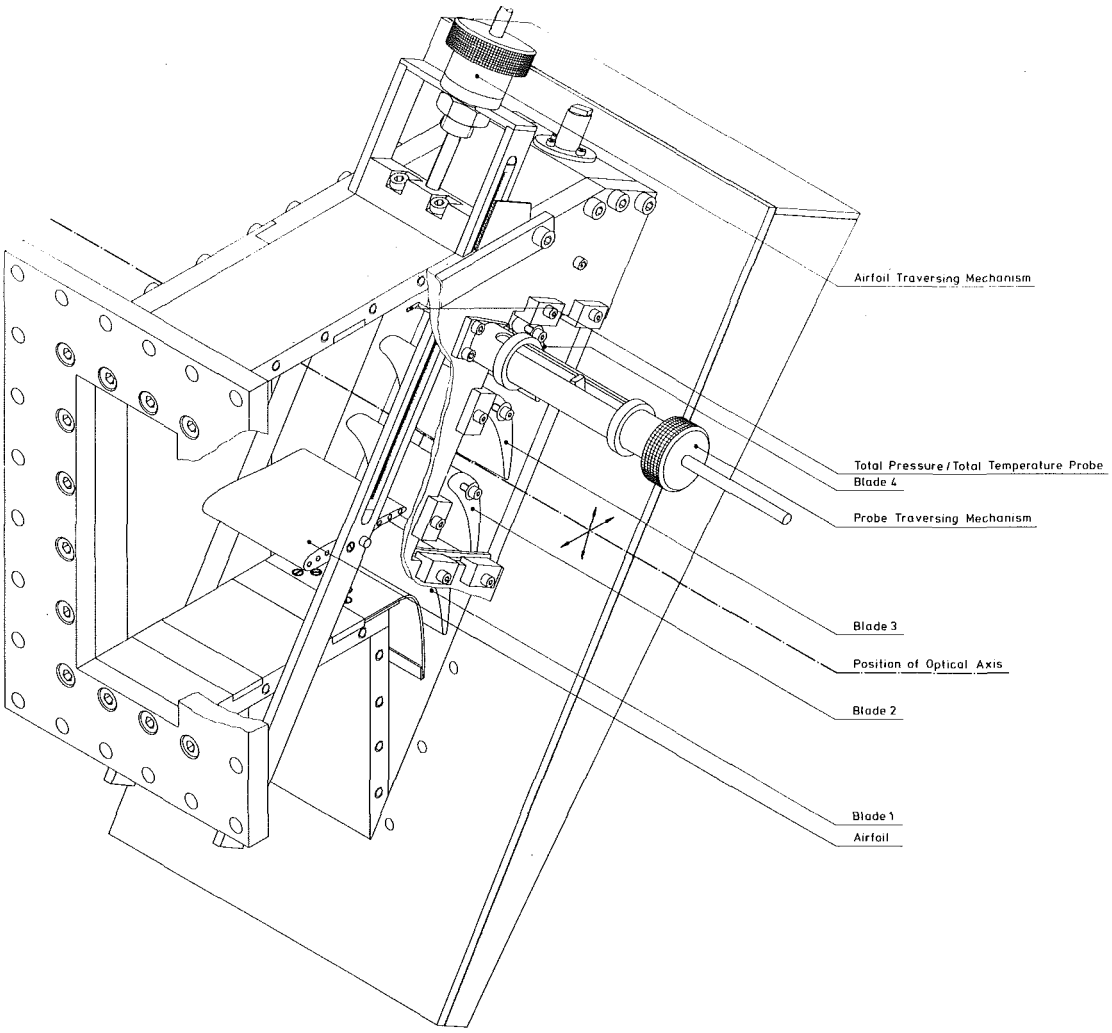

Fig. 2 Test section

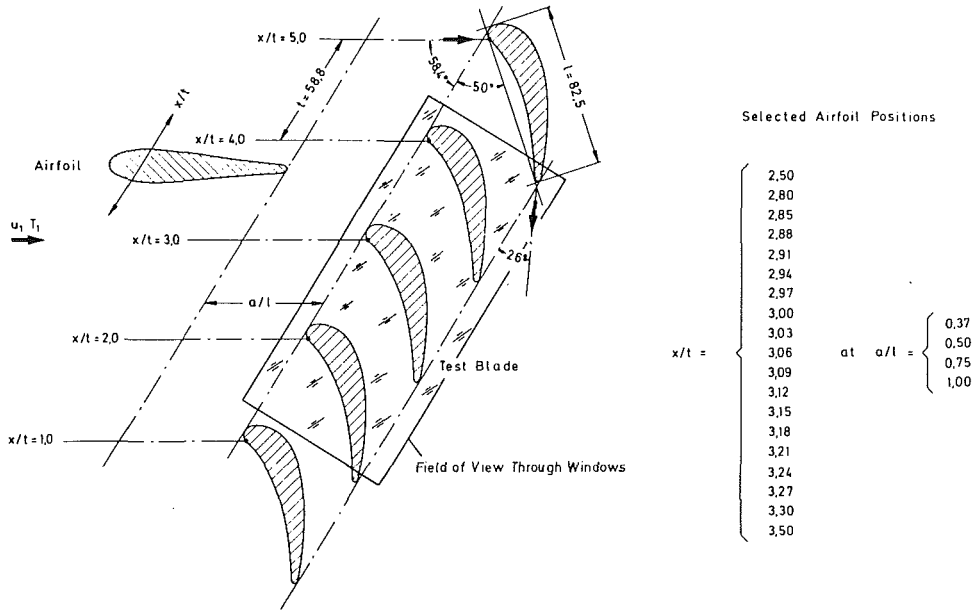

Fig. 3 Arrangement of the cascade and the airfoil

two parallel beams of equal intensity, passing thereafter through a Bragg cell unit in which a frequency shift can be achieved. The following unit serves to reduce the spatial distance between the two beams from 60 mm to 30 mm or 15 mm. The two parallel beams are then brought to a common focus by a lens. The dimensions of the probe volume are 0.22 mm in diameter and 4 mm in length. The scattered light from both beams is collected at the opposite side of the hot gas tun-

nel by a lens and focused by another lens onto a pinhole aperture in front of the photomultiplier tube, reducing the effective diameter of the probe volume to 0.1 mm.

The sending and receiving optics are separately supported by coordinate platforms which facilitate an accurate positioning of the probe volume within ± 10 μm. The Doppler frequencies are detected by means of a TSI 1990 500 MHz signal processor connected via a parallel line unit with a PDP 11/34 computer for fast data acquisition and reduction. Each measuring point is based on 2000 counts for a one-dimensional analysis or 6000 counts for a two-dimensional analysis. These large numbers of single counts provide good reproducibility in the fluctuating components. Calculations of mean values and fluctuating components for one and two-dimensional measurements have been widely discussed in the literature [19, 20], along with the capability to use a single component optic for two-dimensional measurements.

For determination of the fluid velocity, laser-velocimetry techniques depend on tracer particles in the fluid. However, the natural seeding level is often too low. In the present study a seeding of the flow was necessary. In optimizing all parameters of importance, it was found that SiO_2 particles with a mean diameter of 0.5 μm and a density ratio of only 50 – which can be achieved by a special technique – lead to the best results. A detailed description of the special fluidized bed seeding system and the measurements of the size distribution of the particles has been discussed earlier [12, 13].

In recognizing the specific advantages of the laser-dual-focus velocimetry, particularly the high signal-to-noise ratio as well as the small probe volume, additional efforts have been directed toward the application of this technique. Despite excellent results which were achieved in a variety of other studies [12–16], two main disadvantages of the LDF system prevented its convenient use in the present investigation. Primarily the extended measurement times have to be mentioned, as data under at least eight different angles are necessary for a sufficient statistical data base, whereas LDA measurements require only three. In addition, relatively low reproducibility is achieved at low turbulence levels in recording the fluctuating components of the velocities u' and v' with the LDF velocimeter. In the meantime, however, a solution has been found by improving data acquisition and processing.

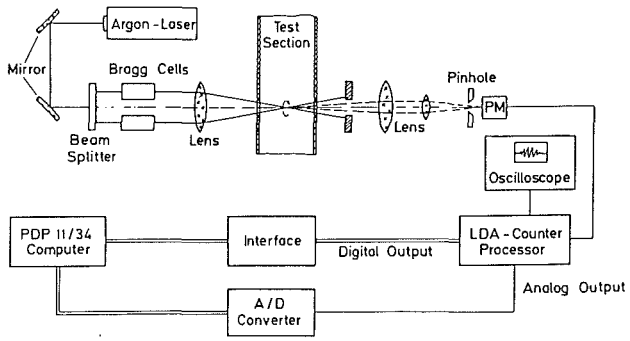

Fig. 4 Laser-Doppler anemometer

Results

As can be seen from Figs. 5–10, velocities as well as turbulence characteristics were recorded within the wake of the airfoil as well as within the cascade. The first step toward a correct interpretation of the measurements was to determine the effect of the wake-producing airfoil on the inlet flow to the cascade. During the measurements, the position of the LDA probe was held constant, whereas the airfoil was moved in discrete steps. It was therefore possible to avoid the possibly cumbersome adjustments of the receiving optics. The location of the probe volume was fixed on the cascade inlet plane between the second and third blade (x/t = 2.50).

The velocity profiles shown in Fig. 5 are normalized by the local undisturbed velocity u^*. For reasons of clarity, the profiles of u/u^*, Tu_u, and Tu_v are shown only for the relative axial positions of $a/l = 0.5$ and 1.0, respectively. As expected, a drastic rise of the turbulence levels can be observed within the wake, whereas the velocity variations are moderate. Furthermore, the turbulence shows an anisotropic characteristic. The results show that the location of maximum turbulence levels as well as the minima of the velocity change with the dimensionless distance from the airfoil. It should be noted that the flow at the cascade inlet plane without airfoil is already slightly skewed due to the cascade itself. The inlet flow angle at the cascade front was determined to be 13 deg. The effect of the inflow skewness, therefore, induces a certain asymmetry to the wake with respect to the measurement blade. The wake causes an increase in the turbulence level as well as a decrease in the velocity.

In principle the developed profiles are independent of the dimensionless distance. However, the size of the region influenced by the wake is proportional to the dimensionless distance a/l, whereas the magnitude of the disturbance caused by the wake is inversely proportional to a/l. The shift of the maxima toward smaller values of x/t with decreasing a/l results from the aforementioned skewness of the inlet flow. The observed increase in the velocity profile for $x/t \geq 2.60$ results from the displacement effect of the airfoil.

In conclusion, the wake primarily induces an increase of the turbulence level. The velocity drop due to the airfoil is – in contrast to the turbulence level – equalized sooner. The max-

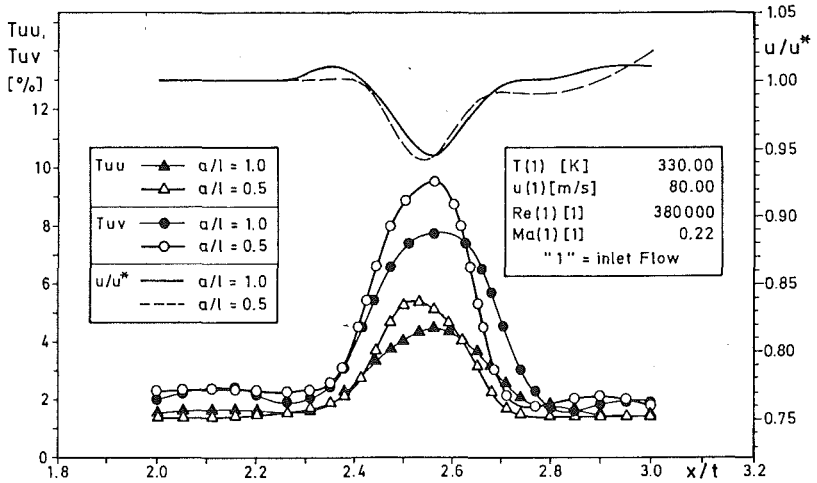

Fig. 5 Velocity and turbulence distribution of the wake flow

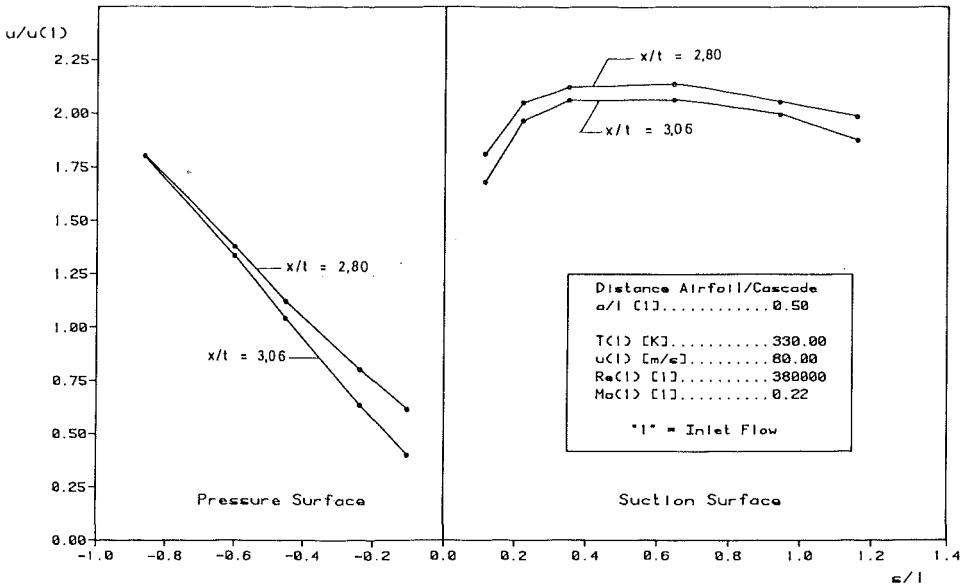

Fig. 6 Velocity distribution along the surface of the blade

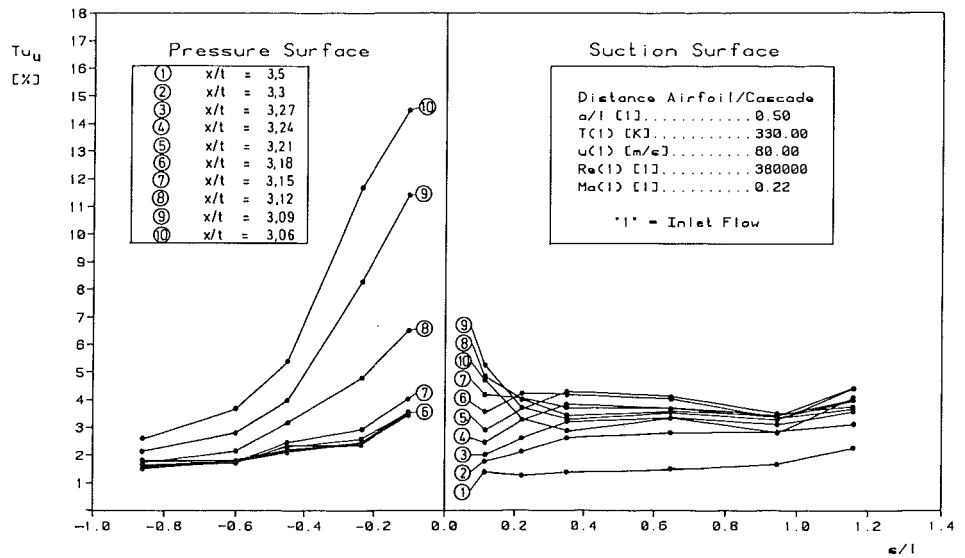

Fig. 7 Turbulence intensity along the surface of the blade ($x/t = 3.50$ to $x/t = 3.06$)

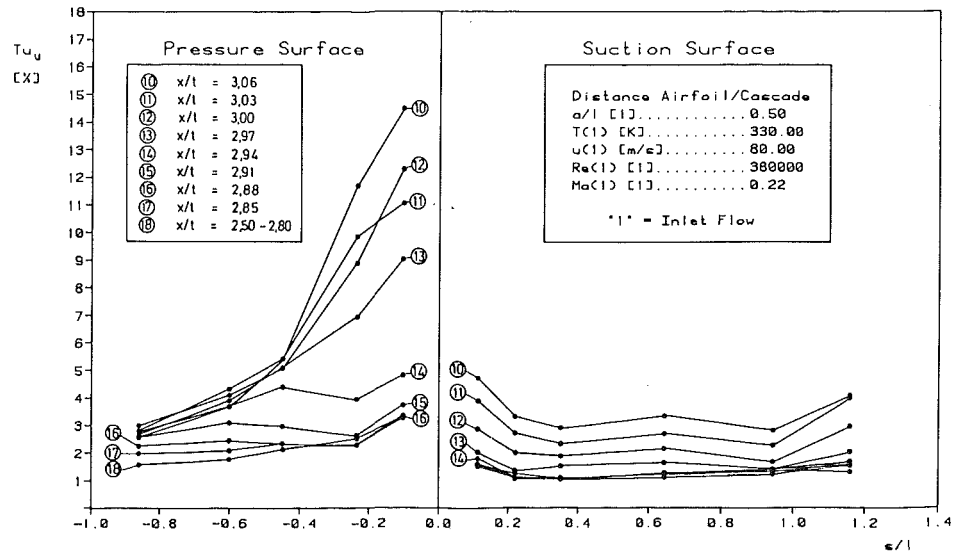

Fig. 8 Turbulence intensity along the surface of the blade ($x/t = 3.06$ to $x/t = 2.50$)

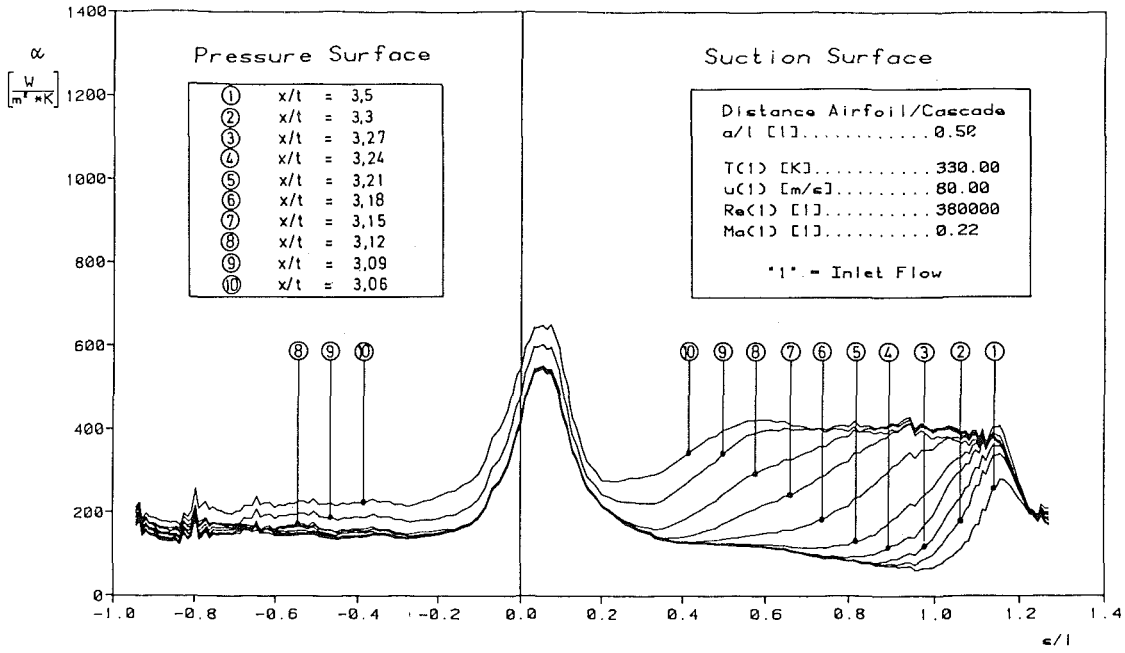

Fig. 9 Heat transfer coefficients along the surface of the blade ($x/t = 3.50$ to $x/t = 3.06$)

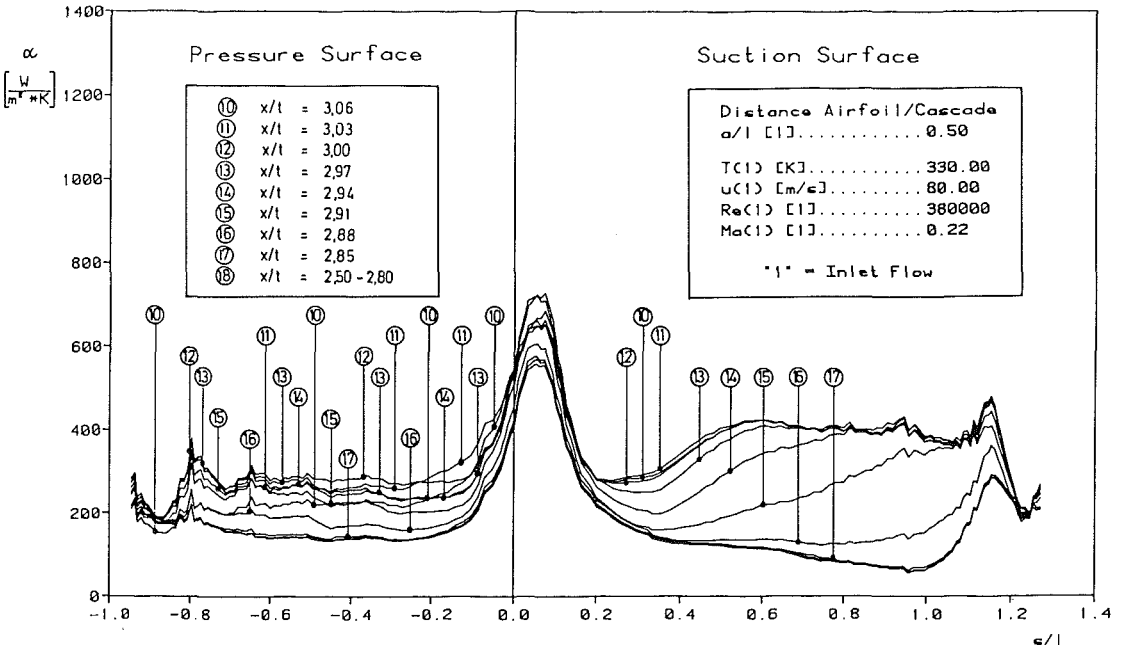

Fig. 10 Heat transfer coefficients along the surface of the blade ($x/t = 3.06$ to $x/t = 2.50$)

imum velocity difference within the wake amounts to approximately 6 percent at $a/l = 0.37$.

The effect of the wake on the velocity and turbulence distribution and finally on the heat transfer along the blades is illustrated in Figs. 6–10. The quantities $u/u(l)$, Tu_u, and α are plotted against the dimensionless surface length s/l, where l is the chord length of the blade. The measurements of the flow around the blade were obtained at the boundary layer edge. However, in regions of very thin boundary layer the measurements were obtained at locations as close as possible to the wall. A problem arose from the geometric arrangement of the LDA with respect to the cascade: As the two laser beams formed a plane parallel to the blade's surface, a relatively small rotation influences one of the beams which is shaded off by the blade itself. Only one-dimensional measurements therefore were conducted. The determination of the magnitude and direction of the actual velocity was iteratively carried out, starting with a probe volume orientation parallel to the tangent of the surface.

For reasons of clarity, only the distance $a/l = 0.5$ between the trailing edge and the entrance plane of the cascade is shown in Figs. 6–10. The Reynolds number in this case was 3.8×10^5.

Specifically the velocity distribution along the blade's surface at $a/l = 0.5$ is shown in Fig. 6 for two limiting cases, namely maximum disturbance due to the airfoil ($x/t = 3.06$), and no disturbance at all ($x/t = 2.80$). The development of the velocity distribution along the blade's surface is characterized by a very fast acceleration in the first part of the suction side, followed by a slight deceleration to the trailing edge. On the other hand, a constant acceleration can be seen along the whole pressure side. Furthermore, the effect of the wake on

the velocity distribution was determined. It is generally weak except in the vicinity of the stagnation point. This is due to the aforementioned equalization of the velocity profile.

As can be seen from Figs. 7 and 8, the effect of the wake on the turbulence is considerably higher. It should, however, be mentioned that the dimensionless turbulence levels depend on the value of the local velocity. This partly explains the differences in the turbulence levels between the pressure and the suction side of the blade. For further use in numerical analysis and correlations, this approach in presenting the data had to be chosen. If the airfoil is moved from the top position (x/t = 3.50) toward the stagnation point position of the test blade, the pressure side remains unaffected for values of $x/t \geq 3.15$. Beyond this position the entire pressure side is affected by the wake almost simultaneously. Due to the constant and moderate acceleration over the pressure side, the wake effects are obviously strong, especially on the leading third. With a decrease of the wake intensities due to the continuing motion of the airfoil, the turbulence decays, with the trailing edge of the pressure side showing the lowest decay rate.

In passing by the airfoil, the suction side of the blades within the cascade is affected prior to the pressure side. As can be seen in comparing the results of Fig. 7, the turbulence level first increases at the trailing edge, as this is the first part to be affected. This is also supported by Fig. 9. The leading part of the blade shows a delayed rise in the turbulence level.

Further positioning of the airfoil to $x/t \leq 3.15$ causes an increase of the turbulence level in the frontal area of the blade followed by a decrease over the whole surface after passing the stagnation point position.

The development of the turbulence levels in the direct vicinity of the stagnation point is of particular interest. In this region, the turbulence levels increase drastically with the drop of x/t below a value of 3.18. A thorough examination of curves 6–8 in Fig. 7 shows that extremely high levels of turbulence are to be expected in the direct vicinity of the stagnation point. This expectation is strongly backed by the high values of the heat transfer coefficients observed in this region, which will be discussed later. Unfortunately, we were unable to obtain reliable data from LDA measurements as strong velocity gradients and curvature effects are of dominant influence.

A comparison of the heat transfer and turbulence measurements illustrates the strong relation between the local values of the free-stream turbulence and the heat transfer coefficients (see Figs. 7 and 9 as well as Figs. 8 and 10). This is especially obvious for the pressure side. By traversing the airfoil toward lower x/t values a significant increase in the heat transfer coefficient was observed at those locations which experience a high turbulence level. Similar observations were discussed in our previous contributions [9–11, 14, 18].

On the other hand, the conditions are significantly more complex on the suction side. Here, the local heat transfer coefficient is not only affected by the turbulence levels but also by the transition region from laminar to turbulent boundary layer. It is interesting to note that the relatively strong rise of the turbulence level in the central and trailing section of the suction side for an airfoil position of $3.30 \geq x/t \geq 3.27$, as illustrated in Fig. 7, did not result in a significant change of the heat transfer coefficient and the onset of the transition region. The transition slowly moves toward the leading edge with further traversing of the airfoil. This effect can be explained by the fact that the turbulence level rises slowly in the leading part of this side of the blade as seen in Fig. 7. It is well known that the turbulence level in the frontal region of the blade has a dominating effect on the boundary layer development. This is also evident from the conditions at $x/t = 3.06$ where the fastest laminar/turbulent transition takes place. Here, the turbulence level in the direct vicinity of the stagnation point is expected to reach its maximum value. When the airfoil assumes positions $x/t < 3.06$ a reversal of the previously described characteristic behavior is observed, i.e., turbulence intensity and heat transfer are reduced.

Conclusions

In summary it can be concluded that results of detailed optical analysis of the flow field in wake-effected cascade flow – i.e., velocity and turbulence characteristics – correspond with those of heat transfer measurements. Additional studies of the leading edge region are planned as this is found to be necessary for a full understanding of the phenomena.

References

1 Bayley, F. J., and Milligan, R. W., "The Effect of Free-Stream Turbulence Upon Heat Transfer to Turbine Blading," AGARD-CP-229, 1977.

2 Bayley, F. J., and Priddy, W. J., "Effects of Free-Stream Turbulence Intensity and Frequency on Heat Transfer to Turbine Blading," ASME JOURNAL OF ENGINEERING FOR POWER, Vol. 103, 1981, pp. 60–64.

3 Bayley, F. J., and Priddy, W. J., "Studies of Turbulence Characteristics and Their Effects Upon the Distribution of Heat Transfer to Turbine Blading," AGARD-CP-281, 1980.

4 Pfeil, H., and Pache, W., "Messungen von Strömungsgrenzschichten unter Turbomaschinenbedingungen," *Zeitschrift für Flugwissenschaft und Weltraumforschung*, Vol. 1, No. 4, 1977.

5 Pfeil, H., and Herbst, R., "Transition Procedure of Instationary Boundary Layers," ASME Paper No. 79-GT-129, 1979.

6 Doorly, D. J., Oldfield, M. L. G., and Scrivener, G. T. J., "Wake-Passing in a Turbine Rotor Cascade," AGARD-CP-390, 1985.

7 Stöcker, U., "Temperaturfeld und örtlicher Wärmeübergang bei instationären Strömungsvorgängen an einer gekühlten Turbinenlaufschaufel," *Fortschritt-Berichte der VDIZeitschriften*, Vol. 7, No. 80, 1983.

8 Stöcker, U., Kühl, W., and Koschel, W., "Über den Einfluss instationärer Strömungsvorgänge auf die Wärmeübergangsverteilung an einer Turbinenlaufschaufel," VDI-Berichte No. 487, 1983, pp. 191–199.

9 Rüd, K., and Wittig, S., "Free-Stream Turbulence and Pressure Gradient Effects on Heat Transfer and Boundary Layer Development on Highly Cooled Surface," ASME Paper No. 84-GT-180.

10 Rüd, K., Sill, H., and Wittig, S., "Einfluss der Freistromturbulenz auf den Wärmeübergang an stark gekühlten Oberflächen," *Thermische Strömungsmaschinen '83*, VDI-Bericht No. 487, VDI-Verlag, 1983, pp. 171–180.

11 Rüd, K., "Transitionale Grenzchichten unter dem Einfluss hoher Freistromturbulenz, intensiver Wandkühlung und starker Druckgradienten in Heissgasströmungen," Dissertation, Universität Karlsruhe, 1985.

12 Eriksen, S., Wittig, S., Sakbani, K., and Rüd, K., "Comparison of Laser-Doppler-, Laser-Dual-Focus- and Probe Measurements in Laminar and Fully Turbulent Boundary Layers," *Proc. of Int. Symposium on Application of Laser-Doppler Anemometry to Fluid Mechanics*, Lisbon, July 1982.

13 Eriksen, S., Sakbani, K., and Wittig, S., "Laser-Doppler- and Laser-Dual-Focus Measurements in Laminar and Fully Turbulent Boundary Layers," *Proc. of the XIV ICHMT Symposium on Heat and Mass Transfer in Rotating Machinery*, 1982.

14 Eriksen, S., Wittig, S., and Rüd, K., "Optical Measurements of the Transport Properties in a Highly Cooled Turbulent Boundary Layer at Low Reynolds Number," *Proc. of the 4th Symposium on Turbulent Shear Flow*, Karlsruhe, West Germany, Sept. 12–14, 1983.

15 Eriksen, S., Wittig, S., and Dullenkopf, K., "The Application of LDA and LDF Anemometry to the Study of Boundary Layer Transport Properties Under Gas Turbine Conditions," *Proc. of the 2nd Int. Symposium on Applications of Laser Anemometry to Fluid Mechanics*, Lisbon, July 1984.

16 Wittig, S., Eriksen, S., Schulz, A., and Hassa, C., "Laser-Doppler- und Laser-Zwei-Focus-Messungen in laminaren und turbulenten Wandgrenzschichten," *Thermische Strömungsmaschinen '83*, VDI-Berichte No. 487, VDI-Verlag, 1983, pp. 181–189.

17 Wittig, S., Schulz, A., Bauer, H. J., and Sill, K. H., "Effects of Wakes on the Heat Transfer in Gas Turbine Cascades," AGARD-CP 390, 1985.

18 Wittig, S., Schulz, A., and Bauer, H. J., "Einfluss der Nachlaufströmung auf den örtlichen Wärmeübergang von gekühlten Gasturbinenschaufeln: Modellierung instationärer Vorgänge," *Thermische Strömungsmaschinen '85*, VDI-Berichte No. 572.1, VDI-Verlag, 1985, pp. 267–286.

19 McLaughlin, D., and Tiederman, W., "Biasing Correction for Individual Realization of Laser Anemometry Measurements in Turbulent Flows," *The Physics of Fluids*, Vol. 16, No. 12, 1973, p. 2082.

20 Stevenson, W. H., Thompson, H. D., Bremmer, R., and Roesler, T., "Laser Velocimeter Measurements in Turbulent and Mixing Flows," Technical Rep. AFAPL-TR-79-2009, Part II, School of Mech. Eng., Purdue University, IN, 1980.

Three-Dimensional Flow in a Low-Pressure Turbine Cascade at Its Design Condition

H. P. Hodson

R. G. Dominy

Whittle Laboratory,
Cambridge University,
Cambridge, United Kingdom

This paper describes an experimental study of the three-dimensional flow within a high-speed linear cascade of low-pressure turbine blades. Data were obtained using pneumatic probes and a surface flow visualization technique. It is found that in general, the flow may be described using concepts derived from previous studies of high-pressure turbines. In detail, however, there are differences. These include the existence of a significant trailing shed vortex and the interaction of the endwall fluid with the suction surface flow. At an aspect ratio of 1.8, the primary and secondary losses are of equal magnitude.

Introduction

The existence of secondary flow and loss mechanisms within axial-flow turbines has long been recognized and many investigations (e.g., [1-4]) have been undertaken in order to study these phenomena and their effects. As a result, the main parameters which influence the growth of secondary flows and losses are now known (e.g., [5]) even if their relative importance is not fully understood. Thus, it is possible to attempt to inhibit their generation by attention to the overall and detailed design of turbines (e.g. [6, 7]).

In high-pressure (H.P.) turbines, the blade profiles are relatively thick, the blade heights are short, and the secondary flows occupy most if not all of the flow field at the blade row exit (e.g., [8]). It is not surprising, therefore, that investigations which are concerned with the development and control of secondary flows are usually designed to meet the needs of the designers of H.P. turbines.

In low-pressure (L.P.) turbines, the Reynolds numbers are much lower and in order to obtain the necessary blade loading the blade profiles are relatively thin. Therefore, it is much more difficult to alter either the detailed or the overall design in order to control the development of secondary flows. Of course, the higher aspect ratios of L.P. turbines tend to reduce the significance of secondary flows and losses. Even so, relatively little detailed information exists which is directly relevant to the problem of limiting the growth of secondary flow and loss in L.P. turbines. Some general information does however exist in the available correlations (e.g., [9, 10]).

The present paper presents the results of an investigation into the three-dimensional flow which exists within a linear cascade of L.P. turbine rotor root sections. It is recognized that a linear cascade cannot simulate the effects of, for example, inlet skew and rotation. Nevertheless, the present investigation can at least begin to provide some information on

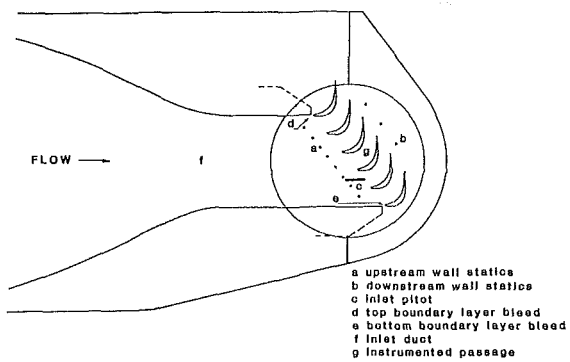

Fig. 1 Cascade installation

Table 1 Blade design, cascade geometry, and operating conditions

No. of blades	6
Chord, C (mm)	55.88
Axial chord, Cx (mm)	52.53
Inlet aspect ratio, h_1/C	1.715
Exit aspect ratio, h_2/C	1.818
Pitch-chord ratio, s/C	0.564
Pitch-axial chord ratio, s/Cx	0.600
Design inlet angle (deg from axial)	38.8
Design exit angle (deg from axial)	−53.9
$\mathrm{Cos}^{-1}(O/s)$	−54.2
Stagger angle (deg from axial)	−19.6
Throat-pitch ratio, O/s	0.585
Leading edge radius-chord ratio	0.016
Isentropic exit Mach number	0.71
Isentropic exit Reynolds number	2.9×10^5

Table 2 Estimate of experimental accuracy

Linear position	+/− 0.01 mm	
Inlet flow angle	+/− 0.2 deg	
Exit flow angle	+/− 0.4 deg	
Stagnation pressure (5 hole probe)	+/− 0.003	$\times (P_{04}-p_4)$
Stagnation pressure (all pitots)	+/− 0.001	
Static pressure (5 hole probe)	+/− 0.005	
Static pressure (surface tappings)	+/− 0.001	

Contributed by the Gas Turbine Division of THE AMERICAN SOCIETY OF MECHANICAL ENGINEERS and presented at the 31st International Gas Turbine Conference and Exhibit, Düsseldorf, Federal Republic of Germany, June 8-12, 1986. Manuscript received at ASME Headquarters January 20, 1986. Paper No. 86-GT-106.

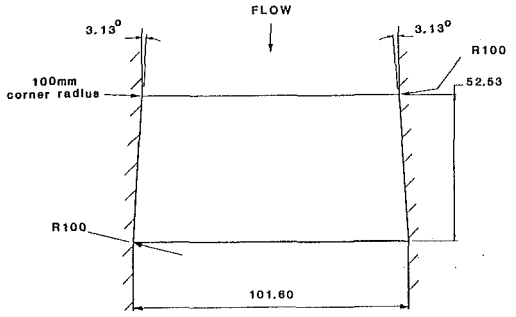

Fig. 2(*a*) Cascade: plan view

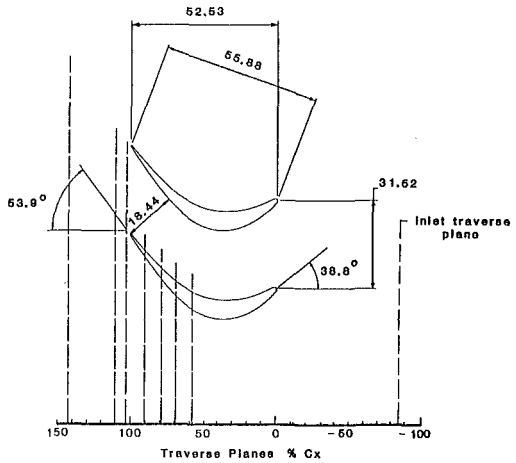

Fig. 2(*b*) Cascade: side view of a single passage

the nature of secondary flows in L.P. turbines and provide an assessment of the relative importance of such flows. Wherever possible, comparisons are made with the flows observed in H.P. turbines and cascades. A companion paper [11] describes the off-design performance of the present profile.

Experimental Details

The experiments described in this report were conducted in the Transonic Cascade Facility of the Whittle Laboratory [12]. The wind tunnel is part of a closed circuit within which the density and pressure ratio can be varied independently. The air is supplied to the test section via a contraction and a short, parallel duct. It exhausts into a large plenum. The general arrangement of the six-blade cascade is shown in Fig. 1.

The profile selected for the current investigation was a thin, hollow, castable root section from the rotor of an L.P. turbine. It was designed to operate at an air inlet angle of 38.8 deg relative to the axial direction and to provide approximately 93 deg of turning. The design velocity ratio across the cascade was equal to 1.41. The nominal aspect ratio was 1.8. This provided a cascade of reasonably sized blades (chord = 56 mm) within which there was no direct interference between the secondary flow fields of the two ends of a blade. In order to simulate the stream-tube height variation which occurs within an L.P. turbine, the cascade endwalls were flared (area ratio 1.06) with a linear variation in aspect ratio between the inlet and exit planes of the cascade. Upstream and downstream of the cascade, the endwalls were parallel. Further details can be found in Table 1, Appendix I, and Fig. 2.

The central passage of the cascade was instrumented with 0.2-mm-dia static pressure tappings which were located along the midspan sections of the blade profiles. The static pressure tappings at the inlet to the cascade were located 0.86 axial chord lengths upstream of the leading edge plane. A conventional pitot was placed at the same location. The inlet stagnation temperature (ambient) was determined using a thermocouple placed within the duct upstream of the working section.

Three different types of pneumatic probe have been employed during the current investigation. The first of these was a fixed direction, 5-hole, 60-deg conical probe with an overall diameter of 2 mm. This was used to traverse the cascade exit flow field at 110 and 142 percent *Cx*, having previously been calibrated in the same facility. Within and just downstream of the cascade (i.e., at 58, 69, 79, 90, and 102 percent *Cx*) a five tube total pressure rake (tube diameter 0.7 mm; spacing 1.55 mm) provided further information about the development of the secondary flow field and losses. The third type of probe was a flattened pitot (0.14 × 1.16 mm overall) which was used to traverse the inlet (−86 percent *Cx*) and exit (142 percent *Cx*) endwall boundary layers. An estimate of the experimental uncertainty associated with these and other pneumatic measurements is provided in Table 2.

The facility is provided with a fully automated, computer-controlled, data acquisition system. Probe movement, for example, can be achieved using the three linear and two angular traverse mechanisms, all of which are mutually independent. All pressures are measured using a Scanivalve system.

Oil-and-dye surface flow patterns were obtained using a mixture of silicone oil and a fluorescent powder which was photographed under the illumination of ultraviolet light. The range of wall shear stresses which occurred within the cascade was such that a variety of mixtures had to be used in order to obtain the maximum amount of information. The results presented, which were obtained during a single test, contain most of this information. That which is not clearly visible is shown in the accompanying interpretations.

All of the tests in the current investigation were conducted at the isentropic design conditions. These were an exit Reynolds number of 2.9×10^5 and a Mach number of 0.7. The free-stream turbulence intensity at inlet to the cascade was 0.5 percent. Further information can be found in Table 3.

Nomenclature

C = chord
Cx = axial chord
h = span
M = Mach number
p = static pressure
P_0 = total pressure
R = reattachment line
Re = Reynolds number
s = pitch
S = separation line
u, U = velocity
x = axial distance
y = tangential distance
Y = stagnation pressure loss coefficient = $(P_{01} - P_0)/(P_{04} - p_4)$
z = spanwise distance
β = pitchwise flow angle (from axial)
δ^* = boundary layer displacement thickness
θ = boundary layer momentum thickness
ρ = density

Subscripts

∞ = free stream
1 = inlet free stream
2 = traverse plane
2s = downstream isentropic
3 = pitchwise mixed out
4 = downstream infinity (i.e., pitch and spanwise mixed out)
s = suction
p = pressure
0–6 = number of separation/reattachment line

Table 3 Test conditions

Inlet flow angle (deg from axial)	38.8
Inlet Reynolds number	2.3×10^5
Inlet Mach number	0.496
Inlet turbulence intensity (percent)	0.5
Isentropic exit Mach number	0.702
Isentropic exit Reynolds number	2.9×10^5

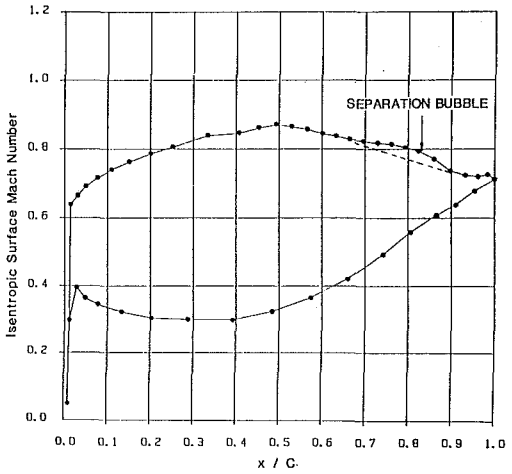

Fig. 3 Midspan surface Mach number distribution (measured)

Results and Discussion

Midspan Flow. Some characteristics of the flow at the midspan section of the central passage of the cascade have been reported elsewhere, e.g., [13]. However, a brief summary is provided below.

The measured midspan isentropic Mach number distribution is presented in Fig. 3. These results show that the profile is relatively midloaded, with significant regions of acceleration and diffusion on both the pressure and suction surfaces. A closer examination indicates the existence of a closed separation bubble near 83 percent C on the suction surface. Previous investigations have also revealed the existence of two other closed regions of separated flow. One of these was found in the diffusing flow near the leading edge of the pressure surface. The other occurs at the leading edge of the suction surface and is caused by an overspeed which occurs close to the blend point of the circular leading edge and the suction surface. In the regions following these leading edge separation bubbles, there is sufficient re-acceleration for relaminarization to occur. On the suction surface, the re-acceleration is immediate and the boundary layer may be regarded as laminar until it separates following peak suction. On the pressure surface, relaminarization is virtually complete by the trailing edge. In an actual machine, where the levels of turbulence and unsteadiness will be much greater, full relaminarization may not occur.

Inlet Boundary Layer. The velocity profile of the incoming endwall boundary layer, obtained at midpitch, 86 percent Cx upstream of the cascade leading edge plane, is plotted in Fig. 4. The integral parameters of this boundary layer are given in Table 4. They were obtained using the compressible form of the appropriate expression or integral. These results show that the upstream boundary layer is turbulent with a shape factor (δ^*/θ) of 1.44 and a displacement thickness-chord ratio (δ^*/C) of 0.011. This boundary layer is thus typical of those found at the inlet to model turbines (e.g., [15]) and of those measured by other investigators during cascade studies (e.g., [3, 4]). Even so, its relevance to actual turbines remains uncertain since the appropriate data do not appear to exist.

Surface Flow Visualization. The use of surface flow visualization in two and three-dimensional flow studies is a well-established technique. It is of course recognized that although important and useful, these flow patterns only provide information about the nature of the near surface flow. Care must therefore be taken when inferences are made regarding the main body of the flow. Conclusions which are drawn are supported either by other measurements (q.v.) or by other investigations of similar phenomena (e.g., [1–8]). In describing the current experiments the nomenclature used in, for example, [5] has been adopted wherever possible.

A perspective photograph of the suction surface and endwall flow visualization patterns is shown in Fig. 5 together with a schematic interpretation of the same. The upstream boundary layer is identified by the speckled pattern in the photograph. It separates along the lines S1s and S1p as it rolls up to form the horseshoe vortex. The stagnation streamline R1 divides the upstream boundary layer into the fluid which enters the suction leg (S1s) and that which enters the pressure

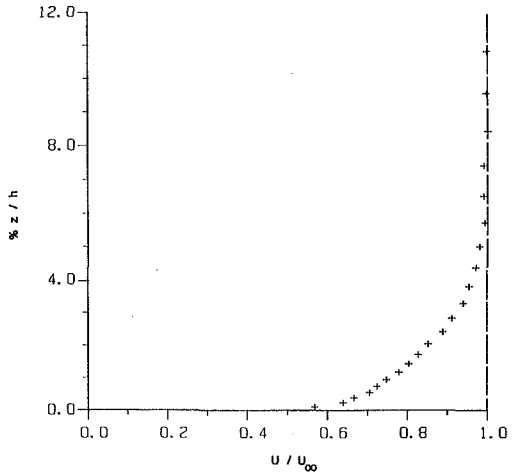

Fig. 4 Inlet boundary layer profile

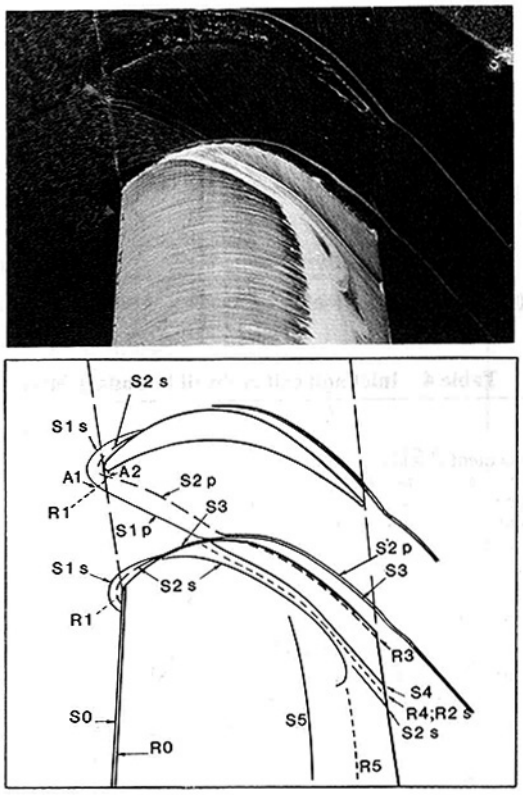

Fig. 5 Suction surface and endwall flow visualization

Fig. 6(a) Endwall flow visualization

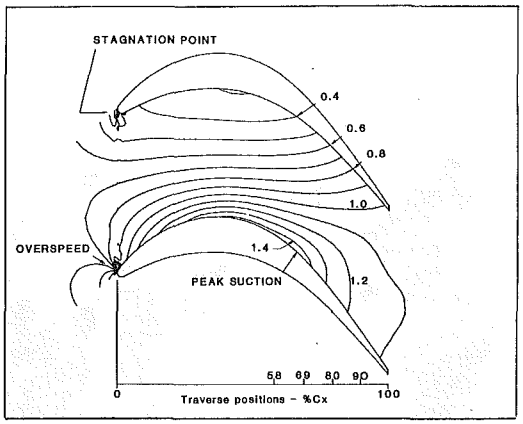

Fig. 6(b) Predicted midspan static pressure contours $(P_0 - P)/(P_0 - P_2)$

Table 4 Inlet and exit endwall boundary layers

	Inlet	Exit
Displacement thickness/chord, δ^*/C	0.0108	0.0027
Momentum thickness/chord, θ/C	0.0075	0.0013
Displacement thickness/span, δ^*/h	0.0063	0.0015
Momentum thickness/span, θ/h	0.0044	0.0007
Shape factor, δ^*/θ	1.44	2.01

side leg (S1p) of the horseshoe vortex. The secondary separation lines (S2s and S2p) which mark the liftoff line of the horseshoe vortex are not visible in the photograph. Investigations in H.P. turbine cascades (e.g., [8]) have also at times failed to reveal a second separation line, but it is usually the separation line of the inlet boundary layer rather than the liftoff line of the horseshoe vortex that is not visible [5]. Evidence which confirms that it is indeed the primary separation line which is easily visible in Fig. 5 was obtained using a different flow visualization mixture, albeit at the expense of the quality of the overall pattern. Although fluid is fed into the separation bubble that is bounded by the stream surfaces corresponding to the primary and secondary separation lines (S1s and S2s, S1p and S2p) the apparent difference in the visibility of the primary and secondary separation lines implies that the energy of the fluid in the separated zone is not as low as suggested by the results of [4]. The results of [16] show that the region in question may be unsteady and that the flow direction is not constant, so it is quite possible that a separation line, which is a representation of the mean flow, may not be detected in the oil patterns.

Figure 6 contains a prediction of the static pressure field made using the quasi-three-dimensional method of Denton [14]. The solution presented is representative of the midspan conditions where the stream-tube height variation (linear from leading edge to trailing edge) was that suggested by the measured axial-velocity-density ratio, rather than the geometric value of 0.94. Static pressure contours are presented

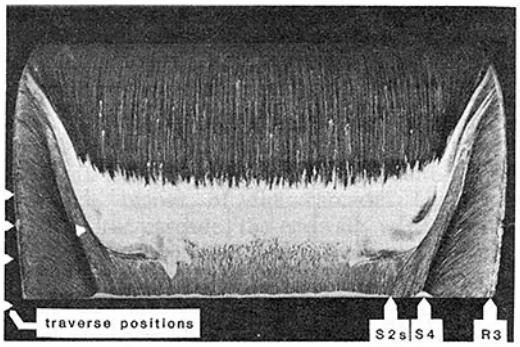

Fig. 7 Suction surface flow visualization

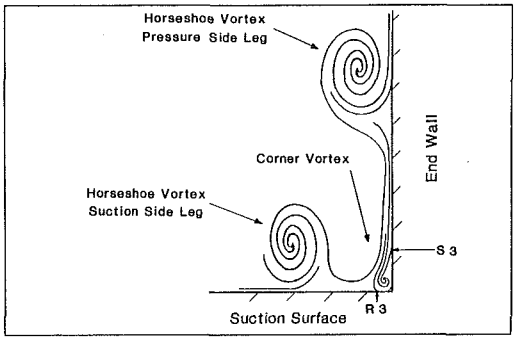

Fig. 8 Vortex structure just downstream from the intersection of the horseshoe vortex (suction leg) and the blade suction surface

with a picture of the endwall flow visualization. It shows that within the passage the endwall limiting streamlines are generally perpendicular to the isobars, particularly near midchord. The location of the overspeed at the leading edge of the suction surface is indicated in the figure. The separation bubble caused by this overspeed can be seen in the flow visualization patterns of Fig. 5. Its limits are defined by the lines So and Ro which extend across the entire span suggesting that the leading edge overspeed is not confined to the region of primary flow. The flow visualization indicates that the secondary flow is not affected by the overspeed.

As the suction side leg of the horseshoe vortex enters the blade passage, it experiences the significant transverse pressure gradients indicated by Fig. 6. Under their influence, the separation lines S1s and S2s merge as they are swept onto the suction surface at approximately 15 percent *Cx*. Figure 7 shows that this vortex then moves toward the midspan as it spirals along the surface toward the trailing edge. At about 60 percent *Cx*, the suction leg of the horseshoe vortex comes into contact with the closed separation bubble which is defined by the lines S5 and R5 in Fig. 5. According to the surface flow visualization patterns, there is little evidence of fluid from the horseshoe vortex entering the separation bubble until it encounters the reattachment zone at the rear of the bubble. At present, the mechanism of this interaction is not fully understood but it is known that the sense of rotation of the flow within the bubble is opposite to that of the vortex which suggests that some cancellation of vorticity is taking place. Nevertheless, it is clear that not all of the fluid within the vortex enters the separation bubble since the separation line S2s which is associated with this vortex remains just visible up to the trailing edge. Therefore in contrast to the situation which often occurs in H.P. turbines (e.g., [17]) the suction side leg of the horseshoe vortex is not forced away from the surface toward the middle of the blade passage under the influence of the passage vortex (see below) nor is it engulfed by the passage vortex.

At the intersection of the separation line S1s with the suction surface, Fig. 5 shows that a new separation line S3

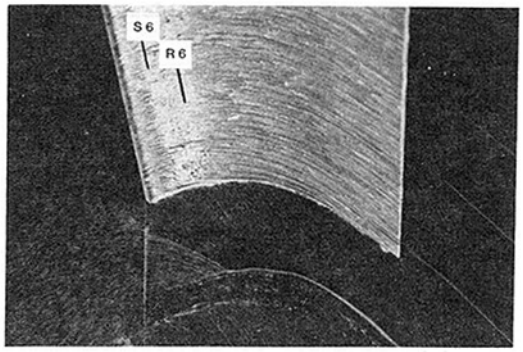

Fig. 9 Pressure surface and endwall flow visualization

develops. This line indicates the presence of a corner vortex. Figure 8 is a schematic representation of the flow which occurs just downstream of the start of this vortex, which is formed as a result of the high angle of attack of the near-surface streamlines onto the suction surface. Associated with the separation line S3 is a reattachment line R3. The sense of rotation of the corner vortex is the same as that of the suction side leg of the horseshoe vortex. Thus it is not unreasonable that it originates from the point where this leg of the horseshoe vortex meets the suction surface. This result is contrary to observations (e.g., [2]) made in H.P. turbines which indicate that, when present, the corner vortex originates where the pressure-side leg S1p meets the suction surface. Thus it is likely that the point of origin of the corner vortex is more a function of the angle of attack of the streamlines than of the locations of the horseshoe vortices.

Figures 5 and 6 show that as the pressure side of the horseshoe vortex enters the passage, it is deflected by the transverse pressure gradient toward the suction surface of the adjacent blade at the same time as it merges with the passage vortex. It therefore becomes impossible to distinguish between these vortices. The line S4 in Fig. 5 denotes the separation of the passage vortex from the suction surface. Between this line and that associated with the liftoff of the suction side leg of the horseshoe vortex is the reattachment line R4/R2s. Figure 7 shows this more clearly. The inclination of the surface streamlines in the region between the separation line S4 and the endwall is an indication of the rate of rotation of the passage vortex.

Behind the secondary separation line S2p (Fig. 5), a new highly skewed endwall boundary layer develops which is also swept toward the suction surface. The high wall shear stress which is associated with this new and therefore thin boundary layer is responsible for the flow pattern observed. Because it meets the suction surface at such a high angle of attack, the corner vortex is enhanced and as a result, the associated separation line S3 and reattachment line R3 move away from the corner along their respective surfaces.

Figure 9 shows a perspective view of the pressure surface and endwall interaction. Near the leading edge of the pressure side, the fluid flows from the surface onto the endwall under the influence of the horseshoe vortex and cross-passage pressure gradient. The separation bubble which is indicated by the separation line S6 and reattachment line R6 is caused by the diffusion which follows the acceleration around the leading edge (Fig. 3). Within this bubble, there is very little movement of the oil except near the endwall where the low-momentum fluid moves onto the endwall under the influence of the transverse pressure gradient. Downstream of the separation bubble, the interaction between the pressure surface and endwall fluid is very weak, no corner vortex is observed, and the flow appears to be two dimensional.

Traverse Results. The patterns obtained during the surface flow visualization experiments, while providing a valuable insight into the nature of the secondary flow, do not necessarily indicate the magnitude of the observed phenomena; nor do they always reflect the development of the flow in the center of the passage. It is for this reason, together with a need to determine the significance of the secondary losses, that a series of area traverses were performed using pneumatic probes.

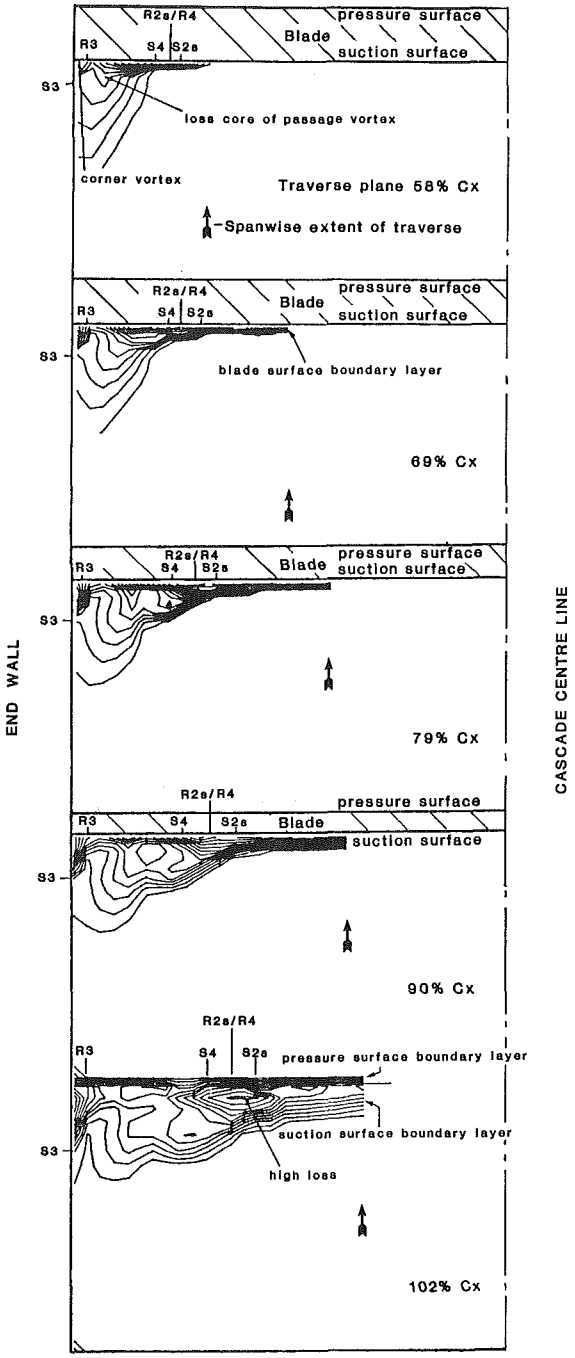

Fig. 10 Total pressure loss coefficient (contour interval 0.06)

The results of the stagnation pressure rake traverses are plotted in Fig. 10 in the form of nondimensional total pressure loss contours (i.e., contours of $(P_{01} - P_0)/(P_{04} - p_4)$). The uppermost figure was obtained closest to the leading edge. The positions of the various separation and reattachment lines taken from the flow visualization are also indicated. Physical constraints within the blade passage prevented the measurement of the flow near to the pressure surface.

The most upstream area traverse was performed at 58 percent *Cx* (Fig. 10, top), which corresponds to peak suction.

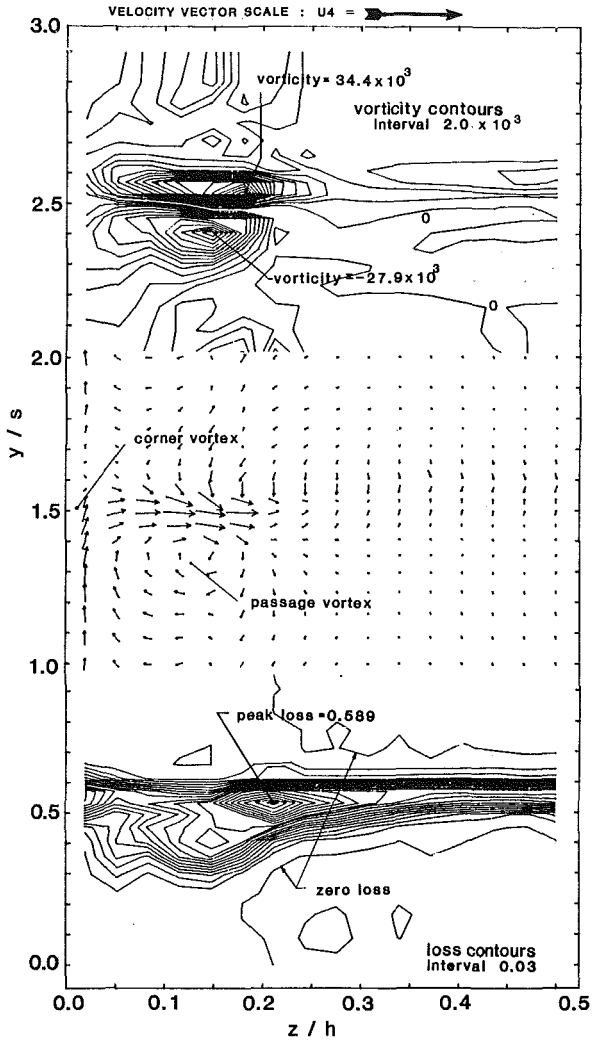

Fig. 11 Total pressure loss coefficient contours, secondary vorticity contours, and secondary velocity vectors at 110 percent *Cx*

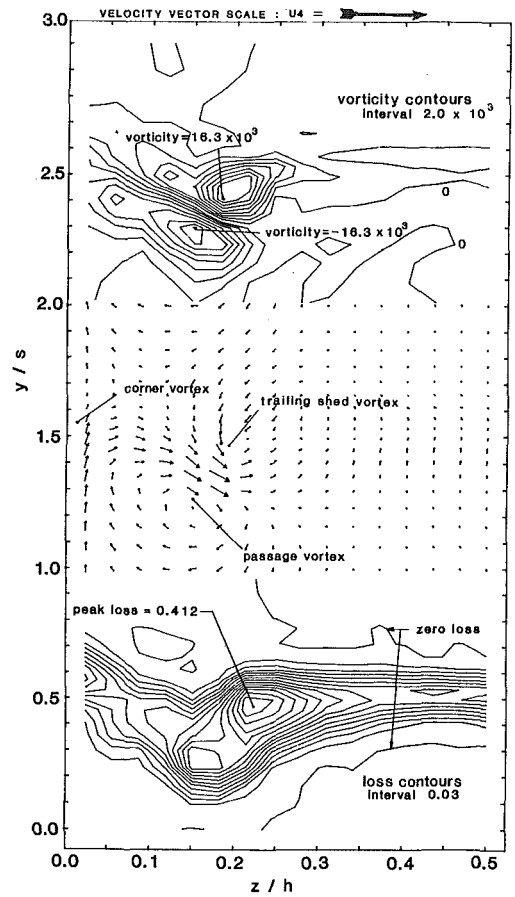

Fig. 12 Total pressure loss coefficient contours, secondary vorticity contours, and secondary velocity vectors at 142 percent *Cx*

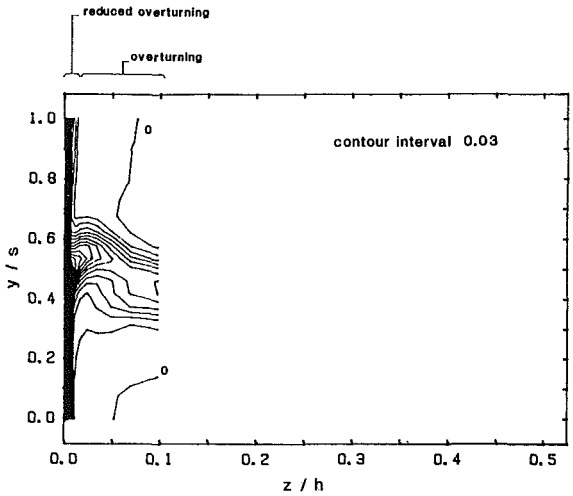

Fig. 13 Near endwall total pressure loss coefficient contours

Here, the separated inlet boundary layer has already rolled up and has largely been engulfed by the passage vortex, the center of which lies between the corner and the separation line S4 as is usually the case. In the corner between the lines S3 and R3, the corner vortex can also be identified by a region of high loss. The high-loss region to the right of the line S2s is thought to indicate the presence of the suction side leg of the horseshoe vortex. Neither the blade surface boundary layer nor the endwall boundary layer could be detected at this location because they have developed under generally favorable pressure gradients and as a result, have remained very thin.

Between 58 percent *Cx* and 69 percent *Cx*, more fluid from the new and the upstream endwall boundary layers has been swept across the passage into the passage vortex, which has moved toward midspan. This flow is driven by the cross-passage pressure gradient. The corner vortex and the reattachment zone between S4 and S2s have both increased in size as a consequence of this secondary flow. The blade surface boundary layer is now visible; the rapid growth is due to the effects of the separation which it has just undergone (see Fig. 7). The new endwall boundary layer however remains undetectable.

The middle plot of Fig. 10 was obtained at 79 percent *Cx*. It shows that the features described above grow as a result of the continuing secondary flow. The passage vortex, for example, has moved further along the suction surface away from the endwall. In addition, the passage vortex now appears to have engulfed almost all of the high-loss fluid associated with the incoming endwall boundary layer which has been replaced by lower loss fluid from the free stream. The flow visualization suggested that most of the suction side leg of the horseshoe vortex was absorbed into the separation bubble on the suction surface. Even so, some of the high-loss fluid which is thought to be associated with this vortex can be identified in the figure.

At 90 percent *Cx*, which lies close to the reattachment line R5 of the suction surface separation bubble, Fig. 10 shows that the passage vortex has further rolled up. It contains more high-loss fluid and occupies approximately 15 percent of the span. Its core, which is identified by the loss peak, continues to lie close to the suction surface, unlike those sometimes observed in H.P. cascades. As at all of the locations in Fig. 10,

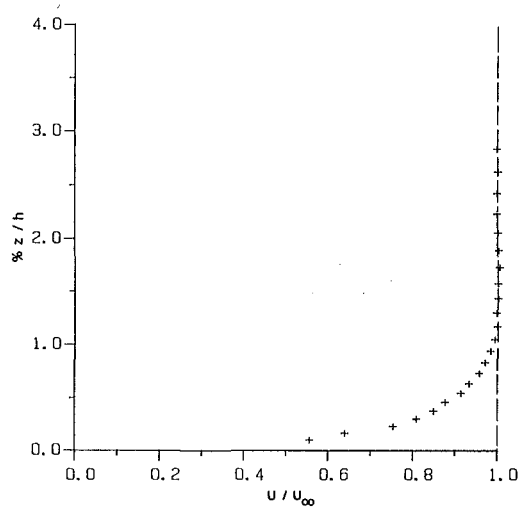

Fig. 14 Wall boundary layer at cascade exit plane (midpassage)

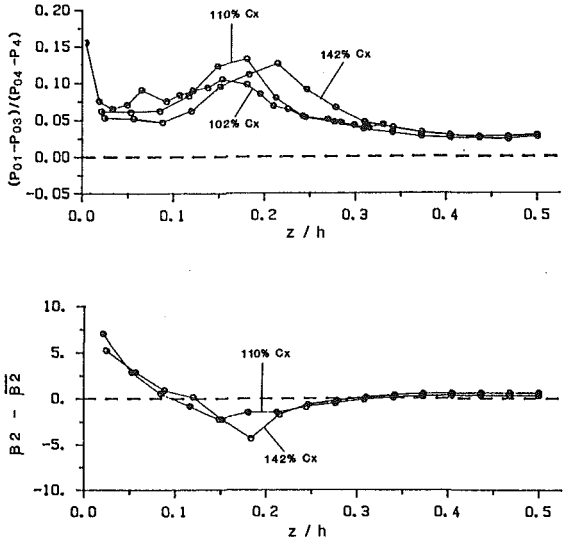

Fig. 15 Spanwise mixed-out stagnation pressure loss and pitchwise flow angle

the highest measured loss is to be found in the reattachment zone between the separation lines S4 and S2s. Due to the increased size of the suction surface boundary layer and/or further spanwise mixing/migration, it is virtually impossible to detect the suction side leg of the horseshoe vortex.

Just beyond the trailing edge at 102 percent *Cx*, Fig. 10 shows that the secondary flows extend to at least 30 percent of the span. This rapid increase in the spanwise extent of the secondary loss region is a result of the spanwise flow which occurs near the rear of the suction surface separation bubble (S5-R5) where it meets the secondary flow field (Figs. 5 and 7). The high loss region which originated between the separation lines S4 and S2s and the corner vortex appear to be similar in size. The peak value of loss in both of these regions is much greater than in the passage vortex. A weak remnant of the suction side leg of the horseshoe vortex can possibly be identified in the lowest plot of Fig. 10, and its location agrees with the separation line (S2s) which is known to exist up to the trailing edge. Like the flow visualization, this is thought to indicate that the suction leg of the horseshoe vortex is not fully dissipated by its interaction with the suction surface separation bubble, but such a conclusion is tenuous.

Area traverses were also performed downstream of the cascade at 110 and 142 percent *Cx* using a calibrated fixed-direction five-hole probe. Due to physical constraints, these traverses were only performed between 2 and 50 percent span. The results of these experiments are plotted in Figs. 11 and 12, respectively, in the form of total pressure and secondary vorticity contours and secondary velocity vectors. The interval between the contours of the total pressure loss coefficient in these figures is one half of that employed in Fig. 10. The secondary velocities were obtained by projecting the velocity vectors onto a plane which was perpendicular to the mixed-out flow direction. The secondary vorticity was then calculated by finite differentiation of the measured data. Although not wholly reliable, this can at the least serve to indicate the relative magnitudes of the vorticity.

The further development of the features noted in Fig. 10 can be seen by examining Fig. 11. Downstream of the cascade, the vortices are not confined by the blade surface. Therefore, the center line of the wake becomes distorted as the fluid rotates. At 110 percent *Cx*, this distortion is just noticeable in the stagnation pressure contours. The maximum value of vorticity in the passage vortex is equivalent to an angular velocity of approximately 14,000 rad/s or one half of a revolution per chord length in the streamwise direction. The position of peak vorticity is used to identify the center of the passage vortex. It can be seen that this position coincides with the loss peak which has already been identified as the passage vortex in Fig. 10.

Like the results of Fig. 10, the loss contours of Fig. 11 show that the region which originated between the separation lines S4 and S2s and the corner vortex contains the fluid with the greatest loss.

Apart from the passage vortex, the vorticity contours of Fig. 11 indicate that there is a significant region of counterclockwise vorticity. This elongated region has a center line which coincides with that of the wake. The peak vorticity in this region is 24 percent greater than and of opposite sign to the peak value of the passage vortex. It lies between the passage vortex and the fluid from between the separation lines S4 and S2s. It is unlikely that it is the suction side leg of the horseshoe vortex. Most probably, it is a combination of the trailing shed vorticity and that due to the relative skew of the blade surface boundary layers. A calculation along classical lines of the relative strengths of the passage and trailing shed vorticities predicts that they should be of about equal magnitude. It is impossible to identify the corner vortex in the vorticity contours, even though it is clearly visible in the loss measurements, as it rotates in the same sense as the trailing shed vorticity. This indicates that the rate of rotation within the corner vortex is not significant. Since the passage and trailing shed vorticities are of opposite sign, the largest secondary velocities occur in the region between these features, where they reach a value equal to one third of the mean exit velocity.

The results obtained with the five-hole cone probe at the most downstream traverse plane (i.e., 142 percent *Cx*) are plotted in Fig. 12. The elongated region of counterclockwise vorticity in Fig. 11, which contained the trailing shed vorticity and which presumably began as a vortex sheet, has now rolled up into a discrete vortex. A comparison of the loss contours of Fig. 12 with Fig. 11 shows that the wake has further decayed due to viscous action and become further distorted as the unbounded vortices rotate. The regions of underturning and overturning which are due to the presence of the passage and trailing shed vortices can be identified by this distortion. The peak vorticities of the passage and counter vortex are now equal with a value which is equivalent to an angular velocity of approximately 8000 rad/s. One other result of the rotation of the fluid is that the centers of the vortices have moved apart as fluid is drawn in between them. Their spanwise positions remain unchanged, however. Figure 12 also shows that the position of peak loss within the passage vortex has remained coincident with its center of rotation. A further comparison of the results obtained at 110 and 142 percent *Cx* reveals that much of the decay has taken place within the wake and trailing shed

vortex. The peak loss within the passage vortex has, for example, remained unchanged while the overall maximum value at 142 percent *Cx* is equal to 70 percent of the maximum at 110 percent *Cx*. Such a variation in the rate of decay is not uncommon and may be taken as an indication of the relative magnitudes of the turbulent and the mean transport properties associated with the various phenomena.

It has already been stated that the five-hole probe was not traversed very close to the endwall and that the endwall boundary layer could not therefore be detected. The wall boundary layer measurements presented in Fig. 13 were thus obtained by traversing the flattened pitot at 142 percent *Cx*. The skew of the wake's center line shows that the amount of overturning is reduced very close to the endwall. This reduction is due to the presence of the corner vortex which is clearly identified by the high-loss region very close to the endwall. The flattened pitot results of Fig. 13 also show that the thickness of the endwall boundary layer varies across the pitch. The variation occurs because the fluid nearest the suction side of the wake will have originated further upstream than that near the pressure side. Figure 14 shows the velocity profile of this boundary layer at midpitch. It extends to approximately 1.5 percent span. The integral parameters are given in Table 4. These results confirm that the exit endwall boundary layer is thin ($\delta^*/C = 0.0013$) with a shape factor ($\delta\theta = 2.0$) which indicates that it is transitional, albeit more turbulent than laminar. It should be noted that these values of the integral parameters are obtained relative to the local free stream, where the total pressure is not equal to the value at inlet as a result of the mixing and redistribution of fluid which has taken place.

The variations across the span of the pitchwise integrated total pressure loss coefficient, deduced from the exit traverse data of Figs. 10, 11, and 12, are plotted in Fig. 15. The quantities shown have been obtained by a constant area mixing calculation at each spanwise position. As the flow develops downstream of the cascade, there is a shift in the loss peak toward the midspan from 15 percent span near the trailing edge to 22 percent span at the most downstream traverse plane. This movement is caused by the convective influence of the passage and counter rotating vortices. The spanwise variation of the pitchwise averaged tangential flow angle, measured using the five-hole probe, is also plotted in Fig. 15. This shows that the maximum amount of underturning increases as the flow develops. This is contrary to expectations. The increase occurs because the underturning effect of the passage vortex is enhanced by the counterrotating vortex which has formed between 110 and 142 percent *Cx* and which contains the trailing shed vorticity. In many of the H.P. turbines investigated, such a strong countervortex does not appear to exist.

Figure 15 also shows that the total pressure loss coefficient varies continuously across the entire span at all of the downstream measurement planes. In particular, the loss at midspan is greater than the minimum value which occurs near 45 percent span. Therefore, it is impossible to identify a region of genuine two-dimensional "profile" loss. The interaction of the secondary flow with the suction surface separation bubble is thought to be at least partially responsible. Other studies in which there was no separation bubble have produced similar results, but only when the aspect ratios were of the order of unity [18], a value which is more typical of H.P. turbines. The aspect ratio of this cascade is approximately 1.8.

The total pressure loss contours of Fig. 12 have been integrated over the area of the traverse using a constant area mixing calculation in which the conservation equations of mass, momentum, and energy are employed. The results of this integration are presented in Table 5, together with a conventional breakdown of the sources of this loss. It has already been noted that the "profile" loss coefficient is not constant in the region of the midspan. Nevertheless, this value (0.028) has been taken as being indicative of the two-dimensional value. The net secondary loss coefficient which is generally thought to represent the new secondary loss generated within the cascade is assumed to be equal to the difference between the total loss and the sum of the inlet and midspan values. It is equal to 0.025. This value does not however include the exit endwall boundary layer. Including those results of Fig. 13 which were obtained with the flattened pitot between zero and 2 percent span raises the total loss coefficient to 0.069 and the net secondary loss coefficient to 0.030. Table 5 also lists the loss of stagnation pressure which is attributed to the mixing calculation. At 142 percent *Cx*, the mixing loss accounts for less than 10 percent of the total. If the midspan flow were to exist over the entire span, then the mixing loss coefficient attributable to the nonuniformity of the two-dimensional flow is equal to 0.0012. Thus, the mixing loss attributable to the three dimensionality of the flow may be said to be equal to 0.0047, or 18 percent of the net secondary loss. Further analysis of the data shows that as expected, virtually all of the mixing loss occurs due to the nonuniformity of the velocity field.

The mixed-out values of the exit flow angles and the axial velocity density ratio calculated from the exit traverse results at 142 percent *Cx* are also given in Table 5. These results show that there is no net spanwise flow. The flow angle in the blade-to-blade plane is equal to -54.1 deg, which compares favorably with the values listed in Table 1. The axial velocity density ratio is equal to 0.917 if the blockage of the inlet endwall boundary layers is taken into consideration, which may be compared to the theoretical value of 0.943. This is equivalent to an error in the exit flow angle of -1.2 deg or an error in the inlet Mach number of 0.014.

The area traverse results obtained at 110 percent *Cx* have also been integrated via a mixing calculation. Within the total loss coefficient of 0.055, the midspan value was equal to 0.025, the net secondary value 0.018, and the mixing value 0.007. The flow angle and axial velocity-density ratio were equal to the values obtained at 142 percent *Cx*. The above data have not been included in Table 5 because it is not clear whether the difference in the overall loss coefficient (0.055 compared to 0.064) is due to the relative size of the probe and flow phenomena at 110 percent *Cx* or viscous effects.

Conclusions

The nature of the development of the secondary flows and losses which exist at the hub of a low-pressure turbine has been investigated in a linear cascade.

It is shown that the general nature of the flow can be

Table 5 Mixed-out traverse results (142 percent *Cx*), stagnation pressure loss coefficients, exit flow angles and mass conservation

Inlet loss coefficient	0.0110
Midspan ("profile") loss coefficient	0.0278
Total loss coefficient (excluding endwall boundary layer)	0.0639
Mixing loss coefficient (excluding endwall boundary layer)	0.0059
Net secondary loss coefficient (excluding endwall boundary layer)	0.0251
Total loss coefficient (including endwall boundary layer)	0.0685
Net secondary loss coefficient (including endwall boundary layer)	0.0297
Pitchwise exit flow angle (deg from axial)	−54.1
Spanwise exit flow angle (deg form axial)	0.2
Axial velocity density ratio	0.917

described using the theories that have been applied to high-pressure turbines. However, differences are observed in the detailed flow structure. In particular these differences relate to the formation of a vortex of significant proportions which contains the trailing shed vorticity, the origin of the corner vortex, the nature of the flow in the region between the suction side leg of the horseshoe vortex and the passage vortex, and the interaction between the closed, suction surface separation bubble and the endwall flow field.

It is also found that for this test case (aspect ratio 1.8), the nominal profile loss and the secondary loss assume similar proportions.

Although many of the flow features and their origins are identified, it is clear that further work is needed if the full implications of secondary flows in L.P. turbines are to be understood.

Acknowledgments

The work described was supported by the Ministry of Defence and Rolls-Royce Limited. The assistance of their representatives, in particular Mr. C. T. J. Scrivener of Rolls-Royce, and their permission to publish the work described in this paper, is gratefully acknowledged. The authors also wish to thank the members of the Whittle Laboratory for their contributions.

References

1 Herzig, H. X., Hansen, A. G., and Costello, G. R., "A Visualisation Study of Secondary Flows in Cascades," NACA Report 1163, 1953.

2 Sjolander, S. A., "The Endwall Boundary Layer in an Annular Cascade of Turbine Nozzle Guide Vanes," Carleton University, Canada, TR-ME/A75-4, 1975.

3 Langston, L. S., Nice, M. L., and Hooper, R. M., "Three Dimensional Flow Within a Turbine Cascade Passage," ASME JOURNAL OF ENGINEERING FOR POWER, Vol. 99, Jan. 1977, pp. 21–28.

4 Marchal, Ph., and Sieverding, C. H., "Secondary Flows Within Turbomachinery Bladings," *AGARD Conf. on Secondary Flow in Turbomachines*, AGARD CP-214, Paper No. 11, 1977.

5 Sieverding, C. H., "Recent Progress in the Understanding of Basic Aspects of Secondary Flows in Turbine Blade Passages," ASME Paper No. 84-GT-78, June 1984.

6 Haas, J. E., "Analytical and Experimental Investigation of Stator Endwall Contouring in a Small Axial Flow Turbine," NASA Technical Paper No. 2023, 1982.

7 Atkins, M. J., "Endwall Profiling in Axial Flow Turbines," Ph.D. Thesis, Cambridge, 1985.

8 Moore, J., and Ransmayr, A., "Flow in a Turbine Cascade, Part I: Losses and Leading Edge Effects," ASME Paper No. 83-GT-68.

9 Dunham, J., and Came, P. M., "Improvements to the Ainley-Mathieson Method of Turbine Performance Prediction," ASME JOURNAL OF ENGINEERING FOR POWER, Vol. 92, July 1970, pp. 252–256.

10 Craig, H. R. M., and Cox, H. J. A., "Performance Estimation of Axial Flow Turbines," *Proc. Inst. Mech. Eng.*, Vol. 1985, 1970–71, pp. 407–424.

11 Hodson, H. P., and Dominy, R. G., "The Off-Design Performance of a Low-Pressure Turbine Cascade," ASME JOURNAL OF TURBOMACHINERY, this issue.

12 Gostelow, J. P., and Watson, P. J., "A Closed Circuit Variable Density Air Supply for Turbomachinery Research," ASME Paper No. 76-GT-62.

13 Hodson, H. P., "Boundary Layer Transition and Separation Near the Leading Edge of a High Speed Turbine Blade," ASME JOURNAL OF ENGINEERING FOR GAS TURBINES AND POWER, Vol. 107, Jan. 1985, pp. 127–134.

14 Denton, J. D., "An Improved Time Marching Method for Turbomachinery Flow Calculation," ASME Paper No. 82-GT-239.

15 Hunter, I. H., "Endwall Boundary Layer Flows and Losses in an Axial Turbine Stage," ASME JOURNAL OF ENGINEERING FOR POWER, Vol. 104, Jan. 1982, pp. 184–193.

16 Ishii, J., and Honami, S., "A Three-Dimensional Turbulent Detached Flow Within a Horse-Shoe Vortex," ASME Paper No. 85-GT-70.

17 Belik, L., "Secondary Flow in Blade Cascades of Axial Turbomachines and the Possibility of Reducing Its Unfavorable Effects," *2nd Int. JSME Symp., Fluid Machinery and Fluidics*, Tokyo, Sept. 1972, pp. 41–49.

18 Sharma, O. P., and Graziani, R. A., "Influence of Endwall Flow on Airfoil Suction Surface Mid-Height Boundary Layer Development," ASME JOURNAL OF ENGINEERING FOR GAS TURBINES AND POWER, Vol. 106, Apr. 1984, pp. 400–408.

APPENDIX

Blade Profile

Leading edge circle center: $x = 0.01650$, $y = 0.36514$, radius $= 0.01650$
Trailing edge circle center: $x = 0.99515$, $y = 0.00485$, radius $= 0.00485$
Blend points denoted by*

X/Cx	Y/Cx	X/Cx	Y/Cx	X/Cx	Y/Cx	X/Cx	Y/Cx	X/Cx	Y/Cx
*0.0034	0.3752	0.4000	0.5689	0.8200	0.2591	0.8300	0.1828	0.4100	0.4374
0.0100	0.3835	0.4200	0.5664	0.8400	0.2330	0.8100	0.2034	0.3900	0.4393
0.0200	0.3954	0.4400	0.5626	0.8600	0.2060	0.7900	0.2237	0.3700	0.4404
0.0300	0.4067	0.4600	0.5577	0.8800	0.1786	0.7700	0.2433	0.3500	0.4407
0.0500	0.4273	0.4800	0.5516	0.9000	0.1508	0.7500	0.2621	0.3300	0.4404
0.0700	0.4460	0.5000	0.5442	0.9200	0.1228	0.7300	0.2800	0.3100	0.4395
0.0900	0.4628	0.5200	0.5357	0.9400	0.0943	0.7100	0.2971	0.2900	0.4381
0.1100	0.4783	0.5400	0.5260	0.9600	0.0654	0.6900	0.3134	0.2700	0.4360
0.1300	0.4923	0.5600	0.5152	0.9800	0.0361	0.6700	0.3285	0.2500	0.4333
0.1500	0.5051	0.5800	0.5031	0.9900	0.0213	0.6500	0.3424	0.2300	0.4298
0.1700	0.5167	0.6000	0.4897	*0.9992	0.0075	0.6300	0.3554	0.2100	0.4257
0.1900	0.5272	0.6200	0.4748	*0.9914	0.0018	0.6100	0.3674	0.1900	0.4205
0.2100	0.5365	0.6400	0.4585	0.9900	0.0034	0.5900	0.3785	0.1700	0.4143
0.2300	0.5446	0.6600	0.4410	0.9800	0.0154	0.5700	0.3887	0.1500	0.4073
0.2500	0.5517	0.6800	0.4221	0.9700	0.0273	0.5500	0.3982	0.1300	0.3997
0.2800	0.5602	0.7000	0.4016	0.9500	0.0507	0.5300	0.4068	0.1100	0.3915
0.3000	0.5645	0.7200	0.3800	0.9300	0.0737	0.5100	0.4144	0.0900	0.3826
0.3200	0.5676	0.7400	0.3576	0.9100	0.0963	0.4900	0.4209	0.0700	0.3733
0.3400	0.5696	0.7600	0.3343	0.8900	0.1186	0.4700	0.4264	0.0500	0.3636
0.3600	0.5705	0.7800	0.3099	0.8700	0.1404	0.4500	0.4309	0.0300	0.3535
0.3800	0.5703	0.8000	0.2847	0.8500	0.1618	0.4300	0.4346	*0.0241	0.3505

Production and Development of Secondary Flows and Losses in Two Types of Straight Turbine Cascades: Part 1—A Stator Case

A. Yamamoto
National Aerospace Laboratory,
Chofu, Tokyo, Japan

The present study intends to give some experimental information on secondary flows and on the associated total pressure losses occurring within turbine cascades. Part 1 of the paper describes the mechanism of production and development of the loss caused by secondary flows in a straight stator cascade with a turning angle of about 65 deg. A full representation of superimposed secondary flow vectors and loss contours is given at fourteen serial traverse planes located throughout the cascade. The presentation shows the mechanism clearly. Distributions of static pressures and of the loss on various planes close to blade surfaces and close to an endwall surface are given to show the loss accumulation process over the surfaces of the cascade passage. Variation of mass-averaged flow angle, velocity and loss through the cascade, and evolution of overall loss from upstream to downstream of the cascade are also given. Part 2 of the paper describes the mechanism in a straight rotor cascade with a turning angle of about 102 deg.

Introduction

As reviewed by Sieverding in his recent paper [1], recent progress in basic secondary flow research by many workers has produced a fairly detailed description of the flow mechanisms in turbine blade passages, such as leading edge vortices and their associated three-dimensional separation and reattachment lines. The present author agrees with one of his conclusions, i.e., "It is absolutely essential to know whether each such flow mechanism occurring within the cascade is of only local or of overall significance, since this conditions, to a large extent, the choice of the appropriate endwall flow analysis method." Such knowledge is also important for practical use by designers in companies and by researchers in the field. This leads to a need for more data to estimate quantitatively the role of each mechanism. Experimental data based on detailed traverse measurements made within various blade rows are especially needed because the real mechanism could be revealed, without the necessity of trying to visualize the mechanism from such results as can be obtained outside the rows. Within the author's knowledge, such complete flow surveys within blade rows have been limited to the following: Langston et al. [2] and Gregory-Smith and Graves [3] for low-speed straight rotor cascades, Sieverding and Wilputte [4] for a high-speed straight stator cascade, and Marchal and Sieverding [5] for both low-speed straight stator and rotor cascades.

In addition to the above straight cascades, Sieverding et al. [6], Boletis et al. [7], Boletis [8], and Yamamoto and Yanagi [9] have presented some detailed traverse data obtained within annular stator cascades.

The present paper intends to give more information on the secondary flow/loss mechanism, based on measurements in two types of turbine cascades with different turning angles.

Test Cascade and Test Conditions

Low-Speed Straight Turbine Stator Cascade. The blade profile is the same as the mean profile of the first-stage high-pressure turbine stator for aeroengine use [10] and is given in the appendix. The major specifications of the present cascade are as follows:

- Blade chord $C = 104.4$ mm
- Axial blade chord $C_{ax} = 81.5$ mm
- Blade pitch $S = 76.77$ mm
- Aspect ratio $H/C = 0.96$
- Solidity $C/S = 1.36$
- Number of blades $N = 5$
- Cascade inlet angle (at design) $\theta_{y,\text{inlet}} = 0$ deg
- Cascade outlet angle (at design) $\theta_{y,\text{outlet}} = -68$ deg
- Turning angle (at design) $= 68$ deg

The cascade is characterized by a large turning angle, thick leading and trailing edges, low aspect ratio, and low solidity.

The suction-type cascade wind tunnel consists of two vertical plates for cascade endwalls, between which a cascade is installed. Two inlet guide plates and two outlet guide plates are set upstream and downstream from the cascade, respectively. A part of one endwall can be moved in the pitchwise

Contributed by the Gas Turbine Division of THE AMERICAN SOCIETY OF MECHANICAL ENGINEERS and presented at the 31st International Gas Turbine Conference and Exhibit, Düsseldorf, Federal Republic of Germany, June 8-12, 1986. Manuscript received at ASME Headquarters February 10, 1986. Paper No. 86-GT-184.

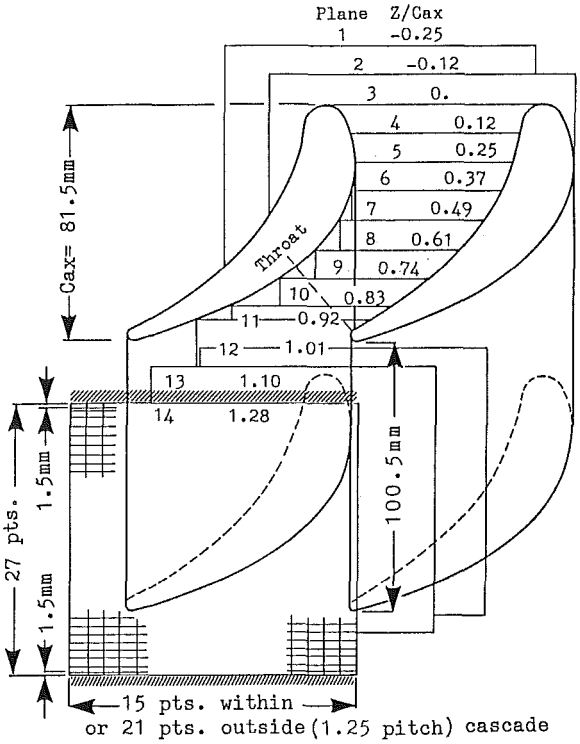

Fig. 1 Traverse measuring planes of straight stator cascade (S3 planes)

direction of the cascade by a pulse motor drive. On the movable wall, there is a radial traverse gear for moving a sensor when a pulse motor drive is set.

The stator blades were made of engineering plastic. Clearance between the movable wall and the blade tip was sealed by felt material. This can be seen in Fig. 1 in Part 2. In the present test of the stator cascade, two sheets of about 5-mm-wide × 0.1-mm-thick aluminum film are attached near two blade tips. This was for making electric contact of the sensor with the blade surface in order to stop the present automatic measuring system, when such contact happens during the traverse measurements.

Test Conditions. The fourteen measuring planes analyzed in the paper are shown in Fig. 1. The cascade outlet flow velocity far downstream of the cascade was kept constant for all traverse measurements. For this, a Prandtl-type total/static pressure probe was used. The test Reynolds number, based on the mass-averaged outlet velocity at the furthest downstream traverse plane (plane 14, $Z/C_{ax} = 1.28$) and the blade chord, was about 2.8×10^5.

Differences between the design and the test flow angles are as follows:

	Design	Test
Inlet flow angle	0 deg	-2.9 deg ($i = -2.9$ at plane 1)
Outlet flow angle	-68 deg	-67.7 deg
Turning angle	68 deg	64.8 deg

The inlet flow conditions and the inlet endwall boundary layer parameters are as follows:

Density $\rho = 1.22$ kg/m^3
Viscosity $\nu = 1.44 \times 10^{-5}$ m^2/s
$\bar{V}_{m,1} = 13.8$ m/s
$\bar{V}_{m,1,\mathrm{mid}} = 14.2$ m/s
$\bar{V}_{m,14} = 38.3$ m/s
Turbulence intensity in free stream $\mathrm{Tu}_1 = 0.5$ percent

	Hub	Tip
Boundary layer thickness δ_{99}/H	0.180	0.210
Displacement thickness δ^*/H	0.0166	0.0301
Momentum thickness δ^{**}/H	0.0136	0.0181
Shape factor δ^*/δ^{**}	1.22	1.66

The above boundary layer parameters were calculated from the spanwise distribution of the pitchwise mass-averaged resultant velocity at cascade inlet plane 1 (i.e., $Z/C_{ax} = -0.25$ in Fig. 5).

The sensor used for traverse measurements was a cobra-type five-hole pitot tube, with a head size of 1.5 mm. All traverse

Nomenclature

A = control area for calculating mass-averaged value
C_{ax} = cascade axial chord
CP_s = static pressure coefficient based on outlet velocity
CP_t = total pressure loss coefficient based on outlet velocity
$CP_{t,1}$ = total pressure loss coefficient based on inlet velocity
C_{sk} = secondary kinetic energy coefficient = $(V_s/\bar{V}_{m,14})^2$
H = blade span
LE = blade leading edge
P_{atm} = atmospheric pressure
P_s = static pressure
P_t = total pressure
TE = blade trailing edge
V_m = resultant flow velocity
V_s = magnitude of secondary flow vector
V_z = axial velocity
Y = spanwise distance from hub endwall
Z = axial distance from blade leading edge
δ_{99} = boundary layer thickness
δ^* = displacement thickness

$$= \int_0^{H/2} (1 - \bar{V}_m/\bar{V}_{m,\mathrm{mid}}) dY$$

δ^{**} = momentum thickness

$$= \int_0^{H/2} (1 - \bar{V}_m/\bar{V}_{m,\mathrm{mid}})(\bar{V}_m/\bar{V}_{m,\mathrm{mid}}) dY$$

Δ = interval of contour plot
θ_y = yaw flow angle measured from cascade axial direction
ρ = density
φ = represents θ_y, V_m, CP_t, V_s, or C_{sk}

Subscripts

1–14 = number of traverse measuring (S3) planes
i = pitchwise number of control areas in one blade pitch
j = spanwise number of control areas in the whole span
mid = midspan

Superscripts

$-$ = pitchwise mass-averaged value
$=$ = overall mass-averaged value

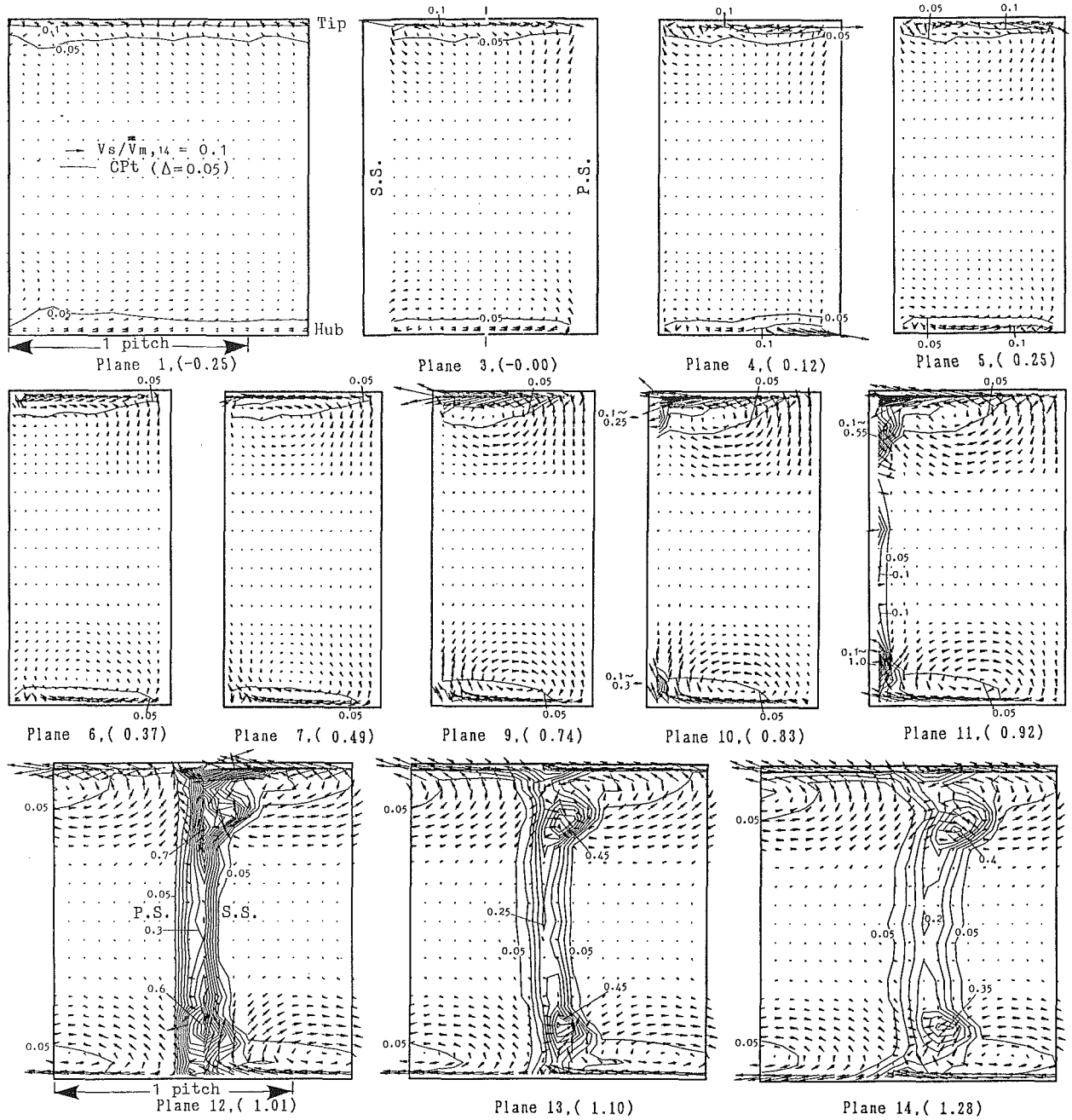

Fig. 2 Development of secondary flows and total pressure losses before, within, and after a straight stator cascade, S3 planes, (Z/C_{ax})

measurements were made under automatic control of a microcomputer. The mechanical resolution of the device was less than 0.01 mm for both spanwise and pitchwise direction of the cascade. All pressures were measured by individual transducers to save the scanning time of the pressures. Yaw direction of the pitot tube was kept in a constant direction during each traverse measurement. Absolute flow directions were then determined by using the pressure data with a calibration map which was programmed on a Vax 11/750 minicomputer.

Analysis Method

Definition of Secondary Flow (Deviation From Flow at Midspan). In the present analysis for straight cascades, the pitchwise local flow directions at midspan were used to determine the secondary flow vectors at other spans; secondary flow vectors were calculated in a way that flows at other spans were projected onto a plane normal to the flow direction at midspan, which is located at the same pitchwise location as the calculated points.

The secondary flow velocities V_s were normalized by the mass-averaged flow velocity at plane 14, i.e., $\bar{V}_{m,14}$ at $Z/C_{ax}=1.28$. The normalized secondary flow vectors were drawn by looking at them from the downstream side of the cascade.

The secondary kinetic energy coefficient C_{sk} is defined by

$$C_{sk}=(V_s/\bar{V}_{m,14})^2 \quad \text{and} \quad C_{sk,1}=(V_s/\bar{V}_{m,1})^2$$

Total and Static Pressure Coefficients (CP_t and CP_s). Total pressures P_t were normalized in the form of total pressure loss coefficients by

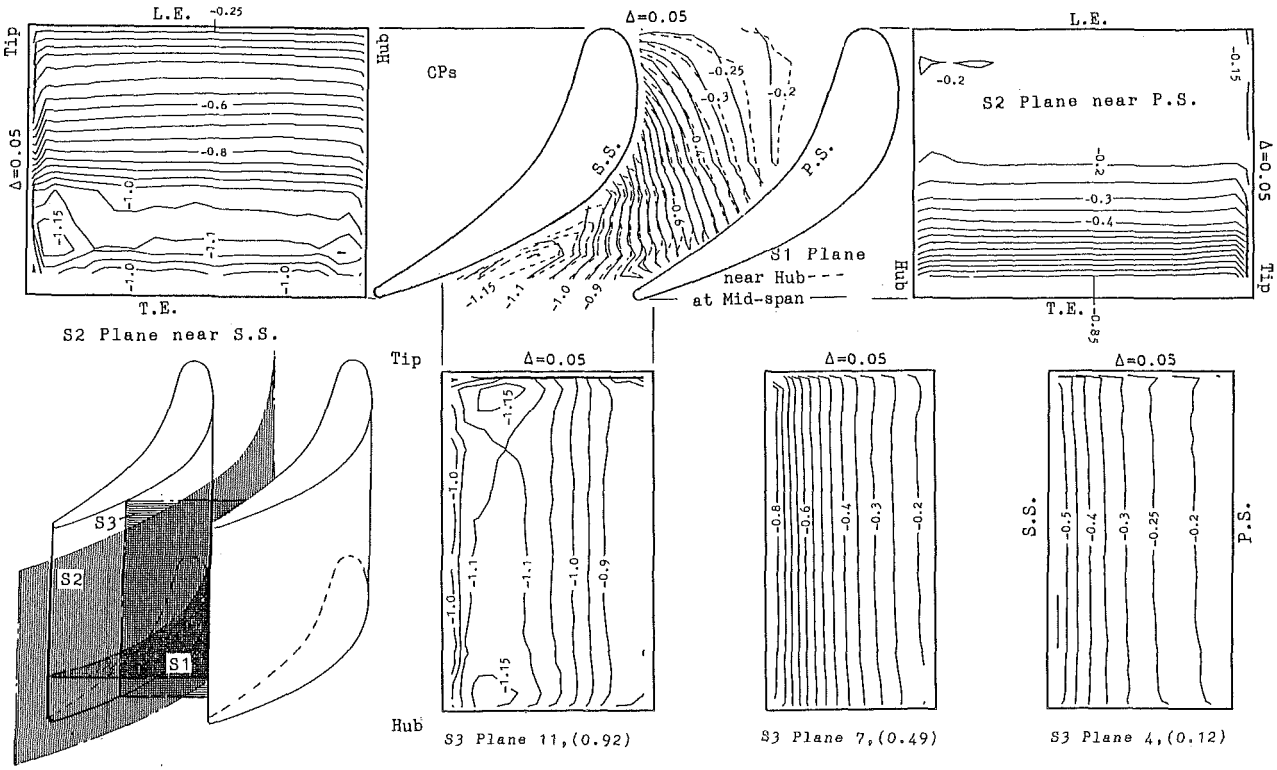

Fig. 3 Static pressure distribution on various planes within a stator cascade

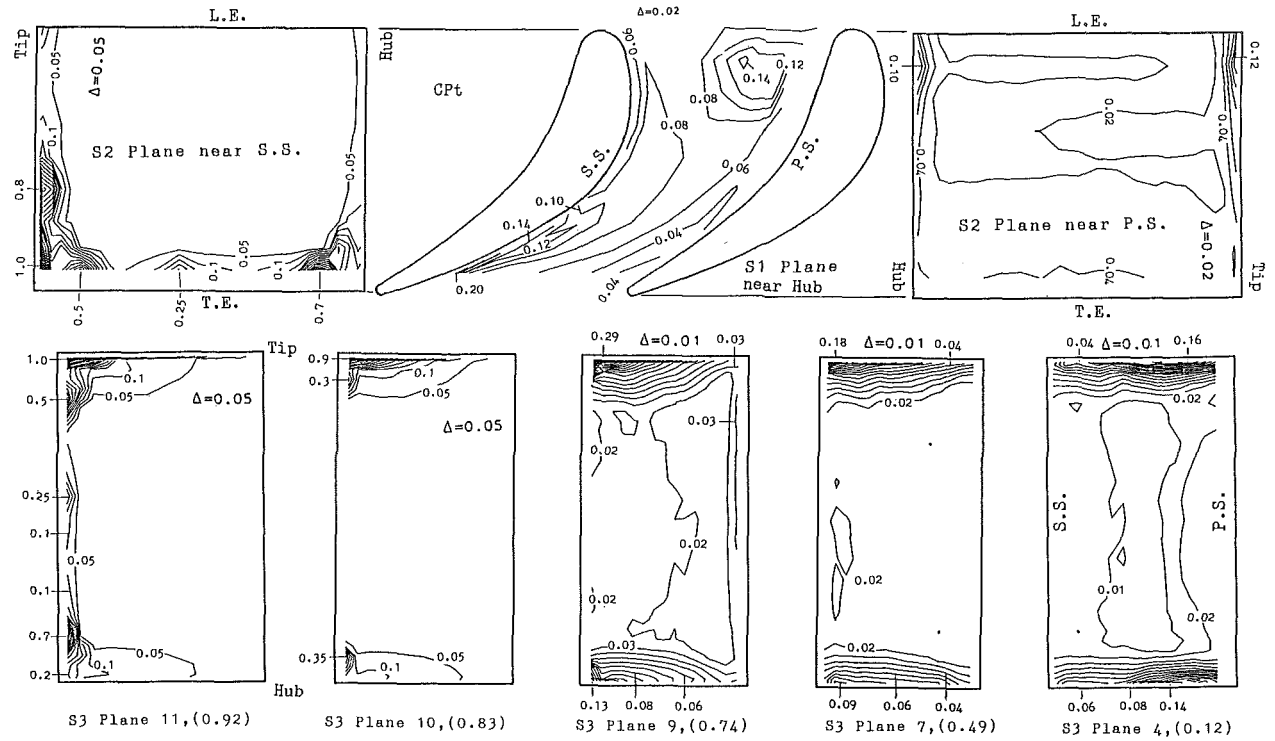

Fig. 4 Total pressure loss distribution on various planes within a stator cascade

$$CP_t = (P_{\text{atm}} - P_t)/(0.5 \times \rho \times \bar{\bar{V}}^2_{m,14})$$

and

$$CP_{t,1} = (P_{\text{atm}} - P_t)/(0.5 \times \rho \times \bar{\bar{V}}^2_{m,1})$$

where P_{atm} is the atmospheric pressure and ρ is density. $\bar{\bar{V}}_{m,14}$ and $\bar{\bar{V}}_{m,1}$ are the mass-averaged cascade outlet velocity at plane 14 and the mass-averaged inlet velocity at plane 1, respectively.

Similarly, static pressures P_s were normalized by

$$CP_s = (P_s - P_{\text{atm}})/(0.5 \times \rho \times \bar{\bar{V}}^2_{m,14})$$

Pitchwise-Averaged Yaw Flow Angle, Velocity, Total

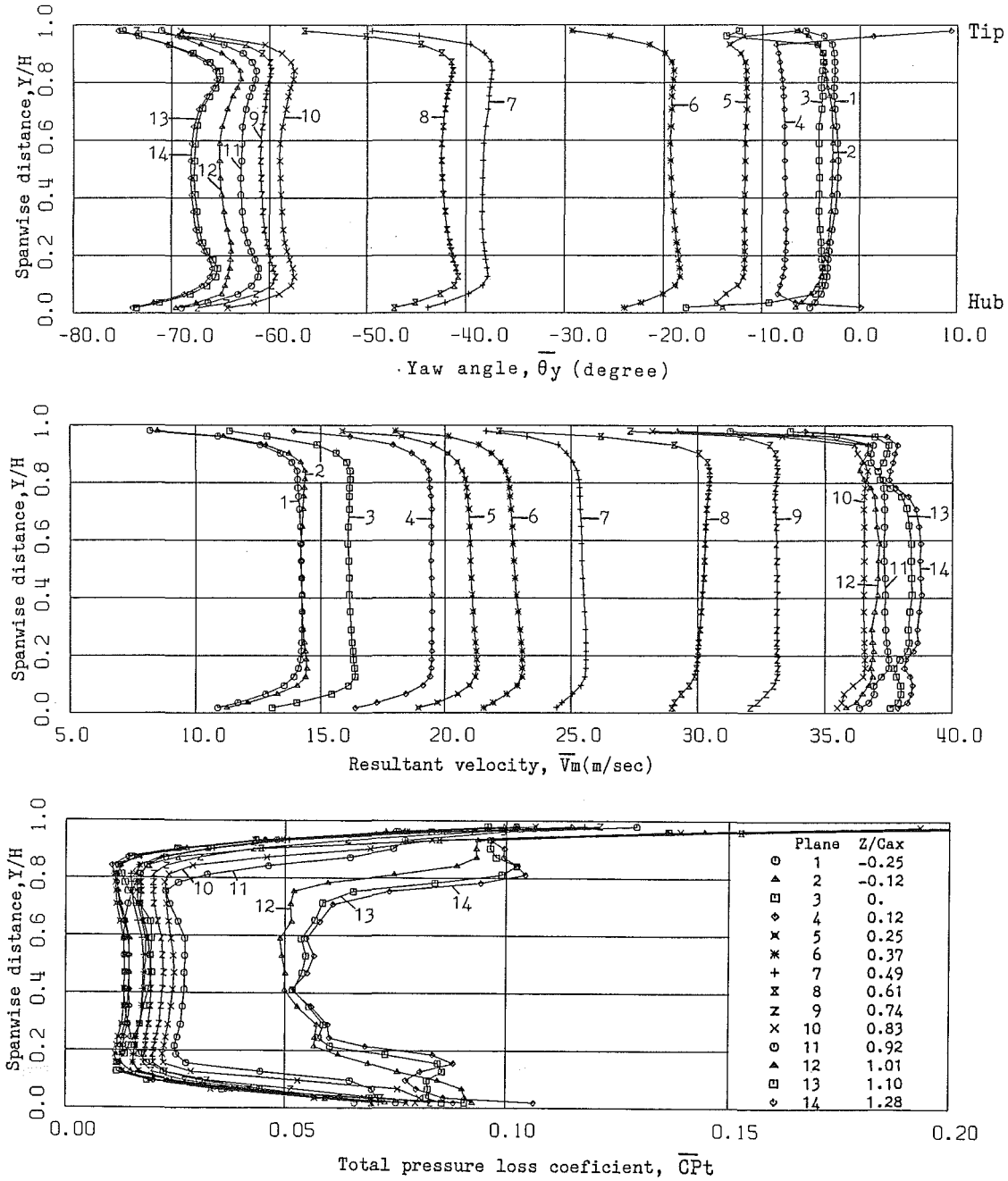

Fig. 5 Spanwise distribution of pitchwise-averaged yaw flow angle, resultant velocity, and total pressure loss coefficient

Pressure Loss Coefficient, and Overall Loss. The averaging method adopted is that of mass averaging. In each small control area (A_{ij}) formed by four neighboring measuring points, the values at the four points of yaw flow angle ($\theta_{y,i,j}$), resultant velocity ($V_{m,i,j}$), total pressure loss coefficient ($CP_{t,i,j}$), axial velocity ($V_{z,i,j}$), and secondary flow velocity ($V_{s,i,j}$) were arithmetically averaged individually. In the region near the blade surfaces and the endwalls, the values on the surfaces and on the walls (i.e., boundary values) were estimated with a linear extrapolation of experimental data, and the same averaging procedure was applied to each control area in the region by using four values: two measured data and two estimated boundary values. Then, pitchwise mass-averaged values ($\bar{\varphi}$) and overall mass-averaged values ($\bar{\bar{\varphi}}$) were calculated by

$$\bar{\varphi} = \sum_i (\varphi \times A \times V_z)_{i,j} \Big/ \sum_i (A \times V_z)_{i,j}$$

and

$$\bar{\bar{\varphi}} = \sum_j \sum_i (\varphi \times A \times V_z)_{i,j} \Big/ \sum_j \sum_i (A \times V_z)_{i,j}$$

where φ represents θ_y, V_m, CP_t, V_s, or C_{sk} ($= V_s^2 / \bar{V}_{m,14}^2$).

S1, S2, and S3 Planes. Similarly to Wu's definition [11], S1 and S2 surfaces for cascade flow analysis, and an additional plane S3, were defined as follows (see also the sketch in Fig. 3): S1 planes are blade-to-blade surfaces parallel to the cascade endwalls; S2 surfaces are meridional surfaces roughly parallel to the blade surfaces; and S3 planes are orthogonal

channel surfaces which are parallel to the cascade pitchwise direction. S3 planes correspond exactly to the traverse measuring planes shown in Fig. 1.

Contour plots on an S1 (blade-to-blade) plane and on two S2 planes near both blade surfaces are obtained by using the data on S3 (traverse) planes.

Experimental Results and Discussion

Secondary Flows and Total Pressure Losses at Traverse Planes (S3 Planes, Fig. 2). Figure 2 shows a general view of production and development of secondary flows and the associated losses within the present cascade. Due to the special treatment made near the blade tips, as mentioned previously, and due to the different boundary layer development on the cascade inlet endwalls, as shown at plane 1 of Figs. 2 and 5, the flow fields are not completely symmetric against the midspan line of the passage. The following discussion will be made mostly on flows at the hub-side half of the passage.

The flows at planes 3–6 show a weak vortex rotating in the counterclockwise direction at the suction surface (SS)/hub endwall corner. This vortex (countervortex) corresponds to the suction-side leg of the leading-edge horseshoe vortex formed on the endwall. Marchal and Sieverding [5] measured this countervortex at the upstream inlet plane and at about $Z/C_{ax}=0.15$ of their straight stator cascade. The position of the vortex in the present case seems to remain at the corner up to $Z/C_{ax}=0.37$, i.e., plane 6. The vortex does not seem to affect loss distribution very much. The vortex tends to shift the loss contour toward the endwall. It has almost disappeared at plane 6, while the passage vortex becomes clear near the endwall. On the other hand, it was difficult to recognize the pressure-side leg of the horseshoe vortex which should exist near the pressure surface (*PS*)/endwall corner of the leading edge. The secondary flow vectors at the corner show weak flows moving toward the endwalls along the *PS*. The flows, then, turn around the endwall corner and pass the endwall from the pressure side to the suction side. The flows finally collide with the countervortex near the *SS*/endwall corner.

The endwall (secondary) flows moving toward the suction side at plane 3 change their flow direction to the pressure side on a part of the endwalls at planes 4 and 5. This part of the endwall may correspond to the reverse flow region located at the pressure side of the leading edge. This region can be seen in Langston's flow visualization [2] and in Hah's analysis [12] of endwall boundary layer flows. This would be due to flow separation at the leading-edge/*PS* corner.

Two passage vortices near both endwalls grow up as they pass further downstream from planes 6–11 within the cascade. The rotational motion of the vortices pushes low-energy fluids of the endwall boundary layers toward the suction side. Similarly to the results obtained by Langston et al. [2], Marchal and Sieverding [5], and Gregory-Smith and Graves [3], the figures from planes 9–11 show that the passage vortices roll up the low-energy fluids onto the *SS* and that they generate high-loss cores there, while they make the loss region near the pressure surface/endwall corners thinner.

Downstream the cascade from planes 12–14, the strength of rolling-up of the passage vortices increases once in the wake at plane 12 and decreases further downstream. The wake width gets wider and the loss values in the loss cores decrease, due to fluid mixing between the low-energy fluids in the wake and the high-energy fluids outside the wake. This mixing causes additional loss which will be seen later on the mass-averaged overall loss shown in Fig. 6. An experimental analysis on this downstream mixing has recently been given by Moore and Adhye [13], who show that the sum of the mass-averaged total pressure loss coefficient and the kinetic-energy coefficient of secondary flow remains almost constant in their case. This

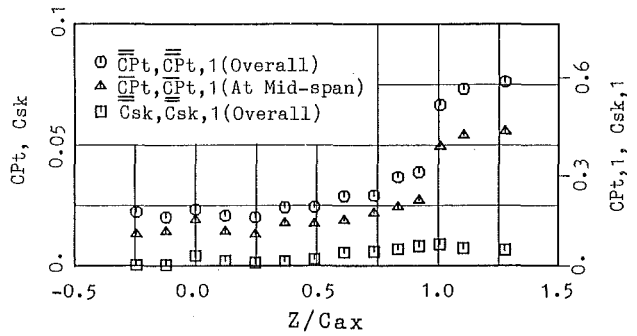

Fig. 6 Evolution of mass-averaged total pressure loss (straight stator cascade)

means that the increase of overall CP_t downstream of the cascade results mainly from the decay of the secondary flows.

The regions where the secondary flows dominate are restricted only within about 1/4 span from the endwalls in the present stator cascade with about 65-deg turning, and passage vortices of this rather flat form are similar to those obtained by Gregory-Smith and Graves [3] for a straight rotor cascade with 110-deg turning. It is noteworthy that the distance of the passage vortex center from the endwall is always constant through this stator cascade.

Static Pressure Distribution on S1, S2, and S3 Planes Within Stator Cascade (Fig. 3). The two S1 (blade-to-blade) planes shown in Fig. 3 correspond to the planes located apart from the hub endwall by 1.49 and 50 percent of the span height. On the other hand, the two S2 surfaces are not located at constant distances from each blade surface and may be seen as the lines connecting all edges at the *SS* side or the *PS* side of the contours on S1 and/or S3 planes in Fig. 3.

Comparison of solid lines and dashed lines on the S1 plane plane indicates that the blade-to-blade static pressure distribution at midspan differs from that near the endwall, due to the endwall shear flows. The differences can be found especially in the regions near the *PS* side of the upstream region and near the *SS* side of the downstream region within the cascade. Departure of the point of minimum static pressure from the *SS* was discussed by Langston et al. [2] based on their endwall static pressure data in a straight rotor cascade. The present results on the two S1 planes show that the points are always located apart from the *SS* not only on the endwall but also at midspan.

Static pressures over the *PS* are fairly uniform along the span except near endwall corners, as seen from the result on a S2 plane near the *PS*. The pressures over the *SS*, however, are fairly nonuniform, especially near endwalls downstream from the passage throat. This was caused by the two passage vortices.

The contours of CP_s at the three S3 planes show the change of the static pressures within the cascade; up to plane 7 ($Z/C_{ax}=0.49$), no significant disturbance occurred.

Total Pressure Loss Distribution on S1, S2, and S3 Planes Within Stator Cascade (Fig. 4). The loss distribution on the S1 plane near the hub endwall reveals two peaks; one is located at the inlet region and the other is located in the flow deceleration region near the *SS* just downstream from the throat. The former may be located in the low-energy region along the pressure side separation line(s) shown by Sjolander [14] and by Marchal and Sieverding [5]. The latter location corresponds roughly to the minimum pressure point near the endwall, as seen previously. It may be interesting to note that there is a corner region along the *SS* (indicated by $CP_t=0.06$) where CP_t is lower than in the neighboring region. The region extends up to $Z/C_{ax}=0.37$ (plane 6). This corresponds to the

plane where the suction-side leg of the leading-edge horseshoe vortex almost disappeared.

The loss distribution on the S2 plane near the *PS* shows that high-loss regions are restricted only to *PS*/endwall corners near the leading edge. The other distribution on S2 near the *SS*, however, shows that low-energy fluids gradually cover the surface from the endwall side toward midspan. Then the low-energy fluids rapidly cover the deceleration flow region downstream of the throat.

The results given at various S3 planes show the migration of endwall low-energy fluids from the pressure side to the suction side. We note especially the movement of the maximum loss values along the walls. Except for the high-loss core on the tip endwall, there exist three local peaks on the *SS* near the trailing edge, as seen at the S3 plane 11 ($Z/C_{ax} = 0.92$) and at the S2 plane near the *SS*. Two of these were produced by the interaction of the passage vortices with the *SS* near the endwalls. The other, at midspan, may be produced by the suction-surface boundary layer fluids plus some of the low-energy fluids transported from both loss cores.

Spanwise Distribution of Pitchwise Mass-Averaged Yaw Angle, Velocity, and Loss Through Stator Cascade (Fig. 5). Figure 5 shows, from the yaw angle variation, that the actual turning angle in the present test is about 65 deg. The incidence is -2.9 deg. The yaw angle at plane 4 ($Z/C_{ax} = 0.12$, just downstream from the cascade inlet plane) shows very large variation close to the endwalls. This was probably caused by endwall separation near the *PS*, as was seen in Fig. 2. All the yaw angle curves from planes 6–14 show typical shapes of yaw distribution under the effect of secondary flows (passage vortices); i.e., the curves have two underturning parts and two overturning parts near the endwalls compared to the angle at midspan.

The velocity distribution of Fig. 5 shows fairly large acceleration of the cascade flow and the change of the boundary layer profiles through the cascade. The ratio of acceleration ($\bar{\bar{V}}_{m,14}/\bar{\bar{V}}_{m,1}$) is about 2.78. The inlet boundary layer thickness is about 0.2 of the span height. Effects of the passage vortices on the velocity curves appear especially at planes 11–14; velocity defects at planes 13 and 14 occur at about $0.18 \times$ span height from both endwalls.

CP_t increased rapidly at plane 12 which is located just downstream from the cascade ($Z/C_{ax} = 1.01$). The value includes the wake loss. Downstream from the cascade (see planes 12–14), the rate of the increase goes down. The local peaks of CP_t at planes 12, 13, and 14 close to the endwalls correspond to the high-loss cores. Apparently they are caused by the passage vortices.

Evolution of Overall Total Pressure Loss Through the Stator Cascade (Fig. 6). Figure 6 presents an evolution of overall total pressure loss and of the loss obtained at the midspan location. The latter might correspond roughly to the cascade profile loss if loss migration from the endwall to midspan were small. The difference between the overall loss and the midspan value may be considered to be roughly equal to the secondary loss, including the endwall boundary layer loss.

The loss in the present cascade shows little growth up to about $Z/C_{ax} = 0.74$ (plane 9) but rapidly increases from there to the trailing edge. Plane 9 corresponds to a plane at which the rolling-up of the low-energy fluids onto the *SS* starts.

The secondary kinetic energy coefficients are also included in the same figure and they grow a little at the cascade inlet and between $Z/C_{ax} = 0.5$ and $Z/C_{ax} = 1.0$.

Downstream from the cascade, the growth rates of both overall loss and midspan loss decrease. The value of the secondary kinetic energy also decreases.

Conclusions

The present study gave fairly detailed experimental data of secondary flows and losses in a straight stator cascade in order to estimate the loss mechanism quantitatively. A weak countervortex, the suction-side leg of the leading-edge horseshoe vortex, appeared at the suction surface/endwall corner in the upstream region of the present cascade but had no significant effects on the loss value. There was a high-loss region on the endwall near the pressure side of the cascade inlet region within the cascade, probably caused by the pressure-side leg of the leading-edge horseshoe vortex. This also did not affect the overall loss to any recognizable extent. Most of the loss produced within the cascade was due to the interaction of passage vortices with the suction surface downstream from the cascade throat.

References

1 Sieverding, C. H., "Recent Progress in the Understanding of Basic Aspects of Secondary Flows in Turbine Blade Passages," ASME JOURNAL OF ENGINEERING FOR GAS TURBINES AND POWER, Vol. 107, 1985, pp. 248–257.

2 Langston, L. S., Nice, M. L., and Hooper, R. M., "Three Dimensional Flow Within a Turbine Cascade Passage," ASME JOURNAL OF ENGINEERING FOR POWER, Vol. 99, 1977, pp. 21–28.

3 Gregory-Smith, D. G., and Graves, C. P., "Secondary Flows and Losses in a Turbine Cascade," in: *Viscous Effects in Turbomachines*, AGARD-CP-351, 1983.

4 Sieverding, C. H., and Wilputte, Ph., "Influence of Mach Number and End Wall Cooling on Secondary Flows in a Straight Nozzle Cascade," ASME JOURNAL OF ENGINEERING FOR POWER, Vol. 103, 1981, pp. 257–264.

5 Marchal, P., and Sieverding, C. H., "Secondary Flows Within Turbomachinery Bladings," in: *Secondary Flows in Turbomachines*, AGARD-CP-214, 1977.

6 Sieverding, C. H., Van Hove, W., and Boletis, E., "Experimental Study of the Three-Dimensional Flow Field in an Annulaur Turbine Nozzle Guidevane," ASME JOURNAL OF ENGINEERING FOR GAS TURBINES AND POWER, Vol. 106, 1984, pp. 437–448.

7 Boletis, E., Sieverding, C. H., and Van Hove, W., "Effects of Skewed Inlet End Wall Boundary Layer on the 3-Dimensional Flow Field in an Annular Turbine Cascade," in: *Viscous Effects in Turbomachines*, AGARD-CP-351, 1983.

8 Boletis, E., "Effects of Tip Endwall Contouring on the Three-Dimensional Flow Field in an Annular Turbine Nozzle Guide Vane: Part 1 – Experimental Investigation," ASME JOURNAL OF ENGINEERING FOR GAS TURBINES AND POWER, Vol. 107, 1985, pp. 983–990.

9 Yamamoto, A., and Yanagi, R., "Production and Development of Secondary Flows and Losses Within a Three Dimensional Turbine Stator Cascade," ASME Paper No. 85-GT-217, 1985.

10 Yamamoto, A., Takahara, K., Nouse, H., Inoue, S., Usui, H., and Mimura, F., "An Aerodynamic Design and the Overall Stage Performance of an Air-Cooled Axial-Flow Turbine," National Aerospace Laboratory, TR-321T, Jan. 1981.

11 Wu, C. H., "A General Theory of Three-Dimensional Flows in Subsonic and Supersonic Turbomachines of Axial-, Radial-, and Mixed-Flow Types," NACA 2604, 1952.

12 Hah, C., "A Navier-Stokes Analysis of Three-Dimensional Turbulent Flows Inside Turbine Blade Rows at Design and Off-Design Conditions," ASME JOURNAL OF ENGINEERING FOR GAS TURBINES AND POWER, Vol. 106, 1984, pp. 421–429.

13 Moore, J., and Adhye, R. Y., "Secondary Flows and Losses Downstream of a Turbine Cascade," ASME JOURNAL OF ENGINEERING FOR GAS TURBINES AND POWER, Vol. 107, 1985, pp. 961–968.

14 Sjolander, S. A., "The Endwall Boundary Layer in an Annular Cascade of Turbine Nozzle Guide Vanes," Carleton University, TR ME/A 75-4, 1975.

15 Carrick, H. B., "Secondary Flow and Losses in Turbine Cascade With Inlet Skew," in: *Secondary Flows in Turbomachines*, AGARD-CP-214, 1977.

16 Moore, J., and Ransmayr, A., "Flow in a Turbine Cascade: Part 1 – Losses and Leading-Edge Effects," ASME JOURNAL OF ENGINEERING FOR GAS TURBINES AND POWER, Vol. 106, 1984, pp. 400–408.

17 Moore, J., and Smith, B. L., "Flow in a Turbine Cascade: Part 2 – Measurement of Flow Trajectories by Ethylene Detection," ASME JOURNAL OF ENGINEERING FOR GAS TURBINES AND POWER, Vol. 106, 1984, pp. 409–413.

18 Graziani, R. A., Blair, M. F., Taylor, J. R., and Mayle, R. E., "An Experimental Study of Endwall and Airfoil Surface Heat Transfer in a Large Scale Turbine Blade Cascade," ASME Paper No. 79-GT-99, 1979.

19 Yamamoto, A., "Production and Development of Secondary Flows and Losses in Two Types of Straight Turbine Cascades, Part 2 – A Rotor Case," ASME JOURNAL OF TURBOMACHINERY, this issue.

APPENDIX

Blade Profile Coordinates

I	X_s	Y_s	X_p	Y_p (mm)
1	5.858	73.000	7.763	59.526
2	10.785	74.764	11.821	57.991
3	16.672	75.806	15.728	56.973
4	22.462	75.682	19.140	55.900
5	29.934	75.100	22.526	54.659
6	35.345	73.093	26.020	53.234
7	41.857	69.254	30.384	51.644
8	47.680	64.493	35.056	49.364
9	53.084	59.078	39.876	46.094
10	57.865	52.299	45.528	42.066
11	62.175	45.488	50.754	37.204
12	66.556	37.852	56.102	31.124
13	70.623	29.570	61.495	24.278
14	74.443	20.534	67.033	16.622
15	78.151	10.524	72.821	7.943
16	81.286	0.689	78.295	−0.660

D_L	(X_L , Y_L)	D_T	(X_T , Y_T)
13.300	(6.903 , 66.037)	3.300	(79.794 , 0.000)
D_{max}	(X_{max} , Y_{max})	chord	
22.000	(30.702, 63.240)	104.416	

where D_L, D_T, and D_{max} represent diameters of blade leading-edge, trailing-edge, and blade maximum thickness, and chord represents blade chord length. The coordinate points were connected smoothly to make the blade profile.

Production and Development of Secondary Flows and Losses in Two Types of Straight Turbine Cascades: Part 2—A Rotor Case

A. Yamamoto
National Aerospace Laboratory,
Chofu, Tokyo, Japan

Part 1 of this paper [1] presents the detailed mechanism of secondary flows and the associated losses occurring within a straight stator cascade with a relatively low turning angle of about 65 deg. The significant contribution of secondary flows on the loss production process was shown only near the blade suction surface downstream from the cascade throat ($Z/C_{ax} = 0.74$) *in which regional flows decelerated due to adverse pressure gradient. In the second part, the same experimental analysis is applied to a straight rotor cascade with a much larger turning angle of 102 deg. Flow surveys were made at 12 traverse planes located throughout the rotor cascade. The larger turning results in a similar but much stronger contribution of the secondary flows to the loss developing mechanism. Evolution of overall loss starts quite early within the cascade, and the rate of the loss growth is much larger in the rotor case than in the stator case.*

Introduction

As clearly shown by Smith [2] in his experimental correlation between stage loading coefficients, flow coefficients, and turbine efficiencies based on a number of experimental data of real turbines, the level of turbine efficiencies depends strongly on the loading coefficients; the efficiency tends to decrease with increase of the loading. The cascade turning angle is related to the blade loading and is one of the main factors affecting the loss developing mechanism.

In this part of the paper, mechanisms occurring within a straight rotor cascade with a larger turning angle than that in Part 1 will be made clear.

Test Cascade and Test Conditions

Most of the test facility is the same as described in Part 1 and only major differences are given here.

Low-Speed Straight Turbine Rotor Cascade. The blade profile is the same as the mean profile of the first-stage high-pressure turbine rotor for aeroengine use [3] and is given in the appendix. The major specifications of the cascade are as follows:

- Blade chord $C = 73.5$ mm
- Axial blade chord $C_{ax} = 72.6$ mm
- Blade pitch $S = 61.42$ mm
- Aspect ratio $H/C = 1.37$
- Solidity $C/S = 1.20$
- Number of blades $N = 6$
- Cascade inlet angle (at design) $\theta_{y,\text{inlet}} = 49.8$ deg
- Cascade outlet angle (at design) $\theta_{y,\text{outlet}} = -63.5$ deg
- Cascade turning angle (at design) $= 113.3$ deg

The cascade is characterized by thick leading and trailing edges, low aspect ratio and low solidity for air cooling, and by a large turning angle for large loading. The present rotor blades were made of aluminum by a wire-cutting manufacturing method. The test cascade is shown in Fig. 1. In the present case of the rotor cascade, two sheets of about 12-mm-wide × 0.1-mm-thick aluminum film are attached to the blade surfaces near the tip. The purpose is the same as described in Part 1.

Test Conditions. Twelve measuring planes analyzed in the paper are shown in Fig. 2. The test Reynolds number, based on the mass-averaged outlet velocity at the furthest downstream traverse plane (plane 12, $Z/C_{ax} = 1.23$) and the blade chord, was about 1.8×10^5. The turbulence intensity of the inlet free stream obtained at plane 1 was about 0.5 percent.

In the present test, differences between the design and the test flow angles are as follows:

	Design	Test
Inlet flow angle	43.6 deg	40.1 deg ($i = -9.7$ deg at plane 1)
Outlet flow angle	−63.5 deg	−61.7 deg
Turning angle	107.1 deg	101.8 deg

The inlet flow conditions and the inlet endwall boundary layer parameters are as follows:

Density $\rho = 1.22$ kg/m^3

Contributed by the Gas Turbine Division of THE AMERICAN SOCIETY OF MECHANICAL ENGINEERS and presented at the 31st International Gas Turbine Conference and Exhibit, Düsseldorf, Federal Republic of Germany, June 8–12, 1986. Manuscript received at ASME Headquarters February 10, 1986. Paper No. 86-GT-185.

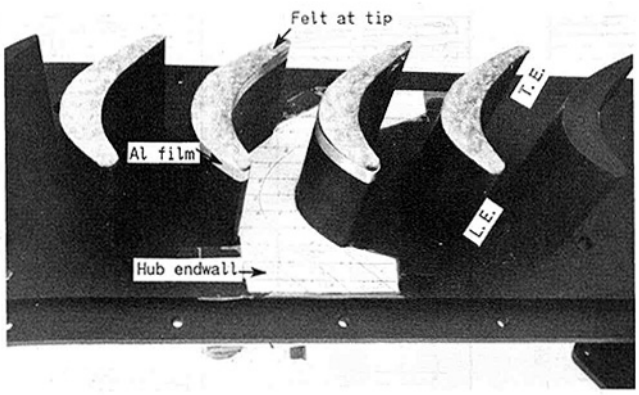

Fig. 1 Test cascade (rotor case)

Viscosity $\nu = 1.44 \times 10^{-5}$ m^2/s
$\bar{V}_{m,1} = 23.9$ m/s
$\bar{V}_{m,1,\text{mid}} = 24.6$ m/s
$\bar{V}_{m,12} = 35.3$ m/s
Turbulence intensity in free stream $\text{Tu}_1 = 0.5$ percent

	Hub	Tip
Boundary layer thickness δ_{99}/H	0.117	0.105
Displacement thickness δ^*/H	0.0132	0.0266
Momentum thickness δ^{**}/H	0.0094	0.0152
Shape factor δ^*/δ^{**}	1.41	1.75

The above boundary layer parameters were calculated from the spanwise distribution of the pitchwise mass-averaged resultant velocity at the cascade inlet plane 1 (i.e., $Z/C_{ax} = -0.26$ in Fig. 6).

Analysis Method

Secondary flow vectors V_s were obtained in the manner given in Part 1. The secondary flow velocities V_s were normalized by the mass-averaged flow velocity at plane 12, i.e., $\bar{V}_{m,12}$ at $Z/C_{ax} = 1.23$. The normalized vectors were drawn by looking at them from the downstream side of the cascade. The secondary kinetic energy coefficients C_{sk} are calculated by

$$C_{sk} = (V_s/\bar{V}_{m,12})^2 \quad \text{and} \quad C_{sk,1} = (V_s/\bar{V}_{m,1})^2$$

Total pressures P_t were normalized in the form of total pressure loss coefficients by

$$CP_t = (P_{\text{atm}} - P_t)/(0.5 \times \rho \times \bar{V}^2_{m,12})$$

and

$$CP_{t,1} = (P_{\text{atm}} - P_t)/(0.5 \times \rho \times \bar{V}^2_{m,1})$$

where P_{atm} is the atmospheric pressure and ρ is density. $\bar{V}_{m,12}$ and $\bar{V}_{m,1}$ are the mass-averaged cascade outlet velocity at plane 12 and the mass-averaged inlet velocity at plane 1.

Similarly, static pressure P_s is normalized by

$$CP_s = (P_s - P_{\text{atm}})/(0.5 \times \rho \times \bar{V}^2_{m,12})$$

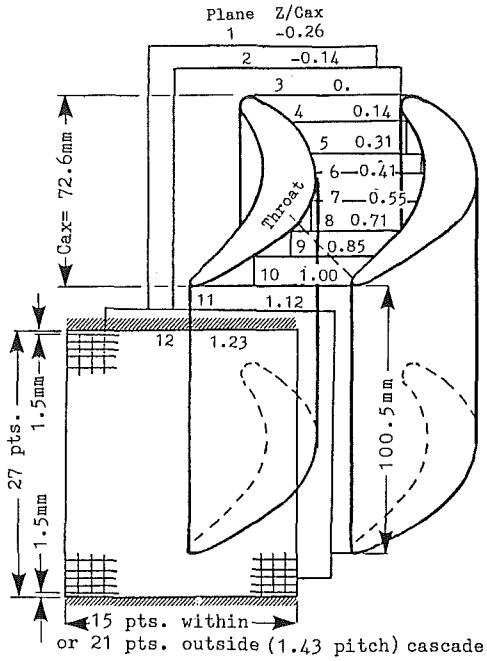

Fig. 2 Traverse measuring planes of straight rotor cascade (S3 planes)

Nomenclature

C_{ax} = cascade axial chord
CP_s = static pressure coefficient based on outlet velocity
CP_t = total pressure loss coefficient based on outlet velocity
$CP_{t,1}$ = total pressure loss coefficient based on inlet velocity
C_{sk} = secondary kinetic energy coefficient $= (V_s/\bar{V}_{m,12})^2$
H = blade span
LE = blade leading edge
P_{atm} = atmospheric pressure
P_s = static pressure
P_t = total pressure
PS = blade pressure surface
SS = blade suction surface
TE = blade trailing edge
V_m = resultant flow velocity
V_s = magnitude of secondary flow vector
V_z = axial velocity
Y = spanwise distance from hub endwall
Z = axial distance from blade leading edge
δ_{99} = boundary layer thickness
δ^* = displacement thickness $= \int_0^{H/2} (1 - \bar{V}_m/\bar{V}_{m,\text{mid}})dY$
δ^{**} = momentum thickness $= \int_0^{H/2} (1 - \bar{V}_m/\bar{V}_{m,\text{mid}})(\bar{V}_m/\bar{V}_{m,\text{mid}})dY$
Δ = interval of contour plot
θ_y = yaw flow angle measured from cascade axial direction
ρ = density

Subscripts

1-12 = number of traverse measuring (S3) planes
mid = midspan

Superscripts

$\bar{}$ = pitchwise mass-averaged value
$=$ = overall mass-averaged value

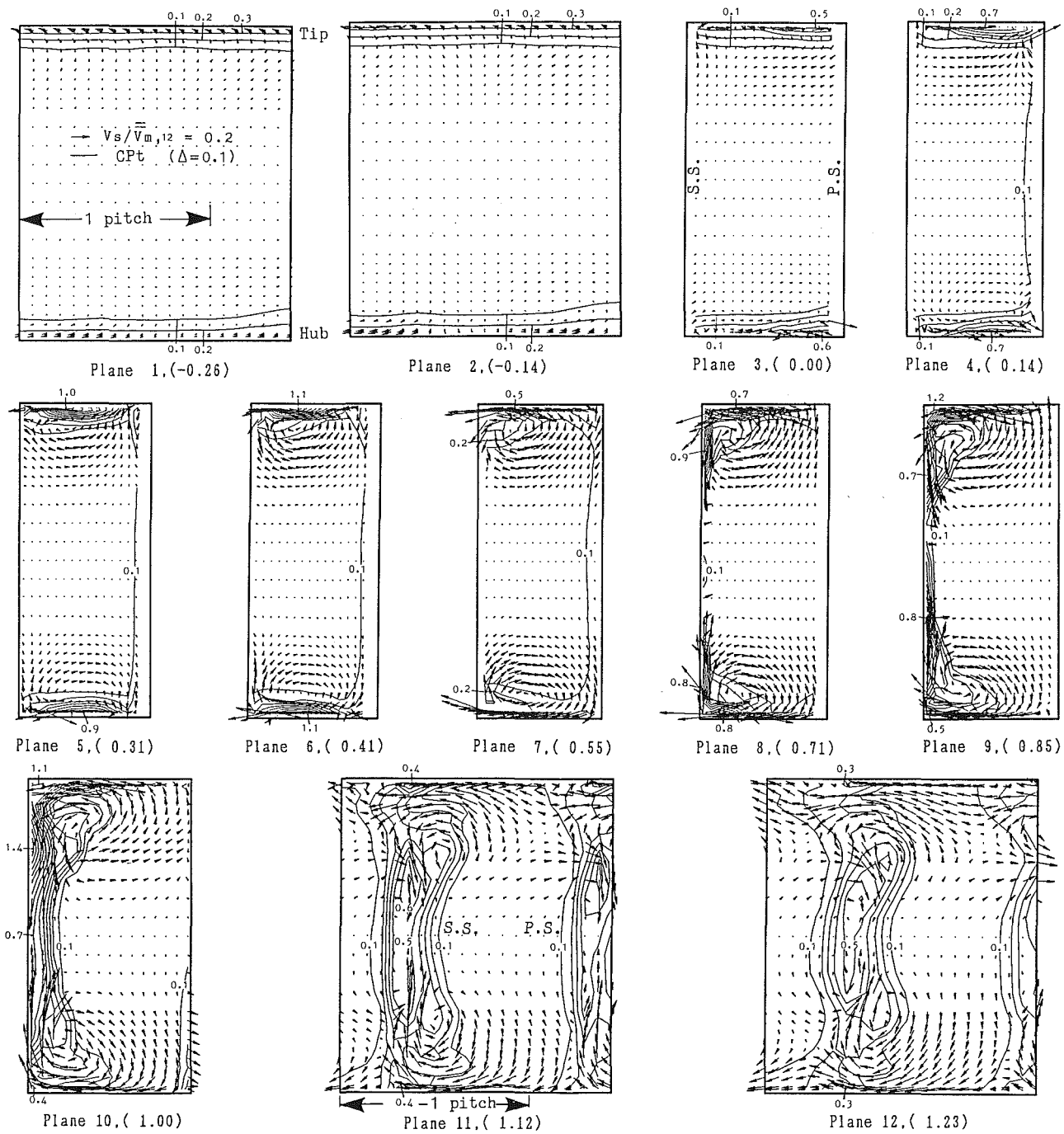

Fig. 3 Development of secondary flows and total pressure losses before, within, and after a straight rotor cascade, S3 planes, (Z/C_{ax})

The mass-averaging procedure for yaw flow angle, resultant velocity, and loss coefficient is given in Part 1. The definitions of S1, S2, and S3 planes are also given in Part 1 and a sketch of them is given in Fig. 4 of the present paper.

Experimental Results and Discussion

Secondary Flows and Total Pressure Losses at Traverse Planes (S3 Planes, Fig. 3). Figure 3 represents a process of production and development of secondary flows and the associated losses through the cascade. Note that the scale of the secondary flow vector adopted in this figure is shortened to half the scale adopted in Part 1, since the magnitudes of secondary flows are generally too large to plot without confusing the vectors with the contours of CP_t.

In the present case with larger turning, the loss production mechanism due to secondary flows is essentially the same as that seen in Part 1, except for the following: The counter-vortex at the suction surface (*SS*)/endwall corner can be clearly seen only at plane 3 ($Z/C_{ax} = 0.0$) which corresponds only to the cascade inlet plane. Gregory-Smith and Graves [4] measured this vortex also at $Z/C_{ax} = 0.03$ of their straight rotor cascade. In the following discussion, a number included in a bracket following a plane number represents the value of Z/C_{ax}, i.e., normalized axial distance from the blade leading edge. The vortex has almost disappeared at the next downstream plane, plane 4 (0.14). Passage vortices have already developed fully at plane 5 (0.31). Rolling-up of low-energy fluids onto the *SS* has started at plane 7 (0.55) which is still located upstream of the cascade throat. The passage vor-

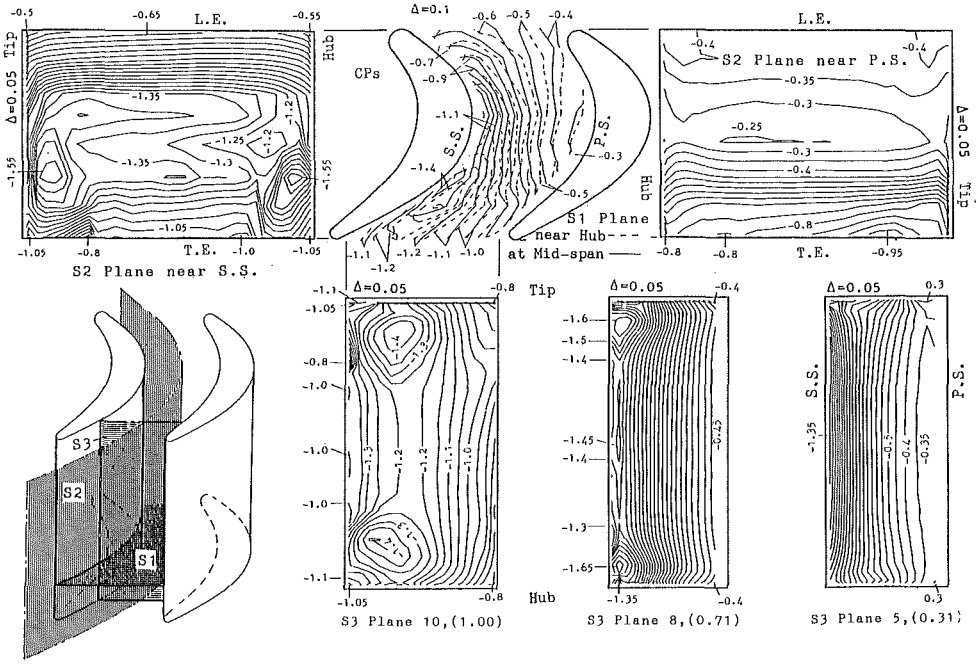

Fig. 4 Static pressure distribution on various planes within a rotor cascade

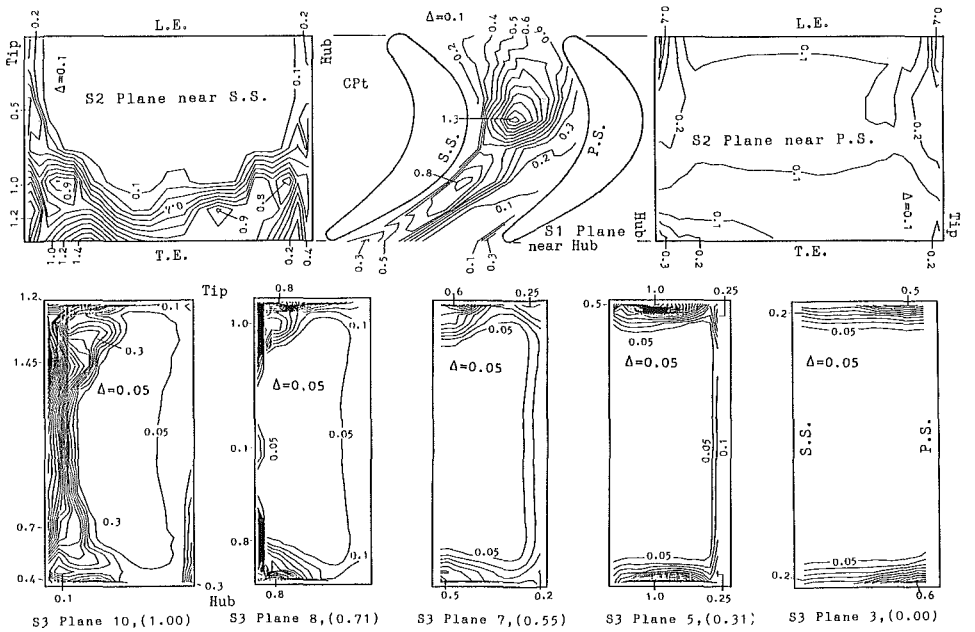

Fig. 5 Total pressure loss distribution on various planes within a rotor cascade

tices are very strong and they concentrate low-energy fluids in very thin loss cores on the *SS*, as seen typically at plane 8 (0.71). The spanwise flows of the low-energy fluids coming from both endwalls meet together at plane 9 (0.85). They rapidly increase the thickness of the high-loss region on the *SS* after the meeting, as seen at plane 10 (1.00). It should be noted that the secondary flow vectors at plane 7 show very smooth circulation and are not disturbed even at the *SS*/endwall corner, while those at planes 6 and 8 show irregular vector plots. This will be discussed later on the loss distribution near the endwalls.

Downstream from the cascade, i.e., at planes 11 and 12, the strong rolling-up of the passage vortices promotes the fluid mixing and energizes the wake flow especially from the endwall sides. These downstream vector plots represent quite similar patterns of secondary flow field shown in Fig. 2 of Sieverding's paper [5], which figure was cited from Armstrong's paper [6]; the figure presents blade shed circulation in addition to passage vortex, as shown here.

The distance of the passage vortex center from the endwall is constant only up to plane 9 (0.85) and increases at the downstream planes in the present rotor cascade, while the distance was always constant in the stator cascade.

Static Pressure Distribution on S1, S2, and S3 Planes (Fig. 4). The two S1 (blade-to-blade) planes shown in Fig. 4 correspond to the planes located apart from the hub endwall by 1.49 and 50 percent of the span height. The difference between the two static pressure distributions on these two S1 planes is more significant in the present rotor case than in the stator

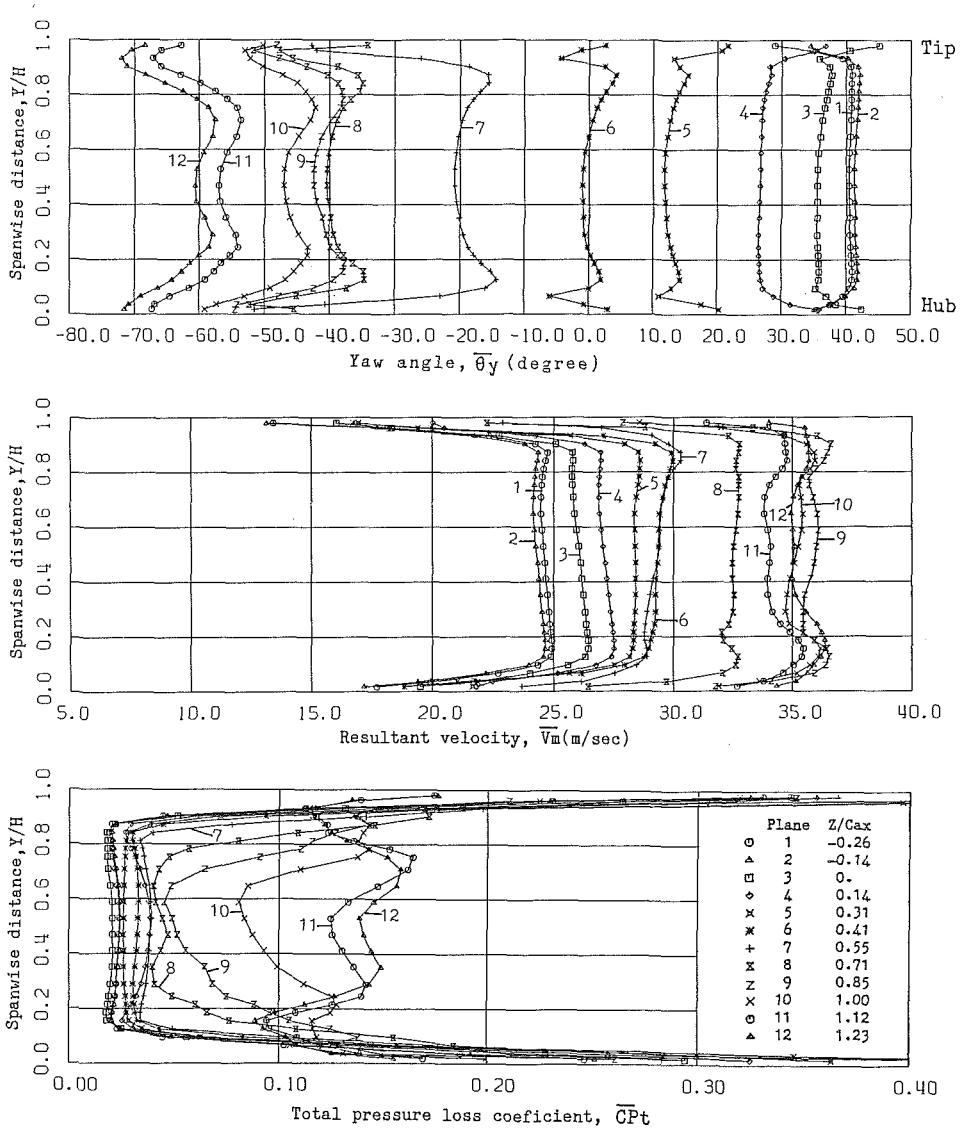

Fig. 6 Spanwise distribution of pitchwise-averaged yaw flow angle, resultant velocity, and total pressure loss coefficient

case. The minimum pressure points on both planes are located apart from the *SS* in the present cascade, too. The distance between these two minimum pressure points is larger in the present case. The point on the midspan S1 plane is located farther upstream and closer to the *SS* than that on the S1 plane near the endwall.

The static pressure contours on the S2 surface near the *PS* reveal a fairly large deceleration region located between the leading edge and the half axial chord. Especially at the *PS*/endwall corners near the leading edge, the rate of flow deceleration is large. As already seen in Fig. 3, the inlet flows near the corners were moving toward the endwalls. Similar corner flows in the regions may be found in Fig. 20 of Gregory-Smith and Graves [4] of their measurements by a pitot tube, and also in Fig. 5(*g*) of Marchal and Sieverding [7] of pressure surface flow visualization of their rotor cascade.

Static pressure contours on the S2 surface near the *SS* reveal that there is a fairly large region with almost constant pressure and with adverse pressure gradient (flow deceleration) between 1/3 axial chord and the trailing edge. Near both endwall corners in this region, strong effects on the pressure field due to the passage vortices can be seen.

Three figures obtained at S3 planes show the effects on the pressure field within the cascade. Significant effects start to appear at plane 8 (0.71).

Total Pressure Distribution on S1, S2, and S3 Planes Within the Rotor Cascade (Fig. 5). The loss distribution on the S1 (blade-to-blade) plane near the hub endwall has two local maximum peaks in the present case too as seen in Part 1. The locations of the peaks, however, are different from those in the stator case; one is located farther inside the cascade. The peak loss value is very large. The other is located near the *SS* (not on the *SS* as in Part 1) just at the cascade throat. These endwall loss contours may relate to endwall shear stress contours. Gaugler and Russel [8], for example, give a figure of endwall shear stress contours within a straight turbine stator cascade with a turning angle of 72 deg; the shear stress contours were obtained by manually sketching the contours of constant relative motion of a number of oil drops taken by movie camera. Their result also presents two local maximum peaks within the cascade; one is located at about 1/2 axial chord from the cascade inlet (i.e., a little closer to the *SS* than one of the present loss peaks), and the other is located on the *SS* downstream from the throat in their case. Further detailed comparison, however, cannot be made at present. The figure also indicates that the *SS*/endwall corner along the *SS* is dominated by lower loss compared to the neighboring region.

Contours of CP_t on the S2 plane near the *PS* show higher loss near the *PS* in the rotor case than in the stator case. This is due to the flow deceleration over the *PS* as was seen in Fig. 4.

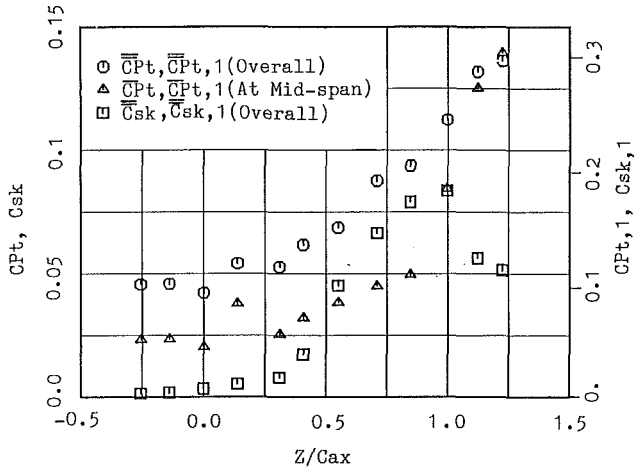

Fig. 7 Evolution of mass-averaged total pressure loss (straight rotor cascade)

The largest loss values near the *PS* can be found at the leading-edge/endwall corners where the flows were much decelerated and were moving toward the endwalls. Another S2 contour plot obtained near the *SS* indicates significant accumulation of low-energy fluids over a large area of the *SS* downstream from the throat. A large part of the loss is apparently produced in the flow deceleration regions where the directions of both pressure force and shear force are opposite each other.

Contour plots at several S3 planes clearly show the migration process of the cascade inlet boundary layers onto the *SS*. We note especially the movement of the maximum loss values along the endwalls. It is noteworthy that the maximum losses on the endwalls decrease once at plane 7 (0.55) and increase again at plane 8 (0.71). This can be seen also on the S1 plane previously discussed. The decrease at plane 7 coincides with the disappearance of irregular vector plots of the passage vortices at the *SS*/endwall corner, as was seen in Fig. 3.

Spanwise Distribution of Pitchwise Mass-Averaged Yaw Angle, Velocity, and Loss Through the Rotor Cascade (Fig. 6). The difference between the two yaw angles at plane 1 and at plane 12 indicates that the mass-averaged turning angle in the present test is about 102 deg.

Every curve of yaw angle distribution downstream from plane 5 has two local maximum values (underturning compared to the midspan flow direction), two minimum values (overturning), and two increased values near the endwalls. The first two and the second two values result from the effects of the passage vortices. The increased values near the walls are probably caused by the wall shear stresses which draw back the overturning flows in the underturning direction. The shear forces may generate corner vortices at the *SS*/endwall corner. Sieverding [5] describes that this kind of underturning shows the existence of corner vortex in the corner. The present plots of secondary flow vectors shown in Fig. 3, however, did not represent any clear circulation of flows near the endwalls, although clear underturning of the flows could be detected in the mass-averaged values. A more detailed survey of the flow near the endwall is needed.

The figure of the resultant velocity shows that the mass-averaged acceleration ratio (i.e., $\bar{\bar{V}}_{m,12}/\bar{\bar{V}}_{m,1}$) is about 1.48, which indicates lower acceleration compared to the value of 2.78 of the stator. The thickness of the inlet boundary layer is about 0.11 of the cascade span height. Flows from plane 9 (0.85) to plane 11 (1.12) decelerate.

The loss curves in Fig. 6 show the spanwise and streamwise development of the pitchwise mass-averaged loss through the cascade. The losses increase first near the endwall regions and finally along the whole span. Downstream from the cascade, i.e., planes 11 and 12, the rate of the loss growth decreases.

Evolution of Overall Total Pressure Loss Through Rotor Cascade (Fig. 7). In the present rotor case with a large turning angle, the curve of mass-averaged overall loss, as shown in Fig. 7, starts to increase at $Z/C_{ax} = 0.25$ near the cascade inlet. The loss grows steadily toward the downstream of the cascade, $Z/C_{ax} = 1.23$.

The mass-averaged loss at midspan also increases in parallel with the overall loss. The difference between the two loss values corresponds approximately to the secondary loss including the loss due to the endwall boundary layers within the cascade. Downstream from the trailing edge, the midspan loss increases more rapidly beyond the overall loss. This is because the migration of the low-energy fluids reaches the midspan of the wake due to the fluid mixing caused by the strong secondary flows (passage vortices).

The secondary kinetic energy coefficient starts to increase at the cascade inlet and rapidly increases from $Z/C_{ax} = 0.25$ up to the trailing-edge plane ($Z/C_{ax} = 1.0$). The coefficient, however, falls abruptly downstream of the cascade.

Among the experimental results on the overall loss evolution reported so far, Langston et al. [9] and Gregory-Smith and Graves [4] indicated steady growth of the overall loss up to about $Z/C_{ax} = 0.9$ and then rapid growth downstream from there in their rotor cascades. Sieverding [5] showed no growth up to about $Z/C_{ax} = 0.4$ for an impulse rotor cascade and up to about $Z/C_{ax} = 0.7$ for both of their rotor and stator cascades. In the theoretical approach on the loss growth, Hah [10] predicted quite an early start of the loss growth, roughly located between $Z/C_{ax} = 0.2$ and 0.4, by full Navier–Stokes equations with an algebraic Reynolds stress model for Langston's straight rotor cascade [9], while Moore and Moore [11] predicted slower loss growth by a fully elliptic Navier–Stokes code with the Prandtl mixing-length turbulence model and with an elliptic pressure correction for the same cascade. The latter could predict the loss development of Langston et al. [9] better than the former. The tendency of the present result of CP_t is similar to Hah's predicted result although the present cascade geometry is different from that dealt with by Hah. The overall behavior of the present experimental C_{sk} is very similar to that predicted by Moore and Moore.

Conclusions

The present study gave fairly detailed quantitative data on the secondary flow/loss mechanism in a straight rotor cascade with a larger turning angle than that of the stator cascade described in Part 1. As expected, the present cascade caused more significant loss (CP_t based on the outlet velocity) due to the stronger secondary flows occurring within the rotor cascade than within the stator cascade. The passage vortices, which were again the most important in the loss production process, started to grow at an early stage within the cascade. Larger turning of flow in the rotor cascade produced higher loss levels near the endwalls and near the blade surfaces. These lead to a rapid and steady growth of the overall loss from a near-inlet plane to the outlet plane of the cascade.

Acknowledgments

The author wishes to thank sincerely Mr. H. Nouse, Director of the Aeroengine Division, for his support of the present study and his helpful discussion, Mr. H. Usui, a staff member of the Turbine Section, for his assistance in the computational work, Mr. H. Tateishi, a staff member of Maruwa Electric Industry, and Mr. H. Tamura, a student of Nihon University, for their assistance in the experimental work.

References

1 Yamamoto, A., "Production and Development of Secondary Flows and Losses Within Two Types of Straight Turbine Cascades: Part 1—A Stator Case," Paper No. 86-GT-184.

2 Smith, S. F., "A Simple Correlation of Turbine Efficiency," *Journal of the Royal Aeronautical Sciences*, Vol. 69, 1965, p. 467.

3 Yamamoto, A., Takahara, K., Nouse, H., Inoue, S., Usui, H., and Mimura, F., "An Aerodynamic Design and the Overall Stage Performance of an Air-Cooled Axial-Flow Turbine," National Aerospace Laboratory, TR-321T, Jan. 1981.

4 Gregory-Smith, D. G., and Graves, C. P., "Secondary Flows and Losses in a Turbine Cascade," in: *Viscous Effects in Turbomachines*, AGARD-CP-351, 1983.

5 Sieverding, C. H., "Recent Progress in the Understanding of Basic Aspects of Secondary Flows in Turbine Blade Passages," ASME JOURNAL OF ENGINEERING FOR GAS TURBINES AND POWER, Vol. 107, 1985, pp. 248–257.

6 Armstrong, W. D., "The Secondary Flow in a Cascade of Turbine Blades," ARC R.M 2979, 1955.

7 Marchal, P., and Sieverding, C. H., "Secondary Flows Within Turbomachinery Bladings," in: *Secondary Flows in Turbomachines*, AGARD-CP-214, 1977.

8 Gaugler, R. E., and Russel, L. M., "Comparison of Visualized Turbine Endwall Secondary Flows and Measured Heat Transfer Patterns," ASME JOURNAL OF ENGINEERING FOR GAS TURBINES AND POWER, Vol. 106, 1984, pp. 168–172.

9 Langston, L. S., Nice, M. L., and Hooper, R. M., "Three Dimensional Flow Within a Turbine Cascade Passage," ASME JOURNAL OF ENGINEERING FOR POWER, Vol. 99, 1977, pp. 21–28.

10 Hah, C., "A Navier-Stokes Analysis of Three-Dimensional Turbulent Flows Inside Turbine Blade Rows at Design and Off-Design Conditions," ASME JOURNAL OF ENGINEERING FOR GAS TURBINES AND POWER, Vol. 106, 1984, pp. 421–429.

11 Moore, J., and Moore, J. G., "Performance Evaluation of Linear Turbine Cascades Using Three-Dimensional Viscous Flow Calculations," ASME JOURNAL OF ENGINEERING FOR GAS TURBINES AND POWER, Vol. 107, 1985, pp. 969–975.

APPENDIX

Blade Profile Coordinates

I	X	Y_p	Y_s (mm)
1	0.000	0.000	−6.329
2	4.083	0.817	−12.250
3	8.167	−2.001	−17.354
4	12.250	−4.614	−21.438
5	16.333	−6.533	−24.500
6	20.417	−7.963	−26.338
7	24.500	−8.657	−27.563
8	28.583	−8.657	−27.767
9	32.667	−8.085	−27.358
10	36.750	−6.860	−26.133
11	40.833	−4.900	−24.214
12	44.917	−2.654	−21.233
13	49.000	0.531	−18.171
14	53.083	4.288	−13.067
15	57.167	8.698	−7.350
16	61.250	13.271	−0.408
17	65.333	18.171	7.146
18	69.417	–	15.108

D_L	(X_L, Y_L)	D_T	(X_T, Y_T)
8.167	(2.654, −3.063)	4.083	(69.090, 19.396)

D_{max}	(X_{max}, Y_{max})	chord
18.906	(29.808, −18.171)	73.5

where D_L, D_T, and D_{max} represent diameters of blade leading edge, trailing edge, and blade maximum thickness, and chord represents blade chord length. The coordinate points were connected smoothly to make the blade profile.

The Off-Design Performance of a Low-Pressure Turbine Cascade

H. P. Hodson

R. G. Dominy

Whittle Laboratory,
University of Cambridge,
Cambridge, United Kingdom

The ability of a given blade profile to operate over a wide range of conditions is often of the utmost importance. This paper reports the off-design performance of a low-pressure turbine rotor root section in a linear cascade. Data were obtained using pneumatic probes and surface flow visualization. The effects of incidence (+9, 0, −20 deg), Reynolds (1.5, 2.9, 6.0 × 10^5), pitch-chord ratio (0.46, 0.56, 0.69), and inlet boundary layer thickness (0.011, 0.022 δ/C) are discussed. Particular attention is paid to the three dimensionality of the flow field. Significant differences in the detail of the flow occur over the range of operating conditions investigated. It is found that the production of new secondary loss is greatest at lower Reynolds numbers, positive incidence, and the higher pitch-chord ratios.*

Introduction

During the preliminary design or redesign of an axial flow turbine, various methods of performance estimation (e.g., [1–4]) are employed. These or similar methods are inevitably based upon correlations and it is therefore recognized that they cannot replace either more detailed design methods or test data. Nevertheless, they are often used to investigate the directions that future aerodynamic developments should take and it is under such circumstances that correlations of this kind are least reliable. Indeed, as it should be, it is often stated by authors that their methods are only applicable to turbines which contain "well-behaved" blades.

In the case of low-pressure turbines, it can be difficult to arrive at a design which will contain such profiles. Near the rotor hub, for example, the common desire to produce a uniform work distribution can lead to a root section with relatively little overall expansion. A companion paper [5] describes a detailed cascade investigation of the three-dimensional performance of such a profile when operating at its design condition. In a turbine, a profile will operate over a large range of conditions, yet there are very few data available from such turbines concerning the primary and particularly the secondary flow.

This paper presents a study of the off-design performance of a low-pressure turbine rotor root section in cascade. Particular attention is given to the three-dimensional aspects of the flow. The effects of incidence, Reynolds number, inlet boundary layer thickness, and pitch-chord ratio are described.

Experimental Apparatus

The experimental results were obtained in the Transonic Cascade Facility of the Whittle Laboratory, Cambridge. This is a closed-circuit tunnel in which the Mach number (M_{2S} < 1.4) and the Reynolds number ($0.3 \times 10^5 < Re_{2S} < 20 \times 10^5$) can be varied independently.

The cascade consisted of six blades which exhausted into a large plenum chamber. The rotor root section is shown schematically in Fig. 1. It was designed to operate at an inlet angle of 38.8 deg and an exit angle of approximately 54 deg from the axial direction at an exit Mach number of 0.7 and a chord-based exit Reynolds number of 2.9×10^5. The cascade was also designed to accommodate the effects of stream tube height variation by specifying a 6 percent flare of the blade span with a linear variation in aspect ratio between the inlet and exit planes of the cascade. Further details can be found in Table 1 and [5].

The middle passage of the cascade was instrumented with static pressure tappings at midspan. Inlet static pressure tappings were located 0.86 *Cx* upstream of the leading edge plane. A pitot was placed at the same position. The inlet stagnation temperature (15–35°C) was measured using a thermocouple which was placed within the ducting upstream of the working section.

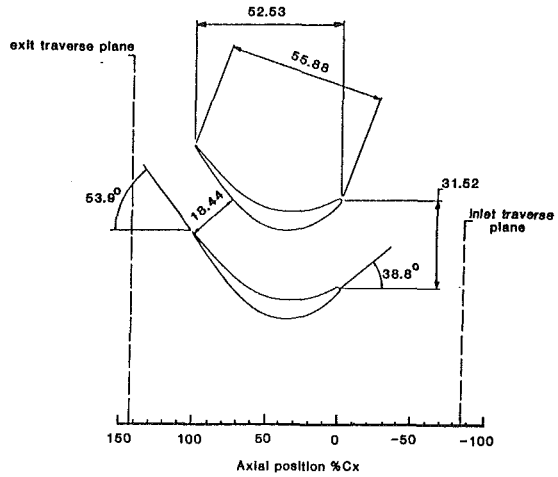

Fig. 1 Cascade: side view of a single passage

Contributed by the Gas Turbine Division of THE AMERICAN SOCIETY OF MECHANICAL ENGINEERS and presented at the 31st International Gas Turbine Conference and Exhibit, Düsseldorf, Federal Republic of Germany, June 8–12, 1986. Manuscript received at ASME Headquarters February 10, 1986. Paper No. 86-GT-188.

Two further probes have been employed during the current investigation. The first consisted of a fixed-direction five-hole 60 deg conical probe with an overall diameter of 2 mm. This was used to traverse the cascade exit flow at 142 percent *Cx*. The second probe was a flattened pitot (0.14 × 1.16 mm) which was used to traverse the inlet endwall boundary layer at −86 percent *Cx*. The facility is provided with a fully automated computer-controlled data acquisition system. The estimated maximum experimental inaccuracies associated with the various measurements and cascade settings are given in Table 2.

Visualizations of the surface flows were obtained using a mixture of fluorescent powder and silicone oil. The mixture was applied to the surfaces prior to the passage of air through the cascade. The viscosity of the mixture and the duration of the experiments were such that the patterns were unaffected by the starting and stopping of the tunnel.

Results and Discussion

The three-dimensional aerodynamic performance of the cascade has been determined over a range of operating conditions. The nominal design point of the cascade is given in Table 1. Unless otherwise stated, the parameters in a given test are identical to those given in the table with the exception of that (e.g., Reynolds number) which is under investigation.

Table 3 summarizes the traverses made through the inlet boundary layer 86 percent *Cx* upstream of the leading edge plane of the cascade. The upstream potential influence of the cascade is negligible at this location. The results show that the inlet boundary layer is turbulent at all of the conditions tested with a displacement thickness-to-chord ratio (δ^*/C) of approximately 0.01 except in the case of the deliberately (using trips) thickened inlet boundary layer. All boundary layer parameters have been determined using the compressible form of the appropriate expression or integral with the assumption that the static pressure is uniform and equal to the value at the wall.

In the following discussion, the results of area exit traverses are presented. Due to physical constraints, these data were only obtained between 2.0 and 50.0 percent of the span. Therefore, the average values which are given do not include the loss, etc., associated with the fluid (including the exit endwall boundary layer) found between the wall and 2.0 percent of the span.

All of the average properties, whether area or pitchwise averaged, have been determined using a constant area mixing calculation in which the inviscid adiabatic equations for the conservation of mass, energy, and momentum are applied. The difference between the mixed-out quantities and the simple mass-averaged values ranged from 7 to 15 percent of the total measured loss, depending upon the nonuniformity of the velocity field which in turn was a function of the operating conditions.

Table 4 provides a breakdown of the exit-based loss coefficient into those associated with the inlet boundary layer, albeit at 86 percent *Cx* upstream of the cascade, the profile loss at the midspan of the blade, and the remainder, the so-called net secondary loss. It is of course recognized that the latter is a concept born out of a need for a convenient method of identification of the losses rather than an understanding of the flow.

The sections which follow concentrate on the major differences which occur in the structure of the flow at the various test conditions.

Table 1 Blade design, cascade geometry, and operating conditions

Number of blades	6
Chord, *C* (mm)	55.88
Axial chord, *Cx* (mm)	52.53
Inlet aspect ratio, h_1/C	1.715
Exit aspect ratio, h_2/C	1.818
Pitch-chord ratio, s/C	0.564
Pitch-axial chord ratio, s/Cx	0.600
Design inlet angle (deg from axial)	38.8
Design exit angle (deg from axial)	−53.9
$\cos^{-1}(0/s)$	−54.2
Stagger angle (deg from axial)	−19.6
Throat-pitch ratio, $0/s$	0.585
Leading edge radius-chord ratio	0.016
Isentropic exit Mach number	0.71
Isentropic exit Reynolds number	2.9×10^5

Table 2 Estimate of experimental accuracy

Linear position	+/−0.01 mm	
Inlet flow angle	+/−0.2 deg	
Exit flow angle	+/−0.4 deg	
Stagnation pressure (five-hole probe)	+/−0.003	
Stagnation Pressure (all pitots)	+/−0.001	$\times(P_{04}-p_4)$
Static pressure (five-hole probe)	+/−0.005	
Static pressure (surface tappings)	+/−0.001	

Table 3 Inlet boundary layers

Test condition	δ^*/C	θ/C	δ^*/θ
Design	0.0108	0.0075	1.44
Re2 = 1.5×10^5	0.0093	0.0065	1.44
Re2 = 6.0×10^5	0.0097	0.0068	1.44
+8.6 deg incidence	0.0108	0.0075	1.44
−20.3 deg incidence	0.0108	0.0075	1.44
s/C = 0.459	0.0108	0.0075	1.44
s/C = 0.688	0.0108	0.0075	1.44
Thickened inlet boundary layer	0.0221	0.0163	1.36

Design Conditions. A description of the development of the primary and secondary flow fields within the cascade at its design point has already been presented in a companion paper [5]. However, for completeness and as an aid to the interpretation of the data presented here, those results are summarized below.

Figure 2 (from [5]) contains an interpretation of the endwall and suction surface flow visualization. The separation lines (*S*1*s* and *S*1*p*) and saddle point associated with the rollup of

Nomenclature

C = chord
Cx = axial chord
h = span
M = Mach number
p = static pressure
P_0 = stagnation pressure
R = reattachment line
Re = Reynolds number
s = pitch
S = separation line
x = axial distance
y = pitchwise distance
Y = total pressure loss coefficient $= (P_{01} - P_0)/(P_{04} - p_4)$
z = spanwide distance
β = pitchwise flow angle (from axial)
δ^* = boundary layer displacement thickness
θ = boundary layer momentum thickness
ρ = density

Subscripts

∞ = free stream
1 = inlet free stream
2 = traverse plane
2s = downstream isentropic
3 = pitchwise mixed out
4 = downstream infinity (i.e. pitch and spanwise mixed out)
s = suction side
p = pressure side
0–6 = number of separation/reattachment line

Table 4 Mixed-out traverse results

Condition	Total loss coefficient	Mixing loss coefficient	Inlet loss coefficient	Midspan loss coefficient	Exit secondary loss coefficient	Axial velocity density ratio	Exit flow angle (deg)
Design	0.0639	0.0059	0.0110	0.0270	0.0259	0.917	54.1
Re2 = 1.5×10^5	0.0715	0.0053	0.0093	0.0354	0.0268	0.916	54.3
Re2 = 6.0×10^5	0.0594	0.0070	0.0101	0.0263	0.0230	0.907	54.1
+8.6 deg incidence	0.1007	0.0148	0.0149	0.0498	0.0360	0.923	54.1
+20.3 deg incidence	0.0810	0.0026	0.0075	0.0598	0.0137	0.907	53.5
s/C = 0.459	0.0625	0.0041	0.0104	0.0344	0.0177	0.929	54.2
s/C = 0.688	0.0680	0.0084	0.0105	0.0278	0.0297	0.935	53.8
Thick inlet boundary layer	0.0764	0.0055	0.0239	0.0280	0.0245	0.928	53.9

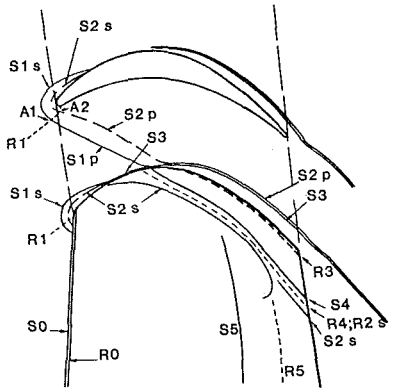

Fig. 2 Suction surface and endwall flow visualization [5]

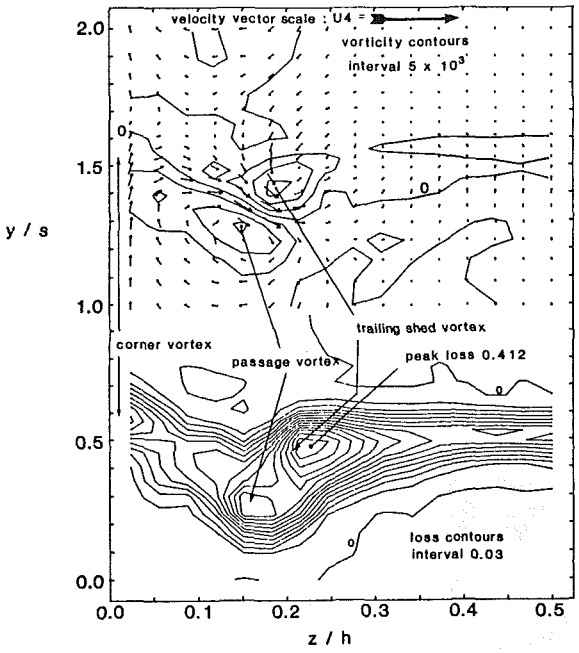

Fig. 3 Total pressure loss coefficient conours, vorticity contours and secondary velocity vectors: design condition

the inlet boundary layer, the separation line (*S*3) and reattachment line (*R*3) of the corner vortex and the separation line (*S*4) of the passage vortex are all shown. The closed separation bubble near the leading edge of the suction surface is caused by an overspeed which is known [6] to have little overall effect upon the suction surface boundary layer which undergoes laminar separation (*S*5), transition and reattachment (*R*5) near the trailing edge. The flow visualization also shows that the suction side leg of the horseshoe vortex (*S*2*s*) interacts with this closed separation bubble. In doing so, some of the high loss fluid is fed into the separation bubble while the rest is convected with the vortex toward the trailing edge. Although not

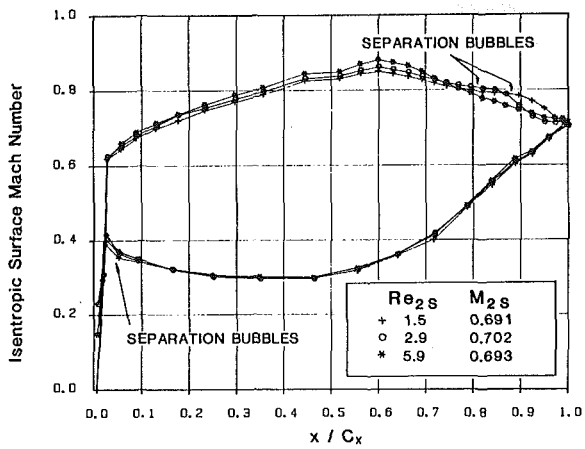

Fig. 4 Blade surface Mach number distributions: Reynolds number variation

shown in the illustration, a closed separation bubble also exists on the pressure side of the blade close to the leading edge. This is caused by the diffusion which follows the acceleration of the flow around the leading edge. In practice, it seems that the pressure side and suction side leading edge bubbles have little overall effect upon the development of the secondary flows and losses at zero incidence.

Some of the above mentioned features can be traced donwstream to the traverse plane located at 142 percent *Cx* (Fig. 3). The secondary velocities in the figure were calculated by projecting the velocity vectors onto a plane which was perpendicular to the mixed out flow direction. In this and in other figures, the contours of secondary vorticity, which were calculated by finite differentiation of the secondary velocities, have been used to identify the centers of the various vortices. The centers of the passage vortex and its associated loss core are indicated in Fig. 3. They are coincident. The locations of the corner vortex (identified using the loss contours) and that which contains the trailing shed vorticity are also shown. The suction side leg of the horseshoe vortex could not be identified even though its path could be traced using the surface flow visualization.

Variation With Reynolds Number. At a Reynolds number of 1.5×10^5, which is one half of the design value, the flow visualization revealed that the suction surface boundary layer separates near 68 percent *Cx* with reattachment just prior to the trailing edge. The isentropic Mach number distributions of Fig. 4 show how the bubble grows in extent as the Reynolds number is reduced from the design value. A consequence of the now extensive separation is that the interaction between the secondary flow and the suction surface boundary layer fluid is greater than at the design condition. The suction surface flow visualization (Fig. 5*a*), for example, revealed that the separation line of the suction side leg of the horseshoe vortex disappeared as it encountered the separated flow. This increase in the strength of the interaction is thought to be

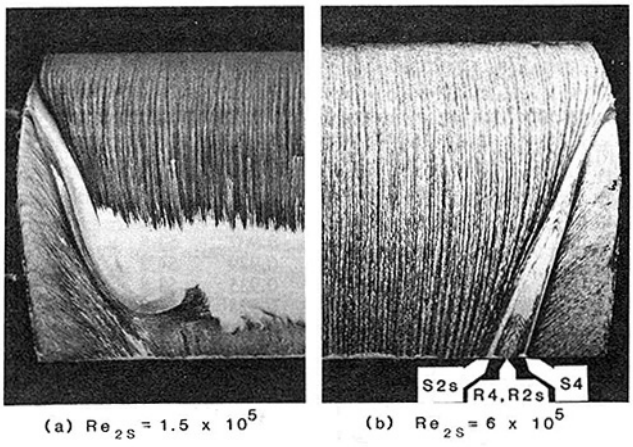

Fig. 5 Suction surface flow visualization

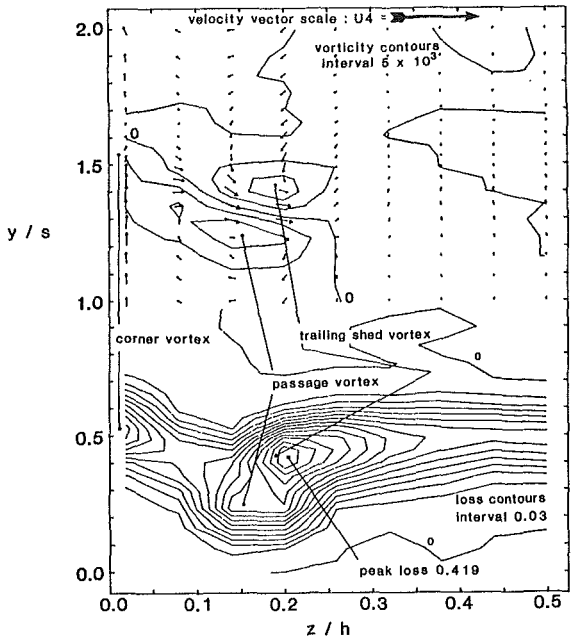

Fig. 6 Total pressure loss coefficient contours, vorticity contours and secondary velocity vectors: low Reynolds number

related to the relatively low static pressure in the bubble as well as the unsteadiness and mixing which would accompany a large separation, phenomena which would also explain the absence of a constant pressure region over the upstream portion of the separation bubble.

Figure 6 contains the results of the exit area traverse at the lowest Reynolds number. It shows that the details within the wake and secondary flow regions are less well defined than at the design condition (Fig. 3). This is partly due to the increased interaction between the secondary and suction surface flow which was indicated by the flow visualization. However, reducing the Reynolds number will also increase the rate of decay of the wake and secondary flow regions and this is thought to be mainly responsible. The secondary velocity vectors are also shown in Fig. 6. Due to the apparent increase in the rate of decay, they are smaller than at the design value. The secondary vorticity contours reveal that the peak strengths of the passage and the trailing shed vortices are 75 percent of the values at the design condition. As a consequence, the distortion of the center line of the wake has reduced. It also appears that the rollup of the trailing shed vorticity is less complete than at the design condition. However,

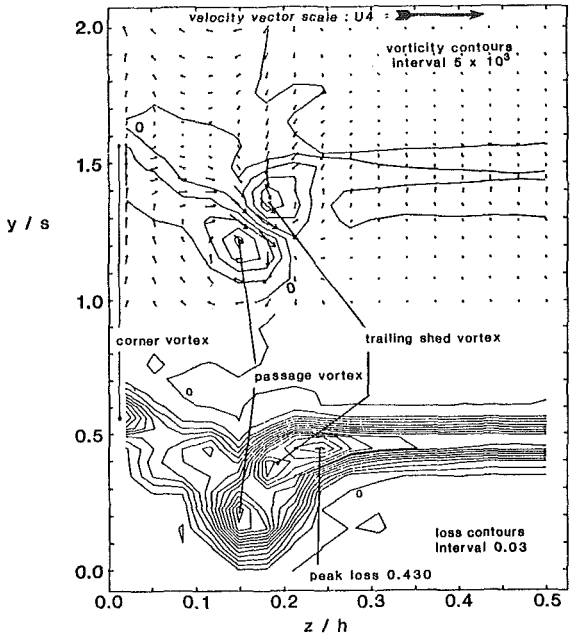

Fig. 7 Total pressure loss coefficient contours, vorticity contours, and secondary velocity vectors: high Reynolds number

the locations of peak vorticity and, therefore, the vortex centers are virtually unchanged.

At a Reynolds number of 6.0×10^5, which is twice that of the design value, transition to turbulent flow is sufficiently complete to prevent the separation of the suction surface boundary. The surface oil flow patterns are shown in Fig. 5(*b*). The absence of the suction surface separation means that the three dimensionality of the suction surface flow is reduced and that the separation line (*S2s*) which is associated with the suction side leg of the horseshoe vortex is clearly visible over the rear of the surface. Otherwise, the development of the surface flow is very similar to that observed at the lower Reynolds numbers.

The absence of a back surface separation and the higher Reynolds number result in more clearly defined wake and secondary flows (Fig. 7). Likewise, the magnitudes of the secondary velocities and therefore vorticities are greater. The peak vorticity within the passage vortex, for example, is increased by approximately 35 percent. The distortion of the center line of the wake is therefore greater, although again, the positions of the passage and trailing shed vortices are unchanged. Figure 7 also reveals that there are now three rather than two loss peaks near 20 percent span and that they all reach similar values, which was not the case at the lower Reynolds numbers. The innermost peak is thought to come from the fluid within the suction side leg of the horseshoe vortex and from the reattachment zone (*R4/R2*) between this and the separation line of the passage vortex. Relatively little vorticity is associated with this loss peak. That which exists is of opposite sign to that of the passage vortex. The middle loss peak is centered on the counterrotating vortex which contains the trailing shed vorticity and the outermost is the passage vortex.

The spanwise variations of the pitchwise mixed-out stagnation pressure loss and yaw angle obtained at the three Reynolds numbers are plotted in Fig. 8. As might be expected from the previous discussion regarding the state of the suction surface boundary layer, the midspan loss decreases with increasing Reynolds number. Similarly, the extent of the constant loss and yaw angle region over the central portion of the blade increases as the Reynolds number is increased and the three dimensionality of the surface flow is reduced. Near the

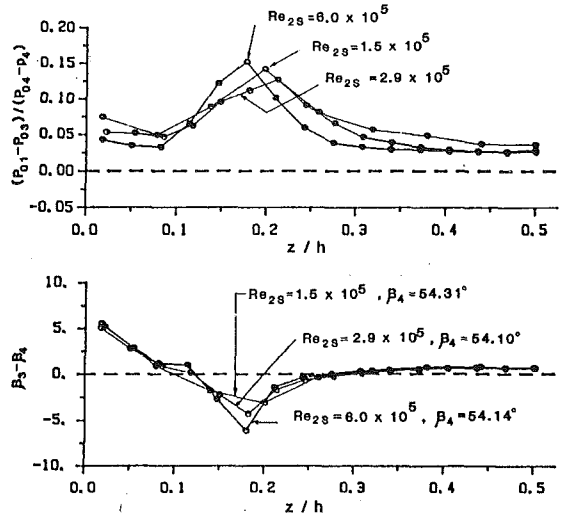

Fig. 8 Mixed-out pitchwise flow angle and stagnation pressure loss: Reynolds number variation

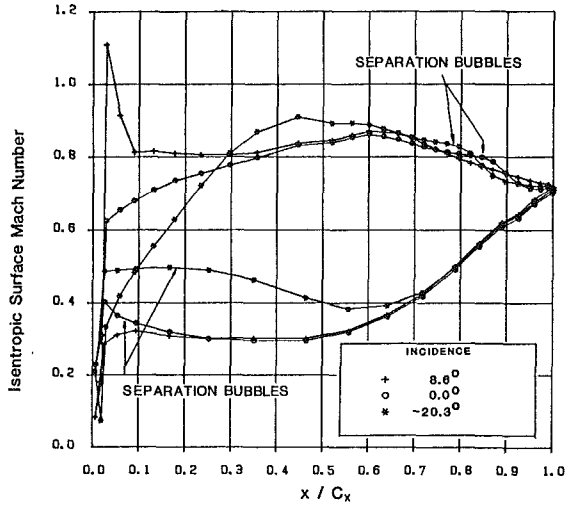

Fig. 9 Blade surface Mach number distributions: incidence variation

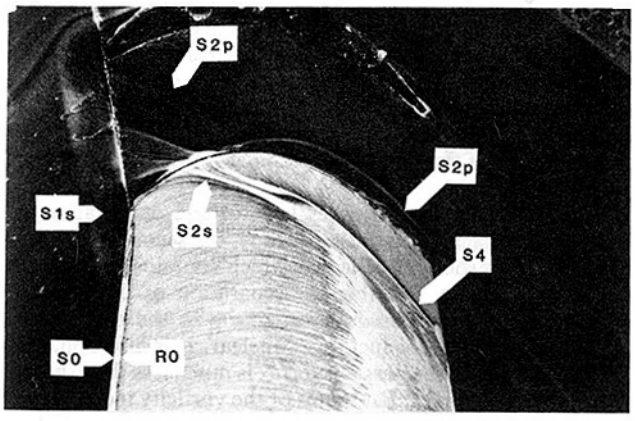

Fig. 10 Surface flow visualization: +8.6 deg incidence

endwall, the amount of overturning and by implication the nature of the growth of the new endwall boundary layer appears to be independent of Reynolds number. However, the variation in flow angle near the center of the passage vortices, in particular the amount of underturning, is Reynolds number dependent. This is a consequence of the changing strengths of the passage and trailing shed vortices as the Reynolds number is varied.

It has already been noted (Fig. 8) that the midspan loss reduces with increasing Reynolds number. Table 4 shows that the same is true of the total loss and the net secondary loss. The latter is derived by subtracting the inlet and midspan loss from the total. The validity of such a calculation has already been questioned. Nevertheless, the indicated trends are undoubtedly valid: Reducing the Reynolds number increases the midspan and the net secondary losses. However the proportions by which these increase are very different. The midspan or "profile" loss for example decreases by 25 percent as the Reynolds number is quadrupled while the net secondary loss decreases by 14 percent. This difference arises because the nature of the suction surface boundary layer changes significantly over the range of Reynolds numbers investigated whereas the secondary flow patterns are virtually unchanged, apart from the interaction of the suction side leg of the horseshoe vortex with the suction surface boundary layer. In several corrrelations (e.g., [4]), the secondary loss is assumed to be proportional to $Re^{-0.2}$ as is the profile loss. In the case of the present cascade no simple power law can be used to describe the variations observed. The overall variation in secondary loss from the highest to the lowest Reynolds number is however much less than this simple relationship implies, although the variation from the design to the highest value does imply a proportionality to $Re^{-0.15}$.

Variation With Incidence. The performance of the cascade was investigated at two inlet flow angles other than the design value. These angles, which are equivalent to incidences of -20.3 and $+8.6$ deg, were chosen to represent the extremes which might be encountered by the profile during operation in a turbine. The midspan isentropic Mach number distributions which correspond to these inlet flow angles are plotted in Fig. 9. It can be seen that the inlet flow angle has a significant effect upon the pressure distribution over much of the blade surface. At positive incidence, the pressure surface diffusion has almost vanished. The flow visualization showed that as a result, there is no pressure surface leading edge separation bubble. Data (unpublished) similar to those in [6] suggest that the pressure side boundary layer remains laminar up to the trailing edge. On the suction surface, operation at positive incidence significantly increases the size of the leading edge overspeed. Behind the separation bubble which follows this overspeed, there is a region of almost constant static pressure within which the reattached, presumably turbulent, boundary layer develops. Therefore, there is no back surface separation.

Figure 10 shows a perspective view of the suction surface and endwall oil flow visualization patterns obtained at positive incidence. The secondary separation line *S2s-S2p* associated with the upstream movement of fluid near the leading edge into the horseshoe vortex is clearly visible. This was not the case at the design condition. The appearance and disappearance of a second separation line associated with the formation of the leading edge vortex has been addressed in [5]. The difference is presumably a consequence of the greater leading edge loading at positive incidence as indeed must be the greater rate of downwash of fluid onto the suction surface. The primary separation line of the pressure-side leg of the horseshoe vortex (*S1p*), for example, meets the suction surface at 25 percent *Cx* rather than at the design condition value of 33 percent *Cx*. However, the saddle points associated with the primary and secondary separation lines of the horseshoe vortex have moved very little. This result must be contrasted with that of [7] which revealed a large shift in the position of the saddle point as the incidence of the flow onto a high-pressure rotor was increased.

Figure 10 also shows that increasing the incidence onto the blades increases the three dimensionality of the suction surface

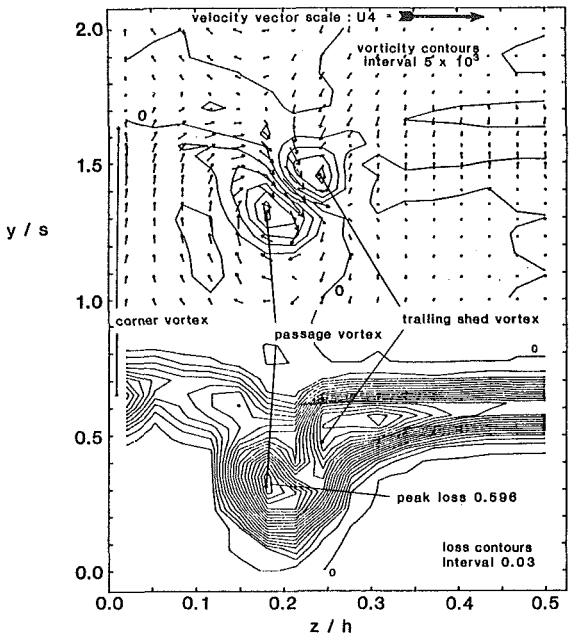

Fig. 11 Total pressure loss coefficient contours, vorticity contours, and secondary velocity vectors: positive (8.6 deg) incidence

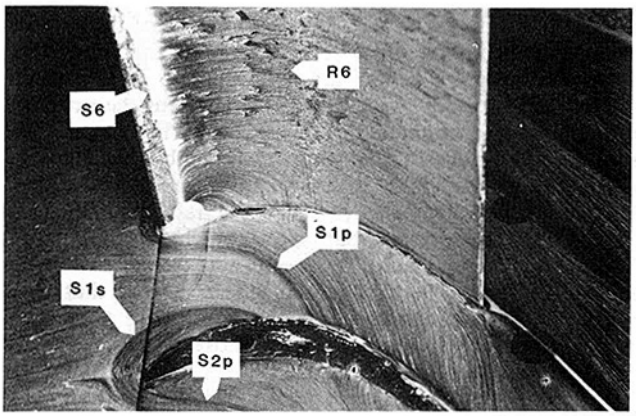

Fig. 12 Pressure side surface flow visualization: – 20 deg

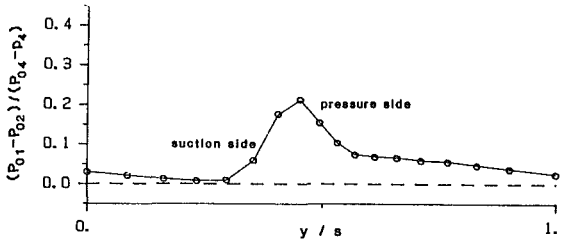

Fig. 13 Mixed-out stagnation pressure loss: – 20 deg incidence

oil flow patterns. The separation lines *S*4 and *S*2*s* associated with the passage and suction side horseshoe vortex are displaced toward midspan, and between them lies a larger reattachment zone. The absence of any truly spanwise flow on the rear of the suction surface is due to the continuous attachment of the blade surface boundary layer. The speckled flow visualization on the back surface is merely a result of the reduced shear stress which follows peak suction. It does not signify separation, but the difference between this picture and Fig. 5(*b*) does suggest that the suction surface boundary layer is not fully turbulent. Unpublished data for similar profiles, which includes transition measurements, support this viewpoint.

Further evidence of the increased three dimensionality of the flow field is contained in Fig. 11. Compared to the design case, the strengths of the passage and counterrotating vortices have increased significantly. For example, the peak vorticity within the passage vortex has increased by 65 percent and the counterrotating vortex which contains the trailing shed vorticity has increased in strength by approximately 35 percent. As a result of the greater downwash of fluid onto the suction surface, the centers of the vortices are now closer to midspan. The center of the passage vortex is coincident with its associated loss peak which is itself of the same magnitude as the peak which lies nearest midspan. The heights of the loss peaks were similarly matched at the highest Reynolds number, when the back surface boundary layer was also attached. The rate of entrainment of fluid into the wake region appears to be greater than at the design condition. This is thought to be due to the increased strength of the vortices, and in particular the passage vortex.

At approximately 20 deg of negative incidence, the Mach number distribution of Fig. 9 shows that the loading becomes negative up to 10 percent *Cx*. The now continuous acceleration over the leading half of the suction surface means that the suction surface boundary layer remains laminar until, following peak suction, it separates, undergoes transition, and finally reattaches near the trailing edge. Thus, the suction surface boundary layer is similar to that which occurs at the design condition. On the pressure surface, however, there is a region of almost constant static pressure between 3 and 25 percent *Cx*, which is indicative of a long separation bubble.

The extent of the pressure side separation bubble can be seen in Fig. 12, which contains a perspective view of the pressure surface and endwall flow patterns. Near midspan, the bubble extends from approximately 5 to 45 percent *Cx*. In the pressure surface endwall corner, the flow is highly three dimensional, with reversed flow occurring on both the blade and endwall surfaces. The positions of the separation and reattachment lines are indicated. This separated flow region is so large that the mixing which occurs between the separated flow and the free-stream results in stagnation pressures which, downstream of the cascade, are everywhere less than the inlet free-stream value. This is illustrated by Fig. 13, which contains some of the data obtained during a midspan pitchwise traverse. Whether this phenomenon should be termed "negative stalling" is, however, unclear since an embedded and attached boundary layer develops over the rear half of the pressure surface. A further consequence of operating at negative incidence can be seen in the flow visualization picture of Fig. 12. The saddle point associated with the primary separation line of the horseshoe vortex now lies on the suction side of the blade.

Because the fluid experiences less turning at negative incidence as it passes through the cascade, the secondary flow is reduced. This is shown by Fig. 14, which contains some of the exit traverse results. Whether the separation of the pressure surface flow and its subsequent mixing with the mainstream also contribute to the reduction is unclear. It is also apparent that the strength of the passage vortex is much less than that of the trailing shed vortex. Estimates of the vorticity indicate that the trailing shed vortex has a strength which is 50 percent of its value at the design incidence. The strength of the passage vortex, which is only just identifiable, is reduced to 25 percent of its value at the design conditions. This difference in the relative strengths of the two vortices and the overall level of secondary flows are thought to explain the appearance of only one loss peak other than the corner vortex, near 15 percent span.

The spanwise variation of loss and flow angle derived from the exit traverses at the three inlet flow angles are plotted in

Table 5 Cascade geometries for modified pitch

	Design	+22 percent *s/C*	−18 percent *s/C*
Pitch-chord ratio	0.564	0.688	0.459
Pitch-axial chord ratio	*0.600*	*0.732*	*0.492*
Stagger	−19.6 deg	−18.2 deg	−20.6 deg
Number of blades in cascade	6	5	7

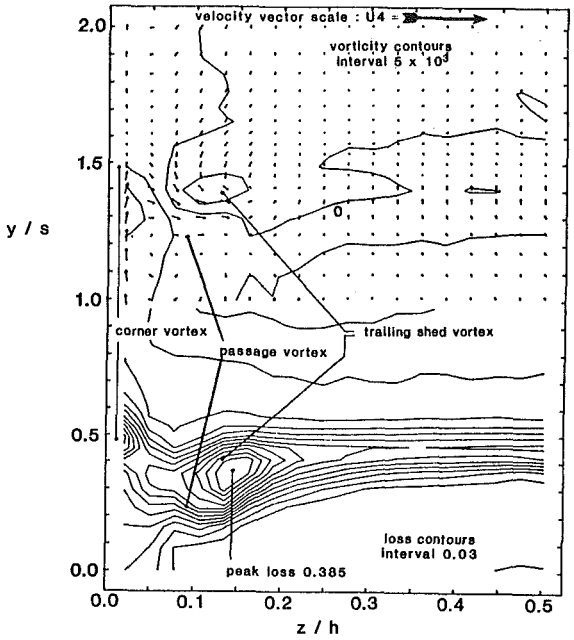

Fig. 14 Total pressure loss coefficient contours, vorticity contours, and secondary velocity vectors: negative (−20.3 deg) incidence

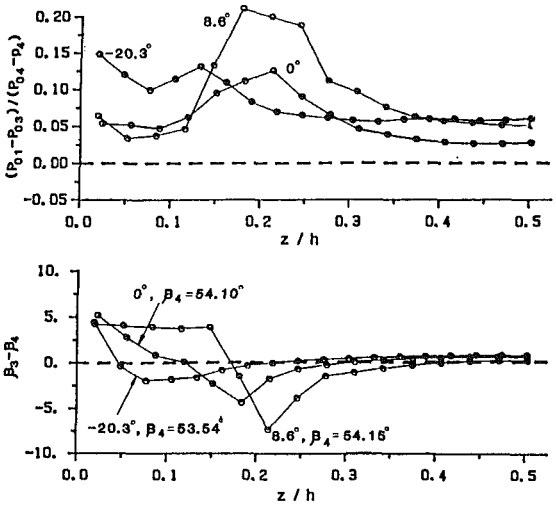

Fig. 15 Mixed-out pitchwise flow angle and stagnation pressure loss: incidence variation

Fig. 15. At midspan the loss is lowest at the design incidence. At positive incidence it is greater because the suction surface boundary layer is turbulent over much of its surface length. At −20.3 deg of incidence the increase is due to the large pressure side separation. As was the case with the Reynolds number variation, the extent of the regions of constant loss and turning decrease and the variation in yaw angle increases with increasing secondary flow. In contrast to the effects of changing the Reynolds number, the overturning near the wall is also dependent upon the flow conditions. This is due to the very different secondary flows which result from the modifications made to the loading distribution as the inlet flow angle is altered.

Table 4 provides a breakdown of the total loss. The apparent variation in inlet loss with inlet flow angle is a result of converting the measured loss at inlet into an exit-based coefficient. Subtracting this and the midspan value of loss from the total reveals, not surprisingly, that the net secondary loss is greatest at positive incidence (50 percent higher) and least at negative incidence, where it is one half of the value of the design condition. Application of the correlation of Craig and Cox [4] reveals that the measured values are approximately one half of those predicted. A comparison between the cascade correlation of Dunham [8] and the turbine correlation of Dunham and Came [3] shows that such a difference is not unreasonable. The relative changes are, however, accurately predicted by [4]. In contrast, [3] and, indeed, the method of Ainely and Mathieson [1] upon which that of [3] is based predict that for this particular cascade the net secondary loss should increase only slightly with increasing incidence over the range investigated.

Variation of Pitch-Chord Ratio. An examination of secondary loss correlations (e.g., [1–4]) shows that it is unclear whether pitch-chord ratio is a parameter upon which secondary losses are dependent. Craig and Cox [4], for example, predict a significant dependence, while the correlation of Dunham [8], for no other reason than a lack of data, does not contain the pitch-chord ratio as an independent variable.

Given this uncertainty, it was decided to investigate the effects of pitch-chord ratio upon the performance of the current cascade. The changes in pitch-chord ratio (i.e., +22 percent, −18 percent *s/C*) necessitated a change in the number of blades in the cascade. The details are given in Table 5. For each pitch a different stagger was selected in order to maintain the same exit flow angle as predicted by a coupled inviscid-boundary layer computation. The measured flow angles show that this requirement was largely satisfied.

Figure 16 contains the isentropic midspan Mach number distributions measured at the three pitch-chord ratios investigated. Increasing the pitch-chord ratio increases the blade loading. At the largest pitch, the leading edge overspeed, which was too short to be detected by static pressure measurement at the design point, has increased in surface length. Presumably this is a result of the greater stagger although the increased loading may also contribute. The effect of this enlarged overspeed upon the suction surface boundary layer is slight however, since separation and turbulent reattachment again occur on the back surface.

The increase in pitch-chord ratio has a marked effect upon the three dimensionality of the flow. Figure 17 shows a view of the suction surface oil-flow patterns. The leading edge separation bubble is just visible. At the rear of the surface, the interaction of the suction side horseshoe vortex with the shortened separation bubble is greater than at the design pitch. It may also be significant that the secondary separation line associated with the leading edge horseshoe vortex was clearly visible in the endwall flow patterns and that the only other condition at which this was so was at +8.6 deg of incidence.

Figure 18 contains the results of the exit traverse at the increased pitch-chord ratio. Like the measurements at the highest Reynolds number (Fig. 7) three loss peaks are visible

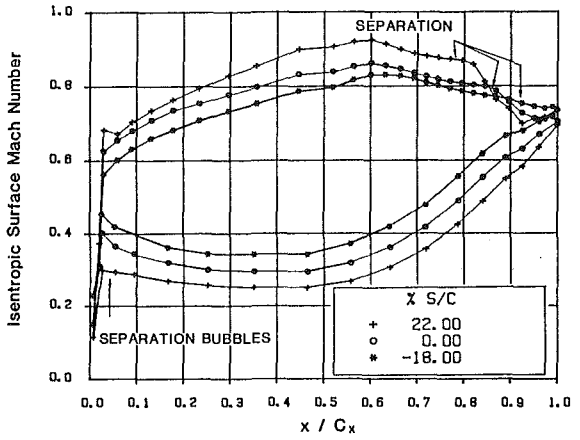

Fig. 16 Blade surface Mach number distributions: pitch-chord ratio variation

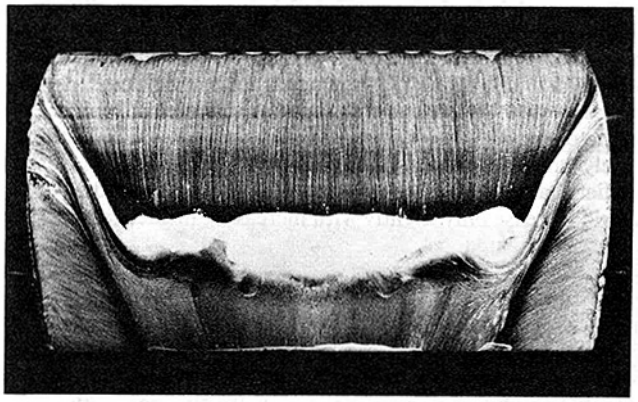

Fig 17 Suction surface flow visualization: +22 percent *s/C*

between 20 and 30 percent span. That nearest the endwall corresponds to the center of the passage vortex, the strength of which, like that of the adjacent vortex of opposite rotation, is greater than at the design value. As a result of the increased secondary flow, the vortices also lie nearer midspan. At positive incidence, where the loading was also greater, a similar shift was observed.

In general, reducing the pitch-chord ratio has an effect opposite to that observed above. The Mach number distribution (Fig. 16), for example, shows that the blade loading is reduced. However, the low base pressure and apparent lack of any reattachment zone suggest that the back surface separation is no longer closed. The flow visualization results also suggested that this was in fact the case.

Figure 19 summarizes the effects of pitch-chord ratio upon the exit flow field. The amount of overturning close to the endwall does indeed depend upon the pitch-chord ratio as does the position and magnitude of the maximum underturning, all of which are related to the stength of the secondary flow. Similarly, the position of the loss peak which is associated with the passage vortex moves toward midspan as the pitch-chord ratio is raised. All of these changes imply that the secondary flow is not independent of the pitch-chord ratio.

Table 4 again provides a breakdown of the losses at exit from the cascade. In terms of the pitch-chord ratio variation, the midspan loss is greatest at the lowest ratio since gross separation of the suction surface boundary layer has occurred. Increasing the pitch-chord ratio above the design value appears to have little effect upon the midspan loss. In contrast, the net secondary loss increases with increasing pitch. For example, the relative increase from the lowest to the highest pitch-chord ratio is 70 percent.

Variation of Inlet Boundary Layer Thickness. The various

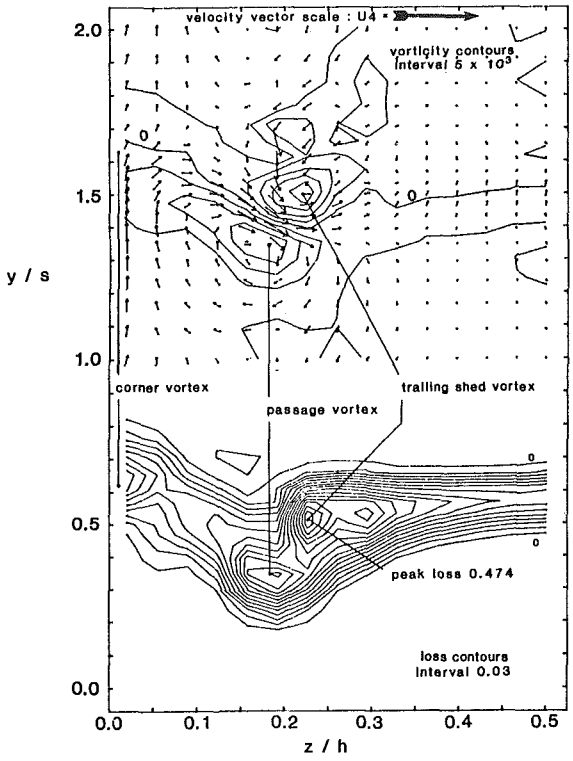

Fig. 18 Total pressure loss coefficient contours, vorticity contours, and secondary velocity vectors: increased pitch-chord ratio

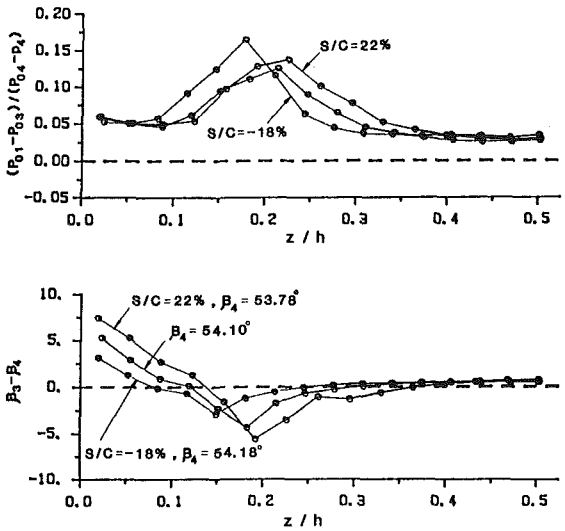

Fig. 19 Mixed-out pitchwise flow angle and stagnation pressure loss: pitch-chord variation

correlations which exist relate the net secondary loss through a cascade to such parameters as deflection, Reynolds number, and aspect ratio. Some, but not all, also attempt to relate the increase in loss to that contained in the upstream endwall boundary layer but such a dependency is only valid if the mechanisms of horseshoe vortex formation generate a significant amount of entropy. Various investigations, e.g., [7, 9, 10], which map the generation of loss through a cascade, suggest that this is not the case. In the present cascade, the thickness of the inlet boundary layer was doubled in a further attempt to determine the extent to which the generation of new loss is dependent upon that which exists at the inlet. Table 3 contains details of the thicker boundary layer.

The results of the surface flow visualization were very similar to those obtained at the design condition. The only

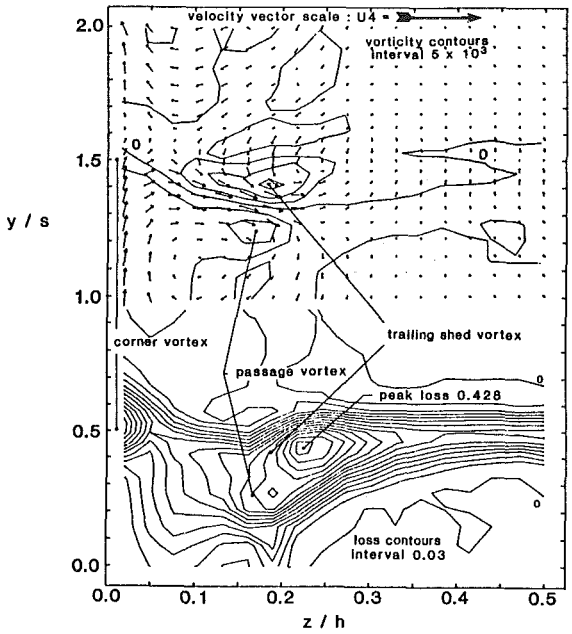

Fig. 20 Total pressure loss coefficient contours, vorticity contours, and secondary velocity vectors: thick inlet boundary layer

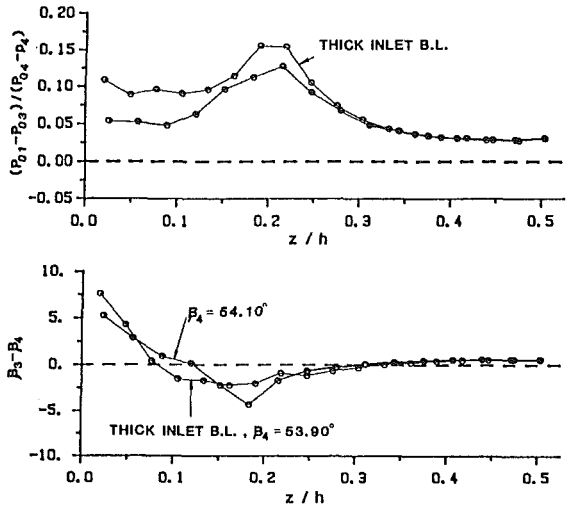

Fig. 21 Mixed-out pitchwise flow angle and stagnation pressure loss: *inlet boundary layer thickness variation*

significant difference was in the distance between the primary separation line of the horseshoe vortex and the leading edge, which reduced from 5.5 to 3.5 leading edge radii as the thickness was doubled. The results of the exit area traverse are plotted in Fig. 20. This shows that a much greater proportion of the flow area is occupied by high loss fluid. The loss peak associated with the passage vortex is only just visible and the center of the passage vortex, which is identified by the position of peak vorticity, lies further from the endwall and suction surface. The magnitudes of the secondary velocity vectors associated with the trailing-shed vorticity are similar to those observed in the case of the thinner inlet boundary layer. The peak strength of the passage vortex is however reduced. Given the decrease in the maximum value of vorticity within the inlet boundary layer, this might be expected.

A comparison of the spanwise variaton of loss and yaw angle at the different inlet boundary layer thickness is provided in Fig. 21. It shows the greater loss and overturning near the endwall in the case of the thicker inlet boundary layer as well as the more gradual variation in under and overturning which is presumably due to the changed distribution of inlet vorticity. The midspan loss is virtually unchanged. Table 4 shows that all of the apparent increase in stagnation pressure loss is due to the increased loss of the inlet boundary layer. Therefore, the production of new secondary loss is not necessarily linked with the magnitude of the inlet endwall boundary layer. The authors of [9, 10] made a similar observation.

Conclusions

The performance of a linear cascade of low-pressure turbine rotor hub profiles has been investigated over a range of paramters. It has been found that the production of new secondary loss increases with increasing Reynolds number, incidence, and pitch-chord ratio. It was apparently independent of the nature of the incoming endwall boundary layer.

The development of the three-dimensional flow field, however, was not as straightforward as the above statement implies. For example, the interaction between the endwall flow and the suction suface separation bubble, when present, affected the number, position and size of the individual loss peaks. Under some but not all conditions, the center of the passage vortex coincided with a loss peak. Furthermore, the strengths and positions of the passage and other vortices, although largely independent of the Reynolds number, were clearly a function of the inlet boundary layer and of the blade loading, the latter being demonstrated by the changes in incidence and pitch-chord ratio.

Undoubtedly, the variation in both the net loss production and the character of the flow field caused by the performed changes in the flow conditions and geometry requires further consideration. As well as the obvious and direct effect of secondary loss production upon machine performance, there exists the question of how the overall and the detailed structure of the exit flow from one blade row affects the performance of the next.

Acknowledgments

The work described was supported by the Ministry of Defence and Rolls-Royce Limited. The assistance of their representatives, in particular Mr. C. T. J. Scrivener of Rolls-Royce and their permission to published the work described in this paper, is gratefully acknowledged. The authors also wish to thank the members of the Whittle Laboratory for their assistance.

References

1 Ainley, D. G., and Mathieson, G. C. R., "A Method of Performance Estimation for Axial Flow Turbines," A. R. C., R. & M. 2974, Dec. 1951.

2 Balje, O. E., "Axial Cascade Technology and Application to Flow Path Designs, Part I," ASME Paper No. 68-GT-5, 1968.

3 Dunham, J., and Came, P. M., "Improvements to the Ainley-Mathieson Method of Turbine Performance Predictions," ASME JOURNAL OF ENGINEERING FOR POWER, Vol. 92, 1970, pp. 252-256.

4 Craig, H. R. M., and Cox, H. J. A., "Performance Estimation of Axial Flow Turbines," *Proc. Inst. Mech. Eng.*, Vol. 1985, 1970-71, pp. 407-424.

5 Hodson, H. P., and Dominy, R. G., "Three-Dimensional Flow in a Low-Pressure Turbine Cascade at Its Design Condition," ASME JOURNAL OF TURBOMACHINERY, this issue.

6 Hodson, H. P., "Boundary Layer Transition and Separation Near the Leading Edge of a High Speed Turbine Blade," ASME JOURNAL OF ENGINEERING FOR GAS TURBINE AND POWER, Vol. 107, 1985, pp. 127-134.

7 Langston, L. S., "Crossflows in a Turbine Cascade Passage," ASME Paper No. 80-GT-5, 1980.

8 Dunham, J., "A Review of Cascade Data on Secondary Losses in Turbines," *Jnl. Mech. Eng. Sci.*, Vol. 12, No. 1, 1970, pp. 48-58.

9 Marchal, P., and Sieverding, C. H., 'Secondary Flows Within Turbomachinery Bladings," AGARD Conference on Secondary Flows in Turbomachines, AGARD CP-214, 1977, Paper No. 11.

10 Gregory-Smith, D. G., and Graves, C. P., "Secondary Flows and Losses in Axial Flow Turbines," ASME Paper No. 82-GT-19, 1982.

H. Hoheisel

R. Kiock

Deutsche Forschungs- und Versuchsanstalt
für Luft- und Raumfahrt (DFVLR),
Institut für Entwurfsaerodynamik,
Braunschweig, W. Germany

H. J. Lichtfuss

Motoren- und Turbinen-Union GmbH (MTU),
München, W. Germany

L. Fottner

Universität der Bundeswehr München,
Institut für Strahlantriebe,
Neubiberg, W. Germany

Influence of Free-Stream Turbulence and Blade Pressure Gradient on Boundary Layer and Loss Behavior of Turbine Cascades

The optimization of the blade surface velocity distribution is promising for a reduction of turbine cascade losses. Theoretical and experimental investigations on three turbine cascades with the same blade loading show the important influence of the blade pressure gradient and the free-stream turbulence on the loss behavior. The results presented demonstrate that it is the boundary layer transition behavior that determines the losses on turbine cascades. An enormous effort in measuring technique is required in order to define the location of transition from cascade experiments very accurately.

Introduction

An important aspect of turbine aerodynamic design is the question of optimum profile shape to reduce the losses. With respect to the boundary layer state of actual turbomachinery blades, it is essential to find velocity distributions with the laminar-turbulent transition point as far downstream as possible. In particular, two factors affect the transition behavior, namely the pressure gradient on the blade surface and the free-stream turbulence. On the other hand, it is well known from turbine cascade experience, especially at low Reynolds numbers, that frequently laminar separation takes place before transition to the turbulent state is attained. Therefore the point at which this condition occurs, and the nature of transition, are the object of several publications, e.g., [1].

One of the first publications about the influence of turbulence on turbine cascade performance was by Hebbel [2]. The importance of investigations on cascades under turbomachinery conditions was demonstrated by Kiock [3, 4] and by Pfeil and Pache [5]. Abu-Ghannam and Shaw [6] investigated natural transition with pressure gradient and turbulence for a flat plate flow. They recommended considering the curvature too. Current turbine velocity distributions were simulated by Sharma et al. [7] to study the transitional boundary layer. The boundary layer behavior with respect to heat transfer is the object of the work by Blair [8] and by Rued and Wittig [9]. In general, no method is available which will predict reliably the influence of parameters like pressure gradient and turbulence on the blade boundary layer behavior. As concluded from a Symposium on Transition in Turbines held recently at the NASA Lewis Research Center a collection of existing transition data should be provided as standard cases against which other models could be tested; see [10].

The references quoted constitute only a selection. In spite of a large number of publications there is little information available about the influence of actual turbulence level on turbine blading performance. The present investigations describe the boundary layer and loss behavior of three turbine cascades of different geometries but with the same loading. Applying a current boundary layer integral calculation method, the influence of different blade velocity distributions and free-stream turbulence levels on the cascade performance was predicted. Experiments performed in the high-speed cascade wind tunnel of DFVLR Braunschweig support these theoretical results.

Theoretical Investigation

Cascade Design. To describe the complicated flow behavior of an axial turbine the "quasi-three-dimensional design" has been applied. First the axial and radial velocity distributions are calculated, followed by several blade-to-blade computations through cascades in order to obtain also the corresponding circumferential distribution of the velocity. The object of the blading design is to find an adequate profile shape to verify the velocity triangle with respect to minimal losses. It is necessary also to incorporate some strong mechanical and turbine cooling constraints [11]. These additional design parameters may be the reason that there is no systematic family for turbine profiles as is the case for compressors (e.g., NACA 65 or C4 profiles). Therefore, the tur-

Contributed by the Gas Turbine Division of THE AMERICAN SOCIETY OF MECHANICAL ENGINEERS and presented at the 31st International Gas Turbine Conference and Exhibit, Düsseldorf, Federal Republic of Germany, June 8–12, 1986. Manuscript received at ASME Headquarters February 19, 1986. Paper No. 86-GT-234.

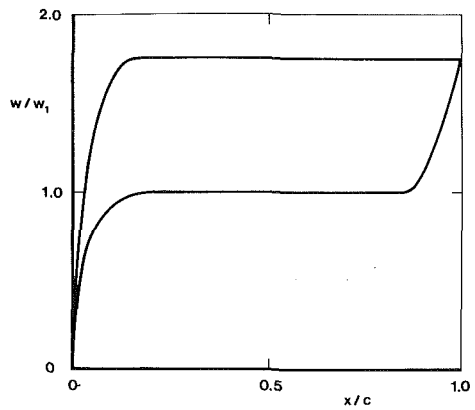

Fig. 1 "Ideal" velocity distribution for accelerating cascades

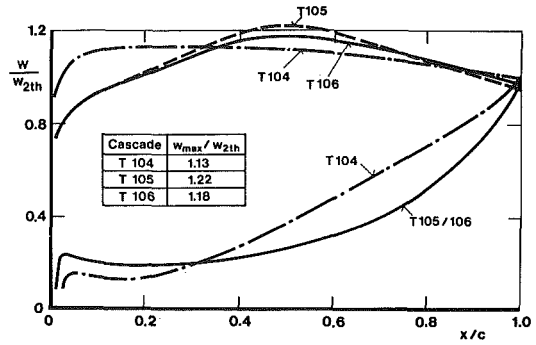

Fig. 2 Design velocity distribution

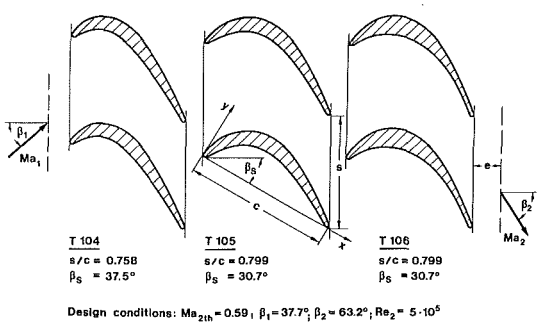

Fig. 3 Cascade geometry and nomenclature

bine profile design is an individual process to be performed in an iterative manner.

The geometric design of the profiles presented in this paper was performed in the traditional manner of superimposing a thickness distribution on a camber line. The camber line is defined by two polynomials of a maximum order of four which are patched to each other at a selected connection point in such a way that the slope remains. Superimposed on the camber line then is a thickness distribution of a similar mathematical character than that of the camber line, starting on the leading edge circle or ellipse at a prescribed wedge angle and ending on the trailing edge circle at another wedge angle. Performing an inviscid blade-to-blade flow calculation then yields pressure or velocity distributions along the pressure and suction surfaces of the profile which serve as a measure of the attained aerodynamic quality (direct method).

Another design procedure which is now available to create the blade shape is the inverse or design method. A very versatile method of this type is given by Schmidt [12] using a compressible inviscid flow model.

Both blading design methods use the profile velociy distribution as a criterion for the aerodynamic quality of the design, i.e., they take into account the close connection between the profile losses (due to blade boundary layer) and the blade surface velocity distribution. Thus, the velocity distribution being input for these methods has to be optimized with respect to low losses of the blading. Since turbine cascades have to accelerate the flow from inlet to outlet, their profile velocity distribution could have in principle a shape without any deceleration region, as shown in Fig. 1. In practical applications this "ideal" distribution will be changed more or less, especially with respect to the above-mentioned mechanical constraints and because of alterations necessary to obtain more desirable boundary layer characteristics.

Experience on several turbine cascades at design conditions shows a mixed laminar-turbulent boundary layer on the suction surface and a mostly laminar boundary layer on the pressure surface. It is therefore necessary primarily to optimize the velocity distribution on the suction surface with

Nomenclature

c = chord
c_{p2} = pressure distribution coefficient, based on exit conditions, see equation (8)
e = standard location of traverse plane
e_{rms} = root mean square a-c CTA (Constant Temperature Anemometer) output voltage
E = mean CTA output voltage, with flow
H_{12} = shape factor = δ_1/δ_2
H_{43} = shape factor = δ_4/δ_3
M_{2th}, Ma_{2th} = isentropic exit Mach number = $f(p_K/p_{01})$
p = static pressure
p_0 = total pressure
q = dynamic head = $p_0 - p$
Re_2 = Reynolds number based on blade chord and exit conditions = $w_2 \cdot c/\nu_2$
s = blade pitch (spacing)
Tu_1 = degree of turbulence at cascade inlet = $\sqrt{\overline{w_1'^2}}/w_1$
w = flow velocity
x, y = profile coordinates, bitangential
β = flow angle, see Fig. 3
β_s = stagger angle, see Fig. 3
δ = boundary layer thickness
$\delta_1, \delta_2, \delta_3, \delta_4$ = displacement, momentum, energy, and density thickness
ζ_{V2} = total pressure loss coefficient, see equation (7)
η = coordinate normal to blade surface
ν = kinematic viscosity
ρ = density
τ = shear stress

Subscripts and Abbreviations

1 = cascade inlet plane
2 = cascade exit plane, homogeneous flow
δ = edge of boundary layer
K = tank (cascade exit condition)
max = maximum
th = theoretical isentropic flow
tr = trailing edge
R = reattachment
S = separation
T = transition onset
TMM = time-marching method

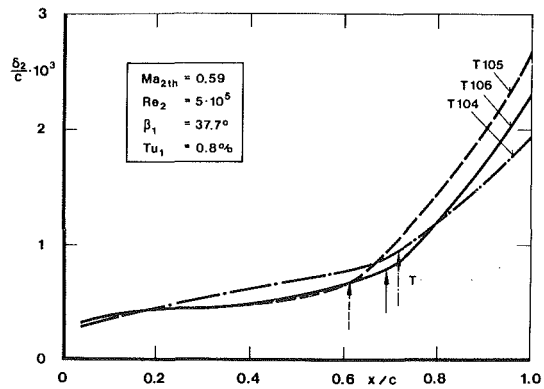

Fig. 4 Calculated momentum thickness of suction surface with Granville's transition criterion

respect to low losses. The laminar boundary layer should be maintained as far downstream as possible. Transition is required to take place without forming a laminar separation bubble. The extent of a rearward deceleration has to be carefully limited to avoid flow separation in this region. In order to obtain information about an optimal velocity distribution on the suction surface considering the boundary layer state, three cascades with different velocity distributions but the same aerodynamic loading were designed for a typical LP turbine condition. These velocity distributions are shown in Fig. 2. The chosen velocity distributions, designated by T104, T105 and T106, can be described as follows:

- Type T104 is front-loaded with an almost uniform suction side velocity, incorporating a small amount of deceleration in the rear part.
- Types T105 and T106 are aft-loaded, showing an acceleration on the suction side over the front part with a maximum velocity at approximately 50 percent chord followed by a deceleration to the outlet velocity. The types T105 and T106 differ only in their peak velocity resulting in different pressure gradients over the rear part of the suction side. The velocity distribution along the pressure side remains nearly unchanged for these cases.

The associated profile shapes and cascade geometries are shown in Fig. 3. These cascades were designed by the direct method.

Boundary Layer Behavior of Different Types of Velocity Distribution. For an assessment of the boundary layer behavior subject to the three velocity distributions, a boundary layer integral method was applied. Starting from Prandtl's boundary layer equations for two-dimensional flow expressing the conservation laws of mass (continuity equation) and momentum

$$\rho u\frac{\partial u}{\partial x}+\rho v\frac{\partial u}{\partial y}=-\frac{\partial p}{\partial x}+\frac{\partial \tau}{\partial y} \tag{1}$$

with the usual assumption on the shear stress τ, integration of equation (1) leads to the compressible integral equation of momentum

$$\frac{d\delta_2}{dx}+\frac{\delta_2}{w_\delta}\cdot\frac{dw_\delta}{dx}[2+H_{12}-M_\delta^2]-\frac{\tau_w}{\rho_\delta\cdot w_\delta^2}=0 \tag{2}$$

and the compressible integral equation of mechanical energy

$$\frac{d\delta_3}{dx}+\frac{\delta_3}{w_\delta}\frac{dw_\delta}{dx}[3+2H_{43}-M_\delta^2]-\frac{2}{\rho_\delta\cdot w_\delta^3}\int_0^{w_\delta}\tau\cdot dw=0 \tag{3}$$

as given by Walz [13] in more detail. In the present paper two different transition criteria are taken into consideration:

- The criterion by Granville [14] describes the influence of turbulent intensity for flat plate flow and flow with pressure gradient at a low free-stream turbulence level.
- An empirical criterion by Seyb [15], analytically given by Dunham [16], describes transition to be dependent on the following three parameters:

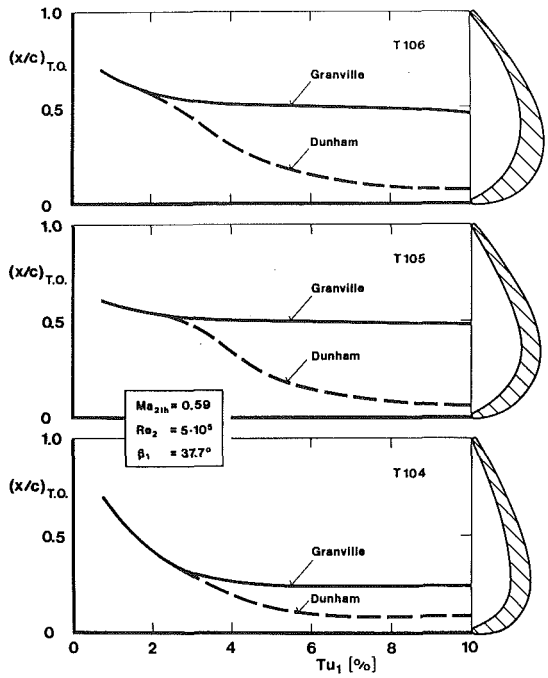

Fig. 5 Influence of degree of turbulence on transition onset on the suction surface

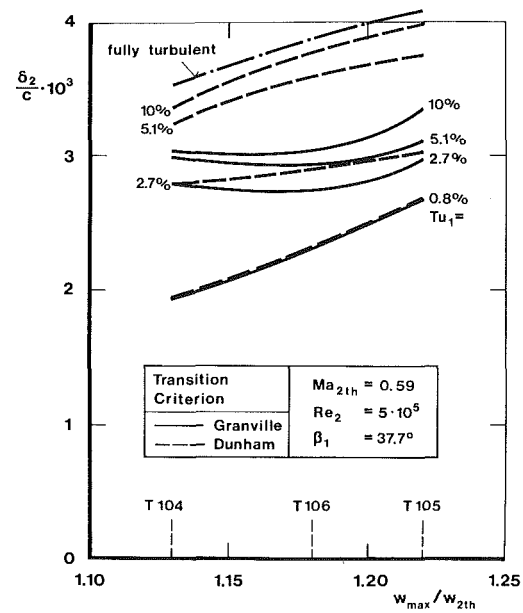

Fig. 6 Effect of deceleration on the momentum thickness at the suction side trailing edge

pressure gradient
$$\lambda=\frac{\delta_2^2}{\nu}\cdot\frac{dw_\delta}{dx} \tag{4}$$

momentum thickness Reynolds number
$$Re_{\delta 2}=\frac{w_\delta\cdot\delta_2}{\nu} \tag{5}$$

local turbulence level
$$Tu=\frac{\sqrt{\overline{w'^2}}}{w_\delta} \tag{6}$$

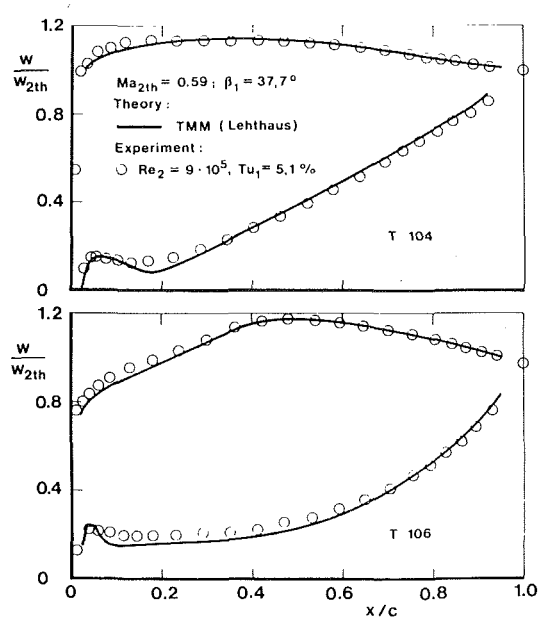

Fig. 7 Blade velocity distribution; comparison of theory and experiment at design conditions

This definition of the degree of turbulence takes into account the local acceleration/deceleration in the blade channel and thus differs from the inlet free-stream value.

At the design condition laminar separation is assumed to be absent or of small extent. For this condition Fig. 4 shows the related momentum thickness versus chord of the three cascades at the low turbulence level of $Tu_1 = 0.8$ percent where the respective locations of transition (T) according to Granville's transition criterion are indicated by the arrows. At this low turbulence level the smallest value of the momentum thickness at the trailing edge is obtained by the type T104 as a result of the transition behavior, and of the moderate deceleration over the rear part of the blade surface. The stronger aftward pressure gradient of T105 causes earlier transition which leads to a larger momentum thickness in the trailing edge region.

Looking at the transition behavior by using the two criteria mentioned above, Fig. 5 shows the influence of the free-stream turbulence on transition onset (T) for the three cascades investigated. With increasing turbulence Dunham's criterion shows transition onset to be located considerably further upstream for all three cascades, whereas the Granville criterion shows a similar strong influence for the T104 type only.

Values of the momentum thickness at the trailing edge calculated by the integral boundary layer method are shown in Fig. 6, where the influence of deceleration attributed to the different cascade types is displayed with the turbulence intensity as parameter. As can be seen a dominant influence of the turbulence level on the trailing edge momentum thickness exists for each cascade type, of which only the front-loaded type T104 attains a low value of momentum thickness at low turbulence level. At actual turbulence levels for turbine cascades the T106 type seems to represent the best compromise between deceleration rate and peak velocity location when Granville's transition criterion is applied.

Experimental Investigation

Apparatus and Test Program. The experimental investigations were carried out in the high-speed cascade wind tunnel of DFVLR at Braunschweig [17]. The tunnel was installed in a tank which could be evacuated from 1 to 0.05 bar. An independent variation of Mach number and Reynolds number was possible. The degree of turbulence was about $Tu_1 = 1$ percent. It could be increased up to $Tu_1 = 8$ percent using grids of crossed bars upstream of the cascade [18]. The tunnel had a test section width of $h = 300$ mm and an adjustable height of 250 to 500 mm depending on the inlet angle. Each cascade consisted of seven blades with chord length $c = 100$ mm resulting in an aspect ratio of $h/c = 3$. No side wall suction was applied. In general, the design point of the cascades only will be considered here: $\beta_1 = 37.7$ deg; $M_{2th} = 0.59$; $Re_2 = 5 \times 10^5$.

Wake traverse measurements (total pressure, static pressure, and outlet flow angle) were performed with a wedge type probe [17] located at 40 percent of chord axially downstream of the blade trailing edge plane. Surface pressure distributions were measured using static pressure tappings on the suction and the pressure sides of the blades adjacent to the center blade.

Boundary layer measurements were carried out at different positions of the blade suction surface by a flattened Pitot probe of 0.15×1.30 mm head size in order to obtain velocity profiles and integral quantities. The probe was calibrated for Mach and Reynolds number, flow angle, and turbulence level. Corrections were applied from these calibrations on the basis of a comparison with flat plate experiments [19] and with measurements by a laser-Doppler anemometer, respectively [20]. Another probe of 0.30×0.80 mm (also a flattened Pitot tube, called Preston type probe) was moved at a constant distance from the blade surface, $\eta = 0.15$ mm, in order to detect boundary layer transition. Details of this technique are described in [21]. Additional tests were performed also in order to detect boundary layer transition by flow visualization method and by the heated thin film technique.

Evaluation of the Experimental Data. The wake data were evaluated by transforming the nonhomogeneous flow in the measuring plane into an equivalent homogeneous flow applying the laws of conservation, see [22]. This evaluation leads to the total pressure loss coefficient which is defined as

$$\zeta_{V2} = \frac{p_{01} - p_{02}}{p_{01} - p_K} \tag{7}$$

For the pressure distribution a nondimensional coefficient is defined as

$$c_{p2} = \frac{p(x/c) - p_K}{p_{01} - p_K} \tag{8}$$

As an alternative the velocity ratio w/w_{2th} with $w = f(p/p_{01})$ and $w_{2th} = f(p_K/p_{01})$ may be used.

All boundary layer data were evaluated under the assumption of constant static pressure across the boundary layer. This leads to the standard definition, e.g., of the momentum thickness

$$\delta_2 = \int_0^{\delta} \frac{\rho(\eta)}{\rho_\infty} \cdot \frac{w(\eta)}{w_\infty} \left[1 - \frac{w(\eta)}{w_\infty}\right] d\eta \tag{9}$$

For the detection of boundary layer transition by a flattened Pitot probe (also called Preston type) the local dynamic heat was evaluated by the Pitot pressure at $\eta = 0.15$ mm and by the local surface static pressure which gives the ratio

$$\frac{q(x/c, \eta)}{q(x/c)} = \frac{p_0(x/c, \eta) - p(x/c)}{p_{01} - p(x/c)} \tag{10}$$

The degree of turbulence in the inlet plane is defined as

$$Tu_1 = \frac{\sqrt{\overline{w_1'^2}}}{w_1} \tag{11}$$

where w_1' is the fluctuating velocity component in the direction of w_1 obtained from a single hot-wire probe placed normal to the free-stream velocity.

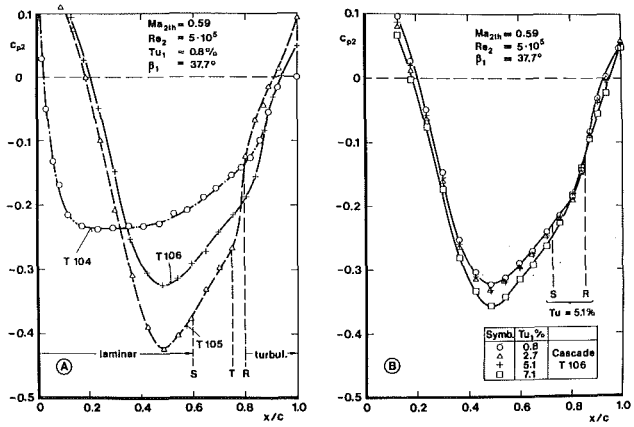

Fig. 8 Pressure distributions on the suction surface: (A) influence of cascade type; (B) influence of free-stream turbulence on cascade T106

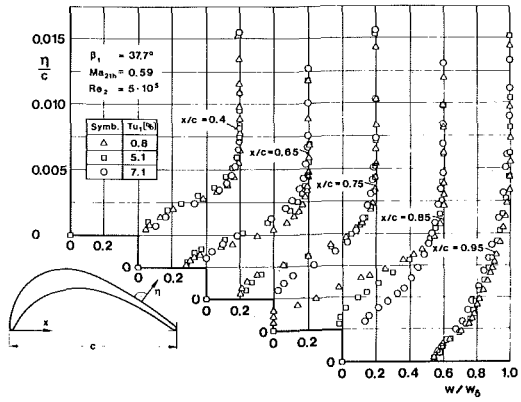

Fig. 10 Boundary layer velocity profiles: suction surface, T106, influence of turbulence

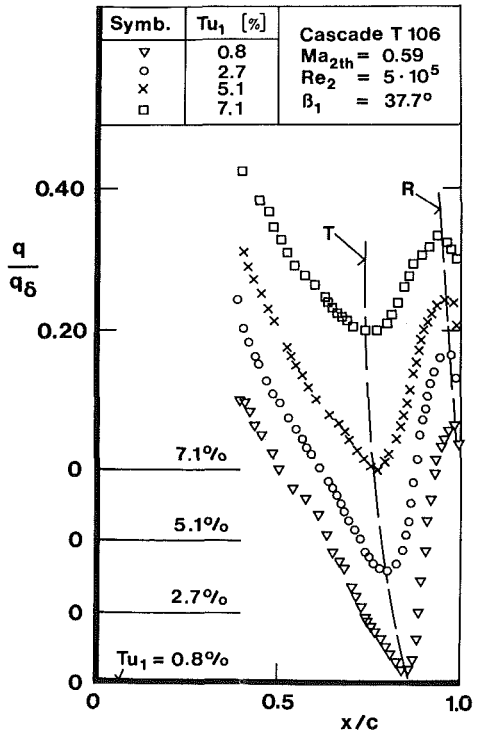

Fig. 9 Boundary layer transition on the suction surface, using Preston type probe

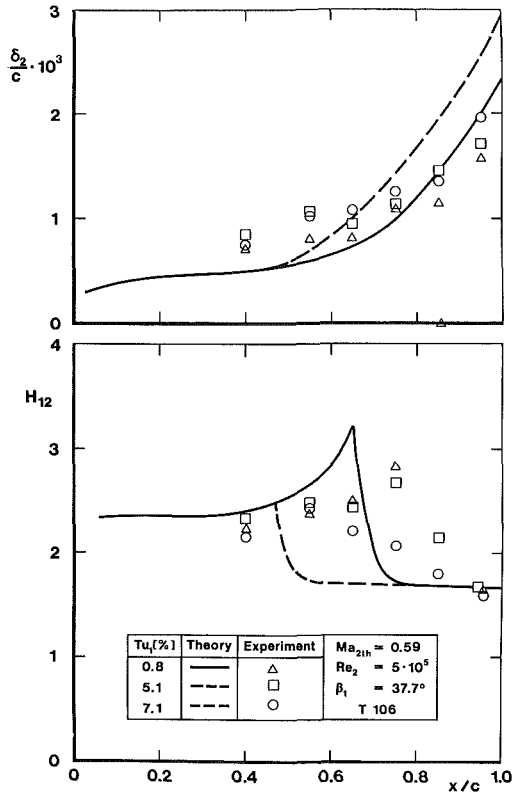

Fig. 11 Integral values of the boundary layer, suction surface T106

Results and Discussion

Measured Pressure Distribution and Comparison With Theory. Figure 7 shows the measured and the calculated velocity distribution of the cascades T104 and T106. The theoretical results were obtained using Lehthaus's time-marching method [23]. From the experiments a case with the relatively high Reynolds number, $Re_2 = 9 \times 10^5$, was chosen in order to keep the influence of laminar separation bubbles low. Very good agreement between the calculated and the measured velocity distributions can be seen to exist for the two different types of turbine cascades. This gives confidence in the cascade design method used. Any differences between theory and experiments in the results presented may therefore be interpreted as inadequacies in the boundary layer method used, and, in particular, in the transition criterion applied.

Boundary Layer Transition Location. The three cascades were investigated at Reynolds numbers of an actual turbine stage. In this Reynolds number range ($Re_2 = 3$ to 7×10^5) laminar separation may occur [24]. Some results of the used measuring techniques are demonstrated and discussed.

Diagram (A) in Fig. 8 shows the pressure distributions on the suction surface of the cascades at the low turbulence level of $Tu_1 = 0.8$ percent. Boundary layer transition from the laminar to the turbulent state via a separation bubble is indicated by the changing pressure gradients on the cascade types T105 and T106. The bubble starts, say, on T105 somewhat downstream of the suction peak at $x/1 = 0.6$ as marked by S. Transition onset (T) occurs for this example at $x/1 = 0.75$. The boundary layer reattaches at $x/1 = 0.80$ (marked by R). On the cascade type T104, with the peak velocity in the front part, the different boundary type states are not clearly determinable from the pressure plot. Other

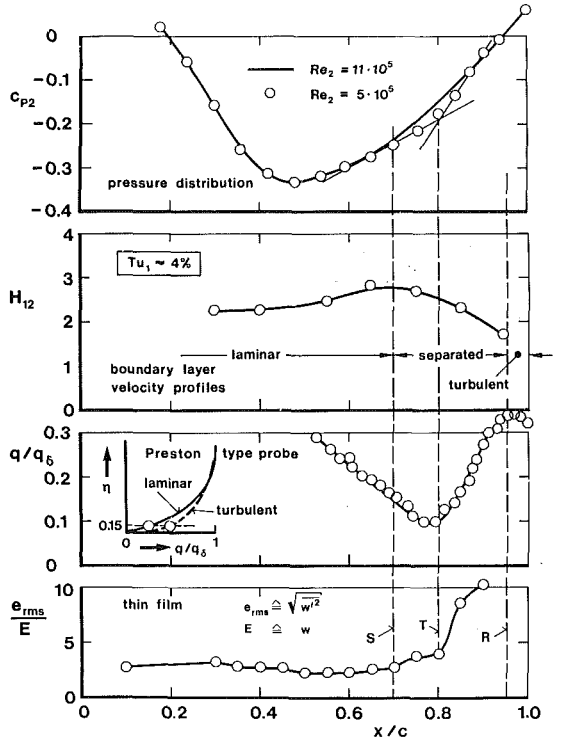

Fig. 12 Determination of transition location from measurements

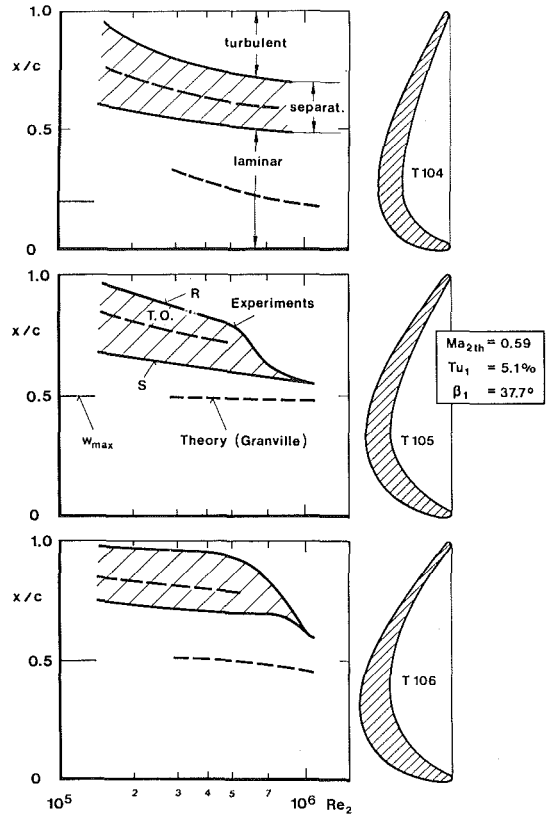

Fig. 13 Effect of Reynolds number on transition location

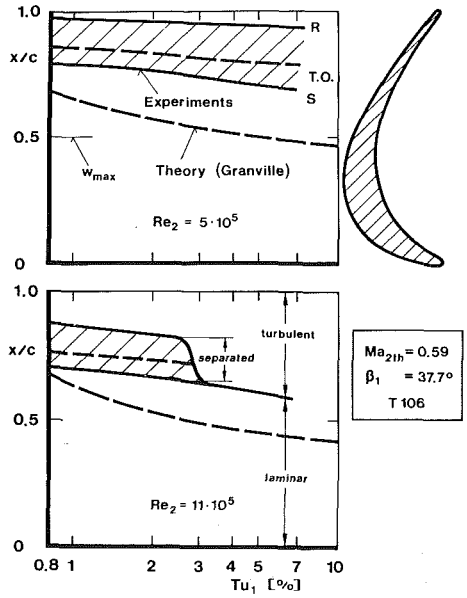

Fig. 14 Effect of free-stream turbulence on transition location, cascade T106

measuring techniques are necessary to clarify this question and will be discussed below. Diagram (B) in Fig. 8 shows the pressure distribution of T106 at different turbulence levels. With increasing turbulence level the detectable laminar separation bubble disappears almost completely.

Another result concerning boundary layer transition is demonstrated in Fig. 9. Here, transition was detected by a Preston type probe. These results show the influence of the turbulence level on cascade T106. With increasing turbulence level the point of transition onset (T) is shifted upstream: All curves have a well-defined minimum, indicating the start of transition, as well as a well-defined maximum, describing the completion of transition (R).

Measurements of the boundary layer velocity profile obtained for different values of the degree of turbulence are presented in Fig. 10 for T106. Velocity profiles w/w_δ are plotted at different locations x/c. These curves demonstrate the progressive change from laminar to "full" turbulent velocity profiles. This change in shape occurs between $x/c = 0.75$ and $x/l = 0.95$ which is in agreement with the pressure distributions (Fig. 8) and with the Preston type probe results (Fig. 9). This range thus defines the extent of a "laminar separated bubble" where a strong influence of the free-stream turbulence is assumed to exist. On the other hand, from comparison with laser-Doppler measurements, it is known that in particular in the reverse flow zone the presence of probes alters the velocity distribution near the wall. This influence disappears with increasing distance of the probes from the surface [20]. These findings are of great importance when comparing test results with empirical correlations on laminar separation bubbles.

From the measured boundary layer velocity profiles some integral values were determined. Plotted in Fig. 11 are the momentum thickness δ_2/c and the shape factor $H_{12} = \delta_1/\delta_2$ versus chord length x/c for the same condition as that used in Fig. 10. The experimental results are compared with theoretical results, obtained by Granville's criterion for transition at different degrees of turbulence between $Tu_1 = 0.8$ and 7.1 percent. For the front part of the blade surface, poor agreement is found for the momentum thickness. In this part the boundary layer thickness is very thin (less than 1 mm). Little is known about the accuracy of measurements in boundary layers where the displacement thickness and the probe height are of the same order of magnitude. An error in measured momentum thickness of about $\Delta\delta_2/\delta_2 = \pm 14$ percent was found in our previous investigations [19]. For the rear part of the blade surface (i.e., downstream of transition) better agreement between theory and experiment is observed

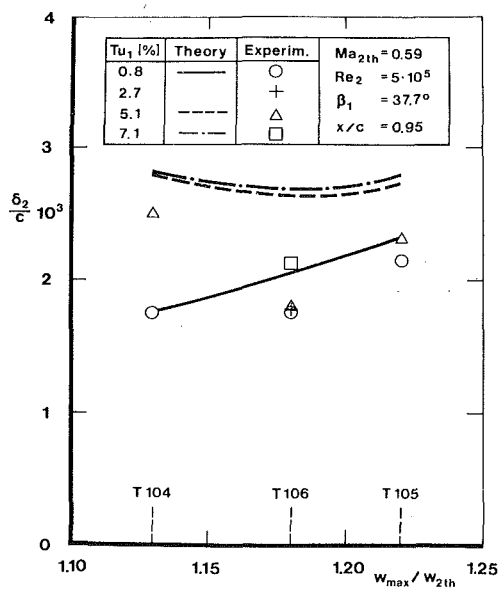

Fig. 15 Effect of blade deceleration on momentum thickness; comparison between theory and experiment

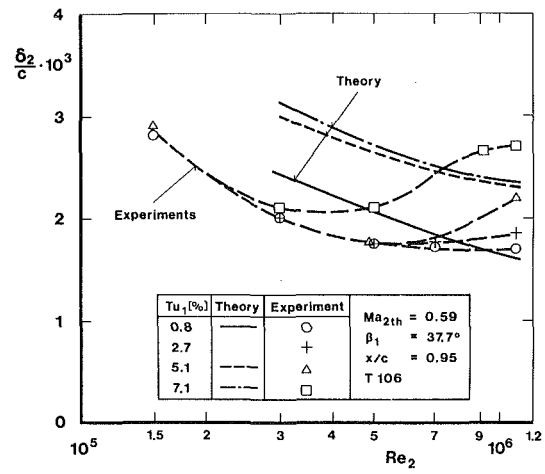

Fig. 16 Effect of Reynolds number and free-stream turbulence on momentum thickness; comparison between theory and experiment

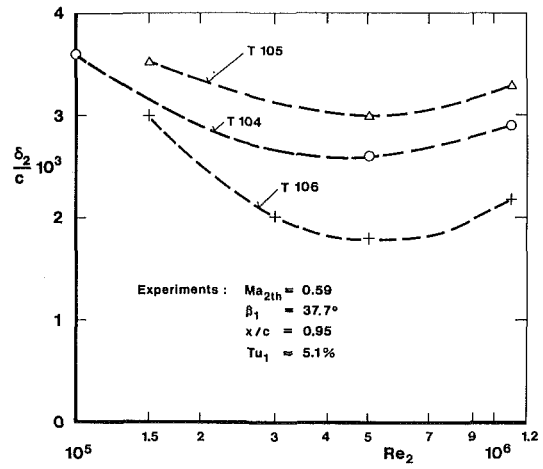

Fig. 17 Effect of Reynolds number on momentum thickness; experiments on different cascades at constant turbulent level

for the momentum thickness. An increase of δ_2 with the turbulence level is seen to exist as was to be expected.

A rather good agreement in the comparison of theory with experiment can also be observed concerning the shape factor H_{12} both for laminar and turbulent boundary layer conditions. The main difference is found in the location of transition (notable by the drop of H_{12}). The theoretical results indicate transition to take place further upstream than the experiments. Obviously, this is due to a deficiency of the transition criterion which does not determine the location and the extent of transition in the correct manner as yet [25].

A comparison of different measurement techniques for the detection of transition is shown in Fig. 12, i.e., curves from heated film technique, Preston type probe results, shape factor H_{12} from boundary layer velocity profiles, and pressure distribution, respectively. As to the thin film technique the distribution of the voltage coefficient e_{rms}/E versus x/c shows a first increase at $x/c \approx 0.7$ which indicates the first change in heat transfer. At this location, the beginning of laminar separation (S) is also indicated by the appearance of turbulent spots detectable from the *a-c* signal on the oscilloscope screen (not shown here), from the pressure distribution, and from the maximum value of the shape factor. Transition onset (T) starts at $x/c \approx 0.8$ indicated by the strong increase of e_{rms}/E. This location coincides with that of the minimum q/q_δ value and with that of the change of the pressure gradient in the pressure distribution. The point of boundary layer reattachment (R) is defined by the maximum q/q_δ value. These findings drawn from different measuring techniques give confidence in the results on boundary layer transition.

The results for the extent of the boundary layer transition regime extracted from the experimental investigations of the three cascades are summarized in Fig. 13 and 14 in comparison with the theoretically determined transition using Granville's criterion. Figure 13 shows the influence of the Reynolds number at a constant turbulence level of about $Tu_1 \approx 5$ percent, while Fig. 14 describes the effect of the turbulence level for two Reynolds numbers in the case of the cascade T106 only. These experimental results stem from:

- pressure distributions
- boundary layer velocity profiles
- Preston type probe measurements along the surface
- flow visualizations
- heated thin film technique (T104 and T106)

In general, the experimental results do not show "natural" transition as assumed in the theoretical investigations, but the "bubble-type" transition is found. A laminar separation bubble is closed by a turbulent reattachment. Start and extension of laminar separation are different depending on the pressure gradient of the three cascades. With increasing Reynolds number laminar separation is moving slightly upstream and the size of the bubbles decreases, which is also found in single airfoil investigations [26]. In the case of the front-loaded cascade type T104 and also for the aft-loaded type T105 with the stronger pressure gradient, transition starts in the same range $x/c = 0.55$ to 0.65. On the aft-loaded type T106 the "transition zone" begins farther downstream than would be expected from the lower pressure gradient.

The influence of turbulence on the aft-loaded type T106 at the most important Reynolds number, $Re_2 = 5 \times 10^5$ (Fig. 14) shows only a small change of transition onset and closure with increasing turbulence level. This experimentally determined behavior is in agreement with the theoretical result, as shown earlier in Fig. 5; however, the locations x/c of theory and experiment differ strongly. At the higher Reynolds number, $Re_2 = 11 \times 10^5$, the laminar separation bubble disappears with increasing turbulence level. This behavior is in agreement with the Granville criterion. However it should be noted that the present results are in disagreement with the correlation formula of Dunham, which was also found by Blair [8].

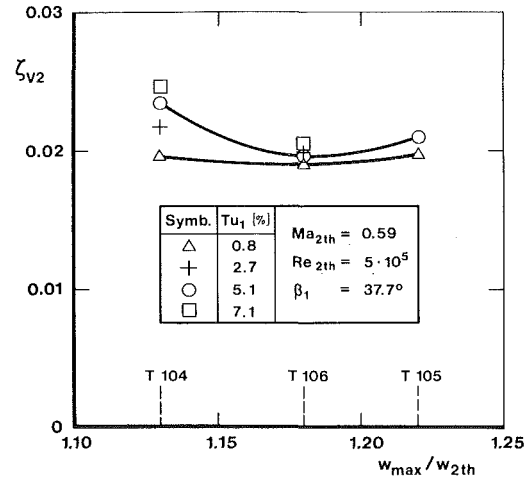

Fig. 18 Effect of blade deceleration on measured loss coefficient at different turbulence levels

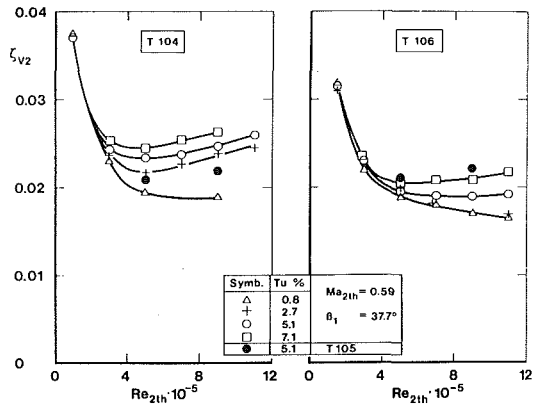

Fig. 19 Effect of Reynolds number on measured loss coefficient at different turbulence levels

Therefore it seems to be necessary to study "natural" and "bubble-induced" transition in more detail in the future, but under the conditions of turbomachinery blades.

Boundary Layer Quantities. The different transition behavior found for the three cascades is also reflected in the momentum loss behavior. Figure 15 shows the momentum thickness versus the flow deceleration (different types of cascade) near the trailing edge, i.e., at $x/c = 0.95$ at design conditions. At the low degree of turbulence $Tu_1 = 0.8$ percent, the same experimental value of δ_2 is obtained for the front-loaded cascade T104 and for the aft-loaded cascade T106. The stronger pressure gradient of cascade T105 leads to higher loss in momentum. The comparison of experiment and theory shows rough agreement, both in level and in tendency. At the higher turbulence levels, a minimum momentum thickness is obtained for the aft-loaded cascade T106 which is qualitatively in agreement with the theoretical results. In view of the different transition mechanisms assumed for the theory and found in the experiments, no quantitative agreement could be expected.

The influence of Reynolds number on momentum thickness of the aft-loaded type T106 is shown in Fig. 16. At the low turbulence level of $Tu_1 = 0.8$ percent, the Reynolds number has the dominant influence, as could be expected. At higher turbulence levels the difference between experiment and theory can again be explained by the insufficient assumptions with regard to the transition criterion.

For the most important turbulence level of $Tu_1 = 5.1$ percent, the momentum thickness of the three cascades, as obtained from experiments only, is plotted versus Reynolds number in Fig. 17. The minimum value of δ_2 at all three cascades occurs near the design Reynolds number, $Re_2 = 5 \times 10^5$. The aft-loaded cascade T106 with the moderate pressure gradient shows the lowest losses in the most important Reynolds number range $2 \times 10^5 < Re_2 < 7 \times 10^5$. For high turbulence levels no advantage in favor of the front-loaded cascade type T104 can be deduced.

Total Pressure Losses. The total pressure losses of the different cascades were determined from wake traverse measurements. Figure 18 shows the loss coefficient ζ_{V2} versus the deceleration rate w_{max}/w_{2th} for the three cascades, at design condition, and with the turbulence level as a parameter. The lowest losses are obtained for the aft-loaded cascade T106, at all turbulence levels; however, the advantage at the lowest turbulence level is small. The front-loaded type T104 shows a stronger influence of the turbulence level, this effect being directly connected to the boundary layer transition behavior (see Fig. 13). The second aft-loaded type T105 shows somewhat higher losses than the type T106, which is attributed to the stronger deceleration on the suction side. Thus, it is in particular this deceleration that has to be limited carefully to avoid increasing losses.

The stronger influence of the turbulence level on the front-loaded type T104 can also be seen to prevail in a wide Reynolds number range in comparison with the aft-loaded type T106 (Fig. 19). The behavior of the loss coefficient confirms the boundary layer results for the suction side perfectly (see Fig. 16). With increasing Reynolds number and increasing turbulence level additional losses are created due to the forward shift of transition.

As discussed before, laminar separation bubbles are, in particular, responsible for the influence of the turbulence level on the total losses. To avoid the occurrence of laminar separation bubbles, several possible measures can be taken. One of these is to design a blade shape to have a slight adverse pressure gradient, which promotes transition without laminar separation. However, this can be done for one particular Reynolds number only. Since a gas turbine blading has to work within a Reynolds number range, laminar separation bubbles will occur rather frequently. In order to avoid or to reduce these phenomena, mechanical or pneumatic turbulators can be used. As demonstrated, e.g., by Hebbel [2], laminar separation bubbles can be made to disappear and consequently losses can be reduced by these devices. Another technique is the application of pneumatic turbulators as used successfully on single airfoils [26]. This principle was also tested with the present cascades by letting air bleed from the pressure to the suction side. Reductions of losses of about 10 to 20 percent can be achieved at Reynolds numbers $Re_2 < 3 \times 10^5$.

The results, discussed so far, pertained to design conditions. The three cascades were also investigated experimentally at different inlet angles (incidences) and Mach numbers. As shown in Fig. 20, for the most important turbulence level of about $Tu_1 = 5$ percent, the aft-loaded type T106 preserves its advantage concerning loss behavior almost over the whole incidence range. At positive incidences, $\beta_1 > 38$ deg, a strong increase of the losses occurs especially on the front-loaded type T104.

With the design inlet angle kept constant, the influence of Mach number on the total pressure losses is plotted in Fig. 21, again for $Tu_1 = 5$ percent. For subcritical Mach numbers, $M_{2th} < 0.85$, the aft-loaded type T106 produces the lowest losses. The comparison with the results for the second aft-loaded type T105 makes again quite clear that the deceleration on the suction surface has to be limited carefully. The front-loaded type T104 offers no advantage in the Mach number range of interest, $M_{2th} < 0.9$.

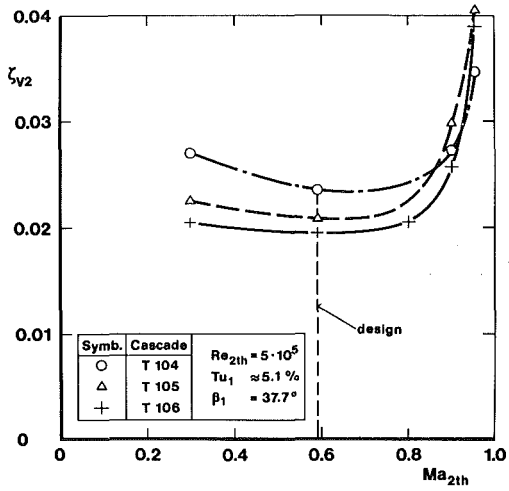

Fig. 20 Effect of inlet angle on loss coefficient of different cascades

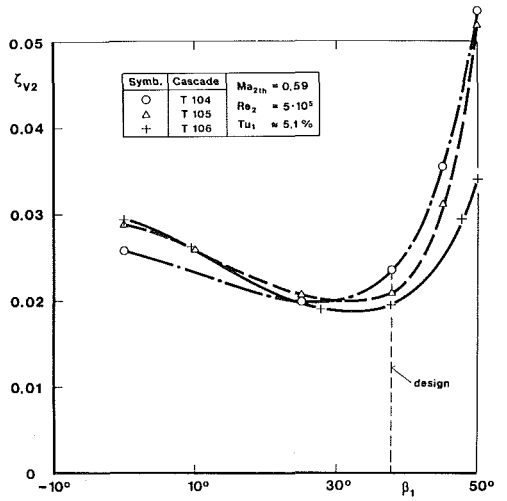

Fig. 21 Effect of Mach number on loss coefficient of design inlet angle of different cascades

Conclusions

The present paper describes theoretical and experimental investigations on the influence of free-stream turbulence for three turbine cascades. These cascades were designed to have a prescribed velocity distribution and the same aerodynamic loading at a Mach number of $M_{2th} = 0.59$ and at a Reynolds number of $Re_2 = 5 \times 10^5$. Flow field calculations were performed using a time marching method to predict the final blade surface velocity distribution. In addition, a boundary layer integral method, including a transition criterion, was applied to predict the influence of the degree of turbulence and pressure gradient on the momentum thickness along the blade suction surface. A series of experiments carried out in the high-speed cascade wind tunnel of the DFVLR Braunschweig which, in general, confirm the theoretical results. Turbulence intensities up to $Tu \approx 8$ percent were generated. The investigations on one front-loaded type and on the two aft-loaded types of turbine cascades led to the following conclusions:

1 The type of velocity distribution in the suction surface is of great importance in view of total pressure losses. The aft-loaded type with a carefully limited rearward deceleration yields low losses.

2 At realistic degrees of free-stream turbulence, $Tu_1 > 2$ percent, this aft-loaded velocity distribution leads to lower losses than the front-loaded velocity distribution. At the design Reynolds number $Re_2 = 5 \times 10^5$, a stronger influence of the free-stream turbulence on the losses is observed for the front-loaded cascade.

3 At a given Reynolds number the laminar-to-turbulent boundary layer transition is, in particular, influenced by the occurrence of laminar separation bubbles. The streamwise location of the onset of transition as measured by different techniques could not be confirmed by the theoretical investigations due to the lack of more reliable transition criteria. In particular, at realistic turbine turbulence levels of $Tu_1 > 2$ percent transition onset is predicted by the theory to lie more upstream than was found from the experiments. Boundary layer transition appears always to be coupled with a laminar separation bubble in the Reynolds number range of interest.

4 The favorable characteristics of the aft-loaded cascade types found at design conditions continue to exist also at different incidences and at high subcritical exit Mach numbers.

Acknowledgments

The work reported herein was supported within the framework of research programs of the German "Bundesministerium der Verteidigung." Permission for publication is gratefully acknowledged. The authors are also indebted to T. Kotlarski, M. Hoeger, and M. Meyer-Glitza for their help in carrying out these investigations. The assistance of P. Geisler, C. Giese, G. Laskowski, and A. Rüberg is also appreciated.

References

1 Gostelow, J. P., *Cascade Aerodynamics*. Pergamon Press, New York, 1984.

2 Hebbel, H. H., "Über den Einfluss der Machzahl und der Reynoldszahl auf die aerodynamischen Beiwerte von Turbinenschaufelgittern bei verschiedener Turbulenz der Strömung," *Forschg. im Ing.-Wesen*, Vol. 30, 1964, pp. 65–77.

3 Kiock, R., "Einfluss des Turbulenzgrads auf die aerodynamischen Eigenschaften von ebenen Verzögerungsgittern," *Forschg. im Ing.-Wesen*, Vol. 39, 1973, pp. 17–28.

4 Kiock, R., "Turbulence Downstream of Stationary and Rotating Cascades," ASME Paper No. 73-GT-80, 1973.

5 Pfeil, H., and Pache, W., "Messungen von Strömungsgrenzschichten unter Turbomaschinenbedingen," *Zeitschr. Flugwiss. Weltraumforsch*, Vol. 1, 1977, pp. 267–277.

6 Abu-Ghannam, B. J., and Shaw, R., "Natural Transition of Boundary Layers – The Effect of Turbulence, Pressure Gradient and Flow History," *Jour. Mech. Eng. Sci.*, Vol. 22, 1980, pp. 213–228.

7 Sharma, O. P., Wells, R. A., Schlinker, R. H., and Bailey, D. A., "Boundary Layer Development on Turbine Airfoil Suction Surfaces," ASME JOURNAL OF ENGINEERING FOR POWER, Vol. 104, 1982, pp. 698–706.

8 Blair, M. F., "Influence of Free-Stream Turbulence on Boundary Layer Transition in Favorable Pressure Gradients," ASME JOURNAL OF ENGINEERING FOR POWER, Vol. 104, 1982, pp. 743–750.

9 Rued, K., and Wittig, S., "Free-Stream Turbulence and Pressure Gradient Effects on Heat Transfer and Boundary Layer Development on Highly Cooled Surfaces," ASME JOURNAL OF ENGINEERING FOR GAS TURBINES AND POWER, Vol. 107, 1985, pp. 54–59.

10 Gaugler, R. E., "A Review and Analysis of Boundary Layer Transition Data for Turbine Application," ASME Paper No. 85-GT-83, 1985.

11 Eckardt, D., and Weiss, H., "Entwicklung der Niederdruckturbine für das Triebwerk PW 2037," Vortrag No. 84-109b, DGLR-Jahrestagung Hamburg, Oct. 1-3, 1984.

12 Schmidt, E., "Computation of Supercritical Compressor and Turbine Cascades With a Design Method for Transonic Flows," ASME Paper No. 79-GT-30, 1979.

13 Walz, A., *Strömungs- und Temperaturgrenzschichten*, Verlag G. Braun, Karlsruhe, 1966.

14 Granville, P. S., "The Calculation of Viscous Drag of Bodies of Revolution," Nav. Dept., The David Taylor Mod. Basin Report No. 849, 1953.

15 Seyb, N. J., "The Role of Boundary Layers in Axial Flow Turbomachines and the Prediction of Their Effects," AGARDograph No. 164, 1972, pp. 241–25.

16 Dunham, J., "Prediction of Boundary Layer Transition on Turbomachinery Blades," AGARDograph No. 164, 1972, pp. 55–71.

17 Hoheisel, H., and Kiock, R., "Zwanzig Jahre Hochgeschwindigkeits-

Gitterwindkanal des Instituts für Aerodynamik der DFVLR Braunschweig," *Zeitschr. Flugwiss. Weltraumforsch.*, Vol. 1, 1977, pp. 17–29.

18 Kiock, R., Laskowski, G., and Hoheisel, H., "Die Erzeugung höherer Turbulenzgrade in der Meβstrecke des Hochgeschwindigkeits-Gitterwindkanals, Braunschweig, zur Simulation turbomaschinenähnlicher Bedingungen," DFVLR-FB 82-25, 1982; see also ESA-TT-815, 1983.

19 Hoeger, M., and Hoheisel, H., "On the Accuracy of Boundary Layer Measurements in Cascades at High Subsonic Speeds," 7th Symposium on Measuring Techniques for Transonic and Supersonic Flow in Cascades and Turbomachines, Aachen, 1983; Mitt. 7184, Inst. Strahlantriebe RWTH, Aachen, 1984.

20 Hoheisel, H., Hoeger, M., Meyer, P., and Koerber, G., "A Comparison of Laser-Doppler Anemometry and Probe Measurement Within the Boundary Layer of an Airfoil at Subsonic Flow," Second International Symposium on Applications of Laser Anemometry to Fluid Mechanics, Lisbon, Portugal, 1984.

21 Oldfield, M. L. G., Kiock, R., Holmes, A. T., and Graham, C. G., "Boundary Layer Studies on Highly Loaded Cascades Using Heated Thin Films and a Traversing Probe," ASME JOURNAL OF ENGINEERING FOR POWER, Vol. 103, 1981, pp. 237–246.

22 Amecke, J., "Anwendung der trasnssonischen Ähnlichkeitsregel auf die Strömung durch ebene Schaufelgitter.," *VDI – Forschungsheft* 540, 1970, pp. 16–28.

23 Lehthaus, F., "Berechnung der transsonischen Strömung durch ebene Turbinengitter nach dem Zeit-Schritt-Verfahren," *VDI-Forschungsheft* 586, 1978.

24 Hoheisel, H., "Ergebnisse experimenteller Untersuchungen an Turbinengittern mit vorgegebener Druckverteilung," Vortrag DGLR-Symposium "Neue Beschaufelungskonzepte für axiale Turbomaschinen," Köln, May 1984.

25 Hourmouziadis, J., "Das Verhalten der Grenzschicht in Turbinengittern," Vortrag DGLR-Symposium "Neue Beschaufelungskonzepte für axiale Turbomaschinen," Köln, May 1984.

26 Horstmann, K. H., Quast, A., and Boermans, L. M. M., "Pneumatic Turbulators – a Device for Drag Reduction at Reynolds Numbers Below $5 \cdot 10^6$," AGARD-CP-365, 1984, Paper No. 20.

Viscous-Inviscid Computations of Transonic Separated Flows Over Solid and Porous Cascades

C. R. Olling
Postdoctoral Fellow.

G. S. Dulikravich
Assistant Professor.

Department of Aerospace Engineering and Engineering Mechanics,
University of Texas at Austin,
Austin, TX 78712

A complete viscous-inviscid interaction is performed that reliably computes steady two-dimensional, subsonic and transonic attached and separated flows for cascades of airfoils. A full-potential code was coupled with both a laminar/transition/turbulent integral boundary-layer/turbulent wake code and the finite-difference boundary-layer code using the semi-inverse methods of Carter and Wigton. The transpiration coupling concept was applied with an option for a porous airfoil with passive and active physical transpiration. Examples are presented which demonstrate that such flows can be calculated with engineering accuracy by these methods. Carter's update formula gives smoother solutions for a strong shock than Wigton's update formulas, although Wigton's formulas are preferred in the early coupling cycles. The computations show that passive physical transpiration can lead to a lower drag coefficient and higher lift coefficient, a weaker shock, and elimination of shock-induced separation. The extent of the porous region and permeability factor distribution of the porous region must be chosen carefully if these improvements are to be achieved.

Introduction

Any meaningful computation of separated transonic two-dimensional flows for cascades requires the inclusion of viscous boundary layer and wake effects. Reviews of procedures for calculating viscous-inviscid interaction in transonic flow about isolated airfoils have been presented by Olling [1], Lock [2], Lock and Firmin [3], Melnik [4], LeBalleur [5], Jameson [6], and Cebeci et al. [7].

The boundary layer can be calculated in the direct or inverse mode. In the direct mode the velocity or pressure on the matching surface between the viscous and inviscid part of the flow field is specified. In the inverse mode some other quantity (the forcing function) is specified, such as the displacement thickness δ^*, mass flux defect Q, or skin friction coefficient C_f. Present finite-difference and integral methods in general must be operated in the inverse mode to calculate extended separated regions in practical computations, when steady-state first-order boundary layer theory is used (see [8] for an exception for a finite-difference method). An alternative way to simulate massive separation is to compute the detached streamline where the boundary layer separates from the airfoil and then use this streamline as part of the effective airfoil surface [9, 10].

The matching between the inviscid and viscous calculations can occur on any of three different surfaces: the surface of the airfoil and the wake centerline, the displacement surface, or the edge of the boundary layer and wake δ [11]. In the first case an equivalent transpiration boundary condition is used in the inviscid calculation. This case will be called the transpiration coupling concept. It obviates the necessity of regenerating the inviscid grid after each coupling cycle and represents the best existing method [1]. Several types of strong interaction methods have been devised. The simplest approach, called the semi-inverse method, computes part or all of the boundary layer and wake in the inverse mode. An initial guess for the forcing function must be made. The resulting viscous boundary-layer edge velocity or pressure is compared with the inviscid velocity or pressure on the matching surface. If these differ then the forcing function and the coupling boundary conditions are updated. Several methods have been proposed for updating the forcing function during the viscous-inviscid iterations by Carter [12], LeBalleur [13], Wigton [14], and Gordon and Rom [15]. This type of strong interaction has been favored by many investigators because it allows one to make the minimum amount of changes to the inviscid code, which is usually more complex than the viscous code.

It should be noted that first-order boundary-layer theory neglects the normal-pressure gradient effect due to the curvature of streamlines inside the boundary layer and wake. In the near-wake region this effect leads to a jump in the tangential velocity component along the wake centerline in the inviscid code. It will be called the wake curvature effect and two approximate theories have been proposed to correct for it [4, 3].

Porous Airfoils

Shock-free or nearly shock-free transonic airfoils and cascades have favorable properties, such as minimum wave drag and no or reduced shock-induced separation. To design

Contributed by the Gas Turbine Division of THE AMERICAN SOCIETY OF MECHANICAL ENGINEERS and presented at the 31st International Gas Turbine Conference and Exhibit, Düsseldorf, Federal Republic of Germany, June 8-12, 1986. Manuscript received at ASME Headquarters February 19, 1986. Paper No. 86-GT-235.

such airfoils, one approach has been to modify the airfoil shape [16]. Another method of achieving shock self-cancellations is to modify the surface boundary conditions on the airfoil, such as by allowing for physical transpiration by making the airfoil surface porous [1, 17–23]. The latter approach may be applied in an active (or forced) transpiration mode or in a passive transpiration mode. An example of a passive method is allowing the plenum (cavity) pressure (under the porous airfoil surface) to adjust to a value that is in equilibrium with Darcy's law for porous material and the external flow. In this case, the net mass flow through the perforated airfoil surface is zero.

The computer codes developed as a part of this [1] study can simulate the passive transpiration effects of a perforated airfoil surface with a cavity located underneath. Darcy's law is used to determine the physical transpiration velocity [17]

$$v_w = \sigma(p_p - p_w)$$

$$\sigma = \bar{\sigma}/(\rho_\infty q_\infty)$$

where p_w is the airfoil surface pressure, p_p is the plenum pressure (assumed to be constant), σ is the permeability factor, $\bar{\sigma}$ is the nondimensional permeability factor, and ρ_∞ and q_∞ are the upstream density and speed, respectively. A value of $\bar{\sigma} = 0.6$ corresponds to a geometric porosity of about 10 percent [18]. The plenum pressure is computed from

$$p_p = \int_s \rho\bar{\sigma}p_w ds \Big/ \int_s \rho\bar{\sigma} ds$$

where s is the airfoil surface arc length. The physical transpiration velocity normalized by the critical speed of sound is

$$\frac{v_w}{a^*} = \frac{\bar{\sigma}\mathrm{M}_\infty^*}{\gamma \mathrm{M}_\infty^2}\left[\frac{\int_s \bar{\sigma}\dfrac{\rho}{\rho^*}\dfrac{p_w}{p_\infty}\dfrac{ds}{c}}{\int_s \bar{\sigma}\dfrac{\rho}{\rho^*}\dfrac{ds}{c}} - \frac{p_w}{p_\infty}\right]$$

where the asterisk denotes a critical value.

Two distributions of $\bar{\sigma}$ can be specified in the input of the present version of the code [24]. These are a uniform distribution and a peaked distribution having a maximum inside the porous region and smooth tapering to zero at the ends of the region. The chordwise coordinates of the beginning (x_1) and end (x_2) of the porous region and the location of the maximum permeability (x_m) on the upper and lower sides of the airfoil are input.

Integral Boundary-Layer Code

Laminar Boundary Layer. The boundary layer is assumed to be divided into laminar, transitional, and fully turbulent regions in the streamwise direction. Near the leading edge of the airfoil the boundary layer is assumed to be laminar. The attached laminar boundary layer is computed in the direct mode by a modified form of a compressible Thwaites method ([25]; see Appendix A for details). The tangential inviscid velocity on the airfoil surface u_i is specified. If laminar separation is indicated, the boundary layer is in the present code assumed to transition abruptly to fully turbulent flow.

Transition Region. Two options are available for determining transition. One option is to enforce abrupt transition at a specified point (no transition region). The other option is to calculate the transition region from the empirical method of Abu-Ghannam and Shaw [26] modified for compressibility. The start of transition is determined from an empirical correlation for the incompressible momentum thickness Reynolds number as a function of the free-stream turbulence level and an incompressible streamwise velocity gradient parameter. Other correlations are used to determine the extent of the transition region and the momentum thickness at the end of transition. Additional correlations then allow the momentum thickness, shape factor, and skin friction coefficient in the transition region to be computed. Stewartson's [27] transformation is used to relate incompressible and compressible quantities. The method is invalid when the transition region includes separated flow or a shock wave or extends into the wake (see Appendix B for details).

Turbulent Boundary Layer. The turbulent boundary layer and wake is calculated with the lag-entrainment integral method of Green et al. [28] modified by East et al. [29] in either the direct mode with u_i specified or in the inverse mode with the mass flux defect Q specified. Here $Q = \rho_i u_i \delta^*$ where ρ_i is the inviscid density on the airfoil or wake centerline. Both attached and thin separated turbulent flow can be calculated. This method is based on the solution of three ordinary differential equations: the momentum integral equation, entrainment equation, and a lag equation derived from the differential turbulent kinetic energy equation. The original integral boundary layer equations of Green et al. [28] were extended to include physical surface transpiration. The extended momentum integral equation is

$$\frac{d\theta}{ds} = \frac{C_f}{2} - (H + 2 - \mathrm{M}^2)\frac{\theta}{u_e}\frac{du_e}{ds} + m_w$$

where $m_w = (\rho_w v_w)/(\rho_e u_e)$ is the nondimensional transpiration mass flux. Here the subscripts e and w denote the edge of the boundary layer and airfoil surface, respectively, s is the arclength in the streamwise direction along the airfoil or wake centerline, θ is the momentum thickness, u is the speed, C_f is the skin friction coefficient, H is the shape factor, M is the local Mach number, and ρ is the density. The equation for the entrainment coefficient C_E given by Green et al. [28] is extended [1] to

$$C_E = \frac{1}{\rho_e u_e}\frac{d}{ds}\int_0^\delta \rho u dn - m_w$$

where $C_E = V_E/u_e$, V_E is the entrainment velocity (positive for entrainment), and n is the coordinate normal to the airfoil surface. Using the definition

$$H_1 = \frac{1}{\theta}\int_0^\delta \frac{\rho u}{\rho_e u_e} dn$$

results in the modified entrainment equation [1]

$$\frac{d\tilde{H}}{ds} = \frac{d\tilde{H}}{dH_1}\left\{C_E + m_w - H_1\left[\frac{C_f}{2} + m_w - (H+1)\frac{\theta}{u_e}\frac{du_e}{ds}\right]\right\}/\theta$$

where $\tilde{H}$ is Head's shape factor

$$\tilde{H} = \frac{1}{\theta}\int_0^\delta \frac{\rho}{\rho_e}\left(1 - \frac{u}{u_e}\right) dn$$

In the method of Green et al. [28] the skin friction coefficient C_f is computed from a correlation depending on the value of the flat-plate (zero pressure gradient) skin friction coefficient C_{f0} coresponding to the moment thickness Reynolds number Re_θ of the flow. The value of this flat-plate skin friction coefficient is modified to account for the effects of transpiration by using the relation given by Kays and Crawford [30]

$$C_{f0} = C_{f0s}\left[\frac{l_n(1+B_f)}{B_f}\right]^{1.25}(1+B_f)^{0.25}$$

where C_{f0s} is the flat-plate (zero pressure gradient) skin friction coefficient for a nonporous surface and $B_f = m_w/(C_{f0}/2)$. The value of C_{f0} is determined by Newton iteration. It is assumed that the other empirical correlations used in the method of Green et al. [28] and modified by East et al. [29]

are approximately the same for the case of a transpired boundary layer.

In the inverse mode the dependent variables are u_e, $\bar{H}$, and C_E. The form of the equations is

$$\frac{du_e}{ds} = -\frac{A}{B} + \frac{1}{B}\frac{dQ}{ds}$$

$$\frac{d\bar{H}}{ds} = C + D\frac{du_e}{ds}$$

$$\frac{dC_E}{ds} = E + F\frac{du_e}{ds}$$

The expressions for the coefficients are given in Appendix C. The boundary layer and wake on the upper and lower sides of the airfoil and wake centerline are computed separately. The wake centerline is taken to be a cubic polynomial with the four coefficients determined from the locations and slopes of the trailing edge and the assumed location of the end of the wake centerline. The skin friction coefficient is set equal to zero in the wake. The starting value for u_e is u_i. When transition is enforced the starting value for Q is determined in either of two ways. One way is to assume continuity of Q. The other way is to compute Q by assuming that it has the value that a flat-plate boundary layer would have at the same distance from the leading edge. The starting values for $\bar{H}$ and C_E are found following the method given by Olling [1]. The correction for longitudinal surface curvature suggested by Green et al. [29] was incorporated by Olling [1]. The system of equations is integrated with a fourth-order Runge–Kutta method [31]. The streamwise step size is clustered toward the leading and trailing edges and is smaller than that of the inviscid code. The first derivative of the forcing function is calculated in the supersonic region by first-order accurate upstream differencing and in the subsonic region by the second-order accurate differencing for a nonuniform step size presented as equation (3.14.3) of Ferziger [31].

Finite-Difference Boundary-Layer Code

The finite-difference compressible boundary layer code presented by Drela [32] was adapted to the present coupling approach. This code can compute compressible laminar, transitional, and turbulent flow that is attached or separated. Modifications were made by Olling [1] to the calculation of the inner eddy viscosity for turbulent separated flow. Surface transpiration effects were incorporated. The intermittency factor of Abu-Ghannam and Shaw [26] was used in the transition region. This code is based on a variation of Keller's box scheme [33, 34].

The governing equations are the continuity equation, the linear momentum equation in the streamwise direction, and the total enthalpy equation. The Cebeci–Smith [34] two-layer algebraic eddy viscosity formulas are used. These equations are nondimensionalized, and then transformed variables are introduced which permit the calculation of flow near the stagnation point. The coupled system of equations is discretized on the shifted box grid [32] and Newton iteration is applied to determine the iterates of the unknown variables. This procedure leads to a block tridiagonal system of equations in which the blocks are 3×3 matrices. The eddy viscosity is also linearized during the Newton iteration procedure and this leads to quadratic convergence of the solution for both laminar and turbulent flow.

Four different forcing functions can be used. In the direct mode u_i is specified. In the inverse mode δ^*, Q, or C_f can be specified. It was found by numerical experiments that the solution would not converge when Q was specified at the stagnation point.

A modified Reyhner–Flugge–Lotz approximation is applied in the separated flow. This consisted of eliminating the contribution of the convective momentum term to the variable iterates (the terms inside the 3×3 blocks) but retaining its contribution to the residues.

The finite-difference code was chosen over a laminar integral boundary-layer code capable of computing laminar separated flow for two reasons. A laminar integral boundary-layer code based on a modified Klineberg–Lees [35] method was developed by Olling [1], but it was found that the code could not be used very near the stagnation point because the integral boundary layer equations possess a singularity there. This would render the method inappropriate if a leading edge separation bubble occurred. Also a laminar integral boundary-layer code cannot compute the transitional region (unless the approximate procedure of LeBalleur [13] is applied) and the empirical method of Abu-Ghannam and Shaw [26] is inapplicable when the transition region contains separation or a shock wave. Thus, for these special cases, the finite-difference method is most appropriate.

Coupling Boundary Conditions—Total Transpiration Velocity

The coupling boundary conditions in the inviscid code on the airfoil and wake centerline are a total transpiration velocity v_n normal to the airfoil and jump conditions on the velocity components normal and tangent to the assumed wake centerline. The total transpiration velocity v_n consists of two parts: an equivalent transpiration velocity v_b due to the boundary-layer displacement effect and a physical mass-weighted transpiration velocity v_c due to suction or blowing through the porous airfoil surface, such that

$$v_n = v_b + v_c$$

where

$$v_b = \frac{1}{\rho_i}\frac{dQ}{ds} \quad \text{and} \quad v_c = \frac{\rho_w}{\rho_i} v_w$$

Here ρ_w and v_w are the density and velocity of the physically transpired fluid, respectively. The sign of v_n is positive for blowing (i.e., a source). It is assumed that ρ_w is equal to the adiabatic wall density

$$\rho_w = \rho_i \Big/ \left(1 + r\frac{(\gamma-1)}{2}\mathrm{M}^2\right)$$

where r is the recovery factor, γ is the specific heat ratio, and M is the local Mach number. For laminar flow, $r = (\mathrm{Pr})^{1/2}$ and for fully turbulent flow $r = (\mathrm{Pr})^{1/3}$, where Pr is the Prandtl number. For transitional flow, it is assumed that $r = (\mathrm{Pr})^{(1/2-\gamma_{tr}/6)}$ where γ_{tr} is the intermittency factor, $0 \le \gamma_{tr} \le 1$, $\gamma_{tr} = 0$ for laminar flow, and $\gamma_{tr} = 1$ for fully turbulent flow. The displacement thickness in the definition of Q is

$$\delta^* = \frac{1}{\rho_{iw}u_{iw}}\int_0^\delta (\rho_i u_i - \rho u)\,dn$$

The velocity jumps on the wake centerline are [3]

$$\Delta v_n = \frac{1}{\rho_{iu}}\left(\frac{dQ}{ds}\right)_u + \frac{1}{\rho_{il}}\left(\frac{dQ}{ds}\right)_l$$

$$\Delta u_t = -\left[K_u^*\frac{Q_u}{\rho_{iu}}(1 + 1/H_u) + K_l^*\frac{Q_l}{\rho_{il}}(1 + 1/H_l)\right]$$

where Δ indicates a jump, the subscripts u, l denote the upper and lower sides of the wake centerline, $H = \delta^*/\theta$ is the shape factor, and K^* is the curvature of the displacement thickness surface

$$K^* = \frac{d\beta}{ds}$$

where β is the streamline slope [19] on the displacement

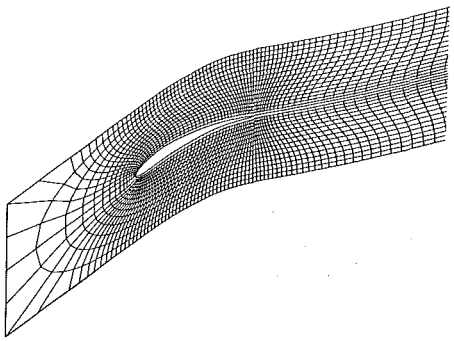

Fig. 1 Computational grid, Sobieczky cascade

thickness surface. A procedure similar to that of Collyer is used to introduce the jumps in the normal and tangential velocity components into the reduced potential at the points on the upper and lower sides of the wake centerline and at the fictitious points on either side of the wake centerline. The detailed procedure is shown by Olling [1].

The semi-inverse coupling method can be summarized as follows:

1 The potential solution is advanced for a certain number of iterations on up to four increasingly refined grids with $v_n = 0$ on the airfoil surface.

2 The boundary layer code was run in the direct mode with u specified from step 1 until separation or a specified point was reached. At that point the boundary layer code was switched to the inverse mode with an initial guess for Q.

3 Wigton's or Carter's formulas for updating the Q values are applied (see Appendix D). The transpiration velocity and jumps in the velocity components along the wake centerline are computed.

4 The potential solution is advanced for one to five iterations on the finest grid being used, with the boundary conditions held constant. During the first nine coupling cycles the relaxation factor was equal to unity. After that the relaxation parameter was equal to 1.7–1.8.

5 The boundary layer code was run in the direct mode on the forward part of the airfoil and in the inverse mode on the rest of the airfoil and wake centerline with the Q values determined from step 3.

6 Steps 3–5 are repeated until the error measure ($u_e/u_i - 1$) is less than a specified value or until a maximum number of interaction cycles has been reached.

Results

Based on the detailed analytic and numerical analysis of Olling [1], a package of computer programs, GSD28, was developed [24]. This software performs automatic computational grid generation, full potential finite area inviscid flow solution [16], integral and finite difference method solution of the complete boundary layer with wake, and automatically iteratively couples the inviscid and the viscous part of the flow field.

The first example is for a cascade of solid Sobieczky [16] airfoils, which are not shock-free. The upstream Mach number is 0.80, the Reynolds number based on the chord is 9.1×10^5, $T_\infty = 288$ K, $c = 0.076$ m, and the freestream turbulence level is 1 percent. The upstream angle of attack with respect to the horizontal is 40 deg and the stagger angle with the horizontal is 27.3 deg. The gap-to-chord ratio is 1.0. The computational wake extends two chord lengths downstream. Three sets of increasingly refined grids were used. The finest grid had 48 cells on both the upper and lower sides of the airfoil, 32 cells along each side of the wake and 16 C-layers of grid cells in the outward direction (Fig. 1). The inviscid code

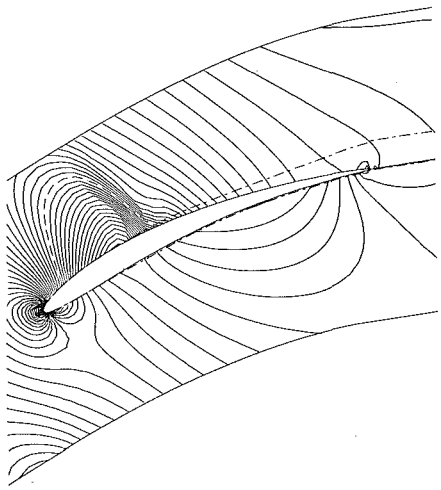

Fig. 2 Mach number field, solid Sobieczky cascade

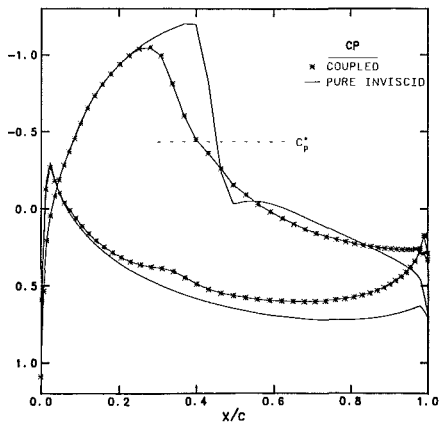

Fig. 3 Pressure coefficient distribution, C_p, solid Sobieczky cascade

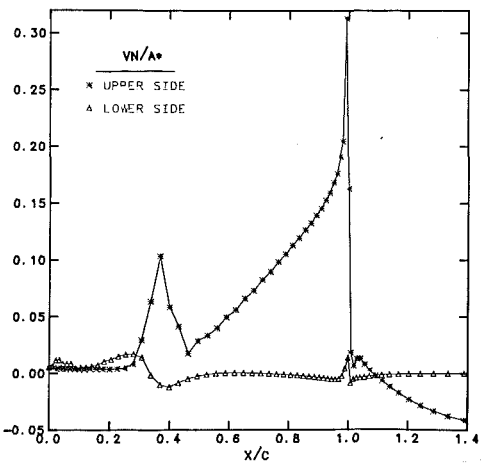

Fig. 4 Total transpiration velocity, v_n/a^*, solid Sobieczky cascade

was run for 10 iterations on the first grid, 10 iterations on the second grid, and 5 iterations on the third grid. Viscous–inviscid coupling was then initiated. During the coupling, one viscous sweep was performed for each inviscid sweep. The overrelaxation factor for the inviscid code during the coupling was 1.697.

Transition was enforced on the upper side of the airfoil at 3 percent of the chord and the boundary layer and wake were computed by the integral method. Natural transition was allowed on the lower side of the airfoil, and the boundary

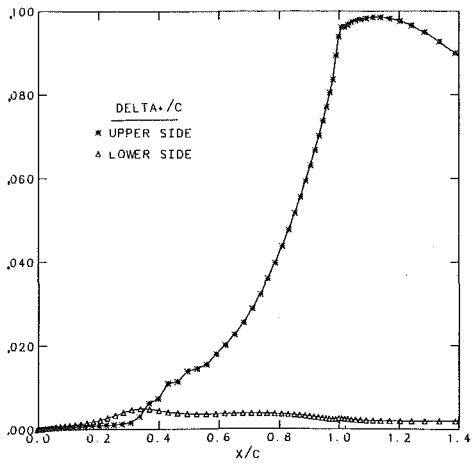

Fig. 5 Displacement thickness, δ^*/c, solid Sobieczky cascade

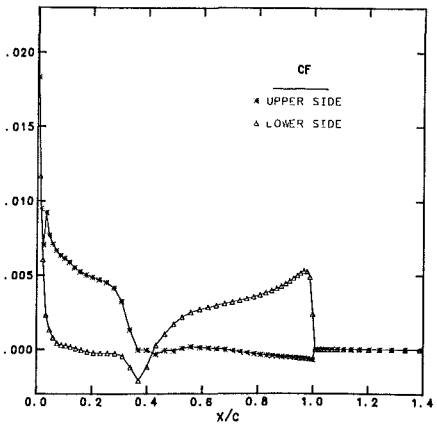

Fig. 6 Skin friction coefficient, C_f, solid Sobieczky cascade

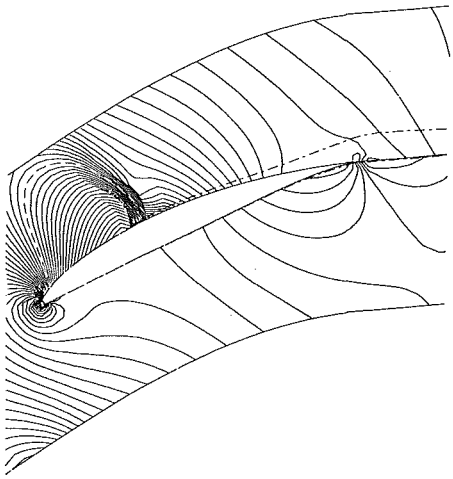

Fig. 7 Mach number field, solid NACA 65-(12)10 cascade

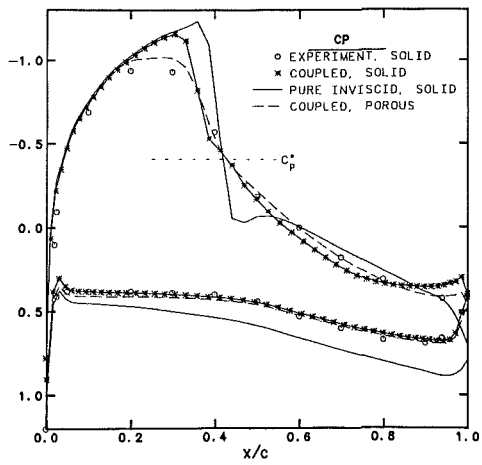

Fig. 8 Pressure coefficient distribution, C_p, solid and porous NACA 65-(12)10 cascades

layer was computed by the finite-difference method with the wake computed by the integral method. Transition started at $x/c = 0.2357$ and ended at $x/c = 0.5554$.

Wigton's update method was used for the first 400 coupling cycles in the regions computed by the integral method. Wigton's method was used because during the initial coupling cycles with Carter's update method with a relaxation factor of 0.1, the boundary layer developed oscillations. Carter's update method, with a relaxation factor of 0.1, was therefore used for the last 240 coupling cycles. At the same time, Carter's update method, with a relaxation factor of 0.1, was successfully used for the regions computed by the finite-difference boundary-layer code. The trailing edge treatment explained by Olling [1] was applied. Mach number field is presented in Fig. 2. The airfoil surface pressure coefficient distribution is shown in Fig. 3. The coupled and pure inviscid solutions exhibit large differences indicating strong viscous-inviscid interaction. The predicted drag coefficient is $C_D = 0.02458$ and the lift coefficient is $C_L = 0.64293$. The predicted turning angle is 16.92 deg. The total transpiration velocity is presented in Fig. 4. A large value is noted at the trailing edge on the upper side of the airfoil. The displacement thickness is shown in Fig. 5. The skin friction coefficient is shown in Fig. 6. On the upper side of the airfoil, the flow has shock-induced separation between $x/c = 0.369$ and $x/c = 0.496$ and separates again downstream of $x/c = 0.683$. On the lower side of the airfoil, laminar separation starts at $x/c = 0.163$ and reattachment occurs at $x/c = 0.427$ as a transitional flow with the itermittency factor $\gamma_{tr} = 0.66$. When this example was computed with a freestream turbulence level of 5 percent, natural transition occurred sooner on the lower side of the airfoil and no separation occurred there.

The second cascade flow example is for both a solid and porous NACA 65-(12)10 cascade. The pressure coefficient was experimentally determined for the solid cascade by Briggs [38]. The upstream Mach number is 0.81, the Reynolds number based on the chord is 9.1×10^5, $T_\infty = 288$ K, $c = 0.076$ m, and the freestream turbulence level is assumed to be 5 percent. The upstream angle of attack with respect to the horizontal is 45 deg, and the stagger angle relative to the horizontal is 28.5 deg. The gap-to-chord ratio is 1.0. The wake extends two chord lengths downstream.

In the porous cascade case, a peaked permeability factor distribution on the upper side of the airfoil was used with $\bar{\sigma}_{\max} = 0.10$, $x_1 = 0.20$, $x_2 = 1.0$, and $x_m = 0.3586$.

Transition was enforced at 3 percent of the chord on the upper side of the airfoil and natural transition was allowed on the lower side. The boundary layer and wake on both sides were computed with the integral method. For the lower side of the solid airfoil, computed transition started at $x/c = 0.085$ and ended at $x/c = 0.244$. For the lower side of the porous airfoil, transition started at $x/c = 0.0925$ and ended at $x/c = 0.262$.

The converged solution Mach number field with a contour interval of 0.02 is presented in Fig. 7 for the solid cascade case. The pressure coefficient is shown in Fig. 8. For the solid cascade, the computations agree fairly well with the experiment except at the beginning of the shock. For the porous cascade, the shock strength is weaker. The C_p curve on the upper side begins to differ from that of the solid case at the start

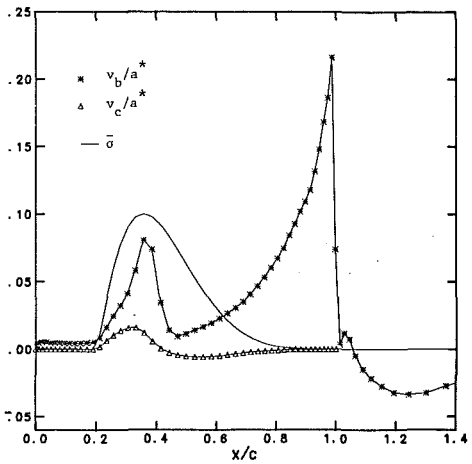

Fig. 9 Equivalent and physical mass-weighted transpiration velocities, v_b/a^* and v_c/a^*, and the permeability factor $\bar{\sigma}$, upper side of porous NACA 65-(12)10 cascade

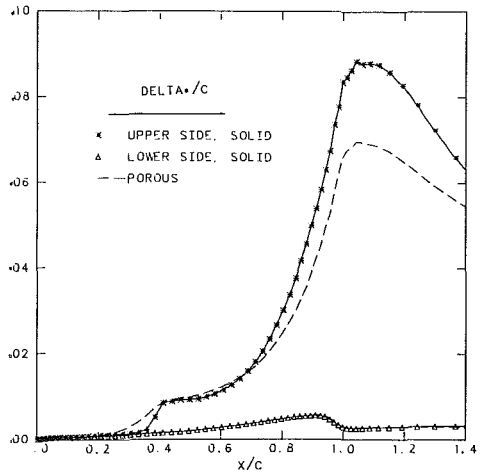

Fig. 10 Displacement thickness, δ^*/c, solid and porous NACA 65-(12)10 cascades

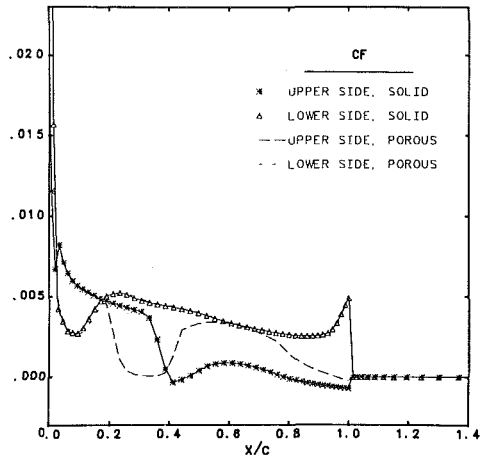

Fig. 11 Skin friction coefficient, C_f, solid and porous NACA 65-(12)10 cascades

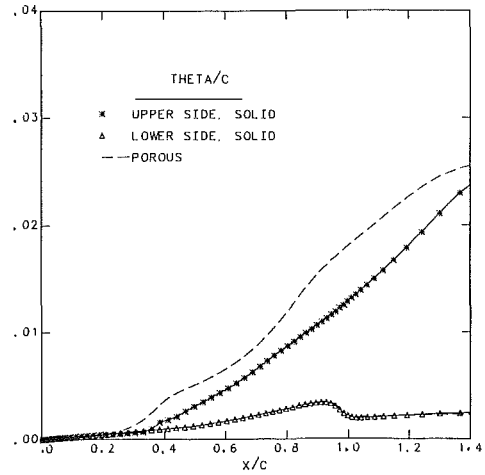

Fig. 12 Momentum thickness, θ/c, solid and porous NACA 65-(12)10 cascades

of the porous region. The computed drag coefficient for the solid cascade is $C_D = 0.03086$ and for the porous cascade is $C_D = 0.02755$, a reduction of 10.7 percent. The computed lift coefficient for the solid cascade is $C_L = 0.74235$ and for the porous cascade is $C_L = 0.76023$, an increase of 2.41 percent. The computed static-pressure rise p_2/p_1 for the solid cascade is 1.2546 while the experimental value was 1.244. The value for the porous case is 1.2622. The computed turning angle for the solid cascade is 19.0 deg while the experimental value was 20.6 deg. The value for the porous case is 19.97 deg. The plenum C_p for the porous airfoil is -0.453 while $C_p^* = -0.406$.

Figure 9 illustrates the equivalent and physical mass-weighted transpiration velocities, v_b/a^* and v_c/a^*, and the permeability factor $\bar{\sigma}$ for the porous cascade. Because the plenum C_p is close to C_p^*, physical blowing occurs in the supersonic region ahead of the shock and physical suction takes place behind the shock. The displacement thickness is shown in Fig. 10. The skin friction coefficient is presented in Fig. 11. For the solid cascade, shock-induced separation occurs between $x/c = 0.41$ and $x/c = 0.45$, and the flow again separates at $x/c = 0.80$. A smooth transition region on the lower side of the airfoil is computed. For the porous cascade, physical blowing ahead of the shock leads to decrease of C_f to near separation, but the flow remains attached. Physical suction behind the shock causes the C_f to increase. Only a small region of trailing edge separation occurs. The momentum thickness, shape factor and mass flux defect are presented in Figs. 12, 13, and 14, respectively.

It should be pointed out that all computations were performed on a medium-size computer, HARRIS 800 II. One sweep of the inviscid code on a typical grid used during the coupling required between 5.35 and 5.87 s of CPU time. The integral boundary-layer code computed the entire boundary layer and wake and coupling boundary condition in about 5.4 s of CPU time. The finite-difference boundary-layer code required an order of magnitude more time, 62.4 s of CPU time, to compute the boundary layer on one side of the airfoil only.

Conclusions and Recommendations

On the basis of the results presented, it can be concluded that coupled viscous–inviscid calculations of transonic separated cascade flows, with or without physical transpiration, are feasible with the present method [1, 24]. However, the semi-inverse coupling method can require a large number of coupling cycles in difficult cases. Part of the reason for this is the slow convergence rate of the SLOR scheme [36] of the inviscid code on the finest grid being used. More efficient inviscid algorithms (e.g., alternating-direction implicit or approximate factorization schemes) are available that could remedy that aspect of the problem. But even without modify-

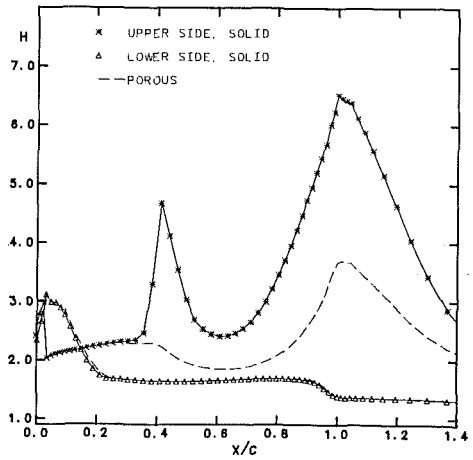

Fig. 13 Shape factor, *H*, solid and porous NACA 65-(12)10 cascades

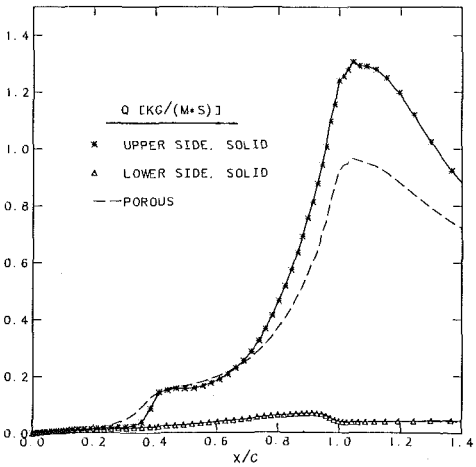

Fig. 14 Mass flux defect, Q, solid and porous NACA 65-(12)10 cascades

ing the inviscid algorithm, some improvement of the global convergence could be achieved by simultaneous calculation of the inviscid and viscous equations in the manner of, for example, Wai and Yoshihara [37] but without their viscous ramp model of shock/boundary-layer interaction. Another advantage of that approach would be the elimination of the necessity of specifying an initial guess for the mass flux defect when separation is encountered. Such calculations were made with a modified version of the GSD28 code [1, 24]. The nonlifting NACA 0012 airfoil was tested using this approach, and the results were encouraging.

For separating cascade flow, Wigton's update formulas are best for the initial coupling cycles, after which Carter's update formula can be used to achieve smoother solutions in the shock region.

The pressure correction theory of Lock and Firmin [3] is inappropriate in the region of strong shock waves. A more sophisticated approach is needed. Boundary-layer displacement effects can be much larger in cascades than for isolated airfoils. The shock wave in cascades will often be in a region of transitional flow unless the freestream turbulence level is high. The present integral boundary-layer code cannot handle this situation and transition must be enforced ahead of or at the shock.

The computations show that passive physical transpiration can lead to a reduced drag coefficient and increased lift coefficient for the permeability factor distributions used in the present work. The shock strength can be diminished and shock-induced separation can be eliminated. If the porosity is too large or the porous region extends too far ahead of the shock, it was observed that the induced blowing ahead of the shock may cause separation there. Actually, the aerodynamic performance of airfoils also can be decreased if the porosity is applied in an ad-hoc manner, just as the incorrectly applied "shaving-off" procedure [16] can make shocked airfoils have even stronger shocks.

Consequently, it would be highly desirable to approach the entire concept of porous airfoil design as an inverse problem. Thus, the optimal porosity distribution and its extent should be found so that it corresponds to a minimal possible total aerodynamic drag for the particular airfoil and given global aerodynamic parameters.

References

1 Olling, C. R., "Viscous-Inviscid Interaction in Transonic Separated Flow Over Solid and Porous Airfoils and Cascades," Ph.D. Dissertation, Department of Aerospace Eng. and Eng. Mechanics, The Univ. of Texas at Austin, Dec. 1985.

2 Lock, R. C., "A Review of Methods for Predicting Viscous Effects on Airfoils and Wings at Transonic Speeds," *Proceedings AGARD Conf. on Comput. of Viscous-Inviscid Interactions*, 1980, AGARD CP 291, 1981, Paper No. 2.

3 Lock, R. C., and Firmin, M. C. P., "Survey of Techniques for Estimating Viscous Effects in External Aerodynamics," in: *Proceedings of the IMA Conference on Numerical Methods in Aero. Fluid Dynamics, Reading, 1980*, P. L. Roe, ed., Academic Press, New York, 1982, pp. 337–430.

4 Melnik, R. E., "Turbulent Interaction on Airfoils at Transonic Speeds—Recent Developments," *Proc. AGARD Conf. on Comput. of Viscous-Inviscid Interactions*, 1980, AGARD CP 291, Paper No. 10.

5 LeBalleur, J. C., "Calcul d'Ecoulements à Forte Interaction Visquese au Moyen de Méthodes de Couplage," *Proc. AGARD Conf. on Comput. of Viscous-Inviscid Interactions*, 1980, AGARD CP 291, Paper No. 1.

6 Jameson, A., "The Evolution of Computational Methods in Aerodynamics," *J. Appl. Mech.*, Vol. 50, 1983, pp. 1052–1070.

7 Cebeci, T., Stewartson, K., and Whitelaw, J. H., "Calculation of Two-Dimensional Flow Past Airfoils," in: *Numerical and Physical Aspects of Aerodynamic Flows, II*, Springer-Verlag, New York, 1984, pp. 1-40.

8 Drela, M., and Thompkins, W. T., Jr., "A Study of Non-Unique Solutions of the Two-Dimensional Boundary Layer Equations at Laminar Separation and Reattachment Points," in: *Second Symposium on Numerical and Physical Aspects of Aerodynamic Flows*, California State Univ., Long Beach, Jan. 17–20, 1983.

9 Hirsch, C., and Janssens, P., "Viscous-Inviscid Interactions in Cascades," *Israel J. Technol.*, Vol. 20, 1982, pp. 109–126.

10 Dvorak, F. A., and Choi, D. H., "Separation Model for Two-Dimensional Airfoils in Transonic Flow," *AIAA J.*, Vol. 22, 1984, pp. 1064–1070.

11 Murman, E. M., and Bussing, T. R. A., "On the Coupling of Boundary-Layer and Euler Equation Solutions," in: *Numerical and Physical Aspects of Aerodynamic Flows II*, Springer-Verlag, New York, 1984, pp. 313–326.

12 Carter, J. E., "A New Boundary Layer Inviscid Interaction Technique for Separated Flow," *Proc. AIAA 4th Comp. Fluid Dyn. Conf.*, 1979, pp. 45–55.

13 LeBalleur, J. C., "Strong Matching Method for Computing Transonic Viscous Flows Including Wakes and Separations – Lifting Airfoils," *La Recherche Aerospatiale* (English edition), No. 1981-3, 1981, pp. 21–45.

14 Wigton, L. B., "Viscous-Inviscid Interaction in Transonic Flow," Ph.D. Thesis, Univ. of California, Berkeley, 1981.

15 Gordon, R., and Rom, J., "Transonic Viscous/Inviscid Interaction Over Airfoils for Separated Laminar or Turbulent Flows," *AIAA J.*, Vol. 19, 1981, pp. 545–552.

16 Dulikravich, G. S., and Sobieczky, H., "Shockless Design and Analysis of Transonic Cascade Shapes," *AIAA J.*, Vol. 20, 1982, pp. 1572–1578.

17 Savu, G., and Trifu, O., "Porous Airfoils in Transonic Flow," *AIAA J.*, Vol. 22, 1984, pp. 989–991.

18 Savu, G., Trifu, O., and Dumitrescu, L. Z., "Suppression of Shocks on Transonic Airfoils," 14th Int'l. Symp. on Shock Tubes and Waves, Sydney, 1983.

19 Thiede, P., Krogmann, P., and Stanewsky, E., "Active and Passive Shock/Boundary-Layer Interaction Control on Supercritical Airfoils," in: *Improvement of Aerodynamic Performance Through Boundary Layer Control and High Lift Systems*, AGARD CP-365, 1984, Paper No. 24.

20 Krogmann, P., Stanewsky, E., and Thiede, P., "Effects of Suction on Shock/Boundary-Layer Interaction and Shock-Induced Separation," *J. Aircraft*, Vol. 22, 1985, pp. 37–42.

21 Nagamatsu, H. T., Ficarra, R. V., and Dyer, R., "Supercritical Airfoil Drag Reduction by Passive Shock Wave/Boundary Layer Control in the Mach Number Range .75 to .90," *AIAA 23rd Aerospace Sciences Meeting*, Reno, NV, Jan. 14–17, 1985, AIAA Paper No. 85-0207.

22 Ram, R. B., Vemuru, C. S., and Harvey, W. D., "Hybrid Approach to Steady Transonic Normal Shock-Compressible Laminar Boundary Layer In-

teractions Over Airfoils With Suction," AIAA Shear Flow Control Conference, Boulder, CO, Mar. 12-14, 1985, AIAA Paper No. 85-0522.

23 Chen, C.-L., Chow, C.-Y., Holst, T. L., and Van Dalsem, W. R., "Numerical Study of Porous Airfoils in Transonic Flow," NASA TM 86713, May 1985.

24 Dulikravich, G. S., and Olling, C. R., "GSD28-Fortran Program for Analysis and Design of Shock-Free Transonic Airfoils and Turbomachinery Cascades Including Viscous/Inviscid Interaction," Computational Fluid Dynamics Group Research Report 100-85, Dept. of Aero. Eng. and Eng. Mech., The Univ. of Texas at Austin, Sept. 1985.

25 Rott, N., and Crabtree, L. F., "Simplified Laminar Boundary-Layer Calculations for Bodies of Revolution and for Yawed Wings," *J. Aero. Sci.*, Vol. 19, 1952, pp. 553-565.

26 Abu-Ghannam, B. J., and Shaw, R., "Natural Transition of Boundary Layers—The Effects of Turbulence, Pressure Gradient, and Flow History," *J. Mech. Eng. Sci.*, Vol. 22, 1980, pp. 213-228.

27 Stewartson, K., "Correlated Incompressible and Compressible Boundary Layers," *Proc. Roy. Soc. London*, Ser. A, Vol. 200, 1949, pp. 84-100.

28 Green, J. E., Weeks, D. J., and Brooman, J. W. F., "Prediction of Turbulent Boundary Layers and Wakes in Compressible Flow by a Lag-Entrainment Method," Aero. Res. Coun., Reports and Memoranda 3791, 1973.

29 East, L. F., Smith, P. D., and Merryman, P. J., "Prediction of the Development of Separated Turbulent Boundary Layers by the Lag-Entrainment Method," R.A.E. TR-77046, 1977.

30 Kays, W. M., and Crawford, M. E., *Convective Heat and Mass Transfer*, 2nd ed., McGraw-HIll, New York, 1980.

31 Ferziger, J. H., *Numerical Methods for Engineering Application*, Wiley, New York, 1981.

32 Drela, M., "A New Transformation and Integration Scheme for the Compressible Boundary Layer Equations, and Solution Behavior at Separation," M.I.T. Gas Turbine and Plasma Dynamics Laboratory, GTL Report 172, 1983.

33 Cebeci, T., and Bradshaw, P., *Momentum Transfer in Boundary Layers*. Hemisphere, Washington, D.C., 1977.

34 Bradshaw, P., Cebeci, T., and Whitelaw, J. H., *Engineering Calculation Methods for Turbulent Flow*, Academic Press, New York, 1981.

35 Klineberg, J. M., and Lees, L., "Theory of Laminar Viscous-Inviscid Interactions in Supersonic Flow," *AIAA J.*, Vol. 7, 1969, pp. 2211-2221.

36 Olling, C. R., and Dulikravich, G. S., "Transonic Cascade Flow Analysis Using Viscous/Inviscid Coupling Concepts," *AIAA 2nd Applied Aerodynamics Conf.*, Seattle, WA, Aug. 21-23, 1984, AIAA Paper No. 84-2159.

37 Wai, J. C., and Yoshihara, H., "Viscous Transonic Flow Over Airfoils," in: *Seventh Int'l. Conf. on Numer. Meth. in Fluid Dynamics*, Springer-Verlag, New York, 1981, pp. 417-421.

38 Briggs, W. B., "Effect of Mach Number on the Flow and Application of Compressibility Corrections in a Two-Dimensional Subsonic-Transonic Compressor Cascade Having Varied Porous-Wall Suction at the Blade Tips," NACA TN 2649, 1952.

APPENDIX A

Laminar Boundary Layer

Rott and Crabtree's [25] compressible Thwaites method for laminar boundary layers is modified as shown below.

From Stewartson's [27] transformation, we have the following relationships between incompressible (subscript I) and compressible quantities

$$ds_I = C\frac{a_e}{a_\infty}\frac{p_e}{p_\infty}ds \tag{A1}$$

$$dn_I = \frac{a_e}{a_\infty}\frac{\rho}{\rho_\infty}dn \tag{A2}$$

$$u_I = \frac{a_\infty}{a_e}u \tag{A3}$$

$$\frac{du_I}{ds_I} = C^{-1}\frac{a_\infty^2}{a_e^2}\frac{p_\infty}{p_e}\frac{T_0}{T_e}\frac{du}{ds} \tag{A4}$$

$$\theta_I = \frac{p_e}{p_\infty}\frac{a_\infty}{a_e}\theta \tag{A5}$$

$$C = \frac{\mu}{\mu_\infty}\frac{T_\infty}{T} \tag{A6}$$

Here, n is the coordinate normal to the airfoil, and the subscripts ∞ and 0 denote upstream infinity and stagnation conditions, respectively. The value of θ is computed from

$$\theta = \left|0.45\,\nu_0\left(\frac{p_\infty}{p_e}\right)^2\left(\frac{a_e}{a_\infty}\right)^8 u^{-6}\int_0^s u^5 C\left(\frac{a_\infty}{a_e}\right)^4 \cdot\frac{p_e}{p_\infty}\,ds\right|^{1/2} \tag{A7}$$

where ν_0 is the stagnation kinematic viscosity coefficient. The incompressible pressure gradient parameter l_I is

$$l_I = \frac{du_I}{ds_I}\frac{\theta_I^2}{\nu_0} = \frac{1}{C}\left(\frac{a_\infty}{a_e}\right)^4\frac{p_e}{p_\infty}\frac{T_0}{T_e}\frac{\theta^2}{\nu_0}\frac{du}{ds} \tag{A8}$$

The incompressible shape parameter H_I is computed from l_I using the curve fits to Thwaites' tabulated values presented by Cebeci and Bradshaw [33]

$$\text{for } l_I \geq 0 \qquad H_I = 2.61 + l_I(-3.75 + 5.34\,l_I)$$

$$\text{for } l_I < 0 \qquad H_I = 0.0731/(0.14 + l_I) + 2.088 \tag{A9}$$

The skin friction coefficient is computed from

$$C_f = 2CP\left(\frac{a_e}{a_\infty}\right)^2 \mathrm{M}_\infty/(\mathrm{MRe}_{\delta_I^*}) \tag{A10}$$

$$\mathrm{Re}_{\delta_I^*} = \frac{u_{I\infty}\delta_I^*}{\nu_{I\infty}} \tag{A11}$$

$$\delta_I^* = \theta_I H_I \tag{A12}$$

$$P = \frac{\delta_I^*}{u_I}\left(\frac{\partial u_I}{\partial n_I}\right)_{n_I=0} \tag{A13}$$

Klineberg and Lees [35] present P and H_I as functions of a parameter "a" for Falkner-Skan velocity profiles. Using a polynomial least-squares fit, the following relation was determined for attached flows

$$a = 8.036555z + 41.54676z^2 - 167.6696z^3 + 300.770z^4 + 1546.605z^5 \tag{A14}$$

where $z = H_I - 0.24711$. Then P was determined from the relation given by Klineberg and Lees [35]. The shape factor is computed from

$$H = H_I\frac{T_0}{T_e} + \mathrm{Pr}^{1/2}\left(\frac{T_0}{T_e} - 1\right) \tag{A15}$$

The displacement thickness is $\delta^* = H\theta$ and the mass flux defect is $Q = \rho_e u_e \delta^*$.

APPENDIX B

Transition Region

The empirical method of Abu-Ghannam and Shaw [26] for calculating transitional boundary layers is modified for compressibility as shown below. By using Stewartson's [27] transformation, the following relations between incompressible (subscript I) and compressible quantities are found (in addition to equations (A1), (A3-A6))

$$R_{\theta_I} = \frac{\theta_I u_I}{\nu_I} = \frac{P_e}{P_\infty}\left(\frac{a_\infty}{a_e}\right)^2\frac{\theta u}{\nu_I} \tag{B1}$$

$$\lambda_I = \frac{\theta_I^2}{\nu_I}\frac{du_I}{ds_I} = \frac{1}{C}\left(\frac{a_\infty}{a_e}\right)^4\frac{P_e}{P_\infty}\frac{T_0}{T_e}\frac{\theta^2}{\nu_I}\frac{du}{ds} \tag{B2}$$

where the subscript ∞ denotes upstream infinity. The value of ν_I is calculated by finding u_I and from this determining the isentropic temperature and density

$$T_I = T_0\left(1 - \frac{\gamma - 1}{2}\left(\frac{u_I}{a_0}\right)^2\right) \tag{B3}$$

$$\rho_1 = p_0\left(1-\frac{\gamma-1}{2}\left(\frac{u_1}{a_0^2}\right)^2\right)^{\frac{\gamma}{\gamma-1}}/(RT_1) \tag{B4}$$

and then using Sutherland's equation

$$\nu_1 = \mu_1/\rho_1 = [1.458\times10^{-6}T_1^{1.5}/(T_1+110.4)]/\rho_1 \tag{B5}$$

The quantities p_0, T_0, a_0 are the stagnation pressure, temperature, and speed of sound, respectively. The incompressible arc length is found by integrating equation (A1).

The start of transition (subscript S) is determined from the relation

$$(R_\theta)_1 \geq (R_\theta)_{IS} \tag{B6}$$

where $(R_\theta)_{IS}$ is defined by equations (11)-(13) of Abu-Ghannam and Shaw [26].

The end of transition (subscript E) is determined from finding when

$$s_1 \geq s_{IE} \tag{B7}$$

where

$$s_{IE} = R_{XIE}\nu_{IS}/u_{IS} \tag{B8}$$

$$R_{XIE} = R_{XIS} + 16.8(R_{XIS})^{0.8} \tag{B9}$$

$$R_{XIS} = s_{IS}u_{IS}/\nu_{IS} \tag{B10}$$

The momentum thickness at the end of transition depends on the value of

$$C_2 = B^2 - 4A\bar{C} \tag{B11}$$

where

$$A = 183.5\ C_1(1.4)\left(\frac{du_1}{ds_1}\right)_E/\nu_{IE} \tag{B12}$$

$$B = u_{IE}/\nu_{IE} \tag{B13}$$

$$\bar{C} = -540 - 183.5C_1 \tag{B14}$$

$$C_1 = R_{IL}10^{-5} - 1.5 \tag{B15}$$

$$R_{IL} = (s_{IE} - s_{IS})u_{IS}/\nu_{IS} \tag{B16}$$

If $C_2 > 0$, then

$$\theta_{IE} = [-B + (C_2)^{1/2}]/(2A) \tag{B17}$$

If $C_2 < 0$, then

$$\theta_{IE} = 0.0368(R_{IL}^{0.8})/B \tag{B18}$$

The value of θ_E is found from equation (A5). This value is used to compute H_E and C_{fE} according to the second method suggested in section A4 of Green et al. [28].

The values of θ, H, and C_f in the transition region are found using equations (24), (26), and (32) of Abu-Ghannam and Shaw [26].

APPENDIX C

Turbulent Boundary Layer

The coefficients used in the integral turbulent boundary layer equations are presented below

$$A = -\rho_e u_e F_1$$

$$F_1 = H\left(\frac{C_f}{2}+m_w\right)+(1+0.2r\mathrm{M}^2)\left[C_E+m_w - H_1\left(\frac{C_f}{2}+m_w\right)\right]\frac{d\bar{H}}{dH_1}$$

$$B = [(1-\mathrm{M}^2)Q+\rho_e u_e F_2\theta]/u_e$$

$$F_2 = -H(H+2-\mathrm{M}^2)+(1+0.2\ r\mathrm{M}^2)(H+1)H_1\frac{d\bar{H}}{dH_1} + 0.4r\mathrm{M}^2(1+0.2\mathrm{M}^2)(\bar{H}+1)$$

$$C = \frac{d\bar{H}}{dH_1}\left\{C_E+m_w-H_1\left(\frac{C_f}{2}+m_w\right)\right\}/\theta$$

$$D = \frac{d\bar{H}}{dH_1}H_1(H+1)/u_e$$

$$E = \bar{F}\left\{2.8[(C_\tau)_{EQ_0}^{1/2}-\lambda(C_\tau)^{1/2}]/(H+H_1) + \left(\frac{\theta}{u_e}\frac{du_e}{ds}\right)_{EQ}\right\}/\theta$$

$$F = -\bar{F}[1+0.075\mathrm{M}^2(1+0.2\mathrm{M}^2)/(1+0.1\mathrm{M}^2)]/u_e$$

where

$$\bar{F} = (0.02C_E + C_E^2 + 0.8\ C_{f_0}/3)/(0.01+C_E)$$

$$C_\tau = \tau/(\rho_e u_e^2)$$

τ is the maximum shear stress, r is the recovery factor, the subscripts EQ and 0 denote equilibrium flow and flat-plate flow, respectively, and λ is a scaling factor for effects due to longitudinal streamline curvature and flow convergence or divergence.

The following changes are made to equilibrium quantities:

$$(C_E)_{EQ_0} = H_1\left[\frac{C_f}{2}+m_w-(H+1)\left(\frac{\theta}{u_e}\frac{du_e}{ds}\right)_{EQ_0}\right]-m_w$$

$$\left(\frac{\theta}{u_e}\frac{du_e}{ds}\right)_{EQ} = \left\{\frac{C_f}{2}+m_w-[(C_E)_{EQ}+m_w]/H_1\right\}/(H+1)$$

APPENDIX D

Wigton's [14] formulas for updating the Q values between each interaction cycle are as follows:

for $M < 1$:

$$Q^{n+1} = Q^n + \frac{\omega_1\tilde{\beta}\rho_i B u_i}{\nu B - \tilde{\beta}\rho_i}\left(\frac{u_e}{u_i}-1\right)$$

for $M > 1$:

$$Q^{n+1} = Q^n + \frac{\omega_2 B\tilde{\beta}\rho_i}{(\nu B)^2+(\tilde{\beta}\rho_i)^2}\left[B\left(\frac{du_e}{ds}-\frac{du_i}{ds}\right) - \tilde{\beta}\rho_i\left(\frac{u_e}{u_i}-1\right)\right]$$

where M is the local Mach number, $\nu = \pi/\Delta s$, Δs is the step size, $\tilde{\beta} = |1 - \mathrm{M}^2|^{1/2}$, B is the coefficient in the momentum integral equation written in the form

$$\frac{dQ}{ds} = A + B\frac{du_e}{ds}$$

and ω_1 and ω_2 are relaxation factors (equal to unity in Wigton's analysis).

Carter's [12] update formula is

$$Q^{n+1} = Q^n\left[1+\omega\left\{\frac{u_e}{u_i}-1\right\}\right]$$

where ω is a relaxation factor.

Predictions of Endwall Losses and Secondary Flows in Axial Flow Turbine Cascades

O. P. Sharma
Senior Research Engineer.

T. L. Butler
Project Engineer.

Engineering Division,
Pratt & Whitney Aircraft Group,
East Hartford, CT 06108

This paper describes the development of a semi-empirical model for estimating endwall losses. The model has been developed from improved understanding of complex endwall secondary flows, acquired through review of flow visualization and pressure loss data for axial flow turbomachine cascades. The flow visualization data together with detailed measurements of viscous flow development through cascades have permitted more realistic interpretation of the classical secondary flow theories for axial turbomachine cascades. The re-interpreted secondary flow theories together with integral boundary layer concepts are used to formulate a calculation procedure for predicting losses due to the endwall secondary flows. The proposed model is evaluated against data from published literature and improved agreement between the data and predictions is demonstrated.

1 Introduction

A knowledge of the magnitude of losses is essential in the preliminary and detailed design phase of a turbomachine. Historically these losses have been divided into three distinct parts, namely profile losses, endwall secondary flow losses, and tip clearance losses. The profile losses are generated on the airfoil surfaces due to the growth of the boundary layers. These losses can be fairly accurately calculated in the detailed design phase for given airfoil surface static pressure distribution by using boundary layer calculation methods. It should be pointed out that a good transitional boundary layer calculation method and a model that accounts for the unsteadiness due to the rotor–stator interaction is essential if reliable estimates of profile losses in a rotating rig environment are to be obtained. For a given family of airfoils designed for prescribed velocity triangles, profile losses can also be fairly accurately estimated in the initial phase of the turbine design. The magnitudes of endwall secondary flow losses and tip leakage losses, however, are almost exclusively obtained from available empirical correlations both in the initial and the detailed design phase of a turbomachine. Tip leakage losses mainly occur in rotors and these are invariably parasitic losses which can be reduced through active control of the tip clearance. The endwall secondary losses, on the other hand, occur because of the annulus wall boundary layers and their interaction with the airfoils in the blade row passage. Since these losses account for almost 30–50 percent of the total pressure loss in any blade row, it is important to understand the physical mechanisms responsible for generating these losses and to define a realistic formulation for estimating them which can be used for turbine designs.

Contributed by the Gas Turbine Division of THE AMERICAN SOCIETY OF MECHANICAL ENGINEERS and presented at the 31st International Gas Turbine Conference and Exhibit, Düsseldorf, Federal Republic of Germany, June 8–12, 1986. Manuscript received at ASME Headquarters February 14, 1986. Paper No. 86-GT-228.

Dunham [1] conducted a detailed review of the available correlations for endwall secondary flow losses and through his comparison with available data concluded that none of the then-existing methods gave a realistic estimate of losses for cascades. He proposed a correlation for the endwall secondary flow losses which was later modified by Came [2], Dunham and Came [3], and Morris and Hoare [4]. The modified formulation of Dunham's correlation is given by the following expression

$$Y=\frac{b}{h}\frac{\sin\beta_2}{\sin\beta_1}\left(\frac{C_L}{\tau/b}\right)^2\frac{\sin^2\beta_2}{\sin^3\beta_m}\left(0.294\frac{\delta^*}{b}+0.011\right) \quad (1)$$

In his paper, Dunham concluded that a fresh approach to estimate endwall secondary flow by using three-dimensional boundary layer concepts was needed to get more realistic predictions of the endwall secondary flow losses.

A number of experimental investigations [5–9] have been conducted over the past decade in large-scale rectilinear and annular cascades to provide more insight into the complex three-dimensional flows in the endwall regions and to provide a data base to facilitate three-dimensional endwall boundary layer and/or three-dimensional viscous flow calculations. Sieverding [10] gave an excellent review of these recently conducted studies in order to outline the state-of-the-art understanding of the basic aspect of the secondary flows in turbine blade passages. In his paper, Sieverding provided detailed insight into the topology of the complex three-dimensional flow field in the endwall regions; however, he did not provide any viable procedure to estimate endwall losses.

To the authors' knowledge, only two endwall loss prediction methods [11, 12] have appeared in the literature since Dunham's correlation which can be used in turbine design process. The formulation provided by Gregory-Smith [11] allows estimation of both the spanwise distribution of endwall losses and the exit air angle deviation due to secondary flow. However, this method can be used only in the detailed design process where airfoil shapes and flowpath geometry have been

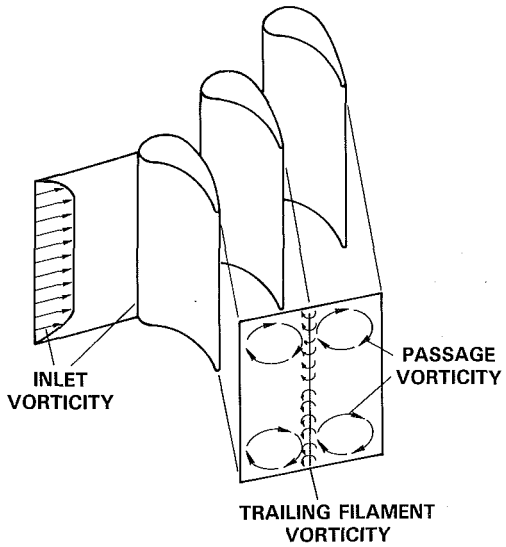

Fig. 1 Cascade vorticity as predicted by classical secondary flow theories

defined. The correlation of Mukhtarov and Krichakin [12] can be used in the initial design phase where optimization and selection of turbine parameters and flow path are being conducted. It should also be pointed out that a number of viscous numerical calculation methods [13, 14, 33] have been developed over the past 15 years which have the potential to influence the optimization of turbines once realistic turbulence models capable of predicting three-dimensional transitional flows become available. These state-of-the-art numerical methods can only be used to guide experimental work and designs at the moment.

The primary objective of the present paper is to demonstrate that the detailed data obtained in the last 15 years have provided sufficient information about the endwall secondary flows in turbine cascades to allow a physically realistic model for the endwall secondary flow losses. In addition, these data have also provided new insight about the effect of inlet boundary layer (normal component of vorticity) on the secondary flow which indicates that the classical approach of inviscid secondary flow theory originally proposed by Squire and Winter [15], and subsequently generalized and applied by many investigators [16–19], may yield misleading results as far as endwall secondary flows in turbomachine cascades are concerned unless proper care is taken while applying these theories. A description of the flow field in the endwall region of turbine cascades is given below with special reference to the effect of inlet boundary layer to substantiate the above statement.

2 Flow Structure in the Endwall Region

An extensive amount of theoretical and experimental work has been conducted over the past forty years to understand and estimate secondary flows in axial turbomachine cascades. Until the recent availability of three-dimensional viscous codes, most of the theoretical work has concentrated on developing and applying inviscid secondary flow theories. The secondary flow vortex system predicted by these classical secondary flow theories is shown in Fig. 1 as described by Hawthorne [16]. It shows the resulting component of exit vorticity in the direction of the flow when fluid with inlet vorticity is deflected through a cascade. Three distinct mechanisms contribute to the secondary vorticity at the exit of the cascade:

(*i*) distributed secondary vorticity which appears as the passage vortex at the exit of the cascade which is generated by the distortion of the vortex filaments of the inlet boundary layer as it passes through a curved passage;
(*ii*) trailing filament vorticity which is generated due to the stretching of the inlet vortex filaments when passing through the cascade with different velocity between the suction and the pressure side;
(*iii*) trailing shed vorticity which is generated due to the spanwise change of the blade circulation.

A number of expressions are available for calculating the distributed secondary vorticity. Almost all of these expressions have been derived by assuming that the flow in the cascade passage is frictionless. These expressions have provided surprisingly good agreement with measured exit air angle data in cascades and curved ducts implying that viscous effects in cascades have a relatively small effect on secondary flows. It should, however, be pointed out that the energy losses estimated by using the theories are an order of magnitude smaller than those measured in cascades.

The sense of rotation of the trailing filament and the trailing shed vorticities are opposite to that of the distributed secondary vorticity and their relative contributions to the total secondary vorticity are much lower than the distributed secondary vorticity.

The secondary vorticity predicted by the classical secondary flow theories relies on the assumption that inlet boundary layer entering the cascade experiences flow turning in the passage resulting in distortion of vortex tubes which causes an

Nomenclature

B = constant
b = chord
bx = axial chord
CR = convergence ratio $\equiv \rho_2 U_2/\rho_1 U_1$
C_L = lift coefficient referred to vector mean velocity $\equiv 2(\tau/b)\ (\cot \beta_1 - \cot \beta_2)\sin \beta_m$
C_f = skin friction coefficient
h = height of the airfoil
H = boundary layer shape factor $\equiv \delta^*/\theta$
H^* = boundary layer shape factor $\equiv \delta^{**}/\theta$
M = Mach number
P_T = total pressure
P_s = static pressure
Ri = Richardson number $= \epsilon/\sqrt{CR}$
s = distance along the streamwise direction
TET = airfoil trailing edge thickness
U = velocity
Y = total pressure loss coefficient $\equiv (P_{Tref} - P_{T2})/(P_{Tref} - P_{S2})$
Z_{TE} = penetration height of the separation line on the airfoil suction surface at the trailing edge
β_m = vector mean air angle = $\cot^{-1}[\frac{1}{2}(\cot\beta_1 + \cot\beta_2)]$
β = gas angle measured from tangential
δ = boundary layer thickness
δ^* = boundary layer mass deficit thickness
δ^{**} = boundary layer energy deficit thickness
ϵ = gas turning in radians
θ = boundary layer momentum deficit thickness
ρ = density
τ = pitch of airfoils in cascades
$1-\phi^2$ = energy loss coefficient

Subscripts

1 = cascade inlet conditions
2 = cascade exit conditions

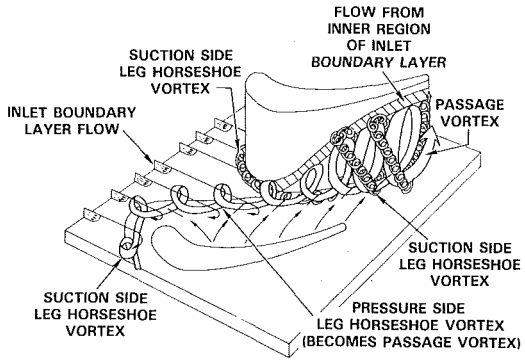

Fig. 2 Cascade endwall flow structure

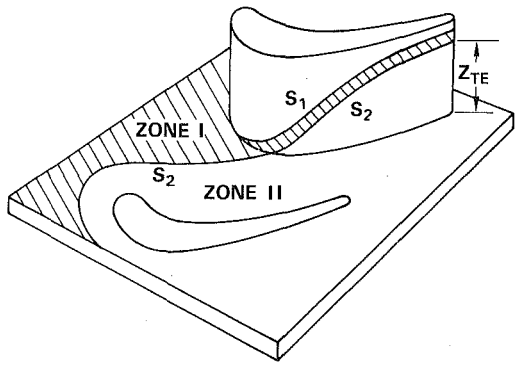

Fig. 3 Cascade endwall region separation lines

increase in vorticity in the streamwise direction. A review of the flow visualization and flow measurements in the leading edge region of cascade appears to dispute this assumption. Details of the flow field in cascades have been fairly well mapped by a number of recent investigators as discussed by Sieverding [10]. Figures 2 and 3 show flow patterns associated with the inlet boundary layer in a turbine cascade. This figure has been generated by utilizing available information from published literature [5, 9, 10, 20, 22, and 24] along with some additional insight obtained by the authors from some recently conducted experiments in full and large-scale cascade wind and water tunnels. As shown in the above figure, the boundary layer entering the cascade separates in the leading edge region forming a horseshoe vortex. A majority of the fluid from the inlet boundary layer gets trapped in this vortex which has two legs. These two legs are normally termed the pressure and the suction side legs. During this interaction the normal component of the vorticity associated with the inlet boundary layer is transformed into the streamwise component of vorticity as soon as the fluid enters the cascade before most turning of the mainstream flow has been achieved. The two legs of the horseshoe vortex entering the cascade are counterrotating, and if both contain equal amounts of fluid, then the net streamwise component of the vorticity would be zero in the exit plane of the cascade if the fluid in the cascade were frictionless. Recently conducted flow visualization tests at P&W indicate that the fluid particles closest to the wall in the cascade inlet boundary layer do not become part of the horseshoe vortex. These fluid particles get convected toward the suction side of the airfoil where they climb the airfoil surface exiting the airfoil on top of the passage vortex.

The pressure side leg of the vortex is immediately influenced by the blade-to-blade pressure gradient as it enters the passage and gets convected toward the suction side, meeting the surface near the minimum pressure point. Since all of the fluid particles from the inlet boundary layer have either become part of the horseshoe vortex or been convected toward the suction side, a new boundary layer starts at the endwall downstream of the separation line defined by the horseshoe vortex system.

As the pressure side leg of the vortex moves across the passage it entrains low-momentum fluid particles from this newly formed passage endwall boundary layer and it grows to become the passage vortex which is the most dominant feature of the flow. This entrainment of the passage endwall boundary layer fluid significantly affects the development of the passage vortex and is a key mechanism in the generation of the secondary flows and endwall losses. Since this mechanism is governed by viscosity one should not expect inviscid secondary flow theories to yield realistic magnitudes of secondary vorticity or endwall losses in cascades.

The suction side leg of the horseshoe vortex has a sense of rotation opposite to that of the pressure side leg of the vortex (and the passage vortex). It tends to follow the contour of the airfoil suction side remaining near the endwall until the point where the passage vortex interacts with the suction side of the airfoil. At this location, which is usually near the minimum pressure point in the cascade passage, the suction side leg of the vortex is forced off the endwall as it interacts with the passage vortex. As the flow proceeds downstream the suction side leg of the vortex orbits around the outside edge of the passage vortex retaining its identity. The location of this suction side leg of the vortex in the cascade exit plane depends on the size and vorticity associated with it and the passage vortex. The countervortex pointed out by Langston [5] at the airfoil suction surface endwall junction in the exit plane is most likely the suction side leg of the vortex which has arrived at the corner by spiraling around the passage vortex.

An important feature of the surface flow visualization on the endwall and the airfoil surfaces is the separation at reattachment lines, which was first identified by Langston [5] in a turbine cascade. Figure 3 shows the schematic of the surface flow visualizations. Zone I in the endwall region represents the region affected by the fluid particles which enter the cascade as the innermost part of the cascade inlet boundary layer. This fluid climbs the airfoil suction surface before the minimum pressure point and appears on the airfoil suction side between lines S1 and S2. The surface streamlines in zone II on the endwall indicate strong crossflows from the pressure to the suction side. This crossflow feeds the pressure side leg of the vortex and it grows to become the passage vortex. This separation line indicates the location where the pressure side leg of the vortex separates from the wall. This line meets the airfoil suction surface at the minimum pressure point and then climbs the airfoil suction surface. The height of the separation line S2 at the trailing edge of the airfoil approximates the diameter of the passage vortex. This line is one of the most prominent imprints of the endwall secondary flow vortex in the axial turbomachine passage. Knowledge of the penetration height of this separation line at the trailing edge on the airfoil suction surface can be used in estimating both endwall losses and secondary flows, as shown in the remainder of this paper.

3 Separation Line Penetration Height

Detailed review of a large body of available cascade data has indicated that the penetration of the separation line toward the midheight of the airfoil suction surface is a good indicator of the magnitude of secondary flow. The data of Langston et al. [5], Marchal and Sieverding [6], and Graziani et al. [9] show the region adjacent to the suction surface, between the separation line and the endwall, to be one of high loss and high external heat load associated with the passage vortex.

Because of the importance of the separation line as an indicator of heat loads and losses both for the midspan and endwall regions of the airfoil, extensive studies of cascade flow visualization experiments were conducted in order to develop

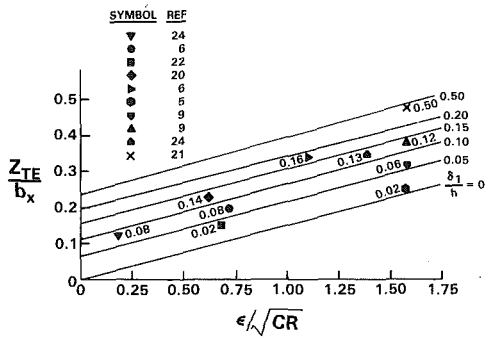

Fig. 4 Penetration height of the separation line on the airfoil suction surface at the trailing edge as a function of the cascade geometry and inlet boundary layer thickness

a correlation to predict its behavior. Figure 4 shows a plot of the penetration height of the suction surface separation line at the trailing edge as a function of cascade turning angle, convergence ratio and inlet boundary layer thickness. These data were obtained from surface flow visualizations reported in [5, 6, 9, 21, 22, 24]. The magnitude of the cascade inlet boundary layer thickness normalized by airfoil height is written next to each data point. The following expression gives a good estimate of the penetration height

$$\frac{Z_{TE}}{bx}=0.15\epsilon/\sqrt{CR}+f\left(\frac{\delta_1}{h}\right) \tag{2}$$

where Z_{TE} = penetration height of the separation line at the trailing edge on the airfoil suction surface; h = height of the airfoil; bx = axial cord; ϵ = flow turning angle in radians; CR = convergence ratio = $(\rho U)_{exit}/(\rho U)_{inlet}$; δ_1 = inlet boundary layer thickness.

The function $f(\delta_1/h)$ in the above expression can be approximated by

$$f\left(\frac{\delta_1}{h}\right)=1.4\frac{\delta_1}{h}-2.73\left(\frac{\delta_1}{h}\right)^2+1.77\left(\frac{\delta_1}{h}\right)^3 \tag{3}$$

It is noted that the curves for different inlet boundary layer thicknesses are parallel lines. This indicates that the increase in separation line penetration due to increasing boundary layer thickness is relatively independent of the cascade geometry (turning angle and convergence ratio). If one considers the penetration height of the separation line at the airfoil suction surface trailing edge to be an indicator of secondary flow, then this result contradicts various secondary flow theories [15–18]. These theories relate secondary vorticity at the exit of the cascade (due to inlet boundary layer) to the airfoil deflection (turning angle). However, these theories assume that the inlet boundary layer enters the cascade without interacting with the airfoil leading edge, in contrast to the observations about the cascade endwall flow discussed above. In cascade flows the inlet boundary layer interacts with the airfoil leading edge and most of the boundary layer fluid (normal component of vorticity) gets wrapped up in the horseshoe vortex (streamwise component of vorticity) before any mainstream flow turning occurs. This streamwise component of vorticity is unaffected by the airfoil deflection. The present correlation indicates that the above assumption used in the secondary flow theories may be unrealistic for typical turbine cascades and that the leading edge/inlet boundary layer interaction may be a more important factor than airfoil deflection in determining secondary flow due to the inlet boundary layer.

4 Effect of Inlet Boundary Layer on Cascade Losses

Although a number of cascade tests have been conducted and published in the literature, few of these tests contain enough information about the airfoils tested such as airfoil shapes, airfoil surface static pressure distributions,

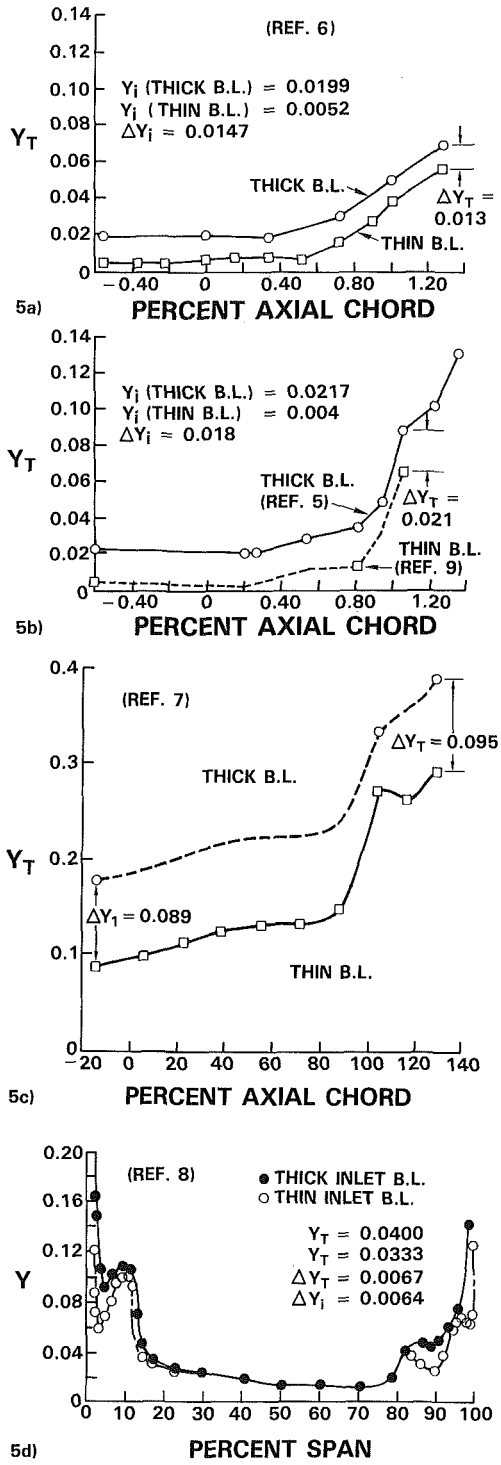

Fig. 5 Loss data from [5–9] indicate that the net cascade passage losses are independent of the cascade inlet boundary layer thickness

measurements of the inlet boundary layer, pitch-averaged exit total pressure profiles, and flow visualization on the airfoil surfaces, to permit detailed analysis of the cascade loss data. Four recently conducted tests, however, do not suffer from the above shortcomings:

(*i*) Tests conducted by Langston et al. [5] and Graziani et al. [9] for a rotor airfoil at low aspect ratio in a large-scale, low-speed rectilinear cascade. These tests were conducted for both thick and thin inlet boundary layers.

(*ii*) Tests conducted by Marchal and Sieverding [6] for both a nozzle and rotor airfoil at high and low Mach numbers

in rectilinear cascades. These tests were conducted at a low aspect ratio for thin and thick inlet boundary layers.

(*iii*) Tests conducted by Gregory-Smith and Graves [7] for a rotor airfoil at an aspect ratio of about two in a large-scale, low-speed, rectilinear cascade. These tests were conducted for three inlet boundary layers.

(*iv*) Tests conducted by Hunter [8] in a large-scale, low-speed annular cascade for a nozzle guide vane. These tests were conducted for two inlet boundary layers.

In the first three of the above tests, measurements of losses were obtained at various axial stations inside the cascade passage including detailed measurements upstream and downstream of the cascade. The development of losses through the cascade for each of these configurations is plotted in Figs. 5(*a–c*) for two test inlet boundary layers. At each station where data are available, the difference in losses between the two tests remains approximately constant and is equal to the difference in loss between the incoming boundary layers. The exit plane pitch-averaged data of Hunter obtained for two inlet boundary layers are shown in Fig. 5(*d*). Here again the difference in loss for the two cases is approximately equal to the difference in inlet boundary layer loss. In each of these four tests the net loss generated inside the passage is approximately the same for both thick and thin inlet boundary layers. This strongly suggests that the inlet losses are additive and that the total loss can be split as follows

$$Y_T = Y_i + Y_{ps} \tag{4}$$

where Y_T = total pressure loss coefficient measured as the difference between the exit total pressure and a reference inlet total pressure; Y_i = inlet loss, contained within the cascade inlet boundary layer; Y_{ps} = passage loss, generated within the passage, this loss is independent of the inlet boundary layer.

A simple expression for the mass-averaged inlet loss can be obtained by integrating the inlet total pressure across the inlet boundary layer assuming the static pressure to be constant to give

$$Y_i = \frac{\delta_1^{**}}{0.5h - \delta_1^*} \frac{\rho_1 U_1^2}{\rho_2 U_2^2} \tag{5}$$

From the discussion in the last sections it is apparent that neither the loss nor the streamwise vorticity attributable to the inlet boundary layer increases as it passes through the cascade passage. This indicates that neither available loss correlations [1–4] nor inviscid secondary flow theories, which relate the amount of secondary loss generated by the inlet boundary layer to the flow turning in the passage, will give physically realistic results for endwall flows in turbine cascades.

It should be noted here that the above conclusions about the effect of inlet boundary layer on turbine cascade secondary flow and loss has been arrived at through the analysis of data obtained for reaction cascades typical of modern high bypass ratio gas turbines used in aircraft transportation. Few detailed data are available for impulse and very low aspect ratio cascades operating with thick inlet boundary layers. In such cases, the inlet boundary layers may have a more pronounced effect on the secondary flows and losses generated in the passage. Until data for such cascades become available the above conclusion cannot be totally generalized.

5 Prediction of Turbine Passage Losses

The losses generated in a turbine passage can be further divided into two components, to facilitate their predictions, as follows

$$Y_{PS} = Y_P + Y_{EW} \tag{6}$$

where Y_P = profile losses and Y_{EW} = endwall secondary flow losses.

The profile losses are generated by the boundary layers developing on the airfoil pressure and suction sides. These losses are independent of the cascade aspect ratio and only for high aspect ratio cascade tests will they be equal to the midheight measured loss. This is because the boundary layers in the midspan regions of cascades are influenced by the endwall secondary flow effects. As pointed out by Dunham [29] and Sharma and Graziani [30], this causes the measured data to be higher than the calculated values. An example of this phenomenon is shown in Fig. 6 where pitch-averaged losses for a cascade test conducted by Langston et al. and Graziani et al. are shown as a function of span. The two sets of data plotted in this figure were obtained at same aerodynamic test conditions except for the thickness of the inlet boundary layer. The total passage losses for these two tests are almost identical as shown in Fig. 5(*a*). If the midspan loses are taken as profile losses, then the thick boundary layer test would yield negative endwall secondary flow losses, which is not physically realistic. Since the measured surface static pressure distributions for both these tests were identical, one would expect the same losses at the midspan. The difference in midspan loss indicates that the endwall secondary flows were affecting the midspan boundary layer development. Measured midspan loss data in almost all cascade tests suffer from the endwall flow effects. Erroneous interpretation of midspan losses as profile losses has invariably resulted in inconsistent estimates of endwall secondary losses from the data and has hindered progress in developing realistic loss prediction models for turbomachinery cascades.

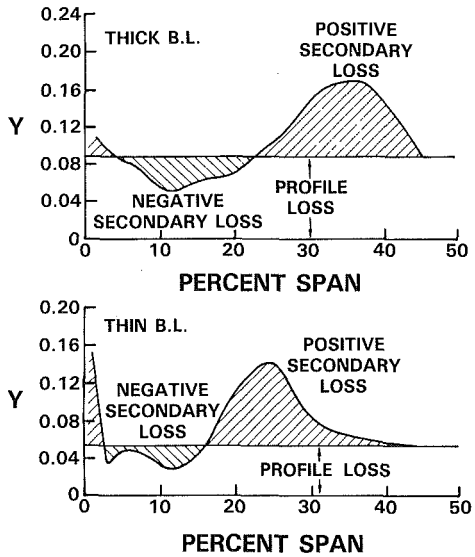

Fig. 6 Data from [5, 9] demonstrate that defining midspan loss as profile loss can result in reduced secondary loss for increased inlet boundary layer thickness

The endwall losses, on the other hand, are generated due to the boundary layer and associated secondary flows in the endwall regions. The procedures adopted in estimating both components of the turbine passage losses are described in the following two subsections.

5.1 Profile Loss Prediction Method. Although a number of correlations are available in published literature for estimating profile losses, as shown by Denton [25] in a review paper, none of these correlations is likely to estimate the profile losses as accurately as boundary layer and mixing calculations conducted for the airfoil pressure distribution as obtained either from measured data or from inviscid flow predictions [26–28].

A number of differential boundary layer calculation methods are available in published literature, for example [30, 31], which can be used to estimate the boundary layer development on turbine airfoils. The method from [30] was used in the present exercise to calculate the two-dimensional boundary

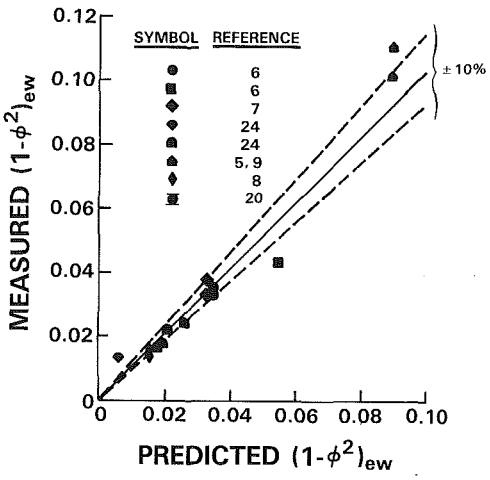

Fig. 7 Predicted endwall losses show good agreement with data

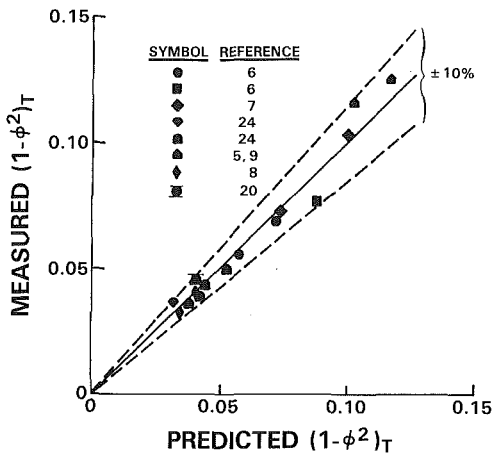

Fig. 8 Predicted total losses show good agreement with data

layer integral parameters, and the mixing analysis developed by Stewart et al. [32] was used to obtain the profile losses for each set of data described below.

5.2 Endwall Secondary Loss Prediction Method. Although in principle a three-dimensional viscous calculation method can be used to estimate endwall secondary losses [13, 14, 33], there is still a need for a semi-empirical model which can be used in the initial design phase of a turbine. Such a semi-empirical model has been developed in the present work by utilizing the classical boundary layer theory developed for the endwall regions of turbomachines. The development of incompressible boundary layer along the pitch-averaged streamline in the endwall regions of a turbine cascade may be written as

$$\frac{d\theta}{ds}+(H+2)\frac{\theta}{U}\frac{dU}{ds}=\frac{C_f}{2} \tag{7}$$

where s = distance along the pitch-averaged streamline; U = pitch-averaged velocity.

θ, H, and C_f are the momentum loss thickness, shape factor, and the skin friction coefficients, respectively, for the boundary layer developing along the pitch-averaged endwall streamline. By using an average value of skin-friction and shape factor in the endwall region and for given velocity and density gradients, equation (7) can be reduced to the following expression for momentum loss thickness at the cascade exit plane

$$\theta_{EW}=S\frac{\overline{C_f}}{2}\left(\frac{U_1}{U_2}\right)^{1+H/2} \tag{8}$$

where $\overline{C_f}$ = average skin friction in the endwall region; U_1/U_2 = ratio of cascade inlet to exit velocity; S = average distance in the endwall region.

Equation (8) can be used to obtain energy loss thickness in the endwall region as

$$\delta^{**}_{EW}=S\frac{\overline{C_f}}{2}H^*\left(\frac{U_1}{U_2}\right)^{1+H/2} \tag{9}$$

Endwall losses can now be obtained by using equation (9) as

$$(1-\theta^2)_{EW}=\frac{2\delta^{**}}{h}=\frac{S}{h}\overline{C_f}\left(\frac{U_1}{U_2}\right)^{1+H/2}H^* \tag{10}$$

An assumption is now made about the behavior of skin friction coefficient for the endwall boundary layer such that it can be obtained by utilizing available correlations from two-dimensional boundary layer theory with a modification to account for the cross flows in the endwall regions. The effect of the crossflow-induced three dimensionality of the boundary layer can be modeled as an extra rate of strain which modifies the skin friction relationship. The proposed relationship for the skin friction may be written as:

$$C_f=C_{f2D}(1+B\mathrm{Ri}) \tag{11}$$

where C_{f2D} = skin friction coefficient for a two-dimensional boundary layer; B = constant; Ri = appropriate Richardson number for endwall boundary layer $= 2(Z_{TE}/bx)=0.3\epsilon\sqrt{CR}$.

The above modification to the skin friction is analogous to the ones proposed by Branshaw [34], for flows over curved and/or rotating surfaces and by Sharma and Graziani [30] for convergence and divergence of streamlines. Here the Richardson number has been assumed to be proportional to the magnitude of the endwall secondary flow as obtained from equation (2). The value of constant B in the above equation can be assumed to be of the order of 14 on the basis of analysis conducted in the above two references.

Substituting equation (11) with appropriate values of B and Ri in (10) yields

$$(1-\phi^2)_{EW}=(1+4\epsilon/\sqrt{CR})\frac{S}{h}\overline{C}_{f2D}\left(\frac{U_1}{U_2}\right)^{1+H/2}H^* \tag{12}$$

The above equation can be simplified as

$$(1-\phi^2)_{EW}=(1+4\epsilon/\sqrt{CR})2\frac{\delta^{**}_{2D}}{h} \tag{13}$$

where $\delta^{**}_{2D}=H^*S\overline{C}_{f2D}(U_1/U_2)^{1+H/2}$; δ^{**}_{2D} = energy loss thickness for two-dimensional boundary layer developing over the endwall surface in the absence of crossflows.

The δ^{**}_{2D} can also be obtained by using two-dimensional boundary layer loss on the airfoil pressure and suction surfaces, as

$$\delta^{**}_{2D}=(1-\phi^2)_{2D}\frac{\tau\sin\beta_2-\mathrm{TET}}{2} \tag{14}$$

where $(1-\phi^2)_{2D}$ = energy loss coefficient for profile losses; H^* = shape factor based on energy deficit thickness.

Substituting equation (14) into equation (13) results in the following expression for endwall losses

$$(1-\phi^2)_{ew}=(1-\phi^2)_{2D}\frac{\tau\sin\beta_2-\mathrm{TET}}{h}\left(1+4\frac{\epsilon}{\sqrt{CR}}\right) \tag{15}$$

The total losses generated in the cascade passage can now be given as

$$(1-\phi^2)_{ps}=(1-\phi^2)_{2D}+(1-\phi^2)_{EW}$$
$$=(1-\phi^2)_{2D}\left[1+\left(1+\frac{4\epsilon}{\sqrt{CR}}\right)\frac{\tau\sin\beta_2-\mathrm{TET}}{h}\right] \tag{16}$$

To demonstrate the predictive capability of equation (15)

for endwall secondary loss, several turbine cascade data sets were analyzed [5–9, 20, 24]. These data consisted of the spanwise distribution of total pressure loss at inlet and exit of the cascade and knowledge of the airfoil midspan surface pressure distribution either from measurement or from inviscid flow calculation, cascade geometry, and test conditions. All of the abovementioned experimental investigations were conducted at near design incidence and loss data were acquired at about 0.5 axial chord downstream of the cascade trailing edge by which time most of the mixing losses have occurred. The major contribution to the mixing losses occur because of dissipation of the secondary flow vortex [35]. In the present model the mixing losses are assumed to be proportional to the secondary loss and these are included in the losses predicted by equation (15).

The proposed method of splitting the total loss allowed the endwall loss to be extracted from this data. The inlet loss was obtained from the measured inlet boundary layer by using equation (5) or from the data if measured directly. Where only the boundary layer thickness was available a power law exponent equal to 5 was assumed to obtain the energy and displacement thicknesses. The two-dimensional profile loss was obtained using the method described in Section 5.1. The input to this boundary layer calculation was the measured midspan pressure distribution when available or the results from an inviscid flow solver [27] when data were unavailable. Subtracting the sum of inlet loss and two-dimensional profile loss from the total loss gave the endwall secondary loss.

A comparison of the measured endwall secondary loss with the loss calculated using equation (15) is shown in Fig. 7. It should be pointed out here that the present procedure deduced endwall secondary losses from measured total losses, thus errors in estimation of profile and inlet losses appear as errors in the prediction of endwall secondary losses. A more realistic evaluation of the present procedure is a comparison between the measured and predicted total losses. Predictions for total loss obtained by adding the inlet loss and the two-dimensional profile loss (as calculated from the method described in section 5.1) to the endwall secondary loss are shown in Fig. 8 compared to the total loss data. Most of the data fall within a ± 10 percent scatter band which must be considered to be within the accuracy of the data for these types of measurement.

6 Conclusions

A method has been described for estimating secondary flows and endwall losses for axial flow turbomachine cascades. Detailed study of available experimental cascade data indicates that the effect of inlet boundary layer as predicted by classical secondary flow theories is incorrect for typical turbomachine configurations because the formation of the leading edge horseshoe vortex transforms incoming normal vorticity to streamwise vorticity independent of flow turning. A simple expression is given which accurately predicts the spanwise extent of the secondary flow region at the trailing edge in terms of meanline geometric parameters and inlet boundary layer thickness. Analysis of cascade loss data has demonstrated that inlet boundary layer losses convect through the passage without causing additional loss and can be distinguished from the passage loss. The passage loss can then be split into a two-dimensional profile loss and an endwall secondary loss. The two-dimensional profile loss can be calculated using an accurate two-dimensional boundary layer calculation method which accounts for the transitional nature of the airfoil boundary layer in the detailed design phase, or it can be correlated to the meanline loading for use in the preliminary design phase. A semi-empirical expression is given for endwall secondary loss based on pitch-averaged boundary layer concepts where the extra rate of strain associated with three dimensionality of the boundary layer is assumed proportional to the spanwise extent of the secondary flow region at the trailing edge. The resulting expression for secondary loss combined with the two-dimensional profile loss calculated using a boundary layer calculation method and the inlet loss gives predictions for cascade losses within ± 10 percent of measured losses.

References

1 Dunham, J., "A Review of Cascade Data on Secondary Losses in Turbine," *Journal of Mechanical Engineering Sciences*, Vol. 12, 1970, pp. 48–59.

2 Came, P. M., "Secondary Loss Measurements in a Cascade of Turbine Blades," Institute of Mechanical Engineers, Conference Publication No. 3, 1973.

3 Dunham, J., and Came, P. M., "Improvements to the Ainley–Mathieson Method of Turbine Performance Prediction," ASME JOURNAL OF ENGINEERING FOR POWER, Vol. 92, July 1970.

4 Morris, A. W. H., and Hoare, R. G., "Secondary Loss Measurements in a Cascade of Turbine Blades With Meridional Wall Profiling," ASME Paper No. 75-WA/GT-13.

5 Langston, L. S., Nice, M. L., and Hooper, R. M., "Three-Dimensional Flow in a Turbine Cascade Passage," ASME JOURNAL OF ENGINEERING FOR POWER, Vol. 99, 1977, pp. 21–28.

6 Marchal, P. H., and Sieverding, C. H., "Secondary Flows Within Turbomachinery Bladings," *Secondary Flow in Turbomachines*, AGARD CP No. 214, 1977, Paper No. 11.

7 Gregory-Smith, D. G., and Graves, C. P., "Secondary Flows and Losses in a Turbine Cascade," *Viscous Effects in Turbomachines*, AGARD CP No. 351, 1983, Paper No. 17.

8 Hunter, I. H., "Endwall Boundary Layer Flows and Losses in Axial Turbomachines," Ph.D. Thesis, University of Cambridge, 1979.

9 Graziani, R. A., Blair, M. F., Taylor, J. R., and Mayle, R. E., "An Experimental Study of Endwall and Airfoil Surface Heat Transfer in a Large Scale Turbine Blade Cascade," ASME JOURNAL OF ENGINEERING FOR POWER, Vol. 102, 1980, pp. 257–267.

10 Sieverding, C. H., "Recent Progress in the Understanding of Basic Aspects of Secondary Flows in Turbine Blade Passages," ASME JOURNAL OF ENGINEERING FOR GAS TURBINES AND POWER, Vol. 107, 1985, pp. 248–257.

11 Gregory-Smith, D. G., "Secondary Flows and Losses in Axial Flow Turbines," ASME JOURNAL OF ENGINEERING FOR POWER, Vol. 104, 1982, pp. 819–822.

12 Mukhtarov, M. Kh., and Krichakin, V. I., "Procedure for Estimating Flow Section Losses in Axial Flow Turbines When Calculating Their Characteristics," *Teploenergetika*, Vol. 18, 1969, pp. 76–79.

13 Dodge, P. R., "Numerical Method for 2-D and 3-D Viscous Flows," *AIAA Journal*, Vol. 15, 1977, pp. 961–965.

14 Hah, C. H., "A Navier–Stokes Analysis of Three-Dimensional Turbulent Flows Inside Turbine Blade Rows at Design and Off-Design Conditions," ASME JOURNAL OF ENGINEERING FOR GAS TURBINES AND POWER, Vol. 106, 1984, pp. 421–429.

15 Squire, H. B., and Winter, K. G., "The Secondary Flow in a Cascade of Airfoils in a Non-uniform Stream," *Journal of Aero Sciences*, Vol. 18, 1951.

16 Hawthorne, W. R., "Secondary Circulation of Fluid Flow," *Proceedings of Royal Society A*, Vol. 203, 1951.

17 Horlock, J. H., and Lakshminarayana, B., "Secondary Flows: Theory, Experiments and Application in Turbomachinery Aerodynamics," *Annual Review of Fluid Mechanics*, 1973, pp. 247–280.

18 Smith, L. H., "Secondary Flow in Axial-Flow Turbomachinery," *ASME Transactions*, 1955, pp. 1065–1076.

19 Lakshminarayana, B., "Effect of Inlet Temperature Gradients on Turbomachinery Performance," ASME JOURNAL OF ENGINEERING FOR POWER, Vol. 99, 1975, pp. 64–74.

20 Kopper, F. C., Milano, R., and Vanco, M., "An Experiment Investigation of Endwall Profiling in a Turbine Vane Cascade," *AIAA Journal*, Vol. 19, Aug. 1981.

21 Barber, T. J., and Langston, L. S., "Three-Dimensional Modeling of Cascade Flows," AIAA Paper No. 79-0047, Jan. 1979.

22 Kopper, F. C., private communication.

23 Bindon, J. P., "Exit Plane and Suction Surface Flows in an Annular Turbine Cascade With a Skewed Inlet Boundary Layer," *International Journal of Heat and Fluid Flow*, Vol. 2, 1980, pp. 57–66.

24 Sharma, O. P., Kopper, F. C., Knudsen, L. K., and Yustinich, J. B., "Low Pressure Turbine Subsonic Cascade Technology Report – Energy Efficient Engine Component Development and Integration Program," NASA CR-165592, PWA 5594-167, 1982.

25 Denton, J. D., "A Survey and Comparison of Methods for Predicting the Profile Loss of Turbine Blades," Inst. Mechanical Engineering Conference, Publication 3, C76/73, 1973.

26 Denton, J. D., "A Time Marching Method of Two and Three-Dimensional Blade to Blade Flows," ARC, R&M #3775, 1974.

27 Caspar, J. C., Hobbs, D. G., and Davis, R. L., "The Calculation of Two-Dimensional Compressible Potential Flow in Cascades Using Finite Area Techniques," AIAA Paper No. 79-0007, Jan. 1979.

28 Ri, R. H., "A Multiple-Grid Scheme for Solving the Euler Equations," *AIAA Journal*, Vol. 20, Nov. 1982.

29 Dunham, J., "The Effect of Stream Surface Convergence on Turbomachine Blade Boundary Layers," *Aeronautical Journal*, 1974, pp. 90–92.

30 Sharma, O. P., and Graziani, R. A., "Influence of Endwall Flow on Airfoil Suction Surface Midheight Boundary Layer Development in a Turbine Cascade," ASME JOURNAL OF ENGINEERING FOR POWER, Vol. 105, 1983, pp. 147–155.

31 McDonald, H., and Fish, R. W., "Practical Calculations of Transitional Boundary Layers," *International Journal of Heat and Mass Transfer*, Vol. 16, 1971, pp. 1729–1744.

32 Stewart, E. L., "Analysis of Two-Dimensional Compressible Flow Loss Characteristics of Turbine Blades in Terms of Basic Boundary Layer Parameters," NACA TN 3515, 1955.

33 Rhie, C. M., "A Pressure Based Navier–Stokes Solver Using the Multigrid Method," AIAA Paper No. 86-0207, Jan. 1986.

34 Bradshaw, P., "The Analogy Between Streamline Curvature and Buoyancy in Turbulent Shear Flow," *Journal of Fluid Mechanics*, Vol. 36, 1969.

35 Moore, J., and Adhye, R. Y., "Secondary Flows and Losses Downstream of a Turbine Cascade," ASME JOURNAL OF ENGINEERING FOR GAS TURBINES AND POWER, Vol. 107, 1985, pp. 961–968.

Effects of Tip Clearance on Blade Loading in a Planar Cascade of Turbine Blades

S. A. Sjolander
Associate Professor.

K. K. Amrud
Graduate Research Assistant.

Department of Mechanical and Aeronautical Engineering, Carleton University, Ottawa, Canada K1S 5B6

The paper examines in detail the structure of the tip leakage flow and its effect on the blade loading in a large-scale planar cascade of turbine blades. The tip clearance was varied from 0.0 to 2.86 percent of the blade chord. One of the blades is instrumented with 14 rows of 73 static taps which allowed a very detailed picture of the loading near the tip to be obtained. In addition to the measurements, extensive flow visualization was conducted using both smoke and surface oil flow. A new feature found in the present experiment was the formation of multiple, discrete tip-leakage vortices as the clearance was increased. Their presence is clearly evident from the surface oil flow and they account for the multiple suction peaks found in the blade pressure distributions. Integration of the pressure distributions showed that for larger values of the clearance the blade loading increases as the tip is approached and only begins to decline very near the tip. The increase was found to occur primarily in the axial component of the force.

Introduction

Flow through the tip gap of axial-flow turbomachinery blade rows has a number of interrelated effects on the performance of the machine, most of them adverse. In the case of axial compressors, surge margin tends to deteriorate with increasing clearance. In both turbines and compressors, the losses associated with the leakage flow account for a significant fraction of the losses in the endwall region. In addition to increasing the losses, the leakage flow alters the blade loading in the tip region thereby affecting the flow turning ability of the blade and complicating the design of the blade profile. Finally, the local regions of under and overturning present in the flow emerging from a blade row with clearance can trigger premature stalling and increase the losses in downstream blade rows.

In the last decade significant progress has been made toward an understanding of the endwall flow behavior in the absence of clearance (e.g., see Sieverding, 1985) and design changes which reduce the effects of the secondary flow are beginning to appear on production engines. With this problem now coming under control, the time seems right for a concerted attack on the leakage flow problem.

Of course much is already known about tip leakage flows. Measurements of the overall machine performance for a range of tip clearances have been correlated and form part of the loss prediction systems for compressors (e.g., Koch and Smith, 1976) and turbines (e.g., Kacker and Okapuu, 1982). Progress has also been made in the understanding and prediction of the details of the leakage flow. Rains (1954) demonstrated experimentally the existence of a tip leakage vortex and devised a simple analytical model for its rollup. Rains also concluded that viscous forces were unimportant except at very small clearances and that the leakage flow rate generally was determined by pressure forces and inertia effects. Lakshminarayana and Horlock (1963, 1967) made extensive measurements of clearance flows both for an isolated compressor blade and in a cascade. They also measured the blade loading at various spanwise stations and found that the blade force increased toward the tip due to the suction pressures induced by the tip leakage vortex. Based on these results, Lakshminarayana (1970) proposed a modified lifting-line analysis of the leakage flow. In recent years, Lakshminarayana and his co-workers (e.g., Davino and Lakshminarayana, 1982; Pandya and Lakshminarayana, 1983) have collected a large body of data on the effects of tip leakage on various aspects of the flow through compressors, such as its effect on the mean velocity in the tip region and the interaction of the leakage flow with the endwall boundary layer. Booth et al. (1982) made leakage flow measurements in water rigs with idealized tip gaps and a cascade of turbine blades with clearance. They agreed with Rains that at normal clearance levels viscous effects play a relatively minor role and they also concluded that the momentum changes parallel and normal to the gap are largely uncoupled. Based on this work, Wadia and Booth (1982) (see also Wadia, 1985) presented a simplified viscous analysis for the flow normal to the gap. The method was used to assess the relative discharge coefficients for various tip geometries rather than to give absolute values of the leakage flow rate. Their calculations showed a roughly 15 percent reduction in the discharge coefficient with tip wall motion. This is presumably the result of the no-slip condition at the tip wall causing fluid to be dragged back over the tip and

Contributed by the Gas Turbine Division of THE AMERICAN SOCIETY OF MECHANICAL ENGINEERS and presented at the 31st International Gas Turbine Conference and Exhibit, Düsseldorf, Federal Republic of Germany, June 8–12, 1986. Manuscript received at ASME Headquarters February 21, 1986. Paper No. 86-GT-245.

it therefore indicates some viscous effect. Graham (1985) also observed reduced leakage due to tip wall motion in his water flow cascade. Very recently, the fully three-dimensional viscous calculation methods currently being developed have begun to be applied to blade passage flows in which tip leakage was present (Moore et al., 1984; Hah, 1985).

Despite the progress that has been made, there seems to be general agreement that tip leakage flow is still far from being fully understood. In addition, there is a need for more data to test both the newest calculation methods and also the more approximate leakage flow and loss prediction schemes. A study is in progress to collect such data and to gain further insight into the physics of the leakage flow. The present paper focuses on the leakage flow structure and its relationship to the blade loading near the tip. It describes an experiment conducted in a large-scale planar cascade of turbine blades for which the tip gap was varied. Extensive measurements were made of the incoming flow, including traverses of the endwall boundary layer, and detailed measurements were made of the blade pressure distributions. The data were supplemented with flow visualization using both smoke and surface oil flow. The experiment is necessarily somewhat idealized: Full-scale Reynolds numbers were matched but the flow was essentially incompressible. The freestream turbulence intensity was also much lower than in an actual engine. Probably more importantly, there was no relative motion of the tip wall. As flow visualization studies (e.g., Phillips and Head, 1982) and measurements (e.g., Graham, 1985) have shown, endwall motion modifies the leakage flow and leads to changes in the blade loading compared with the stationary case. Nevertheless, we feel that our study gives insights into the leakage flow problem which are also applicable to the real flow.

Experimental Apparatus

Cascade Test Section. The measurements were made in the planar cascade test section shown in Fig. 1. The test section is attached to the open jet wind tunnel used previously with another test section to study endwall boundary layers (Sjolander, 1975).

The test section is 675 mm wide and 200 mm deep. The five blades of the cascade are mounted on the 7.9-mm-thick steel backplate which forms the mainstay of the structure. All other walls are made of 12.7-mm-thick plexiglass to facilitate flow visualization. For easy access to the cascade, the tip wall is hinged upstream of the blades. To vary the tip clearance, the tip wall is moved outward by inserting shims between the tip wall and the side walls, beginning about two chord lengths upstream of the leading edge of the blades. Interchangeable ramps provide a step-free transition from the fixed to the movable portion of the tip wall. Tailboards guide the flow downstream of the cascade and they together with the sideflaps are used to establish periodic flow conditions within the flow passages. The periodicity is monitored with pairs of static taps drilled into the backplate near the blade suction and pressure surfaces at about ¼ chord.

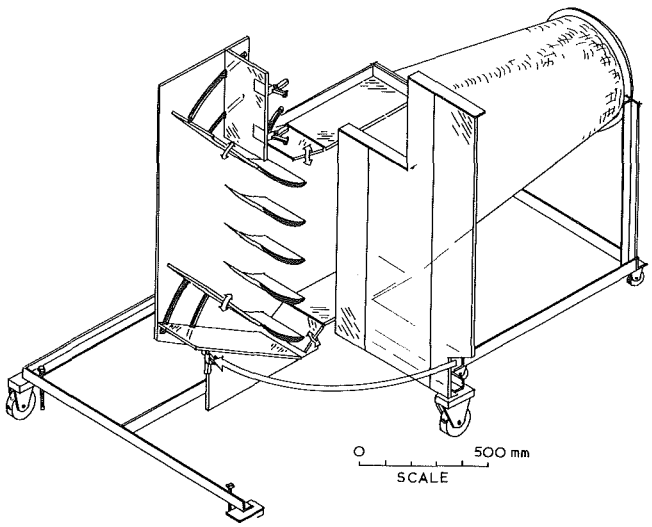

Fig. 1 Cascade test section

Test Cascade. The geometry of the cascade is summarized in Fig. 2. The blade profile corresponds to the tip section of a turbine blade of recent design; it is used here at slightly higher solidity (chord/spacing) and lower incidence than in the actual application. The blades have constant chord and no twist and were machined from solid blocks using a numerically controlled milling machine. The four outboard blades were milled from plexiglass while aluminum was used for the instrumented middle blade. The aluminum blade was made in two halves. The top half has 67 internal channels drilled spanwise around the contour of the blade. The channels were sealed at the tip of the blade and connected to flexible tubes at the other end. Fourteen rows of static taps 0.51 mm in diameter were drilled through the surface to intersect the internal channels. Each row consists of 37 taps on the pressure surface and 36 on the suction surface. The last six channels toward the trailing edge

Nomenclature

A = $(\tau/t_{max})^2 \mathrm{Re}(t_{max}/c)$ = Rains' viscous force parameter
c = blade chord length
C_F = $F/\frac{1}{2}\rho V_{CL}^2 c$ = resultant blade force coefficient
C_L = blade lift coefficient
C_P = $(P-P_{CL})/(\frac{1}{2}\rho V_{CL}^2)$ = pressure coefficient
C_X, C_Y = axial, tangential force coefficients
D = vortex diameter
F = resultant blade force
F_X, F_Y = axial, tangential blade forces
h = blade span
H = δ^*/θ = boundary layer shape factor
L = blade lift force (normal to chord line)
P = static pressure
Re = $\rho V_{CL} c/\mu$ = Reynolds number based on blade chord
s = blade spacing
t_{max} = blade maximum thickness
V = velocity
x, y, z = coordinates in the axial, tangential, and spanwise directions
x' = coordinate in chordwise direction
β = blade angle (Fig. 2)
δ = boundary layer thickness
δ^* = $\int_0^\delta (1 - V/V_e)dz$ = boundary layer displacement thickness
ρ = density
θ = $\int_0^\delta (V/V_e)(1 - V/V_e)dz$ = boundary layer momentum thickness
μ = viscosity
τ = tip gap

Subscripts

CL = undisturbed centerline value
e = boundary-layer edge value
1, 2 = cascade inlet, outlet

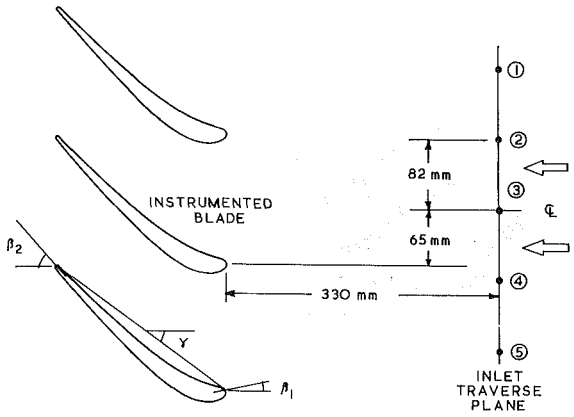

Chord length, *c*: 250 mm
Blade span, *h*: 200 mm
Blade spacing, *s*: 150 mm
Aspect ratio, *h/c*: 0.8
Solidity, *c/s*: 1.667
Stagger angle, γ: 40.5 deg
Blade inlet angle, β_1: 9.2 deg
Blade outlet angle, β_2: 53.6 deg

Fig. 2 Summary of cascade geometry

of the blade are penetrated by taps from both the suction and pressure surfaces. For taking blade pressure measurements, the blade surfaces are sealed with Monokote, a very thin, self-adhesive Mylar film, leaving just the row of taps of interest open to the flow.

The blades are held in place on the backplate by a stem and collar arrangement. The 19-mm-dia steel stems are permanently attached to the blades at about 1/3 chord. In the case of the instrumented blade, the stem is hollow and is used to bring the flexible tubes from the internal channels out of the test section. A simple fixture is used to set each blade at the desired stagger angle, to an estimated accuracy of ± 0.2 deg. The small gap between the blade and the backplate was sealed to prevent leakage.

Instrumentation. The flow field entering the cascade was measured by traversing a pitot probe from the tip to the back wall. The corresponding static pressures were obtained from wall taps located in the same streamwise plane as the pitot probe mouth. The probe is a square-mouthed circular tube with 0.81-mm outer diameter and 0.50-mm inner diameter and the probe mouth is located 19.0 mm from the probe stem which has a diameter of 3.2 mm. The position datum for the probe was determined aerodynamically at each traverse station. With wind on, the probe was moved in small steps until the mouth just contacted the wall, as evidenced by the total pressure levelling off. The displacement from the wall was then obtained from a dial indicator which measured movement of the probe stem. Based on the observed repeatability of the datum, it is estimated that the probe position, near the wall, is known to within ± 0.05 mm. For distances greater than 25 mm from the wall the accuracy of the positioning decreases to about ± 0.15 mm because of the need to reset the dial indicator.

All pressures were measured using capacitance-type differential pressure transducers. A Scanivalve connected to one of the transducers was used to collect the blade static pressures. The analogue pressure signals were converted to digital form using a Hewlett-Packard 3054A Data Acquisition and Control System. The sampling time needed to obtain reliable mean values of the pressure signals was determined experimentally: Representative probe and static pressure signals were recorded for extended periods and the cumulative mean values were then examined. It was found that for wall static and freestream total pressure measurements a sampling time of about 20 s yielded mean values which were within ± 0.2 percent of the very long time averages; for pitot probe measurements within the boundary layers about 30 s was required to obtain the same accuracy.

Smoke for flow visualization was generated by vaporizing Bay oil, a mineral oil used in the cosmetics industry. The resulting dense white smoke is nonirritating, pleasant smelling, and apparently nontoxic. The smoke was injected through the tip wall using a 0.8-mm-dia tube, at a point ½ chord length upstream of the leading edge. To facilitate photography and to avoid fouling the static taps on the instrumented blade, the second blade from the top of the cascade was used. Surface flow visualization was obtained by brushing onto the surface of interest a thin film of SAE-50 motor oil mixed with titanium dioxide pigment.

Experimental Results

Operating Conditions. All measurements and the surface flow visualization were conducted at a constant Reynolds number of $4.3 \times 10^5 \pm 2$ percent, where the Reynolds number is based on the blade chord and the undisturbed upstream velocity. The corresponding velocity was about 30 m/s. The smoke flow visualization was also tried at this condition but the density of the smoke proved to be too low for it to be readily photographed. Therefore, for the smoke pictures the Reynolds number was reduced to 1.27×10^5, about one third the full operating value. To verify that operating at this Reynolds number did not result in any significant changes in the flow field, such as separation of the blade boundary layers, selected blade loading measurements and oil flow patterns were obtained for the lower operating point. The changes were minor and are attributed to the slightly thicker endwall boundary layer observed at the lower Reynolds number.

The freestream turbulence intensity at the inlet to the test section was measured with a normal-wire hot-wire probe. The root-mean-square of the fluctuation in the longitudinal direction u' was found to be about 0.4 percent of the mean velocity.

Five shim thicknesses were used to create the clearances: 0.0, 2.39, 3.96, 5.56, and 7.16 mm, corresponding to 0.0, 0.96, 1.58, 2.22, and 2.86 percent of the blade chord. Using feeler gauges, the gap heights were found to be accurate to ± 0.2 mm. The actual blade has a nominal tip clearance of about 1.9 percent of chord. The values considered therefore roughly span the range encountered in practice under different operating conditions.

Inlet Flow Measurements. Inlet flow measurements were made in a plane 330 mm (1.32 chord lengths) upstream of the leading edge of the cascade, as indicated in Fig. 2. The upstream influence of the cascade should be slight at this plane. As mentioned earlier, total pressure distributions were obtained using the pitot probe and the corresponding static pressures were measured at the wall. No attempt was made to measure the flow angularity, which should be very small.

Seven traverse stations, spaced 82 mm apart, span the width of the test section. Very similar flow conditions were found at all stations although, as expected, the outermost stations showed some influence from the sidewalls and the corner boundary layers. Results are presented here for the five inner stations, which span the streamtube which passes through the two blade channels adjacent to the instrumented blade. Detailed boundary layer measurements were confined to the tip wall since this was the area of primary interest. However, sufficient measurements were made near the back wall to confirm that the thickness of the boundary layer there was essentially the same as at the tip wall.

The five spanwise velocity profiles are plotted in Fig. 3; the

Table 1 Inlet boundary layer parameters

	Station				
	1	2	3	4	5
δ^*/h	0.0118	0.0087	0.0084	0.0091	0.0126
θ/h	0.0075	0.0054	0.0052	0.0059	0.0084
H	1.57	1.61	1.62	1.54	1.50

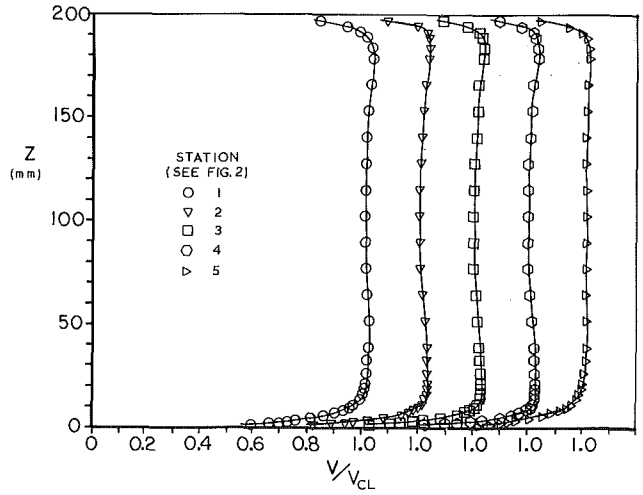

Fig. 3 Cascade inlet velocity profiles

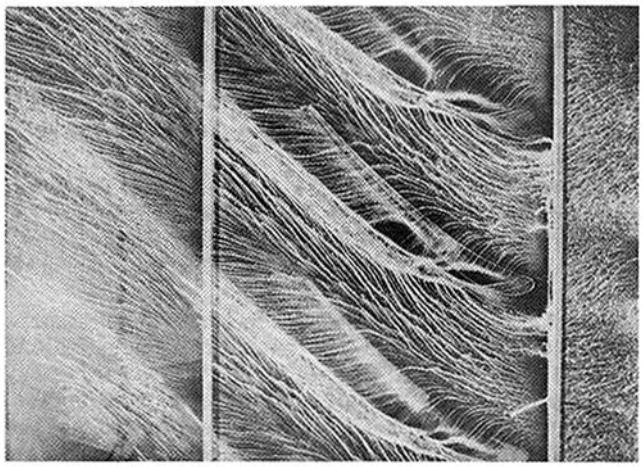

Fig. 4 Surface oil flow visualization on the tip wall for 2.86 percent clearance

traverse stations are numbered from top to bottom, as shown in Fig. 2. It will be noted that there is a small decrease in the velocity, amounting to about 3 percent of the maximum value, near midspan. This is the result of a small deficit in total pressure in the center of the flow delivered by the wind tunnel. As also seen from Fig. 3, the thickness of the endwall boundary layer was about 15 mm, or slightly more than twice the maximum tip clearance. The integral length scales and shape factors for the tip-wall boundary layer are summarized in Table 1. The shape factor values of about 1.6 indicate that the endwall boundary layer was fully turbulent; the values are slightly larger than the 1.4 typical of a zero pressure gradient turbulent boundary layer, probably because there is a small amount of diffusion in the circular-to-rectangular transition immediately upstream of the test section.

The inlet flow measurements reported here were all made with zero tip clearance. However, selected boundary layer traverses were also made for the maximum clearance and they gave essentially the same results. The results in Fig. 3 and Table 1 should therefore apply to all the cases considered.

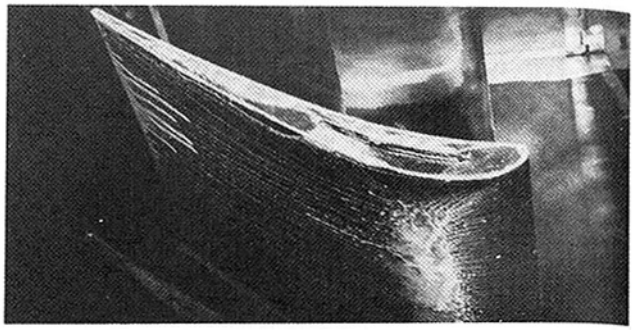

Fig. 5(*a*) Blade suction surface

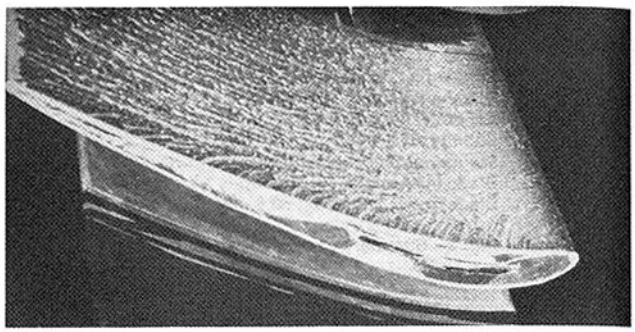

Fig. 5(*b*) Blade pressure surface

Fig. 5 Surface oil flow visualization on the blade surfaces for 2.86 percent clearance

Flow Visualization Observations. Flow visualization was conducted for 0.0, 0.96, and 2.86 percent clearance. For zero clearance the surface oil flow showed the now widely accepted picture of the endwall flow (e.g., Sjolander, 1975; Sieverding, 1985), including the strong horseshoe separation vortex generated around the leading edge of the blade. For the two values of clearance, the flow visualization patterns were similar in broad terms except that, as expected, the tip leakage structures were more clearly defined and obvious for the large clearance. Therefore, only the latter case is presented, although the main differences observed in the low clearance case will be mentioned. Additional flow visualization pictures are reproduced in Amrud (1985).

Figure 4 shows the tip wall oil flow patterns for the large clearance and Fig. 5 shows the corresponding patterns on the blade suction and pressure surfaces. Figure 6 shows a tentative interpretation of the flow structures as inferred from the oil flow. Finally, Fig. 7 shows a sample smoke flow picture along with a schematic summary of the tip-leakage flow directions obtained from a series of similar pictures for which the smoke crossed the tip at different chordwise locations. As evident from Fig. 7, the smoke diffuses too quickly to allow anything other than the broad flow patterns to be discerned.

As seen from Fig. 4, from about 10 to 50 percent of the chord length, the flow close to the tip wall is strongly turned and passes over the blade tip more or less at right angles to the camber line. On the suction side, the first 5 percent of the chord length appears to have little leakage flow emerging from the gap: There is a strong suction peak at about 20 percent of the chord and the leakage flow near the leading edge seems to be following the direction of the maximum pressure gradient over the tip. On the rearward half of the blade the flow is deflected less, consistent with the smaller pressure difference which is present there. Because of the camber of the blade and the stagger angle the net effect is nevertheless for the flow to cross the tip roughly normal to the camber line. Figure 7(*b*) shows that the flow direction for the bulk of the fluid crossing the tip is very similar to the direction of the limiting

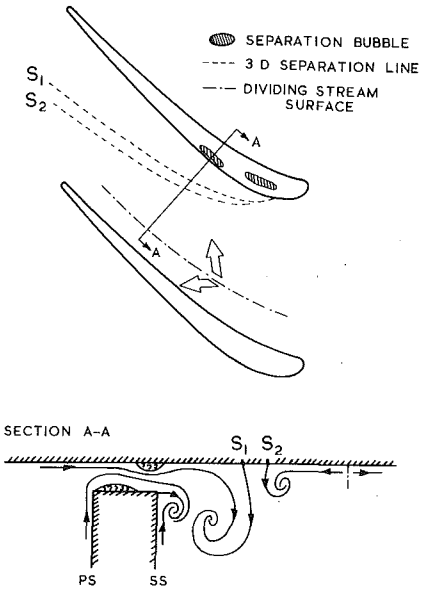

Fig. 6 Tentative interpretation of tip wall flow structures for 2.86 percent clearance

Fig. 7(*a*) Sample smoke flow picture

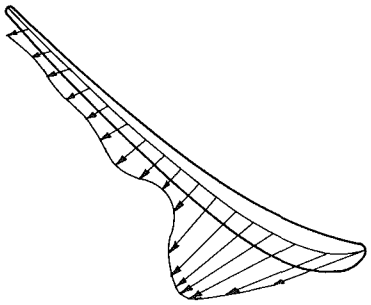

Fig. 7(*b*) Summary of smoke flow directions (vector lengths proportional to local pressure differences)

Fig. 7 Smoke flow visualization for 2.86 percent clearance

streamlines at the tip wall. There is therefore some justification for treating the flow within the gap as quasi-two-dimensional, as is done in some of the simpler leakage flow prediction methods. A few other observations relevant to such methods are worth making. Rains (1954) suggested that for $A = (\tau/t_{\max})^2 * \mathrm{Re} * (t_{\max}/c) > 125$ inertia effects would dominate over viscous forces inside the gap. Since $A = 400$ for our $\tau/c = 0.0096$ flow and $A = 3600$ for the $\tau/c = 0.0286$ flow, it is reasonable to assume that for our cases the leakage flow rate and its direction were primarily determined by the fluid inertia and the pressure forces. We observed that smoke injected within the upstream boundary layer passed over the blade tip within the first 5 to 10 percent of the chord length. The leakage flow along the rest of the blade would therefore be composed of fluid having essentially constant momentum from the blade tip to the tip wall, as determined by the upstream mainflow momentum and the acceleration or deceleration which had occurred up to that point in the blade passage. The local leakage path over the tip should then be determined by the fluid's chordwise momentum (which will change very little since the chordwise component of the pressure gradient is small) and the velocity normal to the camber line induced by the blade pressure difference. The fact that we found that our velocity vectors over the blade tip coincided closely with the direction of the maximum pressure gradient suggests that the chordwise component of momentum can be largely ignored for purposes of determining the leakage flow direction. This is most obviously the case where the pressure difference is the largest, which is also where the leakage flow will be greatest. Likewise, given the dominance of the pressure forces, it should be possible to predict the leakage flow rate from the local blade pressure difference and a suitable discharge coefficient for the tip gap. This assumption has been used, for example, in the leakage flow prediction scheme of Wadia and Booth (1982) and our experiment therefore provides some post facto support for their approach. It should however be noted that the key input to such methods is the blade loading at the tip and, as will be shown later, this loading is itself significantly affected by the leakage.

After emerging from the gap, the tip wall shear stress trajectories converge on a well-defined three-dimensional separation line, marked S_1 in Fig. 6. This is the separation line for the tip leakage vortex. It has been suggested (e.g., Graham, 1985) that for small values of clearance the leakage flow does not roll up into a vortex but simply mixes with the suction side flow after leaving the gap. Rains (1954) found this to be the case for a clearance flow in the range where viscous effects were important ($A < 12$). Our $\tau/c = 0.0096$ flow, which was outside the viscous range, certainly did not exhibit such behavior: The oil film showed an equally well-defined leakage-vortex separation line, although it was much closer to the blade since the vortex was smaller in scale. In both cases, the presence of the tip leakage vortex was also clear from the smoke flow visualization. For the large clearance the vortex starts to form at about 15 percent of the blade chord, as seen from Fig. 4. By comparison, for the $\tau/c = 0.0096$ the rollup process began much closer to the leading edge, at about 5 percent of chord. This forward shift of the starting point of the leakage vortex was also noted by Lakshminarayana and Horlock (1967) in their compressor cascade experiment.

In addition to the aspects of the flow mentioned, Fig. 4 shows a couple of features which do not appear to have been observed previously. In the first place, a second separation line further out in the blade passage is clearly evident (marked S_2 in Fig. 6). The shear stress trajectories for the cross-channel flow converge on this line and it is therefore interpreted as the separation line for the passage vortex. Between the two separation lines is a region of apparently very low wall shear stress, as indicated by the lack of movement of the oil film. The tip leakage and passage vortices do not appear to merge, presumably because of their opposite directions of rotation. In the present case, the passage vortex is undoubtedly rather small, firstly because the incoming boundary layer is thin and also because the vortex is not supplemented by the pressure-side leg of the horseshoe vortex, as would be the case for zero clearance. There is no evidence in the oil flow of separation of the incoming endwall boundary layer as it approaches the leading edge, no doubt because as the tip clearance increases the adverse pressure gradient on the endwall upstream of the leading edge becomes weaker. For $\tau/c = 0.0096$ there did appear to be a small horseshoe vortex, closer to the leading edge than for zero clearance. However, the pressure side leg of the vortex was swept back over the tip of the blade within the first 10 percent of the chord length and again did not contribute to the passage vortex. For the large clearance case (Fig. 4), it

seems clear that a significant fraction of the incoming boundary layer fluid on the pressure side of the leading edge in fact ends up passing over the blade tip and becomes incorporated in the tip-leakage vortex. The dividing stream surface between the endwall boundary layer fluid which passes over the tip and that which crosses the channel to become part of the passage vortex appear to lie at about 20 percent of the passage width, as indicated in Fig. 6.

The other new feature observed in the present work is the occurrence of more than one tip-leakage vortex. Figure 4 clearly shows two distinct structures forming above the blade tip, the first starting at about 15 percent chord, corresponding to the start of the tip leakage vortex, and the second starting at about 35 percent chord. As will be shown later, the presence of two distinct leakage vortices was strongly reflected in the suction surface pressure distributions. The appearance of multiple vortices was progressive with increasing tip clearance: For 0.96 percent clearance a single vortex was present while a third was just beginning to form for 2.86 percent. The nature of the interaction between the two leakage vortices as they progress downstream is not entirely clear. On the one hand, since they have the same direction of rotation they might be expected to merge, perhaps with the second vortex being wrapped around the first. Certainly, we were not able to distinguish separate vortices from the smoke flow visualization. However, there is evidence from the blade pressure measurements (see Fig. 9) that the second vortex remains separate for some distance downstream. Our tentative interpretation of the flow pattern is shown in Fig. 6. We believe that the fluid nearest the tip wall is indeed entrained by the first vortex; this would explain why there is only one leakage vortex separation line apparent on the tip wall. The rest of the leakage flow then rolls up to form the second vortex and in the process probably displaces the first vortex slightly away from the blade surface. As mentioned, the presence of multiple tip leakage vortices does not appear to have been observed previously. We do not know if it is a peculiarity of our cascade, although that seem unlikely since neither the geometry nor the blade loading is very unusual. Predicting the formation of these vortices will present a considerable challenge for current and future three-dimensional calculation methods. Clearly, their occurrence cannot be ignored if accurate predictions of the blade loading in the tip region are required.

A final feature is evident from the tip wall oil flow pattern. In association with the two leakage vortices, there appears to be a pair of nearly two-dimensional separation bubbles formed on the endwall above the tip as evident from the accumulation of oil. The wall flow reattaches quickly and then moves toward the final three-dimensional separation line, S_1. The intervening stretch of wall is obviously a region of very high wall shear stress since the oil and pigment has been scoured away almost completely. There is a separation bubble at the tip of the blade itself (see Fig. 5), as would be expected since the flow will be unable to turn the 90 deg corner at the edge of the pressure surface. This bubble will tend to create a convergent-divergent passage in the tip gap and it may be that a resultant adverse pressure gradient toward the outlet of the gap is the cause of the tip wall separation bubbles.

The oil flow patterns on the blade surfaces (Fig. 5) show that both sides of the blade are significantly affected by the leakage flow. On the pressure surface, the shear stress vectors are turned almost in the spanwise direction near the tip: Near the leading edge, some flow turning is evident as much as 20 mm, or about three clearance heights, from the tip. Evidently a certain amount of pressure-surface boundary-layer fluid is swept over the tip and becomes incorporated in tip leakage vortices. On the suction surface the flow is initially deflected away from the tip, but as the leakage vortices begin to roll up, flow toward the tip is induced. In addition to inducing spanwise flow, it seems likely that the tip leakage vortices will entrain some of the suction surface boundary layer fluid.

It is clear from the smoke pictures such as Fig. 7(*a*) that the tip-leakage vortex affects a very substantial part of the flow in the blade passage. Taking the smoke-filled region to define the extent of the vortex, the size of the vortex was scaled from the smoke pictures. Assuming the structure to be axisymmetric, the width normal to the axis of the vortex is taken as its "diameter" D. For 2.86 percent clearance, the diameter of the vortex as it reached the trailing edge of the blade was about 52 mm, or about 7.2 times the tip gap; for 0.96 percent the corresponding values were about 25 mm and 10.5. For the large clearance, the vortex thus occupied more than half the passage width in the pitchwise plane at the trailing edge. A knowledge of the size of the tip-leakage vortex is useful since, given an estimate of the associated circulation, it allows the crossflows to be predicted. Rains (1954) derived an approximate expression for the vortex diameter, neglecting tip-wall motion and cascade solidity effects and assuming constant loading along the length of the blade. For the trailing edge plane this expression can be written

$$\frac{D}{\tau} = 0.155\left(\left(\frac{c}{\tau}\right)(4+C_L)^{1/2}C_L^{1/2}\right)^{0.85} \tag{1}$$

where C_L is the lift coefficient at the tip of the blade. This relationship is also used in the more elaborate model of Laksminarayana (1970). For the large clearance, equation (1) predicts a D/τ of about 7.3 and for the small clearance about 19. Thus, while Lakshminarayana reported good results for his compressor cases, it appears from the present experiment that Rains' expression must be used with some caution.

Blade Loading Measurements. Preliminary measurements showed that, as expected, the blade pressures varied slowly on the pressure surface and away from the tip generally. Therefore, to save time the final measurements were made at only 8 or 9 of the 14 rows of taps and at 54 of the 73 taps in a given row. Trials showed that for a particular configuration the pressure coefficient at a given tap was repeatable to within ± 0.02. Late in the study, the tip gap was reset to the maximum value and selected measurements were repeated. It was found that near a suction peak the pressure coefficient differed from earlier measurements by up to 0.1, although for most of the taps agreement was considerably better. Since the pressure coefficient varies over a range of 5.0 the uncertainties in individual values are comparatively unimportant.

Although blade loading measurements were made for all five values of the clearance, only those for the maximum gap will be presented in detail. For zero clearance some unloading, corresponding to about 10 percent of the midspan force coefficient, occurred near the tip wall, presumably because of endwall boundary layer effects. The measured midspan force coefficient C_F is 1.77 and will be referred to as the two-dimensional value, although it is recognized that there are probably some three-dimensional effects present at midspan due to the low aspect ratio of the blade. The corresponding C_P distribution is included for reference in Figs. 8 and 10.

Figure 8 shows the blade loading near the tip for 2.86 percent clearance. On the pressure side, the effect of the leakage flow is minor until very close to the tip where some unloading occurs. By comparison, on the suction surface the magnitude and locations of the suction peaks are very substantially altered. For row 1 (2 mm from the tip), two suction peaks are clearly evident at about 20 and 60 percent of chord and a third is just beginning to appear at about 75 percent. These peaks are of course attributable to the multiple tip leakage vortices observed in the flow visualization. It is also clear that near the tip the leakage vortices have the effect of eliminating the basic airfoil suction peak, which occurs at about 5 percent of chord.

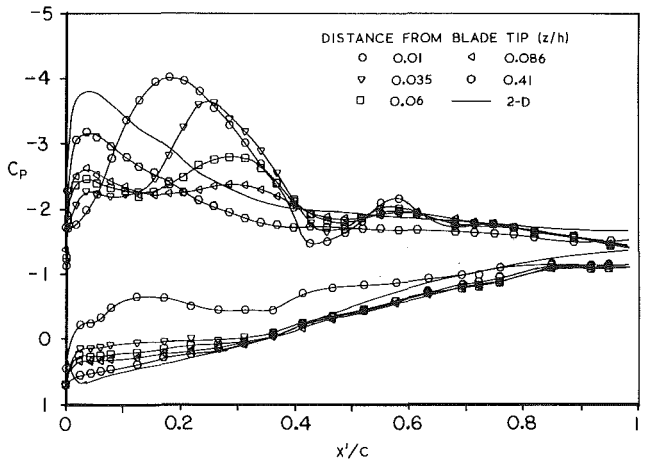

Fig. 8 Blade pressure distributions for 2.86 percent clearance

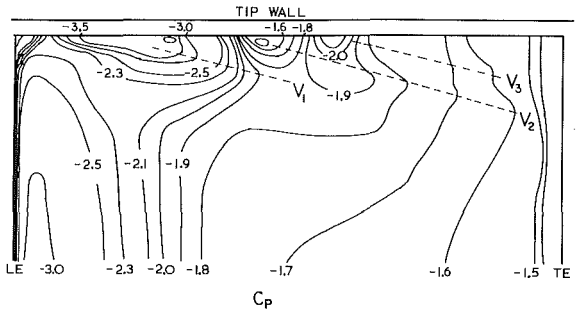

Fig. 9 Blade suction surface static pressure contours for 2.86 percent clearance

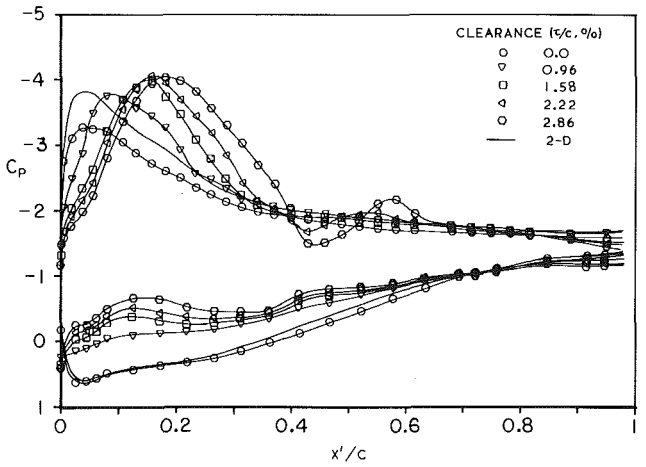

Fig. 10 Variation of blade pressure distributions with clearance ($z/n = 0.01$)

In short, the tip region pressure distributions differ considerably from the two-dimensional distribution and thus any leakage flow predictions based on the latter are likely to lead to erroneous results for both the magnitude of the leakage and its distribution along the blade chord.

Away from the tip, the vortex-induced suction peaks move rearward since the centerline of the vortex must be at an angle to the blade tip in order to accommodate its increase in diameter. This effect is more clearly brought out in Fig. 9 which shows the suction side static pressure contours. The three suction ridges, marked V_1, V_2, and V_3, are seen to be inclined to the tip at an angle of about 14 or 15 deg; this is close to the tip vortex inclination of about 12 deg which Lakshminarayana and Horlock (1967) observed in their compressor cascade. The fact that three separate vortex "tracks" are observable suggests that the downstream vortices retain

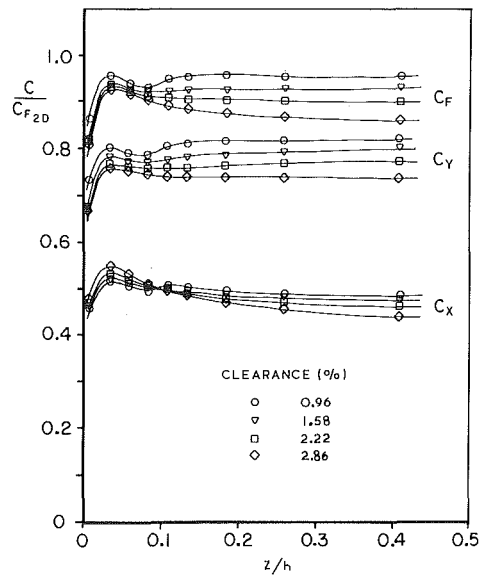

Fig. 11 Variation of resultant, tangential, and axial force coefficients with clearance

their separate identities rather than immediately merging with the first vortex to form a single composite tip-leakage vortex. Figure 9 also indicates the spanwise extent of the influence of the leakage flow: Significant distortion of the pressure contours is seen to occur for about 6 to 8 gap heights away from the tip.

The development of the tip flow with increasing gap is illustrated in Fig. 10 which shows the pressure distributions for row 1 for all the clearances considered. As noted earlier, the start of the first tip-leakage vortex moves rearward with increasing gap and this is reflected in the location of the primary suction peak. The progressive appearance of the second and third vortices is also clear from the pressure distributions: A second suction peak is just discernible for 1.58 percent clearance and it increases in strength as the clearance is increased, while the third peak is just beginning to appear for 2.86 percent clearance.

Finally, to quantify the loading changes due to tip leakage the chordwise pressure distributions were integrated to obtain axial, tangential and resultant force coefficients. The pressure was assumed to vary linearly from tap to tap and to act on a flat panel defined by the coordinates of the two taps. No attempt was made to interpolate a stagnation point or to extrapolate the pressure distributions to the trailing edge. The results are therefore somewhat approximate and it is difficult to estimate the uncertainty. We feel that with the combined effect of the uncertainty in the individual pressures and the approximate integration scheme, the absolute force coefficients probably are accurate to about ± 0.05 at best. The results are normalized on the midspan force coefficient ($C_F = 1.77$).

Figure 11 shows that as the clearance increases the midspan loading of the blade is reduced; this is presumably the result of lower incidence induced by the increasingly strong leakage vortices in an effect analogous to the downwash which occurs for wings of finite span. However, the loading rises again toward the blade tip due to the strong suction peaks produced locally by the leakage vortices. Only at the last row of taps, where significant unloading on the pressure surface was beginning to occur, does the resultant force begin to drop again. For 2.86 percent clearance, the force coefficient has a peak value about 9 percent larger than its midspan value. The lower curves on Fig. 11 show the axial and tangential components of the force coefficient. It is evident that as the force increases toward the tip the force vector is also rotated toward the axial

direction since the increase occurs mainly in the axial component. This implies that little practical benefit would be derived from the higher blade loading induced by the leakage vortices: There would be a small increase in the torque developed by the rotor but a proportionately larger increase in the axial thrust. The latter effect is clearly connected with the tip leakage losses, representing a form of pressure drag or induced drag. In their compressor cascade, Lakshminarayana and Horlock (1967) observed a rise in the normal force coefficient of similar magnitude to the rise in resultant force coefficient observed here. However, they did not present the components of the force.

Conclusions

The present experiment shows that tip leakage flow is, if anything, even more complex than was already suspected. Furthermore, it is clear that many questions remain to be answered experimentally, such as the influence of the inlet boundary layer thickness, the effect of the blade geometry and loading distribution, and of course the effect of relative motion by the tip wall. Recognizing then that ours is a particular case and that the flow patterns observed may not be universal, the picture which emerged is briefly summarized.

The interaction of the blade and the endwall boundary layer is significantly affected by the presence of the clearance. The classic horseshoe vortex separation was found to be present, in a diminished form, only for the smallest gap and even in this case the pressure-side leg of the vortex was swept over the blade tip to become part of the leakage vortex. The endwall boundary layer fluid which was swept across the passage did roll up to form a passage vortex. This vortex appeared to remain separate from the vortices formed by the tip-leakage flow. Within the tip gap the leakage flow appeared to follow closely the direction of the maximum pressure gradient and the velocity vectors at a given station were roughly coplanar. After emerging from the gap the leakage flow began to roll up into a vortex whose starting point moved rearward with increasing clearance. A new feature noted was that more than one discrete leakage vortex was formed at the larger clearances. The vortices retained their individual identities and resulted in multiple suction peaks on the suction side of the blade. The reduction in pressure induced by the leakage vortices on the suction side was larger than the reduction in pressure occurring simultaneously on the pressure side, with the net result that there was a rise in blade force as the tip was approached. It was found that the rise occurred primarily in the axial component of the force.

It is felt that the present study has given new insights into the nature of the tip leakage flow and its effects on the blade loading. Additional measurements are currently being made to document the gap flow and its subsequent development. When they are completed the experiment should form a suitable and challenging test case for the fully three-dimensional viscous calculation methods which are currently being developed.

Acknowledgments

Financial support for this study provided by the Natural Sciences and Engineering Research Council of Canada under Grant A1671 is gratefully acknowledged. Support for the second author through an NSERC Postgraduate Scholarship is also acknowledged. Numerous useful discussions were held with Dr. S. H. Moustapha of Pratt and Whitney Canada.

References

1 Amrud, K. K., 1985, "Tip Leakage in a Planar Cascade of Turbine Blades," M.Eng. Thesis, Department of Mechanical and Aeronautical Engineering, Carleton University, Ottawa, Canada.

2 Booth, T. C., Dodge, P. R., and Hepworth, H. K., 1982, "Rotor-Tip Leakage: Part I – Basic Methodology," ASME JOURNAL OF ENGINEERING FOR POWER, Vol. 104, pp. 154–161.

3 Davino, R. M., and Lakshminarayana, B., 1982, "Characteristics of Mean Velocity in the Tip Region of Turbomachinery Rotor Exit," *AIAA Journal*, Vol. 20, No. 4, pp. 528–535.

4 Graham, J. A. H., 1985, "Investigation of a Tip Clearance Cascade in a Water Analogy Rig," ASME Paper No. 85-IGT-65.

5 Hah, C., 1985, "A Numerical Modeling of Endwall and Tip-Clearance Flow of an Isolated Compressor Rotor," ASME Paper No. 85-GT-116.

6 Kacker, S. C., and Okapuu, U., 1982, "A Mean Line Prediction Method for Axial Flow Turbine Efficiency," ASME JOURNAL OF ENGINEERING FOR POWER, Vol. 104, No. 1, pp. 111–119.

7 Koch, C. C., and Smith, L. H., Jr., 1976, "Loss Sources and Magnitudes in Axial-Flow Compressors," ASME JOURNAL OF ENGINEERING FOR POWER, Vol. 98, No. 3, pp. 411–419.

8 Lakshminarayana, B., 1970, "Methods of Predicting the Tip Clearance Effects in Axial Flow Turbomachinery," ASME *Journal of Basic Engineering*, pp. 467–480.

9 Lakshminarayana, B., and Horlock, J. H., 1963, "Tip-Clearance Flow and Losses for an Isolated Compressor Blade," ARC R&M No. 3316.

10 Lakshminarayana, B., and Horlock, J. H., 1967, "Leakage and Secondary Flows in Compressor Cascades," ARC R&M No. 3483.

11 Moore, J., Moore, J. G., and Timmis, P. H., 1984, "Performance Evaluation of Centrifugal Compressor Impellers Using Three-Dimensional Viscous Flow Calculations," ASME JOURNAL OF ENGINEERING FOR GAS TURBINES AND POWER, Vol. 106, No. 2, pp. 475–481.

12 Pandya, A., and Lakshminarayana, B., 1983, "Investigation of the Tip Clearance Flow Inside and at the Exit of a Compressor Rotor Passage – Part I: Mean Velocity Field," ASME JOURNAL OF ENGINEERING FOR POWER, Vol. 105, pp. 1–12.

13 Phillips, W. R. C., and Head, M. R., 1980, "Flow Visualization in the Tip Region of a Rotating Blade Row," *International Journal of the Mechanical Sciences*, Vol. 22, pp. 495–521.

14 Rains, D. A., 1954, "Tip Clearance Flows in Axial Flow Compressors and Pumps," Report No. 5, Hydrodynamics and Mechanical Engineering Laboratories, California Institute of Technology.

15 Sieverding, C. H., 1985, "Recent Progress in the Understanding of Basic Aspects of Secondary Flows in Turbine Blade Passages," ASME JOURNAL OF ENGINEERING FOR GAS TURBINES AND POWER, Vol. 107, No. 2, pp. 248–257.

16 Sjolander, S. A., 1975, "The Endwall Boundary Layer in an Annular Cascade of Turbine Nozzle Guide Vanes," Tech. Report ME/A 75-4, Department of Mechanical and Aeronautical Engineering, Carleton University, Ottawa, Canada.

17 Wadia, A. R., 1985, "Numerical Solution of Two- and Three-Dimensional Rotor Tip Leakage Models," *AIAA Journal*, Vol. 23, No. 7, pp. 1061–1069.

18 Wadia, A. R., and Booth, T. C., 1982, "Rotor-Tip Leakage: Part II – Design Optimization Through Viscous Analysis and Experiment," ASME JOURNAL OF ENGINEERING FOR POWER, Vol. 104, pp. 163–169.

direction since the increase occurs mainly in the axial component. This implies that little practical benefit would be derived from the higher blade loading induced by the leakage vortices: There would be a small increase in the torque developed by the rotor but a proportionately larger increase in the axial thrust. The latter effect is clearly connected with the tip leakage losses, representing a form of pressure drag or induced drag. In their compressor cascade, Lakshminarayana and Horlock (1967) observed a rise in the normal force coefficient of similar magnitude to the rise in resultant force coefficient observed here. However, they did not present the components of the force.

Conclusions

The present experiment shows that tip leakage flow is, if anything, even more complex than was already suspected. Furthermore, it is clear that many questions remain to be answered experimentally, such as the influence of the inlet boundary layer thickness, the effect of the blade geometry and loading distribution, and of course the effect of relative motion by the tip wall. Recognizing then that ours is a particular case and that the flow patterns observed may not be universal, the picture which emerged is briefly summarized.

The interaction of the blade and the endwall boundary layer is significantly affected by the presence of the clearance. The classic horseshoe vortex separation was found to be present, in a diminished form, only for the smallest gap and even in this case the pressure-side leg of the vortex was swept over the blade tip to become part of the leakage vortex. The endwall boundary layer fluid which was swept across the passage did roll up to form a passage vortex. This vortex appeared to remain separate from the vortices formed by the tip-leakage flow. Within the tip gap the leakage flow appeared to follow closely the direction of the maximum pressure gradient and the velocity vectors at a given station were roughly coplanar. After emerging from the gap the leakage flow began to roll up into a vortex whose starting point moved rearward with increasing clearance. A new feature noted was that more than one discrete leakage vortex was formed at the larger clearances. The vortices retained their individual identities and resulted in multiple suction peaks on the suction side of the blade. The reduction in pressure induced by the leakage vortices on the suction side was larger than the reduction in pressure occurring simultaneously on the pressure side, with the net result that there was a rise in blade force as the tip was approached. It was found that the rise occurred primarily in the axial component of the force.

It is felt that the present study has given new insights into the nature of the tip leakage flow and its effects on the blade loading. Additional measurements are currently being made to document the gap flow and its subsequent development. When they are completed the experiment should form a suitable and challenging test case for the fully three-dimensional viscous calculation methods which are currently being developed.

Acknowledgments

Financial support for this study provided by the Natural Sciences and Engineering Research Council of Canada under Grant A1671 is gratefully acknowledged. Support for the second author through an NSERC Postgraduate Scholarship is also acknowledged. Numerous useful discussions were held with Dr. S. H. Moustapha of Pratt and Whitney Canada.

References

1 Amrud, K. K., 1985, "Tip Leakage in a Planar Cascade of Turbine Blades," M.Eng. Thesis, Department of Mechanical and Aeronautical Engineering, Carleton University, Ottawa, Canada.

2 Booth, T. C., Dodge, P. R., and Hepworth, H. K., 1982, "Rotor-Tip Leakage: Part I – Basic Methodology," ASME JOURNAL OF ENGINEERING FOR POWER, Vol. 104, pp. 154–161.

3 Davino, R. M., and Lakshminarayana, B., 1982, "Characteristics of Mean Velocity in the Tip Region of Turbomachinery Rotor Exit," *AIAA Journal*, Vol. 20, No. 4, pp. 528–535.

4 Graham, J. A. H., 1985, "Investigation of a Tip Clearance Cascade in a Water Analogy Rig," ASME Paper No. 85-IGT-65.

5 Hah, C., 1985, "A Numerical Modeling of Endwall and Tip-Clearance Flow of an Isolated Compressor Rotor," ASME Paper No. 85-GT-116.

6 Kacker, S. C., and Okapuu, U., 1982, "A Mean Line Prediction Method for Axial Flow Turbine Efficiency," ASME JOURNAL OF ENGINEERING FOR POWER, Vol. 104, No. 1, pp. 111–119.

7 Koch, C. C., and Smith, L. H., Jr., 1976, "Loss Sources and Magnitudes in Axial-Flow Compressors," ASME JOURNAL OF ENGINEERING FOR POWER, Vol. 98, No. 3, pp. 411–419.

8 Lakshminarayana, B., 1970, "Methods of Predicting the Tip Clearance Effects in Axial Flow Turbomachinery," ASME *Journal of Basic Engineering*, pp. 467–480.

9 Lakshminarayana, B., and Horlock, J. H., 1963, "Tip-Clearance Flow and Losses for an Isolated Compressor Blade," ARC R&M No. 3316.

10 Lakshminarayana, B., and Horlock, J. H., 1967, "Leakage and Secondary Flows in Compressor Cascades," ARC R&M No. 3483.

11 Moore, J., Moore, J. G., and Timmis, P. H., 1984, "Performance Evaluation of Centrifugal Compressor Impellers Using Three-Dimensional Viscous Flow Calculations," ASME JOURNAL OF ENGINEERING FOR GAS TURBINES AND POWER, Vol. 106, No. 2, pp. 475–481.

12 Pandya, A., and Lakshminarayana, B., 1983, "Investigation of the Tip Clearance Flow Inside and at the Exit of a Compressor Rotor Passage – Part I: Mean Velocity Field," ASME JOURNAL OF ENGINEERING FOR POWER, Vol. 105, pp. 1–12.

13 Phillips, W. R. C., and Head, M. R., 1980, "Flow Visualization in the Tip Region of a Rotating Blade Row," *International Journal of the Mechanical Sciences*, Vol. 22, pp. 495–521.

14 Rains, D. A., 1954, "Tip Clearance Flows in Axial Flow Compressors and Pumps," Report No. 5, Hydrodynamics and Mechanical Engineering Laboratories, California Institute of Technology.

15 Sieverding, C. H., 1985, "Recent Progress in the Understanding of Basic Aspects of Secondary Flows in Turbine Blade Passages," ASME JOURNAL OF ENGINEERING FOR GAS TURBINES AND POWER, Vol. 107, No. 2, pp. 248–257.

16 Sjolander, S. A., 1975, "The Endwall Boundary Layer in an Annular Cascade of Turbine Nozzle Guide Vanes," Tech. Report ME/A 75-4, Department of Mechanical and Aeronautical Engineering, Carleton University, Ottawa, Canada.

17 Wadia, A. R., 1985, "Numerical Solution of Two- and Three-Dimensional Rotor Tip Leakage Models," *AIAA Journal*, Vol. 23, No. 7, pp. 1061–1069.

18 Wadia, A. R., and Booth, T. C., 1982, "Rotor-Tip Leakage: Part II – Design Optimization Through Viscous Analysis and Experiment," ASME JOURNAL OF ENGINEERING FOR POWER, Vol. 104, pp. 163–169.

DISCUSSION

R. G. Williamson[1]

The paper presents detailed information on tip leakage phenomena in a stationary cascade, and the authors are to be congratulated on their careful approach. With this work as a base, it is natural to ask how the inferred vortex structures would be affected by relative movement between the tip and the casing. Clearly, the interpretation of Fig. 6, with stagnation lines on the casing, could no longer be valid, and the presence of multiple vortices might be questioned.

Some corroborative evidence for multiple tip vortices in a rotating blade environment is afforded by the flow visualization photograph presented as Fig. 14 of [19]. Rotor 51 blading clearly shows two dark streaks near the blade tip. Measurements of these surface markings, and a tentative interpretation of the associated multiple vortex structure, are contained in [20], and reproduced here as Figs. 12 and 13. The diameter of the main vortex structure at the trailing edge was estimated as about 10 mm (0.4 in.), or about eight times the tip gap, which correlates well with the measurements of Sjolander

[1]Division of Mechanical Engineering, National Research Council Canada, Ottawa, Canada K1A OR6.

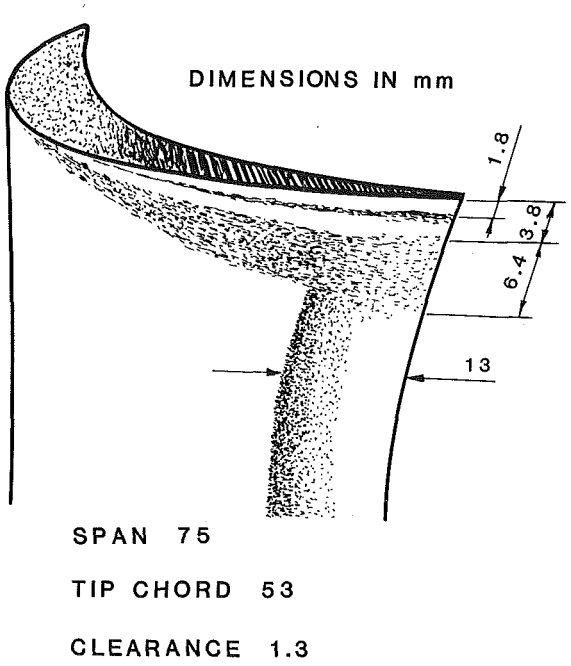

Fig. 12 Flow visualization on rotor blade

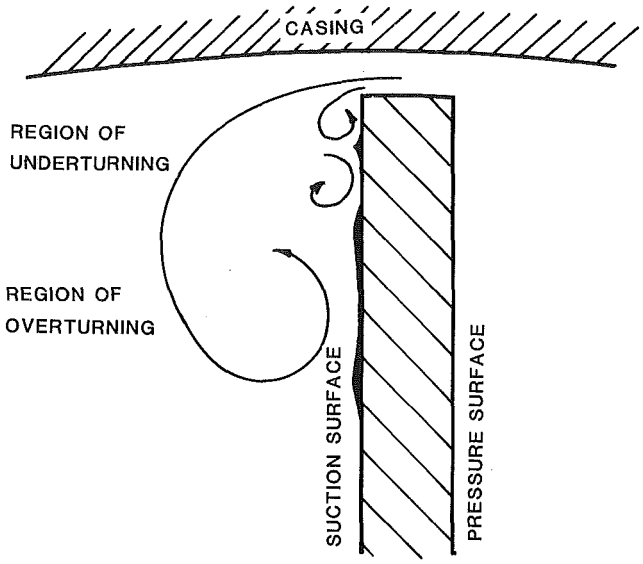

Fig. 13 Possible flow pattern near blade tip

and Amrud. Flow turning of the rotor blade was affected over the outer 20 percent of the span (15 mm or 0.6 in.). It is noted that these data involved a tip clearance of 1.3 mm (0.050 in.), and that the measurements presented in [19] refer to a later build with 1.8 mm (0.070 in.) tip clearance. There is some evidence that the size of the vortex structure increased approximately in proportion to tip clearance. Further work is planned.

References

19 Moustapha, S. H., Okapuu, U., and Williamson, R. G., "Influence of Rotor Blade Aerodynamic Loading on the Performance of a Highly Loaded Turbine Stage," ASME JOURNAL OF TURBOMACHINERY, this issue.

20 Williamson, R. G., "NRC/P&WC Highly Loaded Turbine. Report No. 2: Completion of Performance Mapping—Initial Build," (Company Confidential), NRC LTR-GD-71, June 1982.

Development of an Experimental Correlation for Transonic Turbine Flow

F. Martelli
Professor.

A. Boretti
Research Fellow.

Department of Energetics,
University of Florence,
50139 Firenze, Italy

Optimization of transonic turbine bladings over a broad range of operating conditions calls for better understanding of the relationship between blade profile loss and cascade geometric parameters. In fact, many of the experimental correlations published to date have failed to take into due consideration transonic effects, while others have considered far too few of the numerous geometric parameters affecting profile loss in transonic flows. Through examination of the experimental data gathered by some 20 authors regarding the effects of the most significant blading geometric parameters on profile losses, a loss correlation procedure has been developed. The procedure is especially advantageous in that it allows continuous updating as new experimental data become available.

Introduction

Determination of profile losses in transonic turbine cascades is best implemented via a correlative approach affording the same rapidity and ease as required by through-flow calculations. Using such an approach, profile loss is expressed as a function of only some of the experimentally derived cascade parameters. These results are especially convenient in the preliminary design stage since knowing profile losses in relation to certain key parameters allows determination of geometries capable of minimizing these losses with minimum calculation effort.

The theoretical approach proposed in [1] has been adopted in the present analysis in order to be able to complete the data body necessitated by the correlative approach. In percentage terms, 30 percent of total data have been derived theoretically, while the remaining 70 percent have been obtained experimentally.

Profile Loss

Transonic flow profile losses may be thought of as being composed of three constituents (one basic profile and two shock profile components) of different origins, whose relative importance and evolution in relation to exit flow conditions significantly vary with changes in blading parameters. The basic profile loss originates when a boundary layer develops along the blade surface, thereby giving rise to dissipation in the blade wake. The shock profile losses, on the other hand, are caused by the trailing edge shock waves produced when two supersonic jets meet up at trailing edge. The shock wave on the pressure-surface side traverses the blade passage until reaching the adjacent blade's suction side where it then reflects off the solid boundary. Two shock profile losses result. The first develops across the trailing edge shock waves, while the second is produced by interaction of the pressure-surface trailing edge shock waves with the suction-surface boundary layer. (A more complete description of this process is detailed in [1].)

The following assumptions are applicable to all three loss constituents:

(*a*) Both basic profile and shock profile losses are proportional to the profile loss x_i calculated for incompressible flow.

(*b*) The sum of the three proportionality coefficients x_c can be obtained from an experimental cascade flow analysis as a function of the exit Mach number M_2 for similar blades.

(*c*) The distribution of x_c in relation to M_2 depends on blade type (impulse, reaction, or nearly flat), as well as on the following cascade parameters:

1 Trailing edge thickness (te/g)
2 Blade suction-side curvature
3 Blade turning angle:
$\Delta a = 180 - (a_1 + a_2^*)$, where $a_2^* = \arcsin\ (o/g)$
4 Ratio of blade channel divergence downstream of the throat area (A/A^*).

As this is only valid for convergent-divergent cascades, profile loss for transonic blades thus becomes:

$$x = x_i \cdot x_c \tag{1}$$

Incompressible Flow Profile Loss

Figure 1 shows the cascade notations used in the analysis. Incompressible flow profile loss is dependent upon three factors: the flow acceleration in the blade passage, the pitch-to-chord ratio, and the trailing edge thickness. The blade passage flow acceleration is clearly represented by the degree of blade passage convergence per centerline unit. The convergence gradient [11] is approximately given by

$$G = (o^* - o)/l^* \tag{2}$$

If, on the other hand, the plane cascade is replaced by a uniformly converging duct, the result is a linear variation of

Contributed by the Gas Turbine Division of THE AMERICAN SOCIETY OF MECHANICAL ENGINEERS and presented at the 31st International Gas Turbine Conference and Exhibit, Düsseldorf, Federal Republic of Germany, June 8-12, 1986. Manuscript received at ASME Headquarters January 20, 1986. Paper No. 86-GT-108.

the surface velocities along the centerline. This kind of velocity distribution is adopted in the Truckenbrodt integral equation [8] in which determination of momentum thickness (turbulent boundary layer) serves to obtain the nondimensionalized boundary layer parameters in relation to the pitch-to-chord ratio and the flow acceleration parameter [7, 10]. The kinetic energy loss coefficient resulting from a momentum analysis can be expressed as a function of these magnitudes, as well as of the trailing edge thickness-to-pitch ratio.

The incompressible flow profile loss can hence be calculated using the following empiric relation

$$x_i = K_1(o/cf(o/o^*) - te/cf(o/o^*) - K_2)^{-1} + K_3 te/o \tag{3}$$

where

$$f(o/o^*) = ((1-(o/o^*)^{e_1})/(1-o/o^*))^{e_2} \tag{4}$$

For high deflection blades ($\Delta a \geq 65$) use

$$K_1 = 7.785 \times 10^{-3} \tag{5a}$$
$$K_2 = 4.900 \times 10^{-3} \tag{5b}$$
$$K_3 = 0.1 \tag{5c}$$
$$e_1 = 4.5714 \tag{5d}$$
$$e_2 = 0.7778 \tag{5e}$$

while, for nearly flat blades, use

$$K_1 = 9.342 \times 10^{-3} \tag{6a}$$
$$K_2 = 5.880 \times 10^{-3} \tag{6b}$$
$$K_3 = 0.1 \tag{6c}$$
$$e_1 = 4.5 \tag{6d}$$
$$e_2 = -0.8 \tag{6e}$$

When $g \sin(a_1)$ exceeds o^*, o/o^* is replaced by $o/g \sin(a_1)$.

In the case of nozzles use

$$K_1 = 4.5 \times 10^{-3} \tag{7a}$$
$$K_2 = 2.8 \times 10^{-3} \tag{7b}$$
$$K_3 = 0.1 \tag{7c}$$
$$f(o/o^*) = 1.0 \tag{7d}$$

The effect of the Reynolds number for values other than 10^6 and surface roughness not standard finish can be considered by introducing a loss corrective factor dependent upon the Reynolds number and grain size [2].

Compressibility Coefficient

The compressibility coefficient is given as the sum of several terms

$$x_c = S_1 + S_2 + S_3 \tag{8}$$

where each term is dependent upon M_2. S_1 is the compressibility factor for blades having well-defined cascade parameters that do not exert special effects; the S_2 and S_3 terms are introduced in order to account for these effects.

Most of the data used to plot the impulse, reaction, and nearly flat-blade S_1, S_2, S_3 coefficient curves illustrated in Figs. 2–9 were obtained from recently published experimental results [15–34], with additional data being furnished by the method described in [1]. A breakdown by blade type follows:

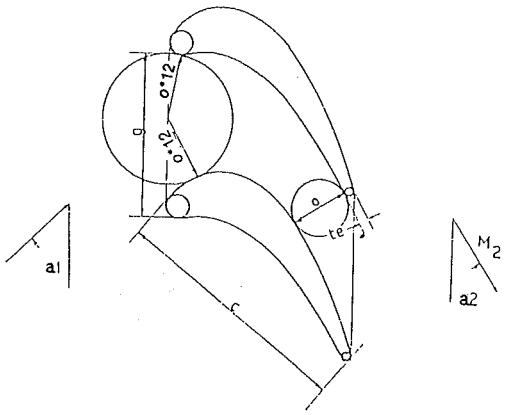

Fig. 1 Cascade notations

(a) Impulse Blades ($x_c = S_1 + S_2$). The distribution of x_c in relation to M_2 for this type of blade can be obtained as the sum of the two terms resulting from linear interpolation between the curves in Figs. 2 (showing the S_1 compressibility coefficient for blades having a trailing edge thickness-to-pitch ratio smaller than 0.04) and 3 (showing the S_2 compressibility coefficient increment introduced to account for trailing edges over 0.04).

(b) Reaction Blades ($x_c = S_1 + S_2$). In this type, blade suction-side curvature considerably affects profile loss. As a result, reaction blades may be classified as one of two types:

1 With a slightly convex rear suction side and gradual variation in curvature radius (the S_1 compressibility coefficient appears in Fig. 4).

2 With a straight rear suction side and marked variation in curvature radius. (The S_1 compressibility coefficient for blades with a trailing edge thickness-to-pitch ratio smaller than 0.035 is shown in Fig. 5; the S_2 compressibility coefficient increment for thicker trailing edges, in Fig. 6.)

Note that blades having a strongly convex rear suction side have not been considered since total flow separation at supersonic exit Mach numbers is so sudden and strong as to make experimental correlation an overly burdensome task.

(c) Nearly Flat Blades ($x_c = S_1 + S_2 + S_3$). The distribution of x_c in relation to M_2 is presented for both convergent and convergent-divergent cascades. (The S_1 compressibility coefficient for blades with trailing edge thickness-to-pitch ratios lower than 0.02 and a unitary area ratio, i.e., convergent cascades, is shown in Fig. 7; the S_2 coefficient increment for blades with a trailing edge thickness greater than 0.02, in Fig. 8; and the S_3 compressibility coefficient increment for convergent-divergent cascades in relation to the

Nomenclature

a = flow angle
A = channel area at trailing edge
A^* = throat area
c = chord
e = standard deviation
g = pitch
K = sand grain size
l^* = centerline length between inlet and exit throat areas
m = mean
M = Mach number
o^* = inlet passage
o = exit throat area
Re = Reynolds number
te = trailing edge thickness
x = kinetic energy loss coefficient

Subscripts

c = compressible
e = experimental
i = incompressible
t = theoretical
1 = inlet
2 = exit

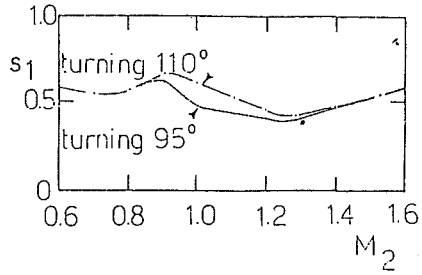

Fig. 2 Compressibility coefficient

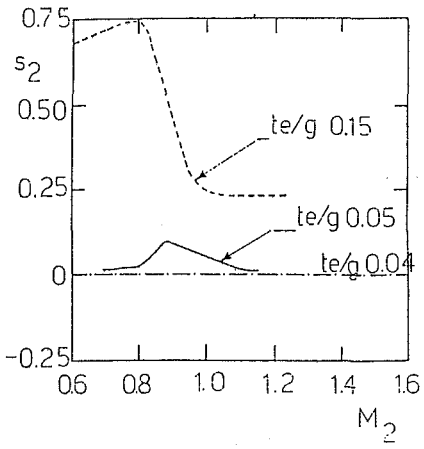

Fig. 3 Compressibility coefficient

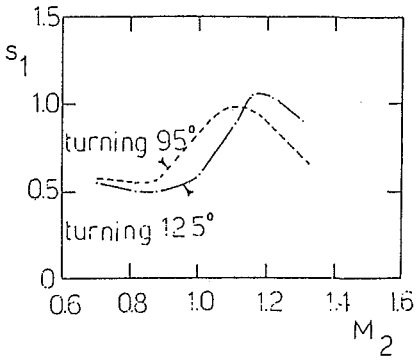

Fig. 4 Compressibility coefficient

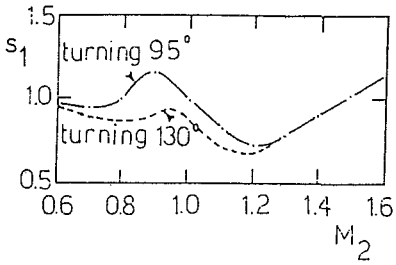

Fig. 5 Compressibility coefficient

blade channel divergence ratio downstream of the throat area, in Fig. 9.)

Results

The above correlation method was compared to an earlier one proposed by Alim [10] for 35 of the 41 convergent cascades that served to create the data body for the profile loss correlation. In order to properly evaluate the benefit of the correlation method, the profile loss versus exit Mach number

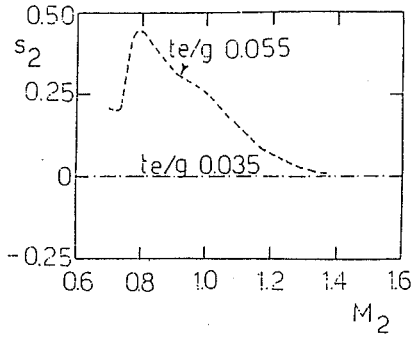

Fig. 6 Compressibility coefficient

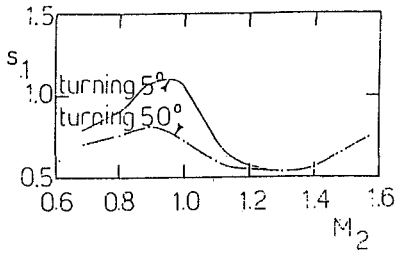

Fig. 7 Compressibility coefficient

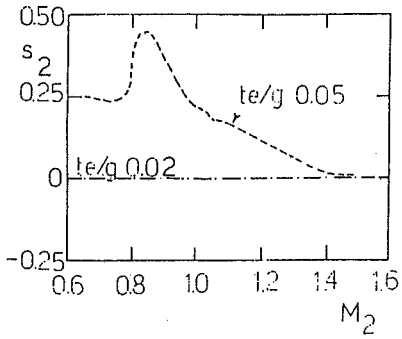

Fig. 8 Compressibility coefficient

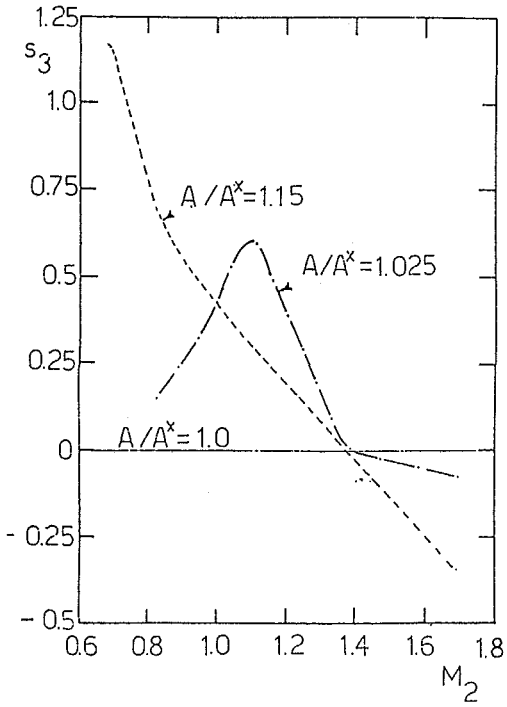

Fig. 9 Compressibility coefficient

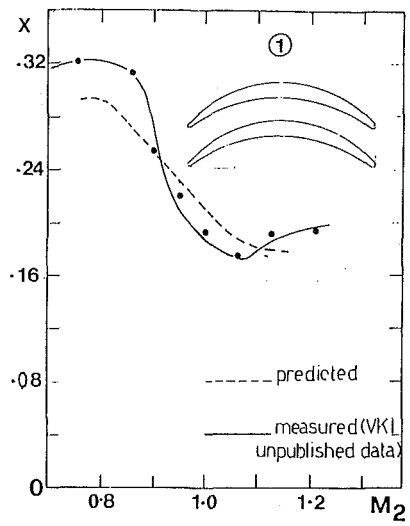

Fig. 10 Comparison of predicted and measured losses: impulse blade

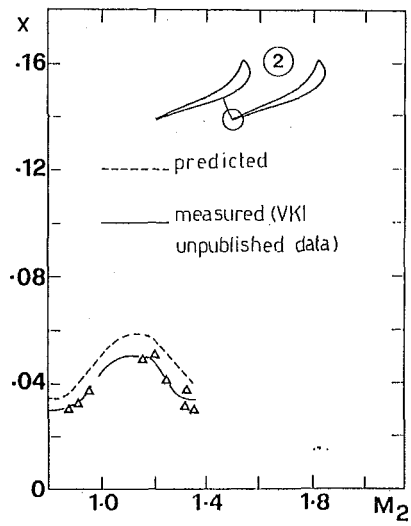

Fig. 11 Comparison of predicted and measured losses: reaction blade

curves were discretized on the basis of 11 values. It was thus possible to compare theoretical and experimental profile losses in groups of the following configurations

$$xk = x_l k - x_e k \qquad k = 1,2, \ldots, n$$

where $n = 400$. The accuracy of the method can be assessed by comparing the arithmetical mean (m) and a standard deviation (e) as estimated from sample data.

Examining the results of the two correlation methods (Alim's and the one presented herein), both of which were obtained from data regarding the same blades, it is evident that profile loss distribution is remarkably sensitive to variations in many of the blading parameters:

Alim method	*Proposed method*
$m = 0.025387$	$m = -0.002113$
$e = 0.041667$	$e = 0.012530$

Alim, in fact, assumed the ratio between compressible and incompressible losses as an exclusive function of the flow turning angle for both straight- and curve-back blades. Consequently, when the other key cascade parameters varied, prediction capability decreased accordingly. In short, experimental correlation methods can achieve an adequate degree of simplicity and reliability only if the blades analyzed share the same design criteria and if there are no great variations in the main cascade parameters. Otherwise, correlation accuracy turns out to be disappointingly poor. In Figs. 10–12 predicted and experimental profile losses were compared for three typical blade geometries. These results can be considered satisfactory.

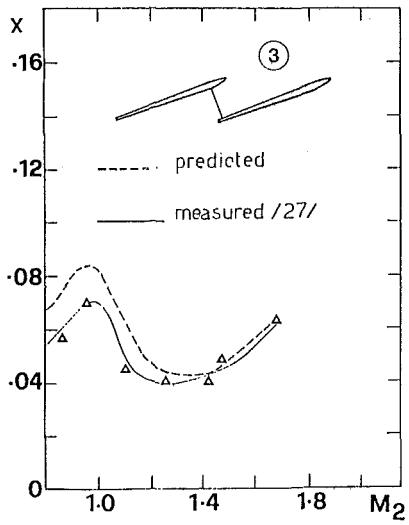

Fig. 12 Comparison of predicted and measured losses: nearly flat blade

Conclusions

Significant relationships between profile loss evolution and certain key cascade parameters in transonic turbine cascades have been clearly brought out by the correlation method described in this paper. The calculation expressions for profile loss obtained by the method are simple enough to fit through-flow procedures and, as a result, are extremely helpful in the preliminary design stage. Moreover, improvement of the expressions can be readily accomplished by adding more profile loss data according to the proposed method and thereby achieving better distribution of the compressibility coefficient terms.

Acknowledgments

The authors wish to express their gratitude to Ansaldo SpA of Genoa and to Prof. C. Sieverding of the von Karman Institute for their valuable aid in preparing the data body without which this project (work carried out within the Progetto Finalizzato Energetica CNR-ENEA, Grant No. 84.02834.59) would never have been possible.

References

1 Boretti, A. A., and Martelli, F., "A Simple Procedure to Compute Losses in Transonic Turbine Cascades," ASME Paper No. 85-GT-21.

2 Denton, J. D., "A Survey and Comparison of Methods for Predicting the Profile Loss of Turbine Blades," *I Mech E Conference Publication 1973-3*, pp. 204–212.

3 Ainley, D. G., and Mathieson, G. C. R., "A Method of Performance Estimation for Axial-Flow Turbines," British ARC, R&M 2974, Dec. 1951.

4 Dunham, J., and Came, P. M., "Improvements to the Ainley-Mathieson Method of Turbine Performance Prediction," ASME Paper No. 70-GT-2.

5 Cox, H. J. A., and Craig, H. R. M., "Performance Estimation of Axial Flow Turbines," *I Mech E Conference Publication 1970-71*, pp. 407–427.

6 Traupel, W., *Thermische Turbomachinen*, Springer, Berlin, 1977.

7 Balje', O. E., and Binsley, R. L., "Axial Turbine Performance Evaluation. Part I: Loss-Geometry Relationships," ASME JOURNAL OF ENGINEERING FOR POWER, Oct. 1968, pp. 341–348.

8 Schlichting, H., *Boundary Layer Theory*, McGraw-Hill, New York; Verlag G. Braun, Karlsruhe, 1968.

9 Stewart, W. L., "Analysis of Two Dimensional Compressible Flow Loss Characteristics Downstream of Turbomachine Blade Rows in Terms of Basic Boundary-Layer Characteristics," NACA TN 3515, July 1955.

10 Alim, A. A., "A Semi-Analytical Blade Loss Prediction Method for High Subsonic and Supersonic Exit Flow," ASME Paper No. 84-GT-2.

11 Qiang, K. F., and Chen, N. X., "New Correlations of the Two Dimensional Turbine Cascade Aerodynamic Performance," ASME JOURNAL OF ENGINEERING FOR POWER, Vol. 104, Apr. 1982, pp. 458–466.

12 Cox, H. J. A., Forster, V. T., and Hobson, G., "Aerodynamic Development of Steam Turbine Blading," *I Mech E Conference Publication 1979–12*, pp. 293–304.

13 Sieverding, C., "On the Use of Transonic Turbine Bladings and the Related Problems in Big Steam Turbines," in: *Transonic Turbines*, VKI LS 30, Jan. 1971.

14 Sieverding, C., "The Confluence of Two Supersonic Jets at the Trailing Edge of Transonic Turbine Blades," in: *Transonic Flows in Turbomachinery*, VKI LS 59, May 1973.

15 Sieverding, C., Stanislas, M., and Snoeck, J., "The Base Pressure Problem in Transonic Turbine Cascades," ASME JOURNAL OF ENGINEERING FOR POWER, Vol. 102, July 1980, pp. 711–718.

16 Purcaru, B. T., and Giess, P. A., "Theoretical and Experimental Investigation of KWU's Most Recent HP/IP Steam Turbine Blade," ASME Paper No. 83-GT-8.

17 Sieverding, C., "The Turbine Blade Definition – Experimental Data on Two Transonic Blade Sections and Comparison With Various Theoretical Methods," in: *Transonic Flows in Turbomachinery*, VKI LS 59, May 1973.

18 Sieverding, C., "The Base Pressure Problem in Transonic Turbine Cascades," in: *Transonic Flow in Axial Turbomachinery*, VKI LS 84, Feb. 1976.

19 Heinemann, H. J., "The Test Facility for Rotating Annular Cascades of the DFVLR and Its Measurement and Evaluation Method," IEE Publication 79 CH 1500-8 AES, Sept. 1979.

20 Lehthaus, F., "Berechnung der transsonischen Stromung durch ebene Turbinengitter nach dem Zeit-Schritt-Verfaheren," *VDI-Forschungsheft 586*, VDI-Verlag, 1978, pp. 5–24.

21 Graham, C. G., and Kost, F. H., "Shock Boundary Layer Interaction on High Turning Transonic Turbine Cascades," ASME Paper No. 79-GT-37.

22 Michel, G. W., and Kost, F. H., "The Effect of Coolant Flow on the Efficiency of a Transonic HP Turbine Profile Suitable for a Small Engine," ASME Paper No. 82-GT-63.

23 Haller, B. R., and Camus, J. J.,"Aerodynamic Loss Penalty Produced by Film Cooling Transonic Turbine Blades," ASME JOURNAL OF ENGINEERING FOR GAS TURBINES AND POWER, Vol. 106, Jan. 1984, pp. 198–205.

24 Camus, J. J., Denton, J. D., Souliis, J. V., and Scrivener, C. T. J., "An Experimental and Computational Study of Transonic Three-Dimensional Flow in a Turbine Cascade," ASME JOURNAL OF ENGINEERING FOR GAS TURBINES AND POWER, Vol. 106, Apr. 1984, pp. 414–420.

25 Oldfield, M. L. G., Kiock, R., Holmes, A. T., and Graham, C. G., "Boundary Layer Studies on Highly Loaded Cascades Using Heated Thin Films and a Traversing Probe," ASME JOURNAL OF ENGINEERING FOR POWER, Vol. 103, Jan. 1981.

26 Nicholson, J. H., Forest, A. E., Oldfield, M. L. G., and Schultz, D. L., "Heat Transfer Optimized Turbine Rotor Blades. An Experimental Study Using Transient Techniques," ASME JOURNAL OF ENGINEERING FOR GAS TURBINES AND POWER, Vol. 106, Jan. 1984, pp. 173–182.

27 Decuypere, R., Hautot, G., and Sieverding, C., "Investigation of Transonic Steam Turbine Tip Section With Various Suction Side Blade Curvatures," *I Mech E Conference Publication 1979–12*, pp. 241–252.

28 Sieverding, C., "Workshop on Two Dimensional and Three Dimensional Flow Calculations in Turbine Bladings. Description of Test Cases and Presentation of Experimental Results. Test Case I: 2-D Transonic Turbine Nozzle Blade," in: *Numerical Methods for Flow in Turbomachinery Bladings*, VKI LS 1982-05, Apr. 1982.

29 Perdichizzi, A., "Analisi sperimentale del flusso transonico in una schiera di pale relative alla sezione di base di uno stadio di bassa pressione," 37th ATI Congress, Padua, 1982.

30 Nealy, D. A., Mihelc, M. S., Hylton, L. D., and Gladden, H. J., "Measurements of Heat Transfer Distribution Over the Surface of Highly Loaded Turbine Nozzle Guide Vanes," ASME JOURNAL OF ENGINEERING FOR GAS TURBINES AND POWER, Vol. 106, Jan. 1984, pp. 149–158.

31 Couston, M., and Morris, A., "Turbine and Compressor Cascade Test Cases. I – Turbine Cascades," in: *Transonic Flow in Axial Turbomachinery*, VKI LS 84, Feb. 1976.

32 Sieverding, C., "The Influence of Trailing Edge Ejection on the Base Pressure in Transonic Turbine Cascades," ASME JOURNAL OF ENGINEERING FOR POWER, Vol. 105, Apr. 1983, pp. 215–222.

33 Consigny, H., and Richards, B. E., "Short Duration Measurements of Heat Transfer Rate to a Gas Turbine Rotor Blade," ASME JOURNAL OF ENGINEERING FOR POWER, Vol. 104, July 1982, pp. 542–551.

34 Scrofani, P., "Studio di una schiera di palette di turbina assiale in regime transonico," *L'Aerotecnica*, Vol. XLVII, Dec. 1976, pp. 214–226.

A. Binder[1]

W. Forster

K. Mach

H. Rogge

Research Engineers,
DFVLR—Propulsion Institute,
Cologne, Federal Republic of Germany

Unsteady Flow Interaction Caused by Stator Secondary Vortices in a Turbine Rotor

Nonintrusive measurements near and within the rotor of a cold-air turbine showed a sudden increase of turbulence energy when the wake portion of the incoming fluid entered the rotor. It has been suggested that this was due to the cutting of the passage vortices and trailing-edge shed vortices which emerge from the stator row. Since these secondary vortices are located very close to the stator wakes, it was very difficult to distinguish between the effects of shed vortex and passage vortex cutting on turbulence intensification. In the present paper, a method is shown which, with the help of time–distance diagrams, made it possible to attribute the turbulence increase to the breakdown of the secondary vortices. Further, the time–distance diagrams made it possible to locate the origin of turbulence production and follow the spreading of the highly turbulent flow regions through the rotor channel.

Introduction

An observer moving with a turbine rotor sees the incoming flow as a sequence of regions of high-velocity and small random velocity fluctuations, i.e., free-stream flow, alternating with regions of lower velocity, high turbulence, and a number of vortices, i.e., wake flow. Both kinds of flow enter the rotor obliquely, striking the pressure side channel before the suction side. Each time a wake region strikes the pressure side, the observer sees an area of increased turbulence, higher than in the incoming wake flow, form on the pressure-side nose and spread across the channel as it is swept downstream.

An observer standing outside the turbine and looking in sees the flow field as depicted in Fig. 1 for one instant in time [5, 9]. The stator wake and secondary vortices leave the stator with absolute angle α with reference to the circumferential direction. Because of the rotor motion, they enter it with relative angle β, striking the pressure-side blade first. As will be shown, the region of increased turbulence propagates back down the wake, which assumes a bowed shape because the velocity in midchannel is higher than in the stagnation region [6, 12]. The roles played by the wake and secondary vortices are difficult to separate because they lie parallel and close to, sometimes even coincident with, one another [2]. However, since it has been shown that unsteady phenomena significantly affect turbomachinery flow and performance, any contribution to their understanding offers the possibility of improved performance in future designs. A recent test series at the DFVLR in Cologne consisted of a careful mapping of the nonstationary and time-averaged flow fields in a turbine rotor; several papers have described different aspects of the work [2–6]. In this paper we propose a mechanism relating the spread of augmented turbulence across the blade channel to the collapse of the stator secondary vortices and describe how the vortices can be identified against the background of the wake flow.

Experimental Apparatus

The research turbine consisted of a single, uncooled, weakly transonic stage, whose essential features are shown schematically in Fig. 2. The stator had 20 airfoils and the rotor had 31. Because of the low aspect ratios (stator 0.56, rotor 0.9) the flow was fully three dimensional and, because the axial

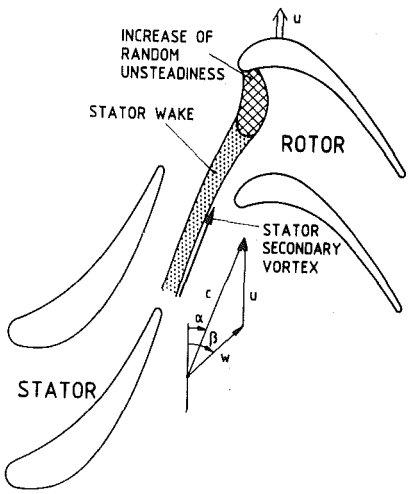

Fig. 1 Schematic of wake and vortex interaction process

[1] Presently at Motoren- und Turbinen-Union, Munich.

Contributed by the Gas Turbine Division of THE AMERICAN SOCIETY OF MECHANICAL ENGINEERS and presented at the 31st International Gas Turbine Conference and Exhibit, Düsseldorf, Federal Republic of Germany, June 8–12, 1986. Manuscript received at ASME Headquarters February 28, 1986. Paper No. 86-GT-302.

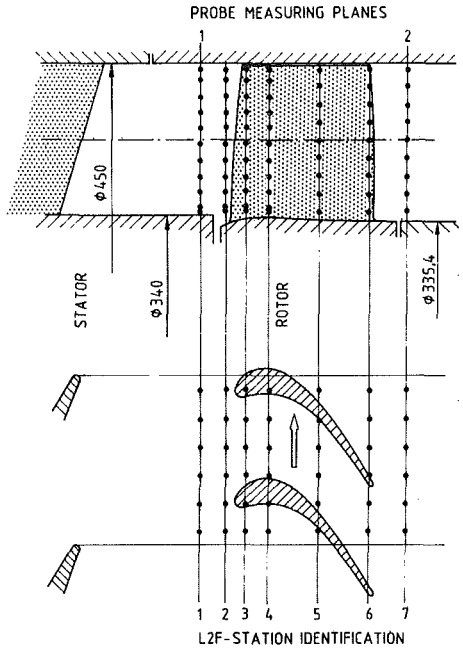

Fig. 2 L2F locations

distance between rotor and stator had been made relatively large in order to provide room for stator exit survey probes, potential (or inviscid) interactions between blade rows could be neglected as a source of nonstationary effects, leaving only the alternating impact of free stream and wake plus secondary vortices as sources of instationary flows into the rotor. Further details of the construction of the rig can be found in [2, 3]. For this test series, a part-load operating point was chosen which, for an average stator exit Mach number of 0.82 and rotor speed of 7800 rpm, yielded approximately zero incidence and completely subsonic flow through the rotor [2]. At each of the points marked with a heavy dot in Fig. 2, a laser-two-focus (L2F) velocimeter measured the ensemble-averaged flow velocity and direction and the components of the random fluctuating velocity parallel and perpendicular to the flow direction. The phenomena described in this paper – the wake and secondary vortex cutting and subsequent vortex breakdown accompanied by the appearance of a region of augmented turbulence – occur before the flow passes through L2F plane 4.

The operating principle of the L2F velocimeter will be only briefly reviewed here. For further details, see [14, 15]. At the desired measurement point, e.g., one of those in the $11 \times 6 \times 7$ array shown in Fig. 2, two laser beams are focused and aligned so that two spots of light form about 0.3 mm apart in the flow direction. As tiny particles (in this case, 0.1-μm oil droplets) are carried through the two spots by the gas stream, the light reflected from them is detected and used to compute the travel time between the two spots. Similarly, two components of the turbulent fluctuating velocity can be measured. A sufficiently large number of data are collected at each point for each of 16 rotor angular positions to allow calculation of statistical averages (phase-locked averaging) [5].

Data Analysis via Time-Distance Diagrams

The flow quantities velocity, direction, etc., in the unsteady three-dimensional flow field of a turbomachine depend on four variables (axial, radial, and circumferential position and time). However, it is not possible to describe this four-dimensional dependence in a straightforward manner. Usually at least two independent variables have to be held constant or averaged. In the initial analyses of the laser anemometry data, the time and either radial or axial coordinate were selected. This yielded a circumferential or axial view of a momentary or time-averaged flow situation. In this investigation, the axial and radial coordinates were held constant and the temporal variation of the flow quantities in the circumferential direction was analyzed by means of time–distance diagrams [3].

Figure 3 shows a schematic example for an axial position ahead of the rotor at midspan. The boundaries in the circumferential direction are on lines which touch the leading edges of two adjacent rotor blades with the design relative inlet angle β (upper figure). An observer moving with the rotor, i.e., in the relative frame of reference, notices an unsteady flow which is periodic with the stator pitch. At each circumferential position between the pressure side (*PS*) and suction side (*SS*) boundary, a perturbation of the incoming flow in the absolute frame (e.g., the wake) is felt at a different time; at the time t no part of the rotor entrance region is influenced by the stator wake. As the rotor moves on, the (stator) suction side of the wake is first felt at the pressure-side boundary of the rotor *PS*. As the rotor continues to move, the rest of the wake passes through *PS*. Locations which are closer to the suction-side end *SS* of the line notice the wake later.

This passage of the wake through the line *PS–SS* appears in the time–distance diagram (Fig. 3, lower) as an oblique line. With proper choice of scale, disturbances which travel along the line with rotor speed are inclined to the horizontal direction with an angle $\theta = 45$ deg. Smaller angles indicate a lower velocity of the disturbance in the circumferential direction and vice versa.

Due to the rotor potential field, a fluid filament which was straight in the absolute frame leaving the stator region (e.g., a filament of the wake) is distorted when it passes through the rotor channel. The deformation of the fluid filament was traced through the measured unsteady flow field with the assumption of two-dimensional flow [6]. In Fig. 4 (left side) a filament is shown entering the upper left corner of the measurement area with absolute inflow angle α_1. The succeeding lines show the filament being convected through the rotor by the nonstationary relative flow. The time interval between two lines is 1/6 of the stator pitch. Near the stagnation pressure fields at the leading edges, the flow is decelerated and the fluid filament becomes bowed.

In the time–distance diagram the deformation of the fluid filament appears as shown in Fig. 4 (right). For axial position I the influence of the rotor potential flow field is weak. The par-

Nomenclature

c = absolute velocity
c' = absolute velocity fluctuation (random part)
L2F = laser-two-focus
PS = pressure side
r = radius
SS = suction side
t = time
T = time period
u = rotational velocity
w = relative velocity
x, y = coordinates
α = absolute flow angle (yaw)
β = relative flow angle (yaw)
θ = slope

Subscripts and Superscripts

1, 2, . . . ,6 = location
L = parallel to absolute velocity
$\tilde{}$ = ensemble averaged
$\hat{}$ = time averaged

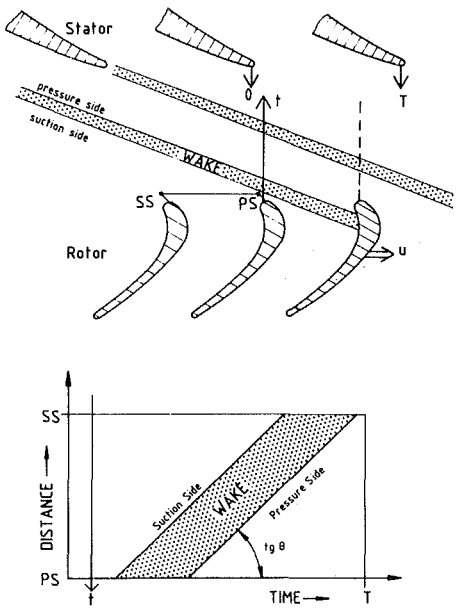

Fig. 3 Relationship between time-distance diagram and physical space

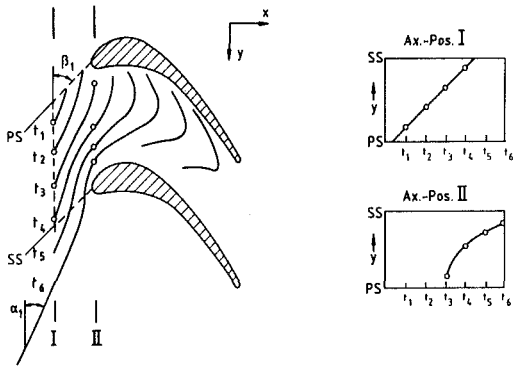

Fig. 4 Filament deformation in the rotor

ticles of the filament cross the circumferential line with their original axial velocity c_x and the intersection of the filament and the line moves from pressure side to suction side with rotor speed; therefore, the filament appears as a straight line with a 45 deg slope. At axial position II the deformation of the filament distorts this trajectory. Near the pressure side of the rotor the inclination is higher, which means that this end of the filament passes more nearly broadside through the line. As the suction side of the adjacent rotor blade gets closer to the filament, the circumferential velocity of the filament is reduced and the inclination of its trajectory in the time-distance diagram becomes smaller.

Locating the Vortex Centers

Behind the stator, the secondary vortices are located in the wake or in its immediate vicinity [2, 4] and it is therefore difficult to track their positions or to relate an observed phenomenon to one or the other. Especially in the rotor region, where the wake and the vortices are cut up by the blades, this fact causes significant difficulties in analyzing the measured results.

In order to get a better understanding of the flow phenomena associated with stator secondary flows, the vortex centers, or axes, were traced as fluid filaments. Behind the stator and in front of the rotor entrance region, these axes are aligned in the absolute flow direction [8, 11]. The original shape and the subsequent deformation of the filaments as they pass through the rotor are shown in Fig. 4. The initial positions of the filaments, which are necessary to calculate the convective deformation, were determined from the distributions of random unsteadiness and yaw angle in L2F plane 1 (Fig. 6).

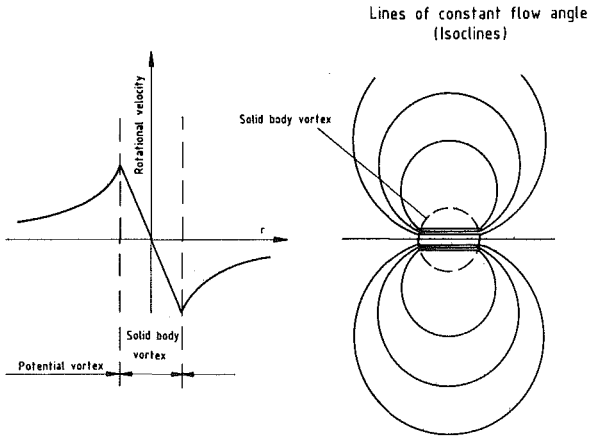

Fig. 5 Isoclines of a real (Rankine) vortex

As described in [4], secondary vortices can be located by means of yaw angle contours. In such yaw angle distributions, the rotation of a secondary vortex leads to characteristic shapes of the isoclinal lines (Fig. 5). A solid body rotation, which is located in the center of every real vortex, is characterized by straight parallel isoclines, usually aligned in the circumferential direction [3]. A free vortex, which usually forms the outer part of a real vortex, is characterized by two groups of circles tangent at the vortex center. Which of these groups indicates underturning or overturning depends on the sense of rotation. This simple model [4] was developed for a measuring plane perpendicular to the vortex axis. In the case of measurement plane 1 (Fig. 2), the secondary vortex axis and the absolute flow direction are inclined about 22 deg to the measurement plane. Consequently, the circles indicating a free vortex flow appear as ellipses whose major axes are about three times longer than their minor axes. By means of this simple model, vortices can be identified in an isoclinal contour map.

Discussion of Results

Four vortices can be found in plane 1 by applying the model just described. In the lower part of Fig. 6, vortices I and II are the well-known passage vortices which arise within the stator passage. Passage vortex I rotates in the clockwise direction, causing overturning and therefore lower values of the flow angle near the casing, and underturning (higher values of $\hat{\alpha}$) on the opposite side of the vortex center. Passage vortex II, which rotates in the opposite direction, is much smaller than passage vortex I because of the radially inward movement of the flow behind the stator [4], causing passage vortex II to move away from the casing and toward the hub. Therefore, vortex I rotates largely free from wall effects, whereas vortex II is suppressed by the hub. Two other vortices, associated with trailing shed vorticity or the remainder of the suction-side leg of the horseshoe vortex, exist in the midspan area.

As seen in the lower part of Fig. 6, the low aspect ratio of the stator leads to secondary vortices, for example III and IV, which are distributed along the entire vane height.

The four vortices whose centers are marked by dashed circles are also marked in the random unsteadiness distribution of the same plane (upper part of Fig. 6). In this figure, the dark contour line indicates the approximate boundary between high and low-turbulence flow regions. The low-turbulence flow indicates the core flow, which is essentially free from viscous effects. The regions showing high turbulence are the wakes and the secondary "loss cores" at the suction

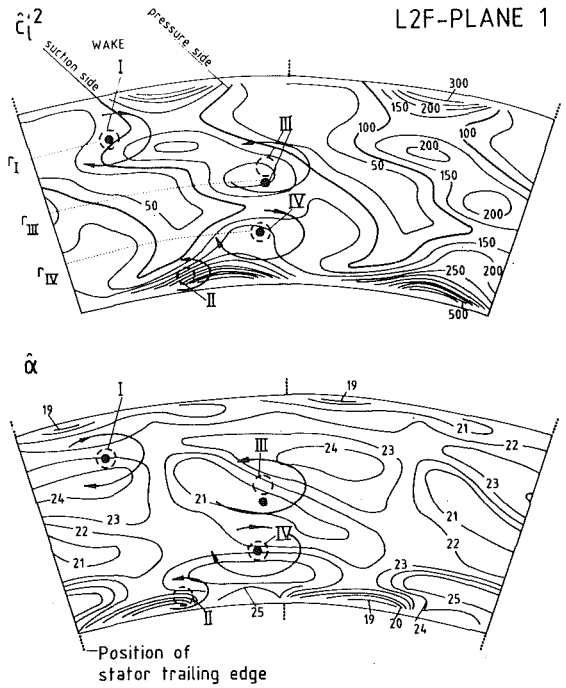

Fig. 6 Contours of time-averaged random unsteadiness $\hat{c}_L'^2$ and absolute flow angle $\hat{\alpha}$ in L2F plane 1

sides of the wakes. These secondary "loss cores" [4], which are located near the hub and the shroud, arise inside the stator passages due to boundary layer accumulation. The accumulation on the suction side of the vanes is caused by the rotational motion of the passage vortices and the cross-passage pressure gradient. Downstream of the stator, i.e., in the wake, these high-loss, high-random-unsteadiness regions [5] are located in or near the centers of the passage vortices.

Looking at the location of the vortex centers relative to the wake, it is apparent that the passage vortices I and II are located at the suction side of the wake, while the secondary vortices III and IV are located within the wake. The location of vortex center III is between the middle of the wake and the pressure side and secondary vortex IV is shifted toward the suction side. The origins of the fluid filaments with which the convection of the stator secondary vortices were followed through the rotor are marked by black dots. Two filaments were located at radii r_I and r_{IV}, corresponding to the centers of vortices I and IV. The filament indicating vortex III is shifted slightly outside the vortex center because no radial measurement location was available at the center itself (Fig. 2).

In the following diagrams the locations of the filaments leaving these dots are always marked by a thick black line.

Figure 7 shows the time history of vortex I from Fig. 6 as it passes through the four axial measurement planes in the rotor entrance region. In the first picture, the vortex and wake pass through L2F plane 1, approximately 25 percent of axial chord upstream of the nose. The vortex center lies toward the suction side of the wake. Recalling from Fig. 1 that the vortex and wake leave the stator with absolute angle α but enter the rotor with relative angle β, we see their intersection with the plane sweep from pressure side to suction side as time advances, i.e., as they pass through the plane (see also Fig. 3). The straight path of the vortex center means that all parts of the vortex pass through the plane at the same velocity and the 45 deg slope of the path means that the intersection between vortex and plane moves from pressure side to suction side at the rotor circumferential velocity u. In other words, we can safely assume the wake and vortex still have their original velocity and direction as they pass through L2F plane 1; they feel no

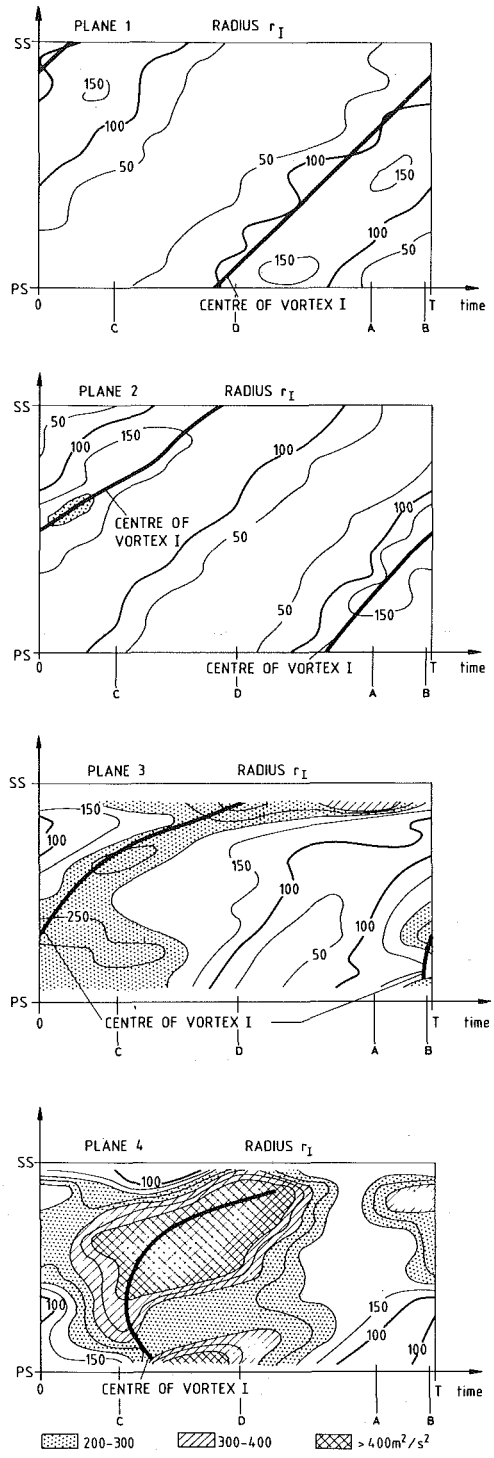

Fig. 7 Time-distance diagrams for vortex I contours of random unsteadiness $\tilde{c}_L'^2$

influence from the rotor yet. The streamwise component of the fluctuating kinetic energy $\tilde{c}_L'^2$ is seen to be in the range of 100 to 150 m^2/s^2.

As the vortex and wake pass through L2F plane 2, approximately 6 percent of axial chord forward of the nose, they begin to feel the influence of the blade. A small spot of higher turbulence appears near midchannel and the contour $\tilde{c}_L'^2 = 150$ m^2/s^2 extends more than halfway across the channel. The slope of the vortex path, i.e., its velocity along line *PS–SS*, decreases between midchannel and the suction side, indicating that the wake and vortex are decelerating in that half of the channel; that is, they arrive at the plane later than they would

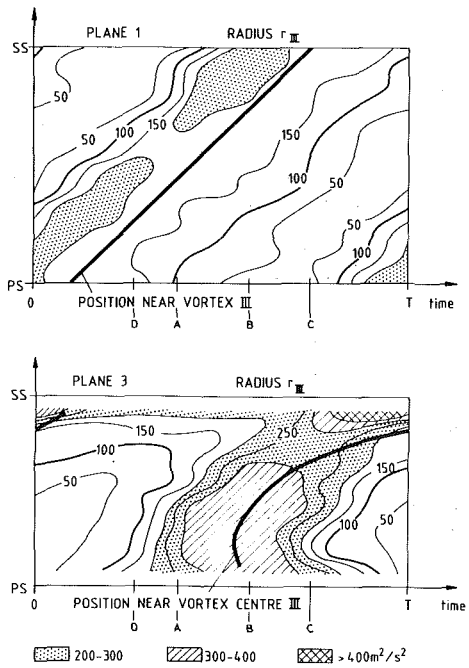

Fig. 8 Time-distance diagrams for vortex III contours of random unsteadiness $\tilde{c}_L'^2$

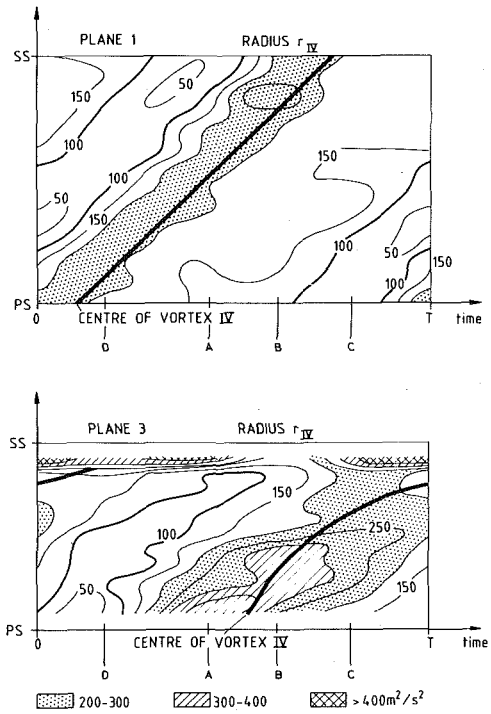

Fig. 9 Time-distance diagrams for vortex II contours of random unsteadiness $\tilde{c}_L'^2$

have with their original velocity. In physical space, the vortex and wake are aligning themselves more nearly in the axial direction as the suction-side velocity decreases and the mid-channel velocity continues. Fluid particles near the suction side cross the plane "behind schedule." In the pressure side the channel, the slope of the vortex path increases, indicating that the vortex and wake are aligning themselves toward the tangential direction. In physical space, the portions of the vortex and wake nearest the pressure side are caught in the stagnation region and therefore decelerate, while those near midchannel proceed with more or less their original velocity.

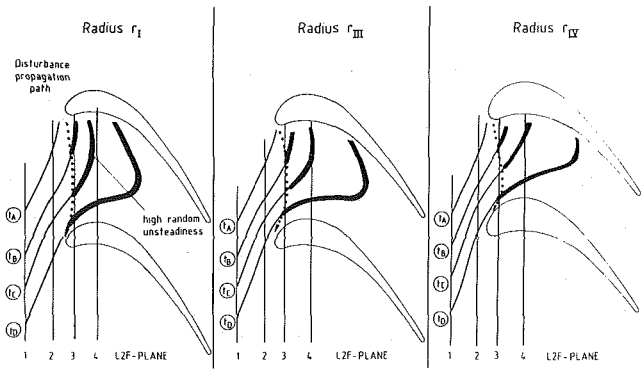

Fig. 10 Schematic of propagation of high turbulence zones

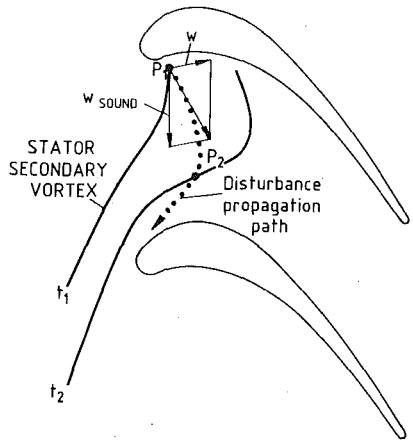

Fig. 11 Schematic of disturbance propagation

Again, the fluid particles near the blade cross the plane behind schedule.

In plane 3, approximately 6 percent of axial chord behind the nose, much the same situation exists, with one important difference. The vortex and wake have been cut off the pressure-side blade and a large zone of turbulence, in which $\tilde{c}_L'^2$ is in the range 200 to 250 m^2/s^2, extends completely across the channel, surrounding the vortex.

In the fourth L2F plane, some 25 percent of axial chord downstream of the nose, near the crown of the blade, the situation becomes chaotic. Very high turbulence, with $\tilde{c}_L'^2 \geq 400$ m^2/s^2 over a large region, fills the channel from side to side and persists for almost the entire vane passing period, although a slender zone of undisturbed fluid can still be seen. The slope of the vortex path is negative near the pressure side, indicating that the vortex is moving toward the blade, rather than away from it as before. In physical space, the vortex and wake have been pulled into the form of a bow whose open end points upstream (see Fig. 4). Therefore, they cross the plane in two places and the points of intersection move toward the two blades.

Figure 8 shows the time-distance diagrams for L2F planes 1 and 3 at radius r_{III}, near midspan. The heavy line marks a path just below that of vortex III, which turned out to lie slightly above the radius at which data were taken. The discussion of Fig. 7 applies here also, with a couple of additional comments. First, the vortex lies toward the pressure side of the incoming wake, whereas vortex I lay toward the suction side. Then, we see two tongues of high turbulence extending from the blade surfaces and following the vortex through plane 1. The incoming turbulence level is higher here than at radius r_I, exceeding 200 m^2/s^2 in the tongues. In plane 3, the situation for vortex III is almost identical to that for vortex I, with the exceptions that the suction side here is continuously bathed in turbulent fluid and the increase in turbulence over the incoming level is

smaller, reaching only 300 m^2/s^2, and is restricted to the pressure-side half of the channel.

The time–distance diagrams for vortex IV, which lies at approximately 1/4 span, are shown in Fig. 9. Note that on crossing L2F plane 1, the vortex is already surrounded by high turbulence, which, considering its location near the hub endwall, is not surprising. The situation in L2F plane 3 is similar to that at the other two radii except that the zone of high turbulence surrounding the vortex is narrower, i.e., it does not last as long, and the free-stream fluid penetrates briefly to the suction side. Note also that the increase of turbulence over the incoming level is again small, reaching only 350 m^2/s^2, and is confined to the pressure-side half and a small part of the suction side of the channel. Finally, note that all parts of the wake and vortex are moving toward the suction side of the channel as they cross plane 3 (the slope of the vortex is positive everywhere), even though they have been pulled into a bow in physical space.

It is clear from Figs. 7–9 that, in the rotor entrance region, the turbulence increases above the levels in the incoming wake, but only in areas associated with the stator secondary vortices. Outside the vortex areas, there was no discernible increase. The most reasonable explanation of this phenomenon is that the vortices break down and some of their kinetic energy is converted into turbulence [7, 13].

The vortex paths shown in the time–distance diagrams of Figs. 7–9 are shown in the blade-to-blade plane in Fig. 10. In Fig. 10(*a*), the locations of vortex I corresponding to the four instants in time *A*, *B*, *C*, and *D* from Fig. 7 are shown. At time t_A the vortex has not yet penetrated plane 3 and the turbulence level along it is essentially that of planes 1 and 2. At times t_B, t_C, and t_D, the vortex is passing through plane 3 and, as seen from the last two diagrams in Fig. 7, all of the vortex downstream of plane 3 is surrounded by high turbulence, indicated by heavy lines in Fig. 10. The upstream end of the high-turbulence area is found by axial interpolation to lie just forward of plane 3. At radii r_{III} and r_{IV} the behavior is similar except that at time t_C the high-turbulence zone does not quite extend forward to plane 3.

It is clear from study of Figs. 10 and 7 that the elevated turbulence spreads from the pressure side back along the vortex axis to approximately plane 3, but no further. Two questions are raised. Where exactly does the turbulence increase begin and why does it stop spreading where it does?

The model sketched in Fig. 11 explains: Slightly after the vortex is cut by the blade, for instance at point P_1, a disturbance is created which propagates along the vortex axis with the speed of sound. Simultaneously, the vortex is swept downstream at the local relative velocity. The resultant path is shown as a sequence of dots.

To get the best fit to the measurements, the origin of the turbulence increase (point P_1) is shifted slightly up- or downstream along the pressure side of the blade. The turbulence propagation paths which best match the measured results are marked by dots in Fig. 10. At each radius, excellent agreement with the measured results is apparent. The origin of turbulence production, as found by this model, occurs near the pressure-side stagnation region of the blades, immediately after the cutting of the stator secondary vortices.

Conclusions

L2F measurements in the rotor region of a single-stage, cold-air turbine have been analyzed with special regard to the unsteady blade row interaction caused by secondary vortices.

The behavior of the stator secondary vortices has been investigated as they propagate through the rotor. The following properties have been shown:

- The stator secondary vortices, which originally are aligned parallel to the stator wakes, are cut off by the rotor blades.
- Immediately after the vortex is cut off, the turbulence in the vortex region increases considerably. Most probably, the vortical motion breaks up and its energy is converted into turbulence.
- The origin of the breakdown is located near the pressure-side stagnation region of the rotor blades.
- The increase of turbulence spreads back along the vortex axis at the speed of sound.

References

1 Ashworth, D. A., La Graff, J. E., Schultz, D. L., and Grindrod, K. J., "Unsteady Aerodynamic and Heat Transfer Processes in a Transonic Turbine Stage," ASME JOURNAL OF ENGINEERING FOR GAS TURBINES AND POWER, Vol. 107, 1985, pp. 1022–1030.

2 Binder, A., "Turbulence Production Due to Secondary Vortex Cutting in a Turbine Rotor," ASME JOURNAL OF ENGINEERING FOR GAS TURBINES AND POWER, Vol. 107, 1985, pp. 1039–1046.

3 Binder, A., "Instationäre Strömungsvorgänge im Laufrad einer Turbine," submitted 1985.

4 Binder, A., and Romey, R., "Secondary Flow Effects and Mixing of the Wake Behind a Turbine Stator," ASME JOURNAL OF ENGINEERING FOR POWER, Vol. 105, 1983, pp. 40–46.

5 Binder, A., Förster, W., Kruse, H., and Rogge, H., "An Experimental Investigation Into the Effects of Wakes on the Unsteady Turbine Rotor Flow," ASME JOURNAL OF ENGINEERING FOR GAS TURBINES AND POWER, Vol. 107, 1985, pp. 458–466.

6 Förster, W., and Mach, K., "Instationäre Strömung in einem Turbinenlaufrad," VDI-Berichte 572, 1985.

7 Hall, M. G., "The Structure of Concentrated Vortex Cores," *Progress in Aeron. Science*, Vol. 107, 1966, pp. 53–110.

8 Hawthorne, W. R., "Rotational Flow Through Cascades, Pt. I: The Components of Vorticity," *Q. J. Mech. and Appl. Math.*, Vol. VIII, Pt. 3, 1955.

9 Hodson, H. P., "An Inviscid Blade-to-Blade Prediction of a Wake-Generated Unsteady Flow," ASME JOURNAL OF ENGINEERING FOR GAS TURBINES AND POWER, Vol. 107, 1985, pp. 337–344.

10 Hodson, H. P., "Measurements of Wake Generated Unsteadiness in the Rotor Passages of Axial Flow Turbines," ASME JOURNAL OF ENGINEERING FOR GAS TURBINES AND POWER, Vol. 107, 1985, pp. 467–476.

11 Horlock, J. H., "Recent Developments in Secondary Flow," AGARD-CP-214, 1977.

12 Joslyn, H. D., Caspar, J. R., and Dring, R. P., "Inviscid Modeling of Turbomachinery Wake Transport," 21st Joint Propulsion Conference, 1985, Paper No. AIAA-85-1132.

13 Leuchter, O., and Solignac, J. L., "Experimental Investigation of the Turbulent Structure of Vortex Wakes," ONERA-Report T. P. 1983–107.

14 Schodl, R., "Entwicklung des Laser-Zwei-Fokus-Verfahrens für die berührungslose Messung von Strömungsvektoren, insbesondere in Turbomaschinen," Dissertation TH Aachen, 1977.

15 Schodl, R., "A Laser-Two-Focus (L2F) Velocimeter for Automatic Flow Vector Measurements in the Rotating Components of Turbomachines," ASME *Journal Fluids Engineering*, Vol. 102, 1980, pp. 412–419.

smaller, reaching only 300 m^2/s^2, and is restricted to the pressure-side half of the channel.

The time–distance diagrams for vortex IV, which lies at approximately 1/4 span, are shown in Fig. 9. Note that on crossing L2F plane 1, the vortex is already surrounded by high turbulence, which, considering its location near the hub endwall, is not surprising. The situation in L2F plane 3 is similar to that at the other two radii except that the zone of high turbulence surrounding the vortex is narrower, i.e., it does not last as long, and the free-stream fluid penetrates briefly to the suction side. Note also that the increase of turbulence over the incoming level is again small, reaching only 350 m^2/s^2, and is confined to the pressure-side half and a small part of the suction side of the channel. Finally, note that all parts of the wake and vortex are moving toward the suction side of the channel as they cross plane 3 (the slope of the vortex is positive everywhere), even though they have been pulled into a bow in physical space.

It is clear from Figs. 7–9 that, in the rotor entrance region, the turbulence increases above the levels in the incoming wake, but only in areas associated with the stator secondary vortices. Outside the vortex areas, there was no discernible increase. The most reasonable explanation of this phenomenon is that the vortices break down and some of their kinetic energy is converted into turbulence [7, 13].

The vortex paths shown in the time–distance diagrams of Figs. 7–9 are shown in the blade-to-blade plane in Fig. 10. In Fig. 10(*a*), the locations of vortex I corresponding to the four instants in time *A*, *B*, *C*, and *D* from Fig. 7 are shown. At time t_A the vortex has not yet penetrated plane 3 and the turbulence level along it is essentially that of planes 1 and 2. At times t_B, t_C, and t_D, the vortex is passing through plane 3 and, as seen from the last two diagrams in Fig. 7, all of the vortex downstream of plane 3 is surrounded by high turbulence, indicated by heavy lines in Fig. 10. The upstream end of the high-turbulence area is found by axial interpolation to lie just forward of plane 3. At radii r_{III} and r_{IV} the behavior is similar except that at time t_C the high-turbulence zone does not quite extend forward to plane 3.

It is clear from study of Figs. 10 and 7 that the elevated turbulence spreads from the pressure side back along the vortex axis to approximately plane 3, but no further. Two questions are raised. Where exactly does the turbulence increase begin and why does it stop spreading where it does?

The model sketched in Fig. 11 explains: Slightly after the vortex is cut by the blade, for instance at point P_1, a disturbance is created which propagates along the vortex axis with the speed of sound. Simultaneously, the vortex is swept downstream at the local relative velocity. The resultant path is shown as a sequence of dots.

To get the best fit to the measurements, the origin of the turbulence increase (point P_1) is shifted slightly up- or downstream along the pressure side of the blade. The turbulence propagation paths which best match the measured results are marked by dots in Fig. 10. At each radius, excellent agreement with the measured results is apparent. The origin of turbulence production, as found by this model, occurs near the pressure-side stagnation region of the blades, immediately after the cutting of the stator secondary vortices.

Conclusions

L2F measurements in the rotor region of a single-stage, cold-air turbine have been analyzed with special regard to the unsteady blade row interaction caused by secondary vortices.

The behavior of the stator secondary vortices has been investigated as they propagate through the rotor. The following properties have been shown:

- The stator secondary vortices, which originally are aligned parallel to the stator wakes, are cut off by the rotor blades.
- Immediately after the vortex is cut off, the turbulence in the vortex region increases considerably. Most probably, the vortical motion breaks up and its energy is converted into turbulence.
- The origin of the breakdown is located near the pressure-side stagnation region of the rotor blades.
- The increase of turbulence spreads back along the vortex axis at the speed of sound.

References

1 Ashworth, D. A., La Graff, J. E., Schultz, D. L., and Grindrod, K. J., "Unsteady Aerodynamic and Heat Transfer Processes in a Transonic Turbine Stage," ASME JOURNAL OF ENGINEERING FOR GAS TURBINES AND POWER, Vol. 107, 1985, pp. 1022–1030.

2 Binder, A., "Turbulence Production Due to Secondary Vortex Cutting in a Turbine Rotor," ASME JOURNAL OF ENGINEERING FOR GAS TURBINES AND POWER, Vol. 107, 1985, pp. 1039–1046.

3 Binder, A., "Instationäre Strömungsvorgänge im Laufrad einer Turbine," submitted 1985.

4 Binder, A., and Romey, R., "Secondary Flow Effects and Mixing of the Wake Behind a Turbine Stator," ASME JOURNAL OF ENGINEERING FOR POWER, Vol. 105, 1983, pp. 40–46.

5 Binder, A., Förster, W., Kruse, H., and Rogge, H., "An Experimental Investigation Into the Effects of Wakes on the Unsteady Turbine Rotor Flow," ASME JOURNAL OF ENGINEERING FOR GAS TURBINES AND POWER, Vol. 107, 1985, pp. 458–466.

6 Förster, W., and Mach, K., "Instationäre Strömung in einem Turbinenlaufrad," VDI-Berichte 572, 1985.

7 Hall, M. G., "The Structure of Concentrated Vortex Cores," *Progress in Aeron. Science*, Vol. 107, 1966, pp. 53–110.

8 Hawthorne, W. R., "Rotational Flow Through Cascades, Pt. I: The Components of Vorticity," *Q. J. Mech. and Appl. Math.*, Vol. VIII, Pt. 3, 1955.

9 Hodson, H. P., "An Inviscid Blade-to-Blade Prediction of a Wake-Generated Unsteady Flow," ASME JOURNAL OF ENGINEERING FOR GAS TURBINES AND POWER, Vol. 107, 1985, pp. 337–344.

10 Hodson, H. P., "Measurements of Wake Generated Unsteadiness in the Rotor Passages of Axial Flow Turbines," ASME JOURNAL OF ENGINEERING FOR GAS TURBINES AND POWER, Vol. 107, 1985, pp. 467–476.

11 Horlock, J. H., "Recent Developments in Secondary Flow," AGARD-CP-214, 1977.

12 Joslyn, H. D., Caspar, J. R., and Dring, R. P., "Inviscid Modeling of Turbomachinery Wake Transport," 21st Joint Propulsion Conference, 1985, Paper No. AIAA-85-1132.

13 Leuchter, O., and Solignac, J. L., "Experimental Investigation of the Turbulent Structure of Vortex Wakes," ONERA-Report T. P. 1983–107.

14 Schodl, R., "Entwicklung des Laser-Zwei-Fokus-Verfahrens für die berührungslose Messung von Strömungsvektoren, insbesondere in Turbomaschinen," Dissertation TH Aachen, 1977.

15 Schodl, R., "A Laser-Two-Focus (L2F) Velocimeter for Automatic Flow Vector Measurements in the Rotating Components of Turbomachines," ASME *Journal Fluids Engineering*, Vol. 102, 1980, pp. 412–419.

DISCUSSION

A. Stewart[2]

I was interested to read the subject paper. Some years ago, I studied the subject of possible errors in gas turbine synthesis calculations due to the fact that the flow between the components was not steady state [16].

The general conclusion was that isotropic turbulence would have no appreciable effect on such calculations but that oscillations and secondary flows might have an appreciable effect. However, the effects of the oscillations and secondary flows are opposed and it was not therefore possible to draw a general conclusion on whether there would be any net effect without knowing the magnitudes of the energy involved in the

[2]Former head of Turbine Aerodynamic and Blade Cooling Development, Rolls-Royce Ltd., Derby, United Kingdom; presently Director, Turbo-Kinetic Design, Ltd., Derby, United Kingdom.

oscillations and the secondary flows (vortices). The necessary experimental evidence was not available at the time but it is possible that it may be available from your work. If this is the case, it would be interesting to know.

References

16 Stewart, A., "The Effect of Turbulence on Thermodynamic Calculations, With Particular Reference to Gas Turbines," Dissertation submitted to the Faculty of Applied Science and Technology, Queen's University, Belfast, Mar. 1975.

Authors' Closure

The authors would like to thank Dr. A. Stewart for his comments.

The development of the random unsteadiness in the secondary flow region was also investigated in previous published papers [2, 3]. In these works the increase of random unsteadiness in the rotor entrance region has been related to the enthalpy drop of the turbine. It has been shown that the energy converted into turbulence by the cutoff process of the secondary vortices is on the order of 1 percent. The energy contained in the oscillations (periodic fluctuations) has not yet been calculated.

J. Moore

D. M. Shaffer

J. G. Moore

Department of Mechanical Engineering,
Virginia Polytechnic Institute and State
University,
Blacksburg, VA 24061

Reynolds Stresses and Dissipation Mechanisms Downstream of a Turbine Cascade

An experimental investigation was performed to measure Reynolds stresses in the turbulent flow downstream of a large-scale linear turbine cascade. A rotatable X-wire hot-wire probe that allows redundant data to be taken with solution for mean velocities and turbulence quantities by least-squares fitting procedures was developed. The rotatable X-wire was used to obtain the Reynolds stresses on a measurement plane located 10 percent of an axial chord downstream of the trailing edge. Here the turbulence kinetic energy exhibits a distribution resembling the contours of total pressure loss obtained previously, but is highest in the blade wake where losses are relatively low. The turbulent shear stresses obtained are consistent in sign and magnitude with the gradients of mean velocity. The measured Reynolds stresses are combined with measured distributions of velocity to show how and where losses are being produced. The mechanisms for the dissipation of mean kinetic energy in this swirling three-dimensional flow are revealed.

Introduction

One of the challenges in turbine design is to understand the sources of the losses in three-dimensional turbulent flow. Design procedures are becoming available which allow changes in blade profiling and stacking, endwall contouring, and blade sweep and lean. The designer can vary these parameters and *measure* the changes in performance of the blading, but much more insight and better modeling of the loss mechanisms will be required before he can accurately *predict* changes in performance.

There is a need for more information about how and where losses are produced in turbomachinery flows. In this paper, we quantitatively explain the rate of loss production downstream of a linear turbine cascade. It is hoped that the explanation for this flow region will contribute to a better understanding of loss production mechanisms in general.

VPI&SU Cascade. The flow considered is that at Plane 2, 10 percent of an axial chord downstream of the trailing edge of the VPI&SU cascade [1] shown in Fig. 1. The cascade is geometrically similar to the UTRC cascade [2]. The airfoil section is that of a reaction turbine rotor with mean camber line angles of $\beta_1 = 43.99$ and $\beta_2 = 25.98$ deg giving a nominal turning angle of 110 deg and a velocity ratio of approximately 1.6.

The operating conditions for the cascade are given in Table 1. With these conditions, the flow downstream of the cascade is dominated by the decay of passage vortices and the dissipation of secondary kinetic energy [1].

Primary and Secondary Velocities. Figure 1 shows the primary flow velocity component U, defined in the direction of the mean camber line at the blade trailing edges ($\beta_2 = 26$ deg). The secondary flow velocity components are then W, in the spanwise direction, and V, perpendicular to U and W.

Figure 2(*a*) shows the secondary velocity vectors (the resultant of the secondary velocities V and W) at plane 2, pictured on the measurement plane. The corresponding contours of total pressure loss coefficient C_{P_t} are shown in Fig. 2(*b*).

Of particular interest in this paper are the large spanwise velocities toward midspan in the blade wake, where W is of the order of -20 to -25 m/s, and the overturning of the flow,

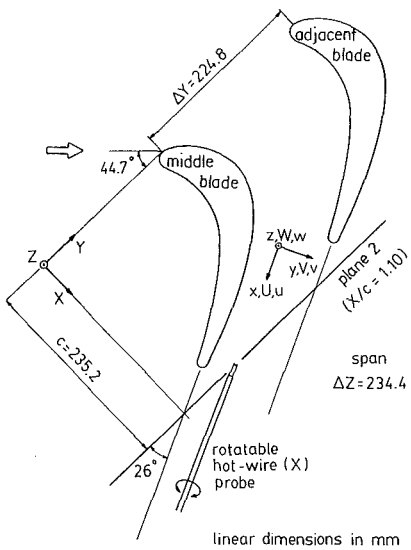

Fig. 1 Cascade geometry with coordinate systems for the cascade (X, Y, Z) and for primary and secondary flow downstream (x, y, z)

Contributed by the Gas Turbine Division of THE AMERICAN SOCIETY OF MECHANICAL ENGINEERS and presented at the 31st International Gas Turbine Conference and Exhibit, Düsseldorf, Federal Republic of Germany, June 8–12, 1986. Manuscript received at ASME Headquarters January 17, 1986. Paper No. 86-GT-92.

Table 1 Operating conditions for VPI&SU cascade

Freestream velocity at inlet	
U_0(m/s)	23.5 (± 0.4)
Freestream turbulence intensity at midspan	
$\sqrt{\overline{u^2}}/U_0$ (percent)	0.3
Endwall boundary layer parameters at inlet $(X/c = -1.20)$	
Boundary layer thickness, δ_{99} (mm)	38.
Displacement thickness, δ^* (mm)	5.41
Momentum thickness, θ (mm)	4.10
Shape factor, $H_{12} = \delta^*/\theta$	1.32
Air properties	
ρ (kg/m^3)	1.12
μ (kg/m s)	0.0000188
Exit Reynolds number based on axial chord	
Re_c	5.2×10^5

between the vortex core and the endwall, with blade-to-blade velocities V of the order of -10 m/s.

Total Pressure Losses and Secondary Kinetic Energy Downstream. More than one third of the losses in this cascade are found to occur downstream of the trailing edge. This rise in total pressure loss is almost entirely explained by a corresponding dissipation of secondary kinetic energy, $(V^2 + W^2)/2$, as shown in Fig. 3 and Table 2. The decrease in the secondary kinetic energy $W^2/2$, associated with the spanwise velocities, represents more than 60 percent of the additional total pressure loss.

One is led to ask, what are the mechanisms governing the decay of the secondary kinetic energy? Can the decay be explained by turbulent and viscous stresses in the flow?

An Apparent Paradox. An analysis of downstream mixing losses [1] showed that the net contribution of the dissipation of primary kinetic energy and the rise in static pressure is very small when compared to the dissipation of secondary kinetic energy. The flow develops downstream of the trailing edge as if the primary flow (in a mass-averaged sense) is reversible and only the secondary kinetic energy decays irreversibly.

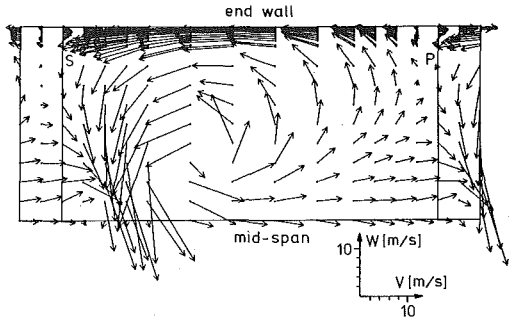

Fig. 2(a) Secondary flow vectors

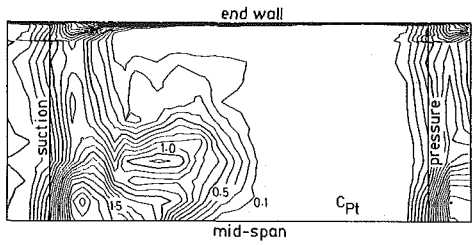

Fig. 2(b) Contours of total pressure loss coefficient C_{Pt}

Fig. 2 Measured flow distribution at plane 2 ($X/c = 1.10$) [1]. Solid line: projections downstream of blades in directions of mean camber lines at trailing edges; suction S: downstream of middle blade; pressure P: downstream of adjacent blade.

One asks whether this finding can be correct given the dissipation of primary kinetic energy which must be occurring in the endwall boundary layers. Again, is the explanation to be found in the turbulence stresses in the flow?

Present Contribution. In this paper, we will:

1 consider the equations for the development of total pressure losses and the individual components of the mean kinetic energy in a three-dimensional turbulent flow;

2 present results of measurements of Reynolds stresses at plane 2 ($X/c = 1.10$) downstream of the VPI & SU cascade;

3 combine the Reynolds stresses with gradients of

Nomenclature

A = area of measuring plane, area of integration

$A_1, \ldots, A_6$ = coefficients, equation (10)

c = blade axial chord, Fig. 1

C_{Pt} = total pressure loss coefficient

$$= (P_{t0} - P_t)/\frac{1}{2}\rho U_0^2$$

D = substantial derivative $= \partial/\partial t + U_j\,\partial/\partial x_j$

e_A, e_B = fluctuating wire voltage

N = nondimensionalization factor

$$= c/\left(\bar{V}_n A\,\frac{1}{2}\rho U_0^2\right)$$

P = mean static pressure

q_A, q_B = fluctuating effective cooling velocity, equation (10)

$\overline{q^2}/2$ = turbulence kinetic energy, equation (11)

rms = root mean square

t = time

U, u = mean and fluctuating primary velocity components, Fig. 1

U_i, u_i = components of mean and fluctuating velocity

U_0 = upstream freestream velocity

V, v = mean and fluctuating lateral velocity components, Fig. 1

V_n = velocity component normal to measuring plane, axial velocity

$\bar{V}_n$ = area-averaged normal velocity, Table 2

W, w = mean and fluctuating spanwise velocity components, Fig. 1

x, y, z or x_i = flow coordinates, Fig. 1

X, Y, Z = cascade coordinates, Fig. 1

ΔY = blade pitch

ΔZ = blade span

α_0 = wire angle, Fig. 4

μ = viscosity

ρ = density

Subscripts

0 = upstream of cascade in freestream

t = total, stagnation

Overbars

$\bar{\ }$ = time average

$\tilde{\ }$ = mass average

Table 2 Average flow properties

	Plane 1	2	3	4
X/c	0.96	1.10	1.25	1.40
$\bar{V}_n(m/s)^{(1)}$	18.74	15.76	15.76	15.76
$\bar{\bar{C}}_{Pt}$	0.220	0.268	0.306	0.343
$\overline{\overline{U^2}}/U_0^2$	2.53	2.58	2.49	2.55
$\overline{\overline{V^2}}/U_0^2$	0.090	0.054	0.049	0.041
$\overline{\overline{W^2}}/U_0^2$	0.103	0.077	0.052	0.025
$\overline{\overline{(V^2+W^2)}}/U_0^2$	0.193	0.131	0.101	0.066
$\bar{\bar{C}}_{Pt}+\overline{\overline{(V^2+W^2)}}/U_0^2$	0.413	0.399	0.407	0.409

(1) Uniform corrections have been applied to the measured yaw angles to obtain mass balances with the inlet flow.

measured mean velocity [1] to give distributions of turbulent deformation work and dissipation of mean kinetic energy;

4 discover the mechanisms governing the decay of secondary kinetic energy and the changes in primary kinetic energy in this swirling three-dimensional flow;

5 suggest an explanation for the paradox of apparently reversible primary flow and irreversible secondary flow, downstream of the VPI & SU cascade.

Equations for Kinetic Energy of the Mean Motion

The equation of motion for turbulent flow of an incompressible fluid is

$$\rho\left(\frac{\partial U_i}{\partial t}+U_j\frac{\partial U_i}{\partial x_j}\right)=-\frac{\partial P}{\partial x_i}+\frac{\partial}{\partial x_j}\left(\mu\left(\frac{\partial U_i}{\partial x_j}+\frac{\partial U_j}{\partial x_i}\right)-\rho\overline{u_iu_j}\right) \tag{1}$$

where U_i are the components of the mean velocity and $-\rho\overline{u_iu_j}$ are the Reynolds stresses[1] due to turbulent velocity fluctuations u_i and u_j.

Following Hinze [3], we multiply the equation of motion by U_i and obtain the equation for the kinetic energy of the mean motion

$$\underbrace{\frac{1}{2}\frac{\partial}{\partial t}(\rho U_iU_i)}_{\text{I}}+\underbrace{\frac{\partial}{\partial x_j}U_j\left(P+\frac{1}{2}\rho U_iU_i\right)}_{\text{II}}+\underbrace{\frac{\partial}{\partial x_j}\rho\overline{u_iu_j}U_i}_{\text{III}}$$

$$\underbrace{-\frac{\partial}{\partial x_j}\mu U_i\left(\frac{\partial U_i}{\partial x_j}+\frac{\partial U_j}{\partial x_i}\right)}_{\text{IV}}=\underbrace{\rho\overline{u_iu_j}\frac{\partial U_i}{\partial x_j}}_{\text{V}}-\underbrace{\mu\left(\frac{\partial U_i}{\partial x_j}+\frac{\partial U_j}{\partial x_i}\right)\frac{\partial U_i}{\partial x_j}}_{\text{VI}} \tag{2}$$

The terms in this equation represent:

(I) local rate of change of mean kinetic energy;

(II) change in convective transport of total pressure;

(III) the rate at which mean kinetic energy is diffused by turbulent fluctuations;

(IV) the rate at which viscous stresses do work on the control volume;

(V) work of deformation of the mean motion by the turbulence stresses per unit volume and time; this term represents the rate at which mean kinetic energy is converted to turbulence kinetic energy;

(VI) the rate at which energy of the mean flow is dissipated through the action of viscosity per unit of volume and of time.

[1] For simplicity, the quantities $\overline{u_iu_j}$ are sometimes referred to as the Reynolds stresses in this paper.

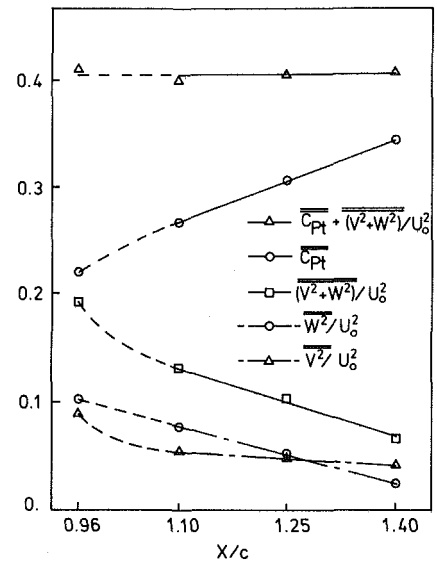

Fig. 3 Variation of mass-averaged flow properties downstream of trailing edge

In a similar manner, we multiply the equation of motion by the individual mean velocity components U, V, and W to obtain the following equations for the individual components of the mean kinetic energy.

In the x direction[2]:

$$\rho D\left(\frac{U^2}{2}\right)+\frac{\partial}{\partial x_j}\rho\overline{uu_j}U-\frac{\partial}{\partial x_j}\mu U\left(\frac{\partial U}{\partial x_j}+\frac{\partial U_j}{\partial x}\right)=-U\frac{\partial P}{\partial x}+\rho\overline{uu_j}\frac{\partial U}{\partial x_j}-\mu\left(\frac{\partial U}{\partial x_j}+\frac{\partial U_j}{\partial x}\right)\frac{\partial U}{\partial x_j} \tag{3}$$

In the y direction:

$$\rho D\left(\frac{V^2}{2}\right)+\frac{\partial}{\partial x_j}\rho\overline{vu_j}V-\frac{\partial}{\partial x_j}\mu V\left(\frac{\partial V}{\partial x_j}+\frac{\partial U_j}{\partial y}\right)=-V\frac{\partial P}{\partial y}+\rho\overline{vu_j}\frac{\partial V}{\partial x_j}-\mu\left(\frac{\partial V}{\partial x_j}+\frac{\partial U_j}{\partial y}\right)\frac{\partial V}{\partial x_j} \tag{4}$$

In the z direction:

$$\rho D\left(\frac{W^2}{2}\right)+\frac{\partial}{\partial x_j}\rho\overline{wu_j}W-\frac{\partial}{\partial x_j}\mu W\left(\frac{\partial W}{\partial x_j}+\frac{\partial U_j}{\partial z}\right)=-W\frac{\partial P}{\partial z}+\rho\overline{wu_j}\frac{\partial W}{\partial x_j}-\mu\left(\frac{\partial W}{\partial x_j}+\frac{\partial U_j}{\partial z}\right)\frac{\partial W}{\partial x_j} \tag{5}$$

Area Integration and Nondimensionalization. The rates of change of total pressure and of the individual components of mean kinetic energy, in the axial (X) direction (see Fig. 1), are obtained at plane 2 by integrating equations (2)–(5) over the measuring plane. The integration is performed at X/c = 1.10, from $Y = 0.$ to $Y = \Delta Y$, and from $Z = \Delta Z/2$ to $Z = \Delta Z$ (the top half of the cross-sectional plane).

The terms in the equations are made dimensionless by multiplying by a factor N, where

$$N=\frac{c}{\bar{V}_nA\frac{1}{2}\rho U_0^2}=0.00001832\ \text{s}^3/\text{kg m}$$

The area A for integration is $\Delta Y\cdot\Delta Z/2$ and the normal velocity $\bar{V}_n$ is 15.76 m/s (see Table 2).

[2] Note: The x, y, z coordinates correspond to the U, V, W of Fig. 1 and not the cascade coordinates X, Y, Z.

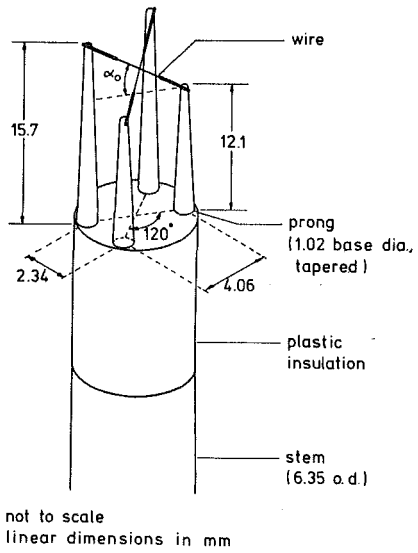

Fig. 4 Schematic of rotatable two-wire hot-wire probe

Upon integration, terms III and IV in equation (2) and the corresponding terms in equations (3)–(5) are found to be of negligible significance. Omitting these terms, the equations become (for steady flow)

$$-\frac{\partial}{\partial\left(\frac{X}{c}\right)}(\bar{\bar{C}}_{Pt}) \cong N\int\int_A \rho\overline{u_i u_j}\frac{\partial U_i}{\partial x_j}\,dA$$

$$+N\int\int_A -\mu\left(\frac{\partial U_i}{\partial x_j}+\frac{\partial U_j}{\partial x_i}\right)\frac{\partial U_i}{\partial x_j}\,dA \qquad (6)$$

$$\frac{\partial}{\partial\left(\frac{X}{c}\right)}\left(\frac{\overline{\overline{P+\frac{1}{2}\rho U^2}}}{\frac{1}{2}\rho U_0^2}\right) \cong N\int\int_A \left(V\frac{\partial P}{\partial y}+W\frac{\partial P}{\partial z}\right)dA$$

$$+N\int\int_A \rho\overline{uu_j}\frac{\partial U}{\partial x_j}dA+N\int\int_A -\mu\left(\frac{\partial U}{\partial x_j}+\frac{\partial U_j}{\partial x}\right)\frac{\partial U}{\partial x_j}\,dA \qquad (7)$$

$$\frac{\partial}{\partial\left(\frac{X}{c}\right)}\left(\frac{\overline{\overline{V^2}}}{U_0^2}\right) \cong N\int\int_A -V\frac{\partial P}{\partial y}dA+N\int\int_A \rho\overline{vu_j}\frac{\partial V}{\partial x_j}dA$$

$$+N\int\int_A -\mu\left(\frac{\partial V}{\partial x_j}+\frac{\partial U_j}{\partial y}\right)\frac{\partial V}{\partial x_j}\,dA \qquad (8)$$

$$\frac{\partial}{\partial\left(\frac{X}{c}\right)}\left(\frac{\overline{\overline{W^2}}}{U_0^2}\right) \cong N\int\int_A -W\frac{\partial P}{\partial z}dA+N\int\int_A \rho\overline{wu_j}\frac{\partial W}{\partial x_j}\,dA$$

$$+N\int\int_A -\mu\left(\frac{\partial W}{\partial x_j}+\frac{\partial U_j}{\partial z}\right)\frac{\partial W}{\partial x_j}dA \qquad (9)$$

In these equations, the terms on the left-hand side can be evaluated from the data in Table 2; for equations (6), (8), and (9) they represent the slopes of curves in Fig. 3. The last terms on the right-hand side can be evaluated from measured velocity distributions at planes 2 and 3 [1]. With the addition of independently measured Reynolds stresses at plane 2, it should be possible to:

(*a*) evaluate the turbulent deformation work terms,
(*b*) balance equation (6), and
(*c*) discover the mechanisms for the production of total pressure losses and for the dissipation of mean kinetic energy.

Reynolds Stress Measurements

Turbulence measurements were made on the upper half of plane 2 (see Fig. 1) using hot-wire anemometry. A rotatable two-wire probe was used from 50.-90.6 percent of span.

Single-wire traverses were done near the endwall, from 100.–90.6 percent of span, where probe blockage effects were expected if the larger two-wire probe was used.

The two-wire probe allowed measurement of the complete set of Reynolds stresses, including turbulence kinetic energy, and all three mean velocity components. The single wire was used to gain an approximation for $\overline{u^2}$ and the turbulence intensity.

Rotatable[3] Two-Wire (*X*) Probe. The two-wire probe, designed for this investigation, combines the advantages of single- and multiple-wire systems and is illustrated in Fig. 4. It consists of two slantwires with a nominal wire angle α_0 of 35.3 deg. These are separated by a fixed angular distance of nominally 120 deg about the probe axis. The probe is designed to be rotated in its support about its axis. This design is an extension of the rotatable single-wire idea [4], while probe complexity is reduced over the three-wire probe [5].

For a wire angle of 35.3 deg, three wire positions separated by 120 deg about the probe axis form a mutually orthogonal set of axes; this probe is designed so that its two wires form two out of three axes of an orthogonal coordinate set. It can be rotated to produce the complete set. In this way, it produces all the wire positions of three-wire systems with mutually perpendicular sensors [6].

The probe was used as an end-flow probe, i.e., with the primary flow in the direction of the probe axis, as shown in Fig. 1. This allowed data to be obtained with the incidence (or cone) angles (relative to the probe axis) of up to 35 deg expected at plane 2 [1].

The two hot-wire sensors were made of 0.0038 mm (0.00015 in.) diameter tungsten wire. The wires were given a copper coating except for about 1.3–1.6 mm exposed length at the middle.

Analysis for Reynolds Stresses. For an orthogonal three-dimensional coordinate system, the Reynolds stress tensor has six components: $\overline{u^2}$, $\overline{v^2}$, $\overline{w^2}$, $\overline{uv}$, $\overline{uw}$, and $\overline{vw}$, where u, v, w represent the fluctuating velocity components in the three coordinate directions. The Reynolds stress quantities can be related to wire voltages by geometry and the method used to model wire response (e.g., the cosine law). The analysis method adopted here is that of Gorton and Lakshminarayana [5].

In this analysis, the mean square of a wire voltage $\overline{e_A^2}$, obtained from the measured rms signal for wire A, is related to the mean square of the corresponding fluctuating cooling velocity $\overline{q_A^2}$. Geometry then relates the cooling velocity to the fixed-coordinate velocity components, which after linearization and time-averaging results in a linear expression

$$\overline{q_A^2} = A_1\overline{u^2}+A_2\overline{v^2}+A_3\overline{w^2}+A_4\overline{uv}+A_5\overline{uw}+A_6\overline{vw} \qquad (10)$$

where the coefficients $A_1, \ldots, A_6$ are functions of the mean velocities U, V, W. The mean velocities are found from the wire mean voltages [7]. From the second wire (B), its mean-square signal, $\overline{e_B^2}$, and the mean-product $\overline{e_A e_B}$ of the two wire signals (obtained from combining the rms sum and difference signals) produce two more equations, also linear in the Reynolds stresses, for $\overline{q_B^2}$ and $\overline{q_A q_B}$.

Solution Procedure for Reynolds Stresses. For each angular setting of the rotatable two-wire probe, three equations for the six Reynolds stresses were obtained. The experimental procedure always called for at least three such

[3] This probe can be rotated into different stationary angular positions, not to be confused with continuously rotating probes.

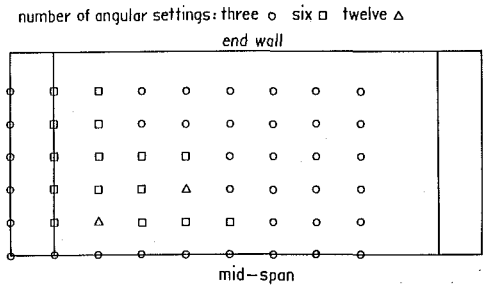

Fig. 5 Grid for X-wire measurement locations at plane 2

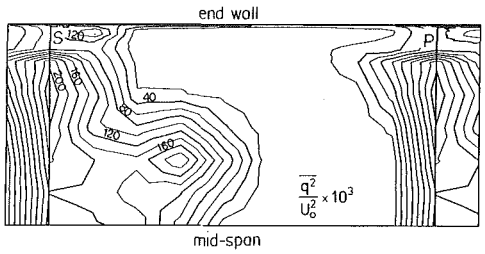

Fig. 6 Contours of turbulence kinetic energy at plane 2

angular settings, resulting in an overspecified set of linear equations.

The solution procedure was then to least-squares fit the system of equations into a set of six equations in six unknowns. This resulted in a more strongly diagonal coefficient matrix, increasing confidence in the results obtained.

It should be noted that the geometry of the *X*-wire probe is such that the two wires could duplicate orientations when the probe was rotated. This occurred when three angular settings equally spaced by 120 deg were used; the two wires assumed nearly the same three mutually orthogonal positions as the probe was rotated. Nine equations were obtained, but only six (three from rms and three from mean product signals) were independent. By increasing the number of settings beyond three, redundant independent information was obtained as opposed to just redundant information as with three settings.

Verification of Two-Wire Probe in Pipe Flow. Verification tests were performed at the exit of a pipe with a Reynolds number of 120,000 based on average velocity and diameter. An uninterrupted length of 240 diameters upstream of the exit insured fully developed flow and the Reynolds number indicates a clearly turbulent flow. The results are compared with those of Laufer [9], and all errors are based on locally expected values.

1 Using three angular settings through 10 deg incidence, the velocity magnitude and flow angle were obtained to within 0.6 percent and 1.0 degree, respectively. The turbulent normal stresses and turbulence kinetic energy were measured to within 28 percent and the primary shear stress ($\overline{uv}$) to within 27 percent. However, the secondary shear stresses ($\overline{uw}$, $\overline{vw}$) were measured as large as 60 percent of the expected primary shear stress when they should have been small in comparison.

2 Using six angular settings, the velocity magnitude was obtained within 0.8 percent and the flow angle within 3.6 deg through 35 deg incidence. The Reynolds stresses and turbulence kinetic energy were obtained within 30 percent through 20 deg incidence, and within 46 percent up to 35 deg incidence.

The verification tests in fully developed pipe flow showed that the *X*-wire probe was capable of measuring the Reynolds stresses and turbulence kinetic energy with the accuracy desired in the cascade flow. They also indicated that six angular settings were desirable when incidence angles were larger than about 15 deg.

Turbulence Measurements at Plane 2

Measurement Locations. Plane 2 was traversed with the *X*-wire probe. Horizontal (pitchwise, *Y*) traverses were made at the following spanwise locations: 50.0, 58.1, 66.2, 74.3, 82.4, and 90.6 percent of span (from the bottom wall). At each spanwise height, measurements were made from $Y = -2.54$ cm to 17.8 cm every 2.54 cm. This defined a grid as shown in Fig. 5, which also indicates the number of angular settings used. Three settings were used in regions of low turbulence and regions of mild secondary velocities (generally cone angles less than 15 deg). The number of settings was increased to six or twelve in those regions of distorted flow exhibiting large secondary velocities and turbulence levels. The vertical lines in Fig. 5 show the trailing edges of the middle and adjacent blades projected in the primary flow direction. The results at $Y = -2.54$, 0, and 2.54 cm were duplicated over the wake region of the adjacent blade to fill in the region to the right.

The region between 90.6 percent of span and the top endwall was traversed spanwise with a horizontal single-wire probe at selected pitchwise locations (not shown).

Mean Velocities. The mean velocities were solved for particularly to complete the coefficient matrix in the Reynolds stress solution (see equation (10), for example). The velocity magnitude was measured to within ±4 percent of earlier five-hole pressure probe results [1] up to cone (three-dimensional incidence) angles of 35 deg. The cone angle was obtained within 4 deg when less than 20 deg, but only within 9 deg for cone angles up to 35 deg.

Turbulence Kinetic Energy. The turbulence kinetic energy $\overline{q^2}/2$ is given by

$$\frac{\overline{q^2}}{2} = \frac{\overline{u^2} + \overline{v^2} + \overline{w^2}}{2} \tag{11}$$

where $\overline{u^2}$, $\overline{v^2}$, and $\overline{w^2}$ are the three Reynolds normal stresses.

Contours of $\overline{q^2}/U_0^2 \times 10^3$ measured by the *X*-wire probe are plotted in Fig. 6. The endwall region was traversed with a single wire, giving information only for $\overline{u^2}$; the turbulence in this region was assumed to be isotropic ($\overline{u^2} = \overline{v^2} = \overline{w^2}$) for the purposes of contour plotting. The computer routine that produced the contours used linear interpolation between grid points, and this should be considered when interpreting the following contour plots.

The contours of $\overline{q^2}/U_0^2$ show a peak of 0.20 in the blade wake downstream of the trailing edge, at about 80 percent of span. Two peaks of 0.16 occur near the center of the passage vortex and in the midspan/suction-side corner region. The latter two peaks correspond to regions of high-total-pressure-loss fluid, as can be seen in Fig. 2(*b*). However, the blade-wake peak is in a region of relatively low-loss fluid ($C_{pt} \cong 0.8$ versus a maximum of 1.8). The turbulence here is probably due to a different mechanism, possibly residual trailing-edge vorticity causing violent mixing of different velocity fluids. The turbulence kinetic energy contours also show the endwall boundary layer to be quite thin, about 2 mm thick at midpassage.

A very low-turbulence region occupies much of the passage, from the passage vortex region to the wake of the adjacent blade. Values of $\overline{q^2}/U_0^2$ here are typically 0.001 to 0.002, with a minimum of 0.0008 (corresponding to an rms turbulence intensity of 1.7 percent of inlet flow velocity) occurring at midspan and 68 percent pitch. This minimum value of turbulence intensity at plane 2 is of the same order as at the edge of the inlet endwall boundary layer (about 1.5 percent).

Mass-Averaged Turbulence Kinetic Energy. The mass-averaged turbulence kinetic energy is defined as

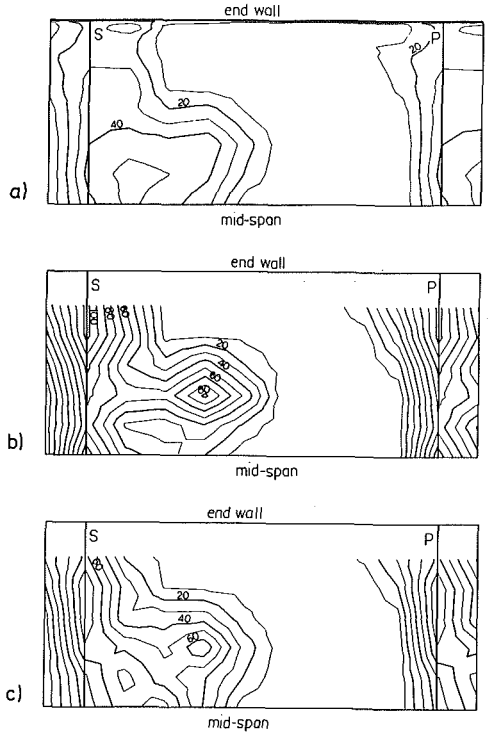

Fig. 7 Contours of Reynolds normal stresses at plane 2: (a) $\frac{\overline{u^2}}{U_0^2} \times 10^3$; (b) $\frac{\overline{v^2}}{U_0^2} \times 10^3$; (c) $\frac{\overline{w^2}}{U_0^2} \times 10^3$

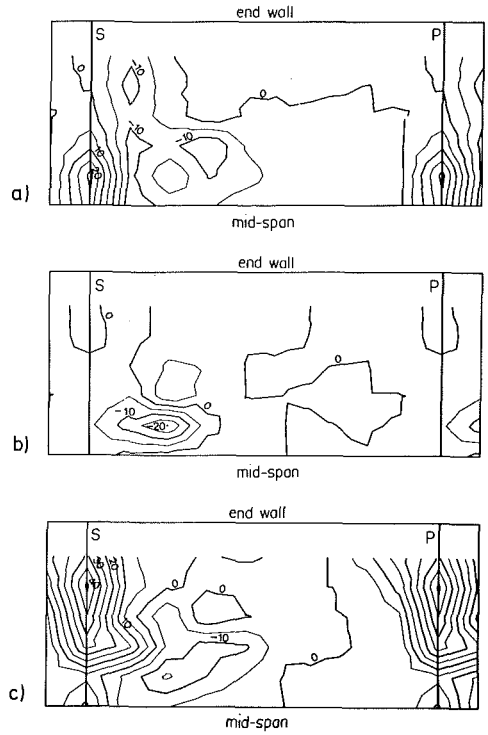

Fig. 8 Contours of Reynolds shear stresses at plane 2: (a) $\frac{\overline{uv}}{U_0^2} \times 10^3$; (b) $\frac{\overline{uw}}{U_0^2} \times 10^3$; (c) $\frac{\overline{vw}}{U_0^2} \times 10^3$

$$\frac{\overline{\overline{q^2}}}{U_0^2} = \frac{\int_0^{\Delta Y}\int_{\Delta Z/2}^{\Delta Z} \frac{1}{2}(\overline{u^2}+\overline{v^2}+\overline{w^2})\rho V_n dZdY}{\frac{1}{2}U_0^2\int_0^{\Delta Y}\int_{\Delta Z/2}^{\Delta Z}\rho V_n dZdY} \tag{12}$$

which is consistent with the definition of $\bar{\bar{C}}_{Pt}$ used in previous investigations [1, 2]. The isotropic approximation made near the endwall did not have a large effect on the answer since overturning there results in a small V_n.

The resultant value for $\overline{\overline{q^2}}/U_0^2$ is 0.062, which can be compared to a $\overline{C_{Pt}}$ of 0.268 at plane 2 (Table 2). The turbulence kinetic energy then accounts directly for about 23 percent of the total pressure loss at plane 2.

Gregory-Smith and Graves [10] believe turbulence may account for 75 percent of the total pressure losses in their cascade. However, their measurement plane (slot 8) was closer to the trailing edge ($X/c = 1.03$) than plane 2 ($X/c = 1.10$). In the VPI&SU cascade, the peak turbulence intensities decay abruptly downstream of the trailing edge, but the decreases would not explain a factor of 3.5 in mass-averaged turbulence kinetic energy.

Normal Stresses. Contour plots of $\overline{u^2}$, $\overline{v^2}$, and $\overline{w^2}$ normalized by U_0^2 are shown in Fig. 7. The secondary normal stresses $\overline{v^2}$ and $\overline{w^2}$ show a distribution similar to $\overline{q^2}/U_0^2$. Local peak values of $\overline{v^2}/U_0^2$ reach 0.10, accounting for half the corresponding local peak turbulence kinetic energies. The $\overline{w^2}/U_0^2$ values are next largest, with peak values of 0.07 occurring in the blade wake.

The primary normal stress distribution is quite different. Contours of $\overline{u^2}/U_0^2$ show a peak of only about 0.05 occurring at midspan, and are more symmetric than the secondary normal stress and turbulence kinetic energy contours. The larger values of $\overline{v^2}$ and $\overline{w^2}$ may result from the rapid dissipation of secondary kinetic energy, $(V^2+W^2)/2$, downstream of the cascade, while the primary flow U behaves as a reversible flow [1].

Shear Stresses. The turbulent shear stresses, $\overline{uv}$, $\overline{uw}$, and $\overline{vw}$, normalized by U_0^2, are contour plotted in Fig. 8. The contours of $\overline{uv}/U_0^2$ show a peak value of $+0.02$ in the blade wake near midspan. This is a region of a high negative $\partial U/\partial y$ velocity gradient and one would expect a large positive $\overline{uv}$ shear stress. There is a corresponding region of not so large positive $\partial U/\partial y$ on the other side of the wake which is accompanied by a region of negative $\overline{uv}$.

Contours of $\overline{uw}/U_0^2$ (Fig. 8(b)) have a large negative (-0.02 peak) region at about 60 percent of span and 20 percent of pitch. This is in a region of large positive $\partial U/\partial z$ as might be expected.

The $\overline{vw}/U_0^2$ shear stress (Fig. 8(c)) has a peak of $+0.04$ in the blade wake closely corresponding to the location of highest $\overline{q^2}$, $\overline{v^2}$, and $\overline{w^2}$. It is more difficult to associate this with a mean velocity gradient since both $\partial W/\partial y$ and $\partial V/\partial z$ may be important and the y direction does not lie in a measurement plane. From the vector plot of secondary velocities (Fig. 2(a)), W is decreasing (becoming more negative) in the Y direction near peak $\overline{vw}$, which is consistent with a positive $\overline{vw}$.

All the shear stresses are small in the undisturbed flow near midpassage with contours of zero appearing there.

The most significant finding here is that the maximum $\overline{vw}$ shear stress is the largest, about twice the maximum value of $\overline{uv}$ or $\overline{uw}$. The $\overline{vw}$ stress was the one not obtained by Gregory-Smith and Graves [10]. It is believed that it may contribute to the rapid decay of mean secondary kinetic energy, particularly $W^2/2$, downstream of the cascade (as discussed below).

Distribution of Deformation Work by Turbulence Stresses

The principal mechanism for the generation of total pressure losses in the flow at plane 2 is the work of deformation of the mean motion by the turbulent Reynolds stresses. This is represented by term V in equation (2), $\rho \overline{u_i u_j}\ \partial U_i/\partial x_j$ and by the corresponding terms in equations (3)-(9). It is the rate of production of turbulence kinetic energy from mean

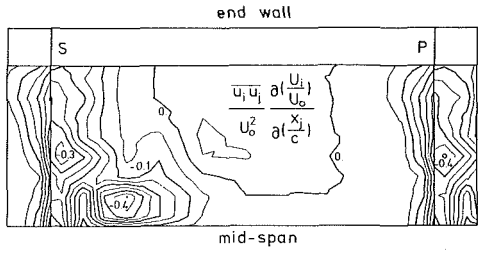

Fig. 9 Contours of turbulent deformation work (rate of production of turbulence kinetic energy) at plane 2

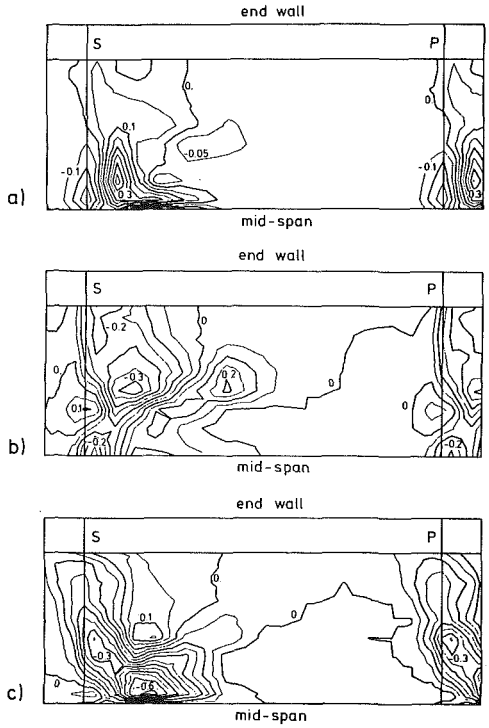

Fig. 10 Contours of contributions to turbulent deformation work from the mean velocity components U, V, and W at plane 2:

(a) $\frac{\overline{uu_j}}{U_0^2}\frac{\partial(U/U_0)}{\partial(x_j/c)}$; (b) $\frac{\overline{vu_j}}{U_0^2}\frac{\partial(V/U_0)}{\partial(x_j/c)}$; (c) $\frac{\overline{wu_j}}{U_0^2}\frac{\partial(W/U_0)}{\partial(x_j/c)}$

kinetic energy. Note that for loss generation and turbulence production, this term has a negative sign. Term V is evaluated at plane 2 by combining the measured Reynolds stresses (Figs. 7 and 8) with measured distributions of mean velocity from planes 2 and 3 [1].

The distributions of deformation work are presented as distributions of the dimensionless quantity

$$\frac{\overline{u_iu_j}}{U_0^2}\frac{\partial(U_i/U_0)}{\partial(x_j/c)}$$

With summation over all nine terms, we get the total turbulent deformation work. This is plotted in Fig. 9. We see loss production throughout the blade wake and in the passage vortex near midspan. In these regions, the turbulence is high (Figs. 6–8) and velocity gradients are large. The distribution has several peaks of the order of -0.3 to -0.4. Deformation work is small in regions of low total pressure loss (Fig. 2(*b*)) where the turbulence is low and velocity gradients are relatively small.

More insight into the specific mechanisms of loss production can be obtained by plotting the distributions of the nine individual terms and by plotting the three sums of three terms that contribute to the dissipation of the three components of mean kinetic energy (the second terms on the right-hand sides of equations (3), (4), and (5) and of equations (7), (8), and (9)).

Deformation Work in the Primary Flow (x) Direction. The sum of the three deformation work terms directly contributing to changes in primary kinetic energy is given by

$$\frac{\overline{uu_j}}{U_0^2}\frac{\partial(U/U_0)}{\partial(x_j/c)}$$

The distribution of this sum is shown in Fig. 10(*a*). The peak of about $+0.3$ is due to $\overline{u^2}\ \partial U/\partial x$, the action of the primary Reynolds normal stress $\overline{u^2}$ on an accelerating flow as the blade wake mixes out three dimensionally. The sense of this term is to cause an *increase* in mean primary kinetic energy $U^2/2$. This surprising observation suggests a reason for the small rate of change of $\bar{P}+\frac{1}{2}\rho\bar{U}^2$ downstream of the VPI&SU cascade [1].

The smaller trough downstream of the trailing edges of the blades between 50 and 65 percent of span is due to $\overline{uv}\ \partial U/\partial y$. This is a region of dissipation of primary kinetic energy on the pressure side of the wake near midspan, and the values are negative.

The contribution due to $\overline{uw}\ \partial U/\partial z$ is not shown in Fig. 10(*a*). This occurs mainly in the endwall boundary layer, where Reynolds stress measurements were not made, but it is also an important mechanism for loss production at plane 2, as discussed below.

Deformation Work in the y Direction. In the y direction, the deformation work terms contributing directly to changes in the secondary kinetic energy component $V^2/2$ are

$$\frac{\overline{vu_j}}{U_0^2}\frac{\partial(V/U_0)}{\partial(x_j/c)}$$

At plane 2, this distribution, shown in Fig. 10(*b*), is dominated by the contribution from $\overline{v^2}\ \partial V/\partial y$. A region of dissipation (negative values) extends throughout the blade wake to midspan, with a peak value of -0.3 at about 70 percent of span. Contours of smaller positive values, also mostly due to $\overline{v^2}\ \partial V/\partial y$, are seen on the pressure side of the blade wake and in the passage vortex.

Deformation Work in the Spanwise (z) Direction. The deformation work terms contributing directly to changes in the spanwise component of secondary kinetic energy $W^2/2$ are

$$\frac{\overline{wu_j}}{U_0^2}\frac{\partial(W/U_0)}{\partial(x_j/c)}$$

The two terms $\overline{vw}\ \partial W/\partial y$ and $\overline{w^2}\ \partial W/\partial z$ both make significant contributions at plane 2. In Fig. 10(*c*), the negative contours in the blade wake between 60 and 90 percent of span are caused by $vw\ \partial W/\partial y$. Here there are large negative spanwise velocities (see Fig. 2(*a*)), large negative velocity gradients $\partial W/\partial y$, and large positive values of vw. The peak value due to $\overline{vw}\ \partial W/\partial y$ is about -0.3.

The term $\overline{w^2}\ \partial W/\partial z$ gives the large negative values, locally as low as -0.6, near midspan in the blade wake on the edge of the passage vortex. This mechanism acts between 50 and 70 percent of span, and results from the high values of $\overline{w^2}$ and the large negative values of $\partial W/\partial z$ due to the symmetry of the flow about midspan.

Area Integrals of Equations for Mean Kinetic Energy

Area Integrals of Individual Deformation Work Terms. The area integrals of the individual turbulent deformation work terms

$$\overline{\rho u_iu_j}\frac{\partial U_i}{\partial x_j}$$

Table 3 Area integrals on plane 2 of individual deformation work terms, $\overline{\rho u_i u_j \frac{\partial U_i^{(1)}}{\partial x_j}}$

Spanwise distance[2]	$\overline{uu_j}\frac{\partial U^{(3)}}{\partial x_j}$	$\overline{u^2}\frac{\partial U}{\partial x}$	$\overline{uv}\frac{\partial U}{\partial y}$	$\overline{uw}\frac{\partial U}{\partial z}$
50.–90.6	+0.017	+0.046[4]	−0.026	−0.003
90.6 – 100.	−0.070	+0.005[4,5]	−0.003[6]	−0.072[6]
50. – 100.	−0.053	+0.051	−0.029	−0.075
	$\overline{vu_j}\frac{\partial V^{(3)}}{\partial x_j}$	$\overline{uv}\frac{\partial V}{\partial x}$	$\overline{v^2}\frac{\partial V}{\partial y}$	$\overline{vw}\frac{\partial V}{\partial z}$
50. – 90.6	−0.041	−0.001	−0.036	−0.004
90.6 – 100.	−0.020	0.000[6]	−0.010[5]	−0.010[6]
50. – 100.	−0.061	−0.001	−0.046	−0.014
	$\overline{wu_j}\frac{\partial W^{(3)}}{\partial x_j}$	$\overline{uw}\frac{\partial W}{\partial x}$	$\overline{vw}\frac{\partial W}{\partial y}$	$\overline{w^2}\frac{\partial W}{\partial z}$
50. – 90.6	−0.116	−0.001	−0.075	−0.040
90.6 – 100.	+0.004	0.000[6]	0.000[6]	+0.004[5]
50. – 100.	−0.112	−0.001	−0.075	−0.036

[1] Values made dimensionless as in equation (6).
[2] Percent of span from bottom wall.
[3] Summation over $j = 1,2,3$ understood.

[4] $\frac{\partial U}{\partial x} = -\frac{\partial V}{\partial y} - \frac{\partial W}{\partial z}$.

[5] In endwall region, single hot wire used for $\overline{u^2}$ and $\overline{v^2} = \overline{w^2} = \overline{u^2}$ assumed.
[6] Turbulent shear stresses calculated using Prandtl mixing length model [11] in endwall region.

made dimensionless by the factor N as in equation (6), are presented in Table 3. The measured Reynolds stresses (Figs. 7 and 8) were used over the region from midspan to 90.6 percent of span. In the region from 90.6 percent of span to the endwall, data from a single hot wire were used for $\overline{u^2}$ and $\overline{v^2} = \overline{w^2} = \overline{u^2}$ was assumed. The turbulent shear stresses in this endwall region were calculated using a Prandtl mixing length model [11] together with the measured mean velocity distributions [1].

The only integrals of the individual laminar deformation work terms

$$-\mu\left(\frac{\partial U_i}{\partial x_j}+\frac{\partial U_j}{\partial x_i}\right)\frac{\partial U_i}{\partial x_j}$$

with values of significance were given by the terms $-\mu \cdot (\partial U/\partial z)^2$ and $-\mu(\partial V/\partial z)^2$ in the endwall boundary layer region. The dimensionless values of the integrals for these two terms are -0.013 and -0.001, respectively.

Table 4 shows the sum of the area integrals of all the turbulent and laminar deformation work terms to be -0.240. The table then ranks contributions in order of significance. Thus, we see the largest single contribution, -0.075 or 31 percent of the total, from the term $\overline{vw}\ \partial W/\partial y$ between 50. and 90.6 percent of span. Other mechanisms for dissipation involve the terms $\overline{uw}\ \partial U/\partial z$ in the endwall region (30 percent), and $\overline{w^2}\ \partial W/\partial z$ (17 percent), $\overline{v^2}\ \partial V/\partial y$ (15 percent), and $\overline{uv} \cdot \partial U/\partial y$ (11 percent) between 50 and 90.6 percent of span. A contribution of the opposite sign comes from $\overline{u^2}\ \partial U/\partial x$ (-19 percent). This was seen in Fig. 10(*a*).

Accounting for the Rate of Increase of Total Pressure Loss. The rate of increase of total pressure loss at plane 2 was

$$\frac{\partial}{\partial\left(\frac{X}{c}\right)}(\overline{\overline{C_{Pt}}}) = 0.25.$$

This was evaluated from the slope of the total pressure loss curve in Fig. 3, using mass-averaged values at planes 2 and 3 (Table 2). Confidence in this value is gained by using the values at planes 2 and 4, which also give a slope of 0.25.

Table 5 shows this measured rate compared with contributions from the deformation work integrals, using the signs of equation (6) and Tables 3 and 4. The terms are grouped as to mean velocity component, U, V, and W, and as laminar and turbulent. The total -0.240 is remarkably close to the measured rate of -0.25.

The deformation work by the primary velocity component gives -0.066, or 27 percent of the loss production rate. The V velocity gives a similar contribution, -0.062 or 26 percent. The largest factor in loss production is the spanwise velocity W, with -0.112 or 47 percent. The secondary velocity components, V and W, combined account for 73 percent of the loss production at plane 2. This supports the earlier finding [1] that loss production downstream of the VPI&SU cascade is dominated by the dissipation of secondary kinetic energy.

At plane 2, Table 5 shows turbulent stresses giving 94 percent of the loss production with 6 percent from laminar shear near the endwall.

Accounting for Changes in Mean Kinetic Energy. The rates of decay of the components of secondary kinetic energy at plane 2 were

$$\frac{\partial}{\partial\left(\frac{X}{c}\right)}\left(\frac{\overline{\overline{V^2}}}{U_0^2}\right) = -0.03 \text{ and } \frac{\partial}{\partial\left(\frac{X}{c}\right)}\left(\frac{\overline{\overline{W^2}}}{U_0^2}\right) = -0.17$$

Again these were evaluated using data from planes 2 and 3. These rates were confirmed by using data from planes 2 and 4, which gave rates for $V^2/2$ of -0.04 and for $W^2/2$ of -0.17.

Combining the measured rates for C_{Pt}, $V^2/2$, and $W^2/2$, we get

$$\frac{\partial}{\partial\left(\frac{X}{c}\right)}\left(\frac{\overline{\overline{P+\frac{1}{2}\rho U^2}}}{\frac{1}{2}\rho U_0^2}\right) = \frac{\partial}{\partial\left(\frac{X}{c}\right)}\left(-\overline{\overline{C_{Pt}}}-\frac{\overline{\overline{V^2}}}{U_0^2}-\frac{\overline{\overline{W^2}}}{U_0^2}\right)$$

$$= -0.25-(-0.03)-(-0.17)$$

$$= -0.05$$

Table 4 Contributions of individual terms to the area integral of the deformation work on plane 2:

$$N\int\int_A \rho u_i u_j \frac{\partial U_i}{\partial x_j}\,dA + N\int\int_A -\mu\left(\frac{\partial U_i}{\partial x_j}+\frac{\partial U_j}{\partial x_i}\right)\frac{\partial U_i}{\partial x_j}\,dA$$

from	(50. − 100.) = −0.240	100.%
$vw\frac{\partial W}{\partial y}$	(50. − 90.6) = −0.075	31.%
$uw\frac{\partial U}{\partial z}$	(90.6 − 100.) = −0.072	30.%
$u^2\frac{\partial U}{\partial x}$	(50. − 90.6) = +0.046	−19.%
$w^2\frac{\partial W}{\partial z}$	(50. − 90.6) = −0.040	17.%
$v^2\frac{\partial V}{\partial y}$	(50. − 90.6) = −0.036	15.%
$uv\frac{\partial U}{\partial y}$	(50. − 90.6) = −0.026	11.%
$-\mu\left(\frac{\partial U}{\partial z}\right)^2$	(90.6 − 100.) = −0.013	5.%
$v^2\frac{\partial V}{\partial y}$	(90.6 − 100.) = −0.010	4.%
$vw\frac{\partial V}{\partial z}$	(90.6 − 100.) = −0.010	4.%
Rest		≤ ±2.%

In Table 6, the measured decay rates are combined in equations (7)–(9) with the area integrals from Table 3. The accounting allows the pressure terms, which represent reversible energy exchanges, to balance the right- and left-hand sides. These extra terms $V\,\partial P/\partial y$ and $W\,\partial P/\partial z$ allow the interchange of mean kinetic energy between the three velocity components. They introduce the possibility that not all the changes in mean kinetic energy are due to irreversible deformation work; and they allow deformation work to be distributed more uniformly between the velocity components.

Table 5 Contributions to the rate of increase of total pressure loss at plane 2

$$-\frac{\partial}{\partial\left(\frac{X}{c}\right)}(C_{Pt}) \cong N\int\int_A \rho\overline{u_i u_j}\frac{\partial U_i}{\partial x_j}\,dA + N\int\int_A -\mu\left(\frac{\partial U_i}{\partial x_j}+\frac{\partial U_j}{\partial x_i}\right)\frac{\partial U_i}{\partial x_j}\,dA$$

$$-0.25^{(1)} \cong \begin{cases} \left(N\int\int_A \rho\overline{uu_j}\frac{\partial U}{\partial x_j}dA = -0.053\right)^{(2)} \\ +\left(N\int\int_A -\mu\left(\frac{\partial U}{\partial z}\right)^2 dA = -0.013\right) \\ +\left(N\int\int_A \rho\overline{vu_j}\frac{\partial V}{\partial x_j}dA = -0.061\right)^{(2)} \\ +\left(N\int\int_A -\mu\left(\frac{\partial V}{\partial z}\right)^2 dA = -0.001\right) \\ +\left(N\int\int_A \rho\overline{wu_j}\frac{\partial W}{\partial x_j}dA = -0.112\right)^{(2)} \end{cases}$$

$$\cong \underset{\substack{\text{Turbulent}\\ \text{contribution (94\%)}}}{(-0.226)} + \underset{\substack{\text{Laminar}\\ \text{contribution (6\%)}}}{(-0.014)}$$

$$\cong -0.240$$

(1) From measurements, Table 2.
(2) Table 3.

Table 6 Contributions to the rates of change of individual kinetic energy components

$$\frac{\partial}{\partial\left(\frac{X}{c}\right)}\left(\frac{V^2}{U_0^2}\right) \cong N\int\int_A -V\frac{\partial P}{\partial y}dA + N\int\int_A \rho\overline{vu_j}\frac{\partial V}{\partial x_j}dA + N\int\int_A -\mu\left(\frac{\partial V}{\partial x_j}+\frac{\partial U_j}{\partial y}\right)\frac{\partial V}{\partial x_j}dA$$

$$-0.03^{(1)} \cong (+0.03)^{(3)} + (-0.061)^{(2)} + (-0.001)$$

$$\frac{\partial}{\partial\left(\frac{X}{c}\right)}\left(\frac{W^2}{U_0^2}\right) \cong N\int\int_A -W\frac{\partial P}{\partial z}dA + N\int\int_A \rho\overline{wu_j}\frac{\partial W}{\partial x_j}dA + N\int\int_A -\mu\left(\frac{\partial W}{\partial x_j}+\frac{\partial U_j}{\partial z}\right)\frac{\partial W}{\partial x_j}dA$$

$$-0.17^{(1)} \cong (-0.06)^{(3)} + (-0.112)^{(2)} + (0.000)$$

$$\frac{\partial}{\partial\left(\frac{X}{c}\right)}\left(\frac{\overline{\overline{P+\frac{1}{2}\rho U^2}}}{\frac{1}{2}\rho U_0^2}\right) \cong N\int\int_A \left(V\frac{\partial P}{\partial y}+W\frac{\partial P}{\partial z}\right)dA + N\int\int_A \rho\overline{uu_j}dA + N\int\int_A -\mu\left(\frac{\partial U}{\partial x_j}+\frac{\partial U_j}{\partial x}\right)\frac{\partial U}{\partial x_j}dA$$

$$-0.05^{(3)} \cong (+0.02)^{(3)} + (-0.053)^{(2)} + (-0.013)$$

(1) From measurements, Table 2.
(2) Table 3.
(3) By difference.

Starting with the equation for spanwise kinetic energy, $\overline{w^2}/U_0^2$, the turbulent deformation work, -0.112, does not completely explain the measured decay rate, -0.17. This suggests that spanwise kinetic energy is also converted reversibly to other forms through the pressure term, $-W\ \partial P/\partial z$ (~ -0.06).

In the equation for $\overline{v^2}/U_0^2$, the turbulent deformation work (-0.061) is larger than the measured decay rate (-0.03). This suggests a production of $V^2/2$ through the pressure term $-V\partial P/\partial y$ ($\sim +0.03$). Similarly, a small production of primary energy, $P+\frac{1}{2}\rho U^2$, is indicated due to $V\ \partial P/\partial y$ and $W\ \partial P/\partial z$ ($\sim +0.02$). This balances equation (9) and accounts for the deformation work by the primary velocity (-0.066) being larger than the measured rate of decrease of primary energy (-0.05).

The rate of decay of $W^2/2$ between planes 1 and 2 was also very close (-0.19) to the rate observed from planes 2 to 4. Thus, there appears to be a steady rate of decay of $W^2/2$, near and downstream of the trailing edge. This suggests that the same mechanisms, $\overline{vw}\ \partial W/\partial y$, $\overline{w^2}\ \partial W/\partial z$, and $-W\partial P/\partial z$, are governing the changes of spanwise kinetic energy at the trailing edge.

Explanation of a Paradox. Two contributing factors have been identified that can explain the paradox of apparently reversible primary flow (in a mass-averaged sense) and irreversible secondary flow, downstream of the trailing edge of the VPI&SU cascade [1]. The first is the conversion of turbulence kinetic energy into primary mean kinetic energy through the action of the primary Reynolds normal stress $\overline{u^2}$ on the primary flow. The magnitude of this term is about 20 percent of the overall rate of loss production at plane 2. The second effect is a reversible energy exchange through the pressure terms in equations (7), (8), and (9). This could be of the order of 10 percent of the overall loss rate. Together these could then offset the 30 percent of the loss rate caused by the endwall boundary layer (Tables 3 and 4). In combination, these factors can explain the turbine designer's rule of thumb that, downstream of a blade row, total pressure is conserved for the primary flow while secondary kinetic energy is dissipated.

Unified Picture of Loss Production. Overall, reversible energy exchanges from $W^2/2$ to $V^2/2$ and $P+\frac{1}{2}\rho U^2$ seem possible. With these exchanges, the measured rates of decrease of mean kinetic energy and the integrated contributions from the deformation work can be reconciled. The results presented in Figs. 9 and 10 and Tables 3–6 then give a unified picture of loss production at plane 2 downstream of the VPI&SU cascade.

Conclusions

A rotatable two-wire hot-wire probe has been developed and used to measure all six turbulent Reynolds stresses on a plane 10 percent of an axial chord downstream of the trailing edge of the VPI&SU cascade. The Reynolds stress measurements have been combined with earlier measurements of mean velocity to evaluate the turbulent deformation work terms (production of turbulence kinetic energy) in the equations for the generation of total pressure loss and the decay of the components of mean kinetic energy.

The measured rate of production of total pressure loss at the measurement plane agrees very closely with the rate obtained by integrating the deformation work terms. Thus, a unified picture of loss production downstream of the VPI&SU cascade has been obtained in terms of turbulent and laminar deformation work. Reversible energy exchanges, through the action of pressure forces, allow the measured rates of decay of the components of mean kinetic energy to be reconciled with the deformation work.

Nearly one half of the deformation work is caused by the spanwise component of mean velocity. Of this nearly two thirds is due to the mechanism, $-\rho\ \overline{vw}\ \partial W/\partial y$, acting on the spanwise velocities in the blade wake; the other one third is associated with the mechanism, $-\rho\ \overline{w^2}\ \partial W/\partial z$, near midspan as the spanwise velocities decrease due to flow symmetry.

The paradox of apparently reversible primary flow and irreversible secondary flow, downstream of the trailing edge of the VPI&SU cascade, can be explained by two mechanisms which can act to produce total pressure in the primary flow direction, $P+\frac{1}{2}\rho U^2$. These are the deformation work term $\rho\ \overline{u^2}\ \partial U/\partial x$, which can act to produce mean kinetic energy from turbulence kinetic energy, and the reversible pressure work terms $V\ \partial P/\partial y + W\ \partial P/\partial z$, which can exchange mean kinetic energy among its three components. These mechanisms combined could offset the nearly one third of the loss production rate caused by shear of the primary flow, $\mu\ (\partial U/\partial z)^2 - \rho\overline{uw}\partial U/\partial z$, in the endwall boundary layer.

Acknowledgments

The authors wish to thank Rolls-Royce Limited, Aero Division, for supporting this work under a cooperative agreement with Virginia Polytechnic Institute and State University.

References

1 Moore, J., and Adhye, R. Y., "Secondary Flows and Losses Downstream of a Turbine Cascade," ASME JOURNAL OF ENGINEERING FOR GAS TURBINES AND POWER, Vol. 107, No. 4, Oct. 1985, pp. 961–968.

2 Langston, L. S., Nice, M. L., and Hooper, R. M., "Three-Dimensional Flow Within a Turbine Cascade Passage," ASME JOURNAL OF ENGINEERING FOR POWER, Vol. 99, Jan. 1977, pp. 21–28.

3 Hinze, J. O., *Turbulence*, 2nd ed., McGraw-Hill, New York, 1975, pp. 68–74.

4 Kool, P., "Determination of the Reynolds-Stress Tensor With a Single Slanted Hot-Wire in Periodically Unsteady Turbomachinery Flow," ASME Paper No. 79-GT-130.

5 Gorton, C. A., and Lakshminarayana, B., "Analytical and Experimental Study of Mean Flow and Turbulence Characteristics Inside the Passages of an Axial Flow Inducer," NASA Contractor Report 3333, Nov. 1980.

6 Lakshminarayana, B., "Three Sensor Hot Wire/Film Technique for Three Dimensional Mean and Turbulence Flow Field Measurement," *TSI Quarterly*, Vol. VIII, Issue 1, Jan.–Mar. 1982.

7 Hirsch, C., and Kool, P., "Measurement of the Three-Dimensional Flow Field Behind an Axial Compressor Stage," ASME JOURNAL OF ENGINEERING FOR POWER, Vol. 99, No. 2, Apr. 1977, pp. 168–180.

8 Shaffer, D. M., "Reynolds Stress Measurements Downstream of a Turbine Cascade," M.S. Thesis, Virginia Polytechnic Institute and State University, Blacksburg, VA, Aug. 1985.

9 Laufer, J., "The Structure of Turbulence in Fully-Developed Pipe Flow," NACA Report No. 1174, 1954.

10 Gregory-Smith, D. G., and Graves, C. P., "Secondary Flow and Losses in a Turbine Cascade," *AGARD Conference Proceedings No. 351 on Viscous Effects in Turbomachines*, Copenhagen, Denmark, June 1983.

11 Moore, J., and Moore, J. G., "Performance Evaluation of Linear Turbine Cascades Using Three-Dimensional Viscous Flow Calculations," ASME JOURNAL OF ENGINEERING FOR GAS TURBINES AND POWER, Vol. 107, No. 4, Oct. 1985, pp. 969–975.

The Segregated Approach to Predicting Viscous Compressible Fluid Flows

J. P. Van Doormaal

G. D. Raithby

Department of Mechanical Engineering,
University of Waterloo,
Waterloo, Ontario, Canada

B. H. McDonald

Atomic Energy of Canada,
Whiteshell Nuclear Research Establishment,
Pinawa, Manitoba, Canada

The SIMPLE method of Patankar and Spalding and its variants such as SIMPLER, SIMPLEC, and SIMPLEX are segregated methods for solving the discrete algebraic equations representing the equations of motion for an incompressible fluid flow. The present paper presents the extension of these methods to the solution of compressible fluid flows within the context of generalized segregated approach. To provide a framework for better understanding the segregated approach to solving viscous compressible fluid flows an interpretation of the role of pressure in the numerical method is presented. With this interpretation it becomes evident that the linearization of the equation for mass conservation and the approach used to solve the linearized algebraic equations representing the equations of motion are important in determining the performance of the numerical method. The relative performances of the various segregated methods are compared for several subsonic and supersonic compressible fluid flows.

Introduction

Many problems of practical interest, such as the analysis of gas turbine flows, require the solution of the equations of motion for a viscous compressible fluid flow. Over the last two decades the numerical methods for treating such problems have evolved rapidly. However, many of the methods that can be used for the prediction of compressible flows, such as those found in [1–4], are not appropriate in the low Mach number limit and not at all applicable to incompressible flows. Another class of methods used extensively for the prediction of viscous incompressible fluid flows and which has been extended to compressible fluid flows is based on the SIMPLE algorithm of Patankar and Spalding [5]. The extension of SIMPLE-based methods to compressible flows was first proposed by Patankar [6] and later by Issa and Lockwood [7] and Hah [8]. While these segregated methods are used, they are based on the extension of the original SIMPLE algorithm which has been, since it was first introduced, the subject of considerable study and enhancement. As a result a number of improved variants of the original SIMPLE algorithm including SIMPLER [9], SIMPLEC [10], and SIMPLEX [11] have been developed. These enhanced variants have not been extended to compressible flows. In the present paper, the extension of these methods to compressible flows is advanced and an understanding of their limitations and knowledge of their relative computational performance is developed.

To provide a framework for understanding the segregated approach to solving viscous compressible fluid flows an interpretation of the role of pressure in the numerical method is presented. With this interpretation of the role of pressure it becomes evident that the linearization of the equation representing mass conservation and the solution method used to solve the linear algebraic equations representing the equations of motion are important in determining the applicability and the computational performance of the method.

To provide a clear understanding of the segregated approach to solving compressible fluid flows, a generalized segregated approach is advanced and the extension of the segregated methods for incompressible flows to compressible flows is presented within this generalized framework. Also, in the interest of clarity, the concepts outlined above are presented within the context of one-dimensional duct flow. Fortunately all of the concepts developed within this one-dimensional context are readily extended to two or three dimensions. To demonstrate the latter and to evaluate the relative performance of the various segregated methods, the results of a number of numerical experiments including one-dimensional flow in a duct and the steady-state two-dimensional supersonic flow around a flat plate obstacle are reported. The numerical experiments were designed to determine the sensitivity of the computational requirements of each of the segregated methods to the size of time step chosen. A simple and stable representation of the equations of motion was used throughout the study; the question of discretization accuracy was not addressed.

Equations of Motion

Differential Equations. The differential equations expressing the conservation of mass, momentum, and energy for a laminar one-dimensional viscous compressible flow of a perfect gas can be expressed as

Contributed by the Gas Turbine Division of THE AMERICAN SOCIETY OF MECHANICAL ENGINEERS and presented at the 31st International Gas Turbine Conference and Exhibit, Düsseldorf, Federal Republic of Germany, June 8–12, 1986. Manuscript received at ASME Headquarters February 11, 1986. Paper No. 86-GT-196.

$$w\frac{\partial \rho}{\partial t}+\frac{\partial}{\partial x}(\rho u w)=0 \tag{1}$$

$$w\frac{\partial}{\partial t}(\rho u)+\frac{\partial}{\partial x}(\rho u w u)=\frac{\partial}{\partial x}\left(w\mu\frac{\partial u}{\partial x}\right)-w\frac{\partial p}{\partial x}+\frac{\mu}{3}\frac{\partial}{\partial x}\left(\frac{\partial}{\partial x}(uw)\right) \tag{2}$$

$$w\frac{\partial}{\partial t}(\rho T)+\frac{\partial}{\partial x}(\rho u w T)=\frac{\partial}{\partial x}\left(w\frac{k}{C_p}\frac{\partial T}{\partial x}\right)+\frac{1}{C_p}\left(w\frac{\partial p}{\partial t}+\frac{\partial}{\partial x}(uwp)-p\frac{\partial}{\partial x}(uw)\right) \tag{3}$$

where the dependent variables u, p, ρ, and T are the velocity, pressure, density, and temperature, respectively, μ is the viscosity, C_p is the specific heat at constant pressure, k is the thermal conductivity, and w is the width of the duct.

To close the set of equations an equation of state, relating pressure, density, and temperature, is required. For an ideal perfect gas this relation is given by

$$\rho=\frac{p}{RT} \tag{4}$$

where R is the gas constant.

Algebraic Equations. To solve the equations of motion a grid is generated to cover the domain of interest and any one of a number of discretization methods applied. In this paper the staggered grid of Harlow and Welch [12], shown in Fig. 1, and the control volume based discretization described by Patankar [9] with the upstream weighted variant of Raithby and Torrance [13] are applied. Also, the recommendation of Issa and Lockwood [7] is adopted whereby densities are upwinded in the discretization of the mass conservation equation. As a result the algebraic equations expressing the conservation of mass momentum and energy for the control volumes shown in Fig. 1 can be expressed as

$$\frac{M-M^0}{\Delta t}=\dot{M}_e-\dot{M}_w \tag{5}$$

$$a_p^u u_P=\Sigma a_{nb}^u u_{nb}-c^u(p_E-p_P)+b^u \tag{6}$$

$$a_p^T T_P=\Sigma a_{nb}^T T_{nb}+b^T \tag{7}$$

where

$$\Sigma a_{nb}^u u_{nb} = a_e^u u_E+a_w^u u_W$$
$$\Sigma a_{nb}^T T_{nb} = a_e^T T_E+a_w^T T_W$$

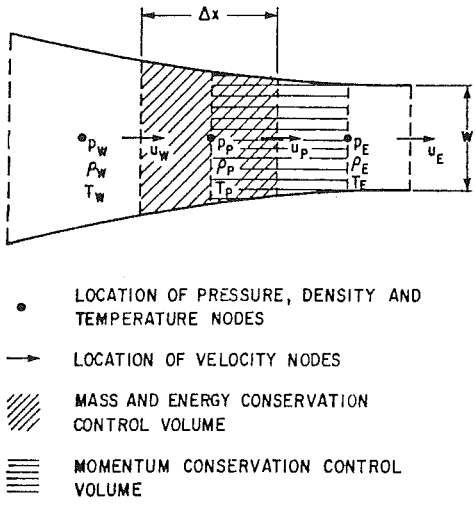

Fig. 1 Geometry and staggered arrangement of mesh, nodes, and control volumes for flow in a one-dimensional variable area duct

and where M is the mass contained in the control volume, the superscript 0 denotes the value at the beginning of the time step, and $\dot{M}$ is the mass flux through the control volume face indicated by the corresponding subscript. The lower case subscript e refers to the location of the control volume face that lies between P and E, and w to the face between P and W. To close the algebraic set of equations the equation of state can be expressed as

$$\rho_P=c^\rho p_P+b^\rho \tag{8}$$

The solution of equations (5)–(8), together with the algebraic representation of the prescribed boundary conditions, advances the solution over a time step Δt. The remainder of this paper is addressed to methods used to obtain this solution.

An Interpretation of the Role of Pressure. Before examining in detail the segregated approach to solving compressible fluid flows it is instructive to consider one interpretation of the role of pressure in a segregated approach.

The treatment of the coupling between pressure and velocity in the solution of *incompressible* fluid flows has in the past been particularly troublesome. This difficulty arises because only velocity and not pressure appears in the mass conservation equation. The mass conservation equation can be interpreted in this case as an indirect constraint equation for pressure whereby the correct pressure distribution is identified

Nomenclature

a_p, a_e, a_w, a_n, a_s = coefficients of pressure equation and algebraic representation of momentum and energy conservation
$\mathbf{A}$ = matrix of a coefficients
$\bar{\mathbf{A}}$ = approximation of $\mathbf{A}$
b = coefficient of pressure equation and algebraic representation of momentum and energy conservation
$\mathbf{b}$ = vector of b coefficients
c = pressure coefficient
$\mathbf{c}$ = vector of c coefficients
C_p = specific heat at constant pressure
$\mathbf{C}$ = matrix of c coefficients
$\mathbf{C}_p$ = matrix of pressure coefficients
d = coefficient of pressure difference influence
$\bar{d}$ = approximation of d
$\bar{\mathbf{d}}$ = vector of $\bar{d}$ coefficients
$\mathbf{D}_p$ = matrix of pressure influence coefficients
$\bar{\mathbf{D}}_p$ = approximation of $\mathbf{D}_p$
k = thermal conductivity
L = length
m_e, m_w, m_n, m_s = coefficients of algebraic representation of mass conservation
M = mass contained in control volume
$\dot{M}$ = mass flux through control volume face
$\mathbf{M}$ = matrix of m coefficients
N = number of control volumes in length L
p = pressure
p^* = estimate of pressure
$\bar{p}$ = improved estimate of pressure
$\bar{\bar{p}}$ = improved estimate of pressure of PUP
p' = pressure correction
p'' = pressure correction of PUP

as that which, when used in the momentum equations, results in velocities which conserve mass.

For *compressible* fluid flows both velocity and density appear as dependent variables in the mass conservation equation. Nevertheless, the algebraic representation of mass conservation can still be interpreted as a constraint equation for pressure and the modified interpretation of the role of pressure for the segregated approach to solving compressible flow becomes that the pressure must influence the velocity through the momentum conservation and the density through the equation of state such that together the resulting velocities and the resulting densities conserve mass.

Nonlinearity. The form of equations (5)–(8) implies that these equations are linear. In fact the coefficients of these equations themselves depend on the dependent variables. To obtain solutions to these nonlinear equations, linearization and iteration are required.

For equations (6)–(8) the linearization adopted is the one implied by the form of these equations whereby the current available estimates of dependent variables are used to evaluate the coefficients. However, the linearized algebraic representation of mass conservation given by equation (5) is not appropriate because the desired dependent variables do not explicitly appear. To remedy this, it is necesary that the coefficients of equation (5) be linearized in terms of density and the components of velocity. This choice is motivated by the interpretation of the role of pressure described previously, that pressure must influence velocity and density such that both velocity and density together conserve mass.

To accomplish this the mass flux term $\dot{M}_e$ is approximated by

$$\dot{M}_e = \{\rho u w\}_e \approx (\rho u^* w)_e + [\rho^* u w]_e - \{\rho^* u^* w\}_e \tag{9}$$

where the superscript * is used to denote that current estimates are to be used to evaluate the corresponding dependent variable. As a result, the mass flux term enclosed in the ( ) brackets is linearized in terms of density and the mass flux term enclosed in the [ ] brackets is linearized in terms of velocity. With ρ_e taken as the upstream nodal value of density, with $\dot{M}_w$ linearized in a similar fashion and upon expanding the control volume mass M in terms of density, equation (5) can be represented by

$$m_p^\rho \rho_P + m_e^\rho \rho_E + m_w^\rho \rho_W + m_e^u u_P + m_w^u u_W = b^c \tag{10}$$

where current estimates of velocity and density are used to evaluate the coefficients of equation (10).

The linearization of the mass conservation equation described above, in terms of both velocity and density, has been adopted to ensure that the linearization is applicable to both incompressible as well as compressible flows. To linearize mass conservation in terms of velocity alone restricts the application of the resulting solution method to low Mach number and incompressible flows; linearization in terms of density alone restricts applications to compressible flows with very small time steps required in the low Mach number limit to maintain stability. The linearization of mass conservation resulting in equation (10) is also a generalization of the linearization of mass conservation suggested by Harlow and Amsden [16] for the ICE method as well as the linearization implied by Patankar [6] in the extension of the SIMPLE approach to compressible flows.

With regards to the linearized algebraic representation of the equation of state, again, the form of equation (8) is motivated by the interpretation of the role of pressure already discussed. For the linearization of the algebraic representation of energy conservation given by equation (7), the assumption is made that the couplings between temperature and velocity as well as between temperature and pressure are not dominant so that in the linear algebraic set of equations the energy equation is decoupled from the mass, momentum and state equations. This allows the focus of the present work to center on the remaining linear equations for pressure, velocity, and density. There are, of course, flows for which such a segregation of the energy equation is inappropriate.

Solution of Linear Equations for Pressure, Velocity, and Density

To advance the solution of the equations for mass, momentum, and energy conservation and the equation of state over a time step, equations (6)–(8) and (10) are solved, the coefficients updated, and the sequence repeated until the effect of the nonlinearities has been adequately treated. Each repetition of the sequence is defined here as a cycle. For small time steps one cycle is adequate while for large time steps several cycles may be required. Because the coupling with temperature has been assumed to be weak only the solution of the linearized algebraic representations of mass conservation, equation (10), momentum conservation, equation (6) and the equation of state, equation (8), for pressure, velocity and density are examined in further detail.

The development of a clear understanding of the segregated approach to solving equations (6), (8), and (10) for compressible flows begins by considering a direct noniterative solution method. Based on this direct method, the framework of a generalized segregated approach is advanced. Different ap-

Nomenclature (cont.)

Re = Reynolds number
u, v = velocity components in x and y directions
u^*, v^* = velocities based on p^*
u^{**}, v^{**} = intermediate velocities of PUP
$\tilde{u}, \tilde{v}$ = improved estimate of velocities
$\bar{\tilde{u}}$ = improved estimate of velocity of PUP
u', v' = velocity corrections
u'' = velocity corrections of PUP
$\hat{u}$ = pseudo-velocity of PUP
V = characteristic velocity
w = width of one-dimensional duct
x, y = Cartesian coordinates
Δt = time step
α_p = underrelaxation factor for pressure correction
μ = viscosity
ρ = density
ρ^* = density based on p^*
ρ^{**} = intermediate density of PUP
$\tilde{\rho}$ = improved estimate of density
$\bar{\tilde{\rho}}$ = improved estimate of density of PUP
ρ' = density correction
ρ'' = density correction of PUP
$\hat{\rho}$ = psuedo-density of PUP

Subscripts

E, W, N, S, P = grid points
nb = neighbor grid point

Acronyms

PUP = Pressure Update of Patankar
SIMPLE = Semi-Implicit Pressure Linked Equations
SIMPLER = SIMPLE-Revised
SIMPLEC = SIMPLE-Consistent approximation
SIMPLEX = SIMPLE-eXtrapolated pressure gradients

proximations introduced into the generalized approach lead directly to segregated methods for compressible flows which are extensions of methods developed originally for incompressible flows.

Direct Solution. For one-dimensional compressible flow in a duct, equations (6), (8), and (10) can be rewritten in matrix notation as

$$\mathbf{A}^u\mathbf{u}+\mathbf{C}_p^u\mathbf{p}=\mathbf{b}^u \tag{11}$$

$$\boldsymbol{\rho}=\mathbf{C}^\rho\mathbf{p}+\mathbf{b}^\rho \tag{12}$$

$$\mathbf{M}^p\boldsymbol{\rho}+\mathbf{M}^u\mathbf{u}=\mathbf{b}^c \tag{13}$$

Extending the method introduced by Watson [14] and further developed by Zedan and Schneider [15] for incompressible flows, equation (11) is rewritten as

$$\mathbf{u}=(\mathbf{A}^u)^{-1}\mathbf{b}^u-\mathbf{D}_p^u\mathbf{p} \tag{14}$$

where $\mathbf{D}_p^u=(\mathbf{A}^u)^{-1}\mathbf{C}_p^u$, and substituting for $\mathbf{u}$ from equation (14) and for $\boldsymbol{\rho}$ from equation (12) into equation (13) the resulting equation for pressure is given by

$$\mathbf{A}^p\mathbf{p}=\mathbf{b}^p \tag{15}$$

where

$$\mathbf{A}^p=\mathbf{M}^\rho\mathbf{C}^\rho-\mathbf{M}^u\mathbf{D}_p^u \tag{16}$$

$$\mathbf{b}^p=-\mathbf{M}^\rho\mathbf{C}^\rho-\mathbf{M}^u(\mathbf{A}^u)^{-1}\mathbf{b}^u \tag{17}$$

The exact solution to equations (11)–(13) can therefore be achieved by solving equation (15) for $\mathbf{p}$, followed by a direct substitution into equations (14) and (12) to obtain $\mathbf{u}$ and $\boldsymbol{\rho}$.

This method for solving the linear equations clearly illustrates how the pressure influences velocity through equation (14) and density through equation (12) such that together velocity and density satisfy the algebraic representation of mass conservation. Also, this method for solving the linear equations for pressure, velocity, and density is relatively straightforward and readily implemented numerically. The computational requirements, in particular, for the evaluation of $\mathbf{D}_p^u$ and the storage of $\mathbf{A}^p$ are considerable. To reduce these computational requirements the iterative segregated approach is adopted where approximations to $\mathbf{D}_p^u$ are introduced.

Generalized Segregated Approach. Given an estimate of pressure, denoted by $\mathbf{p}^*$, the corresponding velocity $\mathbf{u}^*$, which satisfies the algebraic representation of momentum conservation, and the corresponding density $\boldsymbol{\rho}^*$, from the algebraic representation of the equation of state, are given by

$$\mathbf{u}^*=(\mathbf{A}^u)^{-1}(\mathbf{b}^u-\mathbf{C}_p^u\mathbf{p}^*) \tag{18a}$$

or

$$\mathbf{u}^*=(\mathbf{A}^u)^{-1}\mathbf{b}^u-\mathbf{D}_p^u\mathbf{p}^* \tag{18b}$$

and

$$\boldsymbol{\rho}^*=\mathbf{C}^\rho\mathbf{p}^*+\mathbf{b}^\rho \tag{19}$$

Since the $\mathbf{p}^*$ is not in general correct, the $\mathbf{u}^*$ velocity and $\boldsymbol{\rho}^*$ density will not together satisfy mass conservation. To improve the estimate of the $\mathbf{u}^*$ velocity and $\boldsymbol{\rho}^*$ density it is necessary to subtract out the effect of $\mathbf{p}^*$ on $\mathbf{u}$ and $\boldsymbol{\rho}$ and add in the effect of an improved pressure estimate. Approximating the influence of $\mathbf{p}^*$ on $\mathbf{u}^*$ by $-\bar{\mathbf{D}}_p^u\mathbf{p}^*$ and the influence of the improved pressure estimate $\bar{\mathbf{p}}$ by $-\bar{\mathbf{D}}_p^u\bar{\mathbf{p}}$, the improved estimate of velocity $\bar{u}$ is given by

$$\bar{\mathbf{u}}=\mathbf{u}^*+\bar{\mathbf{D}}_p^u\mathbf{p}^*-\bar{\mathbf{D}}_p^u\bar{\mathbf{p}} \tag{20a}$$

or

$$\bar{\mathbf{u}}=\mathbf{u}^*-\bar{\mathbf{D}}_p^u(\bar{\mathbf{p}}-\mathbf{p}^*) \tag{20b}$$

Without further approximation, the improved estimate of density $\bar{\rho}$ is given by

$$\bar{\boldsymbol{\rho}}=\boldsymbol{\rho}^*-\mathbf{C}^\rho\mathbf{p}^*+\mathbf{C}^\rho\bar{\mathbf{p}} \tag{21a}$$

or

$$\bar{\boldsymbol{\rho}}=\boldsymbol{\rho}^*+\mathbf{C}^\rho(\bar{\mathbf{p}}-\mathbf{p}^*) \tag{21b}$$

where $\mathbf{C}^\rho\mathbf{p}^*$ and $\mathbf{C}^\rho\bar{\mathbf{p}}$ represent the influence of $\mathbf{p}^*$ and $\bar{\mathbf{p}}$, respectively, on the density.

By requiring that the $\bar{\mathbf{u}}$ velocity and $\bar{\rho}$ density satisfy mass conservation, given by equation (13), the following equation for $\bar{\mathbf{p}}$ results

$$\bar{\mathbf{A}}^p\bar{\mathbf{p}}=\bar{\mathbf{b}}^p \tag{22}$$

where

$$\bar{\mathbf{A}}^p=\mathbf{M}^\rho\mathbf{C}^\rho-\mathbf{M}^u\bar{\mathbf{D}}_p^u \tag{23}$$

$$\bar{\mathbf{b}}^p=-\mathbf{M}^\rho(\boldsymbol{\rho}^*-\mathbf{C}^\rho\mathbf{p}^*)-\mathbf{M}^u(\mathbf{u}^*+\bar{\mathbf{D}}_p^u\mathbf{p}^*) \tag{24}$$

Solving equation (22) for $\bar{\mathbf{p}}$ the solutions for $\bar{\mathbf{u}}$ and $\bar{\rho}$ are readily determined from equations (20) and (21), respectively.

It is important to note that if $\bar{\mathbf{D}}_p^u$ is chosen to be $\mathbf{D}_p^u$ exactly, then $\bar{\mathbf{p}}$, $\bar{\mathbf{u}}$, and $\bar{\rho}$ will satisfy equations (11), (12), and (13) exactly. However, because an approximate evaluation of $\mathbf{D}_p^u$ is used to obtain $\bar{\mathbf{p}}$, $\bar{\mathbf{u}}$, and $\bar{\rho}$, these solutions will not satisfy equations (11)–(13) exactly unless the choice for $\mathbf{p}^*$ happened to be correct.

Using the approach described above the solutions of equations (11)–(13) can be determined from repeated application of equations (18)–(24) with $\mathbf{p}^*$ to be taken from the previous value of $\bar{\mathbf{p}}$. With an appropriate choice for $\bar{\mathbf{D}}_p^u$ this iterative method will converge but it is not clear that the computational requirements associated with this iterative method would be any less than the requirements of a direct method. However, if $\bar{\mathbf{D}}_p^u$ is a good approximation of $\mathbf{D}_p^u$, then the values of $\bar{\mathbf{p}}$, $\bar{\mathbf{u}}$, and $\bar{\rho}$ after one iteration will adequately represent $\mathbf{u}$, $\mathbf{p}$, and $\boldsymbol{\rho}$. As a result, the computational requirements of the iterative method may be considerably less than those of a direct method.

The resulting segregated approach is implemented by executing the following sequence of steps:

1 Guess a pressure field $\mathbf{p}^*$.

2 Evaluate the coefficients of the momentum conservation equation and the equation of state, equations (11) and (12), and solve for $\mathbf{u}^*$ and $\boldsymbol{\rho}^*$ using $\mathbf{p}^*$.

3 Evaluate the coefficients of the mass conservation equation (13) and the pressure equation (15) and solve for $\bar{\mathbf{p}}$.

4 Evaluate the improved estimate for velocity $\bar{\mathbf{u}}$ and density $\bar{\rho}$ from equations (20) and (21), respectively.

5 Evaluate the coefficients of the energy conservation equation (9), and solve for the temperature T.

6 Using the $\bar{\mathbf{p}}$ found in step 3 as the new $\mathbf{p}^*$, return to step 2. Repeat this cycle, until the desired convergence is achieved, to obtain the solution for $\mathbf{p}$, $\mathbf{u}$, $\boldsymbol{\rho}$, and T at the end of the time step.

7 Repeat steps 1 to 6 for each time step until the solution at the prescribed time, or steady-state conditions, are obtained.

In the approach described above the solutions of the tentative velocity $\mathbf{u}^*$, the tentative density $\boldsymbol{\rho}^*$, the approximate pressure $\bar{\mathbf{p}}$, and the temperature T are determined separately, in an uncoupled manner. This approach to solving the coupled equations can appropriately be described as segregated. In fact, without prescribing how $\bar{\mathbf{D}}_p^u$ is to be evaluated, the method is the compressible flow extension of the generalized segregated approach to solving incompressible fluid flows described previously [11].

It is evident that the performance of a segregated method is dependent on the approximations introduced to determine $\bar{\mathbf{D}}_p^u$. With a detailed discussion of this consideration for incompressible flows already presented by Van Doormaal and Raithby [11], only a summary of the discussion is presented here.

On the Structure of $\bar{\mathbf{D}}_p^u$. In an effort to ensure that the computational requirements of the segregated method are minimized a desirable structure for $\bar{\mathbf{D}}_p^u$ arises from relating

Table 1 Evaluations of $\bar{d}^u$

Method	Approximation	$\bar{d}^u$
SIMPLE	$\sum a^u_{nb} u'_{nb}=0$	c^u/a^u_p
SIMPLER	$\sum a^u_{nb} u'_{nb}=0$	c^u/a^u_p
SIMPLEC	$\sum a^u_{nb}(u'_{nb}-u'_P)=0$	$c^u/(a^u_p-\sum a^u_{nb})$
SIMPLEX	$\Delta p_{ALL}=\Delta p_P$ for u_P	$a^u_p \bar{d}^u_P=\sum a^u_{nb}\bar{d}^u_{nb}+c^u$

each nodal velocity, through $\tilde{\mathbf{D}}^u_p$, to only the two nodal pressures that stagger the velocity node. In this case the $\tilde{\mathbf{D}}^u_p$ matrix would have zero entries everywhere except along two diagonals.

There are at least two advantages to this form of $\tilde{\mathbf{D}}^u_p$. The first is that the diagonal entries of $\tilde{\mathbf{D}}^u_p$ may be readily evaluated, thereby keeping the computational requirements low. Secondly, the computational storage requirements of $\mathbf{A}^p$ from equation (23) are minimal. It is because of these advantages that most segregated methods adopt this simple form of $\tilde{\mathbf{D}}^u_p$. However, there are at least two major shortcomings of this practice.

The first shortcoming is that for high Reynolds number flows and with relatively high values of the time step it has been shown [11] that nodal pressures which are physically distant from a nodal velocity can have a significant influence on the velocity. For such cases the simple form of $\tilde{\mathbf{D}}^u_p$ is not appropriate. Only for smaller time steps does this simple form become appropriate [11]. The second shortcoming of this simple form of $\tilde{\mathbf{D}}^u_p$ is that, without taking special care, the convergence of a segregated method often degrades significantly with grid refinement.

With a knowledge, then, of these potential limitations of segregated methods, these methods can be used in an appropriate fashion. In the next section various approximations to $\mathbf{D}^u_p$ leading to the compressible flow extension of SIMPLE, SIMPLER, SIMPLEC, and SIMPLEX are reviewed. Subsequently, the results of numerical experiments designed to evaluate the relative performance of these methods are presented.

Examples of the Segregated Approach

The preceding description of the generalized segregated approach is given in terms of the dependent variables, pressure, velocity, and density, using matrix notation, with the solution of the temperature, determined from the conservation of energy, being completely decoupled from the solution of the remaining dependent variables. In what follows the segregated approach is reformulated and cast in terms of corrections to the nodal values of pressure, velocity and density. Although the two descriptions are algebraically equivalent, the latter is employed because it is the form most commonly implemented in a computer code. Also, in the interest of minimizing the effects of computer roundoff, use of the correction form is recommended [10].

Segregated Approach in Terms of Nodal Values. Given an estimate for pressure p^*, the nodal values for the u^* velocities and ρ^* densities are determined from

$$a^u_p u^*_P = \Sigma a^u_{nb} u^*_{nb} - c^u(p^*_E - p^*_P) + b^u \tag{25}$$

and

$$\rho^*_P = c^\rho p^*_P + b^\rho \tag{26}$$

Introducing corrections to the p^* pressure and u^* velocity denoted by p' and u' such that

$$p' = \tilde{p} - p^* \tag{27}$$

$$u' = \tilde{u} - u^* \tag{28}$$

approximating that

$$u'_P = -\bar{d}^u(p'_E - p'_P) \tag{29}$$

and combining with the definition of u', the $\tilde{u}$ velocity is given by

$$\tilde{u}_P = u^*_P - \bar{d}^u(p'_E - p'_P) \tag{30}$$

Similarly, introducing a correction to the ρ^* density denoted by ρ' such that

$$\rho' = \tilde{\rho} - \rho^* \tag{31}$$

the $\tilde{\rho}$ density is given by

$$\tilde{\rho}_P = \rho^*_P + c^\rho p'_P \tag{32}$$

By requiring that the $\tilde{u}$ velocities and $\tilde{\rho}$ densities satisfy mass conservation, that is

$$m^\rho_p \tilde{\rho}_P + m^\rho_e \tilde{\rho}_E m^\rho_w \tilde{\rho}_W + m^u_e \tilde{u}_P + m^u_w \tilde{u}_W = b^c \tag{33}$$

the following equation for p' results

$$a^p_p p'_P = a^p_e p'_E + a^p_w p'_E + b^{p'} \tag{34}$$

where

$$a^p_p = m^\rho_p c^\rho + m^u_e \bar{d}^u + m^u_w [\bar{d}^u]_W \tag{35}$$

$$a^p_e = -m^\rho_e [c^\rho]_E + m^u_e \bar{d}^u \tag{36}$$

$$a^p_w = -m^\rho_w [c^\rho]_W - m^u_w [\bar{d}^u]_W \tag{37}$$

$$b^{p'} = b^c - m^\rho_p \rho^*_P - m^\rho_e \rho^*_E - m^\rho_w \rho^*_W - m^u_e u^*_P - m^u_w u^*_W \tag{38}$$

and where the subscripts on the coefficients enclosed by the [ ] brackets refer to coefficients written for the equation of the corresponding subscript. For terms not enclosed by the [ ] brackets the P control volume is implied. Upon solving equation (34) for p', $\tilde{p}$ is obtained from

$$\tilde{p} = p^* + p' \tag{39}$$

$\tilde{u}$ is obtained from equation (30) and $\tilde{\rho}$ from equation (32).

At this point it is instructive to note the algebraic equivalence of equations (18) and (25), equations (19) and (26), equations (20*b*) and (30), equations (21*b*) and (32), and equations (22) and (34). In the case of equations (30), (32), and (34), which are expressed in terms of p', equation (39) provides the simple linear transformation to $\tilde{p}$ which appears in equations (20*b*), (21*b*), and (22). In noting the equivalence of equations (22) and (34) it is worthy to note that the approximate form of $\tilde{\mathbf{D}}^u_p$ results in a tridiagonal matrix for $\tilde{A}^p$ thereby minimizing the computational storage requirements.

Four Segregated Methods. Using the generalized segregated approach described above, a number of segregated methods can be generated by introducing different approximations to evaluate the $\bar{d}^u$ coefficient of equations (29) and (30). The evaluation of $\bar{d}^u$ and the approximation introduced for several segregated methods including SIMPLE, SIMPLER, SIMPLEC, and SIMPLEX, all proposed originally for incompressible flows, are listed in Table 1.

It is important to note here that the evaluations of $\bar{d}^u$ distinguish the segregated methods from one another, and that the same evaluations of $\bar{d}^u$ used for incompressible flows are applicable to compressible flows. The major difference between segregated methods for incompressible flows and segregated methods for compressible flows is the additional consideration in compressible flows of the variations in density in the mass conservation equation.

SIMPLE. In the original form of SIMPLE [5], the approximations which are introduced to evaluate $\bar{d}^u$ often result in an overestimation of the magnitude of p' which in turn leads to slow convergence or to cause divergence of the method. To remedy this, for incompressible flows, the correction of pressure is underrelaxed by

$$\tilde{p} = p^* + \alpha_p p' \tag{40}$$

where Patankar [17] recommends $\alpha_p \approx 0.8$. However, for compressible flows equation (40) is not necessarily appropriate since the pressure now influences both velocity and density.

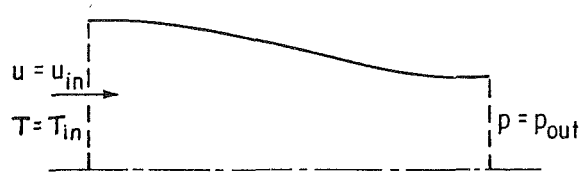

Fig. 2 Probelm of one-dimensional subsonic flow through a 3:2 converging duct with Mach 0.3 inlet

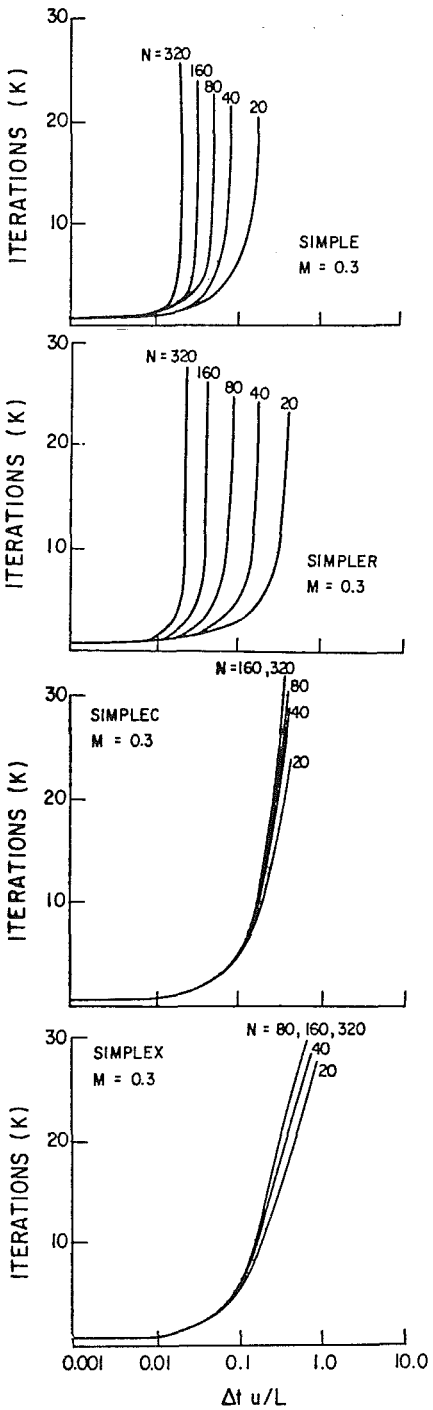

Fig. 3 Iterative convergence behavior of: (a) SIMPLE, (b) SIMPLER, (c) SIMPLEC, and (d) SIMPLEX for one-dimensional subsonic test problem

Therefore, for compressible flows a value of unity for α_p is used.

SIMPLER. In place of underrelaxing p' Patankar [9, 17] in his SIMPLER method for incompressible flows introduces

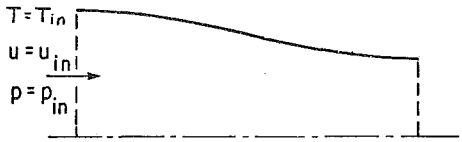

Fig. 4 Problem of one-dimensional supersonic flow through a 3:2 converging duct with Mach 2.0 inlet

the "Pressure Update of Patankar" (PUP) as a second stage to SIMPLE. For compressible flows a similar update of pressure can be adopted. By introducing a second set of improved pressure, velocity, and density estimates, $\bar{\bar{p}}$, $\bar{\bar{u}}$, and $\bar{\bar{\rho}}$, and substituting into momentum conservation and the equation of state

$$a_p^u \bar{\bar{u}}_P = \Sigma a_{nb}^u \bar{\bar{u}}_{nb} - c^u(\bar{\bar{p}}_E - \bar{\bar{p}}_P) + b^u \tag{41}$$

$$\bar{\bar{\rho}}_P = c^\rho \bar{\bar{p}}_P + b^\rho \tag{42}$$

With a second set of pressure and velocity corrections, $p'' = \bar{\bar{p}} - \bar{p}$ and $u'' = \bar{\bar{u}} - \bar{u}$, and introducing the approximation that $\Sigma a^u{}_{nb} u''_{nb} \approx 0$, which is similar to that of SIMPLE, equation (41) becomes

$$\bar{\bar{u}}_P = u_P^{**} - \bar{d}^u(p''_E - p''_P) \tag{43}$$

where

$$u_P^{**} = (\Sigma a_{nb}^u \bar{u}_{nb} - c^u(\bar{p}_E - \bar{p}_P) + b^u)/a_p^u \tag{44}$$

Similarly by introducing a second density correction, $\rho'' = \bar{\bar{\rho}} - \bar{\rho}$, equation (42) can be expressed as

$$\bar{\bar{\rho}}_P = \rho_P^{**} + c^\rho p''_P \tag{45}$$

where

$$\rho_P^{**} = c^\rho \bar{p}_P + b^\rho = \bar{\rho}_P \tag{46}$$

By requiring that $\bar{\bar{u}}$ and $\bar{\bar{\rho}}$ satisfy mass conservation, an equation for p'' similar to equation (34) results

$$a_p^p p''_P = a_e^p p''_E + a_w^p p''_W + b^{p''} \tag{47}$$

where

$$b^{p''} = b^c - m_p^\rho \bar{\rho}_P - m_e^\rho \bar{\rho}_E - m_w^\rho \bar{\rho}_W - m_e^u \bar{u}_P - m_w^u \bar{u}_W \tag{48}$$

Upon solving equation (47) for p'' the improved pressure estimate is determined from $\bar{\bar{p}} = \bar{p} + p''$ and the $\bar{\bar{u}}$ velocities and $\bar{\bar{\rho}}$ densities from equations (43) amd (45), respectively.

The application of PUP differs in two ways from the description of SIMPLER provided by Patankar [9, 17]. The first difference arises from the use of a second pressure correction p'' not used by Patankar. However, PUP can be implemented in terms of the $\bar{\bar{p}}$ pressure by rearranging equations (43) and (45) into the form given by

$$\bar{\bar{u}}_P = \hat{u}_P - \bar{d}^u(\bar{\bar{p}}_E - \bar{\bar{p}}_P) \tag{49}$$

$$\bar{\bar{\rho}}_P = \hat{\rho}_P + c^\rho \bar{\bar{p}}_P \tag{50}$$

where $\hat{u}_P = (\Sigma a_{nb}^u \bar{u}_{nb} + b^u)/a_p^u$ and $\hat{\rho}_P = b^\rho$. Now by requiring that $\bar{\bar{u}}$ and $\bar{\bar{\rho}}$ conserve mass an equation for $\bar{\bar{p}}$ results that is consistent with Patankar's proposal.

The second difference is the order of the SIMPLE and PUP stages. In the preceding description PUP follows SIMPLE where in the SIMPLER described by Patankar, PUP precedes SIMPLE. The order of the PUP and SIMPLE stages described in this paper is identical to the order described by Raithby and Schneider [18] in their study of methods for solving incompressible flows and is in many ways similar to the PISO method [19, 20] developed for solving incompressible and compressible flows. In fact, for steady incompressible flows the PISO method is identical to the method described here. For transient incompressible flows as well as compressible flows further study is required to determine the significance of any difference between the two methods.

SIMPLEC. The introduction of PUP as a second stage is an attempt to correct errors in the pressure which result from

making a poor approximation to $\mathbf{D}_p^u$. In the SIMPLEC method of Van Doormaal and Raithby [10] a more "consistent" approximation is introduced. The results of numerical experiments indicate that for incompressible flows SIMPLEC is substantially more economic than SIMPLE and that SIMPLEC is usually less expensive than SIMPLER.

SIMPLEX. In the three segregated methods described above, no care is taken to ensure that the rate of convergence will not decrease with grid refinement. An attempt to address this concern is made in SIMPLEX [11] where the influence of nodal values of pressure further from a nodal velocity is accounted for. This is accomplished in SIMPLEX by using extrapolation to express all pressure differences in the domain in terms of the pressure difference local to the velocity. Again, for incompressible flows, the computational advantage of SIMPLEX over the previous methods reviewed here, particularly for fine grids, has been demonstrated [11].

One-Dimensional Demonstration Problems

To illustrate the applicability of the segregated methods and to evaluate the relative convergence behavior of these methods numerical experiments were performed on two laminar one-dimensional compressible duct flows.

Subsonic Demonstration Problem. The first demonstration problem is that of a subsonic laminar flow through the 3:2 converging duct shown in Fig. 2 with an inlet Mach number of 0.3. Using a Reynolds number of 10^7 steady-state numerical solutions were determined to within the roundoff limit of the computer using 20, 40, 80, 160, and 320 nodes. Using these solutions, numerical experiments were performed to evaluate the sensitivity of the covergence of the segregated methods to the number of nodes N and the time step Δt. For each grid and for a prescribed time step the coefficients of the linearized algebraic representations of mass conservation, momentum and energy conservation, and the equation of state were determined using the steady-state solutions for p, u, ρ, and T. Subsequently, the pressure was set throughout the domain to the value of the outlet and the convergence of each segregated method was monitored as the solution of the linearized algebraic equations with fixed coefficients was obtained. It is important to emphasize that these tests reveal how well the solution methods used treat the coupling between p, u, and ρ in the linear equation set. Good performance at this level is a prerequisite to the satisfactory solution of the nonlinear set.

In Fig. 3 the number of cycles K required by each of the methods on each of the grids to determine the pressure to within 0.5 percent of its correct value is presented as a function of the size of the time step. The results indicate that for sufficiently small time steps all methods require only one cycle. This is due to the fact that the coefficients of the algebraic equations which are based on the steady-state solution are held fixed. However, as the size of the time step increases the iterative requirements of all methods increase monotonically. This behavior is due to the limitations imposed on all methods by using a very simple structure for $\tilde{\mathbf{D}}_p^u$ which does not appropriately account for the significant influence of nodal pressures which are far from a nodal velocity. The results also show that the behavior of both SIMPLEC and SIMPLEX is relatively independent of the number of nodes while the behavior of both SIMPLE and SIMPLER suffers with grid refinement. In summary, these results indicate that for subsonic flow the behavior of segregated methods using large time steps is determined by the approximations to $\mathbf{D}^u$.

Supersonic Demonstration Problem. The second demonstration problem is that of a supersonic laminar flow through the 3:2 converging duct, shown in Fig. 4, with an inlet Mach number of 2.0. Using the same Reynolds number, the same grids and a similar numerical experiment as in the subsonic case, the sensitivity of the convergence of the segregated methods to the number of nodes and the time step were determined.

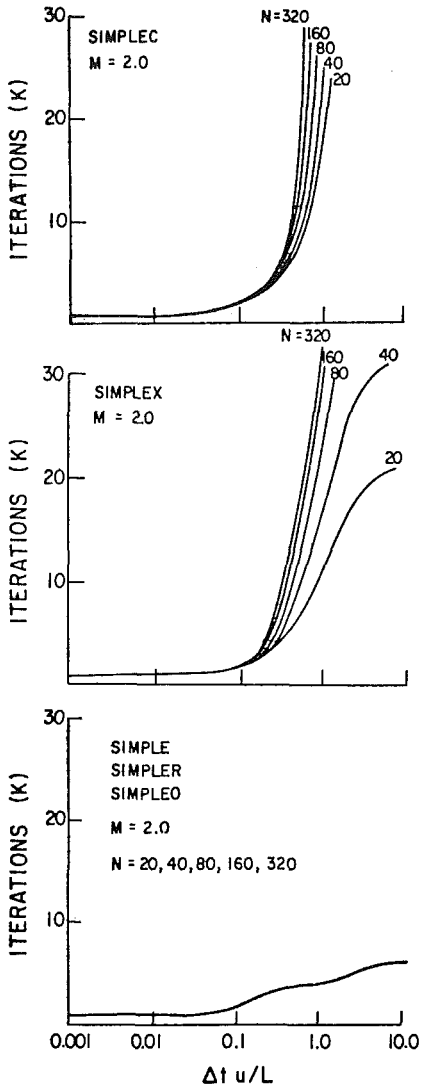

Fig. 5 Iterative convergence behaviour of: (a) SIMPLEC, (b) SIMPLEX, and (c) SIMPLE, SIMPLER, and SIMPLE0 for one-dimensional supersonic test problem

The results shown in Fig. 5 again indicate that for small Δt only one cycle was required by all methods to achieve an accuracy of 0.5 percent and that the behavior of SIMPLEC and SIMPLEX is similar to that found in the subsonic case. However, in contrast to the poor behavior of SIMPLE and SIMPLER on the subsonic problem, the behavior of these methods for the supersonic problem is quite favorable. As shown in Fig. 5(*c*) both SIMPLE and SIMPLER exhibit only a marginal sensitivity to the time step and no sensitivity to spatial discretization. These results, at first, seem surprising especially in light of the poor approximations used to evaluate $\tilde{d}^u$. In fact, in both SIMPLE and SIMPLER the value of $\tilde{d}^u$ is underestimated resulting in an overestimation of pressure corrections for incompressible and subsonic flows. However, for supersonic flows, it appears that the underestimation of $\tilde{d}^u$ is not detrimental to the convergence behavior of SIMPLE and SIMPLER. This is due to the fact that for supersonic flows the primary role of pressure is to influence the density through the equation of state so that mass is conserved. As a result the influence of pressure on velocity can be ignored. To illustrate this point the numerical experiments were repeated for the

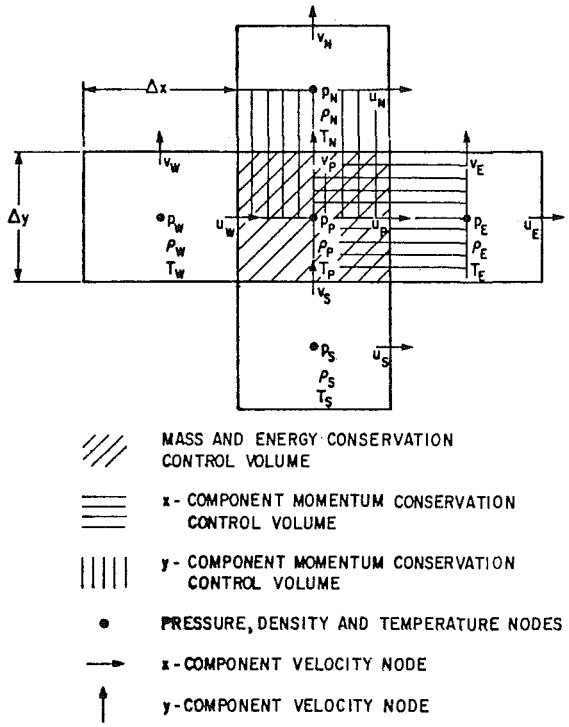

Fig. 6 Staggered arrangement of mesh nodes, and control volumes for two-dimensional flow

supersonic problem using SIMPLE0 where 0 is appended to SIMPLE to denote that $\bar{d}^u$ is everywhere set to zero. The results shown in Fig. 5(*c*) indicate that the iterative convergence behavior is identical to that of SIMPLE and SIMPLER. Therefore, the superior performance of SIMPLE and SIMPLER for supersonic flows is not due to a better approximate evaluation of $\bar{d}^u$ but rather that the underestimation of $\bar{d}^u$ is not detrimental to the performance of these methods. Unfortunately, the same is not true for multidimensional flows.

Segregated Approach for Two-Dimensional Problems

Up to this point the segregated approch and methods have been considered in a one-dimensional context. In what follows the extension of the segregated approach and methods to two dimensions is reviewed. Subsequently, the applicability of these methods is demonstrated on a two-dimensional compressible flow problem.

Differential Equations. The differential equations expressing the conservation of mass, momentum, and energy for a laminar two-dimensional viscous compressible flow of a perfect gas can be expressed in Cartesian coordinates as

$$\frac{\partial \rho}{\partial t}+\frac{\partial}{\partial x}(\rho u)+\frac{\partial}{\partial y}(\rho v)=0 \tag{51}$$

$$\frac{\partial}{\partial t}(\rho u)+\frac{\partial}{\partial x}(\rho uu)+\frac{\partial}{\partial y}(\rho uv)=-\frac{\partial p}{\partial x}$$
$$+\frac{\partial}{\partial x}\left(\mu\frac{\partial u}{\partial x}\right)+\frac{\partial}{\partial y}\left(\mu\frac{\partial u}{\partial y}\right)+\frac{\mu}{3}\frac{\partial}{\partial x}\left(\frac{\partial u}{\partial x}+\frac{\partial v}{\partial y}\right) \tag{52}$$

$$\frac{\partial}{\partial t}(\rho v)+\frac{\partial}{\partial x}(\rho uv)+\frac{\partial}{\partial y}(\rho vv)=-\frac{\partial p}{\partial y}$$
$$+\frac{\partial}{\partial x}\left(\mu\frac{\partial v}{\partial x}\right)+\frac{\partial}{\partial y}\left(\mu\frac{\partial v}{\partial y}\right)+\frac{\mu}{3}\frac{\partial}{\partial y}\left(\frac{\partial u}{\partial x}+\frac{\partial v}{\partial y}\right) \tag{53}$$

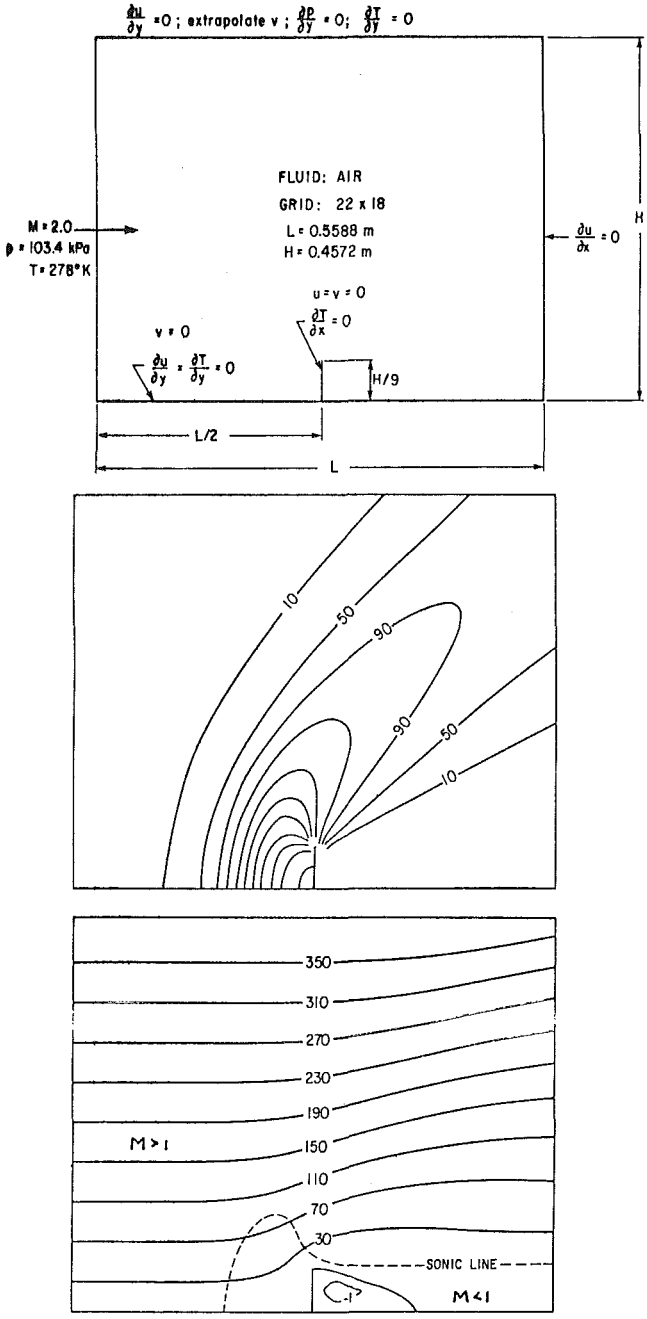

Fig. 7 Flow around a flat plate: (*a*) geometry and boundary conditions, (*b*) isobars (kPa) of pressure in excess of inlet pressure, and (*c*) streamlines

$$\frac{\partial}{\partial t}(\rho T)+\frac{\partial}{\partial x}(\rho uT)+\frac{\partial}{\partial y}(\rho vT)$$
$$=\frac{k}{C_p}\frac{\partial}{\partial x}\left(\frac{\partial T}{\partial x}+\frac{\partial T}{\partial y}\right)$$
$$+\frac{1}{C_p}\left(\frac{\partial p}{\partial t}+\frac{\partial}{\partial x}(up)+\frac{\partial}{\partial y}(vp)-p\frac{\partial u}{\partial x}-p\frac{\partial v}{\partial y}\right) \tag{54}$$

where the additional dependent variable v is the component of velocity in the y coordinate direction.

Algebraic Equations. Employing the staggered grid shown in Fig. 6, the same discretization and linearization techniques described in the one-dimensional context, the linearized algebraic representations of the conservation of mass, momentum, and energy can be expressed as

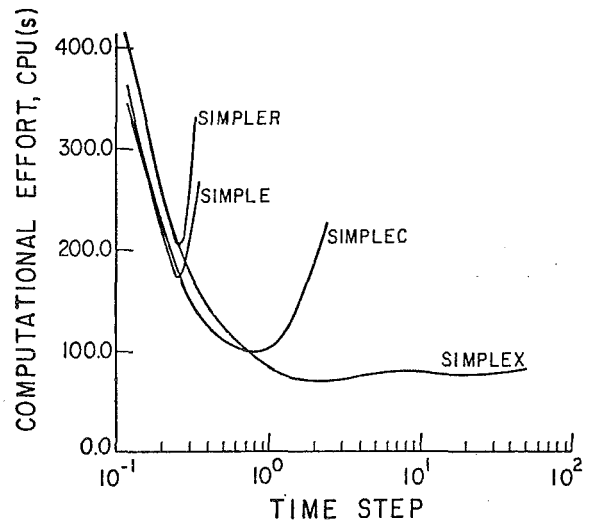

Fig. 8 Computational requirements versus time step of SIMPLE, SIMPLER, SIMPLEC, and SIMPLEX for flow around a flat plate

$$m_p^\rho \rho_P + m_e^\rho \rho_E + m_w^\rho \rho_W + m_n^\rho \rho_N + m_s^\rho \rho_S + m_e^u u_P + m_w^u u_W + m_n^v v_P + m_s^v v_S = b^c \quad (55)$$

$$a_p^u u_P = \Sigma a_{nb}^u u_{nb} - c^u(p_E - p_P) + b^u \quad (56)$$

$$a_p^v v_P = \Sigma a_{nb}^v v_{nb} - c^v(p_N - p_P) + b^v \quad (57)$$

$$a_p^T T_P = \Sigma a_{nb}^T T_{nb} + b^T \quad (58)$$

where

$$\Sigma a_{nb}^u u_{nb} = a_e^u u_E + a_w^u u_W + a_n^u u_N + a_s^u u_S$$

$$\Sigma a_{nb}^v v_{nb} = a_e^v v_E + a_w^v v_W + a_n^v v_N + a_s^v v_S$$

$$\Sigma a_{nb}^T T_{nb} = a_e^T T_E + a_w^T T_W + a_n^T T_N + a_s^T T_S$$

and where the equation of state is again represented by

$$\rho_P = c^\rho p_P + b^\rho \quad (59)$$

Generalized Segregated Approach. The generalized segregated approach presented previously within the context of one-dimensional flow in a duct is readily extended to multiple dimensions. In terms of nodal values and considering only the influence of nodal pressures which are adjacent to the nodal components of velocity, the improved estimates of the components of velocity $\tilde{u}$ and $\tilde{v}$ can be related to the pressure correction by

$$\tilde{u}_P = u_P^* - \tilde{d}^u(p_E' - p_P') \quad (60)$$

$$\tilde{v}_P = v_P^* - \tilde{d}^v(p_N' - p_P') \quad (61)$$

where, given p^*, estimates for pressure, u^*, and v^* are determined from

$$a_p^u u_P^* = \Sigma a_{nb}^u u_{nb}^* - c^u(p_E^* - p_P^*) + b^u \quad (62)$$

$$a_p^v v_P^* = \Sigma a_{nb}^v v_{nb}^* - c^v(p_N^* - p_P^*) + b^v \quad (63)$$

By requiring that the improved estimates of velocity $\tilde{u}$ and $\tilde{v}$ given by equations (60) and (61) and the improved estimate of density given by equation (32) satisfy mass conservation, equation (55), the following equation of pressure correction is obtained

$$a_p^p p_P' = a_e^p p_E' + a_w^p p_W' + a_n^p p_N' + a_s^p p_S' + b^{p'} \quad (64)$$

where

$$a_p^p = m_e^\rho + m_e^u \tilde{d}^u - m_w^u[\tilde{d}^u]_W + m_n^v \tilde{d}^v - m_s^v[\tilde{d}^v]_S \quad (65)$$

$$a_e^p = -m_e^\rho[c^\rho]_E + m_e^u \tilde{d}^u \quad (66)$$

$$a_w^p = -m_w^\rho[c^\rho]_W - m_w^u[\tilde{d}^u]_W \quad (67)$$

$$a_n^p = -m_n^\rho[c^\rho]_N + m_n^v \tilde{d}^v \quad (68)$$

$$a_s^p = -m_s^\rho[c^\rho]_S - m_s^v[\tilde{d}^v]_S \quad (69)$$

$$b^{p'} b^c - m_p^\rho \rho_P^* - m_e^\rho \rho_E^* - m_w^\rho \rho_W^* - m_n^\rho \rho_N^* - m_s^\rho \rho_S^* - m_e^u u_P^* - m_w^u u_W^* - m_n^v v_P^* - m_s^v v_S^* \quad (70)$$

and where the evaluations of $\tilde{d}^u$ are given in Table 1 and, for SIMPLE and SIMPLER

$$\tilde{d}^v = \frac{c^v}{a_p^v} \quad (71)$$

for SIMPLEC

$$\tilde{d}^v = \frac{c^v}{a_p^v - \Sigma a_{nb}^v} \quad (72)$$

and for SIMPLEX

$$a_p^v[\tilde{d}^v]_P = \Sigma a_{nb}^v[\tilde{d}^v]_{nb} + c^v \quad (73)$$

Solving equation (64) for p', the $\tilde{p}$ pressures determined from $\tilde{p} = p^* + p'$, and the $\tilde{u}$ velocities, $\tilde{v}$ velocities and $\tilde{\rho}$ densities are determined from equations (60), (61), and (32), respectively.

Two-Dimensional Demonstration Problem

For the purpose of demonstrating the applicability of the segregated methods and of demonstrating their relative performance, the steady-state supersonic (Mach 2) flow around a flat plate oriented normal to the flow, as shown in Fig. 7(*a*), was considered. The solution of the discrete equations of motion using a uniform coarse 22 × 18 grid was determined to the roundoff limits of single precision FORTRAN-H on an IBM 4341 Group II computer. The isobars and streamlines from this solution are plotted respectively in Figs. 7(*b*) and 7(*c*). Figure 7(*b*) shows that a bow shock is predicted, while Fig. 7(*c*) shows the flow deflection around the plate with a subsonic region surrounding the plate. The shock smearing that is evident results from the coarse grid and from the numerical diffusion that is inherent in the discretization used. Because the present study focuses on the applicability of solution methods, the improvement of accuracy was not considered.

A number of tests were carried out to establish the sensitivity of solution time of the segregated methods to the number of cycles used for each time step and to the accuracy to which each linear set of equations was solved. Details of these tests have been reported by Van Doormaal [22]. It was found that, for each time step, it was best to permit only one cycle (i.e., to solve only on set of linear equations) except for the continuity equation where a second coefficient evaluation and solution were performed. The MSIP solver of Schneider and Zedan [21] was used to solve the segregated linear equation set for each variable.

The performance of the various solution methods was tested by initializing all dependent variables to inlet conditions, and advancing the solution through time steps Δt until the computed variables were all within 0.5 percent of the previously obtained steady-state solution. The computational effort is plotted against Δt in Fig. 8 for each of the four segregated methods. At small Δt the behavior of all methods is similar; the slightly higher effort for SIMPLER and SIMPLEX reflects the need to solve an extra linear equation. For larger Δt SIMPLEC and SIMPLEX become distinctly superior to SIMPLE and SIMPLER. This is due to the relatively poor approximations inherent in $\tilde{d}^u$ and $\tilde{d}^v$ in SIMPLE and SIMPLER. For multidimensional flows this detrimental effect of the underestimation of $\tilde{d}^u$ and $\tilde{d}^v$ is to be expected, even in supersonic cases, because there is likely to be at least one coordinate direction along which the component of the flow is subsonic. An attractive feature of SIMPLEX for this particular test problem is its relative insensitivity to the size of Δt when large time steps are taken.

Concluding Remarks

A number of aspects of the segregated approach to solving viscous compressible fluid flows have been presented in this paper. Included in these are the extension to the solution of compressible flows of an interpretation of the role of pressure in the segregated approach, of the generalized view of the segregated approach, and of the segregated methods SIMPLE, SIMPLER, SIMPLEC, and SIMPLEX developed originally for the solution of incompressible flows. The present paper also develops an understanding of the strengths and shortcomings of the segregated methods. Many of these aspects are demonstrated on one-dimensional and two-dimensional compressible flow problems. In particular, with the appropriate linearization of mass conservation and with the appropriate approximation of the influence of pressure on velocity, the segregated approach has been demonstrated to be equally applicable to supersonic and subsonic compressible flows as well as compressible flows.

Acknowledgments

This work was supported by Atomic Energy of Canada Ltd. (Whiteshell) and by the Natural Sciences and Engineering Council of Canada.

References

1 Peyret, R., and Viviand, H., "Computation of Viscous Compressible Flows Based on the Navier-Stokes Equations," AGARD-AG-212, 1975.

2 NcNally, W. D., and Sockol, P. M., "Computational Methods for Internal Flows With Emphasis on Turbomachinery," NASA-TM-82764, presented at the Symposium on Computers in Flow Predictions and Fluid Dynamics Experiments at the ASME Winter Annual Meeting, Washington, D.C., Nov. 15-20, 1981.

3 Anderson, D. A., Tannehill, J. C., and Pletcher, R. H., *Computational Fluid Mechanics and Heat Transfer*, McGraw-Hill, Washington, 1984.

4 Briley, W. R., and McDonald, H., "On the Structure and Use of Linearized Block Implicit Schemes," *Journal of Computational Physics*, Vol. 34, 1980, pp. 54-73.

5 Patankar, S. V., and Spalding, D. B., "A Calculation Procedure for Heat, Mass and Momentum Transfer in Three-Dimensional Parabolic Flows," *Int. J. Heat Mass Transfer*, Vol. 15, 1972, p. 1782.

6 Patankar, S. V., "Calculation of Unsteady Compressible Flows Involving Shocks," Mech. Eng. Dept., Imperial College, Report UF/TN/A/4, 1971.

7 Issa, R. I., and Lockwood, F. C., "On the Prediction of Two-Dimensional Supersonic Viscous Interactions Near Walls," *AIAA Journal*, Vol. 15, 1977, pp. 182-188.

8 Hah, C., "A Navier-Stokes Analysis of Three-Dimensional Turbulent Flows Inside Turbine Blade Rows at Design and Off-Design Conditions," ASME JOURNAL OF ENGINEERING FOR GAS TURBINES AND POWER, Vol. 106, 1984, pp. 421-429.

9 Patankar, S. V., *Numerical Heat Transfer*, Hemisphere, Washington, D.C., 1980.

10 Van Doormaal, J. P., and Raithby, G. D., "Enhancements of the SIMPLE Method for Predicting Incompressible Fluid Flows," *Numer. Heat Transfer*, Vol. 7, 1984, pp. 147-163.

11 Van Doormaal, J. P., and Raithby, G. D., "An Evaluation of the Segregated Approach for Predicting Incompressible Fluid Flows," ASME Paper No. 85-HT-9, 1985.

12 Harlow, F. M., and Welch, J. E., "Numerical Calculation of Time-Dependent Viscous Incompressible Flow of Fluid With Free Surface," *Phys. Fluids*, Vol. 8, 1965, pp. 2182-2189.

13 Raithby, G. D., and Torrance, K. E., "Upstream-Weighted Differencing Schemes and Their Application to Elliptic Problems Involving Fluid Flow," *Comput. Fluids*, Vol. 2, 1974, pp. 191-206.

14 Watson, P. C., "A Solution Method for the Finite Difference Form of the Steady-State Navier-Stokes Equations Using Computer Program Nasess," M.A.Sc. Technical Project, Univ. of Waterloo, Waterloo, Ontario, Canada, 1981.

15 Zedan, M., and Schneider, G. E., "Investigation Into the Simultaneous Variable Solution of Velocity and Pressure in Incompressible Fluid Flow Problems," AIAA 18th Thermophysics Conference, Montreal, Quebec, Canada, June 1-3, 1983.

16 Harlow, F. H., and Amsden, A. A., "A Numerical Fluid Dynamics Calculation Method for All Flow Speeds," *Journal of Computational Physics*, Vol. 8, 1971, pp. 197-213.

17 Patankar, S. V., "A Calculation Procedure for Two-Dimensional Elliptic Situations," *Numer. Heat Transfer*, Vol. 4, 1981, pp. 409-425.

18 Raithby, G. D., and Schneider, G. E., "Numerical Solution of Problems in Incompressible Fluid Flow; Treatment of the Velocity-Pressure Coupling," *Numer. Heat Transfer*, Vol. 2, 1979, pp. 417-440.

19 Benodekar, R. W., Goddard, A. J. H., Gosman, A. D., and Issa, R. I., "Numerical Prediction of Turbulent Flow Over Surface Mounted Ribs," ASME Paper No. 83-FE-13, 1983.

20 Issa, R. I., "Numerical Methods for Two- and Three-Dimensional Recirculating Flows," in: *Computational Methods for Turbulent, Transonic, and Viscous Flows*, J. A. Essers, ed., Hemisphere, Washington, 1983, pp. 183-211.

21 Schneider, G. E., and Zedan, M., "A Modified Strongly Implicit Procedure for the Numerical Solution of Field Problems," *Numerical Heat Transfer*, Vol. 4, 1981, pp. 1-19.

22 Van Doormaal, J. P., "Numerical Methods for the Solution of Incompressible and Compressible Fluid Flows," Ph.D. Thesis, University of Waterloo, Waterloo, Ontario, Canada, 1985.

Horseshoe Vortex Formation Around a Cylinder

W. A. Eckerle[1]
United Technologies Research Center,
East Hartford, CT 06108

L. S. Langston
Department of Mechanical Engineering,
University of Connecticut,
Storrs, CT 06268

An experimental investigation was conducted to characterize a symmetric horseshoe vortex system in front of and around a single large-diameter right cylinder centered between the sidewalls of a wind tunnel. Surface flow visualization and surface static pressure measurements as well as extensive mean velocity and pressure measurements in and around the vortex system were acquired. The results lend new insight into the formation and development of the vortex system. Contrary to what has been assumed previously, a strong vortex was not identified in the streamwise plane of symmetry, but started a significant angular distance away from it. Rather than the multiple vortex systems reported by others, only a single primary vortex and saddle point were found. The scale of the separation process at the saddle point was much smaller than the scale of the approaching boundary layer thickness. Results of the present study not only shed light on such phenomena as the asymmetric endwall flow in axial turbomachinery but can also be used as a test case for three-dimensional computational fluid mechanics computer codes.

Introduction

The three-dimensional separation of a boundary layer approaching a bluff body, an airfoil, or a cascade of airfoils mounted on a wall is a commonplace phenomenon in fluid mechanics. The separation commences at a wall saddle point of separation, downstream of which a vortex system is formed in front of and around the body. This system, made up of the boundary layer and some portion of the mainstream flow, is generally referred to as a *horseshoe vortex* (or vortices) in the (English) literature.

The symmetric separation of boundary layer flow normal to a single cylinder (or a cascade of cylinders) is perhaps the simplest of geometries that demonstrate the horseshoe vortex phenomenon (e.g., [1]), while the vortex system formed on the endwall of a cascade of turbine airfoils (e.g., [2]) might be considered to be one of the most complex of the family of such flows.

This paper deals with the experimental study of the simple cylinder vortex system. Aerodynamic measurements were made to define the horseshoe vortex system formed around a single cylinder mounted between endwalls in a wind tunnel. Because of the existence of the sidewalls of the tunnel, the cylinder model approximates one element of a cascade of cylinders. The tests were carried out at a relatively high Reynolds number with turbulent boundary layers on the endwalls. The objectives of the study were as follows:

1 There have been a number of studies carried out to measure and explain cylinder endwall flow and these have been reviewed by Eckerle [1]. The conclusion of this review is that few or no measurements have been taken in the vortex region itself, especially in the region of the vortex formation. Also, in most studies, the scale of the experiment was too small for accurate and detailed measurements. In the study presented here, measurements were made in the vortex region, and the cylinder model scale was about 100 times larger than the pressure probe scale.

2 Often it is possible to study and understand a simple member of a fluid flow family to explain and predict the behavior of a more complex member of that family. The study here represents the flow into a cascade of cylinders with zero angle of attack (no lift), at a Reynolds number based on cylinder diameter representative of many turbomachinery applications and with a large scale that would be difficult to achieve in an airfoil cascade. One objective then is to shed more light on the important problem of endwall flows in turbine cascades.

3 The measurements were taken in such a way (i.e., inlet and exit conditions to a control volume with interior flow measurements) that they can be used as a test case for three-dimensional computational fluid mechanics computer codes.

The emphasis of this paper is to elucidate details of the horseshoe vortex structure and to indicate significant differences between the measured vortex characteristics and the vortex structure that has been assumed by others. A more detailed discussion of the results, e.g., pressure distribution on the cylinder surface, is contained in [1].

Experimental Apparatus

Testing was conducted in the University of Connecticut Low-Speed Wind Tunnel. Details of this tunnel and specific modifications for this experiment are contained in [1]. The test-section lower endwall was constructed to facilitate acquisition of static pressures during this program. The lower endwall contained a rotatable disk to which a 29.8-cm-dia

[1]Presently at Department of Mechanical and Industrial Engineering, Clarkson University, Potsdam, NY 13676.

Contributed by the Gas Turbine Division of THE AMERICAN SOCIETY OF MECHANICAL ENGINEERS and presented at the 31st International Gas Turbine Conference and Exhibit, Düsseldorf, Federal Republic of Germany, June 8–12, 1986. Manuscript received at ASME Headquarters February 21, 1986. Paper No. 86-GT-246.

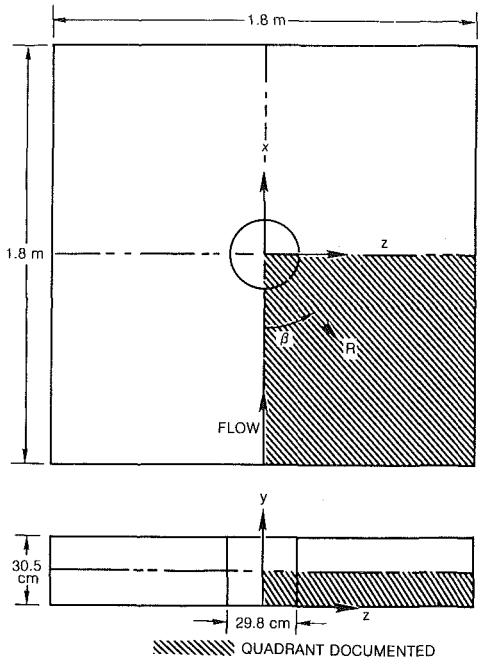

Fig. 1 Schematic showing test section with cylinder and coordinate systems

cylinder that spanned the test section was concentrically mounted. Both the lower endwall and cylinder contained four rows of static pressure taps. The radial position of the taps on the endwall and the vertical position of the taps on the cylinder were staggered so that dense static pressure distributions at any desired angular location on both the endwall and cylinder surfaces could be obtained by sequentially rotating each row of taps to a desired angular location. Accurate and repeatable angular positioning of the disk was achieved with indexing holes machined near the disk's outer edge.

A schematic of the test section along with the coordinate systems used in this effort are shown in Fig. 1. The origin of the coordinate systems coincides with the cylinder and disk center on the lower endwall. Angular and radial positions are denoted by β and R, respectively. Cartesian coordinates representing streamwise, vertical, and transverse locations are x, y, and z, respectively. The experiment was designed to create vertical and horizontal planes of symmetry at the test-section centerline and midheight, respectively. As shown in Fig. 1, the lower quadrant on the right side of the test section, when viewed facing downstream, was chosen for documentation.

Interior fluid measurements were obtained with a five-hole combination probe manufactured by United Sensor Co. (Model No. DC-0.093-24-F). Probe calibrations, which were checked several times during testing, provided local total pressure, static pressure, and velocity magnitude and direction for a range in pitch angle of ± 30 deg. The probe tip diameter, which was aligned with the shaft axis so that the tip rotated but did not translate as the probe was rotated about its shaft axis, was 2.4 mm. This tip diameter was less than one percent of the cylinder diameter and span. Excellent agreement was observed between probe static pressures measured near the bottom endwall and corresponding endwall pressures measured without the probe in the vicinity of the static tap. The probe was positioned vertically and in yaw with a calibrated probe drive that was mounted to a mechanized positioner located on the top endwall. Precise angular (β) and radial (R) probe positions were determined by aligning the probe tip with an endwall static tap that was positioned at the desired measurement location. Estimated experimental uncertainties associated with the five-hole probe measurements and position are:

Angular position	± 0.2 deg
Yaw angle	± 0.5 deg
Cp_T	± 0.0062
Cp_s	± 0.0085
$\frac{Q}{U_0}$	± 0.0085
Pitch angle	± 0.15 deg
Vertical position, y	± 0.05 cm
Radial position, R	± 0.04 cm

Odds are 20 to 1 that the measured values were within the uncertainty intervals listed above.

Velocity profile data for the boundary layer near the test-section entrance were obtained with pitot-static probes. Flow visualization patterns on the endwall and cylinder surfaces were obtained using the ink/oil of wintergreen technique of Langston and Boyle [3].

Test Conditions

All testing for this study was conducted with a velocity at the test-section entrance of 30.5 m/s corresponding to a Reynolds number based on cylinder diameter of 5.5×10^5. Velocity profile data for the approaching boundary layer were

Nomenclature

C_f = skin friction coefficient
Cp_s = static pressure coefficient = $(P_s - P_{s0})/q_0$
C_{P_T} = loss coefficient = $(P_{T0} - P_T)/q_0$
$\tilde{C}_{P_T}$ = mass-averaged loss coefficient, equation (2)
D = cylinder diameter = 29.85 cm
H = boundary-layer shape factor = δ^*/θ
MS = test-section midspan plane
n = exponent in power-law profile representation = $2/(H-1)$
P_s = local static pressure
P_{s0} = reference static pressure near test-section entrance
P_T = local total pressure
P_{T0} = reference total pressure near test-section entrance
Q = local velocity magnitude
q_0 = dynamic pressure near test-section entrance
R = radial distance from center of cylinder, Fig. 1
Re_θ = Reynolds number based on boundary-layer momentum thickness
U_0 = reference velocity near the test-section entrance
$x, y, z,$ = orthogonal coordinate system as defined in Fig. 1
z_0 = lower limit of mass-averaged loss integral, either 0 or $D/2$
z_w = distance from test-section plane of symmetry to sidewall = 0.91 m
β = position angle relative to plane of symmetry, Fig. 1
δ = boundary-layer thickness
δ^* = boundary-layer displacement thickness
θ = boundary-layer momentum thickness
μ = viscosity
ν = kinematic viscosity = μ/ρ
ρ = density

Table 1 Test-section centerline entrance boundary-layer parameters with cylinder installed; $x/D = -2.72$

z/D	δ/D	δ^*/D	θ/D	δ^*/θ	C_f	Re_θ
0	0.099	0.0154	0.0114	1.35	0.0028	6149

acquired near the test-section entrance at $x/D = -2.72$ with the cylinder installed. Table 1 lists the measured boundary-layer dimensions and properties at the test-section centerline.

The test section inlet, carefully constructed of porous plates, honeycomb, and fine mesh screen, created a uniform entrance flow field to within ± 2 percent of the values in the table. The streamwise turbulence intensity of the core flow was less than 1 percent.

Experimental Results

Endwall surface static pressures are presented along with interior fluid measurements obtained with a five-hole probe. The vortex characteristics deduced from these measurements are then integrated with surface flow visualizations to characterize the vortex formation process.

Endwall Static Pressure Measurements. Static pressure distributions are presented in coefficient form using the polar coordinate system defined in Fig. 1. The pressure distribution in the plane of symmetry, $\beta = 0$, is presented in Fig. 2. Radial locations are normalized by the cylinder diameter, and the ordinate corresponds to the cylinder leading edge. Upstream of the separation region, the distribution displays a characteristic rise in pressure due to the blockage of the cylinder. Unlike the potential-flow distribution shown by the solid line, the experimental distribution begins to decrease a short distance downstream of the saddle point determined from the endwall flow visualizations. The distribution displays a local minimum approximately two tenths of a cylinder diameter from the cylinder leading edge, then increases rapidly from that point to a value of one at the endwall-cylinder junction. The coefficient value of one indicates that loss-free core flow stagnated at the junction. Location of the saddle point in an adverse pressure gradient, not at the local peak pressure, is consistent with the work of Langston and Wagner [4]. They applied Oswatitch's model [5] to saddle-point behavior and predict that the saddle point occurs in an adverse pressure gradient.

The difference between experimental and potential-flow values upstream of the saddle point is the result of the mean flow accelerating through the test section due to the increasing boundary layers on the uncontoured endwalls. The experimental values in Fig. 2 that correspond with five-hole probe traverses were corrected for the effect of the thickening boundary layer. The corrected values are close to the potential-flow values.

The experimental distribution in Fig. 2 is plotted with the limited results of Ram [6] and East and Hoxey [7]. These experiments were conducted in large wind tunnels so that corrections for thickening boundary layers are insignificant. Static pressures measured upstream of the saddle point are close to the corrected values from this experiment, although Ram's data are slightly higher than the other two sets. Ram's results in the separation zone exhibit the same trend as data from this experiment.

Potential-flow and measured endwall static pressure contours throughout the documented quadrant are shown in Fig. 3. The potential-flow results are for a cascade of cylinders spaced to simulate the test-section sidewalls. Comparing these two figures, the pressure distributions are, as expected, quite similar outside of the separation region. Inside the separation region, the experimental contours display a large dip near $R/D = 0.72$. This dip, which was observed in the plane of symmetry data, persists around the cylinder up to approximately $\beta = 60$ deg. Beyond this angular plane, the dip is no longer present, and the experimental contours are shaped more like that of the potential-flow contours. This similarity indicates that the strong pressure field associated with the mean flow acceleration around the cylinder, which is represented by the potential-flow solution, negated the local pressure minimum created in the separation region.

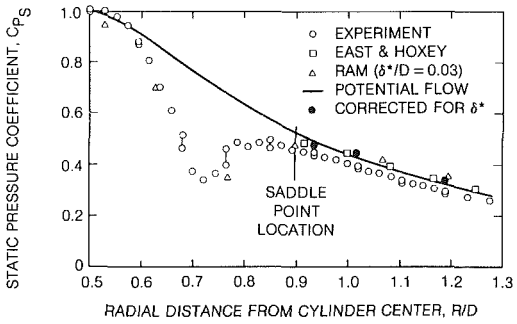

Fig. 2 Comparison of plane of symmetry static pressure distributions

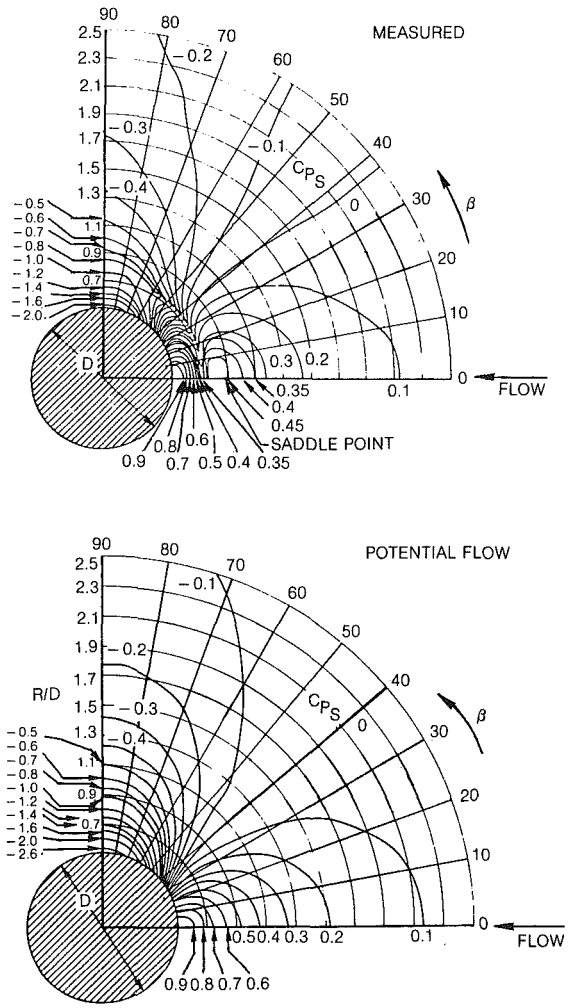

Fig. 3 Comparison of measured endwall pressure distribution with potential-flow pressure distribution

Five-Hole Probe Measurements. Data were acquired with a five-hole probe in the angular planes defined by $\beta = -5$, 0, 5, 25, 45, and 90 deg. The probe was traversed at 81 radial locations to define the flow field adjacent to and inside of the separation region. Data were recorded from $y/D \simeq 0.0085$ to the test-section midspan. This smaller value, approximately

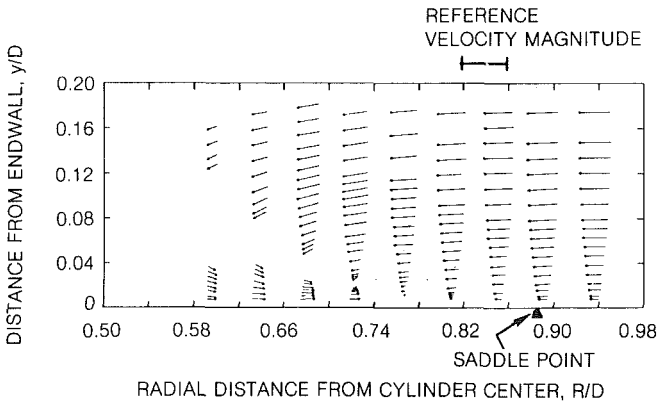

Fig. 4 Velocity vectors in the plane of symmetry

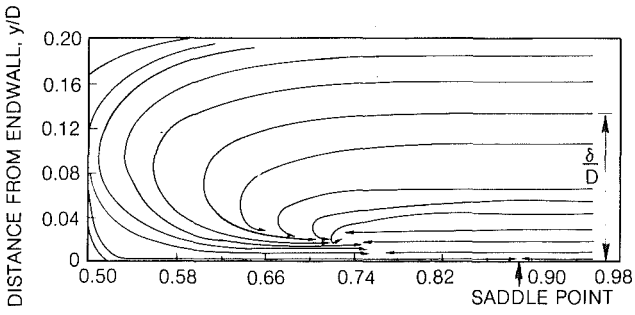

Fig. 5 Flow pattern in the plane of symmetry

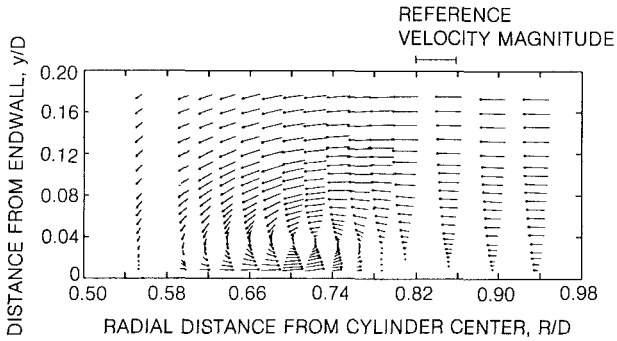

Fig. 6 Velocity vectors in the 25-deg plane

one probe tip diameter from the endwall, represents the lowest point for which data could be acquired without endwall interference. This determination was primarily based on endwall static pressure data acquired in this test program with and without the probe in proximity of a static pressure tap. Data obtained up to 0.2 cylinder diameters from the endwall are discussed. The data in the region between $y/D = 0.2$ and the test-section midspan ($y/D = 0.511$) do not vary substantially from the midspan values. The endwall-region data are presented in the form of in-plane velocity vectors, static pressure contours, and total pressure contours.

The radial velocity components for the angular planes given by $\beta = 0$, 25, and 90 deg are presented. The data are displayed as vectors centered at the measurement point. The in-plane pitch angles are based on the in-plane components, not on the total velocity measured with the five-hold probe. The vectors are normalized by the reference velocity measured at the test-section entrance. The ordinate and abscissa in the figures represent the cylinder o.d. and endwall, respectively.

The plane of symmetry velocity vectors is shown in Fig. 4. Upstream of the endwall saddle point, the vectors take on the appearance of a two-dimensional boundary layer, though vortex stretching is present. The outer edge of the approaching boundary layer at $R/D = 0.94$ is at $y/D \simeq 0.13$. The separation streamline between forward and reverse flow is very

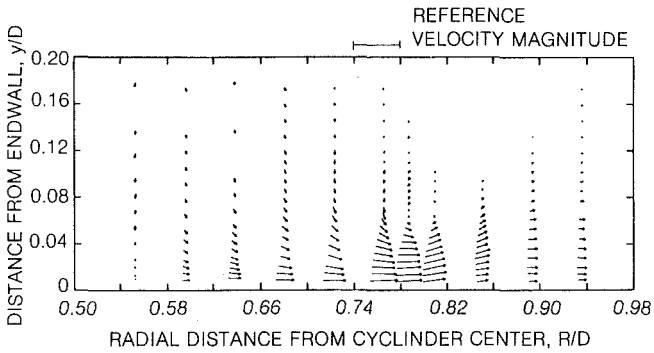

Fig. 7 Velocity vectors in the 90-deg plane

shallow. A straight line drawn from the saddle point to the streamline location at $R/D = 0.766$ represents a separation angle of approximately 4 deg. The shallowness of this line is markedly different from the multiple vortex models developed in the literature, e.g., that of Baker [8]. Following the flow field from the saddle point toward the cylinder, the velocity vectors indicate that flow in the boundary layer and outside of the boundary layer pitched downward, rotated 180 deg, and proceeded toward the saddle point. Blank areas are present in the traverses nearest the cylinder because the flow pitch angle was out of the probe calibration range. Data were acquired in these regions, however, to qualitatively determine the flow direction.

The plane of symmetry flow pattern deduced from the five-hole probe data and surface static pressure data is sketched in Fig. 5. Loss-free fluid outside the boundary layer stagnated at the endwall-cylinder junction. Five-hole probe measurements at $R/D = 0.598$ contain negative pitch angles up to $y/D \simeq 0.3$ indicating that flow from approximately two approaching boundary-layer thicknesses away from the endwall entered the juncture region. The reverse flow accelerated as it moved away from the endwall-cylinder juncture in order to accommodate the incoming flow, which separated at a shallow angle. The favorable endwall static pressure gradient is consistent with this pattern. At approximately $R/D = 0.72$, the reverse flow started stagnating with the incoming flow. The abrupt reverse flow deceleration caused by the blockage is indicated by the strong endwall adverse pressure gradient in this region. The reverse flow did not roll up to form a vortex, however. The vectors clearly show that a closed vortex was not present in the plane of symmetry, although positive pitch angles in a portion of the reverse flow at $R/D = 0.72$ and $y/D = 0.02$ may indicate the start of vortex formation. Rather than rolling up, the reverse flow passed out the plane and proceeded tangentially around the cylinder next to the separation line. Note that the reverse flow was confined to the lower 15 percent of the boundary layer as it passed out of the plane.

Velocity vectors in the 5-deg plane show a flow pattern similar to that shown in the plane of symmetry. Velocity vectors for the 25-deg plane, however, show a well-formed vortex (Fig. 6). The vortex, then, became fully formed between the plane of symmetry and 25-deg plane. The vortex center in the 25-deg plane was at $R/D = 0.71$ and $y/D = 0.035$. This was approximately one third of the incoming boundary-layer thickness from the endwall. The vortex itself was confined to a region that extended less than one boundary-layer thickness from the endwall. The radial location of the vortex center is close to that of the local static pressure minimum on the endwall in this plane.

The velocity vectors in the 45-deg plane are similar to these presented for the 25-deg plane. Between the 25-deg and 45-deg planes, however, the vortex center moved radially outward to $R/D = 0.735$. The vortex structure in the 90-deg plane was much weaker than that in the 45-plane. The velocity vectors in Fig. 7 faintly show a vortex center at $R/D = 0.80$ and $y/D =$

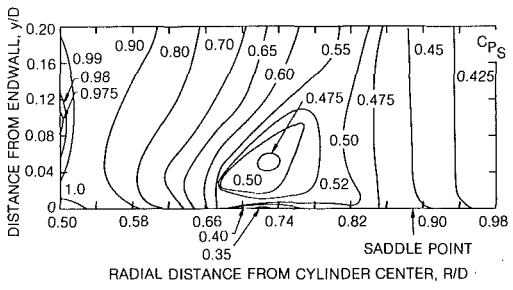

Fig. 8 Static pressure contours in plane of symmetry

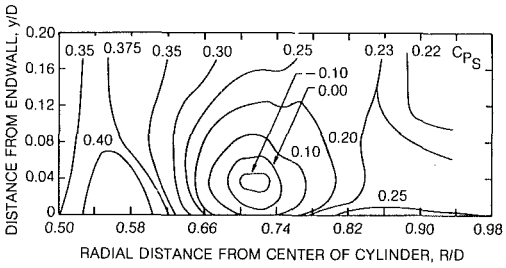

Fig. 9 Static pressure contours in 25-deg plane

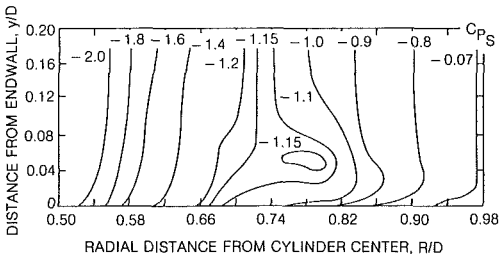

Fig. 10 Static pressure contours in 90-deg plane

0.07. The vortex was not symmetric with the secondary flow near the endwall stronger than that on the core-flow side of the vortex. The reduced vortex strength, which was also indicated by the endwall static pressure distribution, can be attributed to the streamwise acceleration of the mean flow around the cylinder.

Static pressure coefficient contours corresponding to the velocity vector plots are shown in Figs. 8–10. Upstream of the endwall saddle point, the static pressure contours in the plane of symmetry are nearly vertical except near the endwall surface. The pressures adjacent to the endwall were larger than those measured in the core flow. This trend can also be seen in the comparison between potential-flow and corrected endwall static pressures in the plane of symmetry (Fig. 2). The assumption of constant static pressure through the two-dimensional boundary layer at a given streamwise location upstream of the saddle point is inaccurate. The cylinder created a stronger adverse pressure gradient in the viscous sublayer.

The pressure distribution closer to the cylinder was significantly skewed by the recirculating flow. A local pressure minimum at $y/D \simeq 0.04$ and $R/D \simeq 0.73$ is marked by the closed contours. The velocity vectors show that this small minimum is not associated with a vortex. The minimum pressure in the plane was adjacent to the endwall at the same radial location. This minimum is associated with the reverse flow first accelerating away from the cylinder and then decelerating when blocked by the streamwise flow. The coefficients near the cylinder are close to one. They indicate that low-loss fluid from outside the boundary layer passed next to the cylinder at a low velocity prior to stagnating at the endwall cylinder junction.

The contours in the 25-deg plane (Fig. 9) clearly correspond to the well-formed vortex structure shown in the corresponding velocity vector plot. The center of the closed pressure contours corresponds with the vortex center indicated by the velocity vectors. The static pressure coefficient at the vortex center is 40 percent of the test-section entrance dynamic head below the test-section midspan coefficient measured at the same radial position. The pressure contours indicate that the pressure distribution upstream of the separation line was also substantially altered by the vortex structure.

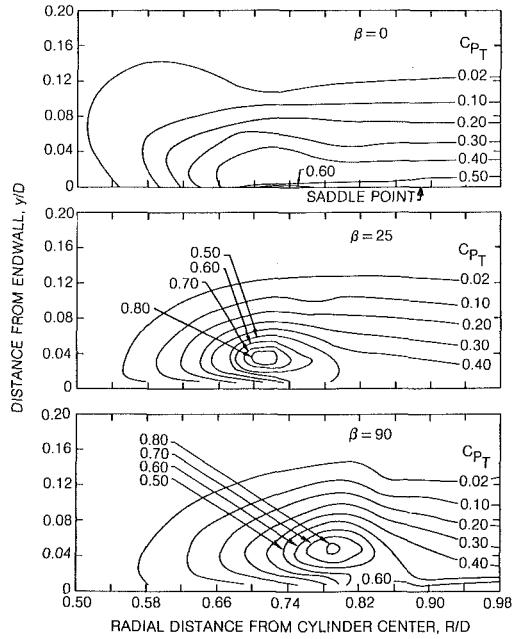

Fig. 11 Total pressure loss

In the 90-deg plane, where the vortex strength was significantly reduced, pressure profiles in Fig. 10 show that pressure at the vortex core was only slightly less than surrounding pressure. The contours tend to be vertical and increase in value radially outward. The pressure field associated with the two-dimensional acceleration of the flow around the cylinder was clearly dominant. The vortex had only a small local effect on the pressure distribution.

Total pressure data from the five-hole probe measurements have been expressed as loss coefficients

$$C_{P_T} = \frac{P_{T0} - P_T}{q_0} \tag{1}$$

where the test-section entrance conditions are again used for references. The loss contours for the same three planes are shown in Fig. 11. Upstream of the saddle point, the contours are nearly horizontal, like an attached two-dimensional boundary layer. The edge of the boundary layer approaching the saddle point was at $y/D = 0.13$. Downstream of the saddle point, the low-loss contour bends around and touches the abscissa at $R/D = 0.54$. This pattern shows the radial extent of the low-loss fluid in front of the cylinder. The contours also show the high total pressure loss associated with this low-loss fluid accelerating away from the endwall-cylinder junction. The region of highest loss, $C_{P_T} = 0.6$, occurred at $R/D = 0.74$, where the reverse flow next to the endwall interacted with the streamwise flow. The loss contours in the 25-deg plane show high losses at the location corresponding to the vortex center. The losses at the vortex center were 80 percent of the entrance dynamic pressure. Although the losses associated with the rollup were high, they were localized. The region of low losses adjacent to the cylinder location is larger than the same region in the plane of symmetry. For the 90-deg plane, the contours indicate that the high-loss region is displaced to the same location as the vortex center. The high-loss fluid created during the rollup process, then, simply

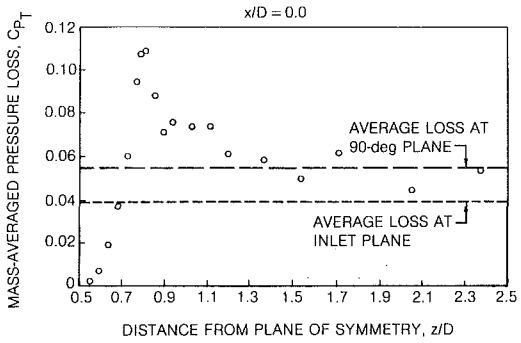

Fig. 12 Pressure loss distribution in the 90-deg plane

accumulated at the vortex center and passed around the cylinder with the vortex. The magnitude of the losses in the vortex did not increase during the passage from the 25-deg to the 90-deg plane. The size of the low-loss fluid region adjacent to the cylinder increased only a small amount from that same region in the 25-deg plane.

The mass-averaged pressure loss at any streamwise plane in the test section is given by

$$\overline{C_{P_T}} = \frac{\int_{z_0}^{z_w}\int_0^{MS} C_{P_T} u \, dy \, dz}{\int_{z_0}^{z_w}\int_0^{MS} u \, dy \, dz} \tag{2}$$

The limits in equation (2) reflect the two planes of symmetry. The sidewall boundary layers were not measured and are not included in the loss calculation. The losses calculated across the entrance plane are quite uniform at 4 percent of the reference dynamic pressure. The loss distribution for the 90-deg plane is shown in Fig. 12. Each point represents the mass-averaged loss of a particular traverse. The 90-deg plane losses are nonuniform. Adjacent to the cylinder, the losses are quite low since low-loss fluid from the core flow occupied this region. Relatively high losses at $z/D = 0.8$ are associated with high-loss fluid that accumulated in the vortex core during the rollup process. Farther away from the cylinder, $z/D > 1.15$, losses level out at around 5 percent of the reference dynamic pressure.

A check on the integration procedure for calculating the above losses was accomplished by comparing the calculated mass flow through each of the planes (the denominator in equation (2)). Mass flow through the 90-deg plane was 3.4 percent above that in the entrance plane. This agreement indicates that the above integration procedure provided accurate values for $\bar{C}_{P_T}$.

A comparison for the above loss calculations is the loss for an equivalent turbulent boundary layer developing on a flat plate without a cylinder. Substituting the power-law formulation for the velocity distribution into equation (2) yields

$$\overline{C_{P_T}} = \frac{\frac{n}{n+1} - \frac{n}{n+3}}{\frac{n}{n+1}\left(\frac{MS}{\delta}\right)^{\frac{n+1}{n}}} \tag{3}$$

The calculated loss coefficient at the test-section entrance centerline, using measured boundary-layer parameters, is $\bar{C}_{P_T} = 0.038$. This value is very close to the 0.039 value calculated by integrating experimental data. In the absence of a pressure gradient, Schlichting [9] gives the following expression for the boundary-layer thickness as a function of streamwise distance

$$\delta(x) = 0.37 \times \left(\frac{Ux}{\nu}\right)^{-1/5} \tag{4}$$

Equation (4) was used to estimate the flat-plate boundary-layer development of a flow starting with the test-section entrance conditions. The boundary-layer thickness was calculated for a length equal to $x/D = 2.72$ (the distance to the 90-deg plane). The calculated value of δ was substituted into equation (3), resulting in a loss coefficient of 0.054. This value is identical to the measured loss in the 90-deg plane. It is concluded, then, that the overall loss associated with the horseshoe vortex formation is small. Losses associated with the vortex rollup are offset by low losses adjacent to the cylinder. Langston et al. [2] found the same trend in their cascade experiment. The measured losses in the initial portion of the cascade were only slightly larger than those measured upstream of the saddle point. Significant losses, measured farther downstream in the passage, were associated with the interaction of the passage vortex with the airfoil suction surface in the region of uncovered turning.

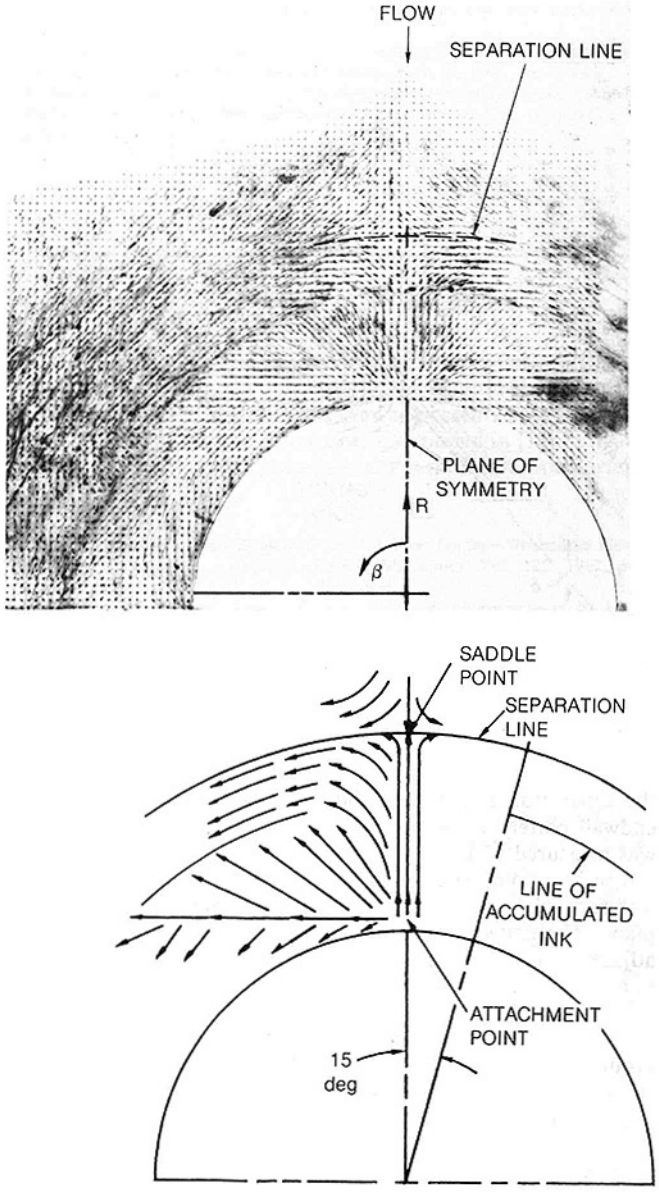

Fig. 13 Endwall flow visualization and flow diagram

Flow Visualization. A photograph of the endwall streaklines and an accompanying flow diagram are contained in Fig. 13. Two singular points, a saddle point and an attachment point, can be seen in the plane of symmetry. No other singular points can be identified in this plane as all streaklines between these two points indicate flow away from the attachment point toward the saddle point. The dashed line indicates

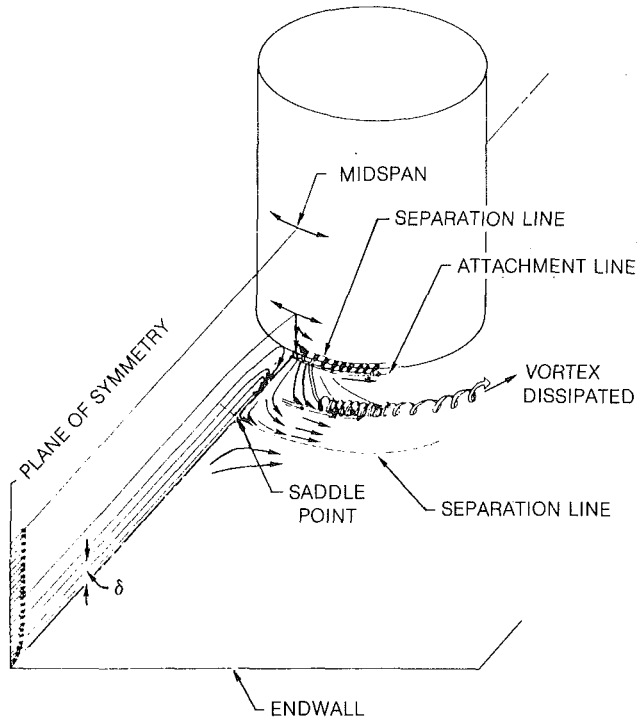

Fig. 14 Horseshoe vortex formation

the separation line corresponding to the saddle point. This endwall pattern is indicative of a single horseshoe vortex, as was measured with the five-hole probe.

The five-hole probe data show that the horseshoe vortex was formed between the plane of symmetry and the 25-deg plane. The endwall flow visualization indicates that the flow adjacent to the endwall rolled up into the vortex at approximately $\beta = 15$ deg. The streak pattern between the plane of symmetry and $\beta = 15$ deg indicates that reverse flow moved toward the separation line and then proceeded tangentially around the cylinder. Beyond the 15-deg plane, reverse flow streaklines abruptly stop where a line of accumulated ink can be seen. This pattern indicates that reverse flow adjacent to the endwall rolled up into the fluid interior beginning in the vicinity of the 15-deg plane. The line of accumulated ink can be interpreted as a separation line. The flow visualization clearly shows, however, that this separation line does not extend from a second saddle point in the plane of symmetry. In the terminology of Tobak and Peake [10], then, this line of accumulated ink represents a *local* separation line.

Discussion

The vortex pattern deduced from the experimental data is shown in Fig. 14. Near the plane of symmetry, low-loss fluid from outside the approaching boundary layer passed next to the cylinder, stagnated at the endwall-cylinder junction, and proceeded back toward the saddle point adjacent to the endwall. Streamwise flow in the boundary layer followed the same pattern but turned inside of the low-loss fluid. The interaction between reverse flow and incoming flow, which separated at a shallow angle, led to the reverse flow accelerating away from the cylinder. Incoming flow eventually blocked reverse flow, forcing the reverse flow to decelerate. Rather than rolling up into a vortex, the low-momentum flow tended to turn and pass tangentially around the cylinder adjacent to the separation lines. Reverse flow away from the plane of symmetry followed the same pattern, but turned at radial locations closer to the cylinder as reverse flow from closer to the plane of symmetry occupied the region next to the separation line. Eventually this accelerating reverse flow contained too much momentum to adjust to the sharp turning required to pass tangentially around the cylinder. The reverse flow then rolled up into a vortex. The five-hole probe measurements show that the vortex was present in the 25-deg plane but not in the 5-deg plane. The endwall visualization pattern indicates that flow adjacent to the endwall became involved in the vortex beginning at $\beta = 15$ deg.

This flow pattern does not support the multiple vortex pattern given by Baker [8] and Moore and Forlini [11]. That pattern was developed from endwall flow visualizations where the local separation line identified in this experiment was interpreted as a global separation line emanating from a second saddle point in the plane of symmetry. Based on the flow topology, a nodal point of attachment must be present between the two saddle points, though the nodal point could not be discerned in the endwall flow visualizations. Based on these results, the experimenters inferred a multivortex system for the separation of the boundary layer from the endwall. This complex vortex system was not present in this experiment. The endwall flow visualization clearly shows a single saddle point, and the flow field measurements indicate a single horseshoe vortex.

Conclusions

This project documented the flow field in the endwall region around a cylinder. This documentation leads to the following conclusions:

1 A single endwall saddle point and a single endwall attachment point were observed in the endwall flow visualization pattern. The multiple singular points required for the multivortex model were not present.

2 The five-hole probe measurements indicate that a single main vortex was formed. Although the rudiments of a vortex were observed in the plane of symmetry and the 5-deg plane, the vortex was fully formed between the 5-deg and 25-deg planes. The flow visualization pattern indicates that the flow adjacent to the endwall initially rolled up near the 15-deg plane.

3 The main vortex was confined to a region less than one boundary-layer thickness from the endwall. The vortex core moved radially outward and slightly away from the endwall as the vortex passed around the cylinder.

4 The losses associated with the vortex rollup were localized and offset by the transport of core flow into the endwall region next to the cylinder.

5 A key implication of these experimental results for gas turbine engines is that flow in the saddle point region does not exhibit swirl.

Acknowledgments

This work was supported by NASA Grant No. NSG-3238 under the direction of L. J. Goldman of the NASA Lewis Research Center.

References

1 Eckerle, W. A., "Horseshoe Vortex Formation Around a Cylinder," Ph. D. Thesis, University of Connecticut, Storrs, CT, May 1985.

2 Langston, L. S., Nice, M. L., and Hooper, R. M., "Three Dimensional Flow Within a Turbine Cascade Passage," ASME JOURNAL OF ENGINEERING FOR POWER, Vol. 99, 1977, pp. 21–28.

3 Langston, L. S., and Boyle, M. T., "A New Surface-Streamline Flow-Visualization Technique," *Journal of Fluid Mechanics*, Vol. 125, 1982, pp. 53–57.

4 Langston, L. S., and Wagner, C. A., "A Streamline Model for a Saddle Point of Separation," submitted to the *Journal of Fluid Mechnics*, Oct. 1983.

5 Oswatitsch, K., "Die Ablosungsbedingung von Grenzchichten," *Symposium on Boundary Layer Research*, International Union of Theoretical and Applied Mechanics, Gortler, ed., Springer-Verlag, Berlin, 1958.

6 Ram, V. V., "Untersuchungen uber die Eckengrenzschicht an einem

Kreiszlyinder mit Seitenwand," Report No. 63/46, Institute of Fluid Mechanics, Technische Hochschule, Braunschweig, 1963.

7 East, L. F., and Hoxey, R. P., "Low Speed Three-Dimensional Turbulent Boundary Layer Data," Royal Aircraft Establishment, Tech. Rep. No. 69041, Parts I and II, 1969.

8 Baker, C. J., "Vortex Flow Around the Bases of Obstacles," Ph.D. Thesis, University of Cambridge, Cambridge, England, Sept. 1978.

9 Schlichting, H., *Boundary Layer Theory*, McGraw-Hill, New York, 1968, pp. 596–651.

10 Tobak, M., and Peake, D. J., "Topology of Three-Dimensional Separated Flows," *Ann. Rev. Fluid Mechanics*, Vol. 14, 1982, pp. 61–85.

11 Moore, J., and Forlini, T. J., "A Horseshoe Vortex in a Duct," ASME JOURNAL OF ENGINEERING FOR GAS TURBINES AND POWER, Vol. 106, 1984, pp. 668–676.

Kreiszlyinder mit Seitenwand," Report No. 63/46, Institute of Fluid Mechanics, Technische Hochschule, Braunschweig, 1963.

7 East, L. F., and Hoxey, R. P., "Low Speed Three-Dimensional Turbulent Boundary Layer Data," Royal Aircraft Establishment, Tech. Rep. No. 69041, Parts I and II, 1969.

8 Baker, C. J., "Vortex Flow Around the Bases of Obstacles," Ph.D. Thesis, University of Cambridge, Cambridge, England, Sept. 1978.

9 Schlichting, H., *Boundary Layer Theory*, McGraw-Hill, New York, 1968, pp. 596–651.

10 Tobak, M., and Peake, D. J., "Topology of Three-Dimensional Separated Flows," *Ann. Rev. Fluid Mechanics*, Vol. 14, 1982, pp. 61–85.

11 Moore, J., and Forlini, T. J., "A Horseshoe Vortex in a Duct," ASME JOURNAL OF ENGINEERING FOR GAS TURBINES AND POWER, Vol. 106, 1984, pp. 668–676.

DISCUSSION

T. V. Jones[2] and P. T. Ireland[2]

Together with the previous work [12] the present paper provides an important picture of the flow field associated with the horseshoe vortex. We wish to comment on two points discussed in the paper: firstly the existence of one main vortex without the presence of a multivortex structure, and secondly the new flow field which is proposed close to the centerline. In a paper to be presented in the near future [13], the horseshoe vortex present at both ends of a cylinder placed across fully developed turbulent flow in a two-dimensional channel is examined. Surface flow visualization indicated only one main horseshoe vortex and a small corner vortex at the wall-cylinder junction. No multivortex system was apparent and in this sense the observations are in keeping with the results reported in the present paper. On the second point, it would appear that heat transfer measurements on the end wall [13] could not be explained by the proposed flow field close to the centerline. The heat transfer coefficient reduced with radial distance from the cylinder, except for a small peak close to the "heart" of the horseshoe vortex, in all angular directions. There was no change in this pattern of heat transfer close to the centerline which might be expected if the flow field was as suggested in the paper. The heat transfer coefficient distribution is similar to that reported by Blair [14], where it is also suggested that unsteadiness may be present. Fast response surface heat transfer measurements mentioned in [13] indicate that unsteady effects are present beneath the horseshoe vortex.

[2]Department of Engineering Science, University of Oxford, Oxford OX1 3PJ, England.

References

12 Langston, L. S., and Boyle, M. T., "A New Surface-Streamline Flow-Visualization Technique," *Journal of Fluid Mechanics*, Vol. 125, 1982, pp. 53–57.

13 Ireland, P. T., and Jones, T. V., "Detailed Measurements of Heat Transfer on and Around a Pedestal in Fully Developed Channel Flow," to be presented at the 8th International Heat Transfer Conference, San Francisco, 1986.

14 Blair, M., "Heat Transfer in the Vicinity of a Large-Scale Obstruction in a Turbulent Boundary Layer," *Prop. & Power*, Vol. 1, No. 2, 1985, p. 158.

Authors' Closure

We thank Dr. Jones and P. Ireland for their comments on our paper, and their independent observation of a single vortex system. Although we have reported on mean flow field measurements only, we do agree that unsteadiness must play some role in the interaction of the vortex system with the endwall. We are currently taking hot-wire anemometer measurements within the vortex system (using the mean flow measurements for mean flow direction) and will report on these at a later date.

The Development of the Profile Boundary Layer in a Turbine Environment

J. Hourmouziadis
F. Buckl
P. Bergmann

Turbine Aerodynamics,
MTU Motoren- und
Turbinen-Union München GmbH,
Munich, Federal Republic of Germany

Cascade testing tries to simulate the actual flow conditions encountered in a turbine. However, it is possible to reproduce neither the free-stream turbulence structure of the turbomachinery, nor the periodic wake effects of upstream blade rows. The usual understanding is that the latter in particular results in a significantly different behavior of the boundary layer in the engine. Experimental results from cascades and turbine rigs are presented. Grid-generated free-stream turbulence structure is compared to that in the turbine. Measurements of the profile pressure distribution, flush-mounted hot films, and flow visualization were used for the interpretation of the test results. Some observations of the boundary layer development in the cascade, on the guide vanes, and on rotor blades with typically skewed boundary layers are shown indicating essentially similar behavior in all cases.

Introduction

The overall performance of a turbine depends primarily on the viscous effects in the flow. This is particularly true for turbines in aircraft engines where large portions of the boundary layer on the airfoils are laminar. In this case early laminar/turbulent transition would increase turbulent friction losses, late transition would tend to increase sensitivity to laminar separation, both leading to performance deterioration. In cooled turbines these phenomena would also have an influence on heat transfer to the blade and may penalize life. Evidently close control of transition is necessary to hold and improve on the present high levels of performance.

It is well known that turbulence can have a strong effect on the transition of shear layers. This has been accepted for some time and extensive experimental work has been carried out to determine the influence of the degree of turbulence on cascade performance. Reviews have been presented by Surugue [1] and Kiock [2]. Adopting the point of view of fundamental boundary layer research, in many cases devices have been used to produce isotropic or at least uniform turbulence at the entry to the test section. This permits a clear separation of turbulence from other effects. Unfortunately, the situation in turbomachinery is more complicated. The turbulence produced in wakes usually does not have sufficient time to become uniform before it interacts with the boundary layer of the next row. The wakes of rotating blades produce discrete frequency fluctuations for the stationary vanes. Changing from the absolute to the relative frame and vice versa directly affects the components of velocity fluctuations. Finally the problem is further complicated by radial movement of the fluid in secondary flows.

Contributed by the Gas Turbine Division of THE AMERICAN SOCIETY OF MECHANICAL ENGINEERS and presented at the 31st International Gas Turbine Conference and Exhibit, Düsseldorf, Federal Republic of Germany, June 8–12, 1986. Manuscript received at ASME Headquarters February 21, 1986. Paper No. 86-GT-244.

To reduce complexity, modeling of these phenomena at the present has to remain essentially two-dimensional. Nevertheless, it is quite obvious that the degree of turbulence alone is not sufficient to describe the flow. It is necesssary to include some more sophisticated considerations of the macroscopic structure of turbulence. These could help to separate, for example, the following different forms of interaction with a shear layer:

- Very slow fluctuations (very large eddy) representing quasi-steady-state flow for the boundary layer
- Slow fluctuations producing true unsteady flow, as in the experiments of Doorly and Oldfield [3]
- Fast fluctuations in the unstable region of the laminar boundary layer initiating transition. These are either introduced into the flow with isotropic turbulence, or with periodic wakes as in the experiments of Pfeil and Herbst [4], or with discrete frequency excitation as for example reported by Kachanov and Levchenko [5].
- Very fast fluctuations (very small eddy) which are damped away in the boundary layer and have no effects

To resolve these phenomena some more detailed information about the turbulence environment in a turbine is required. Measurements in a variety of turbine rigs are presented in this paper, and the characteristics are compared to grid-generated turbulence. The observed behavior of the two-dimensional profile boundary layer in such an environment is shown for guide vanes and rotor blades using different measurement techniques.

Experimental Facilities

Turbulence measurements were carried out in three different turbine rigs and behind grids placed in a jet flow. The experiments with the profile boundary layer were carried out in two of the turbine rigs.

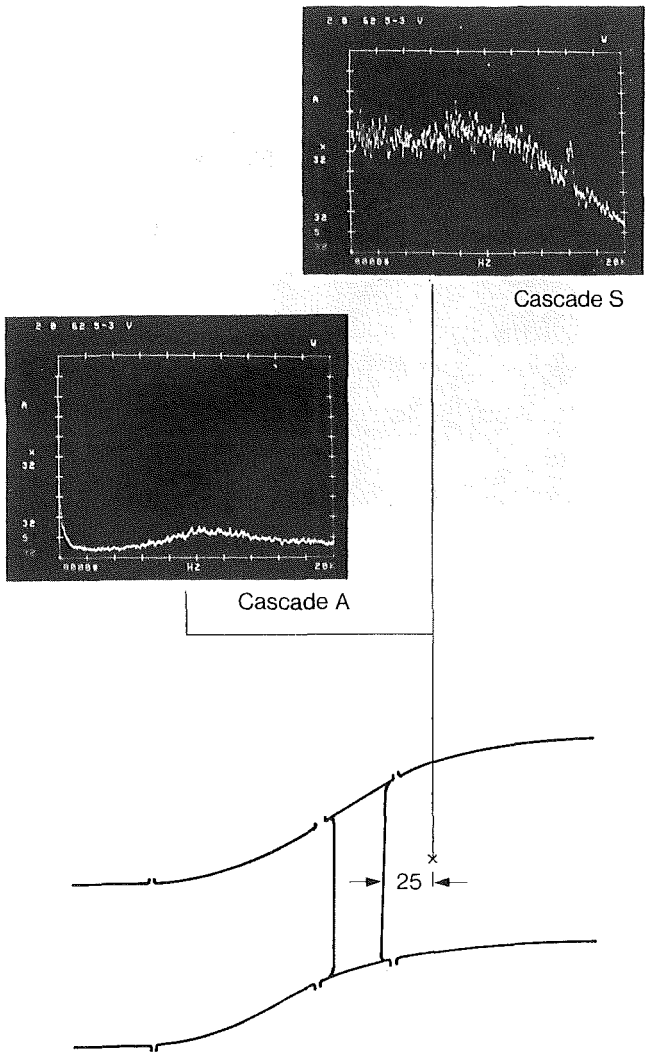

Fig. 1 Annular cascade rig and typical frequency spectra of turbulence for cascades *A* and *S*

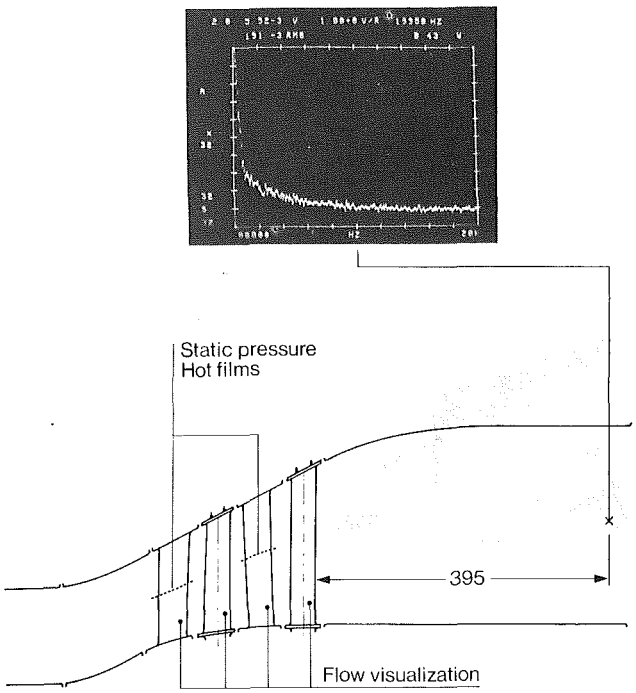

Fig. 2 Two-stage LP turbine rig and typical frequency spectra of turbulence

Figure 1 shows the annular cascade rig for the first guide vane of a low-pressure turbine. Very extensive aerodynamic measurements were carried out in this setup with two different cascades. This included static taps and flow visualization on the airfoil and circumferential traversing of the flow 25 mm downstream of the trailing edge at the mean section both with a five-hole pressure probe and a hot-wire probe.

In the two-stage rig shown in Fig. 2 the measurements concentrated on the profile boundary layer of the guide vanes using static taps and hot films at the mean section. Flow visualization was applied both on guide vanes and rotor blades. Turbulence measurements could be done 395 mm downstream of the trailing edge of the second rotor only. A hot-film cylinder probe was used. The first guide vane was one of the annular cascades used in the rig of Fig. 1.

The third rig, a single-stage high-pressure turbine, is shown in Fig. 3. Turbulence measurements were conducted 5 mm downstream of the rotor trailing edge at the 3 o'clock position and 40 mm at the 1 o'clock position at the mean section. No traversing was done. A hot-film cylinder probe was used for these tests.

The experiments with the turbulence grids were carried out in the jet behind a nozzle of 100 mm diameter shown in Fig. 4. The grids were mounted on the nozzle. Bar diameter/mesh width was 0.3/1.0; 0.8/3.3; 6/19; and 8/20 mm. Both hot-wire and hot-film cylinder probes were used.

The turbine parts were genuine engine hardware. For the turbulence measurements DISA probes were used. The flush-mounted hot films for the boundary layer investigations were developed and manufactured at MTU. Development and calibration techniques will be reported by Pucher and Göhl [7]. A TSI 1050 CTA anemometer was used for the tests. The signals were taken on tape and were further processed with a NICOLET 446B FFT real time analyzer.

Nomenclature

d = diameter, trailing edge thickness, m
e = rms hot film signal, V
E = time-average hot film signal, V
E_0 = time-average hot film signal at zero flow, V
f = frequency, Hz
F = frequency range, Hz
L = length scale of velocity fluctuations, m
P_t = total pressure, Pa
M = Mach number
Re = Reynolds number
s = curved coordinate of the profile surface, m
Sr = Strouhal number
t = cascade pitch, m
u = velocity in the shear layer, m/s
u' = velocity fluctuation, m/s
U = main flow velocity, m/s
V = eddy convection velocity, m/s
α = wave number, l/m
β = Hartree parameter
δ_1 = displacement thickness, m
η = dynamic viscosity, kg/(m•s)
λ = relative length scale of velocity fluctuations
τ = shear stress, Pa

Subscripts

I = integral value
F = frequency range
w = wall

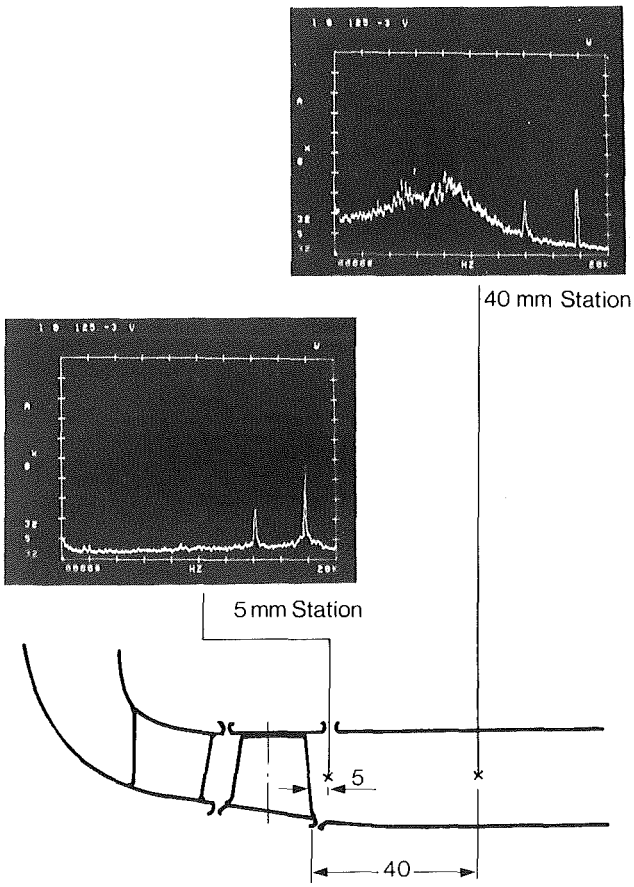

Fig. 3 HP turbine rig and typical frequency spectra of turbulence

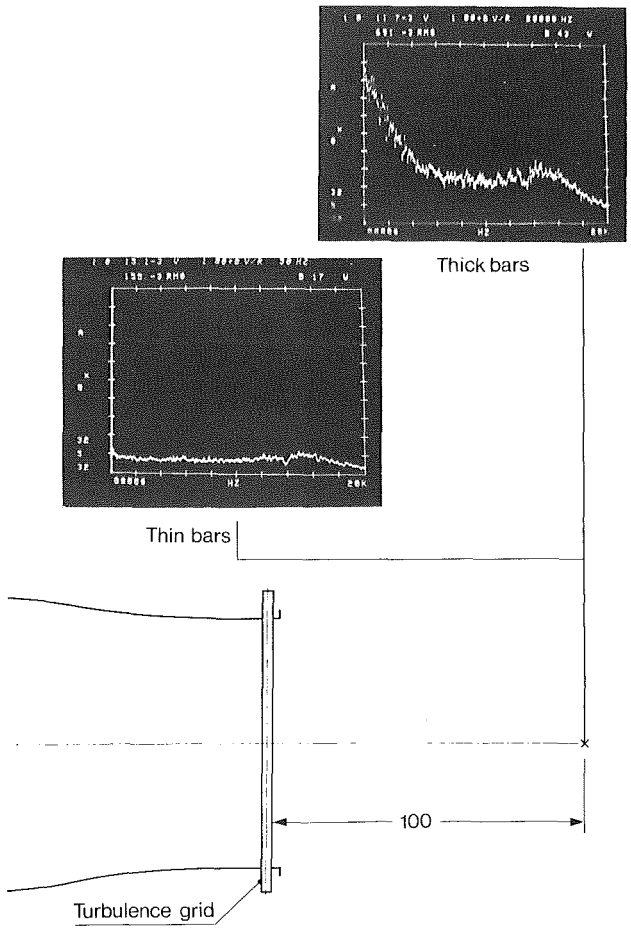

Fig. 4 Nozzle with turbulence grids and typical frequency spectra of turbulence

Macrostructure of Turbulent Fluctuations

For the classification of the interaction between turbulence and a shear layer the size of the eddies has been used in the introduction indicating the necessity for a characteristic length. Originally it was Taylor [6] who presented an analysis of turbulence in 1936 suggesting that not only the amplitude but also the wavelength of the disturbance are the important parameters. Stability theory for laminar flow uses only the wavelength. Frequency spectra can indeed show quite different qualities. In the case of Fig. 2 the amplitude is practically independent of the frequency except for very low values. In the case of Fig. 3 at the 40 mm downstream station, turbulence appears to be rather strong around 4 kHz, falling off at lower and higher frequencies. Additionally strong fluctuations can be observed at the discrete frequencies of 14 and 18 kHz. It should be expected that a shear layer would react differently to these two disturbances.

The individual disturbance can be described using its characteristic frequency f. The disturbance is convected downstream with the velocity V. This velocity can be used to define a length scale L

$$L = \frac{V}{2\pi f} \tag{1}$$

In terms of the eddy model this is the wavelength of the fluctuation. In free shear layers V is assumed to be equal to the local mean velocity of the flow U

$$V = U \tag{2}$$

These definitions can be directly applied to discrete frequency disturbances. For random fluctuations, however, integral scales have to be introduced. An integral frequency $f_{I,F}$ can be defined by an amplitude weighted averaging process over the frequency range of 0 to F kHz

$$f_{I,F} = \frac{\int_0^F f\sqrt{\overline{u'^2}}\, df}{\int_0^F \sqrt{\overline{u'^2}}\, df} \tag{3}$$

Accordingly the integral length scale is

$$L_{I,F} = \frac{V}{2\pi f_{I,F}} \tag{4}$$

For uniform turbulence, where the amplitude is constant, the integral frequency can be readily calculated to be equal to $F/2$. An integral frequency value below $F/2$ indicates that the slower fluctuations are more pronounced, a value above $F/2$ means that the higher frequencies are dominating. This suggests the introduction of relative parameters like the relative integral length λ

$$\lambda_{I,F} = \frac{L_{I,F}}{L_{I,F\ \text{uniform}}} \tag{5}$$

With equation (4) this gives

$$\lambda_{I,F} = \frac{f_{I,\text{F uniform}}}{F_{I,F}} = \frac{F/2}{f_{I,F}} \tag{6}$$

It should be noted that these parameters are still integral values just the same as the degree of turbulence. $\lambda_{I,F} = 1$ does not imply the existence of uniform turbulence. It only in-

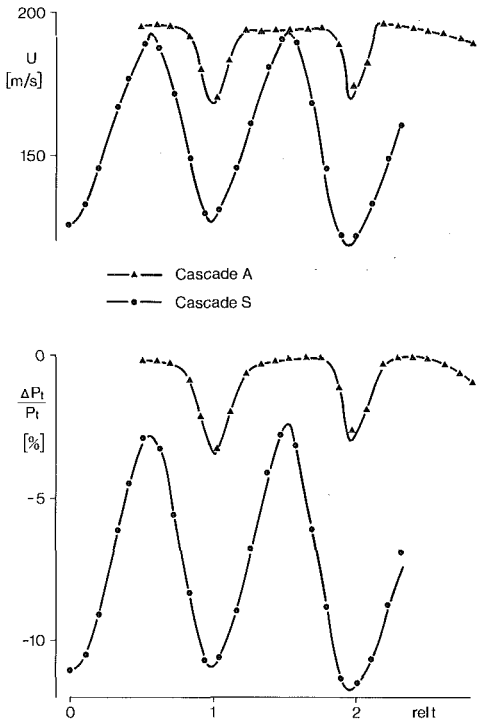

Fig. 5 Velocity and total pressure loss distribution downstream of the annular cascades *A* and *S*

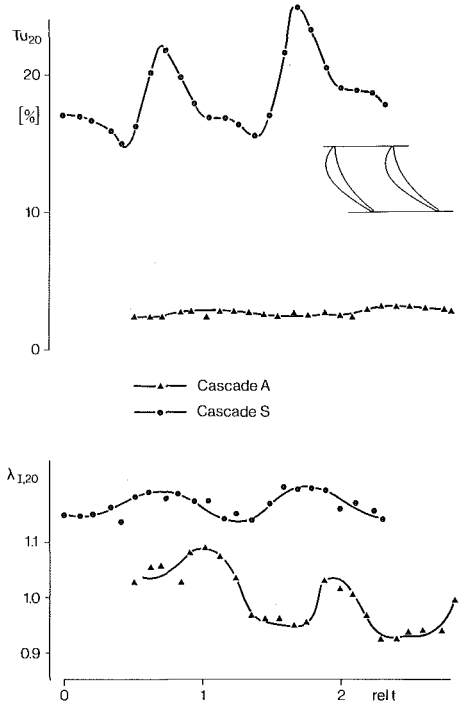

Fig. 6 Degree of turbulence and relative integral lengh downstream of the annular cascades *A* and *S*

dicates that overall turbulence levels below and above $F/2$ are equal, whatever the distribution in these two regions may look like. Nevertheless, the integral length is, besides the degree of turbulence, the second independent parameter which is necessary to describe the overall characteristics of amplitude and frequency.

In general these considerations have to be applied in the three possible directions of the fluctuations. However these are seldom available from measurements in turbomachinery. Results reported here include the streamwise and radial fluctuation. The frequency range has been limited to 20 kHz. This is somewhat low for hot-wire probes, but the experimental setup and other probes used tend to make measurements beyond that unreliable. Unless indicated otherwise, integral values in this study do not include discrete frequency amplitudes.

Turbulence Measurement Results

The most conclusive results were obtained with the annular cascade rig shown in Fig. 1, because one of the cascades investigated showed non-reattaching laminar separation. Test conditions were adjusted to give a Reynolds number of 200,000 defined with exit parameters and true chord.

The flow parameters were traversed tangentially 2.5 times the pitch in width. Figure 5 shows the velocity U and total pressure loss $\Delta P_t/P_t$ wakes versus the relative pitch. Figure 6 shows the overall degree of turbulence Tu and the relative integral length scale $\lambda_{I,20}$. The phase shift between the two cascades is arbitrary.

The total pressure losses increased dramatically from cascade A to cascade S, very similar to the transonic tests of Lawaczek [8] where the phenomenon was also caused by separation. The presence of laminar separation on cascade S was confirmed by the profile static pressure distribution and flow visualization, which also showed that on cascade A the boundary layer remained attached up to the trailing edge.

The measurement station is about one axial chord downstream of the vane row where significant mixing should already have taken place. However, the velocity deficit in the

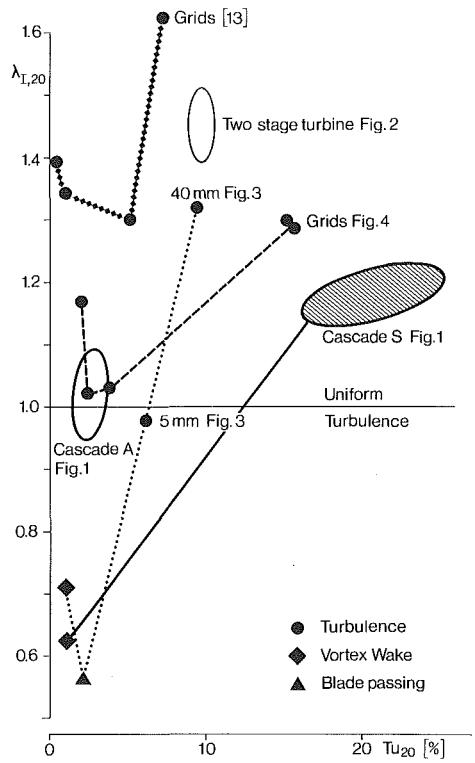

Fig. 7 Integal characteristics of turbulence in turbines and behind grids

wake of cascade A is still 13 percent, and 34 percent for cascade S. Velocity gradients are practically the same for both cases.

Much more interesting are the turbulence wakes. Although velocity gradients still exist, cascade A shows a constant degree of turbulence below 2 percent with relative integral length scales in the vicinity of 1. This confirms the observation

of Kiock [9] that the dissipation of turbulence is signifcantly faster than the decay of the mean velocity wake. He reported on similar levels of turbulence at the same distance from the trailing edge downstream of a compressor cascade.

Sharma et al. [10] obtained 8 percent maximum degree of turbulence 0.1 axial chords downstream of the inlet guide vane of a 1½ stage low velocity rig turbine. Taking the dissipation rate into account, this is also comparable to the present results.

The separate flow of cascade S shows levels of turbulence one order of magnitude higher and relative length scales of about 1.2. The latter indicates that lower frequencies dominate as can also be seen from the rms spectra in Fig. 1. The velocity gradients present in this station would not indicate sufficient turbulence production to explain these values. They are probably due to turbulence produced closer to the cascade where the suction side main flow mixes at the free shear layer with the dead water of the separation zone. In that region the highest velocity gradients in the flow are present. This is in agreement with the distribution of turbulence. The highest levels can be observed on the suction side leg of the wake quite close to the edge of the mixing zone. Kiock [11] identified similar behavior of turbulence in a compressor. It was attributed to laminar separation, which developed when Reynolds numbers were reduced below a critical value.

The rms spectra of Fig. 1 show a strong amplitude at 16 kHz for cascade S which could not be explained by any frequency of the system and which was not observed in cascade A. Assuming a Strouhal number Sr = 0.2 for the wake of a body with a displacement diameter d

$$\mathrm{Sr} = \frac{fd}{U} \tag{7}$$

a value of d = 2.4 mm can be calculated. This is approximately the predicted total displacement effect of pressure side boundary layer, trailing edge thickness, suction side separation zone, and suction side free shear layer, implying the presence of a vortex wake. The corresponding frequency for cascade A was expected to be beyond the range of the measurements. It could be identified at 28 kHz, giving about half the displacement effect of cascade S. In both cases the amplitude of the signal had a peak in the core of the wake. If these observations can be verified they would present a rather simple method of identifying flow separation in turbine cascades.

From the results of these tests two facts should be pointed out:

- High levels of turbulence in turbines can be produced in the mixing out of separation zones and not only by the periodic wakes between stationary and rotating blade rows.
- The measuring station lies within the blade passage of the downstream rotor of the complete stage shown in Fig. 2. It is obvious that turbulence there would by no means have to be uniform. In the case of cascade S for example the rather complex structure shown in Fig. 1 including periodic disturbances would be present.

The integral parameters, degree of turbulence, and relative length scales are shown in Fig. 7. The periodic vortex wake has been separated from the random turbulence for cascade S. It is shown at low levels of relative length scale and degree of turbulence.

Test results of the two-stage rig Fig. 2 are also plotted in the diagram. Turbulence measurements only far downstream were possible in this experiment. Rotor speed was varied between 80 and 120 percent and first vane Reynolds number between 160,000 and 480,000. In all cases the frequency spectra look very similar to that shown in Fig. 2. The distribution is practically constant except for very low frequencies. Obviously the

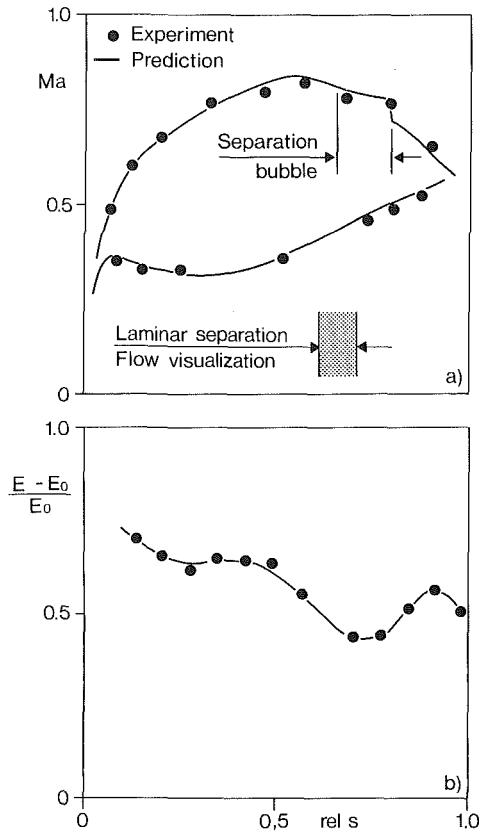

Fig. 8 Mach number distribution and time-average hot-film signal for the first guide vane of the two-stage rig at the mean section

measuring station about 15 axial chords away from the last row is so far downstream that the different operating conditions have no effect. Even the blade passing frequencies do not show. Relative integral length scales are between 1.4 and 1.5, turbulence levels are about 10 percent, which is partly due to the mean velocity reduction in the diffusing annulus of the test rig.

Typical spectra for the high-pressure turbine rig are shown in Fig. 3. Surprisingly, the station 5 mm downstream of the rotor shows a more uniform distribution than the station 40 mm downstream. The blade passing frequency can be readily identified for both stations. Also in both stations a periodic signal can be observed at 14 kHz. After transformation to the relative frame this could be attributed to the vortex wake of the rotor blades. Both discrete frequency signals appear at the very low length scale region of Fig. 7.

The overall degree of turbulence was found to be between 6 and 9 percent in both stations, the lower value corresponding to integral length scales of 1.0, the higher to 1.3. Laser velocimeter measurements 3 mm downstream of the trailing edge triggered to a fixed blade to vane position gave values of 8 to 16 percent along the guide vane pitch.

This sums up the available data on turbulence structure in turbines. It covers a range of Tu = 2 to 25 percent and $\lambda_{I,20}$ = 0.95 to 1.50. Periodic fluctuations lie about Tu = 2 percent and $\lambda_{I,20}$ = 0.5 to 0.6. Because of the limited data base, this does not cover the whole range to be encountered in a gas turbine. It should also be noted that these data only include cold rig experiments. Applying Mach number similarity, blade passing frequencies for example would be about two times higher in a hot engine environment.

For comparison grid-generated turbulence is also shown in Fig. 7. Results from the free jet tests of Fig. 4 give for bar diameters below 0.8 mm values close to uniform turbulence with $\lambda_{I,20}$ = 1 and Tu = 2 to 4 percent. The thicker bars give

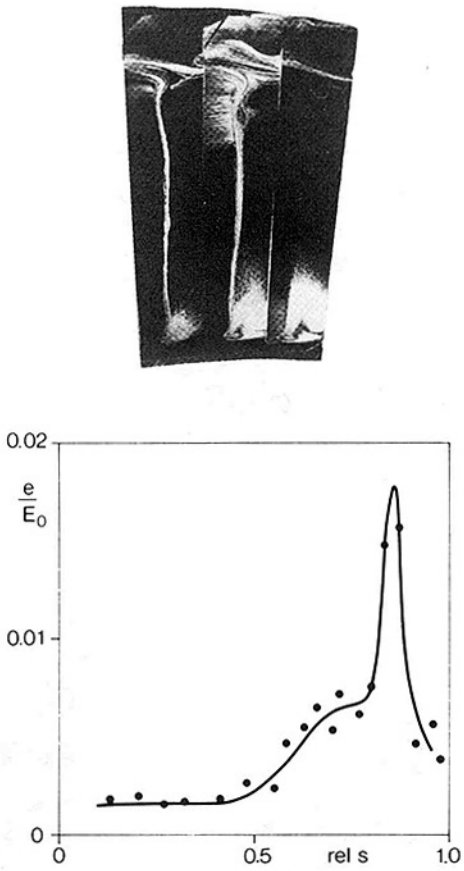

Fig. 9 Total rms hot-film signal and flow visualization for the first guide vane of the two-stage rig at the mean section

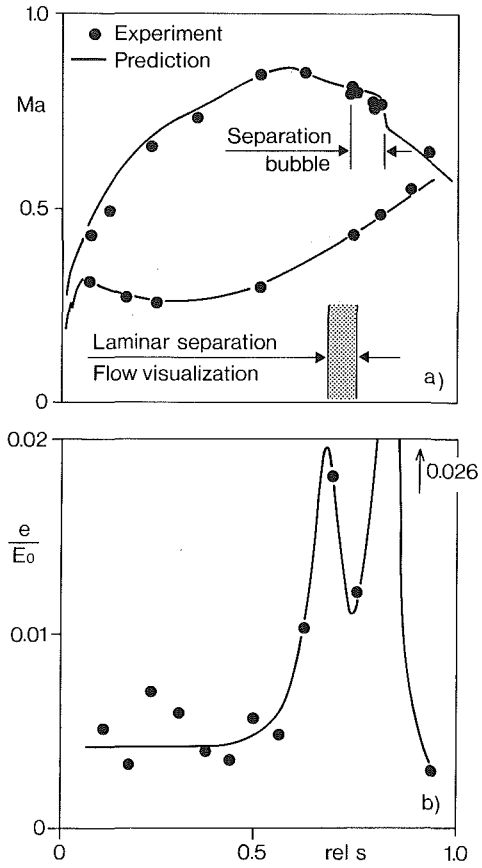

Fig. 10 Mach number distribution and total rms hot-film signal for the second guide vane of the two-stage rig at the mean section

both higher levels of turbulence and length scales. The differences can be easily understood when the spectra in Fig. 5 are compared. In the case of the thicker bars, the distance of the measuring station 100 mm downstream of grids did not fulfill the criterion given by Blair [12] of ten mesh lengths for uniform turbulence.

Further data are included from measurements in a high velocity cascade test facility by Kiock [13]. Degrees of turbulence up to 8 percent with length scales between 1.3 and 1.6 were achieved.

The data collected in Fig. 7 show that grid-generated turbulence is quite similar to that found in turbomachinery as far as overall parameters are concerned. One should not be afraid to put the grids close to the test section. The irregularities appearing there look much like those found in a turbine. Periodic disturbances will have to be introduced separately into the flow.

Boundary Layer Investigation

Because of the fundamental importance of the turbulence intensity and turbulence structure to the boundary layer development, boundary layer experiments were carried out with the two-stage rig shown in Fig. 2. The Reynolds number was set at 200,000 for the first guide vane. As mentioned before, genuine engine parts were used. The measurement techniques applied were:

- Static pressure taps around the profile at the mean section on both guide vanes
- Hot-film probes on the suction side at the mean section on both vanes
- Flow visualization on all four rows

The purpose of the test was to identify the state of the boundary layer along the suction surface and localize transition. The boundary layer behavior of the four rows should be compared in terms of the effects of periodic disturbances from the wakes of the upstream rows.

Figure 8(*a*) shows for the first vane the Mach number distribution, calculated from static to inlet total pressure, over the normalized curved coordinate s of the profile surface. The transition of the separated laminar boundary layer with following turbulent reattachment can be clearly seen on the diffusing part of the suction side. This is in good agreement with the boundary layer prediction.

The time-average hot-film signal E, corrected for the zero flow effect E_0, is plotted on Fig. 8(*b*). For ideal conditions, with no heat transfer from the probe at zero flow, this signal is proportional to $\tau_W^{I/6}$.

Unfortunately the heat loss to the vanes is usually much greater than the heat transfer due to the shear stress. Only with a very difficult calibration procedure would it be possible to calculate wall shear stress from the hot-film results, as Hodson [14] did for his tests. Nevertheless very good relative information can be extracted from the signal. In Fig. 8(*b*) high values of E can be identified in the region of acceleration, because of the thin boundary layer and the high wall shear stress. A minimum is expected at the separation point with zero wall shear stress. It can be found at the same position where the separation bubble was identified from the Mach number distribution. Further downstream the signal is higher, which can be explained by reattachment.

The fluctuating signal e of the hot-film probes is plotted in Fig. 9. The rms value is normalized with E_0. A very pronounced maximum can be observed. It corresponds exactly to the point of turbulent reattachment. The curve also shows a disturbance further upstream, which is close to the laminar

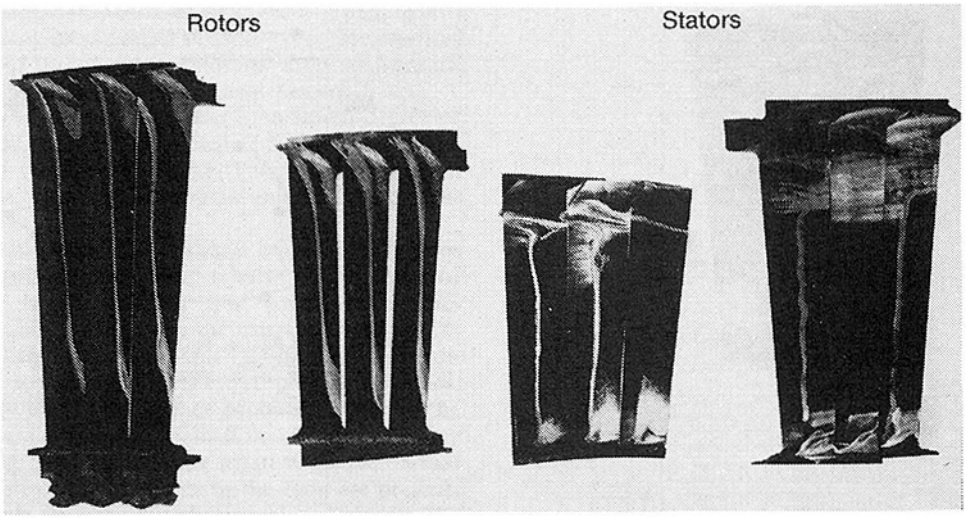

Fig. 11 Flow visualization on the suction side of guide vanes and rotor blades

separation point. These phenomena are discussed in more detail later.

For flow visualization, liquid dye was injected into the flow through static pressure taps during operation. The results, also shown in Fig. 9, confirm the conclusions about the transition process. The laminar separation can be clearly identified. The radial pressure gradients accelerate the stagnating fluid within the bubble towards the hub. A very clear picture of the dead water zone is drawn, similar to that obtained by Rohlik et al., [15] in 1953.

Contrary to the situation with the first guide vane, the second is directly affected by the wakes of the upstream rotor. The Mach number distribution and the rms signal of the hot-film probes for this vane are shown in Fig. 10. Static pressure taps were spaced too far apart in this case to identify a separation, the boundary layer prediction however did show a small bubble on the suction side. This could be confirmed again both by the hot-film measurements and the flow visualization. The rms signal shows in this case two very pronounced maxima: one at the laminar separation and the other at the turbulent reattachment point.

The former obviously corresponds to the disturbance which was also observed on the first guide vane. The difference can be explained in fact by the presence of the rotor wakes in the second vane.

Comparing the two airfoils, the separation seems to be larger on the first vane. One might tend to attribute this to the absence of the upstream rotor. However the boundary layer prediction indicates that this could also be caused by the different pressure distributions alone.

A similar situation with the wakes of the guide vanes is given for the rotor airfoils. Furthermore the boundary layer on the rotating blades is nowhere two-dimensional, because it is skewed by the centrifugal forces acting on the fluid close to the wall. The flow visualization for the four rows is shown in Fig. 11. No fundamental differences in the behavior of the boundary layers can be observed. In all cases transition occurs via a separation bubble. The skewing of the boundary layer on the wall can be clearly seen on the rotor blades. It should be noted that it appears very pronounced on the flow visualization because the density of the liquid dye is higher than that of air.

The applied experimental techniques give a very clear picture of the boundary layer development on the guide vanes. The same behavior was observed as reported by Hodson [16]. A large portion of the suction side boundary layer is laminar. Shortly after the velocity peak laminar separation, transition

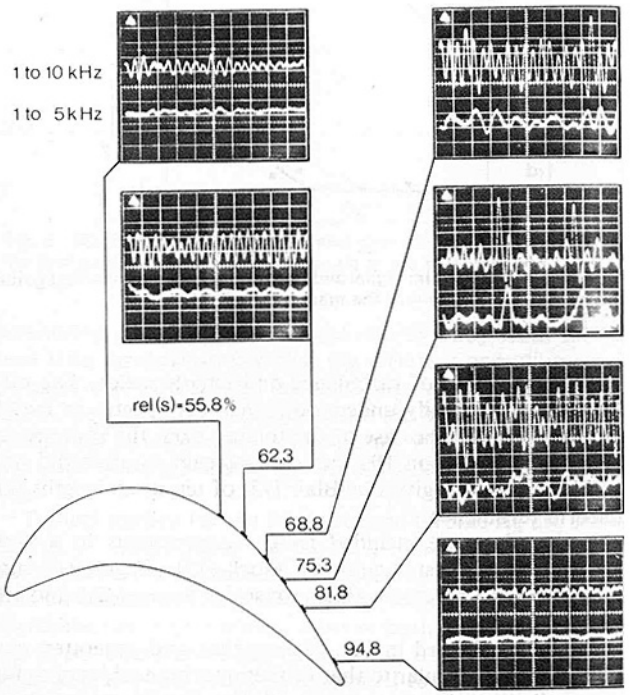

Fig. 12 Evolution of the hot-film signal in the time domain of the suction side of the second vane

in the free shear layer and reattachment occur. The local differences in the overall turbulence environment, including the periodic wake disturbances do not appear to have significant effects. Within the accuracy of the experiments, no differences among the four rows could be identified.

Boundary Layer Stability

The hot-film technique offers the same potential for the investigation of the macrostructure of the boundary layer as the hot-wire technique does for free-stream turbulence. Figure 12 presents an analysis of the signal in the time domain for the second guide vane of Fig. 2 as has been reported by Hourmouziadis and Lichtfuss [17].

The evolution of the signal fluctuation along the wall measured on the suction side of the second vane in a two-stage turbine rig is shown. The probes used have a resolution of approximately 10 kHz. With the passing frequency of the

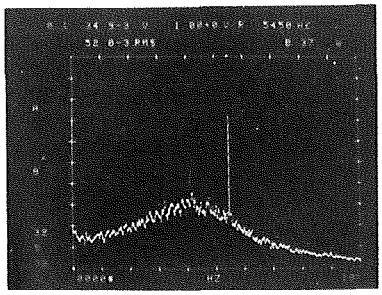

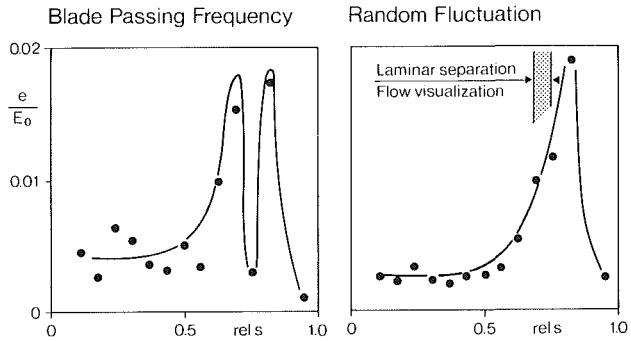

Fig. 13 Separation of the rms hot-film signal into periodic and random fluctuations

upstream blading at about 5.5 kHz the flow disturbances can not be easily isolated from the overall signal. In the lower part of the oscilloscope pictures the passing frequency has been filtered away. The remaining signal shows the expected evolution of the boundary layer along the profile surface coordinate s:

- Stable laminar flow to rel s = 55.8 percent
- Increasing instability until laminar separation occurs between 68.8 and 75.3 percent
- Bursts appearing at 75.3 percent indicating transition in the separated shear layer
- Strong turbulent reattachment fluctuations at 81.8 percent
- Low level of disturbances in the turbulent boundary layer at 94.8 percent which cannot be distinguished from that of the laminar flow at 55.8 percent.

More detailed information can be gained from the analysis of the frequency spectra. A typical example is shown in Fig. 13 for the second guide vane. It can be seen that the periodic fluctuation at the blade passing frequency has a very high rms value. This observation suggests the separation of the total signal plotted in Fig. 10 into a periodic and a random fluctuation. These diagrams are included in Fig. 13. The surprising result was that the first peak of the total e/E_0 signal at the laminar separation point was caused by the blade passing frequency alone. The second peak contained practically equal parts from the discrete frequency and the random fluctuation.

The evolution of the blade passing frequency amplitude on the suction side is presented in Fig. 14:

- From the leading edge up to the velocity maximum at about rel s = 55 percent the amplitude is constant and low.
- In the diffusing part, the signal is strongly amplified until laminar separation occurs between 68.8 and 75.3 percent.
- Within the laminar separation bubble at 75.3 percent the disturbance is totally damped down.
- In the turbulent reattachment zone at 81.8 percent the periodic signal is amplified again.
- Finally the attached turbulent boundary layer at 94.8 percent damps it down to the level of the laminar flow at 55.8 percent.

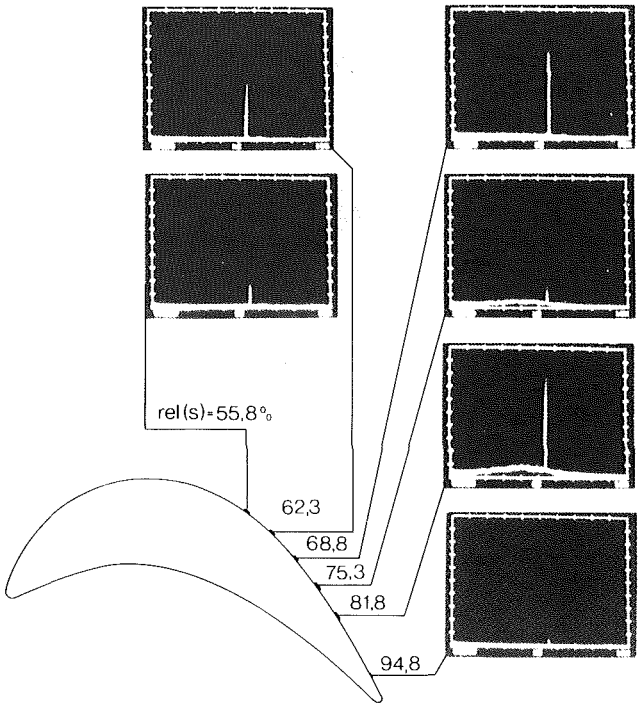

Fig. 14 Evolution of the blade passing frequency signal on the suction side of the second guide vane

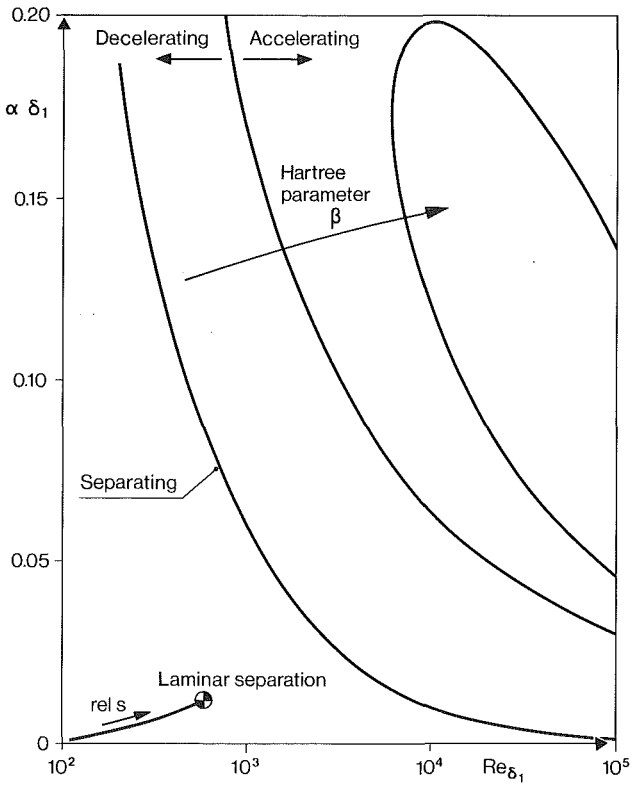

Fig. 15 Laminar flow neutral stability curves for Hartree profiles and boundary layer experimental results

Exactly the same behavior has also been observed on the first vane, however at significantly lower rms levels. This is due to the fact that disturbances are not imposed on the boundary layer by the rotor wakes directly, but by the weaker inviscid upstream effects of the rotor flow field, or by acoustic waves.

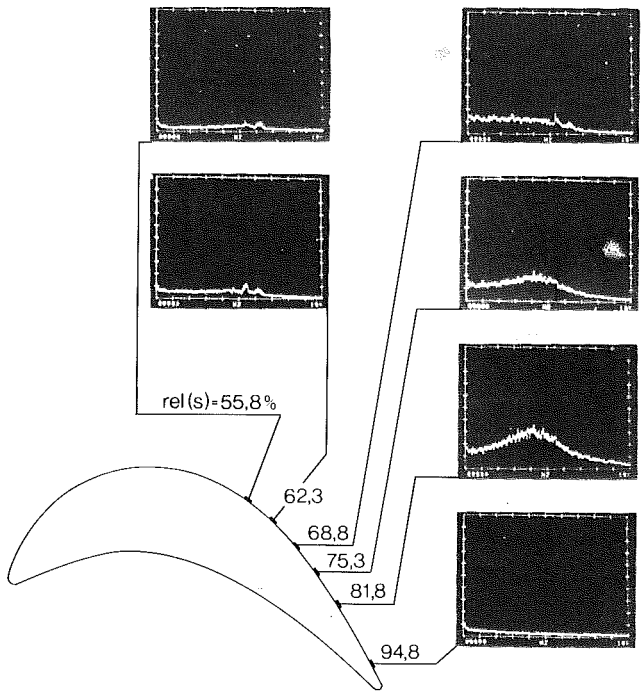

Fig. 16 Evolution of the random fluctuation signal on the suction side of the second guide vane

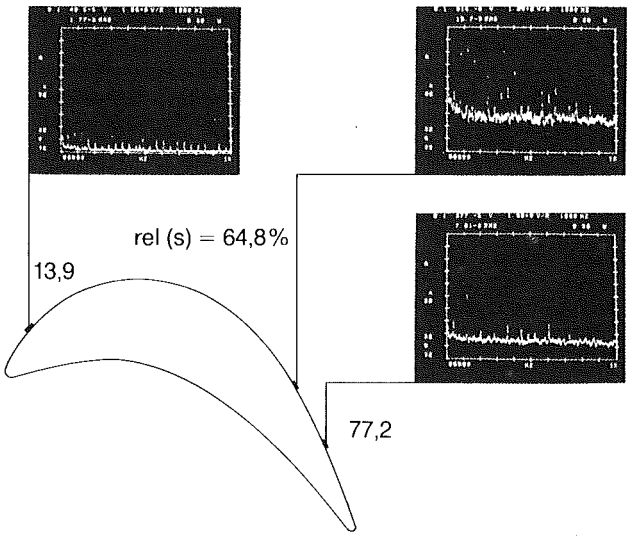

Fig. 17 Low frequency periodic fluctuations on the suction side of the second guide vane

The development up to the separation point looks very much like the stability behavior of the laminar boundary layer. An attempt was made to explain the e/E_0 curve for the blade passing frequency with the linear stability theory developed by Tollmien and Schlichting [18]. This involves the solution of the Orr–Sommerfeld differential equation. Wazzan et al. [19] have made a parametric study for Hartree velocity profiles. The neutral stability curves they calculated are plotted in Fig. 15. The evolution of the profile boundary layer is shown too. It appears that the laminar profile boundary layer remains deep in the stable region. The alternative possibility was also considered: that these are not weak disturbances, which are amplified moving downstream, but strong disturbances, which are damped down upstream. The Orr–Sommerfeld equation however gives practically 100 percent damping rates. Obviously linear stability theory does not give an explanation for this phenomenon.

The evolution of the random fluctuation spectrum is shown in Fig. 16:

- From the leading edge to the velocity maximum the amplitude is low and constant over the whole frequency range.
- In the diffusing part, up to the separation point between rel s = 68.8 and 75.3 percent the signal remains constant over the frequency at inceasing levels.
- Within the separation bubble at 75.3 percent the bursts shown in Fig. 12 lead to a concentration of the fluctuations about 4 kHz.
- In the reattachment region at 81.8 percent the highest levels of random fluctuations appear contributing to the second peak in Fig. 10. The maximum can still be found at 4 kHz.
- The attached turbulent flow at 94.8 percent shows only weak and constant fluctuations similar to those of the laminar boundary layer upstream of 55.8 percent.

The last item together with the observations with the blade passing frequency (Fig. 14) and the analysis in the time domain (Fig. 12) indicates that the state of the boundary layer can not be identified from the individual hot-film signal. It is necessary to follow the complete development history of the flow.

The amplification of the random fluctuations during deceleration is not as pronounced as the periodic signal was. No selectivity of any particular frequency range can be observed either, as should be expected for stability effects. The high levels at 75.3 and 81.8 percent are normal for a reattaching turbulent free shear layer. Rearward-facing step experiments performed by Driver et al. [20] as well as Kelly [21] have shown that the highest levels of turbulence in the flow can be found within the boundary layer at the reattachment point.

At very low frequencies periodic signals from the rotational speed at 39.5 Hz and its higher harmonics were identified on both guide vanes. Figure 17 shows the spectra in the 0 to 1 kHz range for the second vane. Rannacher [22] has carried out a nonlinear stability analysis accompanied by experiments in a plane boundary layer. He found out that excitation by two different frequencies may lead to periodic fluctuations derived from the difference of those two frequencies. This could be the case with the two rotors of the turbine investigated. However the corresponding value is 3 times 39.5 Hz. Probably it is a combination of this effect with vibrations of the vane itself or acoustic excitation. In any case the hot-film signal includes the response of the boundary layer. It can be seen from Fig. 17 that these frequencies are amplified in the same manner random fluctuations are.

Conclusions

The experiments on turbulence in turbines show that a large variety of different macrostructures may be present. This includes periodic fluctuations from blade passing frequencies and vortex wakes. The comparison of integral parameters indicates that grid-generated turbulence can be made to be very similar to that encountered in a turbine. Periodic disturbances however would have to be introduced separately in the flow.

The experimental techniques applied — airfoils profile statics, hot-film probes, and flow visualization — give a complete understanding of the boundary layer development on the airfoils. The two guide vanes and rotor blades of the two-stage rig were exposed to different turbulence environments, particularly in terms of the presence and frequency of rotating upstream wakes. No effects on the fundamental behavior of the boundary layers could be identified. At all rows transition takes place via a laminar separation bubble.

Both guide vanes showed a very characteristic amplification of the blade passing frequency: the first for the inviscid upstream effects of the rotor flow field, the second for the rotor wakes. These phenomena could not be explained by the linear stability theory of the laminar boundary layer.

It can be concluded that experience from plane cascade tests

is a good basis for turbine design. The fundamental boundary layer behavior in a turbomachinery environment is very similar and can be taken into account with the appropriate prediction techniques available today. It should be noted however that the phenomenon of stability and transition as well as the effects of fluctuating flow in turbomachinery are not yet completely understood. Successful design still relies heavily on calibrating transition criteria from experimental results. A large amount of work is still required to provide the aerodynamicist with the precise tools needed to make the best of a turbine design.

Acknowledgments

The authors would like to express their gratitude to Dr. D. Eckardt who originally initiated the investigations; to M. Artmeier, J. Reifenschneider, H. Kneissl, and H. Becker from the MTU turbine test group who carried out efficiently the extensive experimental program and the very precise measurements; to Dr. P. Pucher and R. Goehl who developed the hot-film technique to a standard that could be used in MTU turbine rigs and evaluated the turbulence and hot-film results; and finally to N. Gilbert from the Institut für Theoretische Strömungsmechanik of the DFVLR Göttingen who helped with the solution of the Orr-Sommerfeld equation.

References

1 Surugue, J., ed., "Boundary Layer Effects in Turbomachines," AGARDograph No. 164, Dec. 1972.

2 Kiock, R., "Boundary Layers on Turbomachinery Blades," Course Note 118, VKI Rhode Saint Genese, Feb. 1983.

3 Doorly, D. J., and Oldfield, M. L. G., "Simulation of the Effects of Shock Wave Passing on a Turbine Rotor Blade," ASME JOURNAL OF ENGINEERING FOR GAS TURBINES AND POWER, Vol. 107, 1985, p. 998–1006.

4 Pfeil, H. and Herbst, R., "Transition Procedure of Instationary Boundary Layers," ASME Paper No. 79-GT-128.

5 Kachanov, Yu. S., and Levchenko, V. Ya., "The Resonant Interaction of Disturbances of Laminar-Turbulent Transition in a Boundary Layer," *Journal of Fluid Mechanics*, Jan. 1984, pp. 209–247.

6 Taylor, G. I., "Some Recent Developments in the Study of Turbulence," *Proceedings of the Royal Aeronautical Society*, 1936, pp. 294–310.

7 Pucher, P., and Goehl, R., "Experimental Investigation of Boundary Layer Separation With Heated Thin-Film Sensors," ASME JOURNAL OF TURBOMACHINERY, this issue.

8 Lawaczek, O., "Stoss-Grenzschicht-induzierte Ablösung bei transsonischen Turbinengittern," in: *Beiträge zur stationären und instationären*, DLR-Forschungsbericht 77/34, 1977.

9 Kiock, R., "Turbulence Downstream of Stationary and Rotating Cascades," ASME Paper No. 73-GT-80.

10 Sharma, O. P., Butler, T. L., Joslyn, H. D., and Dring, R. P., "An Experimental Investigation of the Three-Dimensional Unsteady Flow in an Axial Flow Turbine," AIAA/SAE/ASME 19th Joint Propulsion Conference, Seattle, June 27–29, 1983, Paper No. AIAA-83-1170.

11 Kiock, R., "Einfluss des Turbulenzgrades auf die aerodynamischen Eigenschaften von ebenen Verzögerungsgittern," *Forschung im Ingenieurwesen*, Jan. 1973.

12 Blair, M. F., "Influence of Free-Stream Turbulence on Turbulent Boundary Layer Heat Transfer and Mean Profile Development, Part I—Experimental Data," ASME *Journal of Heat Transfer*, Feb. 1983.

13 Kiock, R., Laskowski, G., and Hoheisel, H., "Die Erzeugung höherer Turbulenzgrade in der Messstrecke des Hochgeschwindigkeits-Gitterwindkanals, Braunschweig, zur Simulation turbomaschinenähnlicher Bedingungen," *Forschungsbericht*, DFLVR-FB- 82-25, Mar. 1982.

14 Hodson, H. P., "Boundary Layer and Loss Measurements on the Rotor of an Axial-Flow Turbine," ASME JOURNAL OF ENGINEERING FOR GAS TURBINES AND POWER, Vol. 106, 1984, pp. 391–399.

15 Rohlik, H. E., Allen, H. W., and Herzig, H. Z., "Study of Secondary-Flow Patterns in an Annular Cascade of Turbine Nozzle Blades With Vortex Design," NACA Technical Note 2909, Feb., 1953.

16 Hodson, H. P., "Boundary-Layer Transition and Separation Near the Leading Edge of a High-Speed Turbine Blade," ASME JOURNAL OF ENGINEERING FOR GAS TURBINES AND POWER, Vol. 107, 1985, pp. 127–134.

17 Hourmouziadis, J., and Lichtfuss, H.-J., "Modern Technology Application to Compressor and Turbine Aerodynamics," 7th ISABE, Beijing, Sept. 1–4, 1985.

18 Schlichting, H., *Boundary-Layer Theory*, 2nd ed., McGraw-Hill, New York, 1979.

19 Wazzan, A. R., Okamura, T. T., and Smith, A. M. O., "Spatial and Temporal Stability Charts for the Falkner-Skan Boundary-Layer Profiles," Douglas Aircraft Company, Report No. DAC-67086, 1968.

20 Driver, D. M., Seegmiller, H. L., and Marvin, J., "Unsteady Behavior of a Reattaching Shear Layer," AIAA 16th Fluid and Plasma Dynamics Conference, Danvers, July 12–14, 1983, Paper No. AIAA-83-1712.

21 Kelly, F. J., "Turbulent Flow Reattachment—An Experimental Study of the Flow and Structure Behind a Backward-Facing Step," Stanford University, Ph.D. Thesis, 1980.

22 Rannacher, J., "Kombinationswirbelfeder in realen Strömungen," *ZAMM*, 1982, pp. 657–666.

Transition in Pressure-Surface Boundary Layers

R. I. Crane

G. Leoutsakos

J. Sabzvari

Department of Mechanical Engineering,
Imperial College of Science
and Technology,
London SW7 2BX, United Kingdom

Laminar-to-turbulent transition in the presence of Görtler vortices has been investigated experimentally, in the outer wall boundary layer of a curved water channel. Ratios of boundary layer thickness at the start of curvature to wall radius were around 0.05 and core flow turbulence intensities were between 1 and 3 percent. Measurements of intermittency factor were made by hot film probe and of mean and rms velocity by laser anemometer. At Reynolds numbers low enough to allow considerable nonlinear vortex amplification in the laminar region, transition was found to begin sooner and progress faster at a vortex upwash position than at a spanwise-adjacent downwash position. Measured Görtler numbers at transition onset bore little relationship to those often used as transition criteria in two-dimensional boundary layer prediction codes. Little spanwise variation in intermittency occurred at higher Reynolds numbers, where mean velocity profiles at upwash were much less inflected. Toward the end of curvature, favorable pressure gradients estimated to exceed the Launder relaminarization value corresponded with cases of incomplete transition.

Introduction

Until developments in blade materials are at a considerably more advanced stage than at present, achievement of higher gas turbine engine performance by increasing turbine entry temperature must rely on greater complexity in blade cooling arrangements. To ensure acceptable metal temperatures and component life without sacrificing performance by using excessive amounts of cooling air, detailed and accurate knowledge of heat transfer rates between the combustion gases and the blade surface is of increasing importance. The complex nature of the flow in blade boundary layers, even without film cooling and in regions remote from end walls and blade tips, makes heat transfer prediction a difficult task; quantitative agreement between reliable laboratory measurements and the best of current computational methods is often poor. This is hardly surprising, since the boundary layers contain laminar, turbulent, and transitional regions and are subjected to the combined effects of freestream turbulence, ordered unsteadiness, varying pressure gradient, curvature, compressibility, etc., as reviewed in [1]. Transition, both laminar-to-turbulent and vice versa, can occupy a large fraction of the blade surface.

Predictions of pressure-surface heat transfer are frequently worse than those for suction surfaces, the discrepancies being attributed mainly to the failure to predict the starting location and length of the laminar-turbulent transition. A particular difficulty here is the destabilizing effect of concave curvature, which together with freestream turbulence opposes the stabilizing influence of strong acceleration. Görtler vortices have been observed [2] on a blade with severe pressure-surface curvature, and it was inferred that they acted as a catalyst to transition as well as having a possible effect in augmenting laminar heat transfer.

A good demonstration of the capabilities of five prediction models is provided by the work of Daniels and Browne [3], which compares the models with cascade measurements of heat flux at different Reynolds numbers Re and turbulence intensities *Tu*; with a few exceptions at the extreme combinations of low Re–low *Tu* and high Re–high *Tu*, agreement on the pressure surface was poor even in a qualitative sense, especially over the crucial downstream half of the blade chord. Similar problems are suggested by the recent findings of Nicholson et al. [4]; on two profiles designed to have comparatively short transition regions close to the leading edge, before the start of significant concave curvature, no clear evidence of transition was found from heat transfer measurements for most experimental conditions. In some studies, e.g., [5, 6], transition was believed to occur via a separation bubble in short regions of adverse pressure gradient near the leading edge; the inability of most prediction models to compute through a laminar separation with turbulent reattachment is a problem equally important to that caused by the deficiencies in transition criteria for attached boundary layers.

In the short term, improvements in predictive capability seem most likely to be attained by conducting simplified experiments which attempt to isolate individual effects [7] and incorporating the findings, necessarily in empirical form, into existing finite difference codes which employ low-order turbulence modeling [8]. The present work was undertaken in this spirit, with the aim of providing more information on transition on concave walls in the presence of Görtler vorticity. Together with results from concurrent work elsewhere, e.g.,

Contributed by the Gas Turbine Division of THE AMERICAN SOCIETY OF MECHANICAL ENGINEERS and presented at the 31st International Gas Turbine Conference and Exhibit, Düsseldorf, Federal Republic of Germany, June 8–12, 1986. Manuscript received at ASME Headquarters January 20, 1986. Paper No. 86-GT-104.

[9], it is hoped that this will lead to improved transition modeling for use in codes of the STAN5 or GENMIX-derived type [10, 11].

Following a survey of some current procedures for modeling laminar–turbulent transition, this paper describes experiments on a constant-curvature surface at nominal momentum thickness Reynolds numbers Re_θ and Görtler numbers G_θ not atypical of those expected under gas turbine conditions. Measurements of mean and fluctuating velocities and intermittency factor are presented, extending the velocity measurements reported in [12], and are discussed in the context of existing transition models.

Transition Modeling in Heat Transfer Programs

In typical finite-difference programs in general use, the system of mean boundary layer equations is still closed by relating the turbulent fluxes of momentum and heat to gradients of mean velocity and enthalpy through turbulent diffusivities. To handle transition, an effective diffusivity D_e can be written as

$$D_e = D_l + \gamma D_t \tag{1}$$

where D_l is a molecular diffisivity appropriate to laminar flow, D_t is a turbulent diffusivity, and γ varies from 0 to 1 through the transition region. γ can be taken as the intermittency factor, representing the fraction of the total time during which turbulent "spots" are present at a fixed streamwise location. The required input to such models is therefore the transition starting position where γ first becomes nonzero, the completion position beyond which γ equals unity (unless relaminarization is predicted), and the functional form of the γ versus distance x relationship (or γ versus a boundary layer integral parameter such as Re_θ). Another category of model, which can account for the effect of freestream turbulence on a laminar boundary layer, attempts to predict transition by computing the entrainment of freestream turbulent kinetic energy into the boundary layer; two such models are described briefly in [3]. With higher-order turbulence modeling, this category offers more scope for longer term development; however, the empirical input requirements, e.g., [13], are not directly related to transition and will not be considered here.

For the simpler category of model, several approaches have been reported for specifying the onset and length of transition. To date, most publications have referred to earlier correlations, such as that of Seyb [14] in Gaugler's [15] version of the STAN5 model, although empirical relationships based on more recent and extensive data are now available.

Correlations for transition onset on smooth flat surfaces are now in broad agreement, e.g., those of Abu-Ghannam and Shaw [16] and Blair [17] which also provide some support for the theory of Van Driest and Blumer [18]. These results show that in uniform zero or favorable pressure gradients, $Re_{\theta s}$ (at the start of transition) is a function only of freestream turbulence intensity Tu_∞, provided that Tu_∞ exceeds about 0.5 percent as will be the case in practice. Nevertheless, values of the velocity gradient parameter $K = (\nu/u_\infty^2)(du_\infty/dx)$ greater than around 2.5×10^{-6} may be sufficient to suppress transition by a mechanism similar to that causing relaminarization of a turbulent boundary layer [19]. In uniform adverse pressure gradients, $Re_{\theta s}$ can be expressed as a function of Tu_∞ and the velocity gradient parameter $\Lambda = (\theta^2/\nu)(du_\infty/dx)$; for $Tu_\infty > 3$ percent, the dependence on Λ seems to be weak. Local velocity gradient is not the most appropriate value for use in these correlations, and it is suggested in [16] that flow history effects be taken into account by using the extreme value encountered prior to transition.

The only common treatment of the effect of surface curvature on transition onset seems to be that of Forest [20], who correlated the small amount of early experimental data to give the equation

$$G_{\theta s} = 9 \exp(-17.3\, Tu_\infty) \tag{2}$$

where $G_{\theta s}$ is the transition onset value of Görtler number $G_\theta = Re_\theta (\theta/r_w)^{1/2}$ and r_w is the wall radius of curvature. Brown and Martin [21] plotted this relationship with several sets of data, showing considerable scatter attributable to the influence of parameters other than Tu_∞. The theory of Görtler vortices is insufficiently developed to be able to make use of criteria based on a critical level of amplification of the vortices, as discussed in [22].

Modeling of transition length (or alternatively the location of the end of transition) seems to be less well founded than that of transition onset. A popular prescription is that of Dhawan and Narasimha [23], in which the Reynolds number based on a measure of transition length (between intermittency factor limits of 25 and 75 percent) is proportional to the 0.8 power of length Reynolds number at the start of transition. The correlation for zero pressure gradient in [16] makes $Re_{\theta e}$, the value of Re_θ on completion of transition, proportional to $Re_{\theta s}$, the data being derived from near-wall velocity measurements; for nonzero pressure gradients, a less explicit correlation was presented, relating $Re_{\theta e}$ to $Re_{xe} - Re_{xs}$ and Λ. However, the experiments of [19] indicate the opposite trend, i.e., longer transition zones associated with an early start to transition, attributed to the effects of pressure gradient. Little

Nomenclature

a = channel width
b = free surface height
D = diffusivity
G_θ = Görtler number = $Re_\theta (\theta/r_w)^{1/2}$
K = velocity gradient factor = $(\nu/u_{pw}^2)\, du_{pw}/ds$
r = radial coordinate
Re_s, Re_x, Re_θ = Reynolds number based on s, x, θ
s = streamwise distance measured along the wall ($s = 0$ at contraction exit)
Tu = turbulence intensity = $\tilde{u}/\bar{u}$
u = streamwise velocity component
x = streamwise coordinate on flat surface
y = distance measured normal to wall ($= r_w - r$ for concave surface)
z = spanwise coordinate
γ = intermittency factor
δ = boundary layer physical thickness
θ = momentum thickness = $\int (\bar{u}/u_p)(1 - \bar{u}/u_p)dy$ where $u_p(y)$ = potential (core) velocity profile, extrapolated toward wall
Λ = velocity gradient factor = $(\theta^2/\nu)\, du_\infty/dx$
ν = kinematic viscosity
ϕ = angular coordinate = $(s - s_0)/r_w$

Subscripts

e = end of transition
max = maximum value on profile (at fixed s and z)
pw = value at wall in potential flow
s = start of transition (except when used in Re_s)
w = value at wall
∞ = freestream (above flat surface)

Superscripts

$\bar{}$ = time mean value
$\tilde{}$ = rms value

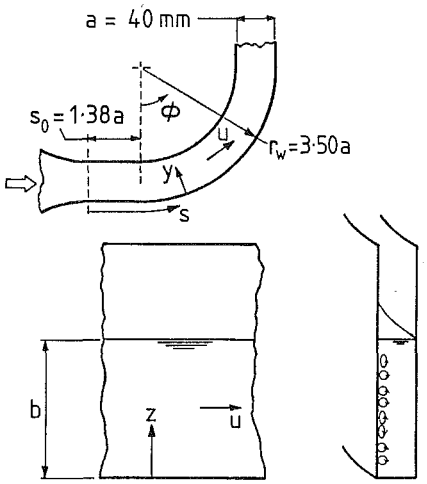

Fig. 1 Test section geometry and notation

is known about the effects of curvature on transition length. An early correlation collected by Schlichting [24] is employed in the heat transfer program of So et al. [5], and applied to both length (in terms of change in Re_θ) and onset of transition. (Onset is defined in So's model in terms of a critical Reynolds number for instability of a laminar layer to small disturbances [25], rather than correlations based on the more usual indicators such as changes in velocity profile, skin friction, or heat transfer.)

Specification of the variation in intermittency from start to end of transition has usually been based on the exponential relationship proposed in [23], regardless of the values of parameters such as turbulence level, pressure gradient, and curvature. So et al. [5] are again unusual in expressing this as a γ versus Re_θ relationship rather than γ versus x.

Finally, mention should be made of attempts to derive transition information by "calibrating" prediction models against experimental heat transfer data (where boundary layer flow measurements are not also available). By adjusting the specified locations of the start and end of transition to achieve the best agreement with heat transfer coefficient distributions, Gaugler [26] has recently obtained several sets of values for $Re_{\theta s}$ and $Re_{\theta e}$, but only for flat and convex surfaces.

Experimental Arrangement

Flow Rig. The closed-circuit water channel described in [12] (where the test section is referred to as "bend B") and [27] was used for the present work. The circuit was comprised of control valves, cone-and-float flowmeters, constant-speed pump, heat exchanger (to maintain constant water temperature), and a Perspex (plexiglass) assembly combining a settling chamber, contraction, and 90-deg-bend test section whose geometry is shown in Fig. 1 together with associated nomenclature. Earlier work with this rig [27] established that the strengths and spanwise spacing of Görtler vortices are characteristic of the final wire gauze screen in the settling chamber. Use of the same final screen as in [12, 27] ensured that a known, repeatable vortex system was produced. The height b of the free surface was chosen as $3.5a$ to give optimum spanwise uniformity of the bend inlet flow; for the present range of conditions, the midspan flow was not noticeably affected by the end-wall secondary flow.

Instrumentation. Local mean and rms fluctuating velocities were obtained by a single-channel laser-Doppler anemometer (LDA) operated in the forward-scatter fringe mode using a 5 mW He–Ne laser. In the present work only the u (streamwise) component was measured, using the optical system described in [28] with the beams passing through the curved walls. Refraction corrections to the beam crossing angle and intersection volume location are given in [29]. Transmitting and receiving optics were mounted on a three-directional traversing mechanism. Around 80 fringes were viewed by the photomultiplier, in an intersection volume of typical dimensions 1.5 × 0.2 mm, with a typical calibration factor of 0.50 MHz per m/s. The effect of the spatial averaging, resulting from having the longer dimension of the intersection volume in the y direction, was examined [29] by comparing results with those from an alternative (and less easy to use) optical system in which the longer dimension was in the z direction. Significant differences occurred only in the region of the narrow troughs which develop in the $u(z)$ distributions prior to transition [12]. Since most phenomena related to transition occur first in the regions of these troughs, it was considered important to localize measurements in the z direction; hence the alternative system was not used for the present work. Signal processing was by a Cambridge Consultants CC08 frequency tracking demodulator. Using where applicable, the uncertainty analysis of [30] with 20:1 odds, the maximum systematic errors in mean velocity $\bar{u}$ and rms velocity $\tilde{u}$ were estimated as ± 3 percent and ± 4 percent, respectively. Intermittency factor cannot be obtained from the discontinuous laser-Doppler signal. A Dantec (DISA) 55R15 boundary-layer fiber film probe was therefore used, having a 70-μm-dia quartz-coated nickel film of active length 1.25 mm, heated by a DISA 56C constant-temperature anemometer (CTA) system. The probe, suitably waterproofed, was mounted on a traversing mechanism with micrometer movement in three directions. The film probe datum positions were set relative to the optically determined LDA datum by focusing the LDA beam intersection on a suitable part of the film probe (while unheated). During operation at an overheat ratio of 1.3, precautions were taken to avoid accumulations of bubbles and minimize contamination of the film.

Conditioned outputs from both the LDA and the CTA were digitized by a Tecmar AD211 12-bit fast analogue-to-digital converter and processed via specially written assembly language programs on an Apple II+ microcomputer. A sampling rate of 4 kHz was used for the CTA signal since the highest fluctuation frequency encountered was below 500 Hz; the same rate was adequate to follow the fastest changes in the LDA frequency tracker analogue output. The available memory allowed a continuous sampling time of 4.25 s per batch of data. For the LDA data, comparison of the processed mean and rms velocities with those from the all-analogue instrumentation formerly used [12, 27] showed that ten successive batches were sufficient at each measurement position. Eight batches were found to be adequate for the CTA data. The contribution to measured rms values of a zero-to-one change in the least significant bit was always negligible.

While it was possible to process the film probe data for mean and rms velocity, this was not done because of problems with calibration drift. Evaluation of intermittency factor was independent of drift, and was carried out as follows.

The CTA bridge voltage signal was first high-pass filtered via a Kemo VBF/8 filter (48 dB/octave attenuation) to remove the mean and low frequency components. A cutoff frequency of about $\tilde{u}/\delta$ was generally satisfactory for eliminating the effect of the large-scale unsteadiness in the Görtler vortex system and the horseshoe vortices which develop from it [12]. A gain of 100 and a 5V offset were next applied by a precision amplifier, to match the signal to the input range and unipolar requirement of the A-to-D converter. Low-pass filtering at 700 Hz cutoff removed the noise before conversion. Intermittency factor was determined as the fraction of all samples for which the digitized amplitude lay outside a preset window (centered on the digital representation of the offset voltage). Window width was chosen on the basis of observations of the recorded signals, using the computer to simulate a storage oscilloscope; a typical digitized signal is il-

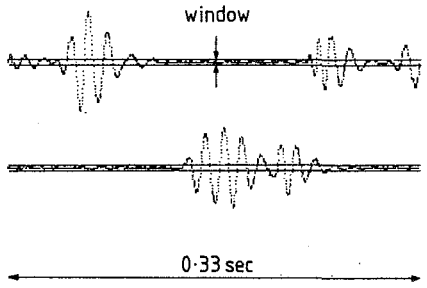

Fig. 2 Example of filtered and digitized hot-film output

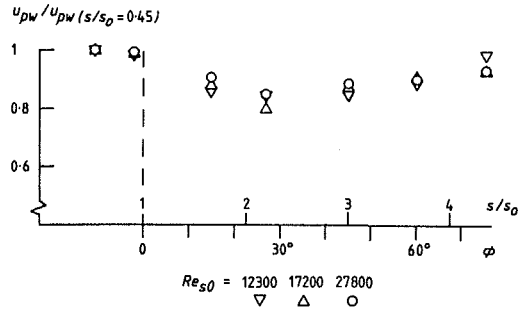

Fig. 3 Streamwise variation of potential wall velocity

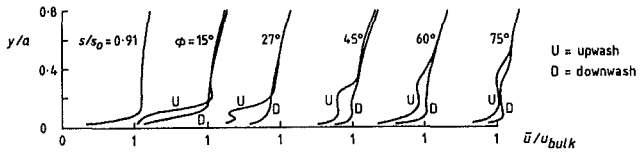

Fig. 4 Mean velocity profiles at Re_{s0} = 12300

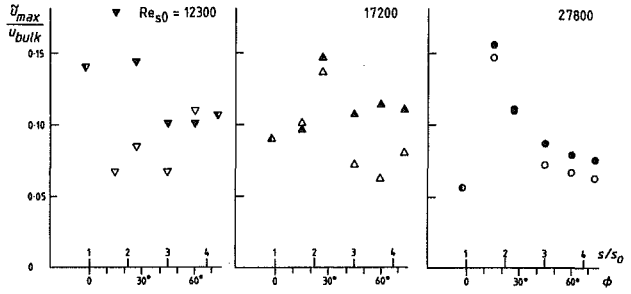

Fig. 5 Streamwise variation of maximum rms velocity; solid symbols: upwash; open symbols: downwash

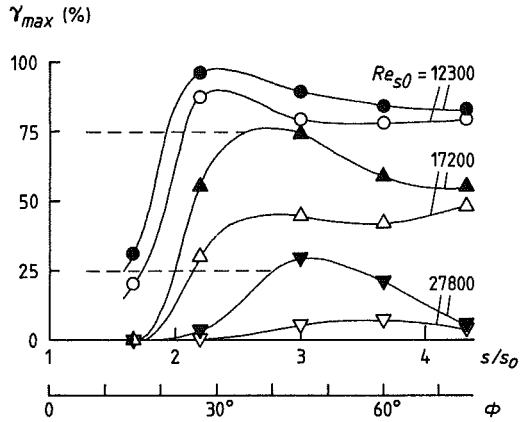

Fig. 6 Streamwise variation of maximum intermittency factor

lustrated in Fig. 2. The count of samples representing turbulent spots included the "window crossings," by requiring a number of *successive* samples to be within the window before finally classifying such samples as laminar. The software to perform this operation was similar in principle to that described in [31], and took around 3 s per data batch to calculate γ; results from the eight batches were averaged. The conversion and the software were first assessed with the aid of simulated signals produced by gating the outputs of two signal generators, one set to give a turbulentlike frequency and amplitude and the other to give a lower frequency and/or amplitude characteristic of an unsteady but laminar flow. Varying the amplitudes, frequencies, and the length and repetition rate of the "turbulent" portions of the simulated signal, the computed intermittency factor (in the range 0 to 1) was found to differ from the set value by not more than 0.01.

Flow Conditions and Procedure. Flow rates will be characterized here by the length Reynolds number Re_{s0} at the start of curvature. Transitional boundary layers were obtained on the concave wall for Re_{s0} between 12000 and 28000 approximately, with measured values of δ/r_w at the start of curvature from 0.04 to 0.06. Core flow turbulence intensities at this location ranged from 3 percent at $Re_{s0} \approx 12000$ to 1.5 percent at $Re_{s0} \approx 28000$. Streamwise pressure distribution, dictated by the duct geometry, varied little with Re_{s0} and is plotted in Fig. 3 in terms of the potential wall velocity u_{pw} (approximated from the LDA data by extrapolating to the wall the variation of $\bar{u}$ with y outside the boundary layer).

LDA and hot-film measurements were made at stations approximately 15 deg apart along the curved wall, covering the full range of flow rates at each station. Data are reported for two spanwise positions, namely "upwash" where, before the vortex system becomes unsteady, the cross-stream flow is directed away from the concave wall and there is a trough in the $\bar{u}(z)$ distribution, and "downwash" where core fluid is swept toward the wall and there is a crest (or plateau) in $\bar{u}(z)$. These two z positions refer to the vortex pair nearest to midspan; their separation (the local semiwavelength, nearly constant with s) ranged from 9–10 mm at Re_{s0} = 12300 to 6–7 mm at Re_{s0} = 27800.

Results

At Re_{s0} = 12300, the mean velocity profiles plotted in Fig. 4 show the full range of Görtler vortex development phenomena identified in earlier work [12, 27], with a severe inflection at the upwash position by ϕ = 27 deg. A large upwash-downwash difference in broad-band rms fluctuating velocity $\tilde{u}$ developed by ϕ = 15 deg but disappeared by 60 deg, as shown in Fig. 5; the value plotted is the maximum $\tilde{u}$ found by traversing normal to the wall. At downwash, the y position of the maximum in $\tilde{u}$ was generally at the closest approach to the wall (y = 2 mm for LDA), but at upwash it correlated well with the y position of the high-shear zone near the boundary layer edge. Because of the distortion in the mean velocity profiles and the subsequent unsteadiness, transition indicators based on change in shape factor or in velocity at a small, fixed distance from the wall are not applicable here.

Hot-film data should be treated with some caution at this flow rate, where there may be some overlap between boundary layer turbulence frequencies and the frequencies associated with Görtler vortex breakdown [32]. The distributions of γ are shown in Fig. 6, again representing the maximum values from a traverse across the boundary layer; as with $\tilde{u}$ the maxima in γ occurred in the high-shear zone at the upwash position. It appears that transition is initiated at the upwash position only. This is consistent with the inflected $\bar{u}$ profile. In [12, 27] and elsewhere, it is shown that this stage of vortex development is associated with rapid narrowing of the troughs in the $\bar{u}(z)$

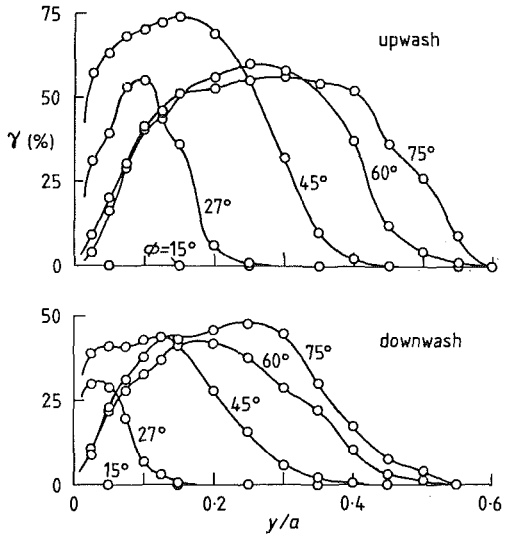

Fig. 7 Intermittency factor profiles at Re_{s0} = 17200

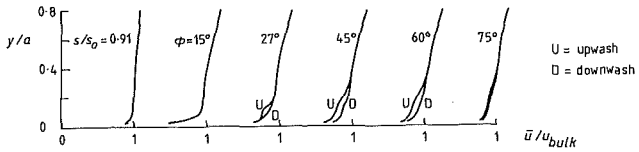

Fig. 8 Mean velocity profiles at Re_{s0} = 27800

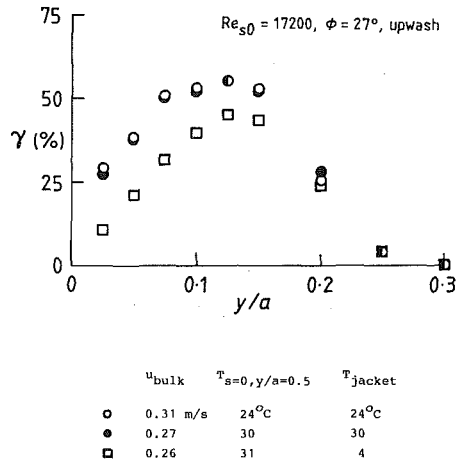

Fig. 9 Effect of heat transfer on intermittency profile

distributions; with high shear in s–y and s–z planes, vortex breakdown follows. This process may be aided here by the preceding region of adverse pressure gradient. At ϕ = 15 deg, the magnitude of the pressure gradient and the upwash profile shape near the wall suggest a possible laminar separation, but the measurements cannot confirm the existence of a shallow bubble. The decrease in γ from $\phi \approx 50$ deg suggests that a turbulent boundary layer cannot be sustained at this Reynolds number in the favorable pressure gradient. There is considerable uncertainty in deriving the pressure gradient from the core flow velocities, owing to the interaction of the vortices and the inviscid flow, but an estimate of the mean K for $\phi > 30$ deg at this Re_{s0} is $\sim 5 \times 10^{-6}$, exceeding the Launder relaminarization criterion [33] of 2.5×10^{-6}.

A more advanced, but still incomplete, transition is evident at Re_{s0} = 17200. Profiles of $\bar{u}$ were similar to those at Re_{s0} = 12300 but progressed more rapidly through the phases of vortex amplification. One result of this was a greater maximum $\tilde{u}$ at the nominal downwash position, seen in Fig. 5, attributed to the spanwise oscillation of the vortex system. A steeper rise in γ occurred, to ~75 percent at upwash but only 45 percent at downwash (Fig. 6). Profiles of intermittency are illustrated in Fig. 7, further demonstrating the spanwise variation. Where an outer-edge zone of very high shear exists in the upwash $\bar{u}$ profile, noticeable only at the ϕ = 27 deg station for this Re_{s0}, the peak in the γ profile coincides with it. The zero values of γ outside the boundary layer indicate that the core-flow fluctuations are all at low frequencies, and in the curved section of the duct are probably associated partly with the unsteady motion of the vortex system. In the region of accelerating flow, with K estimated as $\sim 3 \times 10^{-6}$, the maximum γ approached ~50 percent for both spanwise positions as a spanwise difference developed in the maximum $\tilde{u}$ (the maximum now occurring close to the wall at both positions).

Completed transition is represented by the curves for Re_{s0} = 27800 in Figs. 5 and 6. The $\bar{u}$ profiles in Fig. 8 show much less spanwise variation, as do the distributions of maximum $\tilde{u}$ (Fig. 5). Although a slight lag in transition still occurs at the nominal downwash position, a rapid rise in maximum γ to ~80 percent is seen in Fig. 6, with little attenuation in the favorable pressure gradient which now has a K value estimated as $\sim 1 \times 10^{-6}$. (With the present hardware/software for intermittency evaluation, any computed γ of ~80 percent or more represents a fully turbulent flow.)

The foregoing results all refer to adiabatic flow. However, the effect of heat transfer has been studied briefly by installing a cooling jacket outside the outer wall of the curved and upstream straight sections of the duct. With a stirred ice-water mixture in the jacket and a slightly heated working fluid, a jacket-to-mainstream temperature ratio of 0.91 was obtained, unrepresentative of gas turbine conditions but with the heat flux in the correct direction. The γ profiles in Fig. 9 show, first, that a reduced flow rate, to compensate for the reduced viscosity of the core fluid and maintain a constant Reynolds number Re_{s0}, yields an almost identical intermittency profile in adiabatic flow to that obtained with room-temperature core fluid. Second, the intermittency factor is lower with heat transfer than without, especially near the wall (where the cooler, more viscous fluid may play a part in delaying the spread of turbulence). Prior to the adaptation of the rig for a more extensive study of heat transfer effects, using a liquid crystal sheet plus heater element composite, a plain liquid crystal sheet was mounted inside the concave wall while the cooling jacket was in use. Preliminary observations have shown clear reductions in wall temperature in the upwash zones at flow rates where transition is slow and incomplete, as at Re_{s0} = 12300, particularly in the adverse pressure gradient region from ϕ = 10 to 20 deg.

Discussion

In view of the highly three-dimensional nature of a boundary-layer flow in which Görtler vortex amplification has gone beyond the linear (small disturbance) stage [27, 32], it is not certain that Re_θ or even G_θ are appropriate parameters for a transition criterion. Nevertheless, it is of interest to note their measured values in the present experiments and compare with existing transition criteria. The inaccuracy in estimating θ from the small number of data points in the thin boundary layers at downwash positions must be borne in mind, as must the fact that the distorted velocity profiles will not be predicted by any two-dimensional boundary layer model.

At the streamwise position where Fig. 6 suggests that the measured maximum γ first becomes nonzero, interpolated values of Re_θ at upwash were ~250 for Re_{s0} = 12300 and

~ 270 for $Re_{s0} = 17200$. Core flow fluctuation intensities at these positions were about 2.0 and 1.3 percent, respectively. Perhaps fortuitously, these compare well with the predictions of $Re_{\theta s}$ in [16], for flat surfaces with similar average turbulence levels (prior to transition) and maximum adverse pressure gradient. However, in view of the contribution of global vortex unsteadiness to the local fluctuation intensities, it might be more relevant to compare with flat-surface results at a lower turbulence level; predicted $Re_{\theta s}$ could then easily exceed the present measurements. Corresponding upwash values of G_θ were around 22, some three times those represented by equation (2). (There remains the problem of reconciling definitions of transition onset based on different measurement techniques.) At $Re_{s0} = 17200$, it appears that the downwash values of γ do not initially lag far behind those at upwash, with downwash Re_θ well below 200; this may be attributed to the effect of adjacent upwash zones when spanwise meandering of the vortices occurs. For $Re_{s0} = 27800$, γ was already 25 percent at $Re_\theta \approx 110$–150 and $G_\theta \approx 4$–7; predicted $Re_{\theta s}$ under similar conditions on a flat surface is around 300 [16], and $G_{\theta s}$ from equation (2) is about 7.5. However, it seems unlikely that Görtler vortices have much effect at this flow rate, considering the early transition location ($\phi \approx 15$ deg) and the comparative lack of distortion in the $\bar{u}$ profiles.

Transition length Reynolds numbers $Re_{s(\gamma=75\%)} - Re_{s(\gamma=25\%)}$ are between 8500 and 9500 for all the cases depicted in Fig. 6, compared with 21,000–28,000 given by the Dhawan and Narasimha [23] relationship. Where a trend with transition onset Reynolds number can be detected, it is in the opposite sense to that of [23]. There are insufficient data to compare the shapes of the γ versus s curves with the proposed exponential relationships.

Finally, it should be emphasized that the present results refer to a region of the span affected by one particular vortex pair, originating from a screen-generated disturbance which will be different in strength and character from those in a gas turbine (where the disturbance source might be the blade stagnation region, or the combustors). If those initial disturbances which are in the appropriate wavelength range to be amplified by concave curvature are not of uniform strength, then vortex pairs at differing stages of amplification can coexist at the same streamwise station, as measured in [27]. Hence, if flow conditions are such that Görtler instability promotes transition at some upwash zones, the boundary layer may remain laminar for some distance at other upwash zones. With an unknown distribution of small disturbances in the oncoming flow, it would be impossible to predict where, across the span, vortex breakdown might first occur. Stability theories suggest a vortex pair spacing of a few millimeters only under gas turbine conditions, so that upwash-downwash differences can almost certainly be handled within a two-dimensional boundary layer prediction by a suitable spanwise-averaged transition model; however, the validity of such a procedure is less certain in connection with larger-scale nonuniformity in vortex amplification.

Conclusions

Under the combined influence of concave surface curvature, moderate turbulence level, and varying pressure gradient, a Görtler vortex system has been found to cause significant spanwise differences in the streamwise variation of fluctuation intensity and intermittency factor. At Reynolds numbers low enough to allow considerable nonlinear vortex amplification prior to transition, the intermittency measurements showed transition to begin sooner and progress faster at an upwash location; measured values of Re_θ at transition onset in the upwash location were of similar magnitude to accepted flat-surface values, but upwash values of G_θ greatly exceeded the range of Forest's correlation. At higher Reynolds numbers where transition began soon after the start of curvature, without large distortion in mean velocity profile, little spanwise variation occurred in fluctuation intensity or intermittency.

A velocity gradient factor K greater than the Launder relaminarization value appeared to prevent the completion of transition. This, and the adverse pressure gradient at the beginning of curvature, have complicated interpretation of the results; further experiments are necessary with independent control over pressure gradient.

A very limited test with heat transfer indicated that wall cooling delayed the progress of transition.

Acknowledgments

J. S. is funded by a Science and Engineering Research Council (SERC) Research Grant and G. L. holds a SERC Research Studentship.

References

1 Graham, R. W., "Fundamental Mechanisms That Influence the Estimate of Heat Transfer to Gas Turbine Blades," ASME Paper No. 79-HT-43.

2 Han, L. S., Chait, A., Boyee, W. F., and Rapp, J. R., "Heat Transfer on Three Turbine Airfoils," AFWAL-TR-82-2124 (AD-A128762), Jan. 1983; Han, L. S., and Cox, W. R., "A Visual Study of Turbine Blade Pressure-Side Boundary Layers," ASME JOURNAL OF ENGINEERING FOR POWER, Vol. 105, 1983, pp. 47–52.

3 Daniels, L. C., and Browne, W. B., "Calculation of Heat Transfer Rates to Gas Turbine Blades," *International Journal of Heat and Mass Transfer*, Vol. 24, 1981, pp. 871–879.

4 Nicholson, J. H., Forest, A. E., Oldfield, M. L. G., and Schultz, D. L., "Heat Transfer Optimized Rotor Blades—an Experimental Study Using Transient Techniques," ASME JOURNAL OF ENGINEERING FOR GAS TURBINES AND POWER, Vol. 106, 1984, pp. 173–182.

5 So, R. M. C., Edelfelt, I. H., Elovic, E., and Kercher, D. M., "A Two-Dimensional Boundary-Layer Program for Turbine Airfoil Heat Transfer Calculation," ASME Paper No. 82-GT-93.

6 Consigny, H., and Richards, B. E., "Short Duration Measurements of Heat-Transfer Rate to a Gas Turbine Rotor Blade," ASME JOURNAL OF ENGINEERING FOR POWER, Vol. 104, 1982, pp. 542–551.

7 Metzger, D. E., and Mayle, R. E., "Heat Transfer—Gas Turbine Engines," *Mechanical Engineering*, Vol. 105, No. 6, 1983, pp. 144–52.

8 Nealy, D. A., Mihelc, M. S., Hylton, L. D., and Gladden, H. J., "Measurements of Heat Transfer Distribution Over the Surfaces of Highly Loaded Turbine Nozzle Guide Vanes," ASME JOURNAL OF ENGINEERING FOR GAS TURBINES AND POWER, Vol. 106, 1984, pp. 149–158.

9 Gibbings, J. C., Department of Mechanical Engineering, Liverpool University, private communications, 1984.

10 Crawford, M. E., and Kays, W. M., "STANS—a Program for Numerical Computation of Two-Dimensional Internal and External Boundary Layer Flows," NASA CR-2742, 1976.

11 Spalding, D. B., "GENMIX: a General Computer Program for Two-Dimensional Parabolic Phenomena," Pergamon, Oxford, 1977.

12 Sabzvari, J., and Crane, R. I., "Effect of Görtler Vortices on Transitional Boundary Layers," *International Symposium on Three-Dimensional Flow Phenomena in Fluid Machinery*, ASME Winter Annual Meeting, Miami, FL, 1985.

13 Wang, J. H., Jen, H. F., and Hartel, E. O., "Airfoil Heat Transfer Calculation Using a Low Reynolds Number Version of a Two-Equation Turbulence Model," ASME JOURNAL OF ENGINEERING FOR GAS TURBINES AND POWER, Vol. 107, 1985, pp. 60–67.

14 Seyb, N., "The Role of Boundary Layers in Axial Flow Turbomachines and the Prediction of Their Effects," in: *Boundary Layer Effects in Turbomachinery*, AGARD-AG-164, 1972, p. 241.

15 Gaugler, R. E., "Some Modifications to, and Operational Experiences With, the Two-Dimensional, Finite-Difference, Boundary Layer Code, STAN5," ASME Paper No. 81-GT-89.

16 Abu-Ghannam, B. J., and Shaw, R., "Natural Transition of Boundary Layers—the Effects of Turbulence, Pressure Gradient and Flow History," *Journal of Mechanical Engineering Science*, Vol. 22, 1980, pp. 213–228.

17 Blair, M. F., "Influence of Free-Stream Turbulence on Boundary Layer Transition in Favorable Pressure Gradients," ASME JOURNAL OF ENGINEERING FOR POWER, Vol. 104, 1982, pp. 743–750.

18 Van Driest, E. R., and Blumer, C. B., "Boundary Layer Transition: Freestream Turbulence and Pressure Gradient Effects," *AIAA Journal*, Vol. 1, 1963, pp. 1303–1306.

19 Roberts, G., and Brown, A., "Boundary Layer Transition Regions on Turbine Blade Suction Surfaces," ASME Paper No. 84-GT-284.

20 Forest, A. E., "Engineering Predictions of Transitional Boundary Layers," AGARD-CP-229, 1977, pp. 22.1–22.19.

21 Brown, A., and Martin, B. W., "Flow Transition Phenomena and Heat Transfer Over the Pressure Surfaces of Gas Turbine Blades," ASME JOURNAL OF ENGINEERING FOR POWER, Vol. 104, 1982, pp. 360–367.

22 Kemp, A., "Boundary Layer Development on Turbine Blades in the Presence of Görtler Vorticity," Ph.D. thesis, Cambridge University, 1979.

23 Dhawan, S., and Narasimha, R., "Some Properties of Boundary Layer Flow During Transition From Laminar to Turbulent Motion," *Journal of Fluid Mechanics*, Vol. 3, 1958, pp. 418–436.

24 Schlichting, H., *Boundary Layer Theory*, 4th ed., McGraw-Hill, New York, 1960.

25 Lees, L., "The Stability of the Laminar Boundary Layer in a Compressible Flow," NACA Rep. 876, 1947.

26 Gaugler, R. E., "A Review and Analysis of Boundary Layer Transition Data for Turbine Application," ASME Paper No. 85-GT-83.

27 Crane, R. I., and Sabzvari, J., "Laser-Doppler Measurements of Görtler Vortices in Laminar and Low-Reynolds-Number Turbulent Boundary Layers," *Proc. Int. Symp. on Application of Laser Doppler Anemometry to Fluid Mechanics*, Lisbon, June 1982; also in: *Laser Anemometry in Fluid Mechanics*, R. J. Adrian et al., eds., LADOAN-Instituto Superior Técnico, Lisbon, 1984, pp. 19–35.

28 Winoto, S. H., and Crane, R. I., "Vortex Structure in Laminar Boundary Layers on a Concave Wall," *International Journal of Heat and Fluid Flow*, Vol. 2, 1980, pp. 221–231.

29 Sabzvari, J., "Instability in Laminar and Transitional Boundary Layers on Concave Surfaces," Ph.D. thesis, London University, Jan. 1984.

30 Kline, S. J., and McClintock, F. A., "Describing Uncertainties in Single Sample Experiments," *Mechanical Engineering*, Vol. 75, 1953, pp. 3–8.

31 Shaw, R., Hardcastle, J. A., et al., "Recording and Analysis of Fluctuating Signals Using a Microcomputer," *Int. Conf. on the Use of Micros in Fluid Engineering*, London, June 1983, Paper No. E2.

32 Aihara, Y., and Koyama, H., "Secondary Instability of Görtler Vortices: Formation of Structure," *Transactions of the Japan Society for Aeronautical and Space Sciences*, Vol. 24, No. 64, 1981, pp. 78–94.

33 Launder, B. E., "Laminarization of the Turbulent Boundary Layer in a Severe Acceleration," ASME *Journal of Applied Mechanics*, Vol. 31, 1964, pp. 707–708.

P. Pucher

R. Göhl

MTU Motoren- und Turbinen-Union
München GmbH,
Munich, Federal Republic of Germany

Experimental Investigation of Boundary Layer Separation With Heated Thin-Film Sensors

The heated thin-film method was adapted to meet the requirements of investigations on boundary layer behavior in a turbine rig. Special multisensor probes of vaporized nickel on a polyimide foil were developed and applied to the vanes. Basic experiments with an airfoil in a free stream were carried out and a reliable interpretation of the thin-film results was found by comparison with pressure distribution, flow visualization, and laser measurements. It can be shown that this measuring device is a suitable method for the investigation of separation bubbles and boundary layer transition.

Introduction

In developing a low-pressure turbine with a design point at low Reynolds numbers, it was considered to be of importance to have available a method of measuring the boundary layer to ascertain whether it is laminar, turbulent, separated, or attached. For this purpose special multielement thin-film sensors were developed and used in a full turbine rig test.

Preliminary trials were carried out for testing the sensors and gaining sufficient experience to permit proper interpretation of the signals. For these trials, an airfoil section fitted with thin-film sensors, but also provided with pressure taps, was mounted in a free stream.

This paper describes an investigation carried out in the development of this technique.

Experimental Setup

The thin-film sensors used consist of a nickel film vapor-deposited onto a polyimide foil as shown in Fig. 1. This foil is glued to the airfoil and turbine blades. These thin films are suitable for temperatures up to 250°C.

The thickness of the polyimide film is 0.1 mm, whereas the thickness of the nickel film is 0.3 μm at the actual sensor and 4 μm at the following conducting paths.

The foil was moved around the leading edge to the opposite side of the airfoil. Based on the present experiments, it may be assumed that the film, local heating of the surface at the sensor, or the brazed joints do not affect the boundary layer enough to alter its behavior with regard to transition and separation.

The airfoil in question had a NACA 0018 profile and chord length of 51 mm (see Fig. 2). The first sensor was positioned precisely at the leading edge, with the remaining sensors arranged at intervals of 2.5 mm. They were connected via coaxial cables approximately 20 m in length and a multiway rotary switch to a single-channel constant-temperature anemometer.

The principle involved is based on the relationship between the rate of heat transfer of the heated sensor in the colder fluid and the wall shear stress in the form [1]

$$\frac{I^2 \cdot R}{\Delta T} = a \cdot (\rho \tau_w)^{1/3} + b$$

where I is the current, R is the resistance of the sensor, ΔT is the temperature difference in relation to the fluid, ρ is the air density, τ_w is the wall shear stress, and a and b are constants. Here, a is dependent on the geometry of the sensor and on the properties of the fluid; the constant b represents the heat of the sensor lost to the substrate. Normally, this heat flow into the airfoil or blade is appreciably greater than the amount of heat lost by the sensor directly to the fluid. Hence, in order to ascertain the real wall shear stress, a and b have to be determined by a complicated calibration procedure [1–4].

In the present investigation quantitative determination is not required; it is demonstrated that the boundary layer condition can be recognized by comparing the signals.

The results of the thin-film measurements are evaluated separately according to d-c and a-c voltage. Here, the d-c voltage share E corresponds to the time-averaged heat transfer, whereas the a-c voltage shear e describes the fluctuating part of the heat transfer. In this case, consideration is given only to that part which is dissipated to the fluid by convection. The subscript 0 describes the proportion dissipated without flow. Effects stemming from small manufacturing inaccuracies with the sensors can be suppressed by normalizing with E_0. The changing of the thin-film signals along the surface is compared with the pressure distribution.

In another series of tests, the velocity and turbulence distribution in the immediate vicinity of the airfoil surface were measured using a laser dual-focus anemometer. The smallest distance within the detective capability of the laser

Contributed by the Gas Turbine Division of THE AMERICAN SOCIETY OF MECHANICAL ENGINEERS and presented at the 31st International Gas Turbine Conference and Exhibit, Düsseldorf, Federal Republic of Germany, June 8–12, 1986. Manuscript received at ASME Headquarters March 7, 1986. Paper No. 86-GT-254.

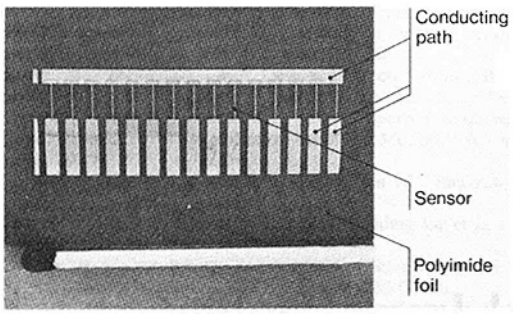

Fig. 1 Thin-film; multi-sensor array

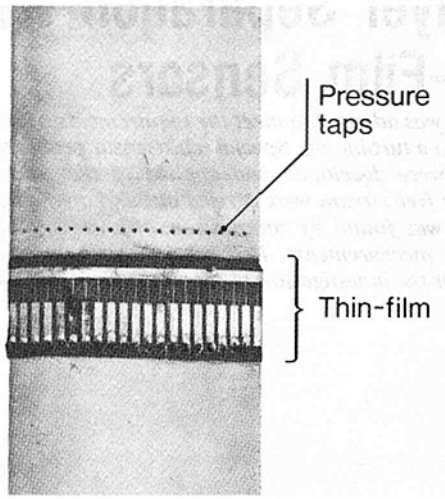

Fig. 2 Thin-film instrumented airfoil

was 0.3 mm; the greatest distance at which measurements were made was 2 mm from the surface.

The airfoil was mounted in a free stream, 100 mm behind the nozzle outlet. The nozzle was of circular configuration with a diameter of 100 mm. Different flow fields around the airfoil were generated by varying the incidence; the Reynolds number was altered in the range $85{,}000 \leq \mathrm{Re} \leq 230{,}000$ by varying the airflow velocity, causing the Mach number to vary between 0.09 and 0.27.

The degree of turbulence in the free stream was about 2 percent at all velocities. Oil was injected into the free stream for visualization of the flow at the surface of the airfoil under different operating conditions.

This paper highlights some of the results obtained in this investigation, and gives an interpretation of the thin-film signals.

Test Results

Pressure Side. Initially, the airfoil was set to give an incidence angle of -12 deg, i.e. with the thin film and pressure taps at the pressure side.

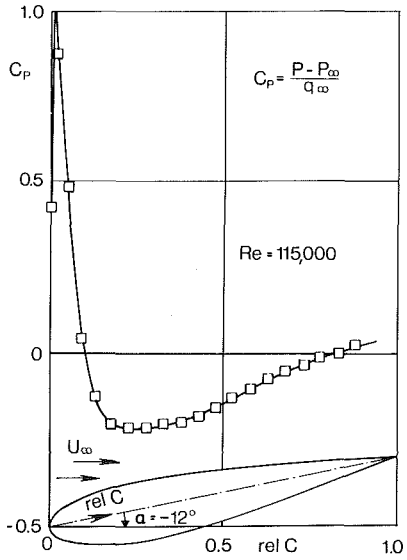

Fig. 3 Pressure distribution on the pressure side of the airfoil, $\alpha = -12$ deg

The pressure distribution at the surface of the airfoil in the direction of flow is shown in Fig. 3. As far as 25 percent of the airfoil chord – starting from the leading edge – the boundary layer is accelerated, after which gradual deceleration sets in.

The course of the relevant thin-film measurement signals is shown in Fig. 4. Up to 25 percent chord the mean signal $E - E_0$ increases, and the fluctuating part decreases somewhat.

This development is consistent with an accelerated boundary layer in which the velocity gradient, and consequently the time-averaged heat transfer, increases at the wall. The boundary layer apparently reacts to the relatively weak deceleration by a rapid decrease of the velocity gradient at the wall, as indicated by the marked decrease in the time-averaged heat transfer.

Immediately downstream of the leading edge, the fluctuating part of the signal first decreases slightly. The first sensors still detect the turbulence in the flow, which then becomes quenched in the developing laminar boundary layer. The flucutation increases in the decelerated section of the boundary layer, but only insignificantly. There is no sign of a transition or even separation of the boundary layer.

A boundary layer calculation, based on the measured pressure distribution, showed that the boundary layer changes from laminar to turbulent at 58 percent chord. The point at which this occurs is shown in Fig. 4. This prediction is not confirmed by the measurements. There are no results in this test downstream of 70 percent chord.

Figure 5 shows signals from individual sensors in the time domain. In accordance with expectations, there is no great difference between the signals of the first and last sensors. The representation is intended rather to serve as a comparison with the findings for the suction side.

Nomenclature

a = constant
b = constant
c = chord length
C_p = pressure coefficient $= (p - p_\infty)/q_\infty$
e = rms thin-film signal (bridge voltage output)
E = time-averaged thin-film signal
I = current through sensor
p = local static pressure
q = dynamic head
rel c = relative chord
Re = Reynolds number $= U_\infty c/\nu$
R = resistance of thin-film sensor
ΔT = temperature difference between thin-film heated element and local ambient
Tu = turbulence intensity
u' = velocity fluctuation
u = velocity in the shear layer
U = main flow velocity
y = distance normal to the wall
α = incidence angle
ν = kinematic viscosity
ρ = fluid density
τ = shear stress

Subscripts

0 = at zero flow conditions
∞ = free-stream conditions
w = wall

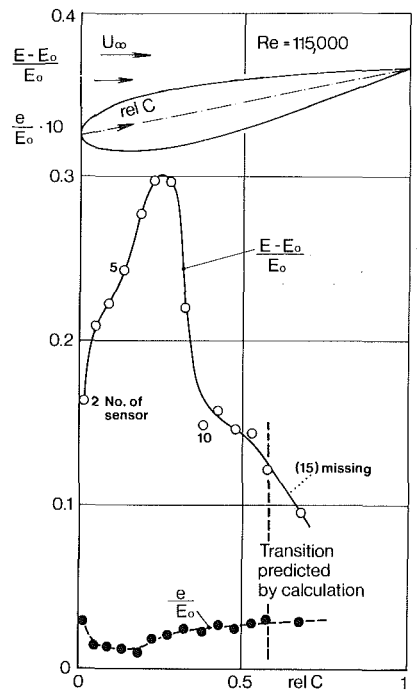

Fig. 4 Thin-film signals from the pressure side of the airfoil, $\alpha = -12$ deg

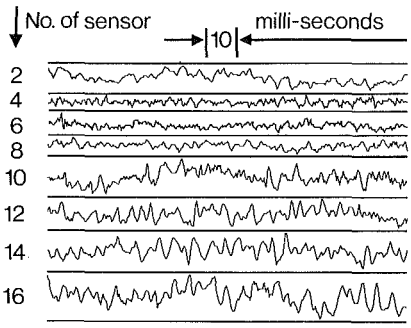

Fig. 5 Unsteady thin-film signals from the pressure side; $\alpha = -12$ deg, Re = 115,000

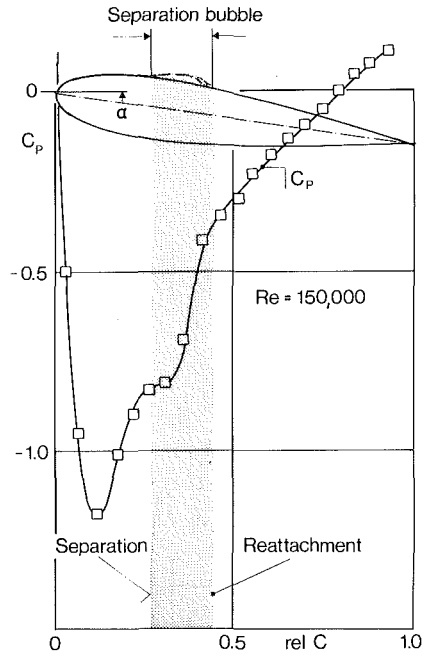

Fig. 6 Pressure distribution on the suction side of the airfoil at $\alpha = 8$ deg

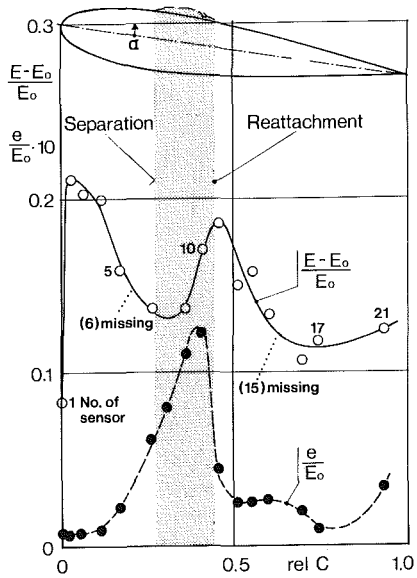

Fig. 7 Thin-film signals from the suction side of the airfoil at $\alpha = 8$ deg

Suction Side With Flow Separation and Reattachment. The results of a test in which the thin film was at the suction side are represented in Figs. 6 and 7. The pressure distribution (Fig. 6) reveals a strong acceleration up to 10 percent chord, after which strong deceleration sets in. The boundary layer separates at approximately 26 percent of the airfoil chord, becoming reattached at around 43 percent. Flow visualization clearly reveals a separation bubble, whose confines are also plotted in Fig. 6.

The thin-film signals from this test are plotted in Fig. 7. Similar to the pressure side measurements, there again occurs an increase in the time-averaged heat transfer, as expressed by $E-E_0$, in the region of accelerated flow. The heat transfer deteriorates in the separation bubble, but is not as low as at the stagnation point. In the region in which the boundary layer becomes reattached to the surface, the heat transfer reaches its maximum, immediately falling off again. Interestingly, the fluctuating content has a clear maximum immediately in front of the reattachment point. The investigations generally demonstrated that this maximum is typical of boundary layer transition, but not of reattachment. The maximum also occurs with separations, where transition of the boundary layer occurs without reattachment. But it must be said that it is much less pronounced in such cases. In marginal cases it is therefore not possible to recognize definitely from the thin-film signals alone whether the boundary layer remains separated or becomes reattached.

These conclusions are in line with Hodson [5] whose results show that the level of fluctuations within the transitional boundary layer is greater than in fully turbulent ones and with Bellhouse and Schultz [2] whose results show a pronounced maximum of mean heat transfer after separation only in reattached boundary layers (see also [1]).

Figure 8 shows how the signals change along the airfoil surface. Whereas there is hardly any difference between the signals of the first sensors and those at the pressure side; from sensor 7 on, there is an increase in the fluctuations, initially in the low frequency range, followed by a marked increase in the

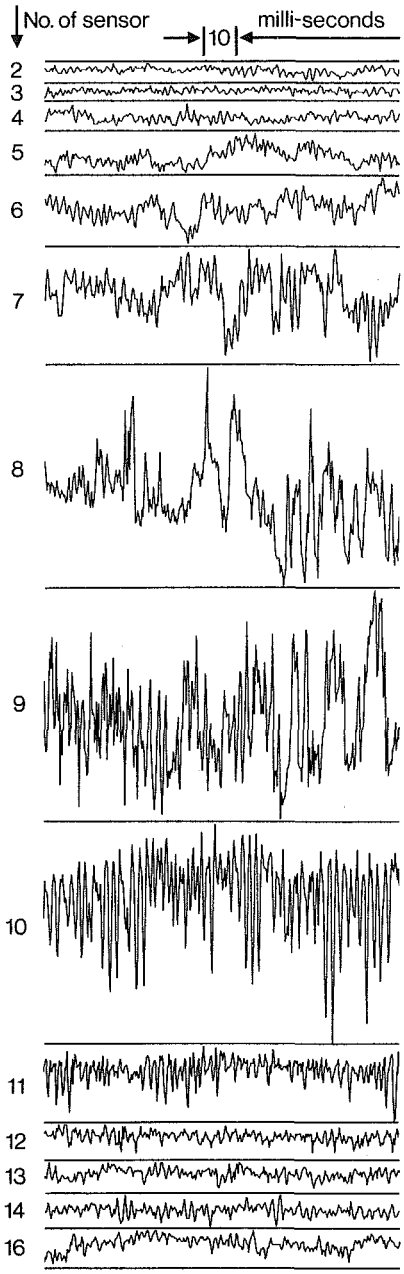

Fig. 8 Unsteady thin-film signals of suction side at $\alpha = 8$ deg, Re = 190,000

amplitude of the high frequency content as well. Sensors 9 and 10 exhibit the highest deflections, where the deflections of sensor 9 clearly always occur from a lower to a higher rate of heat transfer; whereas the situation is reversed with sensor 10. This leads to the assumption that the fluctuation is at its greatest between sensors 9 and 10. The behavior of the e signals as shown in Fig. 7 agrees with this statement. However, it can be seen the maximum of the mean heat transfer lies at sensor 11.

The finding signifies that the point between sensors 9 and 10 is that which is nearest to the boundary layer transition point, and accordingly is where the excessive turbulence makes itself most felt. However, reattachment does not occur until passing sensor 11.

It is surprising that the signal of the sensors lying donwstream of the transition point, i.e., which are in the turbulent boundary layer region (such as No. 14), do not differ appreciably with regard to their fluctuations from those in the region of laminar flow (sensor 4).

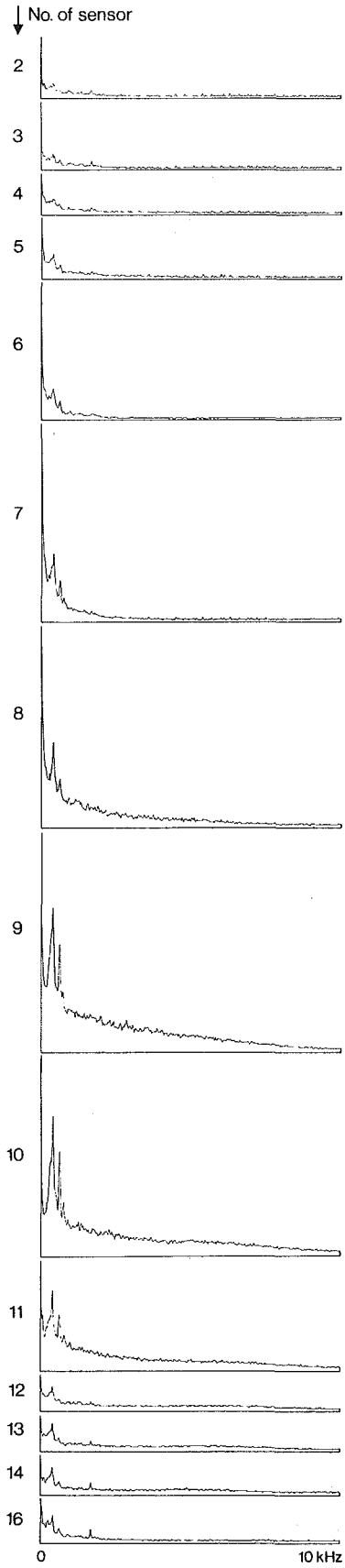

Fig. 9 Thin-film signals in the frequency domain, suction side, $\alpha = 8$ deg, Re = 190,000

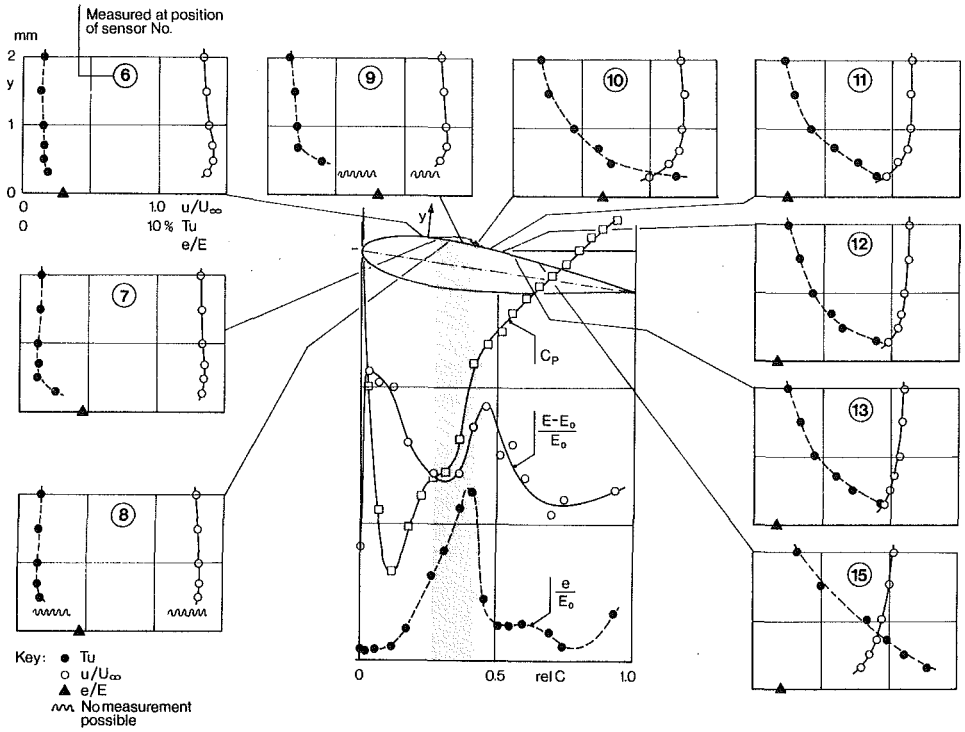

Fig. 10 Laser measurements of velocity and turbulence distribution in the boundary layer; $\alpha = 8$ deg, Re = 150,000

In Fig. 4, the value of the fluctuation e of sensor 14 is indeed greater than that of sensor 4 (these are mean values formed over a long period, whereas only a brief period is represented in Fig. 8), but in comparison with the intervening clearly expressed maximum of e in Fig. 7, it may be said that the fluctuations are of the same magnitude. The signals are represented in the frequency range up to 10 kHz in Fig. 9. The first sensors, e.g., No. 2 and 4, exhibit very slight fluctuations. At sensor 7 the low-frequency share has clearly increased in the frequency range up to 1 kHz. With sensors 9 and 10 the marked increase is exhibited throughout the whole range.

Under similar conditions and with an incidence angle of 8 deg and a Reynolds number of 150,000, measurements were made with the laser dual-focus anemometer. But, for reasons of time, measurements were not made at all locations. The velocity and turbulence profiles normal to the surface are shown in Fig. 10, identifying the position of the sensor. For sake of comparison, in addition to the turbulence intensity Tu measured in the flow, a degree of fluctuation (e/E) has been formed from the thin-film measurement.

Measurement at the level of sensors 8 and 9 at a distance of 0.3 mm from the wall was not possible, because no definite direction of flow could be identified here. All results shown already stemmed from the decelerated part of the boundary layer. With sensor 6 the increase in the fluctuation has already started at the wall, whereas the turbulence at about 1.6 percent at just 0.3 mm from the wall is very low. From sensor 7 the increasing turbulence spreads slowly from the wall also transverse to the direction of flow. A turbulence intensity of 12.7 percent at a distance of 0.3 mm from the wall was measured at sensor 15.

A rapid increase in the fluctuation e/E, which is always higher than the turbulence in the flow, as far as sensor 9 can be read from the fluctuation in the thin-film measurements. The picture reverses at sensor 10; while the fluctuation at the wall decreases again, the turbulence in the flow at a distance of 0.3 mm has already reached 12 percent. This is interpreted to be the place at which, or in whose immediate vicinity, transition

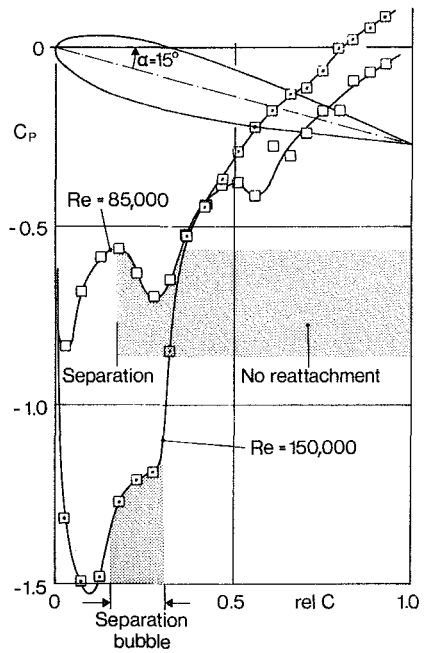

Fig. 11 Pressure distribution on the suction side of the airfoil at incidence $\alpha = 15$ deg at different Reynolds numbers

occurs. Subsequently, the boundary layer turbulence again decreases somewhat, only to rise again as it progresses.

According to these results, the separation bubble must start somewhere around sensor 7; it is at least 0.3 mm thick at sensors 8 and 9 (but not thicker than 0.5 mm), and it disappears again at around sensor 10. This agrees with the other results.

The circumstance that very low fluctuations were measured with the thin film downsteam of the separation bubble, where the boundary layer is turbulent, can be interpreted with the air of the laser measurements at the boundary layer. It appears that the turbulence in the boundary layer certainly in-

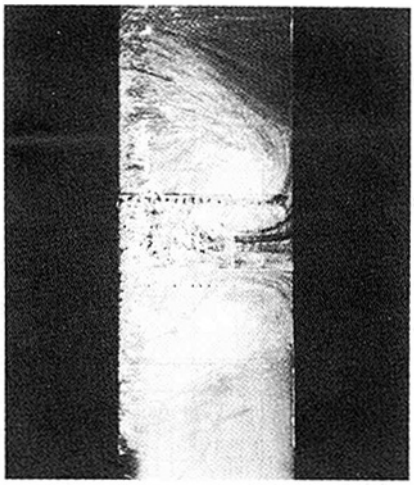

Fig. 12 Flow visualization on the airfoil with separation on the suction side; $\alpha = 15$ deg, Re = 85,000

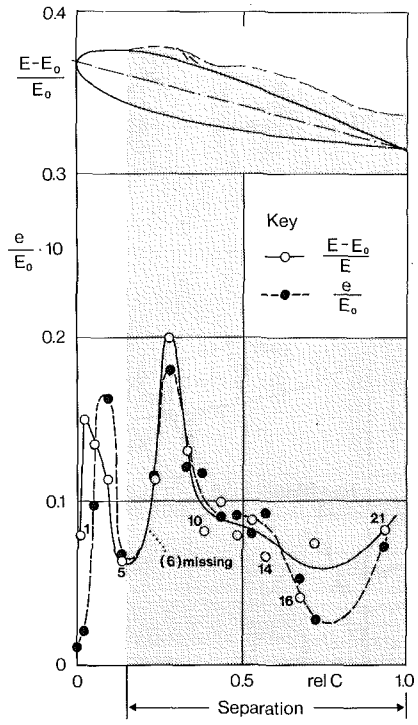

Fig. 13 Thin-film signals from the suction side at $\alpha = 15$ deg, Re = 85,000

creases in the direction of flow, but at the same time a viscous sublayer has already formed, which strongly quenches the turbulence so that it is hardly discernible at the wall itself.

Suction Side With Total Laminar Separation. The results of a test with total flow separation are shown in Figs. 11–14. The incidence of the airfoil was 15 deg. Figure 11 shows a comparison of two pressure distributions for this incidence angle for Reynolds numbers Re = 85,000 and 150,000. While the pressure distribution at the higher Reynolds number shows behavior typical of a boundary layer with a separation bubble and reattachment, the course of the results at Re = 85,000 indicates a boundary layer with total separation, i.e., without reattachment. This interpretation has been confirmed by the flow visualization (see Fig. 12), which shows the total separation. The thin-film signals of the two tests are given in Figs. 13 and 14.

The comparison shows that what was previously taken to be

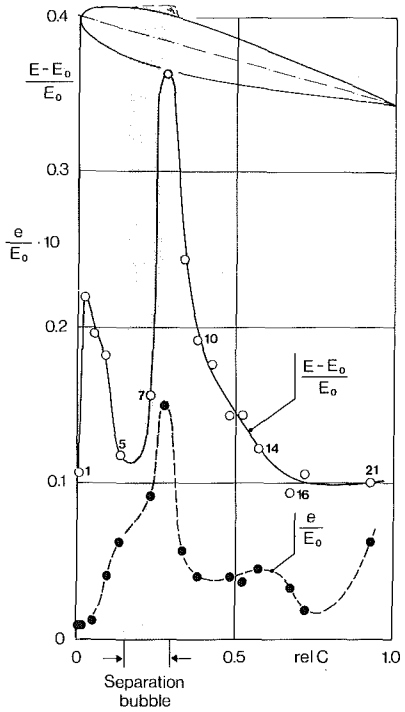

Fig. 14 Thin-film signals from the suction side at $\alpha = 15$ deg, Re = 150,000

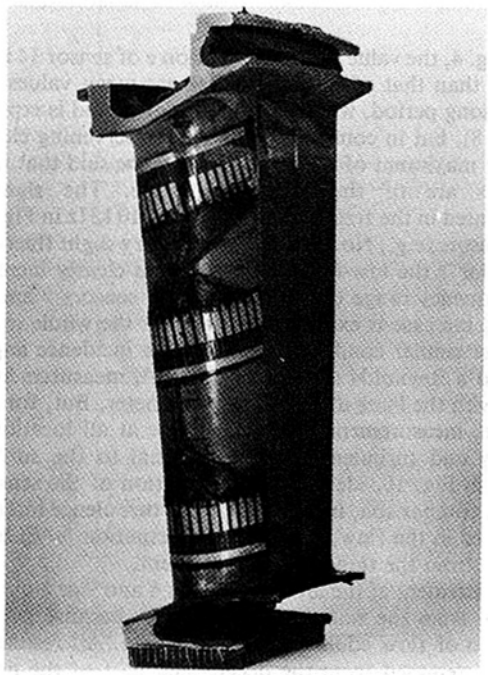

Fig. 15 Thin-film instrumented vane (suction side) of a turbine rig

typical of the signal behavior for separation and reattachment also applies qualitatively to complete separation. Thus it is not possible to recognize reattachment through simple, unmistakable characteristics.

This comparison of results, however, enables the other characteristics distinguishing separation to be established. Four main differences can be found:

- In the range of separation, especially downstream of a relative chord of 30 percent, a remarkable scatter of all results occurs.
- The time-averaged heat transfer increases – as ex-

pected – with the Reynolds number (flow velocity); however the increase at the second maximum, which is supposed to be the point of reattachment, is more than proportional.

- The fluctuation has its maximum at the level of the point of reattachment. At the lower Reynolds number there is another maximum of fluctuation upstream of the separation bubble. This second maximum is not yet fully understood.
- The fluctuation is lower in the case of the higher Reynolds number (reattached flow). This decrease appears very clearly in the range of 40 to 80 percent chord.

From the test results shown above and from similar tests, it can be concluded that these differences can be considered to be typical characteristics of total boundary layer separation. However these effects are not sufficiently clear to determine precisely in every situation if the boundary layer is fully separated or reattached.

For the sake of completeness, it should be mentioned that there are transition conditions between the two Reynolds numbers illustrated, where none of the three methods used was capable of determining with certainty whether the boundary layer had reattached. A great deal more experimental experience is called for here.

Application of Thin-Film Measurement in Rig Test

The thin-film measuring technique was applied several times in a turbine rig test. The sensors were glued on the vanes in a section in the middle of the annulus, as well as in one section each close to the hub and casing (see Fig. 15). With this technique rig tests could be performed successfully which provided information about boundary layer development on the vanes. These test results will be presented by Hourmouziadis et al. [6].

Conclusions

Thin-film sensors have been developed which are suitable for rig tests. Preliminary trials were performed with an airfoil in a free stream to test whether this technique is a reliable method of determining the boundary layer condition.

The experiments were carried out essentially for boundary layer transition in connection with a separation bubble. For boundary layer transition without separation (natural transition) or total flow separation, an insufficient number of tests were performed. Therefore the presented test results do not cover these cases.

The thin-film signals should be evaluated separately according to time-averaged heat transfer and fluctuating part, because only the information provided in both cases will complete the picture of the boundary layer. There is not much sense in using just a single probe or only a few probes on a vane or an airfoil. An interpretation of the results is possible only if information is available about the development of the signals between leading edge and trailing edge.

The thin-film technique has proved itself to be an indicative method with clearly interpretable signals for the majority of experimental conditions. Limitation must solely be made for the range in which the flow is recognizable neither as completely separated nor as clearly attached. In this instance it is impossible to determine the boundary layer condition unambiguously either from thin-film measurements or from the pressure distribution. Nor can the flow picture from the visualization be regarded as reliable in this case, since disturbance by paint particles is certainly influential here.

Great test experience is required to arrive at a clear and reliable interpretation of the thin-film signals for every boundary layer condition.

Acknowledgments

The authors wish to thank D. Schneefeld and J. Wenzl for their assistance in the development and manufacture of the hot films.

References

1 Hanratty, T. J., and Campbell, J. A., "Measurement of Wall Shear Stress," in: *Fluid Mechanics Measurements*, R. J. Goldstein, ed., Hemisphere Washington, 1983, pp. 559–615.

2 Bellhouse, B. J., and Schultz, D. L., "Determination of Mean and Dynamic Skin Friction, Separation and Transition in Low-Speed Flow With a Thin-Film Heated Element," *Journal of Fluid Mechanics*, Vol. 24, 1966, pp. 379–400.

3 Pope, R. J., "Skin-Friction Measurements in Laminar and Turbulent Flows Using Heated Thin-Film Gages," *AIAA Journal*, Vol. 10, 1972, pp. 729–730.

4 Geremia, J. O., "An Experimental Investigation of Turbulence Effects at the Solid Boundary Using Flush Mounted Hot Film Sensors," Dissertation, George Washington University, Washington, D.C., Jan. 1970.

5 Hodson, H. P., "Boundary-Layer Transition and Separation Near the Leading Edge of a High-Speed Turbine Blade," ASME Paper No. 84-GN-179.

6 Hourmouziadis, J., Buckl, F., and Bergmann, P., "The Development of the Profile Boundary Layer in a Turbine Environment," ASME Paper No. 86-GT-244.

Journal of Turbomachinery
Formerly Included in the Journal of Engineering for Gas Turbines and Power

Discussion

Laminar and Transitional Boundary Layer Structures in Accelerating Flow With Heat Transfer[1]

J. W. Polkowski.[2] The authors are to be complimented on a very interesting paper. The experimental results presented are very useful, contributing to a better understanding of the heat transfer mechanism in a boundary layer. It seems, however, that equation (6), which is an extension of the formula

$$\mathrm{St} = 0.0295\ \mathrm{Pr}^{-0.4}\mathrm{Re}^{-0.2} \tag{1}$$

is not a convenient choice for a reference expression for the Stanton number to be further improved and generalized. Formula (1) was derived directly from the classic Reynolds analogy solution which reads:

$$\mathrm{St} = \tfrac{1}{2}\mathrm{Pr}^{-1}C_f \tag{2}$$

(strictly speaking, the Reynolds analogy holds for $\mathrm{Pr} = 1$) and it is valid for $T = \text{const}$ in the streamwise direction and for $p = \text{const}$. Based on the 1/7 power law for the velocity profile, wall shear stress and the thickness of the boundary layer can be written as

$$\tau_w = 0.0225\rho U_\infty^2 \mathrm{Re}_\delta^{-0.25} \tag{3}$$

$$\delta = 0.379x\mathrm{Re}_x^{-0.2} \tag{4}$$

where equation (4) is valid for $U_\infty = const$; it has been derived from the expression

$$\frac{d}{dx}\int_0^\delta u(U_\infty - u)dy = \frac{\tau_w}{\rho}$$

which itself was obtained from the more general von Karman integral relation for a boundary layer assuming $dU/dx = 0$. Using equations (3) and (4), equation (2) can be expressed as

$$\mathrm{St} = 0.0297\ \mathrm{Pr}^{-1}\mathrm{Re}_x^{-0.2} \tag{5}$$

Equation (5) is valid for $T(x) = \text{const}$, $\mathrm{Re}_x < 10^7$, $p = \text{const}$, $U = \text{const}$.

Only the first two conditions have been satisfied in the experiments described in the paper.

Authors' Closure

The authors appreciate Dr. Polkowski's interest and his overall very positive judgment about their work on transitional boundary layers under the influence of various free-stream parameters representative for gas turbine flow.

With respect to his comments on the correlation the authors presented for highly accelerating flows, it seems that there is some misunderstanding. The basic concept of equation (6) indeed refers to the heat transfer correlation for zero pressure gradient flow, which can be derived analytically in the way he described. Equation (6), however, includes as a modification an additional term for taking the influence of velocity gradients into account. This term consequently should compensate for the fact that in accelerating flows the assumption of constant free-stream velocity correlations is no longer fulfilled.

The correlation (equation (6)) is almost identical to that suggested by Kays (1966). The formulation of the additional term for considering pressure gradient effects follows purely empirical evidence as pointed out by Kays. The authors chose this correlation for testing and improving its applicability on flows with high free-stream acceleration and turbulence intensities because it provided the easiest and most obvious access for modifications. The results of these investigations are summarized in the paper and the authors believe they are quite positive.

In general, the authors' intention in using the correlation was simply to provide an easy and convenient tool for predicting turbulent heat transfer coefficients with reasonable accuracy. The extensive data obtained in our experimental studies provided the opportunity for working additionally on this subject. Furthermore, the author observed that it does not make sense to apply the original zero pressure gradient correlations on flows with *high* free-stream acceleration. This is also shown in the paper (see Fig. 14, comparison between measurement and correlation curve for $F_k = 0$).

Certainly the authors are aware of the fact that the applicability of the correlations is restricted to flow situations for which they are experimentally supported. Nevertheless, it should be pointed out that, depending on the individual case, the correlations might be helpful for initial design considerations.

References

Kays, X. X., 1966, *Convective Heat and Mass Transfer*, 1st ed., McGraw-Hill, New York, p. 248.

Stator Endwall Leading-Edge Sweep and Hub Shroud Influence on Compressor Performance[1]

A. J. Wennerstrom.[2] I am gratified to see that the authors' low-speed results have confirmed some of the suspicions we had at the Aero Propulsion Laboratory in the early and mid-1970s concerning some of the effects of sweep. At that time we introduced stator leading-edge sweep in two designs to alleviate shock losses and the experimental results suggested that the sweep had a beneficial effect on the sec-

[1] By K. Rued and S. Wittig, published in the July 1986 issue of the JOURNAL OF TURBOMACHINERY, Vol. 108, No. 1, pp. 116–123.
[2] Gas Turbine Division (TCT), Brown Boveri & Co., Baden, Switzerland.

[1] By D. L. Tweedt, T. H. Okiishi, and M. D. Hathaway, published in the October 1986 issue of the JOURNAL OF TURBOMACHINERY, Vol. 108, No. 2, pp. 224–232.
[2] Aero Propulsion Laboratory, Wright-Patterson AFB, OH.